Dissertation zur Erlangung des Doktorgrades

der Fakultät für Chemie und Pharmazie

der Ludwig-Maximilians-Universität München

Indigoid Molecular Motors and Switches

Ludwig Alexander Huber

aus

Pfarrkirchen, Deutschland

2019

Danksagung

Ich möchte mich bei Dr. Henry Dube bedanken, dass er mir die Chance bot meine Doktorarbeit auf seinem Forschungsgebiet anzufertigen. Es waren spannende und kenntnisreiche Jahre, die ich nicht so schnell vergessen werde.

Bei Prof. Dr. Oliver Trapp bedanke ich mich für die Übernahme des Koreferats.

Bei meinen lieben Kollegen Dr. Sandra Wiedbrauk, Aaron Gerwien, Stefan Thumser, Thomas Bartelmann, Nicolai Bach, Florian Kink, Monika Schildhauer, Kerstin Hoffmann, Dr. Manuel Güntner, Christian Petermayer und Edgar Uhl möchte ich mich im Besonderen bedanken, dass sie mir mit Rat und Tat zur Seite standen. Eine solch kollegiale Atmosphäre, wie sie in unseren Laboren herrscht, ist nicht selbstverständlich.

Lustig war es immer. Allerdings kam der Orangensaft dann doch nie durch die Nase. Das muss wohl die zukünftige Generation übernehmen. Die Chancen stehen 60/60 würde ich sagen.

Ich danke Thomas Bartelmann für die geistreichen Gespräche, die die unendlichen Zeitschleifen so mancher Säule in die Knie zwangen. Thomas, die Lottomillion werden kommen! Der Mann, der seinen Namen schneller wechselt als ein Oktopus sein prächtiges Farbenkleid, brachte mir die theoretische Chemie näher und unterstützte meine Projekte mit seiner Dual-Core Power. Dafür ein herzliches Dankeschön.

Dank an Dr. Peter Mayer für die hervorragende Arbeit in der Kristallstrukturanalyse.

Bei allen Mitarbeitern des Departements. Ohne eure Arbeit geht es nicht. Besonderer Dank gilt Brigitte Breitenstein, David Stephenson, Sonja Kosak, Claudia Ober, Petra Keilholz, Susanne Sauerer, Robert Eicher, Heidi Buchholz und Michael Gayer.

Bei Kerstin Hoffmann möchte ich mich für die super Zusammenarbeit bei unserem gemeinsamen Projekt bedanken. Ebenso bei Roland Wilcken, weil er Spektren schneller misst als sein Schatten. Unsere Kooperation trug viele Früchte und brachte so manche überraschende Erkenntnis. Ebenfalls bedanke ich mich bei Prof. Dr. Eberhard Riedle für die Zusammenarbeit bei unseren Projekten.

Des Weiteren möchte ich mich bei allen Praktikanten und Masteranden bedanken: Konstantin Mallon, Niklas Böcher, Markus Hopf, David Voßiek, Sabrina Hampel und Fabian Huck. Sie alle haben wertvolle Beiträge zu meiner Arbeit geliefert.

Von ganzem Herzen möchte ich mich bei meiner Familie bedanken. Ohne eure Unterstützung wäre ich nie soweit gekommen.

Meiner Frau Johanna. Dir gilt mein größter Dank. Ich freue mich auf unser gemeinsames Leben.

Publications

L. A. Huber, K. Hoffmann, S. Thumser, N. Böcher, P. Mayer, H. Dube*, *Angew. Chem.* 2017, *129*, 14728-14731; *Angew. Chem. Int. Ed.* 2017, *56*, 14536-14539. Direct Observation of Hemithioindigo-Motor Unidirectionality. Highlighted in *Synfacts* 2018, *14*, 0080 and *Laborpraxis* 2017, *41*, 34-35.

L. A. Huber, P. Mayer, H. Dube*, *ChemPhotoChem.* 2018, *2*, 458-464. Photoisomerization of Mono-Arylated Indigo and Water-Induced Acceleration of Thermal *cis* to *trans* Isomerization. (Front Cover)

R. Wilcken[+], M. Schildhauer[+], F. Rott[+], L. A. Huber, M. Guentner, S. Thumser, K. Hoffmann, S. Oesterling, R. de Vivie-Riedle, E. Riedle, H. Dube*, *J. Am. Chem. Soc.* 2018, *140*, 5311-5318. Complete Mechanism of Hemithioindigo Motor Rotation.

[+] contributed equally to the creation of the works

Contributions

[I] *Niklas Böcher*:   Yield improvements and analytical data of **10**, **17**, **24**.

[II] *Dr. Henry Dube*:   Identification of the signals of intermediates **A**-**D** of motor **5** (Figures 63 and 64).

[III] *Dr. Manuel Güntner*:   Investigations on motor **1** in collaboration with *Monika Schildhauer*, provided UV/vis spectra of motor **1**. Condensation attempts of indanones **11** and **12** with benzothiophenone **6** and **9** (Figure 32, entries 1-12).

[IV] *Kerstin Hoffmann*:   Yield improvements and analytical data of **2** and **18**. Crystallization of enantiomerically pure **C**-**2**, Structural confirmation of all enantiomers of motor **2** by chiral HPLC and crystal structure analysis. Experimental assessment of the energy profile of motor **2**.

[V] *Fabian Huck*:   Elaboration of remote influences of bromine substituents on the thermal barriers of the helical inversions of HTI-based motors.

[VI] *Konstantin Mallon*:   Condensation attempt of indanone **12** with benzothiophenone **6** (Figure 32, entry 13).

[VII] *Dr. Peter Mayer*:   Measurement and identification of all structures in the crystalline states.

[VIII] *Monika Schildhauer*:   Experimentally determined energy profile of motor **1** in colloboration with *Manuel Güntner*, UV/vis spectra of motor **1**. Synthesis of **10**, **11**.

[IX] *Stefan Thumser*:   Theoretical assessment of motors **1**, **2** and **5**, transition state structure of mixed indigo **88** and advice with regard to theoretical calculations.

[X] *David Voßiek*:   Crystallization of **A**-**2** and **C**-**3**. Successful elaboration of the synthesis of motor **3** by applying the protocol of motor **2**. Synthesis of **26**.

[XI] *Dr. Sandra Wiedbrauk*:   Provided UV/vis spectra of HTI **14**.

[XII] *Roland Wilcken*:   Transient absorption measurements of motors **1**, **2** and **5**. Quantum yield measurements and revelation of photonic limitations of HTI motors by rate modelling.

Abbreviations

a	annum
Å	angstrom (10^{-10} m)
AIBN	azobisisobutyronitrile
a.u.	arbitrary unit
Boc	*tert*-butoxycarbonyl
c.	concentrated
°C	°C
cal	calorie
calc.	calculated
cis	double bond configuration (indigo, historical nomenclature)
cw	clockwise
ccw	counterclockwise
d	doublet (experimental part, NMR analysis)
d	day(s) (Figure 31)
δ	chemical shifts, delta scale (in ppm)
DADS	decay associated difference spectrum
DBPO	dibenzoyl peroxide
DCE	1,2-dichloroethane
DIPEA	*N*,*N*-diisopropylethylamine
DME	dimethoxyethane
DMF	*N*,*N*-dimethylformamide
DMSO	dimethyl sulfoxide
E	double bond configuration (entgegen)
ε	extinction coefficient [L·mol^{-1}·cm^{-1}]
ECD	electronic circular dichroism
EI	electronic ionization
ESPT	excited state proton transfer
ESI	electron spray ionization
ESP	electrostatic potential
Et	ethyl
EtOAc	ethyl acetate
EtOH	ethanol
eV	electron volt ($1.6 \cdot 10^{-16}$ J)
FC	Franck Condon (vertical excitation)
Fmoc	fluorenylmetoxycarbonyl

FmocCl	fluorenylmethoxycarbonyl chloride
GSB	ground state bleach
h	hour(s)
HMBC	heteronuclear multiple bond correlation
HOMO	highest occupied molecular orbital
HPLC	high performance liquid chromatography
HR	high resolution
HSQC	heteronucear quantum coherence
HTI	hemithioindigo
Hz	hertz [s^{-1}]
IC	internal conversion
iHex	iso-hexane
IR	infrared (spectroscopy)
ISC	intersystem crossing
J	coupling constant (NMR)
J	joule
K	kelvin
L	liter
LDA	lithium diisopropylamide
LOX	lipoxygenase
LUMO	lowest unoccupied molecular orbital
M	helix configuration
M	molecular ion (mass spectrometry; experimental section)
m	meter
m	medium (IR)
M	multiplet (NMR analysis, experimental section)
M	molar
Me	methyl
MEM	2-methoxyethoxymethyl
MEMCl	2-methoxyethoxymethyl chloride
min	minute(s)
m.p.	melting point
MS	mass spectrometry
m/z	mass/charge ratio (MS; experimental section)
$\tilde{v}$	wave number [cm^{-1}]
NBS	N-bromosuccinimide
nBuLi	n-butyllithium

NMR	nuclear magnetic resonance
NOESY	nuclear Overhauser effect spectroscopy
P	helix configuration
pss	photostationary state
q	quartet
R	stereodescriptor
R_a	stereodescriptor (axial chirality)
R_f	retention factor
S	stereodescriptor
S_a	stereodescriptor (axial chirality)
s	strong (IR)
s	second(s)
sep	septet
SET	single electron transfer
t	triplet
TBHP	*tert*-butyl hydroperoxide
TLC	thin layer chromatography
THF	tetrahydrofuran
TICT	twisted intramolecular charge transfer
TMEDA	tetramethylethylenediamine
trans	double bond configuration (indigo, historical nomenclature)
UV	ultraviolet part of electromagnetic spectrum
vis	visible part of the electromagnetic spectrum
vs	very strong (IR)
w	weak (IR)
Z	double bond configuration (zusammen)

Table of Contents

1.   Summary

In the first part of this work the investigations on hemithioindigo (HTI) based molecular motors, were continued and the underlying rotation cycle was elucidated in detail. On the basis of the results[1] of *Manuel Güntner*[III] and *Monika Schildhauer*[VIII], found for the first generation motor **1,** new motor designs for slow motor rotation were elaborated. Motor designs are depicted in Figure 1a.
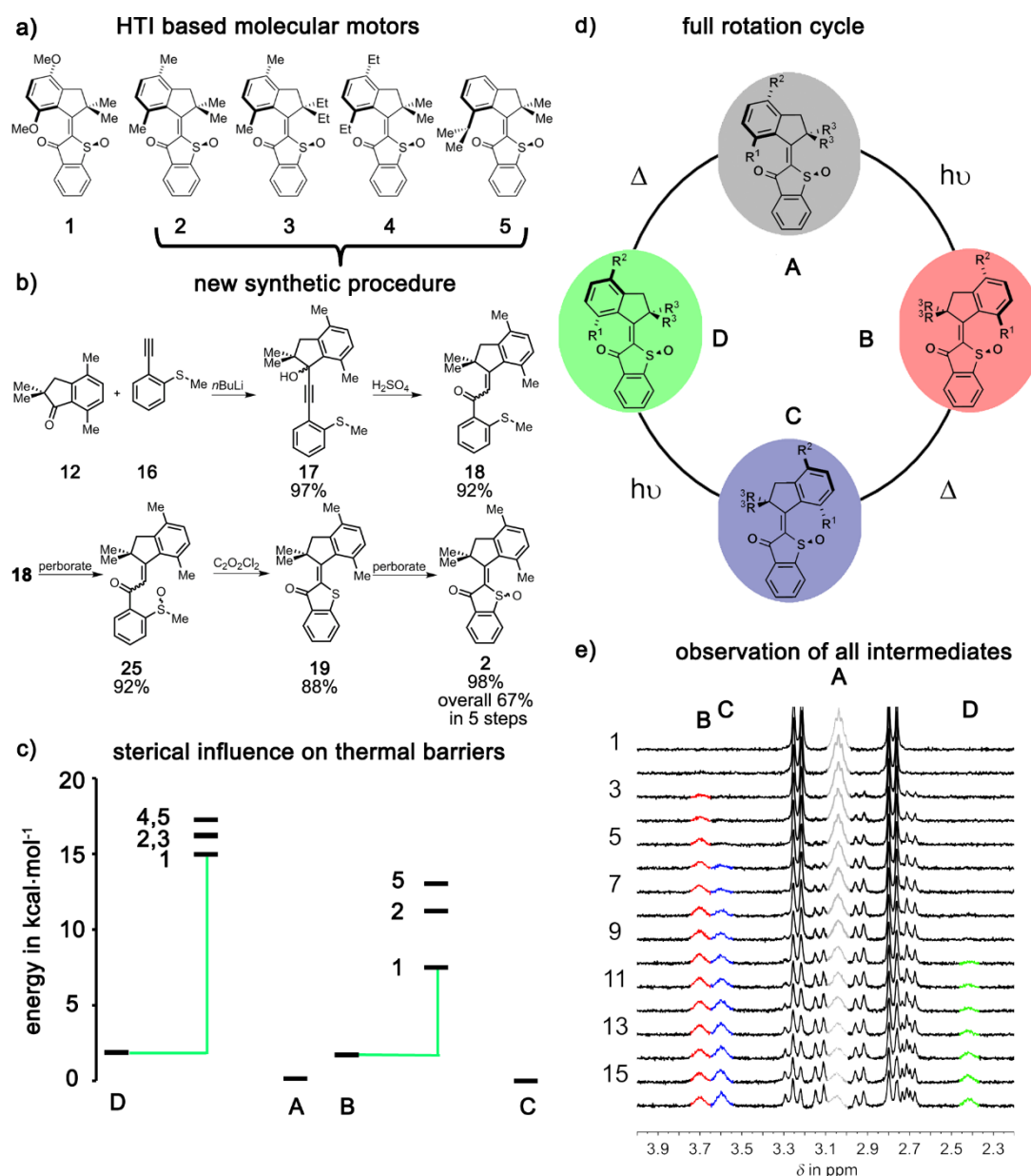
Figure 1:   Summary of motor related findings. a) HTI-based molecular motors with increased sterical hindrance were investigated in this work. b) A new synthetic procedure allowed for the synthesis of motors **2**-**4**. c) Kinetic experiments showed, that sterical hindrance increase the energy barriers for thermal **D**/**A** and **B**/**C** conversion, whith the **B** to **C** conversion showing stronger increases. d) With the herein presented results the four step cycle of the HTI motor rotation could be proven experimentally. e) NMR data of the key experiment, which showed the sequential appearance of all four intermediates, including the so far elusive intermediate **B**.

Therefore a new powerful synthetic method for the preparation of sterically hindered HTI-based molecular motors was developed. The synthetic route is shown in Figure 1b. It allowed for stepwise increase of sterical hindrance in vicinity of the central double bond. Key step of this protocol is the nucleophilic attack of an acetylene moiety at sterically hindered indanones, which turned out to be a powerful tool for the connection of the two motor parts. Further, a hitherto unknown intramolecular cyclization was established. By addition of thionylchloride to **25**, *in situ* generated chlorosulfonium ions are assumed to enable an umpolung of sulfur reactivity. It facilitates a nucleophilic attack of the β-carbon atom of the enone moiety at the sulfur atom, which leads to the HTI structure at the end. With this method at hand, derivatives **2-5** were synthesized, which offered substantial insights into the sterical influences on the rotation speed. In particular, derivative **5** enabled the first observation of the missing intermediate **B** at –105 °C by ^{1}H NMR spectroscopy, which verified the HTI rotation as a four step sequence (see Figure 1d and 1e). Further comparative studies with derivatives **1-5** by ^{1}H NMR spectroscopy as well as ultrafast absorption spectroscopy allowed for quantification of the thermal as well as photonic features of the motor mechanism. Thus, it was uncovered that the aromatic position at the rotor fragment is very sensitive for increasing the thermal barrier for **D/A** conversion by sterical hindrance, while increased sterics at the aliphatic position has only minor effects on the **D** to **A** conversion (see Figure 1c). However, theoretical calculations predicted a considerable decrease of the thermal barrier for the **B** to **C** isomerization in case of increased sterical hindrance at the aliphatic position. The excited state behavior was studied in detail by ultrafast transient absorption spectroscopy. The experiments and data analysis were performed by *Roland Wilcken*[XII]. It was found, that the overall rotation rate at realistic illumination conditions is not limited by the highest thermal barrier of the rotation cycle, but rather by the efficiency to convert the limited amount of photons available into directional motion. Thus, extinction coefficients as well as quantum yields of photoisomerizations were revealed to be the bottleneck of motor rotation speed. On this basis motor derivatives **1**, **2** and **5** were compared and although thermal features are considerably different, their rotation rates at realistic conditions are almost identical, with little tendency of superior rates for derivative **1**, which can be attributed to its improved quantum yields. These studies delivered precious insights for future improvements of motor designs.

In the second part of this work, the photoisomerization of mono- and di-arylated indigos **107** and **108** was investigated (see Figure 2a). Their unique features can be inevitably traced back to the fully intact indigo scaffold, which allowed addressability with light above 600 nm. Mono-arylated indigos surprisingly revealed photochromic behavior under irradiation, too. This was supposed to be unlikely, since its remaining N-bound hydrogen should provide the molecular setup for efficient excited state proton transfer (ESPT). Isomerization yields of moderate 38 % and 72 % of the *cis* isomer in the photostationary state (pss) could be obtained for **107** and **108** by ^{1}H NMR spectroscopy at reduced temperatures, as thermal back reactions turned out to be on minute time scale at ambient temperature in dry THF. For **107** and **108** considerable absorption changes could be observed after irradiation, which

allowed for isomer distinction by the naked eye (see Figure 2b). Detailed studies were carried out for mono-arylated indigo **107** and it was found, that the speed of thermal *cis* to *trans* reaction could be largely influenced by H_2O addition (see Figure 2c top curve). Further, it was found, that not only ground state features could be manipulated by water, but also excited state processes. Deuteration experiments delivered evidence for improved photoisomerization efficiency in present of small amounts of D_2O. A control experiment with equal amounts of added H_2O showed in fact inferior photoisomerization by acceleration of the thermal back conversion (see Figure 2c bottom curve). Thus, improved photoisomerization efficiency is inevitably traced back to excited state processes. In order to scrutinize, if D_2O is manipulating photoisomerization in an intramolecular manner further experiments with increasing D_2O content were carried out and it was confirmed, that more D_2O led to improved photoisomerization efficiency, which would not be expected for a competing intermolecular ESPT. D_2O concentration range, however, may not exceed a certain limit, since thermal back isomerization outcompetes the excited state effects above this limit. The results clearly speak for an intramolecularly working mechanism and the experiments were the basis of the following reaction model: D_2O addition leads to fast deuterium exchange at the nitrogen atom (confirmed by ^1H NMR spectroscopy). Thus, the kinetic isotope effect reduces the efficiency of an ESPT, which is a competing deactivation channel for photoisomerization. Hence, deexcitation can occur predominantly by photoisomerization. In summary, increased D_2O content leads to increased concentration of deuterated indigo in solution, which results in decelerated ESPT and thus enhanced photoisomerization under irradiation. Emission spectra recorded in the presence of D_2O resulted in increased fluorescence quantum yields, which is in agreement with aggravated depopulation of the first excited state by a declined rate for ESPT. In summary, it could be shown, that mono-arylated indigo can undergo photoisomerization and there are indirect spectroscopic evidences for a competing ESPT deactivation. These experiments are the first reports, which can hint at the presence of ESPT in indigo derivatives without the use of fs resolution techniques.
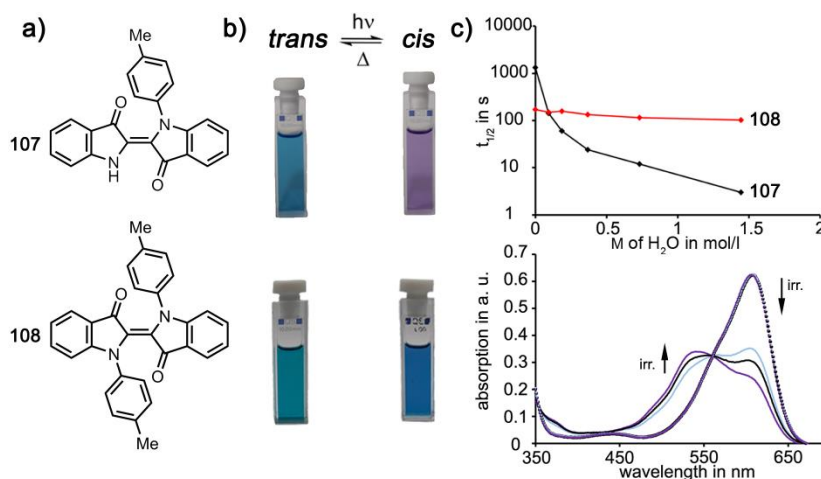
Figure 2: The findings of the investigations on mono- and di-arylated indigos **107** and **108**. a) Structures of *trans*-**107** and *trans*-**108**. b) Photochromism upon irradiation with red light of indigo **107** and **108** solutions in dry THF. The *cis*-enriched indigo solutions after irradiation can be distinguished from the solution in thermal equilibrium (**107**: 100% *trans*, **108**: 82% *trans*) by the naked eye. c) Top: Black/ red curve show water dependency of thermal *cis*/*trans* conversion of indigo **107**/**108**. Bottom: Indigo **107** in the pss in dry THF with 0.09 M H_2O content (blue). Indigo **107** in the pss in dry THF (black). Indigo **107** in the pss in dry THF with 0.09 M D_2O content (violet). Corresponding dotted absorption spectra recorded from *trans*-**107** solutions before irradiation. L. A. Huber, P. Mayer, H. Dube: Photoisomerization of Mono-Arylated Indigo and Water-Induced Acceleration of Thermal *cis* to *trans* Isomerization. *ChemPhotoChem.* **2018**, *2*, 458-464. Copyright Wiley-VCH Verlag GmbH & Co. KGaA. Adapted with permission.

2.   Zusammenfassung

Im ersten Teil dieser Arbeit wurden die Untersuchungen an Hemithioindigo (HTI) basierten molekularen Motoren fortgeführt. Anhand der Ergebnisse von *Manuel Güntner*[III] und *Monika Schildhauer*[VIII] wurden Designprinzipien abgeleitet, die zur Darstellung langsam rotierender Motoren führte (Abbildung 3a). Im Zuge dessen wurde der zugrunde liegende Rotationsmechanismus dieser Motorenklasse im Detail geklärt.

Um langsam rotierende Motoren darzustellen, wurde eine neue effiziente Synthesemetode entwickelt. Sie erlaubt die schrittweise Steigerung der sterischen Hinderung an der Rotationsachse, die für diese Art von Molekülen notwendig ist (Abbildung 3b). Schlüsselschritt dieser Synthese ist der nukleophile Angriff einer Lithium-Acetylid Spezies an einem sterisch gehinderten Indanon. Es stellte sich heraus, dass diese Strategie eine effiziente Möglichkeit darstellt, um die zwei Motorteile zu verknüpfen. Des Weiteren wurde eine bis dahin unbekannte Methode verwendet, um in einer mehrstufigen Zyklisierung die HTI-Vorstufe des Motors herzustellen. Es wird vermutet, dass ein *in situ* generiertes Chlorosulfonium-Ion durch Zugabe von Oxalylchlorid zur Sulfoxid-Spezies, einen nukleophilen

Angriff des β-Kohlenstoffes der Enon-Funktion initiiert. Die sequentielle Oxidation und Chlorierung des Schwefels kann somit als eine Umpolung des Schwefels betrachtet werden, was letztendlich die notwendige Reaktivität erzeugt, um die richtige Bindung zu knüpfen. Mithilfe der neuen Synthesemethode konnten die Derivate **2-5** hergestellt werden, anhand derer wertvolle Einblicke in den Rotationsmechanismus gewonnen werden konnten. Im Besonderen, erlaubte Motor **5** die erste Beobachtung des kurzlebigen Intermediates **B** mittels ^{1}H NMR Spektroskopie bei –105 °C (Abbildung 3e). Dadurch konnte der vierstufige Mechanismus der Rotationsbewegung experimentell belegt werden (Abbildung 3d). Der Vergleich der fünf Motoren anhand der experimentell gewonnenen Daten mittels ^{1}H NMR Spektroskopie und transienter UV/vis Spektroskopie, erlaubte die Quantifizierung der thermischen und der lichtinduzierten Schritte des Rotationszykluses (Abbildung 3c). Dadurch wurde aufgezeigt, dass das Einführen sterisch anspruchsvollerer Gruppen an der aromatische Position einen viel größeren Einfluss auf die Erhöhung der thermischen Barriere der **D**/**A** Inversion hat, während eine vergrößerte sterische Hinderung an der aliphatischen Position nur eine geringe Veränderung der Barriere bewirkt. Darüber hinaus, ergaben theoretische Berechnungen, dass die Erhöhung der Sterik an der aliphatischen Position zu einer stark verminderten thermischen Barriere für die **B**/**C** Inversion führen sollte. Das Verhalten im angeregten Zustand wurde im Detail mittels transienter UV/vis Spektroskopie untersucht. Die Experimente, sowie die Analyse der Daten wurden von *Roland Wilcken*[XII] durchgeführt. Die Messungen führten letztendlich zur Erkenntnis, dass die Rotationsfrequenz unter realistischen Bedingungen mit moderaten Bestrahlungsintensitäten nicht durch die höchste thermische Barriere des Energieprofils bestimmt ist, sondern vielmehr von der Effizienz mit der die vorhandenen Photonen für die Rotationsbewegung genutzt werden können. Daher spielen Quantenausbeuten der Photoisomerisierung sowie die Extinktionskoeffizienten eine viel größere Rolle. Im Zuge dessen wurde aufgedeckt, dass die Motoren **1**-**5** nahezu identische Rotationsfrequenzen unter realistischen Bedingungen aufweisen, obwohl das thermische Energieprofil stark unterschiedlich ist. Motor **1** zeigte aufgrund seiner insgesamt besseren Quanteneffizienz eine etwas höhere Rotationsfrequenz als die anderen Derivate. Aus diesem Grund liefert das Substitutionsmuster von Motor **1** wertvolle Hinweise für zukünftige Motordesigns mit verbesserten Rotationsverhalten.
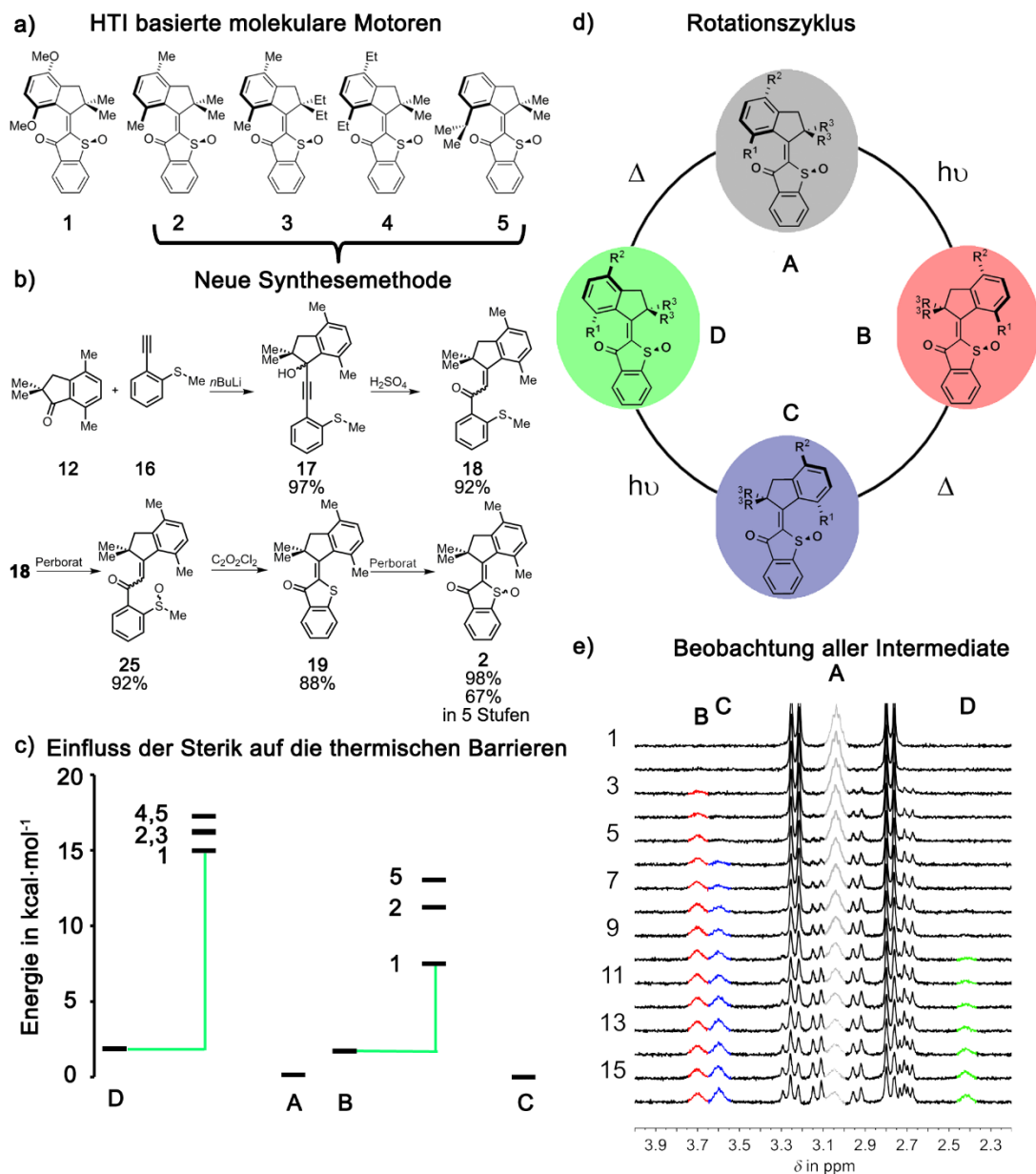
Figure 3: Zusammenfassung der Ergebnisse, die im Zuge der Untersuchung Hemithioindigo basierter Motoren gewonnen wurden. a) Eine Reihe von **5** Motoren, mit steigender sterischer Hinderung an der zentralen Doppelbindung, wurde hinsichtlich ihres Rotationsverhaltens untersucht. b) Mithilfe einer neuen Syntheseroute konnten die Motoren **2**-**5** dargestellt werden. c) Messungen der Kinetiken der thermischen Helixinversionen ergaben, dass, im Allgemeinen, eine erhöhte sterische Hinderung zur Erhöhung der thermischen Barrieren dieser Isomerisierung führen. d) Die experimentellen Ergebnisse dieser Arbeit belegen einen vierstufigen Rotationszyklus. e) Mithilfe des Motors **5** konnten in einem Experiment mittels Tieftemperatur ^{1}H NMR Spektroskopie die genaue Abfolge aller vier Intermediate beobachtet werden, einschließlich des kurzlebigen Isomers **B**, welches bis dato nicht nachgewiesen werden konnte.

Im zweiten Teil dieser Arbeit wurde das Photoisomerisierungsverhalten von arylierten Indigoderivaten untersucht (Abbildung 4a). Ihre einzigartigen Eigenschaften als Photoschalter sind auf das vollständig

erhaltene Chromophorsystem zurück zu führen, was eine Addressierbarkeit im roten Bereich (>600 nm) des elektromagnetischen Spektrums erlaubte. Überraschenderweise zeigten auch einfach arylierte Indigos Photoisomerisierung unter Bestrahlung. Anfangs wurde erwartet, dass diese Moleküle, auf die für Indigo übliche Weise aus dem angeregten Zustand relaxieren. Dabei, so wird angenommen, findet ein Protonentransfer im angeregten Zustand vom Stickstoff zum Sauerstoff statt (ESPT). Die dabei entstehende Enol-Form relaxiert daraufhin in den Grundzustand. Mono-arylierte Indigos besitzen die dafür nötigen Funktionalitäten. Für Indigos **107** und **108** wurden mäßige Isomerenausbeuten von 72 % und 38 % im photostationären Zustand (PSS) mittels Tieftemperatur-^{1}H NMR Spektroskopie gemessen. Tiefe Temperaturen waren notwendig um die thermische Rückisomerisierung zu unterdrücken. Für **107** und **108** wurden beträchtliche Absorptionsänderungen unter Bestrahlung beobachtet. Deshalb war es möglich die bestrahlten und unbestrahlten Indigolösungen mit dem bloßen Auge zu unterscheiden (Abbildung 4b). Kinetische Untersuchungen am einfach arylierten Indigo **107** konnten zeigen, dass die Geschwindigkeit der thermischen *cis/trans* Isomerisierung durch die Wasserkonzentration der Indigolösung beeinflusst werden kann (Abbildung 4c). Des Weiteren zeigte sich, dass nicht nur thermische Eigenschaften durch Wasser manipuliert werden können, sondern auch das Verhalten im angeregten Zustand. Deuterierungsexperimente zeigten, dass sich die Effizienz der Photoisomerisierung durch geringe Mengen D_2O verbessern ließ, obwohl das entsprechende Kontrollexperiment mit normalen Wasser den gegenteiligen Effekt zeigte. Die verringerte Schalteffizienz beim Kontrollexperiment war durch die vorab gezeigte gesteigerte Geschwindigkeit der Rückisomerisierung bei Wasserzugabe zu erwarten (Abbildung 4c). Aus diesem Grund war das verbesserte Schaltverhalten in Anwesenheit von D_2O nur durch verändertes Verhalten im angeregten Zustand zu erklären und nicht durch Grundzustandsreaktionen. Um herauszufinden, ob die D_2O Zugabe in einer intramolekularen Weise auf das Schaltverhalten Einfluss nimmt, wurde eine Konzentrationsreihe gemessen und es bestätigte sich, dass eine erhöhte Konzentration von D_2O in der Tat zu einem verbesserten Schaltverhalten führte. Somit konnte ein dominierender intermolekularer ESPT ausgeschlossen werden. Ab einer Grenzkonzentration überwiegt jedoch der allgemeine Wassereffekt einer beschleunigten Rückisomerisierung und das Schaltverhalten verschlechtert sich wieder mit steigender D_2O Konzentration. Zusammenfassend sprechen die Ergebnisse für eine intramolekulare Wirkweise und führten zur Entwicklung des folgenden Reaktionsmodells: D_2O Zugabe zur Indigolösung führt zu schnellem Austausch von Deuterium mit dem an den Stickstoff gebunden Wasserstoff (bestätigt durch ^{1}H NMR Spektroskopie). Der kinetische Isotopeneffekt führt zu einer verminderten Effizienz für ESPT. Die Relaxation aus dem angeregten Zustand findet folglich bevorzugt über Photoisomerisierung statt. Somit führt die D_2O Zugabe zu einer erhöhten Konzentration an deuteriertem Indigo, welches unter Bestrahlung ein verbessertes Schaltverhalten zeigt. Emissionsspektren, die in Anwesenheit von D_2O aufgenommen wurden, zeigten eine erhöhte Fluoreszenzquantenausbeute, was ebenfalls auf eine erschwerte Relaxation mittels ESPT hinweist. Zusammenfassend konnte gezeigt werden, dass einfach arylierte Indigoderivate Photoisomerisierungsverhalten zeigen und es konnten darüber hinaus Hinweise

gesammelt werden, dass ein konkurrierender ESPT stattfindet. Die gezeigten Experimente sind die ersten experimentellen Befunde, die auf einen ESPT bei Indigoderivaten hinweisen, ohne Spektroskopietechniken mit fs Auflösung zu verwenden.
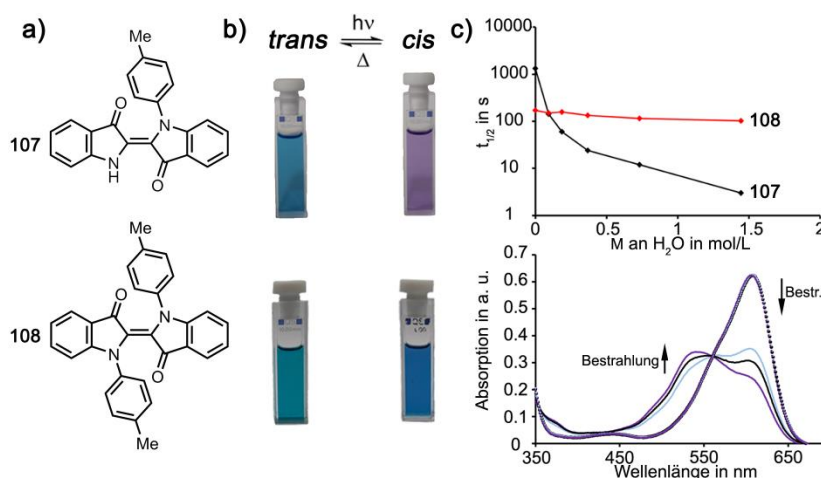
Figure 4:   Die Ergebnisse der Untersuchungen von einfach und zweifach arylierten Indigos **107** und **108**. a) Die Strukturen von Indigo **107** und **108** sind gezeigt. b) Photochromie der Indigolösungen **107** und **108** in trockenem THF nach und vor Bestrahlung mit rotem Licht. Die gesättigten *cis*-Indigo Lösungen nach Bestrahlung können von den Indigolösungen vor Bestrahlung (**107**: 100% trans, **108**: 82% trans) mit dem bloßen Auge unterschieden werden c) Oben: Schwarzer/ roter Graph zeigt die Wasserabhängigkeit der Halbwertszeiten des *cis* Isomers von Indigo **107**/**108**. Unten: UV/vis Spektren. Indigo **107** im PSS in trockenem THF mit einem Wassergehalt von 0.09 M (blau). Indigo **107** im PSS in trockenem THF (schwarz). Indigo **107** im PSS in trockenem THF mit einem D_2O Gehalt von 0.09 M. Die entsprechenden Spektren der *trans*-Indigo Lösungen vor der Bestrahlung mit rotem Licht sind gepunktet dargestellt. L. A. Huber, P. Mayer, H. Dube: Photoisomerization of Mono-Arylated Indigo and Water-Induced Acceleration of Thermal *cis* to *trans* Isomerization. *ChemPhotoChem.* **2018**, *2*, 458-464. Copyright Wiley-VCH Verlag GmbH & Co. KGaA. Mit Erlaubnis verändert.

3.   Introduction: Light-matter interaction

3.1   Nature of light

In 1927 the double-slit experiments of *Davison* and *Germer*[2-3] confirmed the dual nature of matter postulated by *Louis de Broglie*.[4] It expanded *Albert Einstein*'s idea[5] to interpret light as a stream of discrete wave packets and represents the fundamental basis of quantum mechanics. Light waves propagate with constant speed c, which connects the wavelength λ and the frequency ν by the Equation 1:

$$c = \nu \cdot \lambda \qquad \text{(eq. 1)}$$

Thus, different categories of light waves exist, which are characterized by their wavelength λ and frequency ν. Radiation with short wavelengths under 1 nm is called X-ray, while ultraviolet radiation is defined by wavelengths shorter than 400 nm. The visible part of the electromagnetic spectrum ranges from 400-800 nm and is followed by the IR region, which is characterized by wavelengths shorter than 1 μm. Microwaves range up to 10 μm. Waves with wavelengths in the mm, m, or km range are called radio waves.[6]

The beam a light source emits is regarded as a stream of light particles, also called photons. Each photon exhibits an energy portion, which is directly linked to its wavelength by Equation 2:

$$E = h \cdot \nu = h \cdot \frac{c}{\lambda} \qquad \text{(eq. 2)}$$

Thus, photons with shorter wavelengths (e.g. X-rays) exhibit higher energies than photons with longer wavelengths (e.g. the IR region). The visible part of the electromagnetic spectrum ranges from 400 nm to 800 nm, and depicts only a small section of the whole spectrum, which is perceivable for humans without the usage of further spectroscopic devices. In Figure 5 the visible part is illustrated.
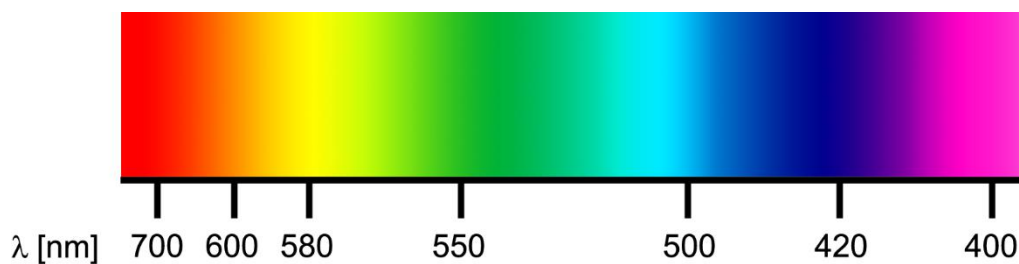
Figure 5:   Visible part of the electromagnetic spectrum. Color perception of yellow and orange is defined by a narrow wavelength range of ca 10-20 nm, while the purple, blue, green and red color impression is attributed to light of wavelengths within a range of 50-100 nm. Electronic transitions are mainly caused by photons from the visible part of the electromagnetic spectrum.

A high resolution of human perception is given at longer wavelengths in the yellow, orange and red region, while the perception of the colors green and blue covers the range of photons with wavelengths of 420 to 570 nm.

Light with a wavelength between 200 and 1000 nm, i.e the near UV, visible part and the near infrared part of the electromagnetic spectrum is capable of electronic excitation of molecules. The corresponding energies vary from 140 kcal to 30 kcal per mole photons. If compared to typical binding energies in organic molecules, it becomes evident, that the intrinsic energy of light can have substantial impact on organic molecules, as bond breaking or structural rearrangements can occur upon absorption. In Table 1, photon energies and typical bond energies are summarized. For example, photons with wavelengths of 300 nm can provide the dissociation energy of a C-C single bond.[6]

Table 1: Summary of wavelength dependent photon energies and typical bond energies at 25 °C.[7]

Wavelength [nm]	Energy [kJ·mol^{-1}]	Energy [kcal·mol^{-1}]	Bond	Binding energy [kJ·mol^{-1}]	Binding energy [kcal·mol^{-1}]
200	598	143	C=C	582	139
300	399	95	O=O	494	118
365	328	78	S=O	420	100
400	299	71	C-H	411	98
460	260	62	C-C	362	87
500	239	57	C-O	358	86
600	199	48	C-Cl	327	78
700	171	41	C-Br	285	68
800	150	36	C-S	272	65
900	133	32	C-I	201	48
1000	120	29	Br-Br	190	45
10000	12	3	I-I	151	36

3.2 Photon absorption

Interaction of light with molecules is commonly described as the absorption of a photon by the molecule and the concomitant transfer of the corresponding energy. Thus, the final energy E_f of the molecule after absorption is defined by the sum of its initial energy E_i and the absorbed photon energy $h\nu$.

$$E_f = E_i + h\nu \qquad \text{(eq. 3)}$$

In particular, absorption is mainly characterized by a specific interaction of molecules with the electric field vector of the electromagnetic radiation. Interactions with the oscillating magnetic field of the light wave are of minor importance, since transitions generated by the magnetic field are much weaker than electric dipole transitions.[6]

The intensity of photon absorption by molecules in solution is described by the *Lambert-Beer* law. The absorbed light intensity I_{abs} depends on the intensity I_0 of the incoming light, the concentration c of the

absorbing material, the path length d of the absorbing solution and the extinction coefficient ε of the material. In short, a substance is strongly coloring, if the value of its extinction coefficient ε is high. The absorbed light intensity I_{abs} is given by Equation 4:

$$I_{abs} = I_0 \cdot 10^{-\varepsilon dc} \qquad \text{(eq. 4)}$$

The absorbance A, which is commonly measured by a spectrometer can be derived from equ. 5:

$$A = \log\left(\frac{I_0}{I_{abs}}\right) = \varepsilon dc \qquad \text{(eq. 5)}$$

By measuring an absorption spectrum of a solution with known substance concentration in a cuvette with a defined path length d (usually 1 cm), the extinction coefficient ε can be easily calculated. So it can be determined, if the substance is a strong or weak colorant in comparison to other materials.[6]

A mathematical description of the absorption of a photon by a particle is given by the time dependent perturbation theory. The ground state of a particle is described by the Schrödinger equation:

$$\hat{H}_o \Psi_i = E\Psi_i \qquad \text{(eq. 6)}$$

Light absorption is introduced as a perturbation with time. Thus, $\hat{H}_o$ no longer describes the state of the particle and has to be extended by the perturbation operator $\hat{H}'$, which includes the effect of the electromagnetic field on the particle. As excitation is a temporal phenomenon, the wave function also becomes a function of time:

$$(\hat{H}_o + \hat{H}')\Psi(x,t) = E\Psi(x,t) \qquad \text{(eq. 7)}$$

The new time dependent wave function can be derived from the initial wave function by introducing a time dependent coefficient $a_f(t)$. This coefficient is directly proportional to the transition moment TM of the absorption and the probability of a transition rises with larger transition moments. Taking into account the Born-Oppenheimer approximation[8] and the Condon approximation,[9] the wave function can be factorized into the product of an electron wave function, a vibrational wave function, and its corresponding spin function. The transition moment TM is then given by Equation 8:[6]

$$TM = \int \phi_i \hat{\mu} \, \phi_f \, d\tau_e \; \int S_i \, S_f \, d\tau_S \; \int \theta_i \theta_f \, d\tau_N \qquad \text{(eq. 8)}$$

| Electronic transition moment | Spin overlap integral | Overlap integral of nuclear vibration |

The first term is the *electronic transition moment*, which is defined by the overlap and symmetry of the initial and final orbitals. The second term is called *spin overlap integral,* which takes into account the spin state of the initial and final orbital. In the last term, the *overlap integral of the vibrational modes* of the participating orbital is calculated. From the TM it can be estimated if a transition is likely to take place or if a transition is forbidden. For example, transitions are called spin forbidden if the spin state multiplicity of ground and excited state are different. Since this is derived from approximations, which do not incorporate all minor, i. e. magnetic interactions, generally weak absorption bands are still observed for forbidden transitions. Transitions are called symmetry forbidden, if the symmetry of the ground state orbital does not fit the excited state orbital. Thus, $n \rightarrow \pi^*$ transitions generally show weak intensities, whereas $\pi \rightarrow \pi^*$ transition are symmetry allowed and exhibit high absorption intensities. Within a further approximation for allowed transitions, called the Franck-Condon principle,[9-10] also the overlap integral of vibrational modes of two electronic states determines the shape and intensity of an absorption band. The Franck-Condon principle describes an electronic transition as a vertical process, because the transition happens on a very short time scale (as-fs), while the nuclei are literally "frozen"[11] and maintain their positions. The corresponding energy diagram is illustrated in Figure 6. The so called Franck-Condon excited state, which is populated after absorption, is "literally born with the structure of the ground state",[11] with the distinct difference of its electronic distribution.[6, 11]
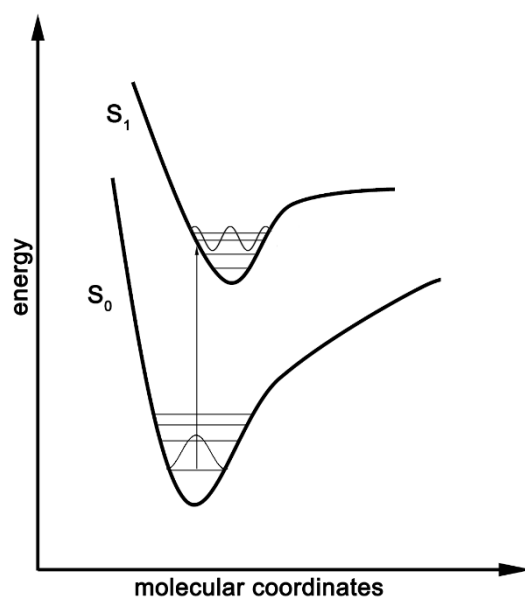
Figure 6:   The energy diagram illustrates the Franck-Condon principle. The transition between electronic states is described as a vertical process, since no nuclear motion occurs on the very short timescale (fs) on which photon absorption happens. Thus, the overlap integral of the vibronic wave functions of the ground state and the excited state determines the band shape of the absorption.

3.3   Relaxation processes of molecules in the excited state

After excitation, molecules relax to the ground state with time, while the excess energy is transferred to their surroundings either by emission of light or by thermal deactivation (collision with other surrounding molecules). The main relaxation processes are tightly connected to the structural setup of the excited molecules. Excited state deactivation may lead to the initial molecule (photophysical processes) or a different chemical species by conformational changes, redox processes or bond breaking/generation within the original molecule (photochemical processes). All photophysical processes from absorption to various deactivation processes can be illustrated in a Jablonski energy diagram (see Figure 7). The Franck-Condon states (FC), initially populated by absorption of photon energy (blue arrows), are usually characterized by vibrational modes of high energy levels. Since collisions are generally the fastest intermolecular processes with rates around 10^{13} s^{-1}, excess energy is dissipated by vibrational relaxation. Transitions between electronic states of isoelectronic vibrational modes are called internal conversions (red wavy arrows (2)) and proceed without energy loss. A similar process, but with change of overall spin multiplicity, is called intersystem crossing (red wavy arrows, (3) and (4)), but generally exhibits low transition probabilities for most organic molecules, with an exception if heavy atoms are present (strong spin-orbit coupling causes spin flipping). In general, the large energy gap between ground state and first excited state in comparison to higher excited states results in reduced transition probabilities for radiationless deactivation from the first excited state. Thus, initial relaxation processes generally end in the vibrational minimum of the first excited singlet state. Further relaxation processes happen after the very fast vibrational relaxation from the Franck-Condon state to the vibrational ground state of the first excited state. The reduced probability for radiationless deactivation derived from the high energy difference between S_1 and S_0 increases the importance of radiative deactivation for these transitions. Fluorescence (i.e. $S_1 \rightarrow S_0$, green arrow (6)) describes the transition with maintained spin multiplicity and emission of light. In contrast to the spin allowed fluorescence, which proceeds within 10^{-9} s, the spin forbidden phosphorescence (i.e. $T_1 \rightarrow S_0$, orange arrow (5)) occurs on the ms time scale. A generalized rule of thumb, the Kasha rule, can be derived, which states that emission always occurs from the lowest excited state to the ground state. An exception to this rule is the $S_2 \rightarrow S_0$ emission of azulenes,[12] which exhibit an exceptionally high energy difference between S_2 and S_1 excited state.[6]
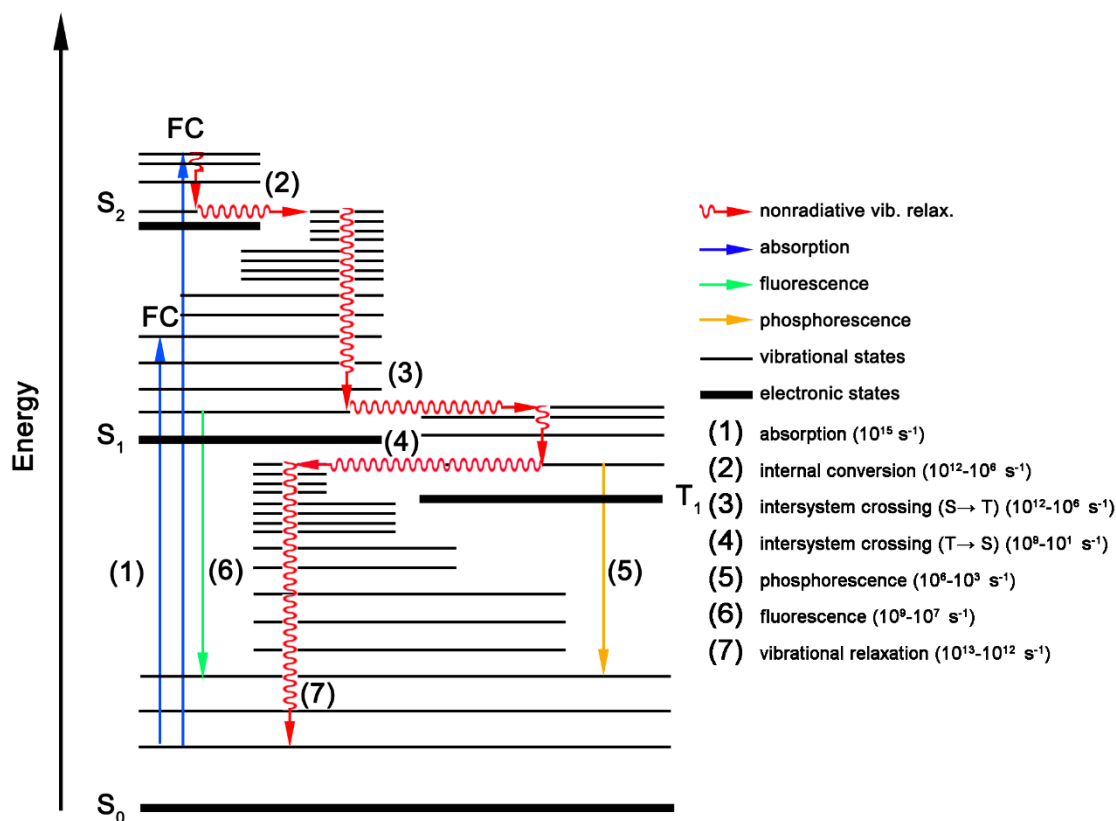
Figure 7:   Jablonski energy diagram, which depicts all possible photophysical processes from excitation to deactivation of excited states. Rate constants of the processes are given in brackets on the right side. Energy differences are in general smaller between higher electronically and vibrational excited states. S_0: electronic singlet ground state. S_1: first singlet excited state. T_1: first triplet excited state. FC: Franck-Condon region initially populated after excitation.

Electronic states can be regarded as potential energy surfaces, which are characterized by the molecular geometry and the corresponding energy. However, for molecules with low symmetry and a ground state energy close to the S_1 energy, the probability of $S_1 \rightarrow S_0$ deexcitation by radiationless transition is increased in comparison to molecules with a large energy difference between these states.[13] A transition is then possible by passing through a conical intersection, which is an effective deactivation pathway between two electronic states. A conical intersection is characterized as one or more points on the potential energy surfaces, where the wave functions of ground and first excited state are degenerate. A further prerequisite for funneling through conical intersections is the breakdown of the Born-Oppenheimer approximation as thermal equilibration is impeded by exceptionally fast transfer rates for these processes. Conical intersections can lead to the initial ground state (photophysical process) or to a new chemical species (photochemical process).[13] In the following chapter, different types of photochemical processes are discussed, with focus on light induced double-bond isomerizations.

3.4   Photochemical reactions

As described above, deexcitation of molecules after photon absorption can lead to the initial ground state by inherent deactivation processes (photophysical processes). However, the absorption of photon energy creates a highly reactive new molecular species, which alternatively can readily undergo chemical rearrangements or reactions with other molecules in order to dissipate the excess energy. The result after deactivation can be an isomeric form of the absorbing molecule or a completely new chemical compound. Excited molecules exhibit different electron density distribution with excess energy, as well as a different molecular structure. Thus, they do not necessarily possess simply an enhanced ground state chemical reactivity, but should rather be regarded as a completely new chemical species. Light induced chemical reactions exhibit generally low activation barriers, which allows for competition with very fast photophysical processes.[6, 13]

As mentioned earlier, the preferred light induced deactivation is tightly bound to the structural features of the excited molecule. For example, radical species are generated from bromine after light induced homolytical cleavage, which is used in radical bromination reactions. Further radical generating molecules are AIBN or DBPO, which release molecular nitrogen and carbon dioxide besides generation of reactive carbon radical species upon irradiation. The examples for radical generation are depicted in Figure 8. Alternatively, the usage of external photocatalysts for radical generation has expanded vividly in recent years, as it provides mildness and high compatibility with functional groups. This renders radical chemistry ideal for the synthesis of complex and highly functionalized natural products.[14] By usage of photocatalysts, however, radicals are generated by single electron transfer (SET) of a light activated dye and not by a homolytical cleavage of labile bonds via direct excitation of the corresponding molecule.
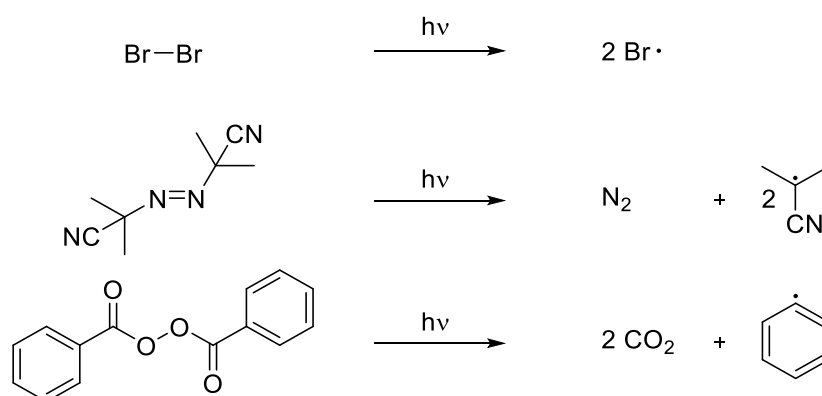
Figure 8:   Light induced homolytical cleavage of covalent bonds leads to reactive radical species, which are widely used for chemical transformations such as brominations,[15-17] or as initiators for polymerization reactions.[18-19]

Suitable photo or photoredox catalysts[14, 20-22] are molecules possessing the potential for electron release and acceptance as well as for energy transfer in the excited state. Which process dominates over the other is mainly determined by the thermodynamic and kinetic aspects of the regarded reactions.[14] Transition metal complexes like $[Ru(bpy)_3]^{2+}$ offer superior features for photoredox catalysis and are widely used in this research area. Since transition metals provide strong spin orbit couplings, triplet states play a much more important role, as it is the case for classical organic molecules. Thus, excited state lifetimes are generally much longer (for $[Ru(bpy)_3]^{2+}$ $\tau = 1$ μs), which increase the probability for collision with reaction partners. Furthermore, the redox potential of metal complexes is strongly influenced by their electronic state. By photon absorption, an electron initially occupying a HOMO experiences a quantum transition into the LUMO. This electronic configuration renders transition metal complexes both suitable reducing and oxidizing materials at the same time. Less energy for electron fission is needed, as the electron already occupies a highly energetic orbital (LUMO) after photon absorption. At the same time, electron acceptance is facilitated as the less energetic HOMO is only singly occupied after excitation and can be filled with an external electron. In Figure 9, the photoredox catalyst $[Ru(bpy)_3]^{2+}$ is depicted and its possible reaction types are shown. A very prominent example was published in 2008 by the group of *MacMillan*,[21, 23] which reports on an enantioselective α-alkylation of aldehydes under $[Ru(bpy)_3]^{2+}$ catalysis. It initiated, amongst other seminal publications,[24-25] an ever expanding interest for the field of photoredox catalysis.

a)

b)

Light activation	$[Ru^{II}(bpy)_3]^{2+}$	$\longrightarrow$ $^1[Ru^{III}(bpy^-)(bpy)_2]^{2+*}$	$\longrightarrow$ $^3[Ru^{III}(bpy^-)(bpy)_2]^{2+*}$	
Energy transfer	$^3[Ru^{III}(bpy^-)(bpy)_2]^{2+*}$ + Q	$\longrightarrow$	$[Ru^{II}(bpy)_3]^{2+}$ + Q^*	
Oxidation	$^3[Ru^{III}(bpy^-)(bpy)_2]^{2+*}$ + A	$\longrightarrow$	$[Ru^{III}(bpy)_3]^{3+}$ + A^-	
Reduction	$^3[Ru^{III}(bpy^-)(bpy)_2]^{2+*}$ + D	$\longrightarrow$	$[Ru^{II}(bpy^-)(bpy)_2]^{+}$ + D^+	

c)

63-93% yield
88-96% *ee*
12 examples
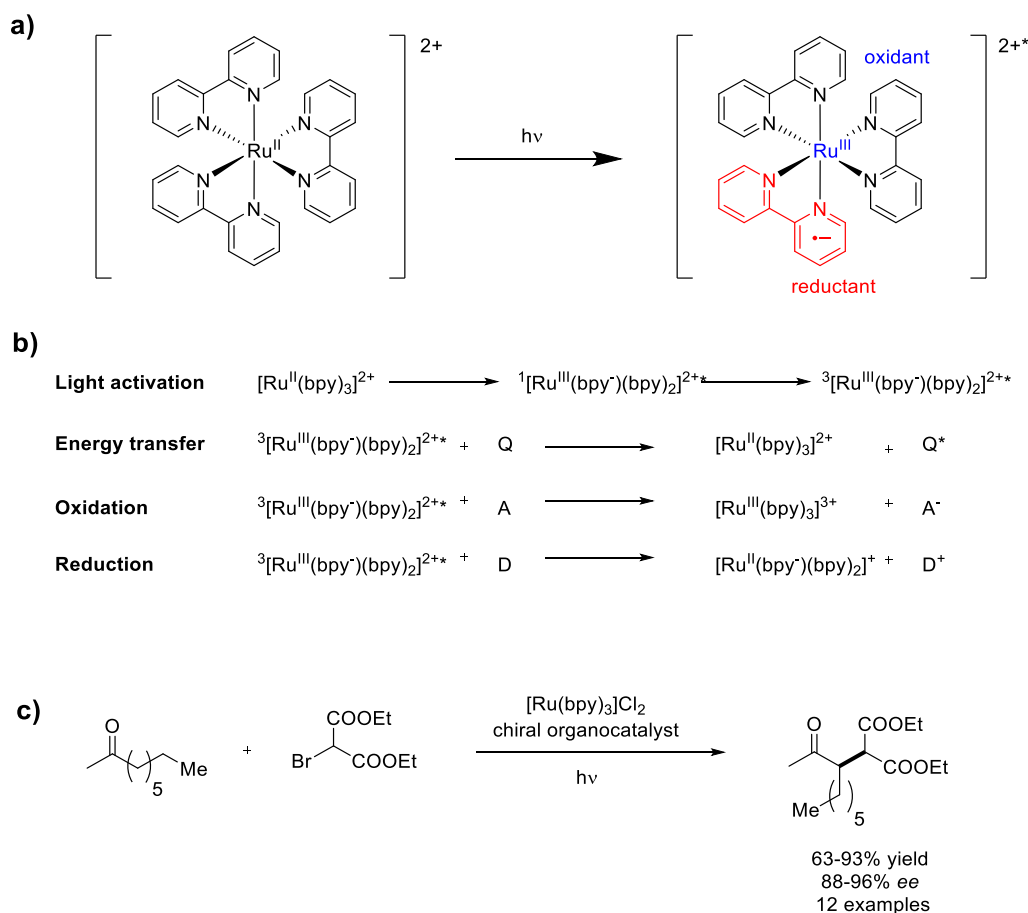
Figure 9:   Photoredox catalyst $[Ru^{II}(bpy)_3]^{2+}$ provides suitable redox potential for reduction (-0.86 V) and oxidation of substrates (+0.84 V) after photon absorption.[14] After excitation, $[Ru^{II}(bpy)_3]^{2+}$ readily converts to the triplet state with an approximate lifetime of 1 µs. The induced charge separation enhances the reducing power of the ligand, while the oxidizing power is located at the central metal. A third possibility for deactivation is the energy transfer to another molecule. a) Excitation of $[Ru^{II}(bpy)_3]^{2+}$ leads to charge separation with reduced electron density at the central metal atom and enhanced electron density at the bipyridine ligands. Hence, photoredox potential can be derived from the oxidizing power of the metal and the reducing power of the ligands. b) Light activation as well as the possibilities for deactivation are illustrated. Q means suitable quenching molecule (quencher), to which the excess energy is transferred. A/ D means accepting/ donating molecule (acceptor/donor) of the electrons. c) Seminal work of the *MacMillan* group, which combined photoredox catalysis with the enantioselectivity of organocatalysis.[21, 23]

Besides electron/energy transfer and homolysis of chemical bonds, light induced rearrangements of organic molecules are an important class of photochemical reactions and mainly concern molecules containing double bonds.
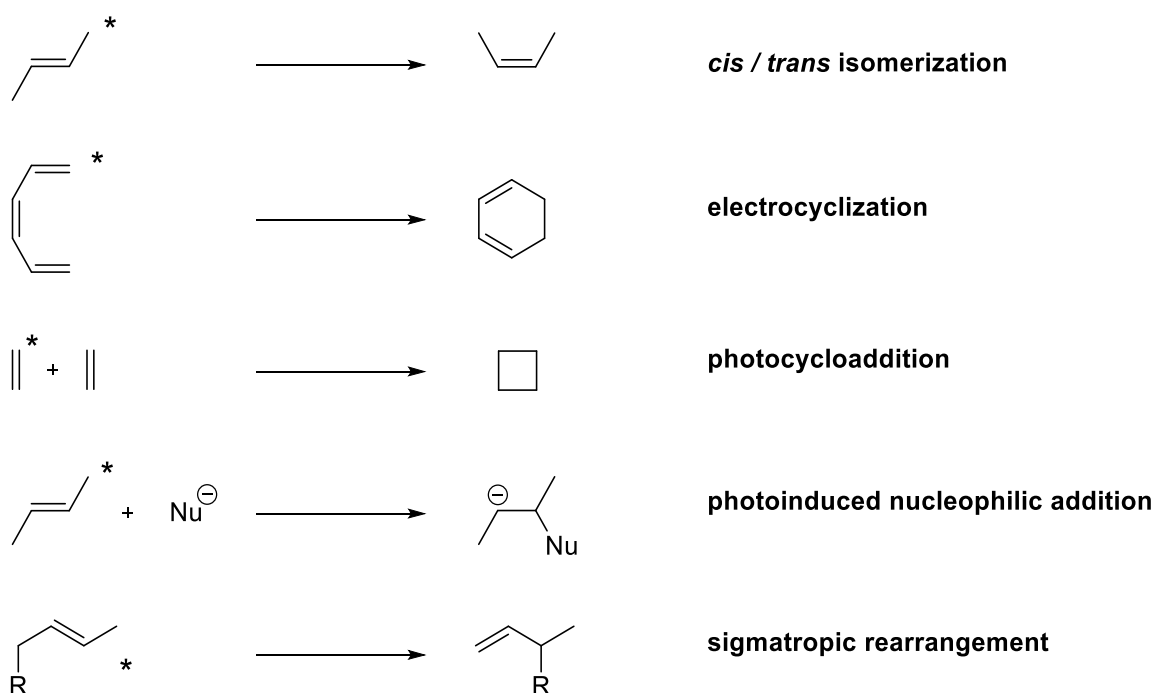
Figure 10:   A variety of photoreactions are depicted.[6] In some cases, the transformations are not limited solely to carbon containing compounds. * indicates a light activated reactive species. The photocycloaddition as well as the photoinduced nucleophilic addition require a second reaction partner. Thus, they are fundamentally different to the rearrangements also shown in this Figure.

In Figure 10, an excerpt of possible photoreactions is depicted. For a more detailed summary of possible photochemical reactions see references.[6, 26] For small organic molecules, it can be generalized that the majority of light induced reactions mainly focus on intramolecular rearrangements, since first excited singlet states have only limited half-life, which reduces the probability for collision with possible reaction partners. In particular, the *cis/trans* isomerization, electrocyclization and the photoinduced nucleophilic addition are of special interest. There are many examples, which not only undergo light induced isomerizations, but are also capable for the reverse reactions under light or thermal input. Thus, it is possible to trigger processes and motions on the molecular scale by varying input with the possibility to return to the starting point. These unique features opened up the flourishing field of photoswitches[27] and are discussed in the following chapter.

3.5 Photoswitches

Photoswitches are a unique tool for manipulation of molecular processes. Light input enables the generation of a new isomeric species, which does not only differ in the structural arrangement of atoms, but also in its inherent chemical properties. Structural changes compulsorily result in a different electron distribution, which alters the chemical and physical properties of the new isomer. Thus, the initial molecule (isomer A) can be distinguished from the photogenerated isomer B by e.g. its absorption spectrum. Molecules with the ability to exist in different isomeric forms with individual absorptions are called photochromic compounds.[28] A further advantage besides the clear distinctness is the resulting selective addressability of both isomers with light. This feature allows for population of two different isomers (states), which is a fundamental requirement for switching devices. For example, molecules which are capable for switching with over 90% yield in both directions, offer great potential for applications. There are also molecular switches available, which do not operate under light control, but can be addressed under acid/base[29-31] or redox control.[29, 32] These are typical switching modes for rotaxane based shuttles (shuttles are not necessarily switching devices; for a shuttle with degenerate binding modes see reference[33]).

Isomers not only differ in their photophysical properties, but also in their relative minimum energies. Metastable isomers can be highly energetic in case of norbornadienes[34-36] (almost 23 kcal·mol^{-1} for unsubstituted nobornadiene), which can be advantageous for certain applications such as solar energy storage.[37] There are also examples, like di-arylated indigos or certain HTI derivatives with metastable isomers exhibiting almost the same energy as the corresponding stable isomers.[38-39] For most applications, a considerable energy difference, which allows for quantitative population of the stable isomer under equilibrium conditions, is advantageous. For instance 2 kcal·mol^{-1} energy difference means 97% population of the more stable isomer at 23 °C.

Another feature of photoswitches, which is often but not necessarily linked to the thermodynamic aspects, is the thermal energy barrier (kinetic stability) between stable and metastable isomers. In general, it can be stated that highly energetic isomers also show lower kinetic stability. The opposite relation however is not always true, since di-arylated indigos are kinetically unstable, although they show almost similar energies for their isomers.[39] In contrast, some HTI derivatives also reveal similar energies for their isomers, but provide high kinetic stability of over 30 kcal·mol^{-1}.[38] Advantageous kinetic features cannot be generalized, as it strongly depends on the requirements of the particular application. For photopharmacological applications[40] photoswitches with low kinetic stability in combination with full thermal recovery of the stable isomers are used, since the biological activity should be activated only under irradiation conditions. In Figure 11, several different types of photoswitches are illustrated.
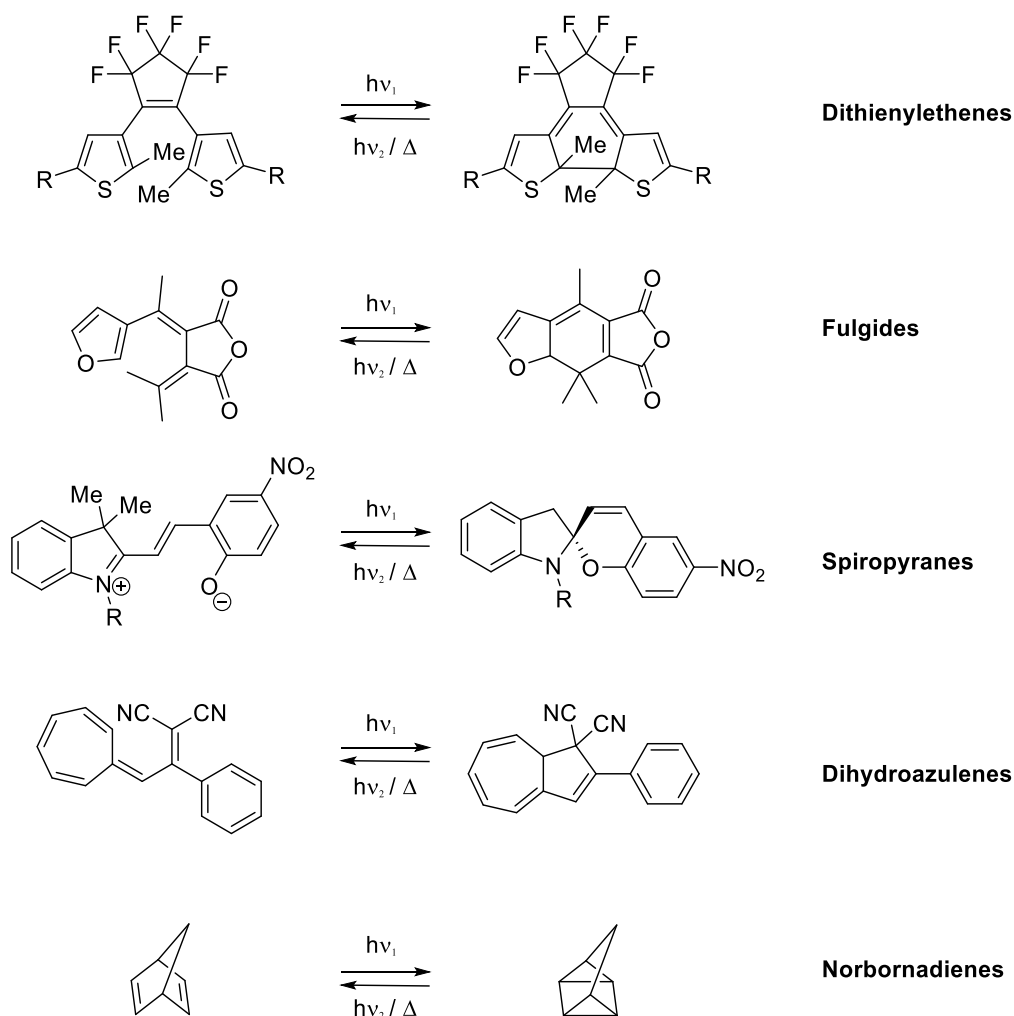
Figure 11: A selection of photoswitches is presented, which can be addressed with light at least in one direction. Back reaction occurs either by light input or thermally. Each example represents a typical class of switches, which share the inherent switching scaffold but may vary in substitution pattern, as different applications need different functionalization.

At present, several different kinds of photoswitches are available. Diarylethenes[41-42] and fulgides[43-44] comprise independent classes of photoswitches, which undergo electrocyclization under irradiation. It is defined by a light induced 4n+2 conrotatory ring closing reaction of the hexatriene moiety after excitation.[45] The initial state can be restored either by light or thermal input. A characteristic of these kind of switches is their considerable photochromism and hence their potential for optical recording.[46-47] Many efforts have been made for the development of thermally stable switches[48-50] with high fatigue resistance.[41, 51] Diarylethenes also reveal a tendency for electrochromism[52], which was investigated in the last years for potential application as dual mode devices. Since only minor structural changes accompany the photoisomerization processes, the usage for molecular mechanics is limited. Both types of switches often appear colorless in the open forms, while an intensive color can be observed for the closed forms.

Light induced nucleophilic addition and heterolytic C-O cleavage is the fundamental switching mechanism of spiropyranes.[53-54] Photochromic behavior of spiropyranes was first reported by *Hirshberg* and *Fisher*.[55] The merocyanine form shows a strong tendency for aggregation which can lead to the formation of nanostructured beads. If an electric field is applied, these beads can be further organized in threads oriented along the electric field lines.[56] Thus, not only molecular processes can be controlled but also nano- or micrometer sized structures can be manipulated with light. Spiropyranes were further implemented in liquid crystals[57], and are known for their unique property of high second order NLO (non linear optics) coefficients[58].

Norbornadienes[34-35] are of potential interest for solar energy storage,[59] as they provide considerable storage capacities (up to 23 kcal·mol⁻¹ for unsubstituted norbornadiene, 36 kcal·mol⁻¹ for a norbornadiene derivative) within their metastable isomers, which thermally convert to the stable isomers. The switching in norbornadienes occur via a 2+2 cycloaddition. The fundamental switching mechanism of dihydroazulenes[60-61] is believed to proceed via a zwitterionic state[62-63] after photoexcitation in a 10π electron rearrangement reaction. Dihydroazulene derivatives were investigated for potential energy storage[64], but they were found to provide unfavorable high kinetic stabilities (stable for 24h at 60 °C) with moderate calculated storage capacities (calc. 13.8 kcal·mol⁻¹) in comparison to norbornadienes.

Switches working with *cis/trans* isomerizations are most prominently stilbenes[65], azobenzenes[66-68], imines/hydrazones[69-72] as well as the class of indigoid photoswitches.[73] Most commonly used are stilbenes and azobenzenes as depicted in Figure 12. Both switches exhibit absorption in the ultraviolet part of the electromagnetic spectrum.

X = C stilbene
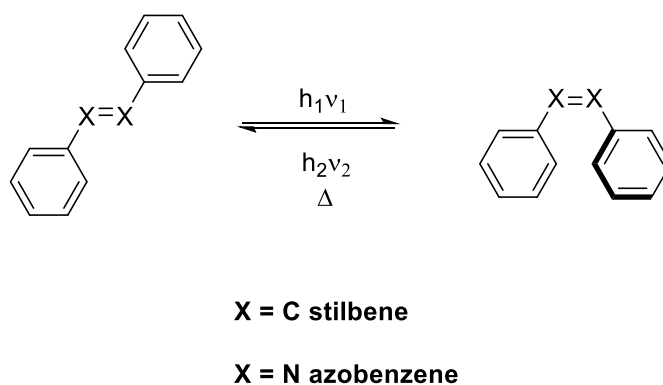
X = N azobenzene

Figure 12: Stilbenes and azobenzenes are the archetypal photoswitches based on double-bond isomerization.

Unsubstituted stilbenes can be addressed with UV light in both directions and provide very good *trans* to *cis* switching of over 90% as well as a considerable thermal barrier of 43 kcal·mol⁻¹ for back reaction. Very good quantum yields of 52% and 35% for *trans* to *cis* as well as *cis* to *trans* were found.

Nevertheless, alternative photoreactions are known, which can be regarded as minor loss channels, such as electrocyclization, which is often followed by irreversible oxidation to anthracene (this side reaction was the basis for the development of highly applicable dithienylethenes). The *trans* isomer exists in a planar form, while the *cis* isomer is forced into a distorted geometry due to sterical hindrance between the aryl residues. Stilbenes earned great popularity, since they were used for the development of light driven rotary molecular motors (rewarded with the Nobel Prize in 2016) and were further applied in molecular force probes[74] and for solar energy storage.[75] Azobenzenes, as the nitrogen containing analogue, offer similar geometry changes upon irradiation, although alternative modes of isomerization have been discussed.[66] Azobenzenes are widely used, especially in photopharmacology[40], for incorporation in foldamers[76] and biomolecules[77] as well as for potential solar energy storage[78] and molecular machinery.[79-80]

3.5.1   Indigoid photoswitches

Indigoid photoswitches[73] include hemithioindigos (HTI)[81-82], hemiindigos (HI)[83-84], substituted indigos[39, 85-90] as well as thioindigos[91] (Figure 13). These kinds of switches incorporate indigo related chromophores and are capable of low energy usage for photoisomerization. Especially HTI and HI combine quantitative on/off switching with light and high thermal stabilities. Distinctive structural changes can be achieved with indigos and thioindigos, but they often exhibit low thermal stabilities as well as decreased switching efficiency. The following chapter focuses on hemithioindigo and indigo.
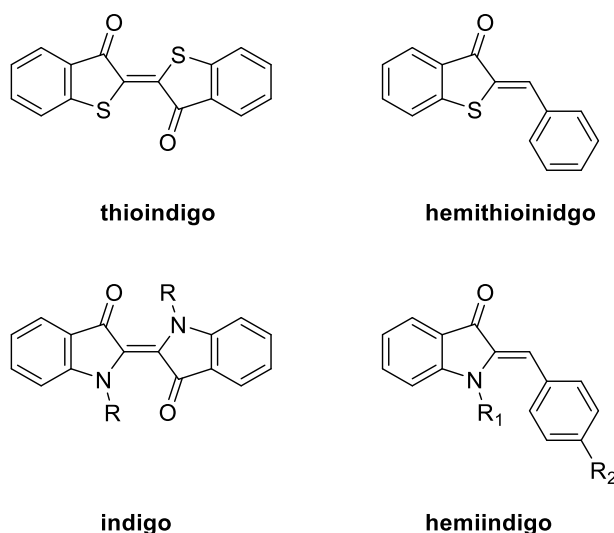
Figure 13:   Summary of indigoid photoswitches with bathochromic addressability.

3.5.1.1 Hemithioindigo

Hemithioindigo (HTI) was first described by *Friedländer*[92] in 1906, while its potential for photoisomerization was discovered by *Mostoslavskii*[93] in 1961. The asymmetric molecule consists of a thioindigo fragment and a stilbene fragment, which are connected by a central double bond (Figure 14). The incorporation of a chromophoric scaffold results in a considerable red shift of the absorption spectrum (λ_{max} = 433 nm for *Z*-HTI and 457 nm for *E*-HTI) in comparison to stilbenes (λ_{max} = 294 nm for *trans* stilbene and 278 nm for *cis* stilbene).[81] Thus, the switching can be addressed with visible light input. Under irradiation with 430 nm light the *Z* isomeric form can be transferred to the *E* isomeric form. Back reaction proceeds thermally but also under irradiation conditions with 500 nm light. It was shown, that this switching process can be cycled 10^4 times without significant degradation.[94-96] The absorption spectra reveal a moderate photochromism of 20-30 nm measured for the absorption maxima, which allows for quantitative photoswitching (>95%) in both directions. The absorption of the *E* isomer is bathochromically shifted and significantly decreased in intensity (5600 Lmol^{-1}cm^{-1} for *E*-HTI in comparison to 12600 Lmol^{-1}cm^{-1} for *Z*-HTI at the corresponding absorption maxima). Quantum yields were measured to be moderate with $\phi_{Z/E}$ = 23% and $\phi_{E/Z}$ = 5%, but they do not negatively influence switching efficiency.[97] Due to the incorporation of a stilbene fragment, unsubstituted HTI is a highly bistable photoswitch, as it provides a thermal energy barrier of 31.4 kcal·mol^{-1}. Usually the *Z* isomer is the thermodynamically more stable isomer with quantitative thermal *E* to *Z* conversion at 100°°C for unsubstituted HTI, which corresponds to an energy difference of at least 3.41 kcal·mol^{-1}.[97]
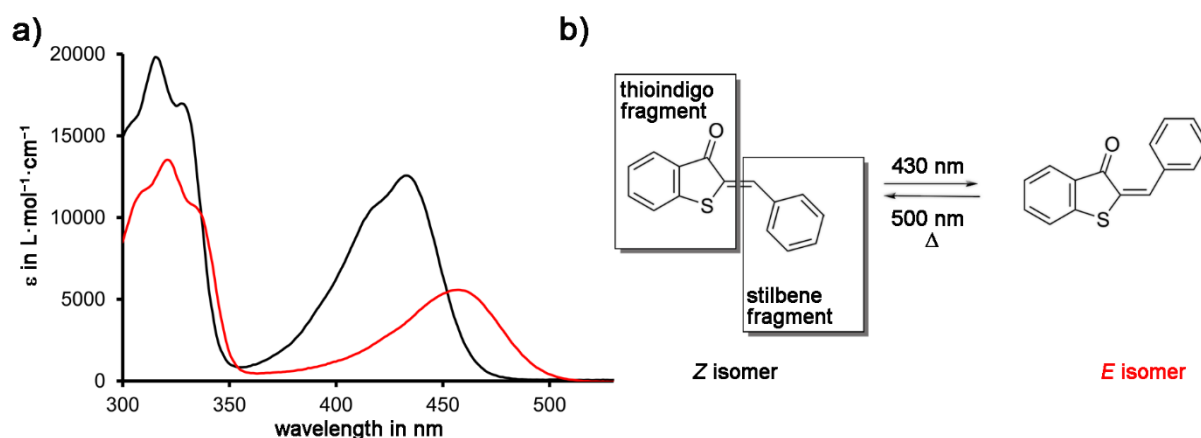
Figure 14: Photoisomerization of unsubstituted HTI. a) Extinction coefficients of the thermodynamically stable *Z* isomer (black) and metastable *E* isomer (red) in CH$_2$Cl$_2$. The spectrum of the *E* isomer is bathochromically shifted but is characterized by substantial loss in absorption intensity at the maximum. b) *Z*-HTI can be quantitatively converted to *E*-HTI by irradiation with 430 nm. Full reversion can be obtained by 500 nm irradiation or by thermal energy input.

The excited state processes leading to isomerization around the central double bond were investigated in detail by transient absorption spectroscopy,[98-100] as well as by theoretical calculations.[101] The derived reaction model is shown in Figure 15.[81] After excitation, the FC region FC_{S1Z} is populated, and the molecule initially relaxes to the S_1 minimum Min_{S1} by vibrational relaxation. The electron distribution is characterized by high electron density at the carbonyl oxygen, as well as low electron density at the sulphur atom. Thus, a vertical polarization at the thioindigo fragment is present, while the stilbene fragment exhibits more or less undisturbed electron distribution. Another excited state minimum S_2 is mixing with S_1 at a geometry representing 90° rotation around the central double bond. Substantial change in electron distribution accompanies the double bond rotation leading to a horizontal polarization at the Min_{S2}, with low electron density at the stilbene fragment and a remaining high density at the carbonyl oxygen. A low energy barrier separates S_1 and S_2 and determines the overall isomerization speed of HTI switches. After overcoming the barrier, the excited molecule further relaxes on the electrostatic potential surface S_2 and funnels in a conical intersection which connects S_2 with the ground state potential energy surface. Double bond distortion is anticipated to be around 90° as the molecule enters the ground state. Thus, geometry and potential energy highly resemble the thermal transition state between *E* and *Z* isomers. Further relaxation compulsorily leads either to the initial molecule or to the corresponding isomer with different double bond configuration. For both *Z/E* and *E/Z* isomerizations similar pathways were found, but with further competitive loss channels for the *E/Z* isomerization, which decrease the quantum yield $\phi_{E/Z}$.

The isomerization proceeds in an ultrafast time regime of 38 ps and 23 ps for *Z/E* and *E/Z* isomerization respectively. Furthermore, the isomerization speed can be manipulated by varying the electronic character of a *para*-situated functionalization at the stilbene fragment. It was found that moderate electron donors lead to a considerable acceleration of the isomerization speed up to 3.6 ps for methoxy substituted HTI derivatives. Substitution with even stronger electron donating groups on the contrary lead to a deceleration. The correlation of isomerization speed with the donor capacity matched well with the developed reaction model.[97] The fastest isomerization speeds were found for HTI derived motors which switch under 1 ps.[102] Very recently it was found that not only the substitution pattern influences the isomerization speed, but it is also changed by the polarity of the surrounding solvent. In contrast to the effects of moderately donating substituents, which lead to speed acceleration of photoisomerization by lowering the energy level of the S_2, polar solvents such as CH_2Cl_2 lead to energetic stabilization of the S_1 excited state. At the same time, the transition state is nearly unaffected because of almost homogeneous electron distribution (no dipole moment), which results in an overall considerable deceleration of the photoisomerization.[103]
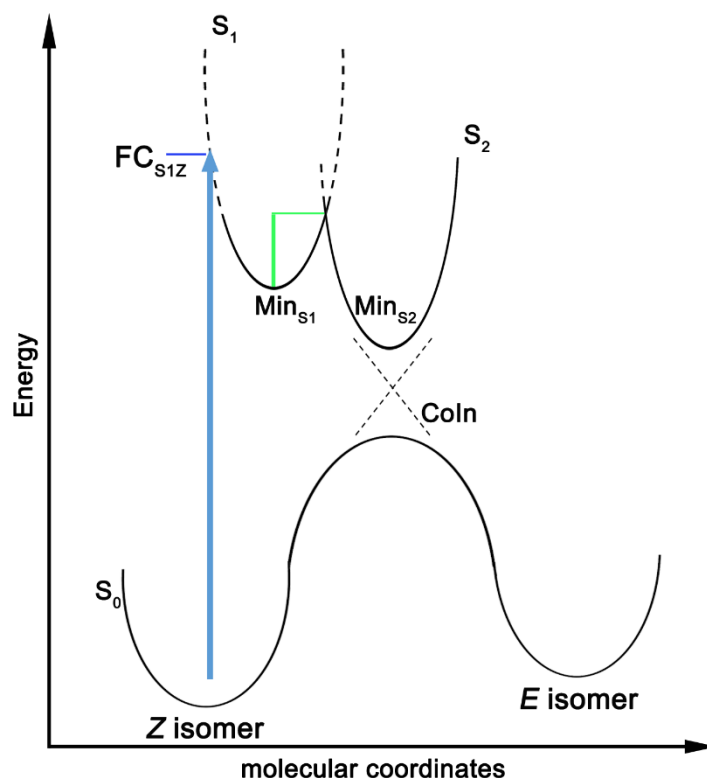
Figure 15:   Model of the excited state behavior of HTIs. S_0: Ground state. S_1: First excited state. FC_{S1Z}: Vertical excitation into the Frank Condon region. Min_{S1}: Minimum of S_1 populated after initial relaxation. S_2: Excited state populated by torsion around the central double bond. Min_{S1}: Minimum of S_2. CoIn: Conical intersection between S_0 and S_2, which is passed during relaxation to the ground state. A 90°-distorted double bond leads either back to the *Z* isomer, or to the *E* isomer by vibrationally cooling in the ground state.

The electronic distribution in the excited state can be further manipulated by different substitution pattern leading to alternative deexcitation channels, which can compete with the photoisomerization. HTI derivatives with tilted stilbene fragment and a strong donor, such as a Me_2N or julolidine moiety in *para* position to the double bond, show dual fluorescence, most pronounced in moderately polar solvents, such as CH_2Cl_2.[104-105] Dual fluorescence hints at an additional excited state with substantial lifetime. Photoisomerization rates were further investigated and it was additionally found that they were strongly diminished, if the measurements were carried out in more polar solvents. This is in agreement with the assumption of an additional excited state, which increasingly diminishes population of S_2 from which isomerization occurs in solvents with increased polarity. From transient absorption spectroscopy a consistent reaction model could be derived, which proposes a new excited state intermediate (TICT state[106-109]) with pronounced twisting around the single bond of the stilbene fragment and a horizontal charge transfer electron distribution with a deexcitation channel to the ground state. Thus, deexcitation can be manipulated solely by solvent polarity.

Ephemeral TICT intermediates with distorted single bonds occur in the excited state but relax back to the initial ground state via rotation around the single bond connecting the photoisomerizable double bond and the stilbene fragment. Two different photoreactions were found for sterically locked chiral HTI derivatives. Sterical locking was achieved by a bulky *tert*-butyl substituent at the central double bond and an asymmetric *ortho* substituted stilbene fragment. The rotation around the aforementioned single bond was consecutively impeded by a high thermal barrier leading to two different atropisomeric arrangements of the stilbene fragment for each double bond isomer. In combination with a sulfoxide stereocenter, these rotamers were rendered diastereotopic, which allowed for clear seperation of all four possible isomers. With crystal structures for each isomer at hand, photochemical behaviour could be followed for each isomer by ^{1}H NMR spectroscopy and it was found that irradiation leads not only to the photoproducts obtained by simple double bond rotation, but also by a single bond rotation[110] and by a concomitant combination of both rotations (Hula Twist mechanism[111-115]). Thus, two new deexcitation processes could unambiguously be revealed for these unique derivatives of HTI photoswitches.[116] In Figure 16, the light induced motions, such as TICT formation, hula twisting, double-bond isomerization and single bond rotation are depicted.

| TICT formation | double bond isomerization | Hula twist | single bond rotation |
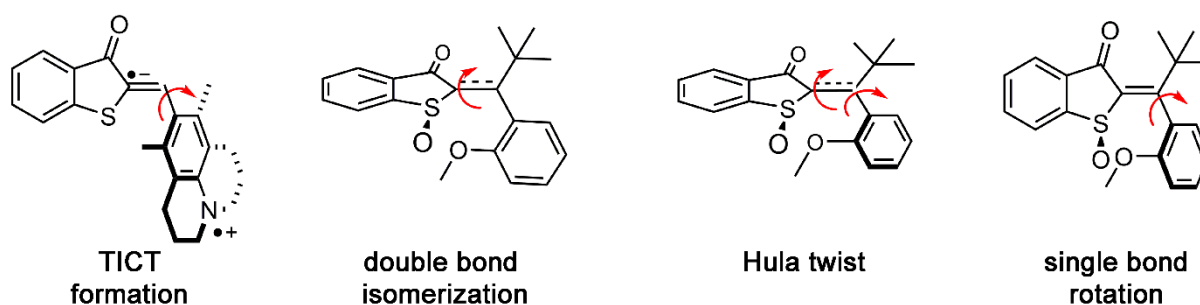
Figure 16:   Light induced motions observed for HTI derivatives. TICT formation is observed for twisted HTI substituted with strong donors. For sterically locked HTI derivatives three independent light induced motions could be evidenced by different photoproduct formation. TICT formation as well as single bond rotation occur around the same rotation axle but they differ from each other significantly as efficiency of single bond rotation for sterically locked HTI derivatives is not enhanced by polar solvent media. It can be assumed that single bond rotation does not involve a charge transfer excited state in the latter case.

HTI photoswitches were successfully implemented in molecular tweezers[117-118], β hairpin peptides[119] and were used as inhibitors for the enzyme lipoxygenase LOX-12/15[120], for supramolecular shuttles[121] as well as for selective guest exchange in supramolecular capsules[122]. The first generation tweezers, which are able to perform light addressable binding of electron deficient aromatic guest molecules, are based on a helical bis-hemithioindigo scaffold with flexible binding sites bound to the switching unit. They exhibit limited light responsiveness and moderate binding constants.[118] The tweezer design was further improved by rigidity enhancement as well as by reduction of switchable functionalities for

selective light addressability. Thus, high binding constants as well as improved switching was obtained. A further advantage of the new molecular architecture was the possibility for preparation of two regioisomeric tweezers, which were capable for simultaneous complementary photoswitching and dynamic guest relocation.[117]

3.5.1.2 Substituted indigos

Since the structure of indigo[89, 123-129] was elucidated by *Baeyer*[130] in 1883, a variety of investigations were performed in order to scrutinize the deep color of indigo[127] and outstanding stability, which made it an excellent dying material for textiles. In 1897, BASF started the first industrial production of indigo using aniline as starting material by applying the *Heumann/Pfleger* route, which widely replaced production from *indigofera* plants. With the synthesis of a truncated derivative "urindigo" in 1980, which spares both phenyl rings, it was found by *Wille* and *Lüttke*,[125] that the deep color can be attributed to the push-pull substituted H-chromophore situated at the central double bond. Thus, the scientific interest for indigo did not originate from its potential as switching device. After several spectroscopic[131-133] and theoretical studies[134-136] had been reported, a commonly accepted theory crystallized, which attributed the photostability of indigo to an efficient deactivation mechanism after light absorption. This pathway was believed to be an intramolecular proton transfer in the excited state (ESPT), which proceeds in an ultrafast time regime, outcompeting alternative deexcitation channels. In Figure 17a, indigo and the discussed ESPT mechanism are shown.
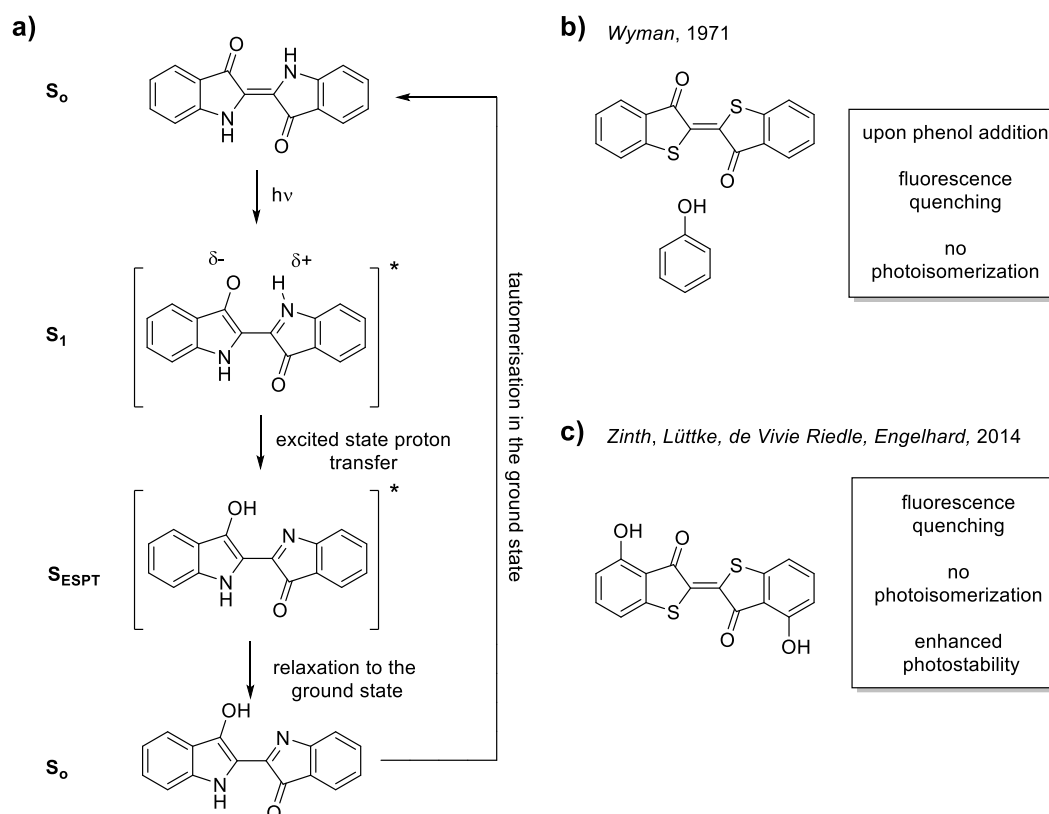
Figure 17: The photostability of indigo is attributed to an ultrafast ESPT. a) Deexcitation by excited state proton transfer from the amine to the carbonyl oxygen, which leads to an enol/imine tautomeric form. The tautomer converts back to the ground state, which is believed to be a highly energetic short lived ground state intermediate. Fast thermal relaxation restores the initial ground state. b) Initial observations of *Wyman* on fluorescence quenching of thioindigo by phenol led to the proposal of ESPT. c) Directly bound hydroxyl groups had same fluorescence quenching effect on thioindigo excited state behaviour and it could be shown that the photostability was greatly enhanced.

Wyman first suggested the possibility of an excited state proton transfer as the mechanism responsible for the high photostability.[137] Experimental background for this assumption was found by the observation of fluorescence quenching and suppressed photoisomerization of thioindigo, when phenol as additive was present in the solution (Figure 17b). It was concluded, that the hydroxyl group readily acts as deactivating reagent by transferring a proton to the highly polarized carbonyl oxygens, which results in deexcitation to the ground state of thioindigo ("formation of a donor acceptor encounter complex"). It was further believed that the hydroxyl group containing additives mimic the N-H groups of indigo, which should hence deactivate in the same manner. First ultrafast spectroscopic studies on the ps time scale in 1986 could not confirm this assumption.[138] However, two decades after this study, transient spectroscopy on the fs time scale reported on the observation of OH stretching modes, which are characterized by a lifetime of only 500 fs after excitation of indigo.[131] Thus, it could be explained

why the earlier study on the ps time scale missed these stretching modes, which hinted at the formation of an enol structure in the excited state. A further study in 2014 by the groups of *Engelhard* and *Zinth* reported on the investigation of the photostability of thioindigo derivatives, which incorporated a hydroxyl group at the aromatic rings in vicinal position to the carbonyl group. In analogy to the results of *Wyman* obtained by phenol addition to thioindigo solutions, they could observe supressed fluorescence and photoisomerization (Figure 17c).[133] This resulted in improved photostability, as the hydroxyl functionalized thioindigos showed no decomposition in comparison to thioindigo or methoxy group bearing analogues when exposed to sunlight for several weeks.

Most investigations were carried out with soluble indigo derivatives, as the parent chromophore exhibits only limited solubility, which rendered spectroscopic studies difficult. Amongst other derivatives, *N,N'*-disubstituted indigos were also investigated, and it was found that these compounds showed photochromic behaviour under irradiation.[87-88] Thus, it was directly shown that removal of N bound hydrogens lead to suppression of ESPT. It was, however, reported that the initial absorption is restored in a very short period of time (s time scale for methylated indigos). Over the last decades less efforts have been made for further elaboration of the photoisomerization potential until an Austrian group reported on twofold Boc-protected indigos in 2015.[86] The electron withdrawing protecting groups lead to a substantial loss of the unique red-shifted absorption, but considerably increased the kinetic stability of the *cis* isomer. In 2017, while investigations on photoswitchable aryl-substituted indigo derivatives were being carried out in our own group, *Huang et al* reported on indigo derivatives, which maintained the unique absorption features of indigo with improved thermal stability. This combination was accomplished by introduction of electron deficient alkyl groups as well as aryl substituents. With electron deficient aryl-substitution it was possible to substantially increase the thermal stability from minutes to hours.

Di-arylated indigos were first reported by *Friedländer*[139] in 1922. In 2010, an improved synthetic strategy was published by *Tanaka*[140], which allowed for the facile one step synthesis of mono- and di-arylated indigos by Cu catalysis. The procedure, however, only allowed zero to low yields for electron deficient aryl substituents, which was further improved by the report of *Huang et al* mentioned above.

3.6   Molecular machinery

The research field of molecular machinery[141-143] gained much interest since in 2016 *Ben L. Feringa*, *Jean-Pierre Sauvage* and *Sir Frasier Stoddart* were awarded with the Nobel Prize in chemistry. The approach to control states and motions at the molecular level can be traced back to *Richard Feynman*, who presented his vision of a bottom up design of machines and computing devices in a forward-looking lecture in 1959.[144] Based on the laws of physics, profound design principles of molecular machines can be derived. *Richard Feynman* and *Marian Smoluchowski* showed with a tiny "thought machine",[145-146]

that at the molecular scale, machines operate under the principles of the second law of thermodynamics as well.

3.6.1   The Smoluchowski-Feynman ratchet

The "thought machine"[143, 145-146] consists of two boxes at molecular scale, which are filled with gas (Figure 18). In box 1 a ratchet and pawl is placed, which is connected to an axle with vanes. This paddle wheel is situated in box 2. Boundary conditions of the thought experiment is that the two boxes are isolated from each other. No heat may be transferred between the boxes, which is mediated by random vibrational fluctuations. Communication between the boxes is limited only to the axle and it is allowed just rotary motion of the axle to occur. Under this limitation heat may be transferred between the boxes. The ratchet has an asymmetric profile with teeth on its surface, which allows only directed motion. This can be accomplished with a pawl connected to an elastic spring, which pushes the pawl against the ratchet. Brownian motion in box 2 leads to collisions of particles with the vanes of the wheel. If the direction, in which the particle is hitting the vane matches the asymmetry of the ratchet, a directional motion occurs. A particle hitting the paddle wheel with opposite directionality may not be able to induce a rotation. Thus, it seems that Brownian motion can be used to drive a cyclic process. Taking a closer look at box 1 will show that this is not the case. At the molecular scale all components of the machine have to be built up from atoms or molecular components. Thus, it is an intrinsically very flexible device, which can populate vibrational modes and undergo conformational changes. As the pawl has to be pushed away from the ratchet when motion transfer occurs from box 2 to 1, the spring consequently restores the positon of the pawl at the ratchet by pushing it back onto the next tooth. This results in an elastic vibration of the spring, which means that at the timepoint the pawl accidently bounces up from the ratchet no mechanical barrier is left to prevent a backward rotation. The vibration of the pawl is fading as heat dissipates to the surrounding gas reservoir. As the temperature is rising, the probability of reactivating the vibration of the pawl is increasing as well. In consequence, with constantly rising temperature the pawl is as much detached from the ratchet as it is attached to it. As the pawl bounces back to the ratchet, it hits an inclined surface given by the asymmetric teeth of the ratchet. While the pawl is detached from the ratchet the Brownian motion in box 2 leads to minor oscillation of the ratchet around its own axis. The position, where the pawl reattaches to the ratchet is gaussian distributed around the position, where it was before it bounced off. Thus, it is much more probable, that the ratchet is rotating in the opposite direction and directional motions are cancelling out each other. This example showed that no directional process can occur, if both boxes have the same temperature (adiabatic process).
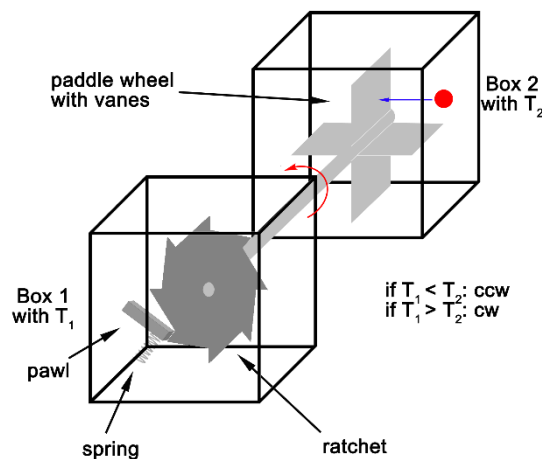
Figure 18:   The ratchet and pawl proposed by *Smoluchowski* and *Feynman* should be capable of exploiting a thermal energy gradient for directional motion.[145-146] The two boxes are filled with gas as well as the depicted machine components. As it could be assumed from first glance, this "thought machine" cannot use random thermal fluctuation for unidirectional rotation, if $T_1 = T_2$.

The following aspects should be regarded by this thought experiment: First, it showed that, it is not possible to construct a *perpetuum mobile* at the molecular scale as well. It is always necessary to supply energy to drive a system out of equilibrium. Second, the herein demonstrated machine is only operable under the restrictive boundary conditions. E.g. the reduction of the communication between the boxes to solely rotational motion of the axle is only possible at macroscopic scale. A particle hitting the paddle wheel induces population of high energetic vibrational modes of the machine. This is not limited to the components in box 2, but is also valid for the components in box 1. It points out, that separation into two boxes as well as maintaining a temperature gradient at this length scale is not possible. Moreover, at molecular scale directionality is not dictated by the steepness of a surface, but by the overall height of the energy barriers.[147] For the thought experiment this means, that a particle hitting the paddle wheel from opposite direction, which forces the ratchet to rotate along the steep gradient may induce a rotation with the same probability as a hitting particle, which rotates the paddle wheel along the shallow gradient, because the barrier height is equal in both cases.

For the design of molecular motors, capable for exploiting a thermodynamic energy gradient, three important conclusions can be drawn from the thought experiment. Asymmetric information leads to an asymmetric energy landscape of the machine (Figure 19b), which allows that energy input may generate a potential energy gradient (population of high energy states, e. g. heating one of the two boxes results in the pawl being shifted to a "higher" position on the inclined surface of the ratchet) and Brownian motion, as equilibrating driving force, leads to depletion of the gradient (operation of the machine levels out the temperature gradient of the two boxes). In Figure 19 energy potentials for demonstration of the deduced design principles are shown. Under equilibrium conditions transfer rates between states cancel

each other out even in an asymmetric energy landscape, which means that no net directional motion occurs (Figure 19 a and b). Under non-equilibrium conditions (e. g. if one box is hotter than the other box), however, a net directional flux is generated (Figure 19c), until equilibrium is reached again. Brownian motion is the driving force for the reestablishment of equilibrium conditions. These design principles are valid for machines, capable of exploiting a thermodynamic energy gradient. In the following chapters these machines are termed as energy ratchets and are to distinguish from information ratchets.
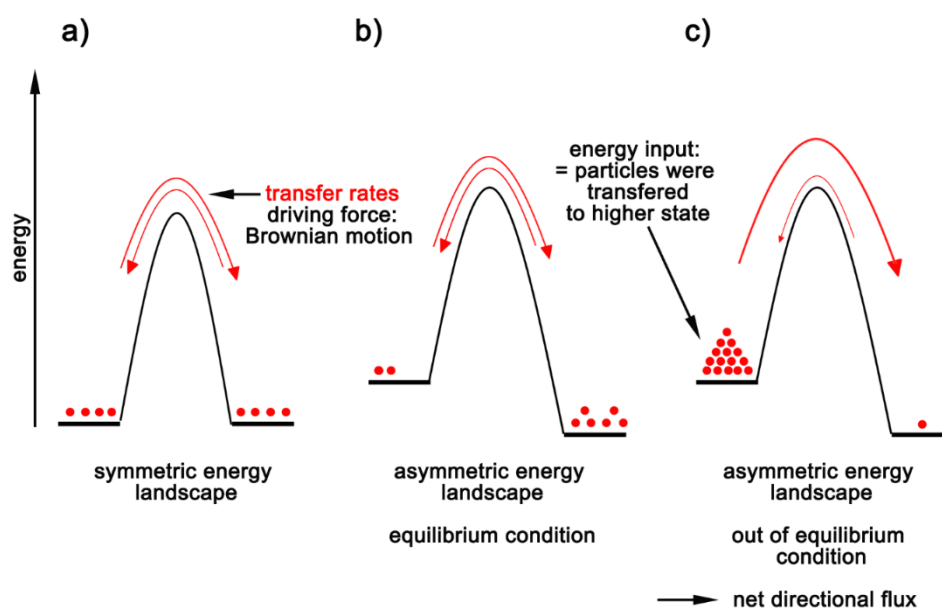
Figure 19:   Three features have to be considered for the design of a molecular machine capable for exploiting a thermodynamic energy gradient. For molecular machines without usage of a thermodynamic gradient energetic minima may be equal. In these cases directionality is achieved by entropy release (see information ratchets below). a) Brownian motion is essential for restoration of equilibrium conditions. b) and c) An asymmetric energy landscape allows for population of higher energetic states under energy consumption. If all these conditions are fulfilled, the gradient is depleted and leads to net directional flux.

3.6.2   Macroscopic scale vs. molecular scale

Brownian motion is an equilibrating driving force at the molecular scale, but also macroscopic objects are confronted with Brownian motion, as it contributes to the macroscopic phenomena of friction, which dampens moving particles with time. A particle experiences strong friction/dampening, if the surroundings are highly viscous. In this context, Brownian motion can have opposing effects on the viscosity of the surroundings. Temperature increase can lead to reduced viscosity, e.g. in case of liquids, but can also increase the viscosity/friction in case of gases.In particular, intermolecular (cohesive) forces in liquids are outcompeted by brownian motion at increased temperatures, which reduces the viscosity.

In the case of gases increased Brownian motion directly leads to heavier collisions at the molecular scale, which enhances viscosity in this case.

In summary, common dampening is linked to the mass/volume ratio, the velocity of the regarded object and, in a general sense, the dragging forces of the surroundings.[143] For large sized objects inertia (depends on mass/volume ratio plus velocity) is governing motion, while at molecular scale inertia is outcompeted by Brownian motion.[143] Under the regime of inertia the information about the direction of a motion is preserved over a distinct period of time, which facilitates the design of macroscopic machines. A comparison of a piston driven motor and a molecular motor is illustrated in Figure 20. No information about the directionality is mechanically implemented in the macroscopic motor. The information about directionality is given at the beginning of motor operation by an external trigger (e. g. a starter, formerly a crank was used to compress the gasoline air mixture as well as to transfer directionality manually). Under motor operation the directionality is preserved by the continuity of motion e. g. inertia. At molecular scale continuity of motion is impeded by Brownian motion and can therefore no longer transfer motor directionality. Molecular motors require a stereochemical information installed in order to provide the direction of motion constantly during operational mode. Further molecular machines affronting Brownian motion must provide structural resistance against the equilibrating powers. These requirements strongly affect the challenges of machine synthesis. In consequence sterically hindered as well as mechanically interlocked molecular designs are indispensable. Increased sterics raise the energy barriers for molecular displacements, which would cancel out directed motion or disassemble molecular components of the machine. In addition, gravitational force is surmounted by Brownian motion and can hence not influence machine operation and efficiency at the molecular scale.
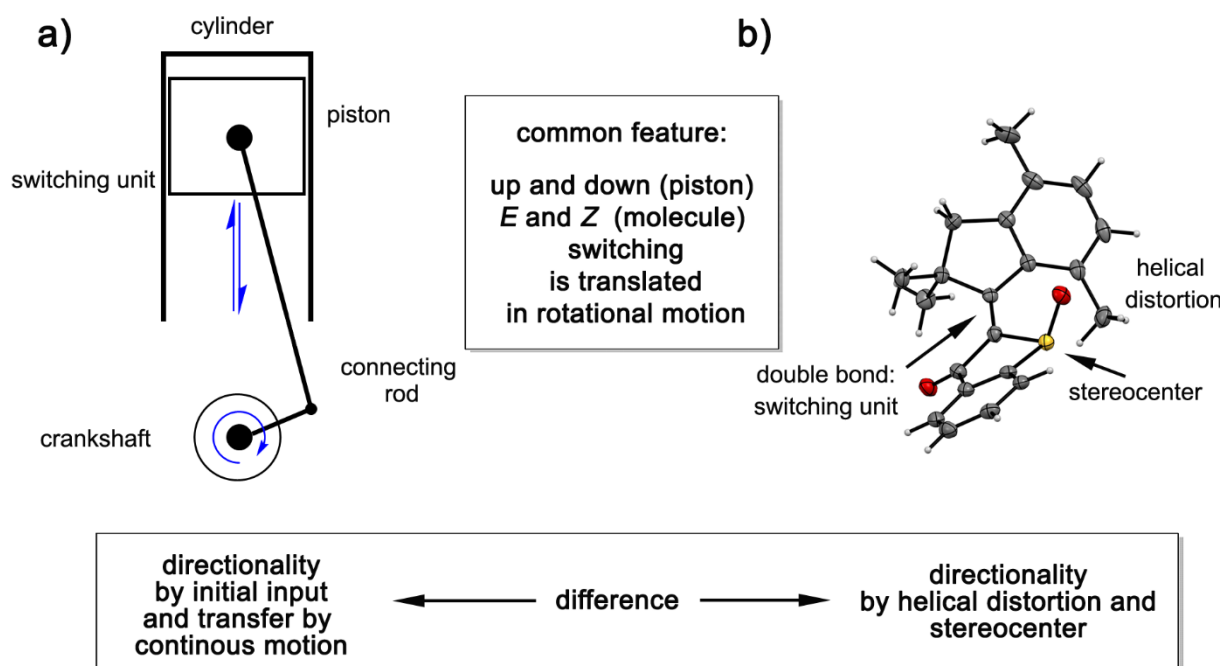
Figure 20: Juxtaposition of a piston driven motor and a molecular motor. a) In a piston motor initial induction of directionality is maintained by inertia and no mechanically implemented asymmetry is needed for the machine setup. b) Inertia is outcompeted by Brownian motion at the molecular scale. Thus, asymmetry is incorporated in the molecular structure of the motor. In both cases a switching processes is used for directional motion.

3.6.3 The first light driven molecular motor

In 1999 *Koumura* and *Feringa* reported on the first light driven molecular motor,[148] which is capable of continuous rotary motion under light and thermal energy input. The chiral overcrowded stilbene combines the three design principles suggested from the *Feynman* ratchet. Asymmetry is given by two carbon based stereocenters, as well as by sterically induced helicity around the central double bond. *Cis* and *trans* configuration of the double bond can be interconverted by light input, as a common feature of stilbene photoswitches. In summary, the molecule can exist in four energetically different diastereomers, which are characterized by the configuration of the double bond and the helical torsion of the subcomponents. The structures are depicted in Figure 21. The configuration of the carbon based stereocenters determines the direction of the rotation. Since the configuration does not change during motor operation, it will be omitted for simplicity reasons in the following description. Isomer **A** exhibits (*P,P*)-*trans*, isomer **B** (*M,M*)-*cis*, isomer **C** (*P,P*)-*cis* and isomer **D** (*M,M*)-*trans* configuration. Under irradiation with UV light, isomer **A** undergoes photoisomerization and is transferred to the metastable isomer **B** with opposite configuration of the double bond and helical twisting. The light induced transfer fulfills the second requirement revealed from the *Feynman* ratchet, as energy input leads to population of a higher energetic state. Isomer **B**, less stable in terms of energy, can be converted thermally into the more stable isomer **C** by a helical inverting step. This can be regarded as the last design principle, as it

exploits Brownian motion as an equilibrating driving force to reinstall equilibrium conditions. This leads to a net directional flux and prevents light induced back isomerization. A second light induced isomerization towards isomer **D**, which is consecutively transferred thermally to isomer **A** restores the starting point of the rotation cycle. In summary, the sequential population of four different intermediates by light and thermal energy input leads to a fully directional 360° rotation around the central double bond. As this requires all four steps to proceed with identical directionality, this will be discussed in more detail in the next chapter.
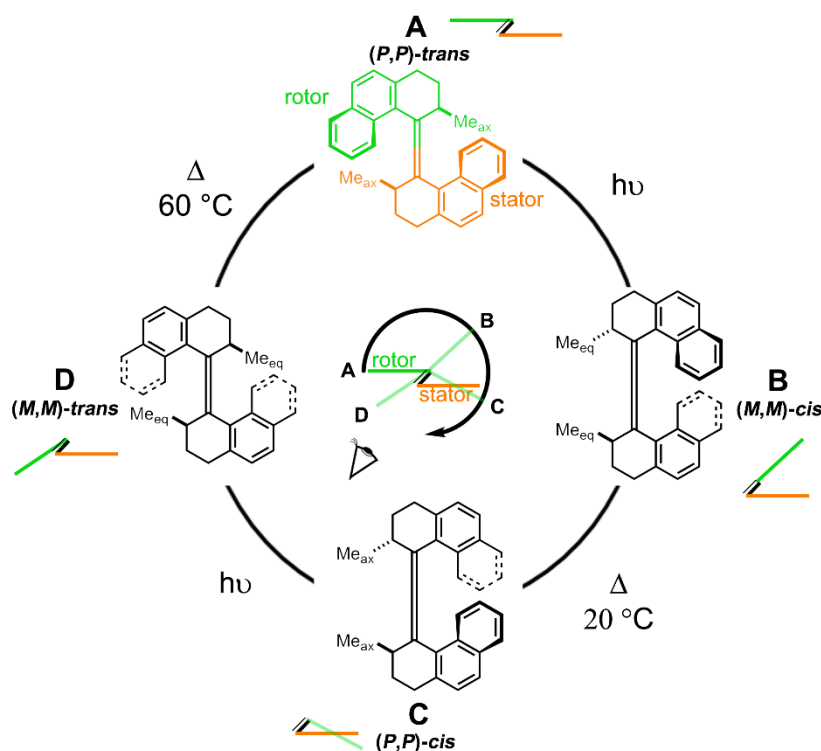
Figure 21:   The rotation cycle of the *Feringa* motor is depicted. Sequential population of four distinct isomers **A**-**D** leads to rotational motion as long as light and sufficient thermal energy supply is available. Center of the Figure: For reconstruction of the directionality look from the stator part along the central double bond to the rotor part. The relative position of the rotor fragment to the stator fragment for each isomer **A**-**D** shows the directional 360° motion in clockwise fashion.

3.6.4   Preservation of directionality

The molecular motor sequentially populates four distinct intermediates **A-D** under operation, which results in a unidirectional 360° rotation around the central double bond. This requires preserved unidirectionality for each isomerization step contributing to the cycle. Common non-chiral photoswitches undergo *E*/*Z* isomerization, which is accomplished by a 180° rotation around the double bond with no preferred direction. Thus, clockwise and counterclockwise rotation can be regarded as enantiomeric pathways, which are energetically equal. In consequence, photoisomerization will take

place in 50% clockwise and 50% counterclockwise fashion, which cannot be distinguished from each other. In the molecular motor a considerable sterically induced twist around the double bond furnish two possible conformations, **A/D** as well as **B/C,** with opposite helicity for each double bond configuration. The additional introduction of stereocenters leads to one helical isomer (**A** and **C**), which is energetically favored in contrast to the isomer with opposing helicity (**B** or **D**) and same double bond configuration. In conclusion, energetic separation leads to 100% population of the favored isomer (**A** and **C**) in equilibrium. Thus, irradiation leads to exclusive excitation of the stable isomers (**A** and **C**). Their helical pretwist dictates the direction of the photoisomerization, as it mechanically impedes a backwards rotation (**A** to **D/C** or **C** to **B/A**). This can be translated into an asymmetric energy potential surface in the excited state, which forced the molecule to relax along the favored reaction coordinate. Thus, only clockwise or counterclockwise rotation occurs depending on the helical pre-twist of the isomer. Both stable isomers **A** and **C** exhibit the same pretwisting and hence photoisomerization of both, equally leads to clockwise rotation. In Figure 21 the rotation cycle is illustrated. For reconstruction of directionality, look from the stator part along the central double to the rotor part (point of view illustrated in the middle of Figure 21). The rotor part must rotate in clockwise fashion to deliver isomers **B** and **D**.

Photoisomerization leads to population of metastable isomers **B** and **D** in a clockwise fashion, which thermally relax to their stable counterparts with the same double bond configurations. Thus, the directionality is only preserved, when these thermal ratcheting steps also proceed in the same direction, as it is the case for the photoisomerization steps. For reconstruction of the directionality a viewpoint from the stator part along the central double bond to the rotor part is defined in Figure 21. The rotor part must rotate again in a clockwise fashion to furnish isomer **C** and **A**. For this rotation to occur the naphthyl rings either have to slip over each other (**B** to **C**), or they have to slip over the methyl groups (**D** to **A**). Concomitantly, a conformational change of the cyclohexyl groups takes place, which leads to repositioning of the methyl groups from equatorial to axial position in both thermal steps.

All four isomerization steps, which in sum contribute to a 360° rotation must exhibit same directionality. This, however, does not exclude that different unproductive isomerization processes with opposite directionality do not take place under operational conditions. For example photoisomerizations from metastable isomers **B** and **D** delivering isomers **A** and **C** are also possible to take place. Depending on the thermal features of the motor rotational cycle, these unproductive photoreactions reduce photonic efficiency of the overall cycle. For high thermal barriers, as it is the case for the first generation *Feringa* motor (Figure 21), under irradiation photoequilibira between isomers **A** and **B** as well as between **C** and **D** are established, where clockwise and counter-clockwise rotations cancel each other out. Under thermal energy supply helix inversions from **B** to **C** and **D** to **A** break microscopic reversibility of these photoisomerizations to drive the system out of equilibrium. Reverse helical inversions (from **C** to **B** and **D** to **A**) are impeded by a high energy difference between the stable isomers **C/A** and the metastable

isomers **B**/**D**. These thermal ratchetings steps ensures directionality, despite the existing photoequilibria between isomers **A** /**B** and **C**/**D**.

3.6.5   Evolution of Feringa Motors

Since 1999 the *Feringa* group consequently improved the motor design and studied the mechanism[149-151] of motor rotation. New motor generations were developed with improved thermal behavior[152-154] for realization of motors working under photonic limitations.[155] The motor designs are depicted in Figure 22a. In the course of these investigations surprising results were found, which anew illustrated the fundamental differences between macroscopic and molecular machines.[156] One example is a molecular motor, which counterintuitively exhibited thermal acceleration, although sterical hindrance was increased in proximity to the rotation axle.[157] This is made possible only by the step by step functionality, which is not the working principle of macroscopic machines. Furthermore, many efforts have been made to shift light addressability out of the region of damaging UV light. This was, on the one hand achieved by expanding the aromatic system[158] and by push/pull substitution,[159] as well as by an energy transfer approach on the other hand.[160-161] The corresponding motor designs are shown in Figure 22b.
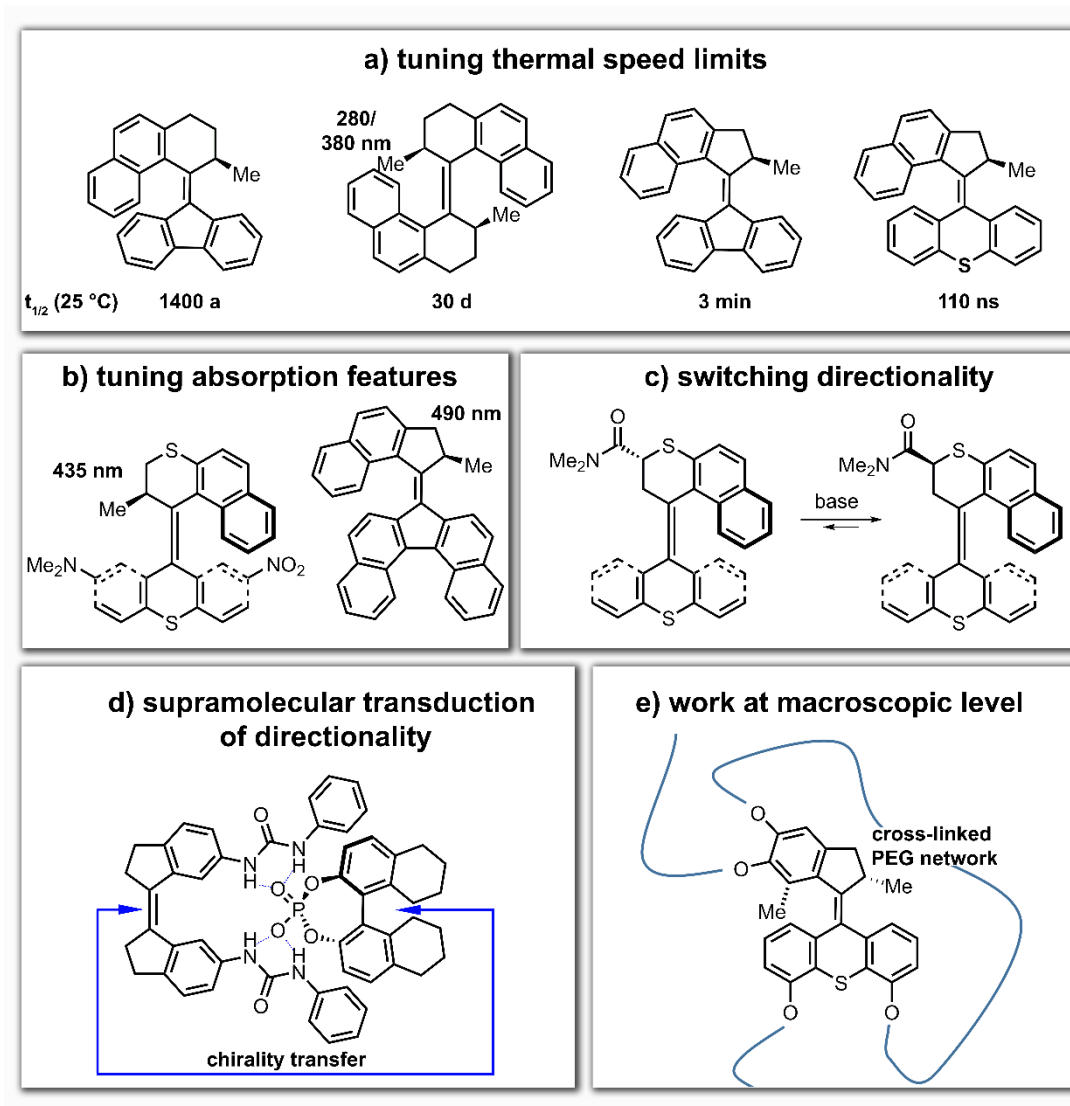
Figure 22: In recent years, Feringa motors were further developed, with regard to reduced thermal speed limits (a) and use of visible light for motor operation (b). Additional functionality was embedded, e.g. the option to change the direction of motor rotation. This can be on the one side achieved by a covalently linked epimerizable stereocenter (c) or by a supramolecular approach (d), where the stereoinformation is induced by an external trigger. Sucessful translation of unidirectional molecular processes to the macroscopic level was achieved by the group of *Giuseppone* (e).

The control of motor functionality was further extended. For instance thermal ratcheting steps can be manipulated by addition of metal ions (not depicted),[161-162] while in an extended molecular setup, a pseudorotaxane subcomponent can impede motor rotation under the presence of protons (not depicted).[163] A milestone in gaining control over motor function was the establishment of a motor molecule with the possibility of switching the directionality of motor rotation under basic conditions (Figure 22c).[164] This was achieved by triggering an epimerization of the directionality determining

stereocenter, while the motor assumes different metastable conformations. Meanwhile, supramolecular induction of motor directionality was also reported,[165] but was not unambiguously proven by the provided experimental data. Axial chirality of a bound guest molecule induces a helical twist around the double bond of a motor-receptor molecule in *cis* configuration. Thus, photoisomerization from *cis* to *trans* should occur, at least, to a certain extent directional. A locked synchronous rotor motion alongside the motor was achieved more recently (not depicted).[166] This reported system provided further valuable insights into the intricate opportunities and challenges of molecular mechanics.

Transfer of molecular into macroscopic motion was also investigated intensively. Valuable contribution of the *Feringa* group was made by using molecular motors as dopant for cholesteric liquid crystal films (not depicted).[167-168] Thus, under irradiation a macroscopic rearrangement of the film was observed, which was nicely illustrated by the rotation of a glass rod mounted on the liquid crystal. It has to be noted, however, that such microscopic directional rotation was also achieved by using a chiral photoswitch as dopant instead of a motor. Therefore, it has to be concluded, that rather the change of the helical twisting power of different motor isomers is responsible for directional macroscopic motion, and not the intrinsic unidirectional rotation of the motor molecules. For real transduction of motor unidirectionality the working group of *Giuseppone* [169-170] delivered valuable contributions. Their presented studies show, that molecular motors with rotor and stator parts interconnected by a PEG-linker network were able to actively collaps a macroscopic gel upon irradiation. The motor rotation leads to a winding up of the PEG chains and the macroscopic gel shrinks as a result

Unidirectional rotation around double bonds, was also achieved for HTI based molecules,[1, 38] which is discussed in detail in this thesis. Furthermore chiral imine derivatives, as successfully shown by the group of *Lehn*[69, 171] are capable for directional motion. A 120° directional rotation around a single bond was achieved by the group of *Kelly*,[172-173] while directional rotation around biaryl axes was investigated,[174-176] leading to a fully directional molecular setup developed by the group of *Feringa* in 2005.[177]

3.6.6 Mechanically interlocked molecules

Besides the development of rotary motors based on overcrowded alkenes, mechanically interlocked molecules (rotaxanes[33] and catenanes[178-181]) were engineered for creation and maintenance of non-equilibrium conditions. These molecules were subsequently improved in order to exploit Brownian motion for transduction of non-equilibrium conditions into directional motion. To accomplish out-of-equilibrium conditions two underlying strategies were followed, e.g. the realization of the energy ratchet and the information ratchet mechanism.[182] Note, that the ratchet mechanisms always regard the processes of gradient installation.

In an energy ratchet[142], a stimulus manipulates the relative energies of different states of an energy profile. Consequently, the formerly stable states (red wells, Figure 23a, inset 1) are metastable after the stimulus was applied and the formerly unstable states were stabilized (green wells, Figure 23a, inset 2). Brownian motion drives a particle towards the new stable state (Figure 23a, inset 3). Restoration of the initial energy profile ensures, that the particle is located again in a metastable state. Subsequently, the particle translocates to the next stable state following the potential gradient (Figure 23a, inset 4). By repetition of this sequence the particle is moved along the energy profile. This is only possible, as the kinetic barriers for forward reactions are lower than the backward reactions. In an information ratchet [142], it is not the relative thermodynamic energies which were altered, but rather the kinetic barriers for forward and backward reaction. This can be realized if the information, what forward and backward actually means, is given. Is a particle situated in a defined state, its presence impacts the potential energy surface. Thermal barriers in forward direction are lowered, and/or thermal barriers in backwards direction are increased. Hence equilibrating forces lead the particle to move to the state separated by the smaller kinetic barrier. In the next step barriers are restored. A net forward directed motion occurred.
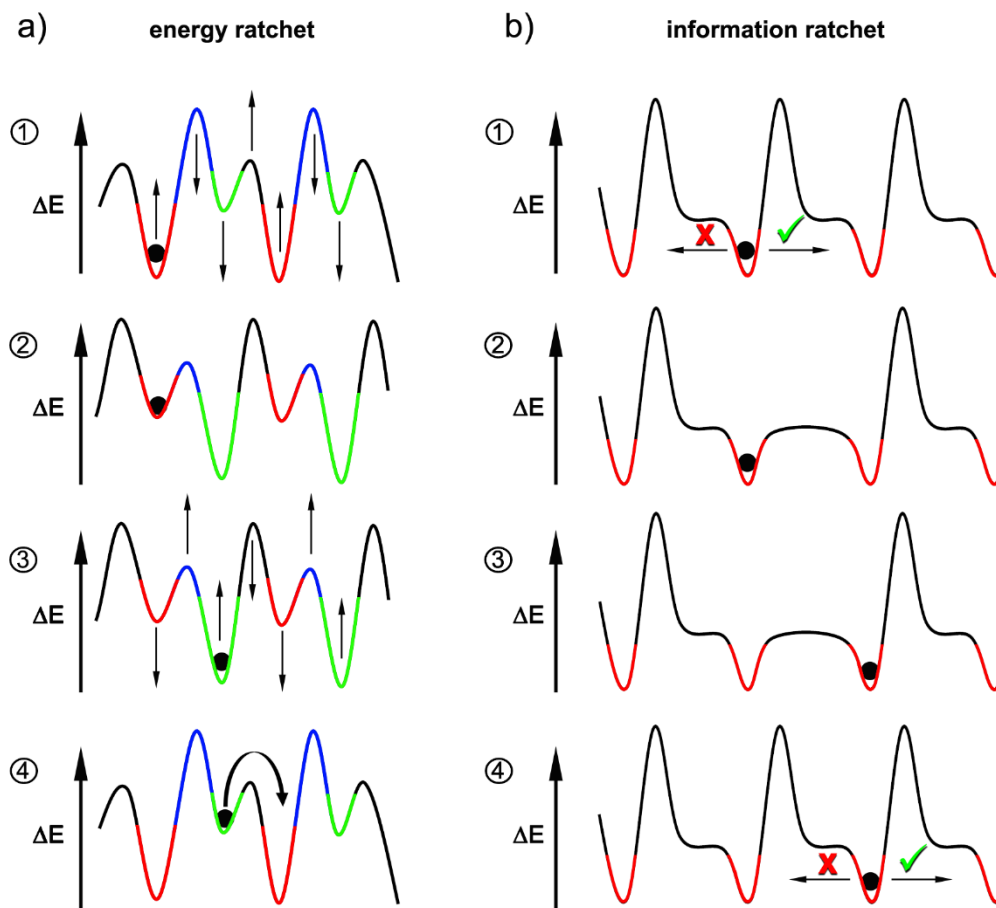
Figure 23:   The energy ratchet mechanism and the information ratchet mechanism are shown. a) The energy ratchet is driven by a sequential change of the thermodynamic energies of the stations. b) Rational design of the potential surface (depicted by the asymmetric barriers with the long shoulder) provide information (indicated by the black arrows) at which stage a particle is located and manipulation of the kinetic barrier of forward reaction or backward reaction is induced.

The energy ratchet principle was successfully applied by the group of *Leigh* for the first time.[183] They developed a rotaxane, which consists of a thread with two binding sites and a macrocycle surrounding the thread. Unthreading of the macrocycle is sterically hindered by bulky stoppers at each end of the thread. The binding sites consist of fumaramide and succinamide groups, which differ in binding affinity for the macrocycle. Larger affinity is supplied by fumaramide, which leads to a ring distribution of 85% to 15% (Figure 24 step 1). Since fumaramide contains a double bond, light exposure induces isomerization to the corresponding *Z*-configured isomer, maleamide (Figure 24 step 2). In the pss 50% maleamide can be achieved. This *Z*-configuration has a lower binding affinity than succinamide. Thus, after irradiation the macrocycle distribution changes to reinstall statistical balance. A new distribution with 56% of the rings binding succinamide and 44% binding the maleamide/ fumaramide position is achieved. By addition of piperidine or thermal energy supply, maleamide is converted back to

fumaramide and the initial ratio of occupancy can be restored. The mechanism described does not differ from a rotaxane shuttle mechanism, which represents a switching process. Hence, a hydroxy function was incorporated in the middle of the thread, which can be further functionalized to a bulky silyl ether. The bulkiness of the silyl ether is sufficient for preventing the ring to slip over it. After irradiation and installation of the new ring distribution, the bulky stopper is connected to the thread (Figure 24 step 3). A further balance-breaking stimulus restores the fumaramide station, but the macrocycles are prevented to restore equilibrium by the bulky stoppers (Figure 24 step 4). This was the first rotaxane-based example for generation and maintenance of a potential energy gradient by energy input, which is one of the prerequisites for realization of directional motion at the molecular scale. In the following years further examples of rotaxane based energy ratchets were established, which work with alternative energy inputs.[184] This working principle was further developed by the working groups of *Stoddart*[185] and *Credi*[186-187] by using energy input for directional threading and dethreading of linear axles through a macrocycle. Based on these results the group of *Stoddart* engineered a molecular pump, capable of threading several rings on a molecular axis.[188]
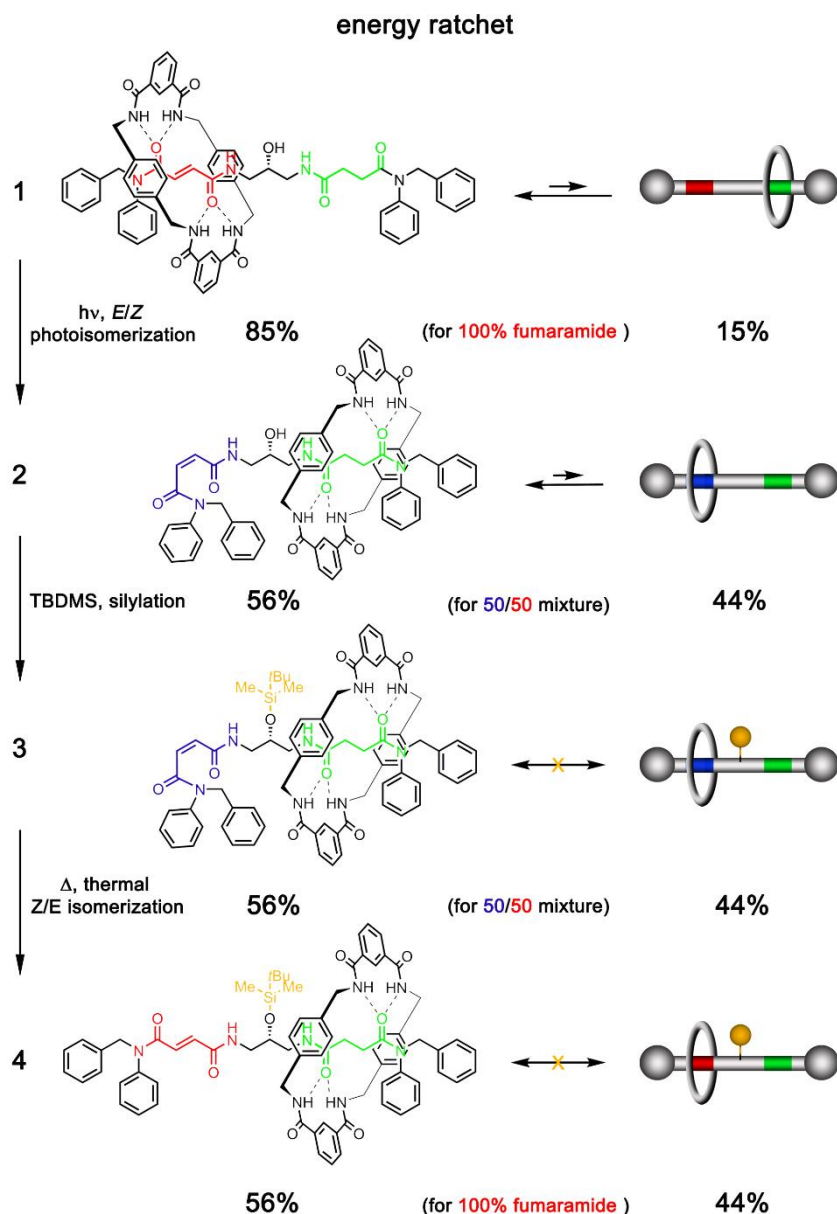
Figure 24: The light sensitive rotaxane demonstrates the energy ratchet mechanism. Ring positioning/population can be shifted by varying the relative binding affinities of different stations via external energy input. 1: 85% of the macrocycles bind the fumaramide stations (red) and 15% are located at the succinamide station (green). 2: After the light stimulus was presented 50% of the fumaramide stations are converted to maleamide stations (blue). For simplicity reasons only rotaxanes with newly formed maleamide stations are shown. The depicted ring distribution of 56% represents the total sum of rings binding either to the remaining fumaramide or to switched maleamide. 3: By increasing the kinetic stability of the metastable ring distribution, maintenance of out of equilibrium conditions is ensured. 4: Ring distribution does not alter after the fumaramide station is recovered. A major advantage is, that kinetic stability can be in turn decreased easily by removal of the blocking group, which allows for gradient release.

A very similar rotaxane setup was used for the successful realization of an information ratchet,[189] which is shown in Figure 25. The rotaxane consists again of a macrocycle surrounding a thread with bulky stoppers at each end. The thread incorporates two binding sites with identical binding affinities. This was achieved by two fumaramide groups, while one of them bears two deuterium at the double bond. Thus, the fumaramides can be distinguished by ^{1}H NMR spectroscopy. By neglecting deuteration the rotaxane with the macrocycle binding at the left station and the reversely occupied rotaxane can be regarded as enantiomeric structures. Between the two binding sites again a hydroxyl function is incorporated. In the following an esterification of the hydroxyl group takes place under presence of a chiral catalyst. The hydroxyl function is close enough to the binding sites for the macrocycle to sterically interfere with the acylation reaction. The DMAP-based catalyst and the benzoic anhydride form an activated chiral species, which favorably reacts with the hydroxy group of the rotaxanes, where the macrocycles show less sterical interference. As result an enantiomeric access of macrocycle distribution is achieved. If a catalyst with opposite chirality is used, inverse macrocycle distribution is achieved, while a 50/50 distribution results from an achiral catalyst. In summary, this information ratchet can shift a 50/50 distribution towards a 67/33 ratio by using a chiral catalyst for introduction of the blocking group. As the installed ester hinders the macrocycle to flip between the compartments, the out-of-equilibrium condition is maintained. Thus, in contrast to the energy ratchet shown above, the population gradient as well as kinetic inertness is installed simultaneously. The group of *Leigh* further developed an information ratchet with three stations[190] as well as a light triggered ratchet.[191]

information ratchet
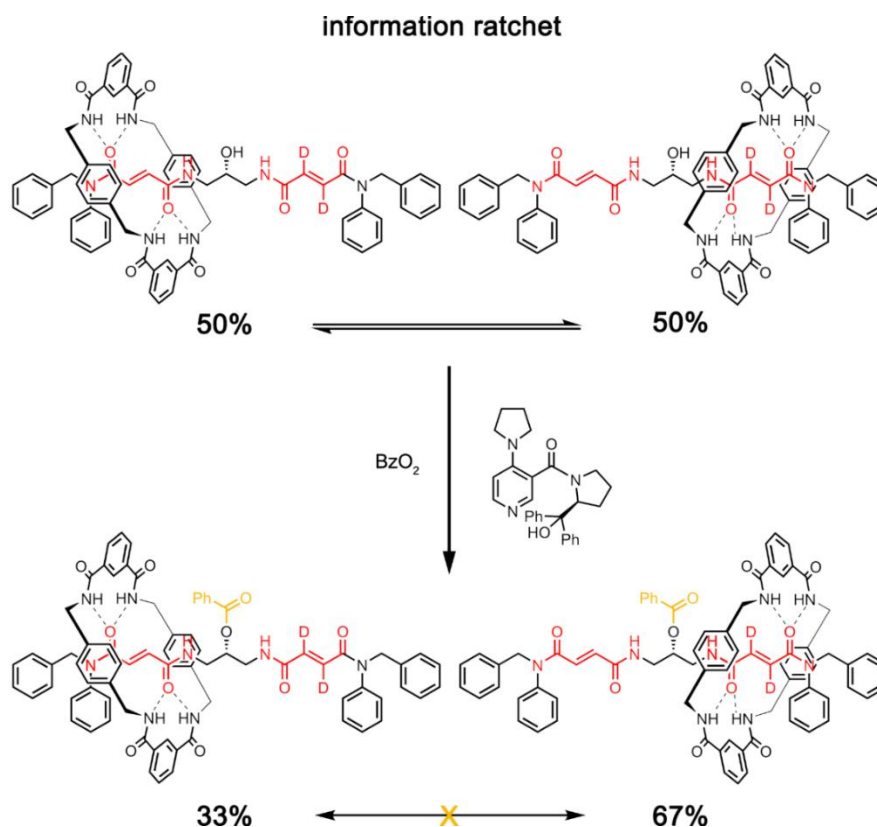
Figure 25:   The illustrated rotaxane works on the basis of the information ratchet mechanism. Binding stations are energetically equal, which results in a 50/50 distribution in equilibrium conditions. By introduction of a blocking group in the presence of a chiral catalyst ring distribution can be shifted in favour of the enantiomer shown in the right. The catalyst literally senses the position of the ring, which leads to an increase of the kinetic barrier for backwards reaction.

3.6.7   Catenane based rotary motors

Based on the results of the rotaxane based ratchets, mechanically interlocked catenanes were developed, which were capable of energy transduction into unidirectional motion. Catenanes are similar to rotaxanes, but the thread's ends are covalently linked to form a ring. In contrast to conventional rotaxanes, these molecules allow for exploiting an energy gradient to generate a directional motion, which does not cancel out directionality accompanied with gradient installation. The group of *Leigh* successfully applied the energy,[192] as well as the information ratchet mechanism[193] for rotational motion of a macrocycle around a cyclic thread. Both examples are illustrated in Figure 26. The energy ratchet is based on a catenane, with a cyclic thread incorporating two different binding sites, e.g. a fumaramide station and a succinamide station (see Figure 26a). A benzylic amide macrocycle surrounds the thread. The succinamide station is flanked with two blocking groups, e.g. a silyl protecting group and a trityl protecting group, which exhibit orthogonal addressability. At the beginning of the rotation cycle, the macrocycle is attached to the fumaramide station (Figure 26a step 1). Removal of the silyl group and consecutive *E*/*Z* isomerization via light input, leads the macrocycle to translocate preferably

to the succinamide station (Figure 26a step 2 and 3). Since the succinamide station is only available from the unprotected compartment, motion occurs in clockwise fashion. Reprotection impedes a backwards reaction (Figure 26a step 4). *Z/E* isomerization can be achieved by addition of piperidine, which restores the fumaramide station with the highest binding affinity for the macrocycle (Figure 26a step 5). Establishment of detailed balance is achieved by removal of the trityl protecting group, which allows for ring translocation in a clockwise fashion (Figure 26a step 6). In summary, a 360° clockwise rotation of the macrocycle in relation to the cyclic thread occurred. Directionality is easily inverted, if the sequence of blocking group attachment is reversed. Overall, a sequence of several inputs is necessary for the directional motion to occur, in contrast to the information ratchet (see Figure 26b), which is capable of continous directional rotary motion, if sufficient fuel supply is available.
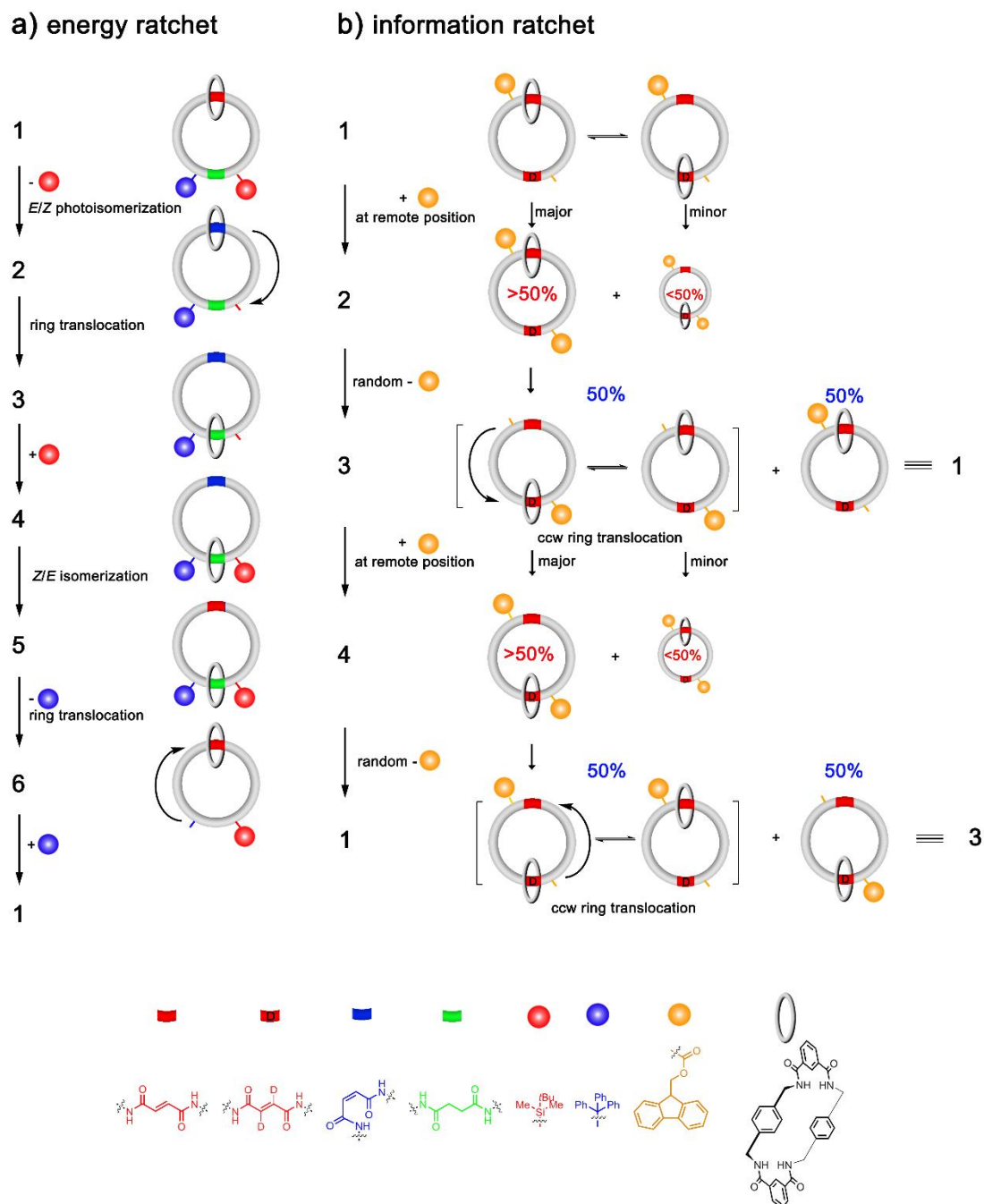
Figure 26:   Both catenanes perform unidirectional rotation of the macrocycle in relation to its cyclic thread. a) The energy ratchet principle is applied. A sequence of several inputs leads to rotary motion. By facile reversal of blocking group detachment and attachment, the directionality can be inverted. b) The information ratchet principle is applied. A continous unidirectional rotation occurs as long as sufficient fuel is supplied, but directionality cannot be changed.

The information ratchet based catenane (Figure 26b) consists of a cyclic thread, which incorporates two fumaramide binding sites with identical binding affinity. Magnetic distinctness was achieved by using

one deuterated fumaramide station. Each station is onesidedly neighbored by a hydroxy group. The rotation cycle starts with one Fmoc protecting group linked to one hydroxyl group (Figure 26b step 1). Under the provided conditions, protection and deprotection are constantly repeated as long as the fuel FmocCl is available. FmocCl concentration is sufficiently high to minimize the concentration of fully unprotected catenane. Installation of the second protecting group proceeds preferably at the hydroxyl group situated next to the unoccupied binding site, since steric interference with the macrocycle is avoided (Figure 26b step 2). The following deprotection reaction is unbiased, since the underlying reaction mechanism is inherently different and not prone to steric hindrance. Thus, a 50/50 distribution of deprotected catenanes can be observed. If the previously installed protecting group is removed, the initial starting point is restored and the rotation cycle is reset (Figure 26b step: 2, right arrow). If the protecting group located next to the macrocycle is removed a translocation in counterclockwise fashion, until equilibrium condition is reached, occurs (Figure 26b: step 3). Reprotection proceeds again in remote position to the macrocycle and hinders a backwards rotation (Figure 26b: step 4). Random deprotection leads either to restoration of an earlier stage of the rotation cycle analogue to the first deprotection (Figure 26b: step 4 right arrow), or to detachment of the blocking group next to the macrocycle (Figure 26b: step 5). In the second case a counterclockwise fashioned translocation leads to the starting point of the rotation cycle. The overall directionality is determined by the biased attachment of the blocking groups. Unbiased deprotection diminishes unidirectional motion yield per consumed FmocCl, but does not cancel out directed motion accompanied with the biased blocking group attachment.

4. Hemithioindigo based molecular motors

The data available at the beginning of this work are described in the following and accentuates the need for new HTI motor derivatives. Based on the findings of the investigations on motor **1**, derivatives **2-5** were synthesized to decipher intricate details of the rotation cycle of HTI-based molecular motors.
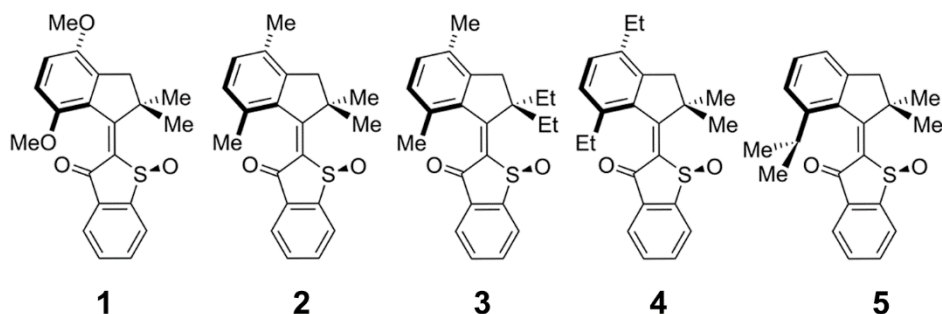
Figure 27:   HTI-based molecular motors **1-5**. Only *E*-(*S*)-(*P*)-configured isomers are shown for clarity.

4.1   Aim

In 2015 the working group of *Dube* reported on the first HTI based molecular motor **1**.[1] Directionality of the rotational motion was proven by low temperature ^{1}H NMR spectroscopy using an *in situ* irradiation technique. As depicted in Figure 27, irradiation of a solution of isomer **C** with 460 nm at – 90 °C leads to the formation of the metastable isomer **D**, which thermally converts to the thermodynamically more stable isomer **A**. First-order kinetic analysis of this process revealed a thermal barrier of 13.10 kcal·mol^{-1}, which is in good agreement with the theoretically predicted value of 14.6 kcal·mol^{-1}. Another light induced isomerization, should lead, as predicted by theoretical assessment, to the formation of the metastable isomer **B**, which is again followed by a thermal process converting the metastable isomer **B** to the stable isomer **C**. As the thermal barrier for this helix inversion was calculated to be 5.52 kcal·mol^{-1} ($t_{1/2} = 2$ µs), it was not possible to detect a new set of signals derived from the metastable isomer **B** even at –100 °C (($t_{1/2} = 2$ µs at –100 °C) by ^{1}H NMR spectroscopy. Hence irradiation of pure isomer **A**, resulted directly in the observation of the stable isomer **C** in the low temperature measurements. Irradiation of pure isomer **C** however initiated the formation of the metastable isomer **D**, which is then accompanied by a delayed thermal formation of the stable isomer **A** at suitable temperatures. The absence of the metastable isomer **D** in the case of the irradiation of isomer **A** indicates that two different photoinduced processes for each stable isomer have to be present, which do not cancel each other out in directionality. In combination with the thermal helix inversion of the metastable isomer **D**, which breaks microscopic reversibility for the overall process, the observations evidenced a completely directional cycle.
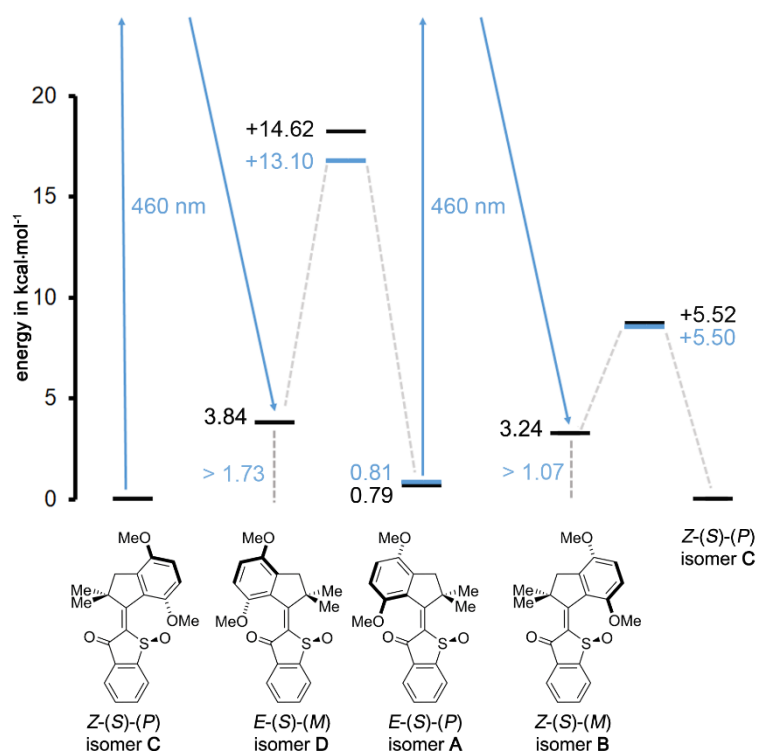
Figure 28: Energy profile of HTI based motor **1**. Only the (*S*)-configured enantiomer is shown for clarity. Calculated energies at the MPW1K level of theory with 6-31 + G(d,p) basis set are labelled in black and measured values are labelled in blue. Light induced processes are depicted as blue arrows. Thermal processes are indicated with grey dashed lines. All experimental values were obtained by variable temperature ^{1}H NMR spectroscopy[1] with the exception of the Gibbs free energy of activation of the thermal helix inversion from the metastable isomer **B** to isomer **C**, which was obtained by ultrafast UV/vis spectroscopy.[102] For details on isomer numbering and stereodescriptors see chapter 2.3.1.

But still, the experimental evidence of the theoretically predicted metastable isomer **B** remained elusive. The presented analysis does not allow a clear and evidence based deduction of the underlying motion of the light triggered transformation of isomer **A** to isomer **C**. By detection of isomer **B**, it could be concluded that the major displacements proceed via a clockwise (cw) rotation around the central double bond. In principle a counterclockwise (ccw) rotation induced by photoexcitation of isomer **A** could also be possible, but if so, the existence of isomer **D** observed as the photoproduct of isomer **C** requires necessarily additional trajectories (e.g. kinking or pyramidalization, see Figure 29b) to accompany the ccw rotation, prohibiting the formation of isomer **D** in this excited state pathway. Thus, the only plausible option should be a strongly distorted or kinked, but still counterclockwise fashioned motion. By observation of the elusive isomer **B** this unlikely alternative could be excluded unambiguously.
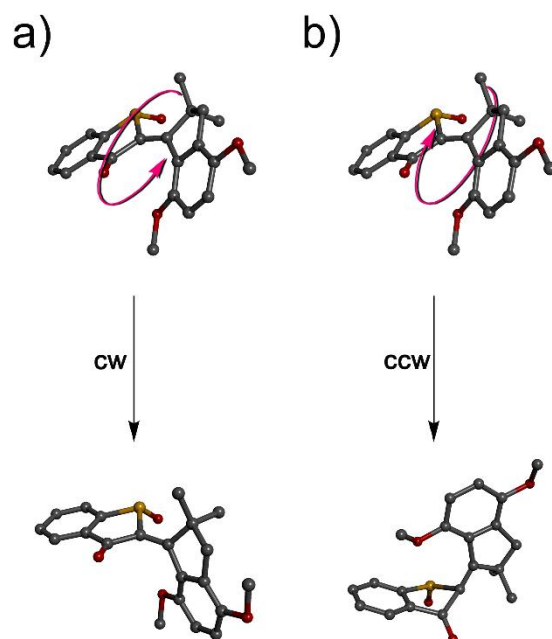
Figure 29:   Two possible rotational modes for the photoisomerization of **A-1**. a) The clockwise rotation is depicted by an arbitrarily selected intermediate at about 90° of rotation around the central double bond. b) The counterclockwise mode of rotation is depicted by a strongly distorted molecular structure at a rotational degree of about 90° of the central double bond. Clockwise and counterclockwise are defined by using the benzothiophenone part as the fixed point of view.

To elucidate the light induced process(es) behind the **A** to **C** conversion, time resolved absorption spectroscopy of isomer **A** was conducted. The obtained spectra revealed a hitherto unknown exited state species, which could be attributed to a triplet state, because of its unusual red shifted absorption (up to 550 nm) and lifetime (100 ns). The predominance and long lifetime of this absorption band hampered the observation of the elusive isomer **B**. These results did not exclude the likely existence of the metastable isomer **B**, but brought into play the possibility of an optional isomerization pathway via a triplet state, which could also, in theory, be consistent with the earlier observations of two different photoequilibria made by ^{1}H NMR spectroscopy. Also, the underlying motion behind this triplet pathway could be the aforementioned distorted and counterclockwise rotation. A further drawback, if the conversion of the isomer **A** to isomer **C** is mediated by a triplet state, is that details about the underlying trajectories of this conversion are hardly accessible because conformational analysis in the excited state is aggravated by short excited state lifetimes and low spectral resolution power.
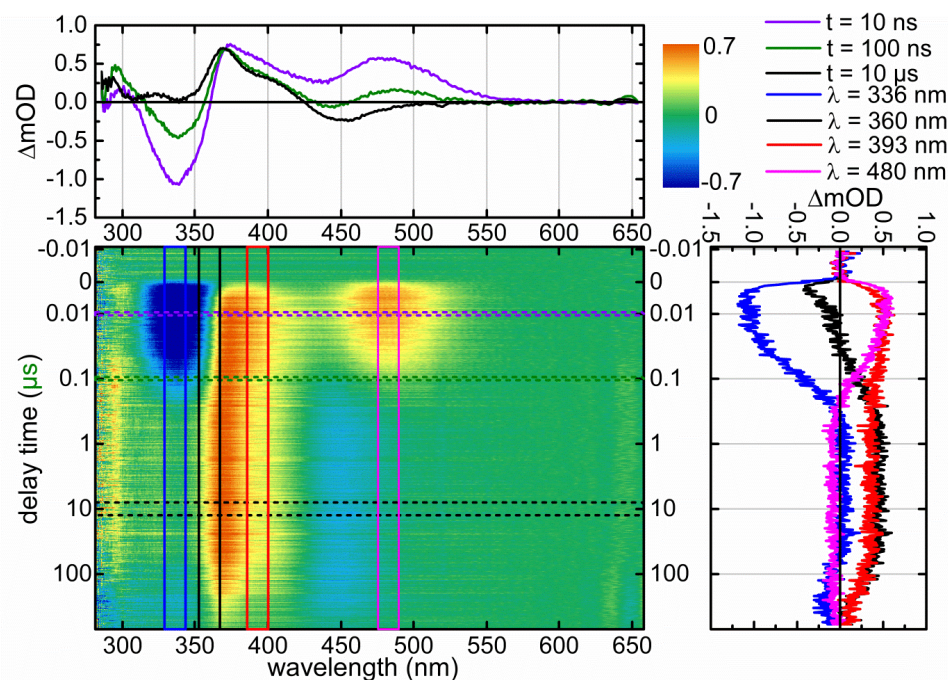
Figure 30: The time resolved absorption spectra of **A**-**1** after optical excitation with 460 nm in CH₂Cl₂ at 22 °C on the ns/µs time scale. The red shifted absorption revealed an unusual shoulder up to 550 nm and decays with a time constant of 100 ns. Reprinted with permission from *J. Am. Chem. Soc.* **2018**, *140*, 5311-5318. Copyright 2018 American Chemical Society.

The observations made by time resolved absorption spectroscopy stressed the importance of synthesizing new derivatives of HTI-based molecular motors, which rotate slow enough to observe both thermal processes by ^{1}H NMR spectroscopy. The apparent approach to increase the thermal barriers for the helix inversions, especially the conversion from **B** to **C**, is to raise the sterical hindrance in close proximity to the rotational axis, i.e. the central double bond. By installing bulky groups either at the aromatic ring of the indanyl part next to the double bond, or at the five-membered ring of the indanyl part in vicinal position to the double bond, the rotation around the central double bond should be aggravated, leading to higher barriers of the thermal helix inversions. In Figure 31b the promising positions for introducing sterical bulk are marked with blue circles. In order to ensure unambigous observation of the missing intermediate, it was deemed necessary to use a high resolution analytical method, i. e. to conduct low temperature ^{1}H NMR spectroscopy. The lowest temperature, which can be achieved with the Jeol NMR spectrometer setup available in our department is –105 °C. Under ideal conditions of high irradiation intensities and minimal acquisition time of a single ^{1}H NMR spectrum, intermediates should at least encounter a thermal activation barrier of about 11 kcal·mol⁻¹ (which can be translated to a half-life of about 40 sec at –105 °C) in order to have a chance for their detection. The energy scheme in Figure 31a shows that the thermal barrier of the **B** to **C** helix inversion of the first HTI-based molecular motor has to be raised by about 6 kcal·mol⁻¹ to be in a detectable range for low temperature ^{1}H NMR spectroscopy (green area in the energy profile of Figure 31a).

a)

b)
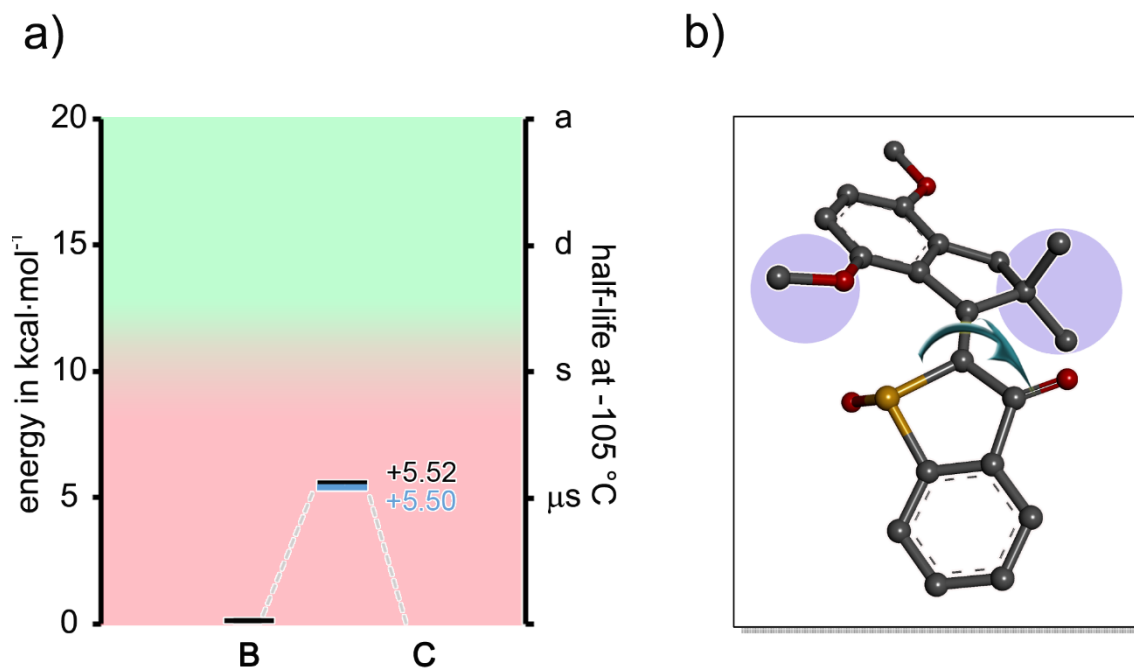
Figure 31: Increased sterical bulk in HTI molecular motors should raise the thermal activation energy barrier for the **B** to **C** helix inversion. a) Energy profile of the **B** to **C** helix inversion. The red area of the background indicates activation energy barriers, that are too low for observation by ^{1}H NMR spectroscopy at $-105°$ C. The green area depicts the convenient range for the observation of intermediates with thermal activation energy barriers higher than 11 kcal·mol^{-1}. b) The most promising positions for substitution, where increased sterical bulk should lead to higher activation energy barriers for both helix inversions, are highlighted with blue circles.

The first HTI-based molecular motor **1** was synthesized by a Lewis acid catalyzed condensation,[1] connecting a benzothiophenone **6** with an indanone **7** as key step. Final oxidation of HTI **8** leads to the corresponding sulfoxide **1** in a moderate yield of 12% over two steps as depicted in Figure 32a. To further increase the sterical hindrance around the double bond, *Guentner*[III] tried to condense indanones **9** and **10** with larger ethyl or *iso*-propyl groups in *ortho* position to the carbonyl function, either with benzothiophenone **6** or with its oxidized form **9** with different Lewis acids (Figure 32c entries 1-12). Indanones **10** and **11** were provided by *Schildhauer*[VIII]. In all cases no conversion could be observed. Further, by applying the original BF$_3$·OEt$_2$ mediated method *Mallon*[VI] tried to condense methylated indanone derivative **12** with benzothiophenone **6** (entry 13). But also in this case the condensation approach failed. In summary, all synthetic attempts to generate sterically hindered HTI motors using indanones **10**-**12** failed with the tested condensation conditions.
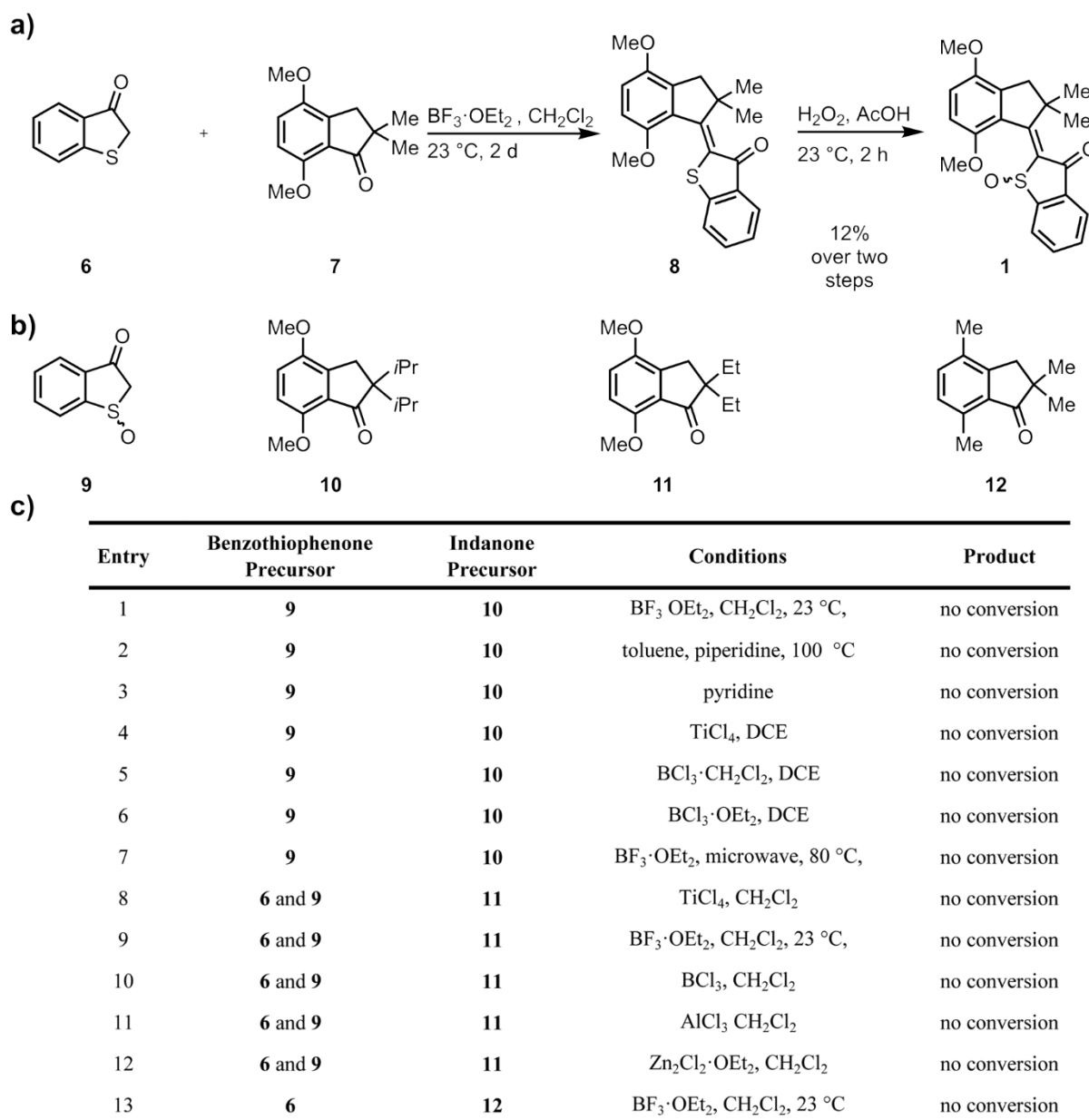
Figure 32: The preparation of the first HTI based molecular motor is presented.[1] a) Readily available precursor **7** is condensed under BF$_3$·OEt$_2$ catalysis with benzothiophenone **6** in CH$_2$Cl$_2$ at ambient temperatures for 2 days. **6** can easily be prepared from thiosalicylic acid over two steps employing an intramolecular *Friedel-Crafts* ring closing reaction.[194] A final oxidation of **8** with H$_2$O$_2$ in glacial acetic acid at ambient temperature furnishes the sulfoxide motor **1** in a moderate yield of 12% over two steps. b) Sterically more hindered indanones **10**, **11** and **12** were subjected to condensation with either **6** or **11**.[III, VI] c) The entries are summarized in the table.

4.2 Synthetic approach

4.2.1 Starting point of a new synthetic strategy

After the failed attempts to prepare sterically hindered HTI molecular motors revealed the limits of the condensation approach, different synthetic strategies were considered. Eventually it became clear that, instead of connecting the double bond in the final synthetic step, it would be favorable, if a different bond is formed at the end of the synthesis. Thus, the double bond could be installed at an earlier stage of the synthesis, where sterical hindrance is less pronounced. In the literature an interesting protocol by *Gang Zheng et al.*[195-196] for the synthesis of HTIs was found, with an iodine mediated intramolecular thiolation of the double bond as key step. The reaction is depicted in Scheme 1.
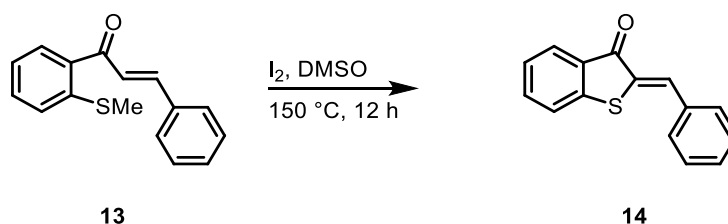
Scheme 1: 2-Methylthiophenyl vinyl ketone **13** can be cyclized to the corresponding HTI **14** upon treatment with I$_2$ as catalyst in DMSO at elevated temperatures.

4.2.2 Retrosynthetic analysis

A retrosynthetic analysis for sterically hindered HTI motors based on a late stage iodocyclization furnishes an α,β-unsaturated ketone **18** as intermediate structure. It could be obtained by an acid catalyzed *Meyer-Schuster* rearrangement[197] from propargylic alcohol **17** (Scheme 2). Access to **17** might be possible via nucleophilic attack of an *in situ* prepared lithiated acetylide species Li-**16** at the carbonyl function of **12**. Precursor **16** can be synthesized according to literature procedure[198] by a Pd-catalysed *Sonogashira* cross-coupling reaction[199] from aryl iodide **15**.

The key step of this synthetic strategy is arguably the nucleophilic attack of Li-**16** at the sterically hindered indanone. In order to get a rough estimate about the potential of this transformation to overcome sterics an investigation of chemical databases was carried out. Several examples report a successful nucleophilic attack to ketones with considerable sterical hindrance.[200-201] It seems that lithiated acetylide species, because of their high reactivity and minor size, could be the ideal nucleophile to get access to the key intermediate **17**.
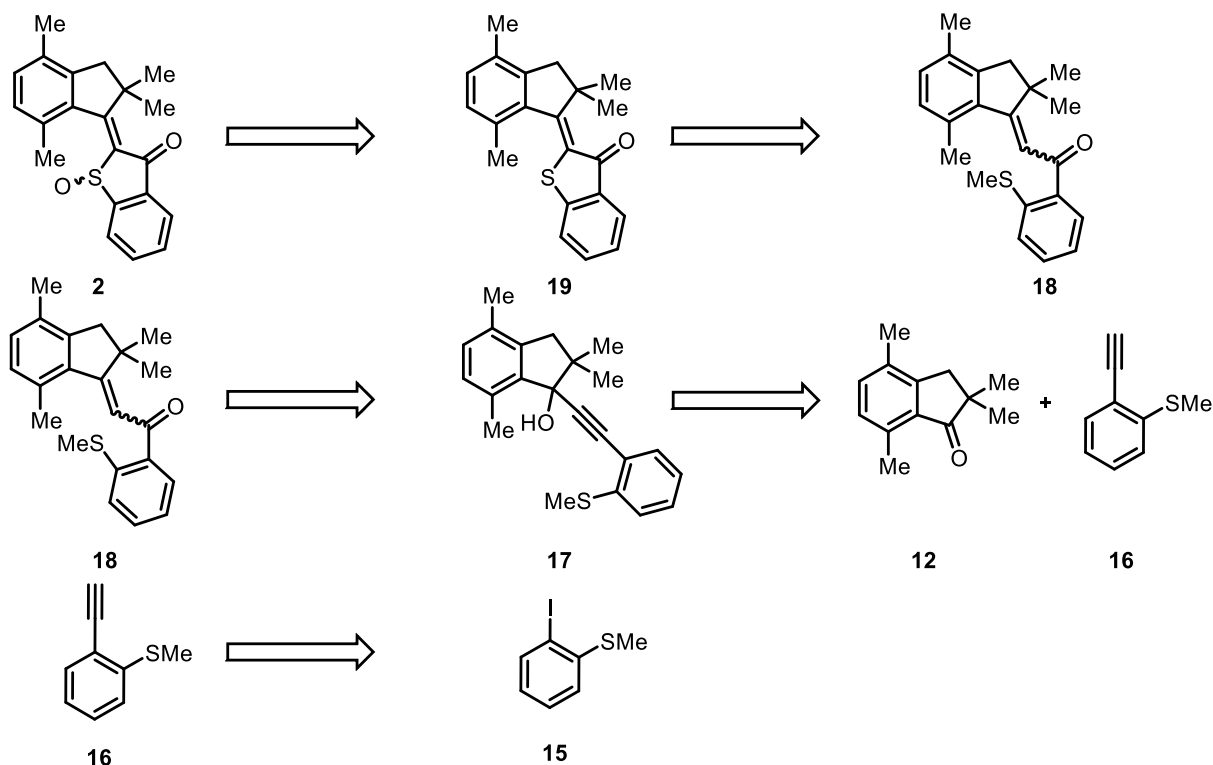
Scheme 2: A retrosynthetic analysis of sterically hindered HTI based motors illustrated exemplarily with motor **2**. Motor **2** could be obtained by oxidation of HTI **19**. Derivative **19** should be available by iodocyclization of compound **18** adapting the procedure of *Gang Zheng et al.*[196] A *Meyer-Schuster* rearrangement of propargylic alcohol **17** should deliver the precursor **18** for the cyclization. Propargylic alcohol should be accessible by nucleophilic attack of Li-**16** at the overcrowded indanone **12**. A Pd-catalyzed *Sonogashira* cross-coupling reaction should supply precursor **16**.

4.2.3 Model compound investigation using fluorenone 20

After establishing the retrosynthetic analysis, precursor 2-ethynyl thioanisole **16** was synthesized by a *Sonogashira* cross-coupling reaction[199] of aryl idode **15** with TMS-protected acetylene in a mixture of THF and N(Et)₃ according to a literature procedure.[198] After deprotection with KF **16** was obtained in an excellent yield of 92% (Scheme 3).
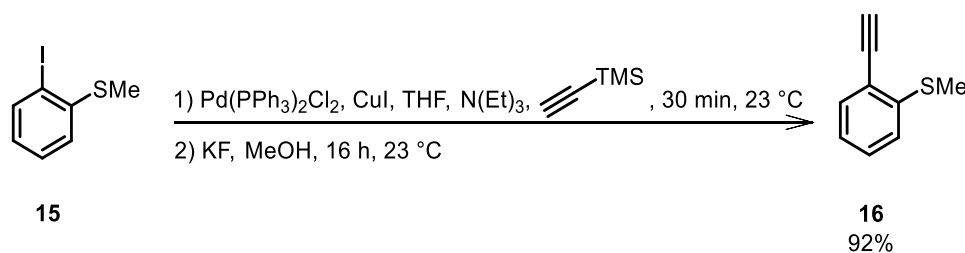
Scheme 3: 2-Iodo thioanisole **15** is converted to 2-ethinyl thioanisole **16** in a *Sonogashira* cross-coupling reaction, which proceeds in an excellent yield of 92% after deprotection with KF.

In order to test the potential of the addition of **16** to ketones with moderate reactivity, fluorenone **20** was used as a model compound for the new synthetic approach. After the *in situ* lithiation of **16** with *n*BuLi in dimethoxyethane, a solution of fluorenone **20** was added to the lithiated species. As a good starting point the reaction proceeded with a moderate yield of 56% (Scheme 4).
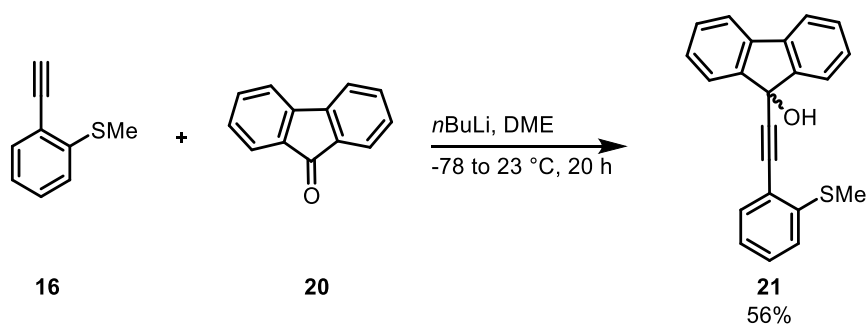
Scheme 4: Nucleophilic addition of *in situ* prepared Li-**16** to fluorenone **20**. Lithiation was performed at 78° C in dry dimethoxyethane over the course of 30 min. A solution of **20** in dimethoxyethane, was then added to the Li-**16** solution.

Next the *Meyer-Schuster* rearrangement[197] was investigated. Propargylic alcohol **21** was treated with c. sulfuric acid in glacial acetic acid. The colorless solution changed immediately into a deep red followed by a green to yellow color. After workup and purification the analytical data revealed the isolated product not as the excepted enone **22**, but the already cyclized HTI **23** (Scheme 5).
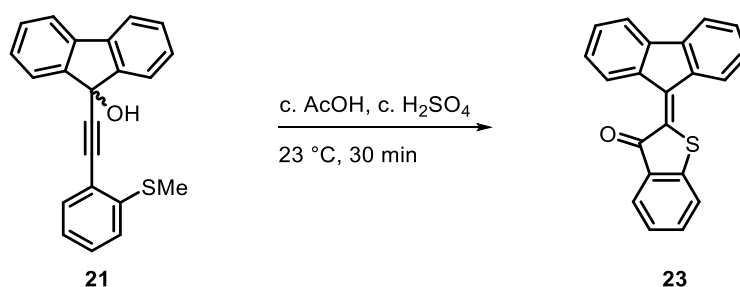
Scheme 5: Propargylic alcohol **21** is treated with c. AcOH and c. H$_2$SO$_4$ to furnish HTI **23** in a multi-step cascade reaction. Yield of the synthesis was not determined.

Further elucidation of this multi-step cyclization by testing different solvents and additives should reveal, if a *Meyer-Schuster* rearrangement product is a possible intermediate in this cascade reaction. The results are summarized in Table 2. Analyses were done exclusively by TLC.

Table 2: Testing the reactivity of propargylic alcohol **21** towards acidic additives in different solvents.

entry	solvent	additive	observation by TLC after 10 min	observation by TLC after 24 h	addition of I$_2$
1	AcOH	H$_2$SO$_4$	Enone **22** + HTI **23**	HTI **23**	Not added
2	EtOH	H$_2$SO$_4$	Enone **22**	Enone **22**	Not added
3	CH$_2$Cl$_2$	BF$_3$·OEt$_2$	Enone **22**	Enone **22**	Not added
4	THF	H$_2$SO$_4$	Enone **22** + HTI **23**	-	HTI **23**

As entry 1 and 4 show, the *Meyer-Schuster* rearrangement product **22** could be detected by TLC after short reaction times. Furthermore, addition of I$_2$ in the case of entry 4 yielded conversion to HTI **23**, proving that the iodocyclization as described in the literature, furnishes indeed the desired HTI **23**. Entry 2 was repeated to verify the reaction product as the enone **22**. NMR spectroscopic analysis of the purified product confirmed this assumption.
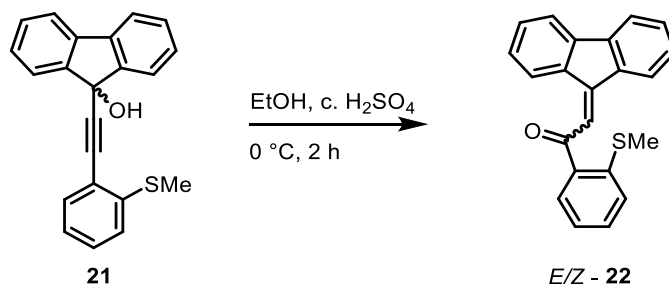
Scheme 6:   At lower temperatures, using EtOH as solvent, propargylic alcohol **21** can be transformed to the *Meyer-Schuster* rearrangement product **22**.

4.2.4   Synthesis of tetramethylated motor 2

These findings allowed the conclusion, that the multi-step cascade reaction from propargylic alcohol **21** to HTI **23** proceeds most likely via a *Meyer-Schuster* rearrangement product **22**, which consecutively reacts to HTI **23** under acidic conditions (table 2, entry 1), but also by treatment with I_2 (table 2, entry 4). Since the preliminary investigations on the model compound were successful, the synthesis of a potential molecular motor with high energy barriers of rotation was explored next. A suitable indanone precursor is tetramethylated indanone **12**, which should exhibit greater steric demand as methoxy-substituted indanone **7**. The synthesis of indanone **12** is described in Scheme 7.[202-204] Commercivley available *p*-xylene was treated with 3-chloro propionic acid chloride in the presence of $AlCl_3$ and was consecutively refluxed in c. sulphuric acid to undergo a *Friedel-Crafts* acylation and alkylation reaction to yield indanone **24**. The optimized yields, presented in Scheme 7, were obtained by *Niklas Böcher*[I] after reducing the reaction times, including a workup and using CH_2Cl_2 as solvent instead of previously used CS_2 (increased the yield from 40% to 84% for the first step from *p*-xylene to indanone **24**).
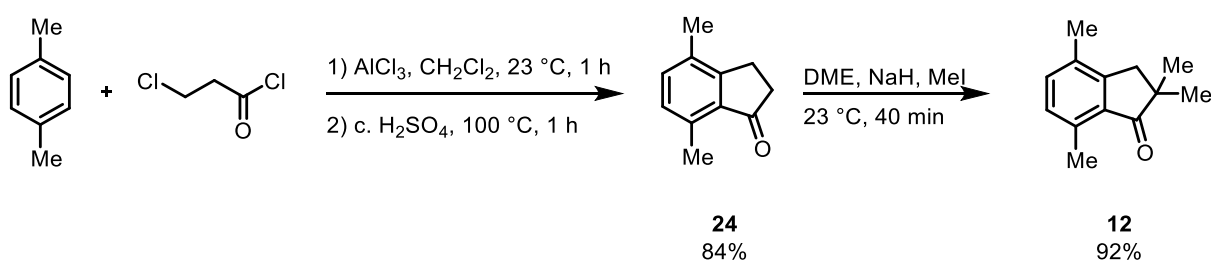
Scheme 7:   Synthesis of indanone **12** over two steps by applying a consecutive *Friedel-Crafts* acylation alkylation method and a twofold nucleophilic substitution reaction.

The nucleophilic addition of **16** to indanone **12** and the following *Meyer-Schuster* rearrangement to enone **18** was successfully explored as depicted in Scheme 8. The desired multi-step cyclization reaction

however, which was observed with fluorenone-derived propargylic alcohol **21**, did not take place in the case of propargylic alcohol **17**, when treated with c. H$_2$SO$_4$ in c. acetic acid.

For the nucleophilic addition acetylene **16** was treated with *n*BuLi in THF at –78°C before indanone **12** was added to the reaction mixture to furnish propargylic alcohol **17** in a moderate yield of 49%. After scrutinizing the ideal conditions *Niklas Böcher* could achieve an excellent yield of 97% by establishing an optimized lithiation protocol (addition of *n*BuLi at –78 °C and warming up to 0 °C within 15 min) as well as using freshly titrated *n*BuLi and dry THF. A very good yield for the *Meyer-Schuster* rearrangement of 92% was achieved after changing the solvent from EtOH to THF.
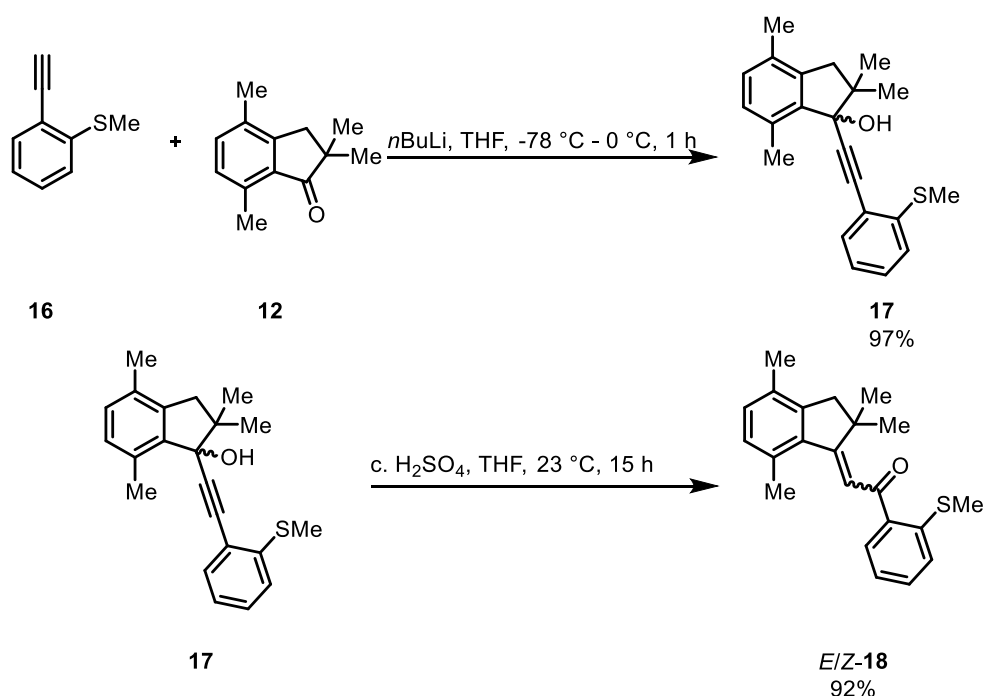
Scheme 8:   Synthesis of propargylic alcohol **17** in an excellent yield by *in situ* lithiation of acetylene **16** and consecutive quenching with indanone **12.** Acid catalyzed *Meyer-Schuster* rearrangement afforded enone **18** in a very good yield.

Unfortunately the multi-step cyclization under acid catalysis from propargylic alcohol did not occur in case of **17**. Thus, iodocyclization of enone **18** should provide HTI **19** instead. However, treatment of enone **18** with I$_2$ in DMSO at elevated temperatures showed no conversion. In Table 3 the conditions to synthesize HTI **19** either from enone **18** or directly from propargylic alcohol **17** are summarized. Also a radical mediated approach was investigated in entries 3 and 4.

Table 3: Applied conditions to convert propargylic alcohol **17** or enone **18** to the HTI **19**.

entry	compound	additive	solvent	observation by TLC
1	**18**	I_2	DMSO	No conversion
2	**18**	c. H_2SO_4	c. AcOH	No conversion
3	**18**	DBPO	-	No conversion
4	**18**	SO_2Cl_2	-	No conversion
5	**17**	c. H_2SO_4 then I_2	EtOH	No conversion
6	**17**	$BF_3 \cdot OEt_2$ then I_2	CH_2Cl_2	No conversion

The possible reason why the iodine mediated cyclization failed in case of enone **18** could be the pronounced sterical hindrance at the double bond of **18**, which prevents the intermittent formation of an iodonium ion, postulated by the investigators of the iodocyclization protocol.[196] Furthermore, bond connection between the sulfur atom and the α-carbon of the enone functional group is aggravated by the nucleophilic character of sulfur, which would rather react, either with the electrophilic carbonyl function, or with the soft charactered β-carbon of the enone function. Both reactions would not lead to the desired product. The solution was found by studying the mechanism of the *Swern* reaction[205] - an oxidation protocol for primary and secondary alcohols. The mechanism is depicted in Scheme 9a. This very powerful, but mild oxidation method uses the inherent reactivity of an *in situ* generated chlorosulfonium ion by treatment of DMSO with oxalyl chloride. The chlorosulfonium ion is subsequently attacked by the nucleophilic alcohol. Deprotonation of an acidified hydrogen atom geminal to the hydroxy function leads to the oxidation of the alcohol to the corresponding ketone or aldehyde, while dimethylsulfide is formed as side product. Further studies reported about the reactivity of chlorosulfonium salts,[206-207] e.g. the hexachloroantimonate or tetrafluoroborate, with various different sulfur-, oxygen- and carbon-based nucleophiles, as depicted in Scheme 9b.

a)

b)
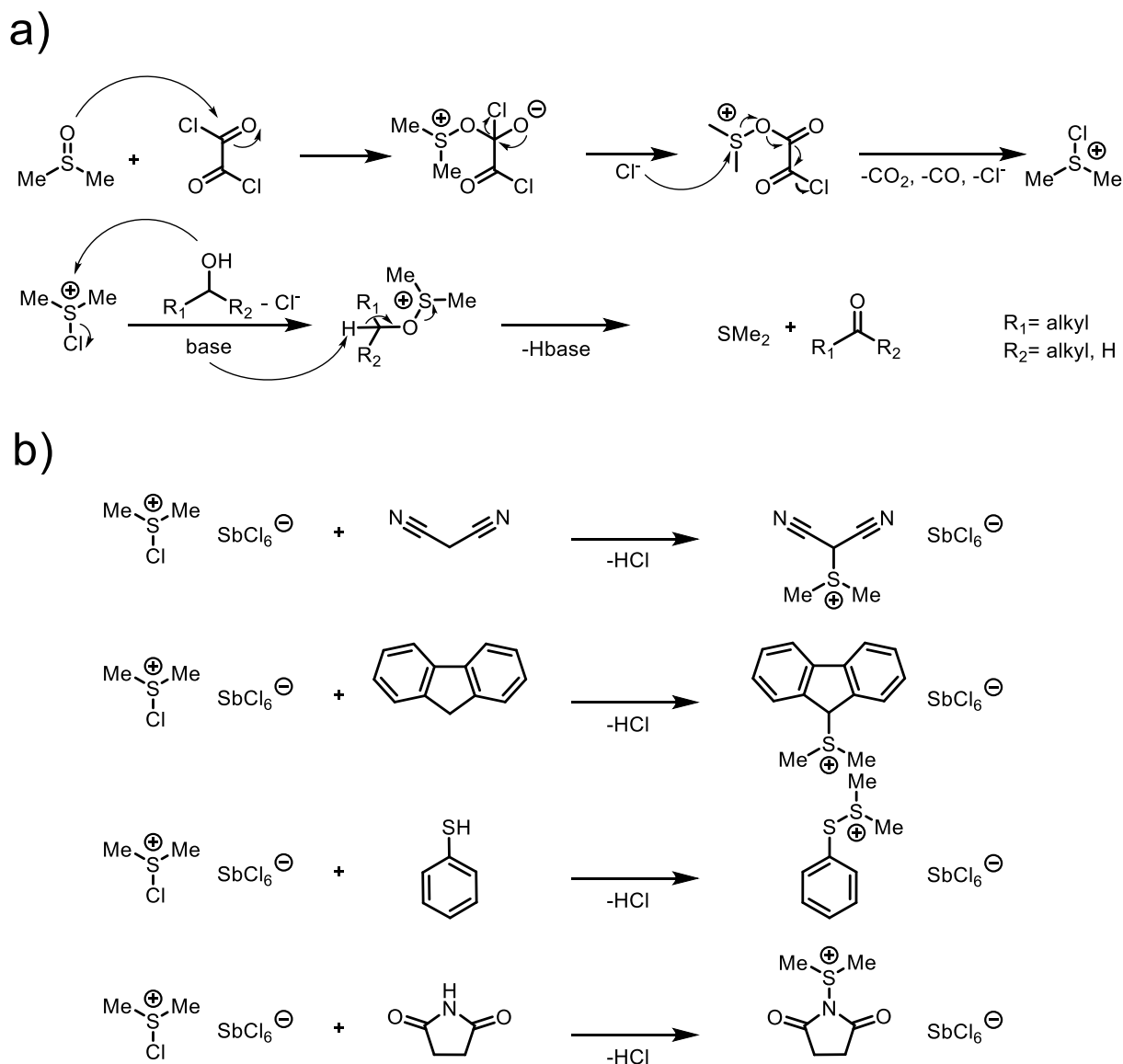
Scheme 9: Chlorosulfonium ions exhibit electrophilic character, which can be used for the oxidation of alcohols or for nucleophilic substitutions. a) The mechanism of the *Swern* oxidation is depicted. b) Several nucleophiles are capable of reacting with chlorosulfonium salts.

Based on these results, it was elucidated if the electrophilic character of a chlorosulfonium ion could supply enough driving force to initiate a nucleophilic attack of the double bond of the enone function at the sulfur atom. To verify this hypothesis enone **18** was oxidized to the corresponding racemic sulfoxide **25** with sodium perborate tetrahydrate in c. acetic acid in a very good yield of 92% (Scheme 10). Sulfoxide **25** was then treated with oxalyl chloride in ethyl acetate. A colour change occurred from pale yellow to deep orange, accompanied by vigorous gas evolution. Spectroscopic analysis of the purified product confirmed the formation of HTI **19** in a moderate yield of 56%. After optimization of this protocol, the cyclization of sulfoxide **25** in CH$_2$Cl$_2$ at lower temperatures furnishes HTI **19** in a very good yield of 88%. Final oxidation with sodium perborate tetrahydrate, lead to the product **2** in a

moderate yield of 56%. *Kerstin Hoffmann*[IV] could increase the yield to excellent 93% by reduced reaction times and addition of 3-4 equivalents of oxidizing agent. [IV]

E/Z-**18**

perborate, c. AcOH

23 °C, 45 min

E/Z-**25**

92%

(CO)$_2$Cl$_2$, CH$_2$Cl$_2$

-50 to -30 °C, 2 h

E/Z-**19**

88%

E/Z-**19**

perborate, c. AcOH

23 °C, 3 h

E/Z-**2**

93%
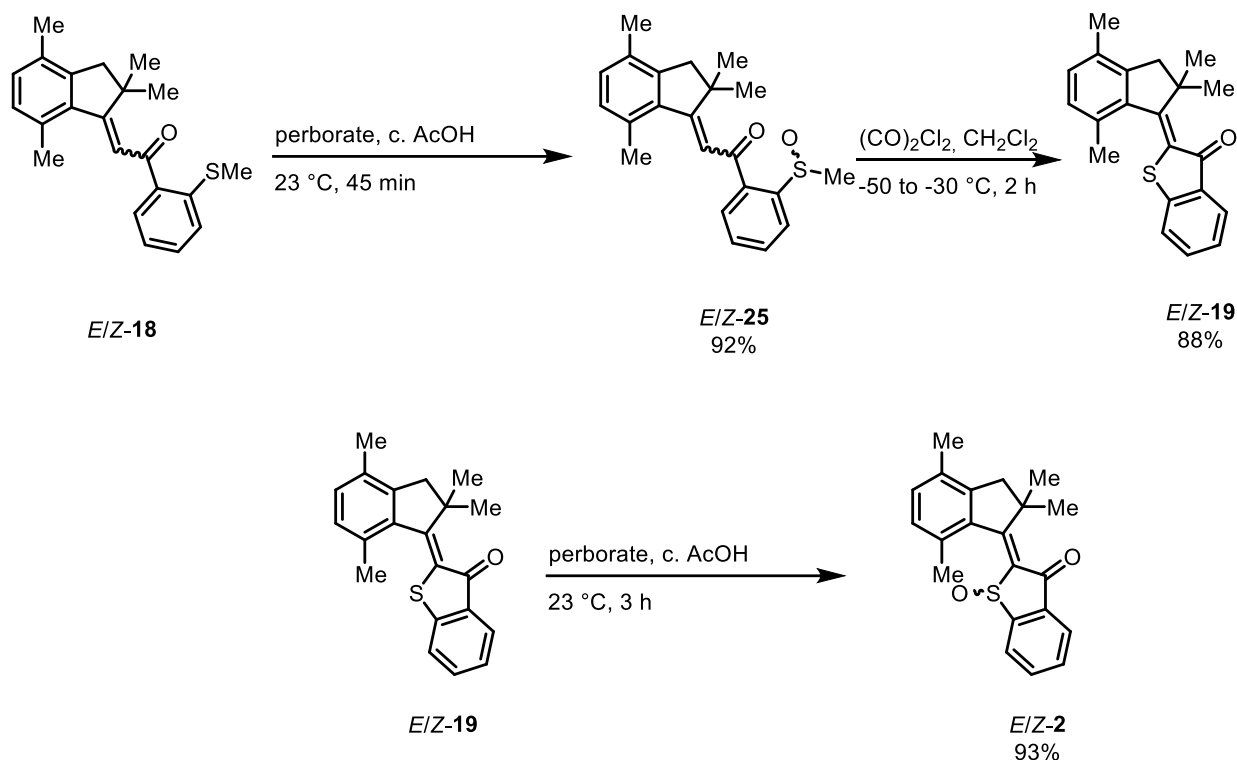
Scheme 10: Reaction pathway towards motor **2** over three steps. Oxidation of enone **18** to racemic sulfoxide **25**. *In situ* generation of the chlorosulfonium ion from sulfoxide **25** efficiently reacts to the HTI **19**. A final oxidation provides the motor **2**.

The overall yield of the second HTI-based molecular motor over 5 steps starting from acetylene **16** and tetramethylated indanone **12** could thus be optimized to excellent 67% proving the potential of the new synthetic route as a very efficient and powerful tool to get access to sterically hindered molecular motors. A detailed mechanistic exploration of the intramolecular cyclization of sulfoxide **25** induced by the addition of oxalyl chloride was not performed due to time restrictions. A likely mechanistic explanation is depicted in Scheme 11. As already mentioned the generation of a chlorosulfonium ion is expected, according to the mechanism proposed for the *Swern* oxidation. As a result a nucleophilic attack of the double bond at the sulfur atom should occur to expel a chloride ion in a substitution reaction. Subsequently, a doubly charged intermediate is formed, which is deprotonated by a chloride anion to reinstall conjugation between the two aromatic fragments. HTI **19** is created in the final step by an SN$_2$-type nucleophilic substitution reaction at the carbon atom with a chloride anion as nucleophile and the sulfonium ion as leaving group, leading to methyl chloride as side product.
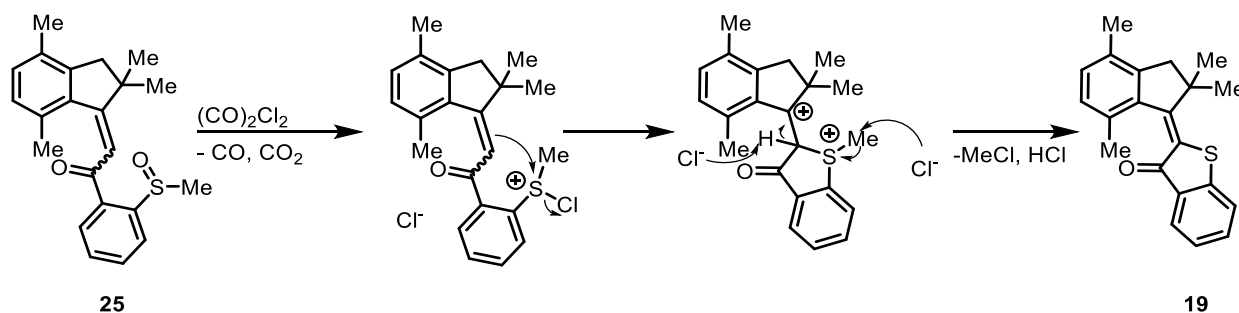
Scheme 11:   Proposed mechanism for the intramolecular cyclization reaction of sulfoxide **25** to HTI **19**.

4.2.5   Exploration of suitable indanone precursors for slow rotating molecular motors

In order to explore the scope of the synthesis, sterically more hindered indanones were prepared according to Scheme 12. In most cases the same synthetic approach[202-203] was applied to provide indanone derivatives. Derivative **26** was synthesized by *Voßiek*.[X] [208] The protocol using NaH to deprotonate the indanone **30** in α-position to the carbonyl function did not furnish the expected twofold methylated indanone **31** but, as reaction control by GCMS indicated, a debromination. An *ipso*-substitution of the bromide, facilitated by the electron withdrawing effect of the carbonyl function and the enhanced ability of a bromide anion to act as leaving group could be a mechanistic explanation. Indanone **31** was therefore synthesized using KO*t*Bu as base instead. Interestingly, the yield for the alkylation decreased significantly from 84% for indanone **26** to 43% for indanone **29**. This could likely be attributed to the increased sterical hindrance of the *iso*-propyl groups compared to ethyl groups. Indanone **36** was obtained by aldol addition with 68% yield by adopting a literature procedure.[209]
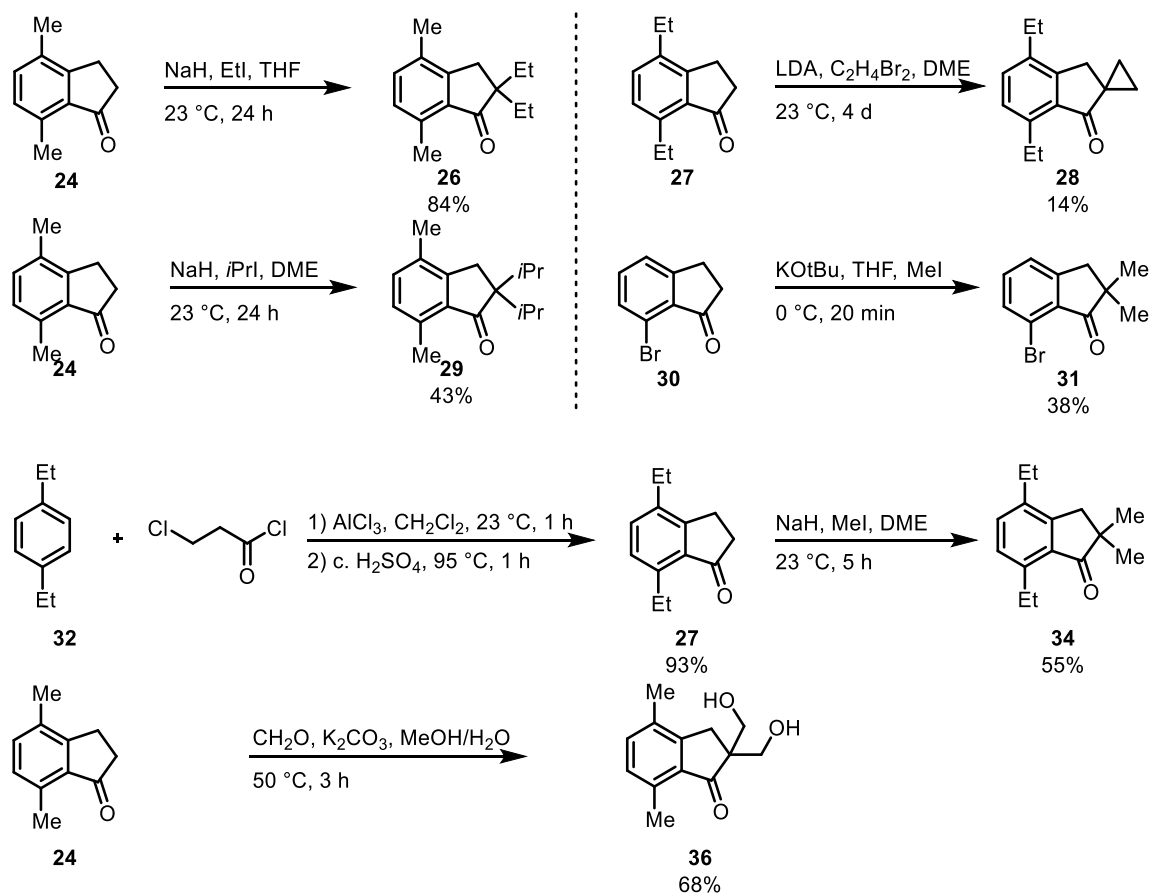
Scheme 12: Several different indanones were synthesized in order to explore the scope of the synthesis and finding a motor derivative, which provides slow rotation to analyze the full motion cycle. Derivative **26** was synthesized by *Voßiek*.[X] [208]

4.2.6 Syntheses of ethylated motor derivatives 3 and 4

The synthesis of motor derivative **3** commences with the addition of Li-**16** at indanone **26**, bearing ethyl groups at the five membered ring in vicinal position to the carbonyl function. The reactions proceeds with 75% yield of propargylic alcohol **38** by applying an optimized protocol variant from the above mentioned method by using two equivalents of the Li-**16** to ensure full conversion of indanone **26**. *Meyer-Schuster* rearrangement towards enone **39** and oxidation of the latter yielded racemic sulfoxide **40**, which was converted to the corresponding HTI **41** by addition of oxalyl chloride. Final racemic oxidation delivers the third motor derivate **3** in 79% yield. The protocol works without purification of synthetic intermediates, starting from propargylic alcohol **38**. The overall yield is hence 59% over five steps. The synthesis of motor derivative **4**, starting with indanone **34**, bearing ethyl groups at the aromatic core, was scrutinized, too. The formation of propargylic alcohol **42** proceeded with a very good yield of 89%. The same protocol, which omits purification of intermediates, was applied and delivered the fourth motor derivate **4**, starting with **42** in an excellent yield of 69%. The overall yield is 61% over five steps. The syntheses of motor derivatives **3** and **4** are summarized in Scheme 13.
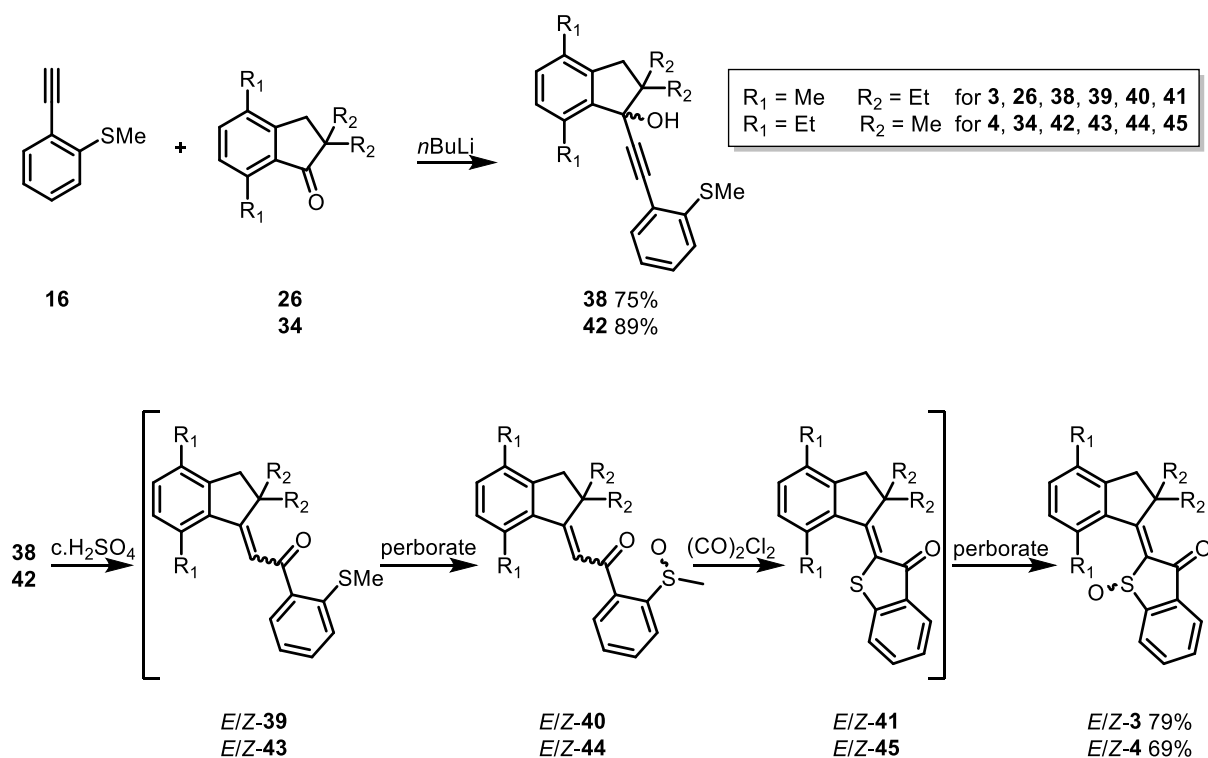
Scheme 13: Summary of the syntheses of motor derivatives **3** and **4**. For derivative **3** and **4** a concise protocol was applied which omits the purification of intermediates **39**-**41** and **43**-**45**. The scope of the new protocol could be extended to more sterical demanding motors.

4.2.7 Synthetic approach towards motors with cyclopropyl- and *iso*-propyl groups

Since none of the new derivatives could supply sufficient thermal barriers for the observation of the missing intermediate **B** (*Z*-(*S*)-*M*) by low temperature ^{1}H NMR spectroscopy, the synthesis of more prospective motor derivatives was explored next. The preliminary theoretical assessment of a motor, which bears a cyclopropyl-ring at the aliphatic position revealed a very promising thermal barrier for the *Z*-(*S*)-*M* to *Z*-(*S*)-*P* isomer helix inversion.[210] The synthesis of indanone **28** is depicted in Scheme 12 and delivered a poor yield of 142-methoxyethoxymethyl ether %.[210] GCMS analysis indicated successful addition of Li-**16** to indanone **28**. Further investigation of the *Meyer-Schuster* rearrangement of the propargylic alcohol however revealed decomposition by addition of c. H$_2$SO$_4$, as monitored by TLC. Apparently the *in situ* generated carbocation in vicinal position to the cyclopropyl-ring is prone to various side reactions. Alternative precursors of prospective motor derivatives are indanone **29** and **31**. **31**, which bears a bromine substituent at the aromatic core, could provide a motor derivative capable for late stage functionalization. That would either allow introduction of sterically demanding groups at the end of the synthesis, or the introduction of substituents for advanced molecular machinery. In case of indanone **31** propargylic alcohol was synthesized successfully as mass spectrometry and TLC analysis confirmed. The *Meyer-Schuster* rearrangement also proceeded successfully, as indicated by TLC.

However, future investigations have to be carried out to explore the concluding steps of the synthesis. Hydroxymethyl group bearing indanone **36** was modified with 2-methoxyethoxymethyl ether (MEM) as protecting groups of the hydroxyl functions, in order to avoid side reactions in basic media applied in the course of propargylic alcohol formation. Successful protection was indicated by ^{1}H NMR and mass spectrometry. TLC analysis and mass spectrometry also indicated the successful access to the corresponding HTI based on MEM-protected indanone MEM-**36**. However, the deprotection of the hydroxyl groups by BCl$_3$·OEt$_2$ led to decomposition as monitored by TLC. In conclusion, first investigations delivered very promising results of a prospective motor derivative, which bears hydroxyl groups, capable for late stage functionalization and access to dynamic covalent chemistry. Nevertheless, future investigations have to be carried out, testing different deprotection protocols or alternative protecting groups.

The synthesis of a motor derivative based on indanone **29** with *iso*-propyl groups at the α-position of the carbonyl function was tested next (Scheme 14 and Table 4). The decreased yield observed by the introduction of the *iso*-propyl groups already indicated the enhanced sterical demand, making this precursor a promising, but challenging candidate. Unfortunately, despite various conditions tested, no synthetic access to propargylic alcohol **46**, as the key intermediate, could be achieved. After preliminary observations with previously used acetylene **16**, smaller acetylide species **47**-**51** were tested. As depicted in Scheme 14b, the smallest possible acetylide species **49** was conveniently generated *in situ* by addition of two equivalents of *n*BuLi to dibromoethylene. This allowed to circumvent the handling of very explosive gaseous acetylene and its mechanistic background is most likely related to the *Corey-Fuchs* protocol,[211] which consists of a consecutive elimination of bromine and a lithium-bromine exchange reaction. Other nucleophiles as Mg- or Cu-based acetylides, as well as the stable and commercially available lithium acetylide ethylene diamine complex **48** were tested in order to explore higher temperature ranges. After several attempts failed, it was investigated if a single electron transfer with sodium would succeed, followed by trapping the generated radical with **49** – **51**, as depicted in entries 21, 22 and 30, but analysis by TLC and GCMS showed no conversion. However, the generation of the radical was seemingly successful as an intensive red color was observed after refluxing a THF or toluene solution of indanone **29** with sodium.
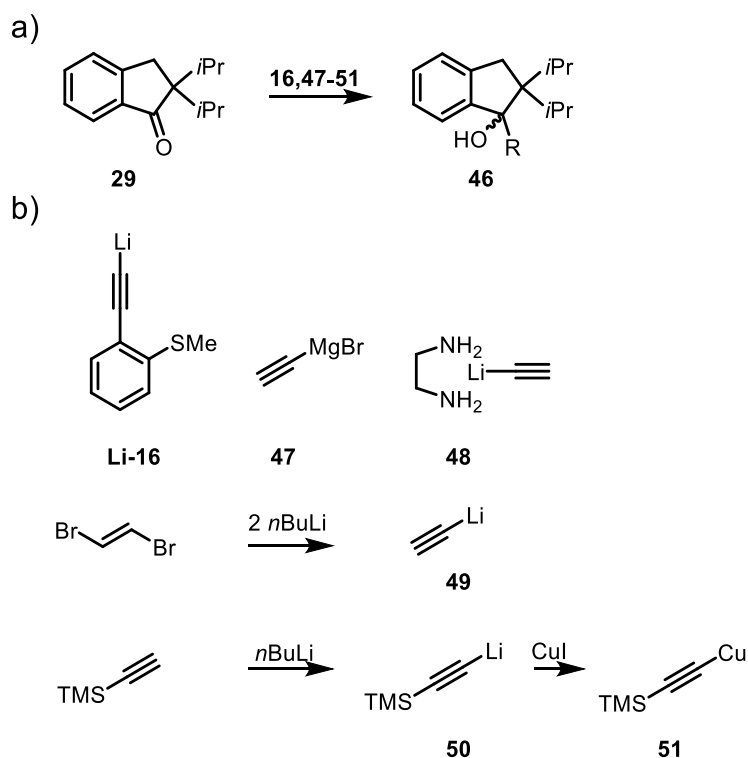
Scheme 14: Synthetic investigations towards propargylic alcohol **46**. a) General reaction scheme of the nucleophilic addition of acetylides **16** and **47**-**51** to the carbonyl function of indanone **29**. b) Various acetylide species tested in the course of the investigations towards the synthesis of **46**.

All applied conditions for the synthesis of propargylic alcohols derived from **46** are summarized in Table 4. As the reactivity of the nucleophile is not solely dependent on its size, but also on its level of aggregation in solution several different additives as TMEDA (entry 5), DMSO (entry 6), and crown ether (entries 10, 11, 14), as well as strongly coordinating solvents as DME (entries 3 and 4) and diglyme (entries 5, 6, 23, 24 and 32) were tested. Also a coordination approach of the carbonyl function by addition of Lewis acids such as LiCl (entries 4, 8, 16 and 31), Ce(Cl)$_3$ (entries 2 and 18), BF$_3$·OEt$_2$ (entries 9 and 19) and BCl$_3$ (entry 20) in order to increase its reactivity, failed as monitored by TLC and GCMS. Apparently, the limit of the synthetic access to indanones by nucleophilic addition of acetylides was found with indanone **29**.

Table 4*:*   Investigated conditions to convert indanone **29** to the corresponding propargylic alcohol**s**.

entry	nucleophile	solvent	additive	observation by TLC/ GCMS
1	**16**	THF		no conv.
2	**47**	THF	Ce(Cl)$_3$	no conv.
3	**49**	DME		no conv.
4	**49**	DME	LiCl	no conv.
5	**49**	diglyme	TMEDA	no conv.
6	**49**	diglyme	DMSO	no conv.
7	**49**	THF		no conv.
8	**49**	THF	LiCl	no conv.
9	**49**	THF	BF$_3$ · OEt$_2$	no conv.
10	**50**	THF	crown ether	no conv.
11	**49**	THF	crown ether	no conv.
12	**49**	THF	AlCl$_3$ crown ether	no conv.
13	**50**	THF		no conv.
14	**50**	THF	crown ether	no conv.
15	**50**	THF		no conv.
16	**50**	THF	LiCl	no conv.
17	**50**	THF	TMEDA	no conv.
18	**50**	THF	Ce(Cl)$_3$	no conv.
19	**50**	THF	BF$_3$·OEt$_2$	no conv.
20	**50**	THF	BCl$_3$	no conv.
21	**49**	Toluene	Na	no conv.
22	**50**	Toluene	Na	no conv.
23	**49**	Diglyme		no conv.
24	**50**	Diglyme		no conv.
25	**48**	DMSO		no conv.
26	**48**	DMSO		no conv.
27	**48**	Pyridine		no conv.
28	**48**	neat		no conv.
29	**48**	Pyridine		no conv.
30	**51**	THF	Na	no conv.
31	**48**	Pyridine	LiCl	no conv.
32	**48**	Diglyme		no conv.

4.2.8   Syntheses of indanone precursors bearing *iso*-propyl groups at the aromatic position

Since access to a motor derivative with bulky *iso*-propyl substituents at the five-membered ring was not accomplished, the synthetic effort was concentrated on motor derivatives, which bear sterically demanding groups at the aromatic core of the indanyl part. Therefore, the synthesis of indanones **53** and **55** with *iso*-propyl groups at the aromatic part was studied next. The conventional method by *Friedel-Crafts* acylation/alkylation of symmetric benzene derivative **52**, unfortunately lead to structural isomers **53** and **54**. Apparently, an *iso*-propyl group migration under Lewis acid catalysis occurred to furnish a mixture of regioisomers. Since the separation by column chromatography was not successful, the synthesis of an alternative indanone precursor **55** was envisioned to circumvent time consuming separations by HPLC at an early stage of the synthesis.
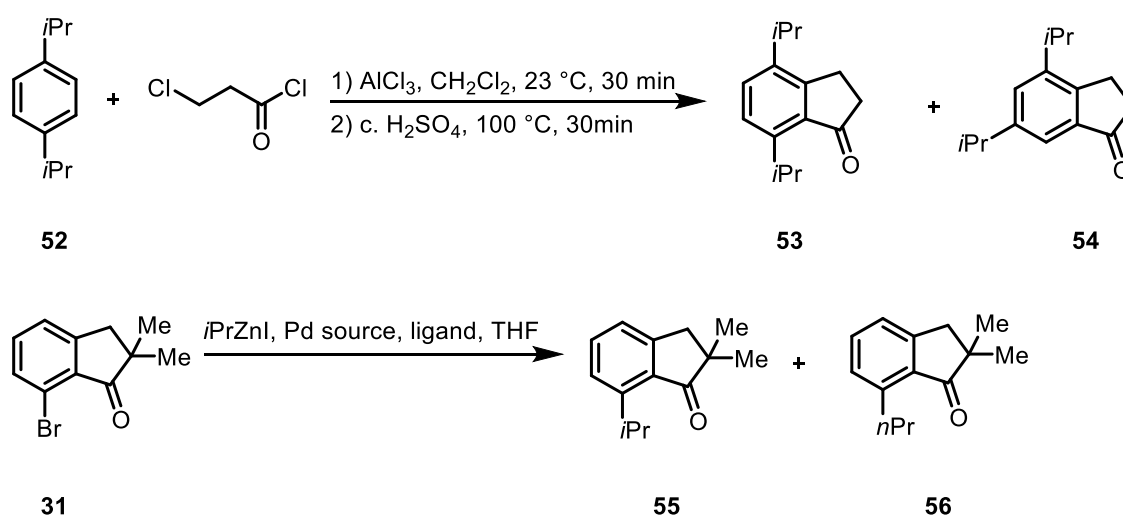
Scheme 15:   Synthetic investigation towards *iso*-propyl indanones. The *Friedel-Crafts* method, which proved to be a powerful method to prepare steric demanding indanones, showed major drawbacks because of regioisomerization. Also *Negishi* type cross-coupling[212] revealed β-hydride elimination and migratory insertion leading to regioisomer **56.**

Alternative indanone **55** should be accessible by a *Negishi* cross-coupling[212] reaction starting from indanone **31**. The reaction proceeds in moderate yields of up to 55%, but *iso*-propyl groups are prone to β-hydride elimination and migratory insertion, which leads to indanone **56** with a linear propyl chain as side product. In Table 5, the tested conditions are summarized. Entries 2 and 6 show a very successful suppression of branch migration. The Pd-PEPPSI-IPent[Cl] catalyst, whose capability in cross-coupling of secondary organozinc reagents was scrutinized by *Organ* and coworkers[213], seemed to be superior, since no additional side products were formed (entry 6). The yield however could not be increased to more than 55%. Since the separation of the regioisomers **55** and **56** was not successful by conventional column chromatography and even minute amounts of impurity could turn out severe drawbacks in the

low temperature NMR analysis of motor rotation, another synthetic route towards indanone **55** was investigated.

Table 5: Investigated cross-coupling conditions for the synthesis of indanone **55**.

entry	catalyst	ligand	regioisomerization	observation	yield
1	sSPhos Pd G2	-	considerable (ratio 1.5/1)	side product	n. d.
2	$Pd(OAc)_2$	sPhos	traces (ca. 5%)	homo-coupling	34-42%
3	$Pd(PPh_3)_4$	-	no sp^2-sp^3 coupling obs.	homo-coupling	n. d.
4	$Pd(OAc)_2$	APhos	considerable (ratio 1.5/1)	side product	n. d.
5	$Pd(dppf)Cl_2$	-	considerable (ratio 1/1.5)	decomposition	n.d.
6	Pd-PEPPSI-IPent^{Cl} cat.	-	traces (ca. 5%)	no side product	34-55%

An alternative synthetic approach towards indanone **55**, shown in Scheme 16, is based on a published procedure.[214] Commercially available 2-*iso*-propylbenzoic acid **57** is converted to the Weinreb-amide **58** in 89%. Treatment of **58** with vinylmagnesium bromide solution in THF furnished enone **59** in the next synthetic step with a good yield of 74%. To avoid considerable decrease in yield it is necessary, that the reaction mixture is diluted in 2M HCl solution after the reaction is finished. Otherwise significant amounts of a side product, which are most probably generated by nucleophilic addition of the hydrolysis-by product *N*,*O*-hydroxylamine at the β-position of the enone **59**, can be observed. An acid catalyzed *Nazarov* cyclization[215-216] delivered indanone **60** in a good yield of 80%. Good yields are only accessible if temperature, reaction time, as well as concentration of acid and enone **59** are strictly adhered to. Purification was performed through a short pad of neutral aluminium oxide, since silica as stationary phase revealed decomposition during column chromatography. A precise protocol to synthesize **60** is given in the experimental section. Subsequently, after deprotonation with NaH and addition of MeI twofold methylated indanone **55** could be obtained in a moderate yield of 58%.
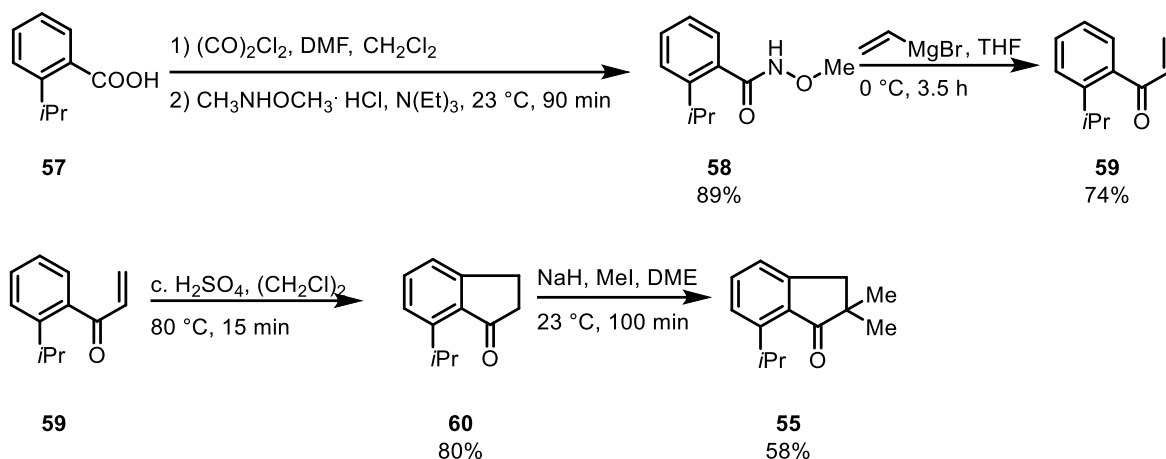
Scheme 16: Synthesis of indanone **55** by consecutive installation of the five-memberd ring.

4.2.9   Synthesis of *iso*-propyl group bearing motor 5

After indanone **55** was accessible in sufficient amounts, the synthesis of a HTI based motor **5** could be explored next. Nucleophilic addition of Li-**16** in THF delivered propargylic alcohol **61** in a good yield of 82%. After acid catalyzed *Meyer-Schuster* rearrangement in THF proceeded in an excellent yield of 99%, oxidation of enone **62** with sodium perborate tetrahydrate in c. acetic acid furnished racemic sulfoxide **63** in a good yield of 71%. Subsequently, sulfoxide **63** was treated with oxalyl chloride in CH_2Cl_2 to initiate intramolecular cyclization yielding HTI **64**, which was finally oxidized with sodium perborate tetrahydrate in c. acetic acid to the corresponding motor **5** in a moderate yield of 36% over two steps starting from *E*-**63**. The sole yield of the cyclization from **63** to **64** is 67%. A concise protocol towards motor **5** was also applied, which started from indanone **55** and acetylene **16** and omits, with exception of propargylic alcohol **61**, purification of intermediates. The overall yield obtained in this case was 52%. Motor derivative **5** finally provided thermal barriers high enough to directly observe the missing intermediate **B** (*Z*-(*S*)-*M*), which allows the deduction of the underlying motion of the motor system. The complete synthesis is shown in Scheme 17.
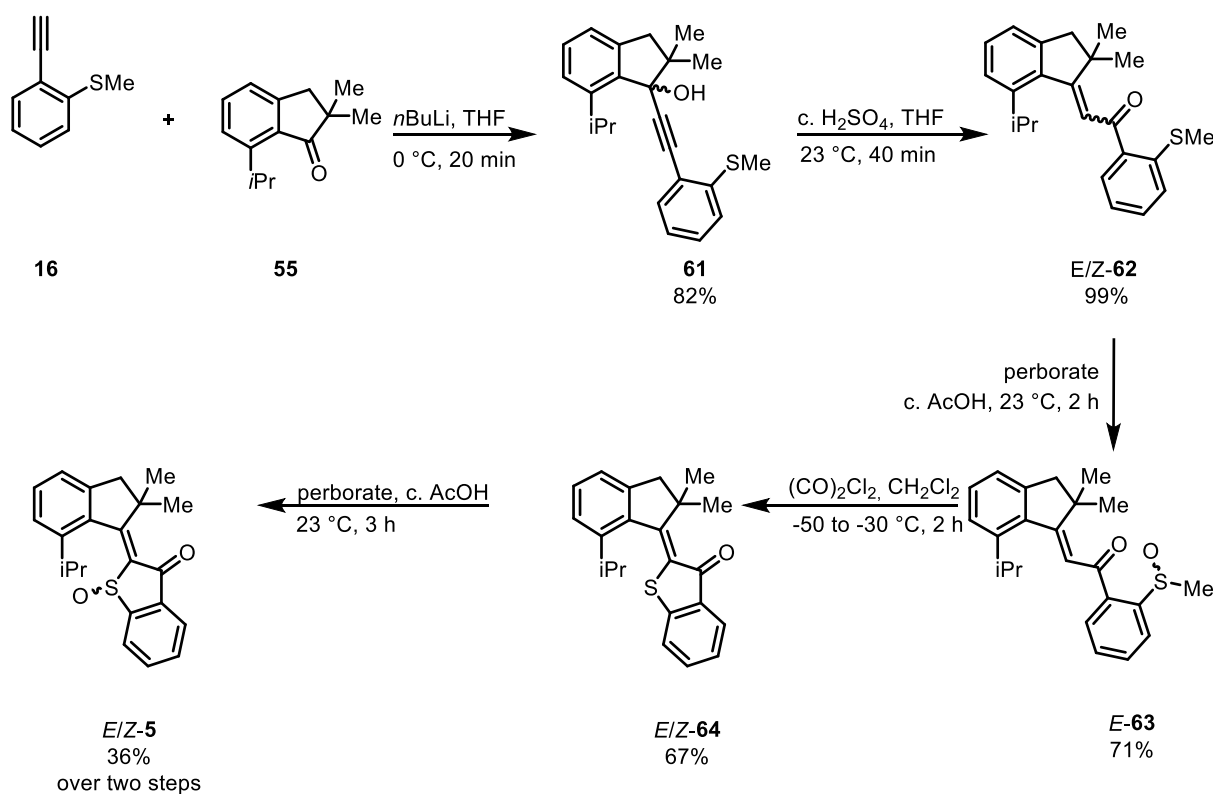
Scheme 17: Synthesis of motor **5**, starting with acetylene **16** and indanone **55** to furnish propargylic alcohol **61** in a nucleophilic addition reaction. After *Meyer-Schuster* rearrangement to enone **62** and subsequent racemic oxidation to sulfoxide **63**, an intramolecular cyclization to HTI **64**, induced by oxalyl chloride, takes place. Final oxidation leads to motor derivative **5**.

4.2.10 Syntheses towards a fluorenyl-based HTI, with two-step motor potential

Because of its inherent symmetry tetramethylated fluorenone **70** exhibits great potential for an interesting motor design, which is based on a reduced two-step cycle. The synthesis, depicted in Scheme 18, commences with homo-coupling of (3,5-dimethylphenyl)boronic acid **67** towards tetramethylated biphenyl **66** in a good yield of 81%.[217] Biphenyl **68** is also accessible by a *Negishi* cross-coupling reaction starting from aryl bromide **65** with an inferior yield of 34%. A twofold *Friedel-Crafts* alkylation delivers fluorene derivative **69** from biphenyl **68** in the presence of $AlCl_3$ and CH_2Cl_2 in a moderate yield of 53%.[218-219] Final oxidation with *tert*-butyl hydroperoxide yielded tetramethylated fluorenone **70** in a good yield of 79%.[220] Further investigations to explore the possibility to introduce asymmetry by simple bromination exhibited mono-brominated fluorene **71**, as proven by mass and NMR spectroscopy.
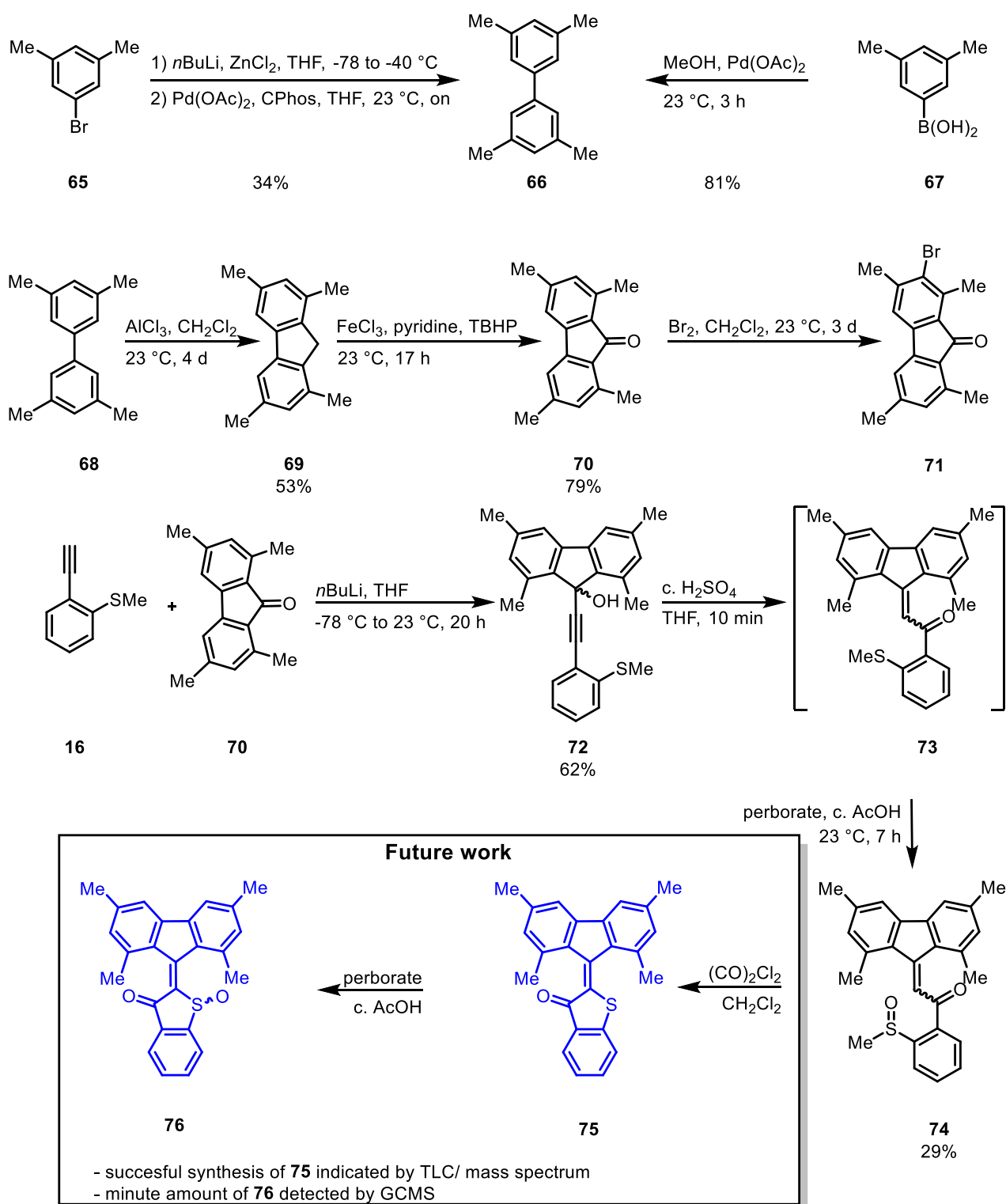
Scheme 18: Synthesis towards motor **76**, starting with acetylene **16** and fluorenone **70** to furnish propargylic alcohol **72** in a nucleophilic addition reaction. After successful *Meyer-Schuster* rearrangement to enone **73** and subsequent racemic oxidation to sulfoxide **74**, the intramolecular cyclization to HTI **75**, induced by oxalyl chloride, was tested. Also final oxidation to motor derivative **76** was tested.

With fluorenone **70** at hand the motor synthesis could be explored next. The nucleophilic addition of acetylene **16** in THF proceeded in a moderate yield of 62%. *Meyer-Schuster* rearrangement provided enone **73**, which was used without purification in the subsequent racemic oxidation with sodium perborate tetrahydrate to furnish sulfoxide **74** in 29% over two steps. The cyclization of sulfoxide **74** and the final racemic oxidation were explored briefly, but the successful outcome could not be proven adequately. TLC and mass spectrometric analysis of HTI **75** indicated a successful cyclization, even though a possible side reaction towards a demethylated enone could also have taken place, as a prominent peak in the mass spectrum indicated. Conformational analysis by NMR spectroscopy was not possible due to time restrictions. Reaction monitoring of the final oxidation revealed considerable amounts of fluorenone **70**, while motor **76** was detected in minute amounts by GCMS. It is likely that HTI **75** is sensitive to hydrolysis leading to fluorenone **70** and benzothiophenone **6** in a retro-*Aldol* reaction. Despite these positive preliminary results, future investigations have to be carried out, especially in finding mild, non-acidic conditions for the final oxidation.

4.2.11 Investigations towards a one-pot protocol for HTI-based molecular motors

The new protocol for sterically hindered HTI based motors proved to be very efficient in synthesizing a series of new motor derivatives, but a considerable number of five linear steps have to be carried out, which offers possibilities for further improvement. The scaffold of the molecular motor is already installed in the first step towards the propargylic alcohol, while the following transformation are solely focused on rearranging bonds and installation of reactivity. Thus, it could be advantageous if the required reactivity, e.g. the sulfoxide is installed before the propargylic alcohol is formed. Since *Meyer-Schuster* rearrangement is promoted by acidic additives, an *in situ* approach is envisaged via formation of a sulfoxidated propargylic alcohol from indanone and a suitable acetylene precursor **77**, followed by addition of acid as well as oxalyl chloride to generate a HTI in a one pot reaction. At this point a serious safety aspect has to be mentioned, as the protocol inevitably involves the consecutive addition of *n*BuLi solution and acidic reagents, such as c. H_2SO_4, which can lead to a violent neutralization reaction. With regard to this aspect, it has to be ensured that no lithiated species is present in the reaction mixture when acidic reagents are added, which can be achieved by the cautious prior addition of water to the reaction mixture. The reaction scheme after initial exploration of suitable conditions is depicted in Scheme 19.
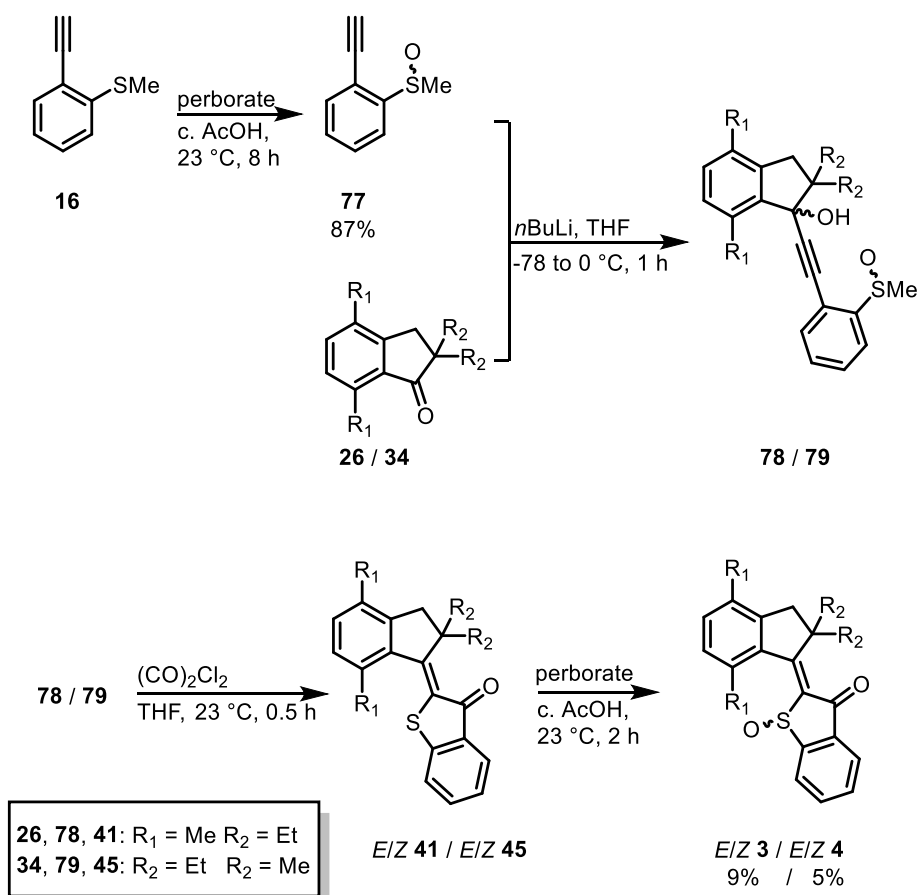
Scheme 19: Synthesis of motor precursor **41** and **45**, starting with the oxidation of acetylene **16** to sulfoxidated acetylene **77**. Nucleophilic addition of Li-**77** to indanones **26** and **34** leads to sulfoxidated propargylic alcohols **78** and **79**. A one-pot approach delivered HTIs **41** and **45** after addition of water and oxalyl chloride to the propargylic alcohols **78** and **79**. After extraction and final oxidation motors **3** and **4** could be obtained.

The oxidation of acetylene **16** to the sulfoxide analogue **77** was achieved by sodium perborate tetrahydrate in c. acetic acid in a good yield of 87%.[221] Lithiation of **77** and consecutive addition of indanones **26** and **34** delivered propargylic alcohols **78** and **79**, as confirmed by TLC. Since a one-pot protocol was aimed, no purification and elaborate analysis of propargylic alcohols **78** and **79** was performed. Subsequently, after addition of one equivalent of water to ensure the absence of lithiated species, several equivalents of oxalyl chloride were added at ambient temperature, which caused a promising color change from colorless to orange. Preliminary investigations revealed, that the H_2SO_4 addition is dispensable, and can be omitted. Reaction control by TLC confirmed the successful synthesis of HTIs **41** and **45**, although several side products were observed. After extraction and final oxidation motors **3** and **4** were obtained in a low overall yield of 9% and 5% starting from indanones **26** and **34**. The mechanistic details for the conversions of **78**/**79** were not elucidated at this point. It is likely that the one pot synthesis consists of the same sequence, beginning with *Meyer Schuster* rearrangement and

consecutive ring closing reaction as it is observed for the stepwise protocol. A direct ring closing reaction of propargylic alcohols **78** and **79**, induced by the generation of a chlorosulfonium ion cannot be fully excluded, however. The dispensability of H_2SO_4 addition is a first indication for this proposal.

At this stage, the one-pot procedure cannot compete with the excellent yields obtained from the stepwise protocol, but it can be regarded as a good starting point for future inquiries, which could investigate usage of reduced equivalents of oxalyl chloride and decreased temperature for the ring closing reaction. It can also be considered, to change the solvent during different steps of the synthesis. The first step could also be done in combination with, or if possible without an alternative base for deprotonation for the formation of propargylic alcohols **78** and **79**. In the stepwise protocol CH_2Cl_2 was used for the ring closing reaction, which could be in principle a promising candidate for the one pot protocol, too.

4.2.12 Synthesis of potential molecular motors based on a mixed indigoid structure

Apart from HTI based motors the synthesis of molecular motors with even more pronounced chromophoric core would be a worthwhile aim. The classical indigo dye would therefore be an ideal candidate in terms of superior absorption behavior. The disadvantage is that the central double bond is already blocked by the functional groups determining the unique absorption profile, which aggravates further functionalization while the chromophore should stay intact. Since the installation of a stable stereocenter is a basic requirement for molecular motors, it could be promising if the already established sulfoxidated HTI fragment would be incorporated, too. Even though a loss in red-shifted absorption can be expected, it would hopefully, amongst the installed stereoinformation, boost sterical hindrance around the double bond to establish a further requirement, e.g. helical distortion around the rotation axle. The molecular design behind these considerations, would furnish a mixed indigoid molecule, consisting of an oxidized thioindigo fragment as well as an *N*-containing indigo fragment. By substitution of the hydrogen, bound to the nitrogen atom, by alkyl or aryl groups, a competitive proton transfer (ESPT), which suppresses photoisomerization in indigo, could be prevented. Additionally, sterical hindrance for a pronounced helical distortion around the central double bond would be increased. The molecular design of a mixed-indigo based molecular motor is depicted in Figure 33.
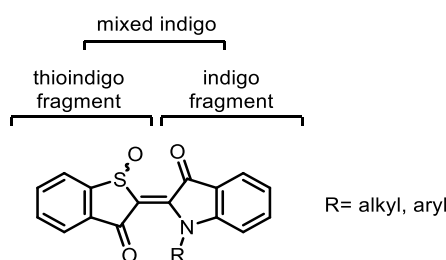
Figure 33: Design of a potential molecular motor based on a mixed indigoid chromophore

Since indigo dyes in general exhibit poor solubility, a *tert*-butyl group substituted benzothiophenone precursor was envisioned first. The synthesis commences with an established preparation of a benzothiophenone precursor **83** in three consecutive steps, which is depicted in Scheme 20. 4-*Tert*-butylthioanisol **80** was transformed into carboxylic acid **81** by nucleophilic substitution with 2-bromoacetic acid in quantitative yields. Oxalyl chloride was used for *in situ* preparation of the corresponding acid chloride, which underwent intramolecular *Friedel-Crafts* acylation to yield benzothiophenone **82**. After workup this light and air sensitive intermediate **82** was oxidized to **83** in the presence of sodium perborate tetrahydrate in c. acetic acid in a good yield of 57% over two steps. An established oxidation protocol with $Mn(OAc)_3$ was successfully used to prepare thioindigo from benzothiophenone precursors.[133] This protocol delivered the desired mixed indigo **85**, when sulfoxidated benzothiophenone **83** and indoxyl acetate **84** were treated with $Mn(OAc)_3$ in c. acetic acid with a low yield of 7%. Mixed indigo **85** is a suitable precursor for *N*-substitution with alkyl or aryl groups. Treatment of **85** with MeI under basic conditions furnished methylated mixed indigo **86** in a moderate yield of 23%. A *Chan-Lam* coupling procedure[222] was used to synthesize a tolyl-substituted derivative **87** in a Cu-mediated cross-coupling reaction of mixed indigo with tolylboronic acid in a moderate yield of 28%. The attempt for acylation of the nitrogen atom failed, as treatment of mixed indigo **85** in acetetic acid anhydride lead to reduction of the sulfoxide function.
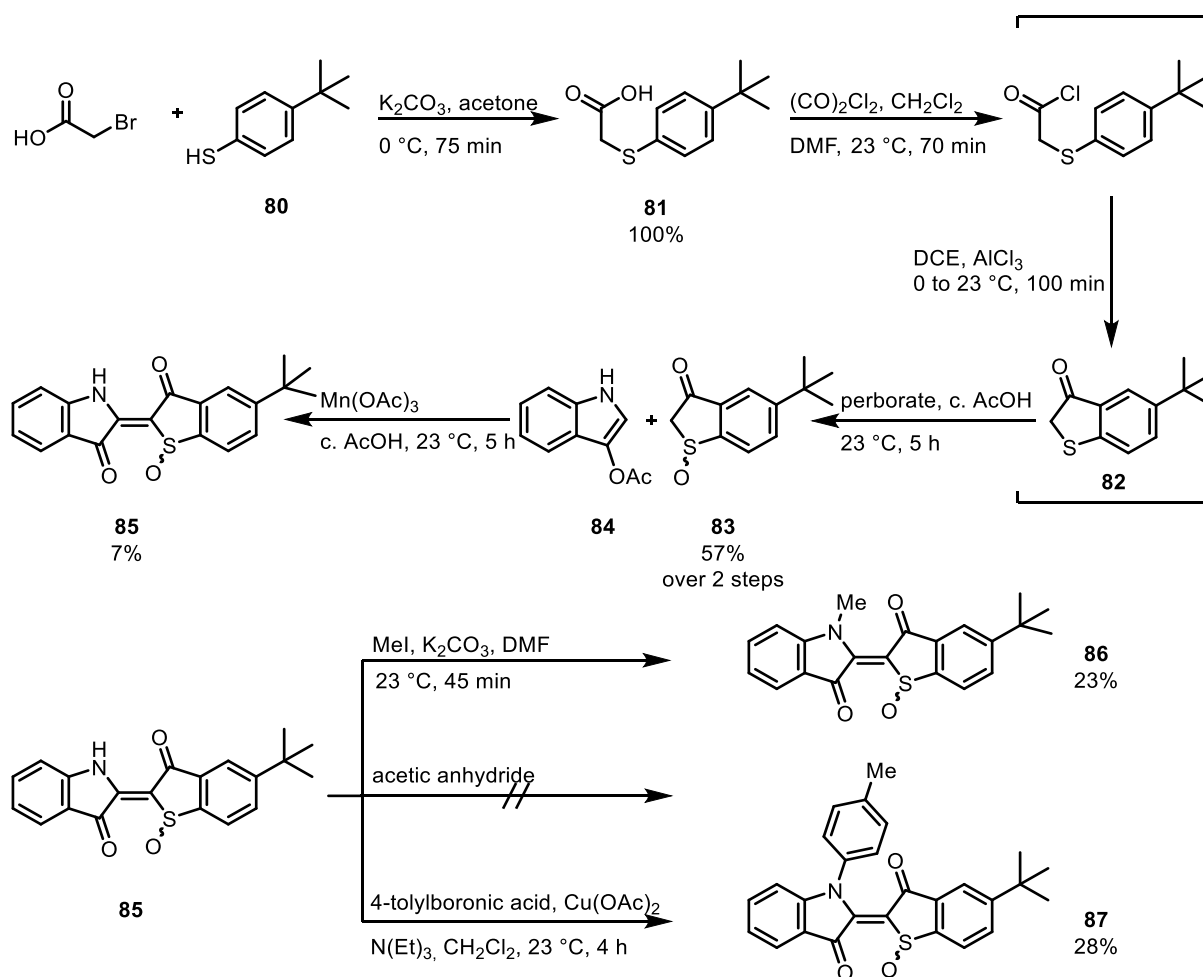
Scheme 20: Synthesis of mixed indigos **86** and **87**. Benzothiophenone precursor **83** was synthesized after an established protocol, which starts with the preparation of carboxylic acid **81** and the corresponding acid chloride. In the presence of AlCl₃ an intramolecular *Friedel-Crafts* acylation takes place to furnish benzothiophenone **82.** After oxidation to the sulfoxide **83**, mixed indigo **85** is formed by treatment of **83** and indoxyl acetate **84** with Mn(OAc)₃. Substitution was achieved on the one hand by simple methylation towards *N*-methyl mixed indigo **86** and on the other hand by a *Chan-Lam* coupling reaction towards *N*-tolyl mixed indigo **87**.

4.3 Theoretical description of the energy profile of motors 1-5

In the following chapter five HTI based motor derivatives were investigated by theoretical means. The theoretical treatement of meethoxy bearing motor **1** has already been reported[1] and is presented herein for comparative reasons. Derivatives **1**, **2** and **5** were theoretically assessed by *Stefan Thumser*.[IX]

4.3.1 Stereochemical configuration of motor isomers

Theoretical assessment of motors **1-5** with (*S*)-configured sulfoxide on the MPW1K/6-311G(d,p) level of theory revealed four energetically different diastereomers. They are further characterized by the configuration of the double bond and the helical distortion of the rotor part relative to the stator part. In Figure 34 all possible isomers are depicted including the ones with (*R*)-configured sulfoxide. The four pairs of enantiomers have mirror-image symmetry, but are identical in terms of energy. *E/Z* is describing the relative configuration of the central double bond, the descriptor *P/M* means the handedness of the helical distortion and (*R*)/(*S*) stands for the configuration of the sulfoxide stereocenter. For simplicity reasons the enantiomeric pairs *E-(S)-(P)/E-(R)-(M)*, *Z-(S)-(M)/Z-(R)-(P)*, *Z-(S)-(P)/Z-(R)-(M)* and *E-(S)-(M)/E-(R)-(P)* are termed as isomers **A**, **B**, **C** and **D** in the following. Frequency analysis confirmed all optimized structures to be stationary points.

1: R^1 = OMe; R^2 = OMe ; R^3 = Me;
2: R^1 = Me   ; R^2 = Me   ; R^3 = Me;
3: R^1 = Me   ; R^2 = Me   ; R^3 = Et;
4: R^1 = Et   ; R^2 = Et   ; R^3 = Me;
5: R^1 = *i*Pr   ; R^2 = H   ; R^3 = Me;
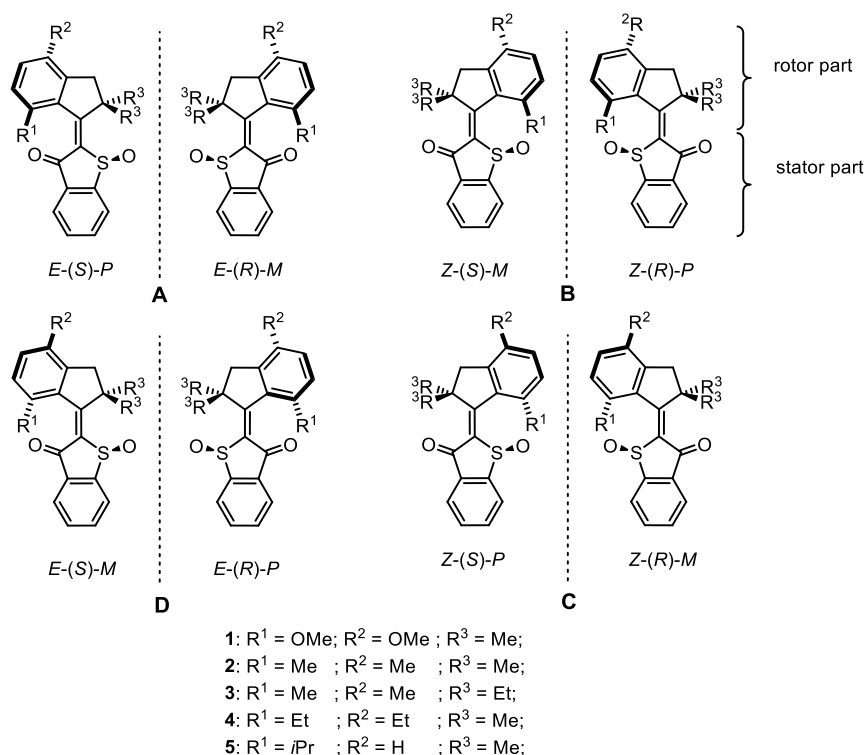
Figure 34:   Stereochemical configuration of all isomers of motors **1**-**5**. Structural features are the double bond configuration, indicated by the descriptor *E/Z*, the helical twist marked as *P/M* and the absolute configuration of the sulfoxide stereocenter, which can be identified by the descriptor (*R*)/(*S*). Stator part is defined as the benzothiophenone-derived lower half of the molecule. The upper part of the molecule is defined as the rotor part.

4.3.2   Ground state energy profile

The diastereomeric isomers **A** and **D** exhibit *E* configuration of the double bond, but differ in their helical twist and hence in energy. Theoretically obtained Gibbs Free energies confirmed isomer **A** more stable than the corresponding isomer **D** and they are interconnected by a transition state **TS$_{D-A}$**, as it was also revealed by theoretical calculations. Isomer **B** and **C** show analogue behaviour, while **C** is the more stable isomer with *Z* configuration. Also in this case theoretical assessment delivered transition state **TS$_{B-C}$**. One imaginary mode was obtained for each transition state, showing that they are first order saddle points on the hyper-potential energy surface. Both transition state structures are characterized by planarized dihedral angles at the central double bonds and exhibit thermal barriers between 5.5 to 15.8 kcal·mol^{-1}. Thus, it can be derived, that **D**/**A** and **B**/**C** transitions take place readily at ambient temperature by pushing R^1 over the sulfoxide or the carbonyl group of the stator part. Exemplarily, the theoretically obtained structures of HTI motor **2** is depicted in Figure 35 and illustrates the underlying movement of the helix inversions of **D**/**A** (Figure 35a) and **B**/**C** (Figure 35b).
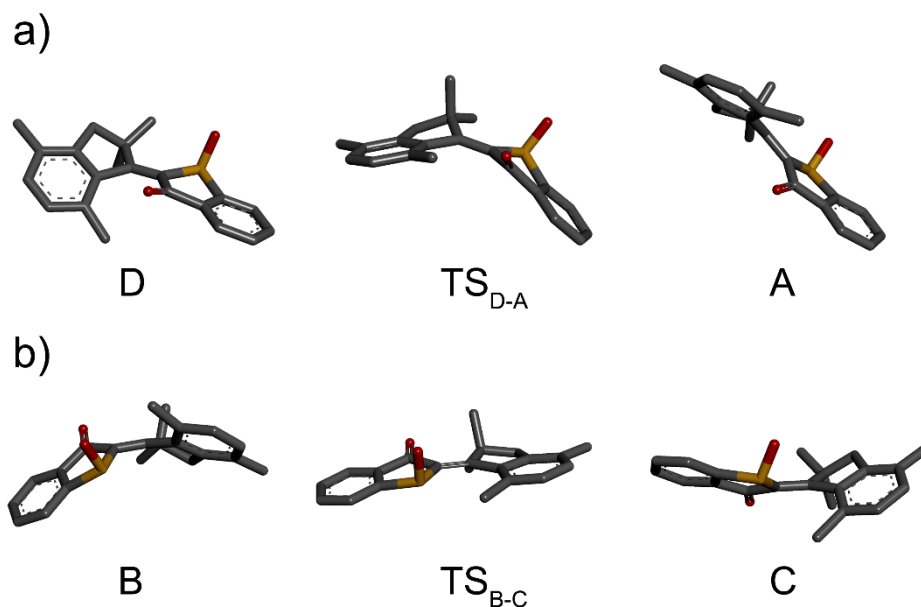
Figure 35:   Theoretically obtained minimum and transition state structures of motor **2** on the MPW1K/6-311G(d,p) level of theory. Structures were provided by *Stefan Thumser*.[IX] a) It can be seen that a helical inversion process is determined by slippage of R^1 over the carbonyl group in case of the **D**/**A** helical inversion b) R^1 is sliding over the sulfoxide stereocenter in case of **B**/**C** helical inversion.

The thermal double-bond isomerizations of isomer **A** to **B** and **C** to **D** was not investigated by theoretical means, but experimental data proved a thermal barrier of >30 kcal·mol^{-1} for motors **1**, **2** and **5**. It can be stated therefore for all investigated derivatives **1-5**, that the helix inverting steps **D** to **A** and **B** to **C** show much smaller thermal barriers, as it is the case for double-bond isomerizations. Thus **D**/**A** and **B**/**C**

isomerization already occur at ambient temperature, while no thermal **A/B** and **C/D** transition is possible. In Figure 36 a general energy profile is depicted.
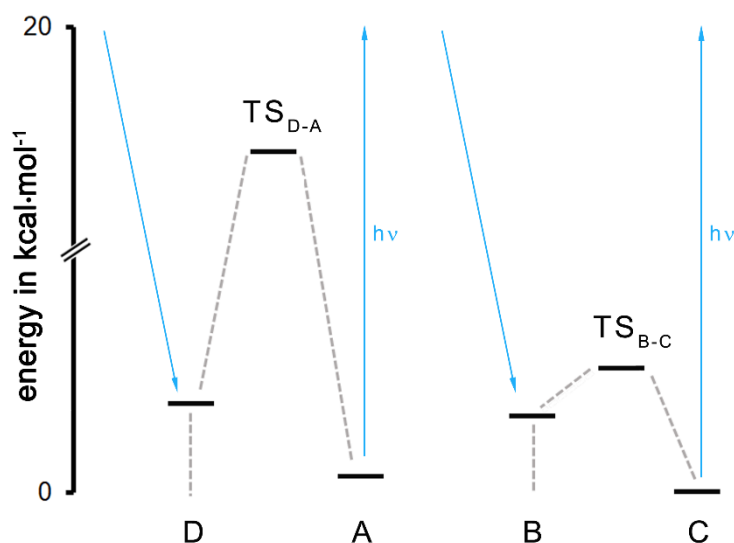
Figure 36:   General energy profile of HTI-based molecular motors. Isomer **D** and **A** as well as **B** and **C** are interconnected by thermal barriers. The corresponding transitions states reveal highly planarized dihedral angles at the central double bond. For all HTI motor derivatives **1**-**5** the **TS$_{D-A}$** is higher in energy than the TS$_{B-C}$. Both do not exceed 16 kcal·mol^{-1}.

A general feature of HTI-based molecular motors is a relatively high thermal barrier for the **D** to **A** conversion (13.5 -15.8 kcal·mol^{-1}), as well as a lower barriers for the **B** to **C** conversion (5.5 -13.5 kcal·mol^{-1}). The global energetic minimum varies with substitution pattern. All motors **2**-**5** with alkyl groups exhibit isomer **A** as their minimum, while isomer **C** is the overall minimum of motor **1** with methoxy-substitution. The energetic differences between isomers **D** and **A** vary from 2.70 to 4.31 kcal·mol^{-1} and from 2.46 to 4.30 kcal·mol^{-1} in case of **B** and **C** isomers. Based on these values, theoretical description predicts 100% population of stable isomers **A** and **C**, while population of the corresponding metastable isomers **D** and **B** can be neglected at ambient temperature. The theoretical energy profile supplies a profound basis for the anticipated rotation mechanism of HTI-based molecular motors.

HTI derivatives are known to be capable of photoisomerization, e. g. a light-induced double bond rotation. Thus *E*-configured isomers can be readily converted to *Z*-configured isomers and vice versa simply by irradiation at ambient temperature. Furthermore, the helical distortion of the rotor part relative to the stator part should guide the light induced rotation in a distinct direction.[1] Hence, excitation of isomer **A**, should exclusively deliver isomer **B** by photoisomerization. As we know from the theoretical calculation a consecutive thermal helix inversion should completely convert metastable **B** to stable

isomer **C**. A second excitation of isomer **C** should furnish isomer **D**, which isomerize thermally to the more stable isomer **A**, as-the starting point of the rotation cycle. As long as light input and sufficient thermal energy is available, a fully directional 360° rotation around the central double bond should occur.

Most parts of the rotation cycle were already confirmed with motor **1** exemplarily.[1] It could be shown that the theoretical predictions of the ground state profile, as well as the anticipated directional rotation are in very good agreement with experimental results obtained for **1**.

4.3.3   Ground state exploration of derivatives 3 and 4

Motor derivatives **3** to **4** were investigated by theoretical means on the MPW1K/6-311G(d,p) level of theory using the Gaussian09 Revision A.02 program package.[223-224] Calculations of **1**, **2** and **5**[1, 38] were performed by *Stefan Thumser*.[IX] Theoretical assessment of derivative **3** started with a relaxed optimization on the basis of calculated structures of motor **2**. As expected four energetic minima were found. The determination of the ethyl group conformation of **3** was obtained by a concomitant scan of both dihedral angles of the ethyl groups (C(9)-C(17)-C(18)-C(19) and C(9)-C(17)-C(20)-C(21); for numbering see experimental part) on the semiempirical PM7 level of theory. The obtained minimum structures were optimized on the MPW1K/6-311G(d,p) level of theory. In case of isomer **D** dihedral angle scan of the ethyl groups led to a helical inversion, which omitted the localization of all minima. For that reason the ethyl groups of isomer **D** were displaced manually before optimization and it was found a coplanar arrangement of the ethyl groups with respect to each other, as the lowest lying energy minimum. In most cases this coplanar arrangement of the ethyl groups with respect to each other was found to be the lowest lying energy minimum. Frequency analysis revealed all structures to be minimum structures as no imaginary vibrational modes were found. For all isomers two low lying minima were found, which vary only little in energy (see Table 6). Transition state structures were obtained on the basis of calculated structures of motor **2**. By manual displacement of the ethyl groups the lowest lying transition states were found. Both transitions states display ethyl group conformations with coplanar arrangement analogous to most minimum structures. Frequency analysis confirmed the structures as first order saddle points on the energy potential surface as only one imaginary mode was found.

Calculated structures of motor **2** were used again as template in case of motor **4** in order to assess its four ground state minima. All obtained preliminary minima were scanned along the dihedral angle of the ethyl group at the aromatic position 14 (see experimental part for numbering) first. The obtained structures were further optimized at the MPW1K level of theory with the 6-311G(d,p) basis set. Finally the ethyl group (aromatic position 11) pointing towards the stator part was rotated for exploration of the ground state minima. Again optimization on the MPW1K level of theory with the 6-311G(d,p) basis set followed. Further, it was found by manual displacement that an additional set of low lying minima is

present with oppositely arranged ethyl group at aromatic position 14 (see Figure 37). All structures were confirmed to be minimum structures by frequency analysis since no imaginary vibrational modes were found. Transition states were assessed by using again template structures of motor **2**. Further, manual displacement of the ethyl groups was used for exploration of transition states of minimal energies. Optimized structures on the MPW1K level of theory with the 6-311G(d,p) basis set were confirmed to be first order saddle points on the energy potential surface, since only one imaginary vibrational mode was found.

Due to pronounced rotational freedom of the ethyl groups present in derivatives **3** and **4** various ground state minima as well as transition states were found for these derivatives. Two low lying minima relevant for each configurational setup - **A**, **B**, **C**, and **D** were found. The energetic differences of the minima are in the range of 0.02 - 0.4 kcal·mol^{-1}, meaning that both minima are contributing to the conformations in solution. For illustration an energy difference of 0.4 kcal·mol^{-1} at 23 °C can be translated to an isomeric composition of 2 to 1. The contribution of higher energetic minimum structures, however, can be neglected as their energies are too high to warrant population at ambient temperatures. In most cases similar conformations of the ethyl groups, were found for the minima **A**, **B**, **C**, **D**. In Table 6 the obtained energies of all transition states as well as ground state minima are summarized for derivatives **3** and **4**.

Table 6: Calculated ground state energies of various minima of motors **3** and **4** on the MPW1K level of theory with the 6-311G(d,p) basis set.

Isomer	ΔG_0 [Hartree]	ΔG_0 [kcal·mol^{-1}]	$\Delta G^{\ddagger}$ [kcal·mol^{-1}]	Isomer	ΔG_0 [Hartree]	ΔG_0 [kcal·mol^{-1}]	$\Delta G^{\ddagger}$ [kcal·mol^{-1}]
A-3-I	-1439.103791	**0**	-	**A-4**-I	-1439.106311	**0**	-
A-3-II	-1439.103767	**0.02**	-	**A-4**-II	-1439.105977	**0.21**	-
B-3-I	-1439.095357	**5.29**	-	**B-4**-I	-1439.099813	**3.87**	-
B-3-II	-1439.095207	**5.38**	-	**B-4**-II	-1439.099543	**4.24**	-
B-3-III	-1439.092123	7.32	-	**B-4**-III	-1439.097381	5.60	-
C-3-I	-1439.102217	**0.99**	-	**C-4**-I	-1439.104339	**1.24**	-
C-3-II	-1439.101805	**1.25**	-	**C-4**-II	-1439.104030	**1.43**	-
C-3-III	-1439.097597	3.88	-	**D-4**-I	-1439.099458	**4.30**	-
D-3-I	-1439.097908	**3.69**	-	**D-4**-II	-1439.099186	**4.47**	-
D-3-II	-1439.097643	**3.86**	-	**D-4**-III	-1439.096439	6.19	-
D-3-III	-1439.092911	6.82	-	**TS$_{D-A}$-4**-I	-1439.074273	20.09	**+15.79**
TS$_{D-A}$-3-I	-1439.075267	17.9	**+14.20**	**TS$_{D-A}$-4**-II	-1439.074232	20.16	**+15.82**
TS$_{D-A}$-3-II	-1439.073449	19.03	+15.34	**TS$_{B-C}$-4**-I	-1439.081098	15.81	**+11.95**
TS$_{B-C}$-3-I	-1439.082402	13.41	**+8.12**	**TS$_{B-C}$-4**-II	-1439.081073	15.83	**+11.96**
TS$_{B-C}$-3-II	-1439.081281	14.12	+8.83	**TS$_{B-C}$-4**-III	-1439.079103	17.06	+13.20

For motors **3** and **4** isomers **A** are depicted in Figure 37 for illustration of typical ethyl group conformations, which were prevalently found for most isomers. Interestingly in the crystal structure of **A-3** a coplanar ethyl group conformation is observed as it is predicted from theory (Figure 37a). **C-3**

however exhibits a twisted ethyl group conformation in the crystalline state. In both cases an ethyl group conformation with coplanar arrangement was found to be the overall minimum in the theoretical description.
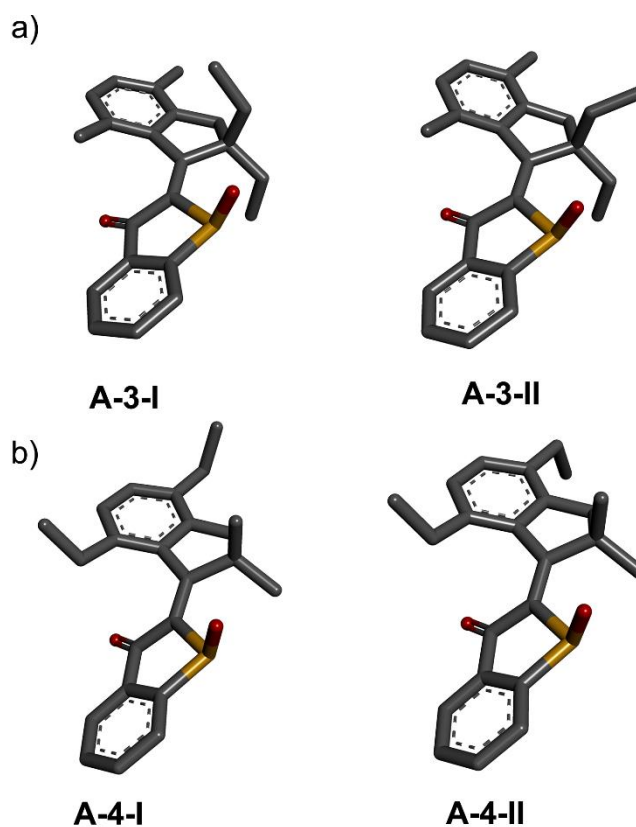
Figure 37: Theoretically obtained minimum structures of motors **3** and **4** on the MPW1K/6-311G(d,p) level of theory. a) Relevant minimum structures of isomers **A-3**. Structure **A-3-I** is the overall minimum, while **A-3-II** is only 0.02 kcal·mol^{-1} higher in energy. The ethyl groups of the overall minimum (**A-3-I**) show coplanar conformation with respect to each other, while **A-3-II** exhibits a twisted conformation. b) Relevant minimum structures of isomer **A-4**. Structure **A-4-I** is the overall minimum, while **A-4-II** is only 0.21 kcal·mol^{-1} higher in energy. The ethyl group at position 14 is pointing in opposite direction.

A comparative study of the molecular motors **1**-**5** with regard to the influences of different substitution on the thermal isomerization processes is presented in chapter 2.19 combining experimentally obtained data with the theoretical description.

4.4   Absorption spectra of 2, 3, 4 and 5 and comparison with theory for 2 and 5

For motor derivatives **2** and **5** UV/vis and ECD spectra were calculated by employing time dependent B3LYP/6-311+G(d,p) calculations based on structures optimized at the MPW1K/6-311G(d,p) level of theory with implementation of CH_2Cl_2 solvent effects by the polarizable continuum model (PCM). Data obtained for **2** and **5** are illustrated in Figures 38 and 39.
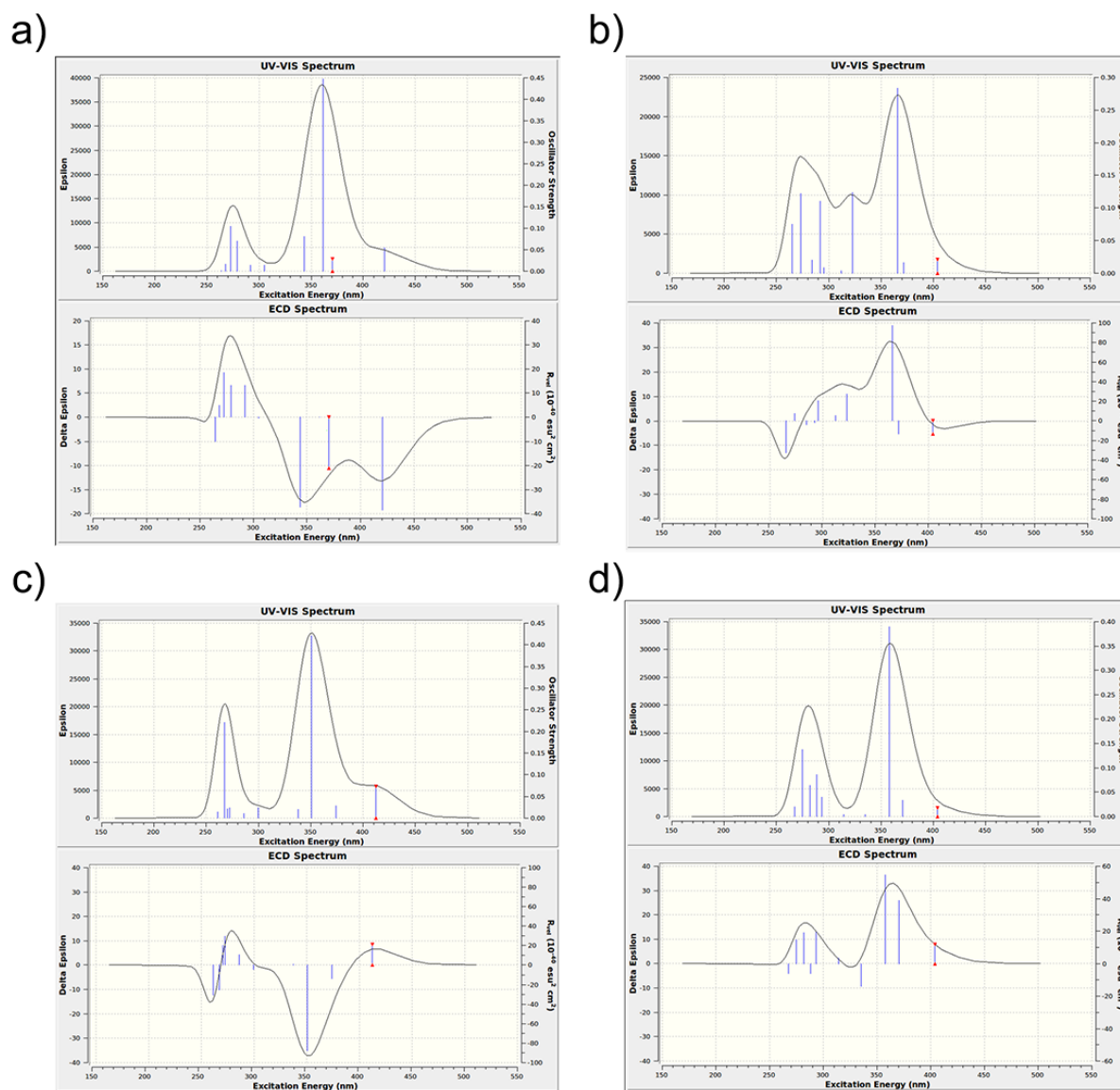
Figure 38:   Theoretically obtained extinction coefficients (top) and ECD spectra (bottom) of motor **2** for all four isomers **A**-**D**. Structures were optimized on the MPW1K/6-311G(d,p) level of theory in the gaseous phase. Only (*S*)-configured isomers were used for theoretical assessment. Prediction of spectral properties was performed on time dependent B3LYP/6-311+G(d,p) level of theory. Additionally the polarizable continuum model (PCM) was employed for the implementation of CH_2Cl_2 solvent effects. a) Isomer **C-2** b) Isomer **D-2**. c) Isomer **A-2**. d) Isomer **B-2**. Reprinted with permission from *Angew. Chem. Int. Ed.* **2017**, *56*, 14536-14539. Copyright 2017 Wiley and Sons.
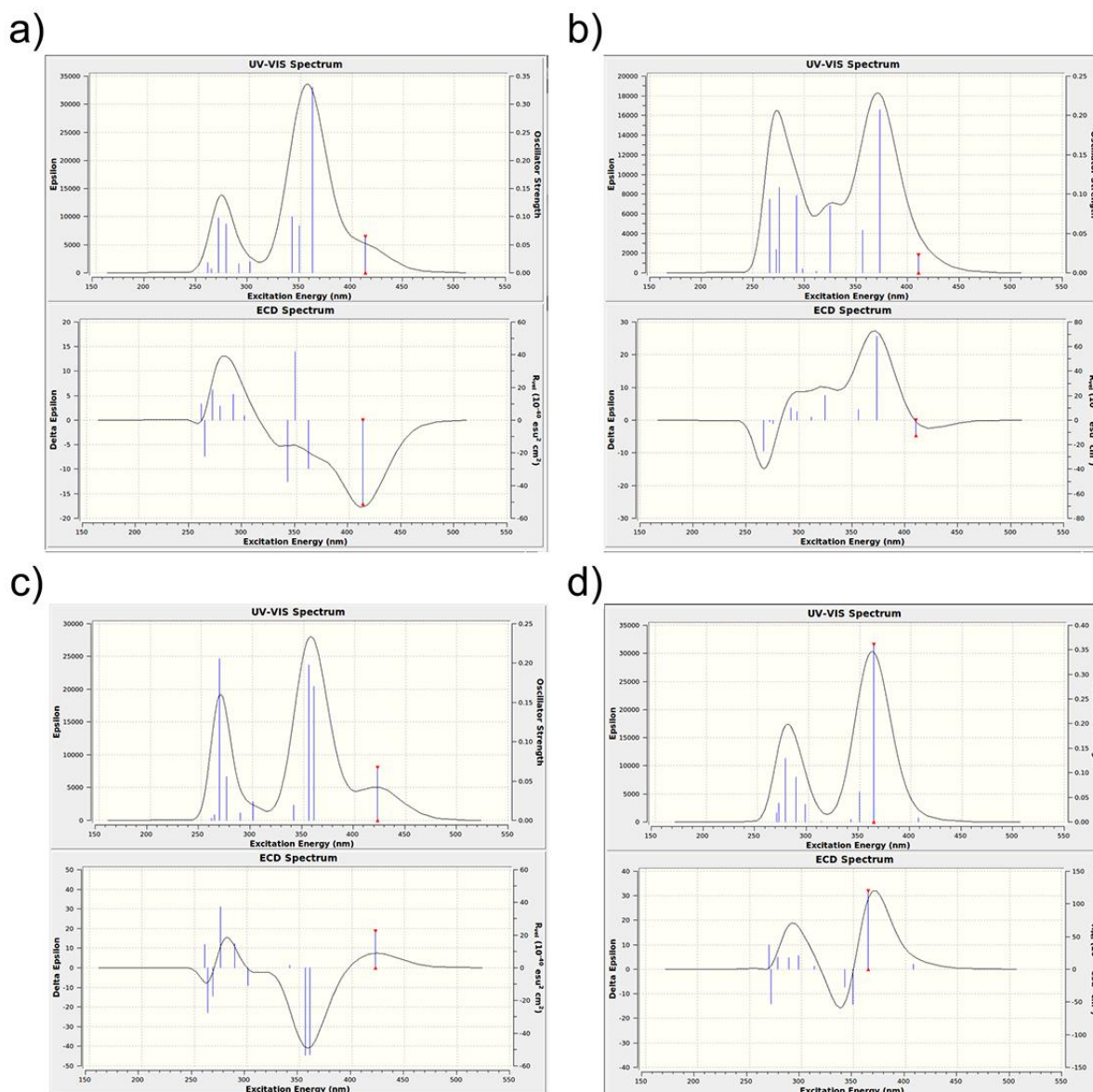
Figure 39:   Theoretically obtained extinction coefficients (top) and ECD spectra (bottom) of motor **5** for all four isomers **A**-**D**. Structures were optimized on the MPW1K/6-311G(d,p) level of theory. Only (*S*)-configured isomers were used for theoretical assessment. Prediction of spectral properties was performed on time dependent B3LYP/6-311+G(d,p) level of theory. Additionally the polarizable continuum model (PCM) was employed for the implementation of CH_2Cl_2 solvent effects. a) Isomer **C-5**. b) Isomer **D-5**. c) Isomer **A-5**. d) Isomer **B-5**. Reprinted with permission from *Angew. Chem. Int. Ed.* **2017**, *56*, 14536-14539. Copyright 2017 Wiley and Sons.

In Table 7 the calculated absorption maxima and the corresponding oscillator strengths as well as the experimentally determined overall absorption maxima are summarized. The predicted overall maxima range from 350 to 375 nm. Theory reliably predicts, that stable isomers **C** exhibit a red shifted absorption maximum in comparison to the stable isomers **A**. The calculated oscillator strengths do not present the extinction coefficient ratio of isomer **A** and **C** of **2** and **5** consistently.

Table 7: Calculated and experimentally determined overall absorption maxima, as well as the calculated corresponding oscillator strengths are summarized. Calculated values are provided only for **2** and **5**.

motor	**2**			**5**			**4**	**3**
	calc.		exp.	calc.		exp.	exp	exp.
isomer	f	λ_{max} (nm)	λ_{max} (nm)	f	λ_{max} (nm)	λ_{max} (nm)	λ_{max} (nm)	λ_{max} (nm)
A	0.4202	350.6	350	0.1976	355.42	351	352	355
B	0.3890	357.77	-	0.3610	363.81	-	-	-
C	0.4481	361.49	364	0.3303	361.34	366	368	370
D	0.2838	365.54	-	0.2075	373.38	-	-	-
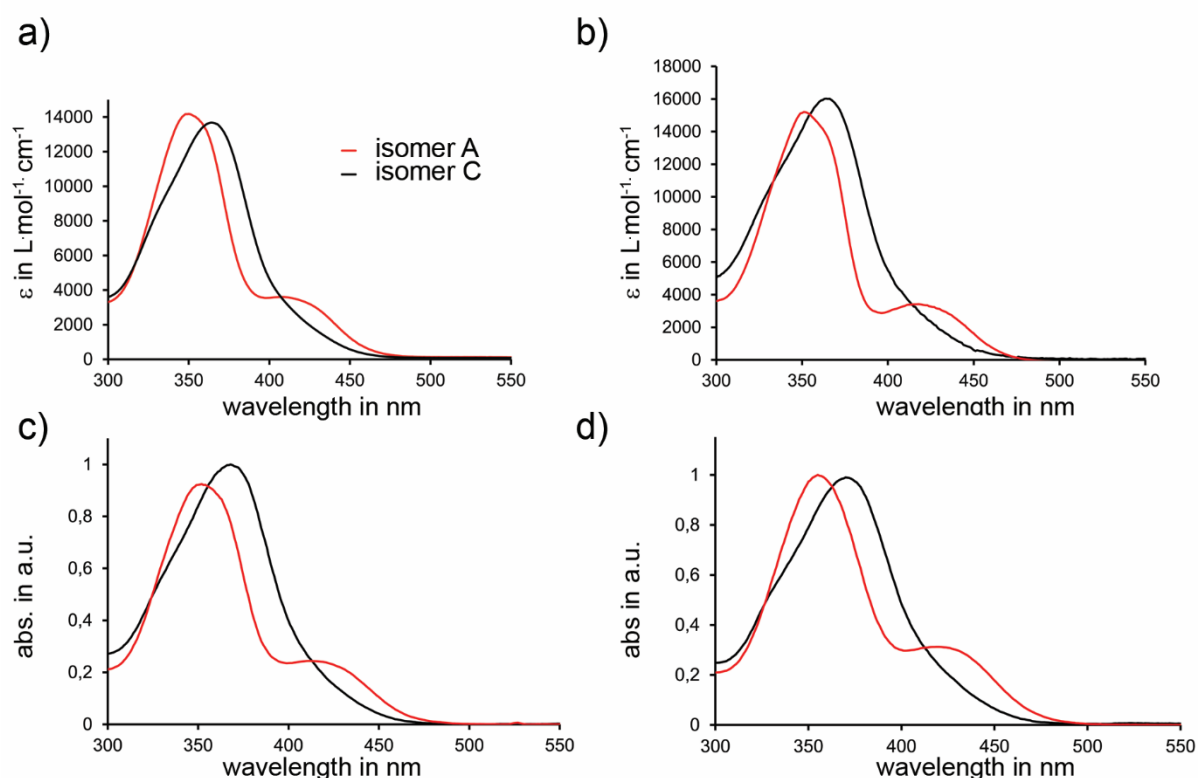
Figure 40: Extinction coefficients (**2** and **5**) and absorption spectra (**3** and **4**) of **A** (red) and **C** (black) in CH$_2$Cl$_2$ at ambient temperature. a) Extinction of **2**. b) Extinction of **5**. c) Absorption spectra of **4**. d) Absorption spectra of **3**.

In Figure 40 the experimentally measured absorption behavior in CH$_2$Cl$_2$ at ambient temperature of motors **2**, **3**, **4** and **5** is illustrated. All derivatives show very similar absorption features, with a red shifted shoulder or maximum for isomers **A** and a red shifted absorption maximum at shorter wavelengths for isomers **C**. Both stable isomers of all motor derivatives shown in Figure 40 absorb blue light up to wavelengths of 450-470 nm.

4.5 Enantiomer separation of stable isomers A and C for motors 2 and 5

Theoretical calculations support the existence of four enantiomeric pairs **A**, **B**, **C** and **D** for HTI-based molecular motors. Since two of these (**B** and **D**) are only accessible in case of irradiation combined with low temperature conditions, a separation of their enantiomers is not possible at ambient temperature. The *E*- and *Z*-configured ground state minima **A** and **C**, however, are perfectly stable and **A/C** separation as well as separation of their enantiomeric pairs *E*-(*S*)-*P*/*E*-(*R*)-*M* and *Z*-(*S*)-*P*/*Z*-(*R*)-*M* is possible. The isolation by chiral HPLC was performed for derivative **5**. The corresponding HPLC traces are shown in Figure 41. For further information on the analysis of motor **1** see referecence 1[1] and on motor **2** see reference 38[38].
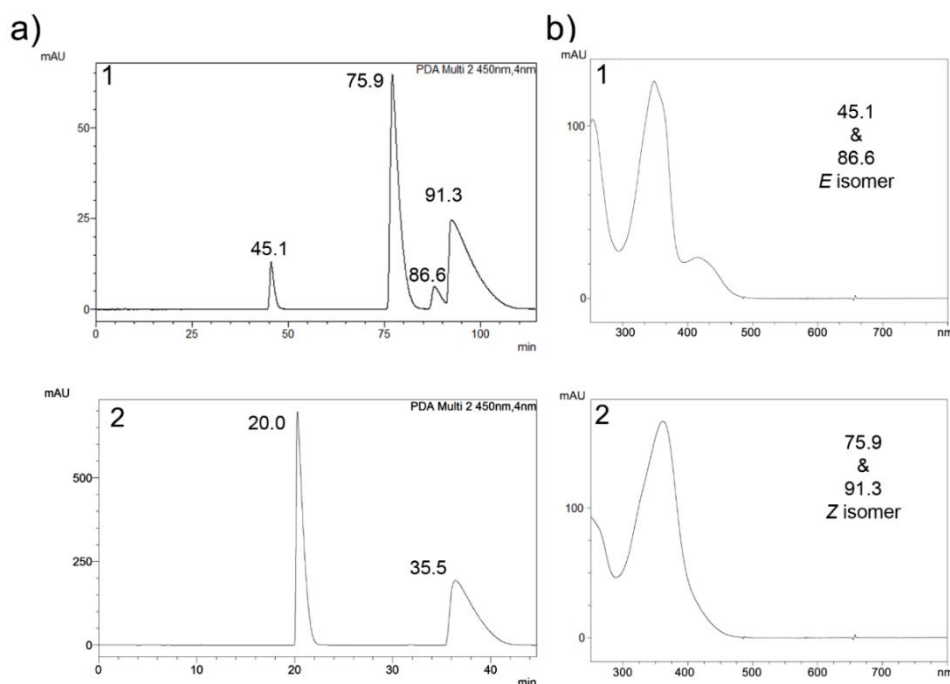
Figure 41:   Enantiomer separation of a mixture of **A** and **C** of motor **5** by chiral HPLC leads to four distinct fractions. Two pairs exhibit the same absorption spectrum, which shows their enantiomeric character. a) 1. Enantiomer separation was performed by using a CHIRALPAK® ID column from Diacel (*n*-heptane : 2-PrOH = 95 : 5, at 40 °C). 2. Since enantiomers eluted between 80 and 95 min are badly separated, racemic *Z*-**5** was separated from racemic *E*-**5** by column chromatography (SiO₂, *i*Hex:EtOAc, 7:3 v/v) first and then separation of the Z-configured enantiomers was performed by HPLC using a CHIRALPAK® ID column from Diacel (*n*-heptane : 2-PrOH = 85 : 15, at 40 °C) The corresponding HPLC trace is shown. b) 1. Absorption spectrum of enantiomers *E*-(*S*)-*P* and *E*-(*R*)-*M* eluted after 45 and 87 min. Since the absorption spectra are identical only the spectrum of one enantiomer (45 min) is shown. 2. Absorption spectrum of enantiomers *Z*-(*S*)-*P* and *Z*-(*R*)-*M* eluted after 76 and 91 min. Since the absorption spectra are identical only the spectrum of one enantiomer (76 min) is shown. Reprinted with permission from *Angew. Chem. Int. Ed.* **2017**, *56*, 14536-14539. Copyright 2017 Wiley and Sons.

Separation by chiral HPLC of solutions of **A**/**C** mixtures of **5** furnished four distinct fractions, as it can be observed in the HPLC traces depicted in Figure 41. Two pairs exhibit each the same absorption spectra, which is expected for enantiomers. Thus, it was possible to separate *E*-(*S*)-*P* and *E*-(*R*)-*M* enantiomers as well as *Z*-(*S*)-*P* and *Z*-(*R*)-*M*. Additionally, for motor **2** a toluene solution of the enantiomer *Z*-(*R*)-*M* was heated to 100 °C for 12 h and eluted afterwards by chiral HPLC. The experiment, performed by *Kerstin Hoffmann*[IV], showed besides *E*/*Z* isomerization no thermal racemization of the sulfoxide stereocenter, which proves an inversion barrier of at least 32 kcal·mol^{-1}.[IV] For unambiguous determination of the stereochemistry of all enantiomers it is necessary to crystalize at least one pure enantiomer obtained from chiral HPLC. From the structure in the crystalline state the stereochemistry of the sulfoxide moiety can be derived. By irradiation of a solution of the very same batch the measured crystal grew, a mixture of *E*/*Z* isomers with identical configuration of the sulfoxide stereocenter can be obtained. By subsequent separation using chiral HPLC with the very same settings as for the separation of all four enantiomers, retention times and configuration of the sulfoxide can be correlated.[IV] This experiment was successfully performed for motor derivative **2** by *Kerstin Hoffmann*[IV] (for analogue experimental details of motor **1** see reference 1[1]). ECD spectra of the isolated enantiomers were acquired and very good agreement with the calculated spectra (Figure 38 and 39) was found. The determination of the stereochemistry by calculated ECD spectra matches the results from the crystallization protocol. Therefore, the stereochemical assignment of the enantiomers of **5** was performed by comparison of calculated ECD spectra with experimentally obtained ECD spectra (Figure 42 and 43) only.
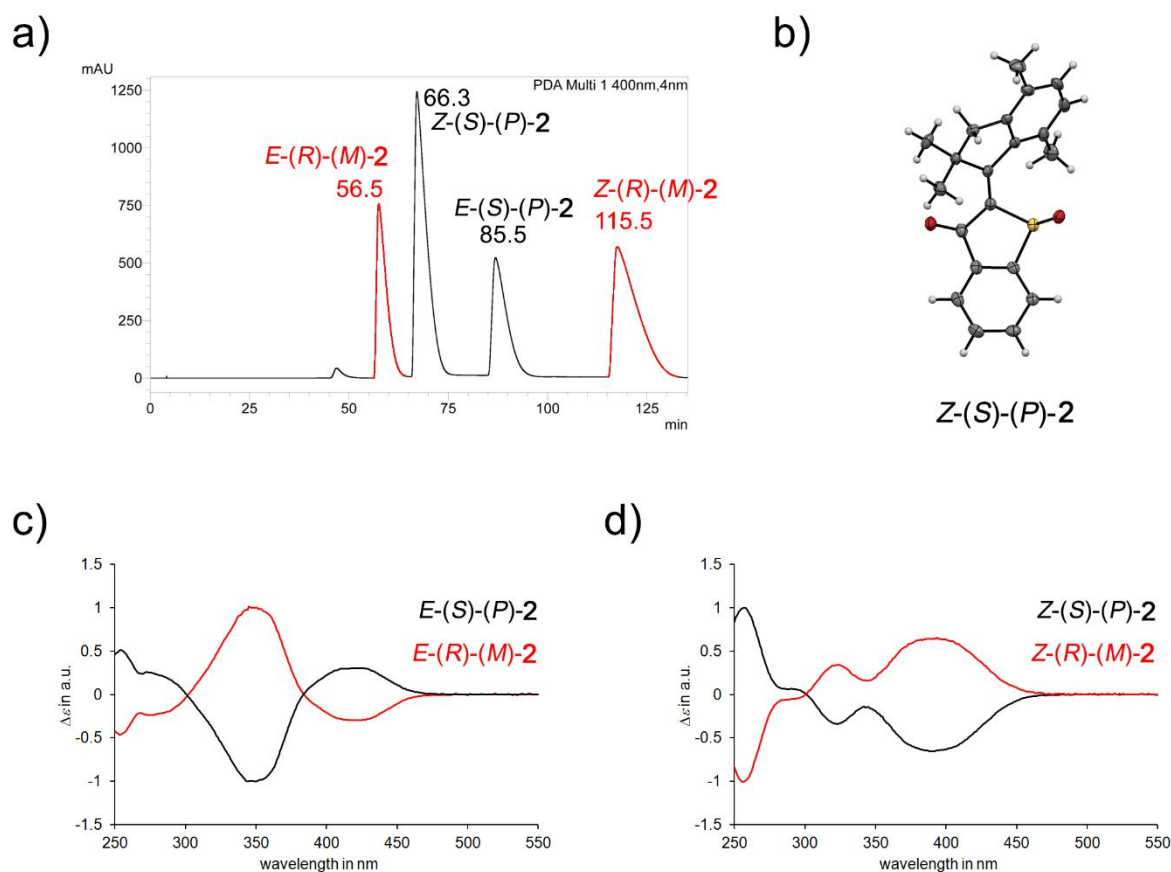
Figure 42:   ECD spectra of pure enantiomers of motor **2** obtained by chiral HPLC separation and assignment of the absolute stereochemistry of all stable enantiomers by comparison to the configuration of Z-(*S*)-*P* in the crystalline state. Experiments were performed by *Kerstin Hoffmann*.[IV] a) HPLC trace obtained from separation of a mixture of **A**/**C** isomers by using a CHIRALPAK® IC column from Diacel (*n*-heptane : 2-PrOH = 95 : 5, at 40 °C). (*R*)-configured enantiomers are highlighted in red, (*S*)-configured enantiomers in black. b) Structure of Z-(*S*)-*P*-**2** in the crystalline state. c) Normalized ECD spectra in *n*-heptane : 2-PrOH (95 : 5) at ambient temperature of isomers *E*-(*S*)-*P* (black) and *E*-(*R*)-*M* (red). d) Normalized ECD spectra in *n*-heptane : 2-PrOH (95 : 5) at ambient temperature of isomers Z-(*S*)-*P* (black) and Z-(*R*)-*M* (red). Adapted with permission from *Angew. Chem. Int. Ed.* **2017**, *56*, 14536-14539. Copyright 2017 Wiley and Sons.
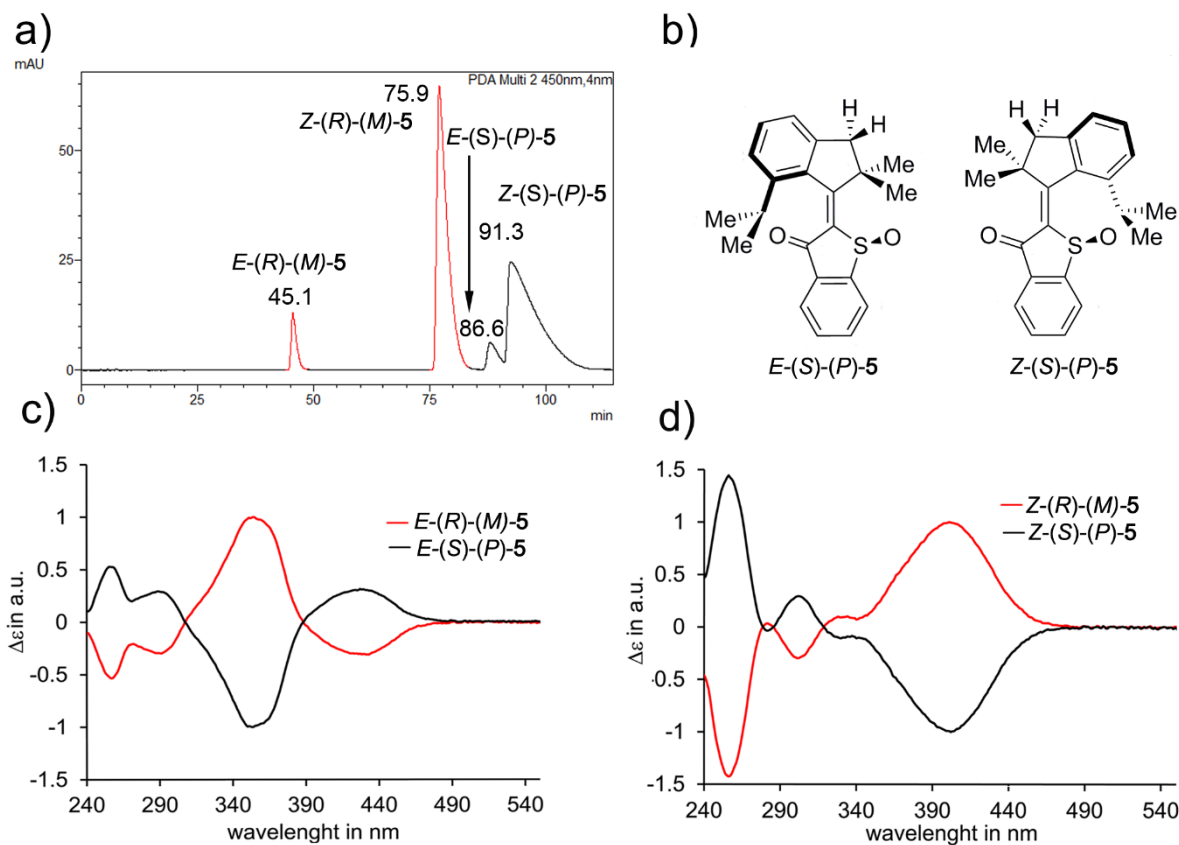
Figure 43:   ECD spectra of pure enantiomers of motor **5** obtained by chiral HPLC separation and assignment of the absolute stereochemistry of all stable enantiomers by comparison to calculated ECD spectra. a) HPLC trace obtained from separation of a mixture of **A**/**C** isomers by using a CHIRALPAK® ID column from Diacel (*n*-heptane : 2-PrOH = 95 : 5, at 40 °C b) First (*R*)-configured enantiomers were eluted (highlighted in red). (*S*)-configured enantiomers are labelled in black. b)Molecular representations of the *E*-(*S*)-*P* and *Z*-(*S*)-*P* isomers. c) Normalized ECD spectra in CH₂Cl₂ at ambient temperature of isomers *E*-(*S*)-*P* (black) and *E*-(*R*)-*M* (red). d) Normalized ECD spectra in CH₂Cl₂ at ambient temperature of isomers *Z*-(*S*)-*P* (black) and Z-(*R*)-*M* (red). Adapted with permission from *Angew. Chem. Int. Ed.* **2017**, *56*, 14536-14539. Copyright 2017 Wiley and Sons.

4.6   Conformational analysis in the crystalline state for motors 2-5

Structures in the crystalline state could be obtained for isomers **A** and **C** of derivatives **2**, **3** and **5**. Crystal structures of motor isomer **C**-**3** as well as of **A-2** were obtained by *David Voßiek*.[X][208] Enantiomerically pure **C-2** was obtained by *Kerstin Hoffmann*.[IV] Only isomer **A** of motor **4** could be crystallized, but X-ray crystallographic analysis revealed a high remaining electron density caused by defectively ordered sulfur atoms. All structures were measured and solved by *Peter Mayer*.[VII] At first sight a great resemblance to theoretically obtained structures can be observed. All structures exhibit a strong helical twist of the rotor part with regard to the stator part. As predicted by the minimum structures from theoretical assessments, the obtained structures with (*S*) configuration show (*P*) helical twisting and (*R*)-configured isomers exhibit (*M*) helical distortion. This can be stated for both, **A** and **C** isomers.
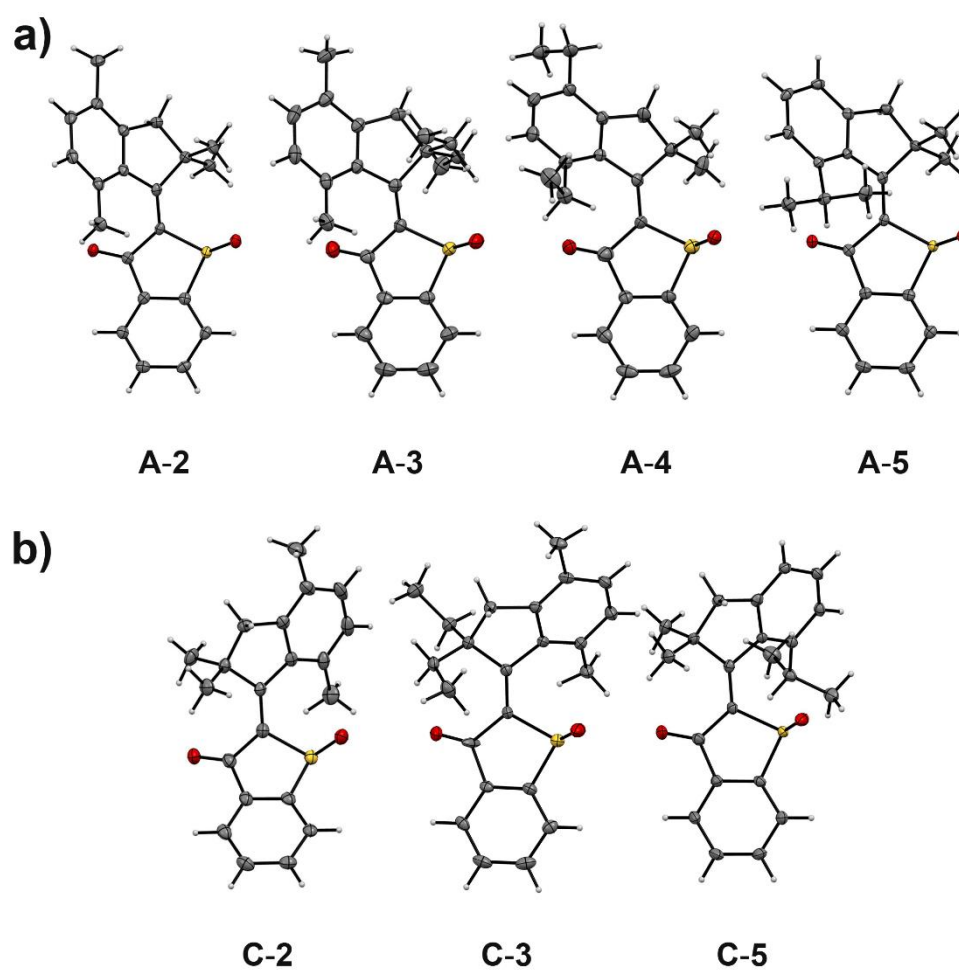
Figure 44:   Structures in the crystalline state of isomers **A** and **C**.[IV, VI, X] a) Racemic isomers **A** of motors **2**-**5**, analyzed by X-ray crystallographic analysis. b) Enantiomerically pure (*S*)-configured **C-2** and racemic **C-3** and **C-5** analyzed by X-ray crystallographic analysis.

Table 8: Comparison of torsional angles, bond lengths and distances of motor derivatives **2-5**. Arbitrary labelling of atoms. Only the (*S*)-configured isomers **A** and **C** are depicted. Distances including varying alkyl residues R^1 always refer to the carbon atom directly bound to the aromatic core of the rotor part. Negative values of **C-3** are owed to the (*R*)-configured sulfoxide of the crystal structure.
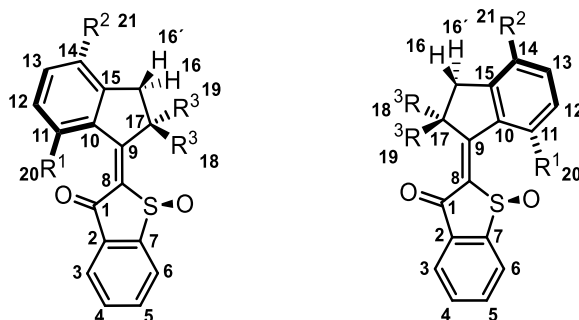
motor isomer	**A-2**	**A-3**	**A-4**	**A-5**		**C-2**	**C-3**	**C-5**
torsional angle					**torsional angle**			
C1-C8-C9-C10	21.54	16.75	18.92	18.61	C1-C8-C9-C17	18.16	–20.20	27.73
C8-C9-C10-C11	31.53	32.97	29.90	36.32	C8-C9-C10-C11	27.62	–34.97	38.43
S-C8-C9-C17	22.26	15.62	17.10	19.05	S-C8-C9-C10	19.68	–16.75	19.45
C9-C10-C11-C20	–1.80	3.25	13.33	10.33	C9-C10-C11-C20	6.89	–13.60	14.40
bond length in Å					**bond length in Å**			
C1-O	1.220	1.207	1.197	1.221	C1-O	1.225	1.233	1.217
S-O(S)	1.492	1.488	1.460	1.497	S-O(S)	1.479	1.470	1.497
C8-C9	1.353	1.356	1.358	1.356	C8-C9	1.361	1.364	1.362
distance in Å					**distance in Å**			
O(1)-C20	2.963	2.924	2.946	3.167	O(S)-C20	3.333	3.753	4.307
O(S)-C18	3.317	3.353	3.454	3.385	O(C)-C18	3.263	3.029	2.959
O(S)-C19	3.449	3.459	3.599	3.411	O(C)-C19	3.333	3.424	3.489

Bond lengths and intramolecular distances show some variations within the series of HTI motor molecules **2-5**. It can be observed that *E*-configured **A** isomers exhibit shorter double bond lengths as it is the case for *Z*-configured isomers **C**. Torsional angles of the central double bond reveal considerable twisting of the rotor part with regard to the stator part. It can be observed, that not only the aromatic rings of the rotor parts are distorted with respect to the plane, defined by C1-C8-S, but also the aliphatic part of the rotor fragment. Torsional angles (C1-C8-C9-C10 / S-C8-C9-C17 for isomers **A** and C1-C8-C9-C17/ S-C8-C9-C10 for isomers **C** determine a (*P*) helical structure for (*S*)-configured crystal structures and (*M*) helices for (*R*)-configured crystal structures. With respect to the directionality of the photoisomerization processes, this helical twist can be assumed to be a unique prerequisite, since a light induced rotation around the central double bond would experience least steric repulsion in the preferred direction. An induced rotation would suffer from pushing two substituents of the double bond against each other and would therefore require much more energy.

4.7   Conformational analysis in solution for motors 3-5

Conformational analysis in solution was conducted by NMR spectroscopy. For more detailed analytical data of motor derivatives **2** and **5** see the Supporting Information of reference 38[38]. The NMR spectroscopic analysis confirmed the molecular structures obtained by X-ray crystallographic analysis and theoretical calculations. In Figure 45 and 46 the HMBC spectra of isomers **C-5** and **A-5** are shown. In Figure 45 and 46 Karplus analysis[225-227] reveals that several structural features observed for calculation and crystallographic analysis coincide also with the conformation in solution. For instance the dihedral angles H(16)-C(16)-C(17)-C(9) as well as C(19)-C(17)-C(16)-H(16') are close to 90° in solution, as it was predicted by calculations and crystal structure analysis, since no cross peak signal in the HMBC spectrum can be observed.
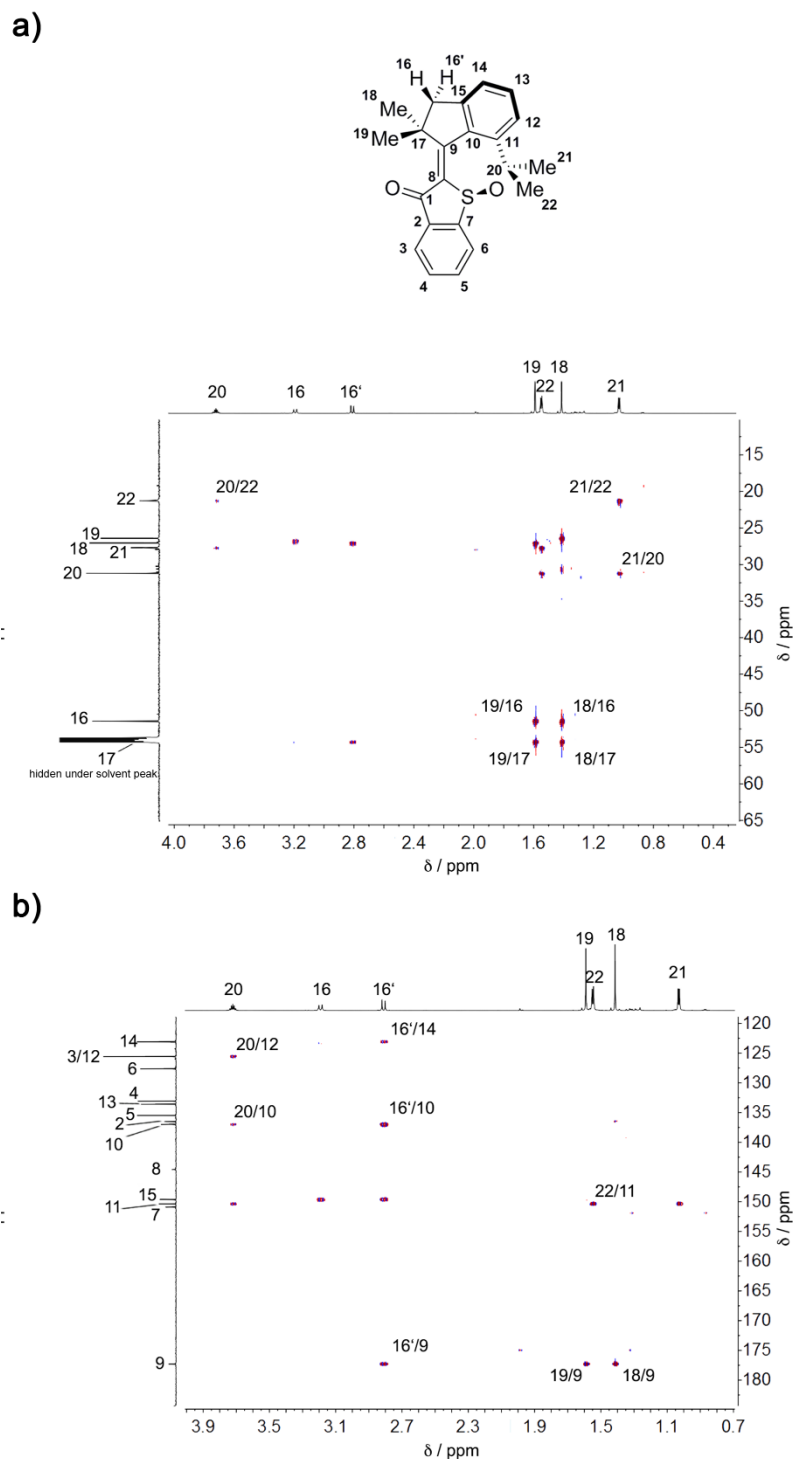
Figure 45: HMBC NMR spectra (800 MHz) of racemic **C-5** in CD_2Cl_2 at ambient temperature and assignment to the (*S*)-configured isomers. a) Aliphatic part of **C-5** acquired at 27 °C. d) Aliphatic aromatic part of **C-5** acquired at 27 °C. No cross peak signals between hydrogen 16 and carbon 9 and hydrogen 16' and carbon 19 for **C-5** can be observed because of almost perpendicular C(9)-C(17)-C(16)-H(16) and C(19)-C(17)-C(16)-H(16') dihedral angles. The absence of these cross peaks match theoretically obtained and crystalline structures. Adapted with permission from *Angew. Chem. Int. Ed.* **2017**, *56*, 14536-14539. Copyright 2017 Wiley and Sons.
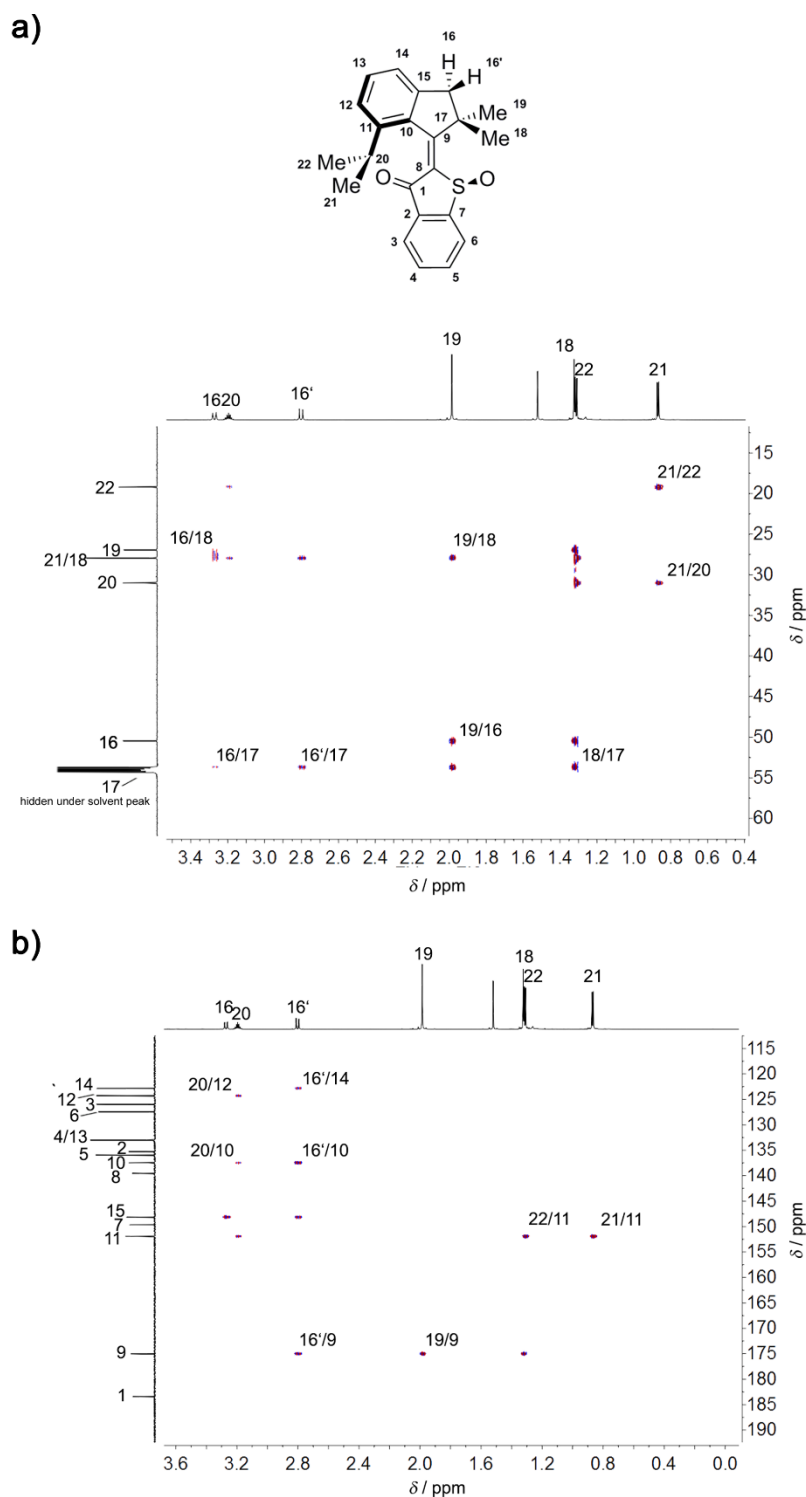
Figure 46: HMBC NMR spectra (800 MHz) of racemic **A-5**, in CD_2Cl_2 at ambient temperature and assignment to the (*S*)-configured isomers. a) Aliphatic part of **A-5** acquired at 27 °C. b) Aliphatic aromatic part of **A-5** acquired at 27 °C. No cross peak signals between hydrogen 16 and carbon 9 and hydrogen 16' and carbon 19 for **A-5** can be observed because of almost perpendicular C(9)-C(17)-C(16)-H(16) and C(19)-C(17)-C(16)-H(16') dihedral angles. The absence of these cross peaks match theoretically obtained and crystalline structures. Adapted with permission from *Angew. Chem. Int. Ed.* **2017**, *56*, 14536-14539. Copyright 2017 Wiley and Sons.

The calculated structure of **C-5** is depicted in Figure 47a exemplarily for illustration of the above mentioned dihedral angles, which were measured to be –89.33° for H(16)-C(16)-C(17)-C(9) and –84.51° for C(19)-C(17)-C(16)-H(16') in case of the calculated structure of **C-5**. The calculated structure of the highly planar transition state **TS_B-C-5** is shown in Figure 47b with dihedral angles of –141.78° for H(16)-C(16)-C(17)-C(9) and –146.10° for C(19)-C(17)-C(16)-H(16'). Thus, it can be concluded, that the absence of cross peak signals in the HMBC are indicative for a similarly helical structure in solution as depicted in Figure 47a. A planar structure with much larger dihedral angles, like the **TS_B-C-5,** would in contrast lead to observable cross peak signals in the HMBC and can therefore be excluded. Analogous behavior was observed for the *E*-configured isomer **A-5**. In fact, all motor derivatives **1-5** exhibit the absence of the discussed cross peak signals, which confirms a helical distortion for all HTI-based motors in solution in the isomeric states **A** and **C**.
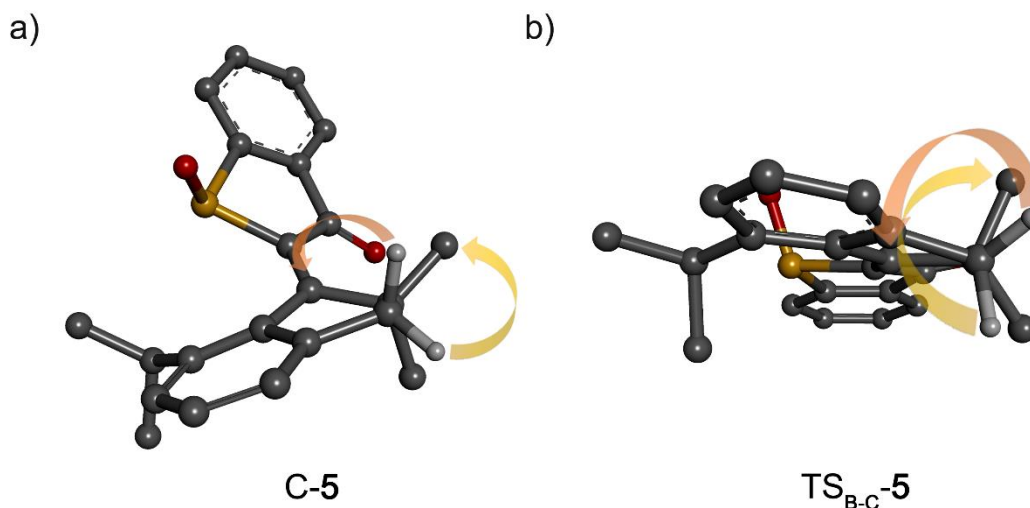
Figure 47:   Calculated structures of **TS_B-C-5** and **C-5** for illustration of the indicative dihedral angles within the rotor fragment. Only the relevant hydrogens H(16) and H(16') are depicted. a) The calculated structure of **C-5** reveals –89.33° for the H(16)-C(16)-C(17)-C(9) dihedral angle and –84.51° for the C(19)-C(17)-C(16)-H(16') dihedral angle. b) The calculated transition state structure of **TS_B-C-5** exhibits –141.78° for H(16)-C(16)-C(17)-C(9) dihedral angle and –146.10° for C(19)-C(17)-C(16)-H(16') dihedral angle.

Comparison between the calculated structures and the experimentally obtained structures in the crystalline state of motor derivative **5** revealed a significant deviation of the dihedral angle of the *iso*-propyl group. As signal intensities of the NOESY cross peaks between the *iso*-propyl group and adjacent aromatic protons hint in favor of the calculated structures, it is most likely the better description of the conformation in solution than the structure in the crystalline state.

In case of motor derivative **3** the crystal structure of isomer **C** shows an orientation of the ethyl groups different from the predicted overall theoretical minimum. However, another low lying minimum with ethyl-group conformation very similar to the crystal structure was found in the calculation. It is only 0.26 kcal·mol^{-1} higher in energy than the global minimum of isomer **C**. Further information of the exact configuration in solution could not be obtained by Karplus analysis in this case. It is probable that both structures contribute to the conformation in solution. In case of isomer **A-3** theoretical prediction and crystal structure analysis reveal very similar ethyl-group conformation. In addition, a second low lying minimum with different ethyl-group conformation was found. Therefore, conformation in solution could be dominated by both structures in this case, too. Derivative **4** also shows several conformations for all isomers received by theoretical assessment. Since the crystal structure of **A-4** lacks of appropriate data, it is not possible to derive a conclusion with regard to the conformation in solution. However, by interpretation of the theoretically obtained data, it can be derived that at least two minima are populated in solution for all isomers, which are predominantly characterized as the rotary conformations of the ethyl group at aromatic position 14. In addition, for aromatic position 11 different minima could be found, which show varying ethyl-group conformation. However, these minima are energetically too high to contribute significantly to the conformations in solution. Also in this case a NMR spectroscopic analysis could not confirm the minimum structure in solution by experimental means.
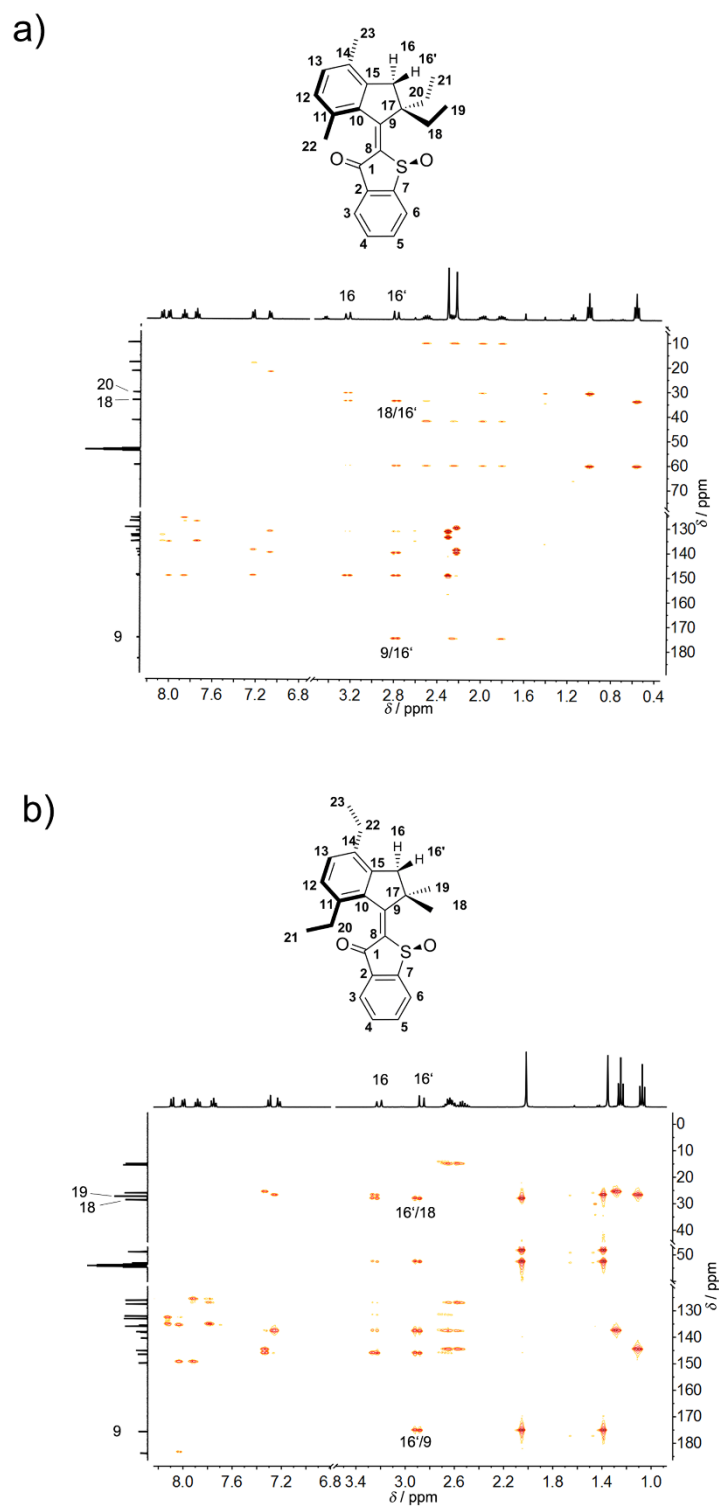
Figure 48: HMBC NMR spectra (400 MHz) of racemic **A-3** and **A-4** in CD$_2$Cl$_2$ at 27 °C and assignment to the (*S*)-configured isomer. a) HMBC spectrum of **A-3**. b) HMBC spectrum of **A-4**. No cross peak signals between hydrogen 16 and carbon 9 are observed because of dihedral angles C(9)-C(17)-C(16)-H(16) and C(20)-C(17)-C(16)-H(16') are close to 90°. Theoretically obtained structures of **A-3** and **A-4** as well as the crystal structure of **A-3** exhibit similar dihedral angles, hinting at similar conformations in solution.

The unambiguous assignment of the configuration of the double bond was performed by NOESY NMR spectroscopy. Long range cross peaks of signals were observed between indicative protons H(19) and H(3), H(22) and H(6) and H(20) and H(6) for isomer **C** of motor derivative **5**, as can be seen in Figure 49. The spectrum was acquired with a Bruker AVANCE III HD 800 (800 MHz) NMR spectrometer with 3 s mixing time at 27 °C. The distances between these hydrogens were derived from the crystal structures and range between 4.59 Å (**C**-**5**: H(19)/H(3)), 4.65 Å (**C**-**5**: H(22)/H(6)) to 5.01 Å (**C**-**5**: H(20)/H(6)). The use of long range NOE coupling for double-bond assignment was previously used for motor derivative **1**.[1] Also in the case of **A** isomers of **3**, **4**, and **5** the configuration of the double bond in solution was determined by NOE coupling, as illustrated in Figures 49, 50 and 51. For double-bond assignment of motor **2**, see reference 38.[38] The indispensable assignment of the configuration of the double bond by experimental means then allowed for direct quantification of photophysical properties such as quantum yields and isomer composition in the pss, as well as the identification of the metastable isomers **B** and **D**.

a)

b)
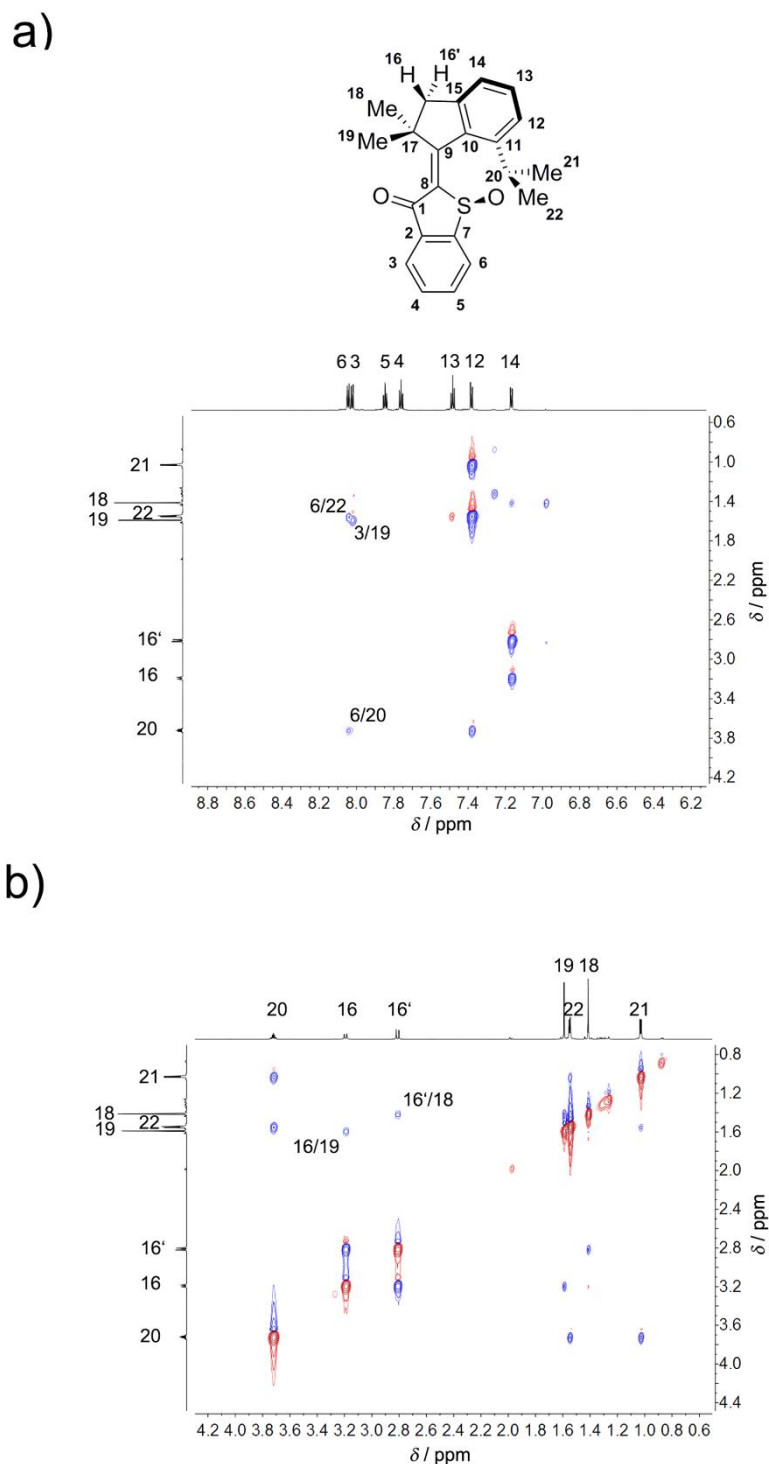
Figure 49:   NOESY NMR spectra (800 MHz, 3 s mixing time) of racemic **C-5** in CD$_2$Cl$_2$ at 27 °C and assignment of the signals to the (*S*)-configured isomer **C**. a) Aliphatic-aromatic part of the spectrum. NOE coupling between hydrogen 6 and 22 as well as 6 and 20 can be observed proving the *Z* configuration of the central double bond. b) Aliphatic-aliphatic part of the spectrum. NOE couplings between hydrogen 16 and 19 as well as 16' and 18 can be observed, indicating that these hydrogen pairs exhibit exhibit *syn* arrangement. Adapted with permission from *Angew. Chem. Int. Ed.* **2017**, *56*, 14536-14539. Copyright 2017 Wiley and Sons.
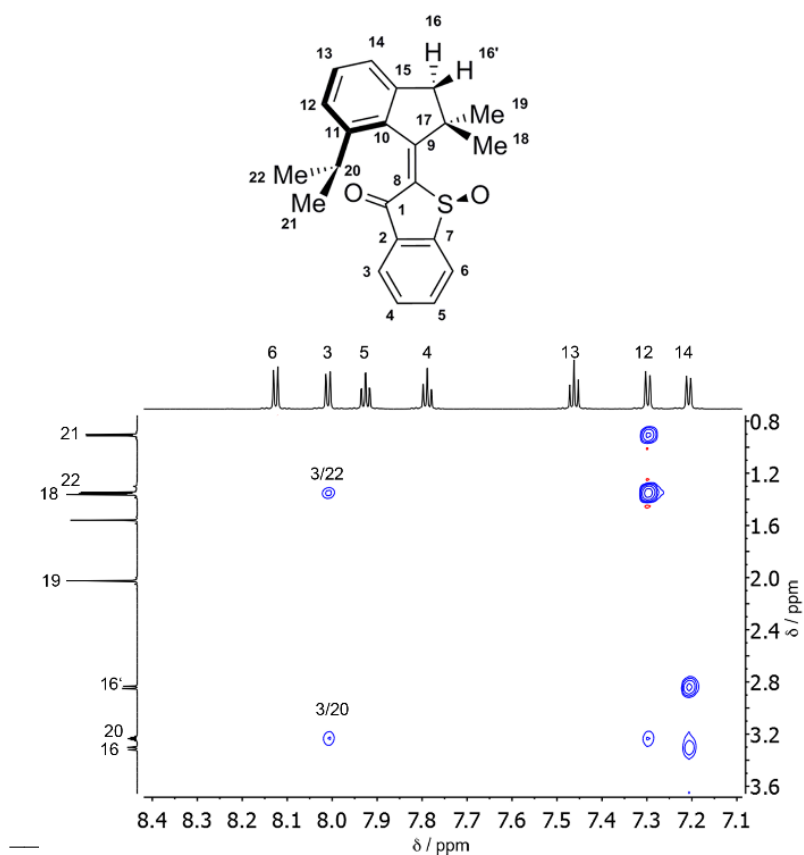
Figure 50: NOESY NMR spectra (800 MHz, 3 s mixing time) of racemic **A-5** in CD$_2$Cl$_2$ at 27 °C and assignment of the signals to the (*S*)-configured isomers **A**. Aliphatic-aromatic part of **A-5**. NOE couplings between hydrogen 3/20 and 3/22 prove the *E* configuration of the central double bond. Similar coupling intensities of hydrogen 12 to hydrogens 21 and 22 indicate a rather symmetric *iso*-propyl arrangement as predicted from theory. Adapted with permission from *Angew. Chem. Int. Ed.* **2017**, *56*, 14536-14539. Copyright 2017 Wiley and Sons.
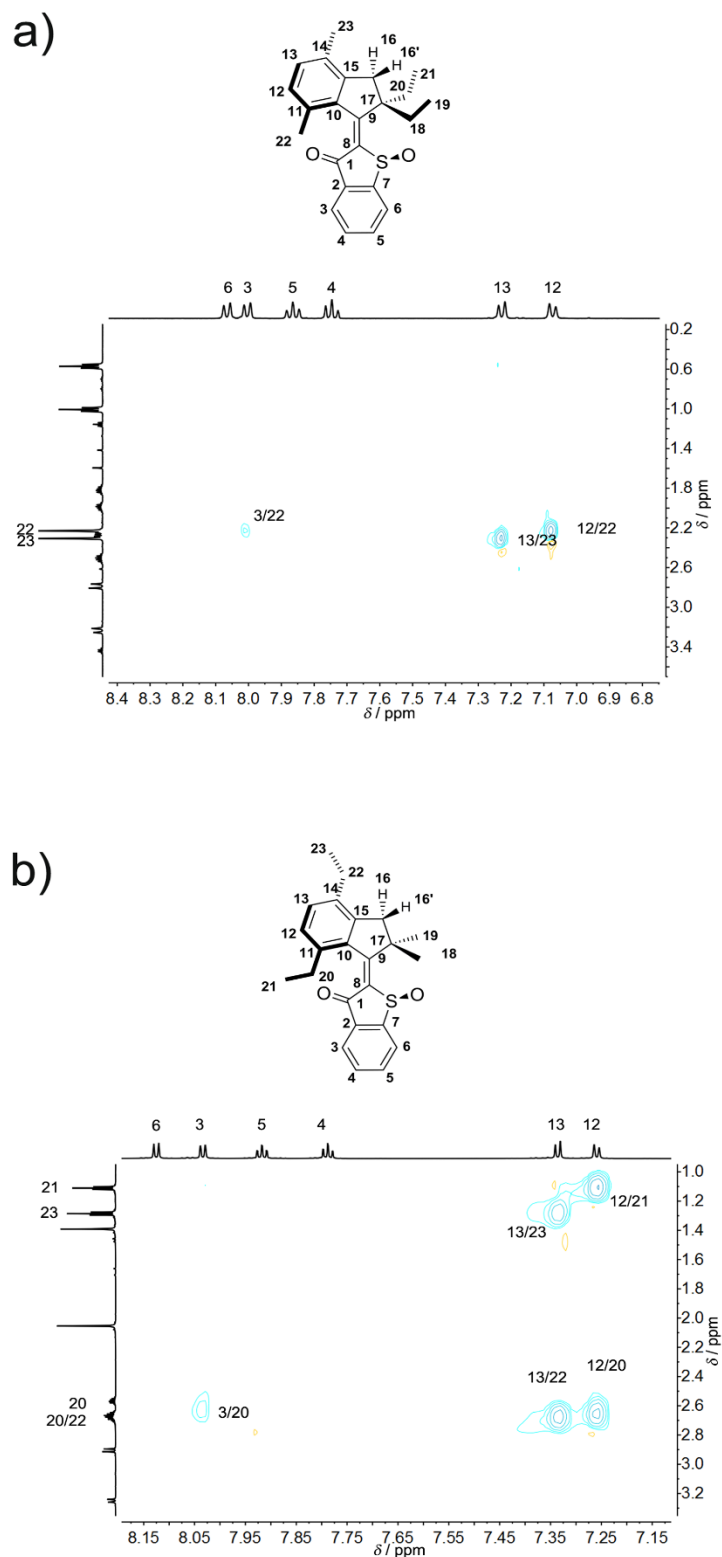
Figure 51: NOESY NMR spectra (800 MHz) in CD$_2$Cl$_2$ at 25 °C of isomers **A-3** and **A-4** and assignments to the (*S*)-configured isomer. a) NOESY spectrum of **A-3**. NOE coupling between hydrogens 3 and 22 proves the *E* configuration of the central double bond. b) NOESY spectrum of **A-4**. The NOE coupling between hydrogens 3 and 20 proves the *E* configuration

4.8   Light induced *E/Z* isomerization

HTIs are known to undergo photoisomerization of the central double bond under light input. The induced geometry change is accompanied by different absorption behavior, which can be easily monitored by steady state UV/vis spectroscopy. At ambient temperatures HTI-based molecular motors seem to behave as regular photoswitches with only two interconvertible species, since fast decaying metastable species **B** and **D** do not contribute to the steady state absorption spectra. Therefore, only two interconverting species, e.g. stable isomers **A** and **C** are observed with the limited time resolution of steady state absorption spectroscopy and the corresponding absorption spectra are just the sum of the contributing isomer spectra. Irradiation with different wavelengths leads to changes of isomeric ratios of isomers **A** and **C**. Under prolonged irradiation a wavelength specific equilibrium is reached (pss) with a characteristic isomeric ratio. This ratio can be determined if the corresponding absorption spectra of pure isomer **A** and isomer **C** are known. A summary of the isomeric ratio in the pss after irradiation with different wavelengths for motors **2** to **5** is given in Table 9. Pure isomer spectra are available either by physical separation of the isomers and subsequent measurement of the absorption spectra, or by a combined method using NMR spectroscopy for determination of isomeric ratio and UV/vis spectroscopy for detection of the corresponding absorption spectrum.[83] In Figure 52 the absorption changes of motors **3** to **5** are depicted for illustration of the photochromic behavior of HTI-based molecular motors under irradiation conditions.
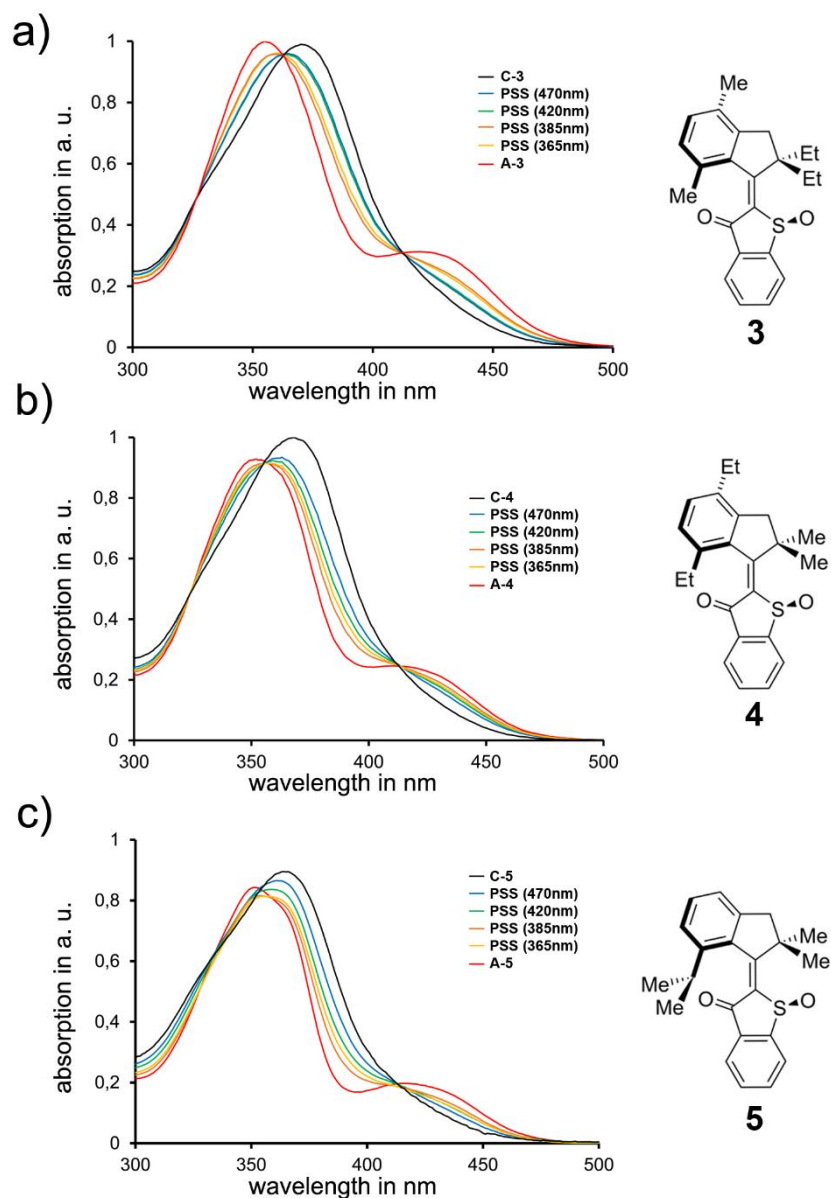
Figure 52:   Steady state UV/vis spectroscopic measurements were performed in CH_2Cl_2 at ambient temperatures. Spectra recorded in the pss at different wavelengths of irradiation. Photostationary state is reached when no spectral changes can be achieved under prolonged irradiation. Pure isomer **A** is shown in red. Pure isomer **C** is shown in black. It can be observed that 100% of **A** or 100% of **C** are not accessible by irradiation. a) Absorption spectra of motor **3**. b) Absorption spectra of motor **4**. c) Absorption spectra of motor **5**.

Table 9:   Isomeric ratio in the pss obtained by irradiation of motors **2** to **5** in CH_2Cl_2 at ambient temperature with different LEDs (wavelength at the maximum of the LED-emission spectrum). Data of motor **2** were provided by *Kerstin Hoffmann*.[IV]

wavelength [nm]	A-2	C-2	A-3	C-3	A-4	C-4	A-5	C-5
470	**39**	**61**	**32**	**68**	**35**	**65**	**31**	**69**
450	-	-	35	65	38	62	35	65
435	41	59	-	-	-	-	40	60
420	46	54	50	50	50	50	50	50
405	57	43	60	40	60	40	60	40
385	**67**	**33**	**63**	**37**	**68**	**32**	**68**	**32**
365	61	39	55	45	59	41	56	44
305	-	-	-	-	-	-	56	44

For all investigated molecular motors **2** to **5** individual isomeric yields, obtainable by irradiation, are moderate. The maximum yields of isomer **C** (56% to 69%) can be obtained by irradiation of motor solutions with 470 nm. Isomer **A** can be accumulated up to 63% - 68% by irradiation with 385 nm. Higher isomeric yields were obtained for methoxy-substituted motor **1**[1] (83% of isomer **C** by irradiation with 490 nm and 78% of isomer **A** by irradiation with 405 nm). In comparison to unsubstituted HTI, which is capable of almost quantitative switching (94% *E* isomer by irradiation with 420 nm and 100% *Z* isomer by irradiation with 505 nm[81]) photoswitching performance is somewhat diminished. A detailed explanation for this behavior is difficult, since a combination of photochromism and quantum yield of photoisomerization contributes to the pss. In general, high isomeric yields in the pss can be obtained if the interconverting species provide minimal spectral overlap. For example a good yield of **C** can be obtained, if isomer **A** exhibits large extinction coefficients, while isomer **C** possess only small extinction coefficients at the same wavelength. The opposite is required for obtaining high isomeric yields of isomer **A** at a different wavelength of irradiation. In Figure 53 the wavelength dependent absorption ratios of isomers **A** and **C** of methoxy-substituted motor **1**, *iso*-propyl bearing motor **5** and unsubstituted HTI **14** as well as the isomeric ratios in the pss are illustrated.
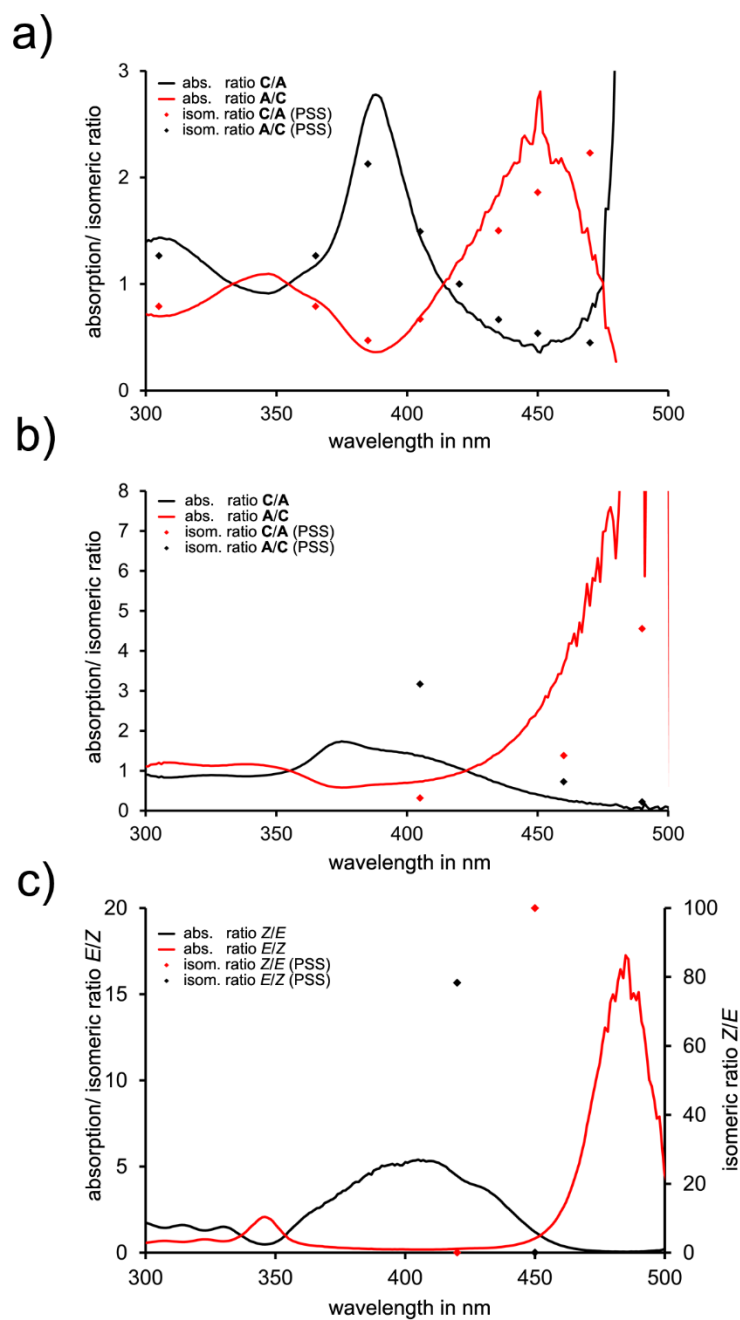
Figure 53: Wavelength dependent absorption ratios and isomeric ratios in the pss of motors **5** (a) and **1** (b) as well as unsubstituted HTI **14** (c) in CH₂Cl₂ at ambient temperature. Isomer ratios in the pss of HTI **14** at different wavelenghts were measured in toluene. Isomeric and absorption ratios are represented by the y-axes. Absorption spectra of both pure isomers of HTI **14** were provided by *Sandra Wiedbrauk*[XI]. Absorption spectra of both pure stable isomers of motor **1** were provided by *Monika Schildhauer*[VIII] and *Manuel Güntner*[III].

For motor **5** a clear correlation between isomeric ratios in the pss and absorption ratios can be observed. Isomeric yields of almost 70% are obtained, if absorption ratios reach a maximal value of almost 3. LEDs with relatively broad emission spectra (±20 nm) were used for the irradiation. The correlation should be further increased if monochromatic light is used for these measurements. Surprisingly, motor **1** exhibits relatively low absorption ratios in the range of 360 nm to 420 nm in comparison to motor **5,** as can be seen in Figure 53b. Nevertheless, higher isomeric ratios of 78% **A** / 22% **C** can be obtained by irradiation with 405 nm in comparison to motor **5**. Thus, superior switching behavior of **1** under 405 nm irradiation must originate mainly from the ratio of the quantum yields of **C** to **A** isomerization and **A** to **C** isomerization.

Table 10:   Quantum yields of motor derivatives **1**, **2** and **5**[XII] as well as of HTI **14** in CH_2Cl_2.[97, 102]

derivative	$\phi_{Z/E}$	$\phi_{E/Z}$	$\phi_{Z/E}$ / $\phi_{E/Z}$	$\phi_{E/Z}$ / $\phi_{Z/E}$
HTI **14**	23%	5%	4.6	0.22
motor **1**	24%	7%	3.4	0.29
motor **2**	15%	10%	1.5	0.67
motor **5**	11%	9%	1.3	0.78

In Table 10 the corresponding quantum yields as well as quantum yield ratios are shown. A ratio of 3.4 in favor of *Z* to *E* photoisomerization can be observed for derivative **1**, which leads to hight yields of isomer *Z*, despite inferior absorption ratios. Also a high yield of isomer *E* is obtained in the pss at 450 nm irradiation. In this case the high absorption ratio can outcompete the diminished quantum yield of 7%. Similar behavior is observed for unsubstituted HTI 14, although the effects are much more pronounced. Excellent yield of isomer *E* is the result of a high quantum yield $\phi_{Z/E}$ of 23% as well as a high absorption ratio of 5. Quantitative generation of isomer *Z* is again provided by an excellent absorption ratio of over 15, which outcompetes the low quantum yield $\phi_{E/Z}$ of 5%. In the case of motor **5** almost identical quantum yields cancel each other out. Hence, isomeric yields in the pss are dominated by the absorption ratios, which is nicely observable in highly correlating absorption ratios and isomeric ratios in the pss. On the basis of these data the excellent photoswitching behavior of unsubstituted HTI **14** can be summarized as a beneficial quantum yield ratio, with high yielding *Z* to *E* photoreaction and a relatively low yielding back isomerization, as well as minimal spectral overlap in the red-shifted part of the visible spectrum. In the case of molecular motors, however, quantitative photoswitching is of minor importance. For increased motor efficiency the quantum yields of both photoreactions should be as high as possible. Hence, the ratio of quantum yields is not an appropriate dimension for evaluation of motor functionalities.

4.9   Quantum yield determination for motors 2 and 5

The quantum yields $\phi_{Z/E}$ and $\phi_{E/Z}$ for motor derivatives **1**, **2** and **5** were measured by *Roland Wilcken*.[XI] Details on the measurements can be found in the Supporting Information of reference 102.[102] Quantum yields of motors **1** and **2** were obtained by transient absorption spectroscopy, whereas quantum yield of motor **5** was additionally determined by a steady state absorption technique. An instrumental setup of the *Riedle* group was used for this purpose.[228] Quantum yield measurement of HTI **14** was reported in reference 97.[97] A profound discussion on quantum yields in combination with other photophysical properties, which were determined by transient absorption spectroscopy can be found in chapter 2.20. The quantum yield of a photoreaction is defined as the ratio of generated photoproduct and absorbed photons:

$$\phi = \frac{c_{prod} \cdot V \cdot N_A \cdot h \cdot c}{P_{abs} \cdot f \cdot \lambda_{ex} \cdot \Delta t} \; ;$$

$$\text{with } P_{abs} = (P_{\text{reference}} - P_{\text{sample}}) \; ; \qquad\qquad \text{(eq. 9)}$$

$$\text{and } f = \frac{1 + R \dfrac{P_{\text{sample}}}{P_{\text{reference}}}}{1 - R} \; ;$$

with V = volume of the sample

N_A = Avogadro constant

h = Planck constant ($6.626 \cdot 10^{-34}$ J·s)

c = speed of light

f = correction factor of reflection

R = the reflection coefficient of the cuvette

λ_{ex} = the excitation wavelength

The absorbed power (P_{abs}) is the difference of transmitted power of the sample containing cuvette (P_{sample}) and the same cuvette containing pure solvent ($P_{reference}$). Light is reflected at the inner side of the cuvette, which leads to slightly increased irradiation intensities. For correction the reflection coefficient R of the glass is taken into account by introducing f as correction factor. The number of photons absorbed is given by the absorbed power P_{abs}, the wavelength of irradiation λ_{ex} and irradiation time Δt. The number of photoproducts is represented by the concentration of the product (c_{prod}) and the volume of the cuvette.

4.10 Thermal double-bond isomerization of motor 5

Since unambiguous assignment of the configuration of the double bond is possible by NOESY experiments, the thermal conversion between *E*- and *Z*-configured HTI-based molecular motors, their kinetics, their associated activation energies, as well as the relative minimum energies of all isomers can be investigated next. For the thermal isomerization of methoxy-based motor **1** a thermal barrier of 29.5 kcal·mol^{-1} was found in toluene, while isomer **C** is 0.82 kcal·mol^{-1} lower in energy. This can be translated into 75/25 isomeric ratio at equilibrium conditions at 100 °C.[1] The thermal barrier found for motor **1** is slightly decreased with regard to the measured thermal barrier of 31 kcal·mol^{-1} of unsubstituted HTIs.[81] The small effect could be likely derived from the helical twisting or from the increased electron donation caused by methoxy substitution at the rotor fragement. It is already known that HTI-derivatives with strong electron donating groups like NMe$_2$-substituents in *para*-position show strongly diminished thermal barriers of 21 to 23 kcal·mol^{-1} for the *E* to *Z* isomerization.[104-105] Therefore, electron donation could be the most probable explanation in this case, too. Theoretical calculations predicted isomer **A** as the overall thermodynamically minimum for alkylated HTI-based motors in stark contrast to the methoxy-substituted motor **1**. Hence, for investigation of the thermal isomerization pure isomer **C** or isomer **C** enriched toluene solutions were heated for several hours to 100 °C. The isomer composition was monitored by ^{1}H NMR spectroscopy at different time intervals. In Figure 54 the thermal isomerization of derivative **5** is illustrated. Kinetic data of motor **2** can be found in reference 38.[38]

For the thermal **C** to **A** conversion of motor **5** a first order kinetic was found for the decay of isomer **C** at 100 °C. A dynamic equilibrium with 19/81 **C/A** composition for **5** was established after prolonged heating. That means the observed decays are influenced by both thermal transitions, **C** to **A** and **A** to **C** conversion as described in Equation 10.

$$\ln\left(\frac{c(\boldsymbol{C}0)-c(\boldsymbol{C}\text{eq})}{c(\boldsymbol{C}t)-c(\boldsymbol{C}\text{eq})}\right) = (k(\boldsymbol{C} \rightarrow \boldsymbol{A}) + k(\boldsymbol{A} \rightarrow \boldsymbol{C}))t \qquad \text{(eq. 10)}$$

with $c(\mathbf{C}_0)$ = initial concentration of the **C** isomer at the starting point of the experiment, $c(\mathbf{C}_{\text{eq}})$ = concentration of isomer **C** at equilibrium conditions, $c(\mathbf{C}_t)$ = concentration of the isomer **C** at the distinct point in time, $k(\boldsymbol{C} \rightarrow \boldsymbol{A})$ = rate constant of **C** to **A** isomerization, $k(\boldsymbol{A} \rightarrow \boldsymbol{C})$ = rate constant of **A** to **C** isomerization, and t = elapsed time.

Hence the slope $m = 0.000036$ s^{-1} for motor **5** of the logarithmic plot represent the sum of both rate constants governing the thermal **C** to **A** and **A** to **C** conversions. From the slope of the logarithmic plot

and the equilibrium ratio of both isomers, the rate constant for **C** to **A** isomerization can be calculated according to Equation 11.

$$k(\textbf{\textit{C}} \rightarrow \textbf{\textit{A}}) \; = \; \frac{m}{1 + \frac{c(\textbf{\textit{C}}\text{eq})}{c(\textbf{\textit{A}}\text{eq})}} \tag{eq. 11}$$

Considering the law of mass action (Equation 3):

$$\frac{c(\textbf{\textit{C}}\text{eq})}{c(\textbf{\textit{A}}\text{eq})} = \frac{k(\textbf{\textit{A}} \rightarrow \textbf{\textit{C}})}{k(\textbf{\textit{C}} \rightarrow \textbf{\textit{A}})} \tag{eq. 12}$$

with $c(\textbf{\textit{A}}\text{eq})$ = concentration of isomer **A** and $c(\textbf{\textit{C}}eq)$ = concentration of isomer **C** at equilibrium conditions.

Hence the thermal **C** to **A** isomerization of motor **5** is characterized by a first order rate constant $k(\textbf{\textit{C}} \rightarrow \textbf{\textit{A}})$ = 0.000031 s⁻¹ at 100 °C. Next, $\Delta G^{\ddagger}_{\text{C-A}}$ for the thermal **C**/**A** conversion can be determined by applying the Eyring equation:

$$k(\textbf{\textit{C}} \rightarrow \textbf{\textit{A}}) \; = \; \frac{k_B \, T}{h} \, e^{\frac{-\Delta G^{*}}{RT}} \tag{eq. 13}$$

with $\quad k_B$ = Boltzmann constant (1.381·10⁻²³ J·K⁻¹)

T = temperature in K

h = Planck constant (6.626·10⁻³⁴ J·s)

Rearrangement of Equation 13 and insertion of the gas constant, the *Boltzmann* constant and the *Planck* constant as well as the temperature delivers $\Delta G^{\ddagger}_{\text{C-A}}$:

$$\Delta G^{\ddagger}_{\text{C-A}} \text{ (in J mol}^{-1}) = \; 8.314 \cdot T \cdot \left[23.760 + \ln\left(\frac{T}{k(\textbf{\textit{C}} \rightarrow \textbf{\textit{A}})} \right) \right] \tag{eq. 14}$$

For derivative **5** $\Delta G^{\ddagger}_{\text{C-A}}$ = 131.9 kJ·mol⁻¹ = 31.5 kcal·mol⁻¹ was obtained for the free activation enthalpy of its thermal **C** to **A** conversion.

For motor **5** a ratio of 81% of isomer **A** and 19% of isomer **C** was found in the thermal equilibrium at 100 °C. The ratio can be translated into the corresponding energy difference according to:

$$-\Delta G = \ln K \cdot R \cdot T \tag{eq. 15}$$

with $\quad K$ = equilibrium constant = [isomer **A**]/[isomer **C**]

R = ideal gas constant = (8.314 J·K⁻¹·mol⁻¹)

T = temperature in K

Therefore an energy difference of 1.1 kcal·mol⁻¹ between isomers **A** and **C** could be determined for derivative **5**.
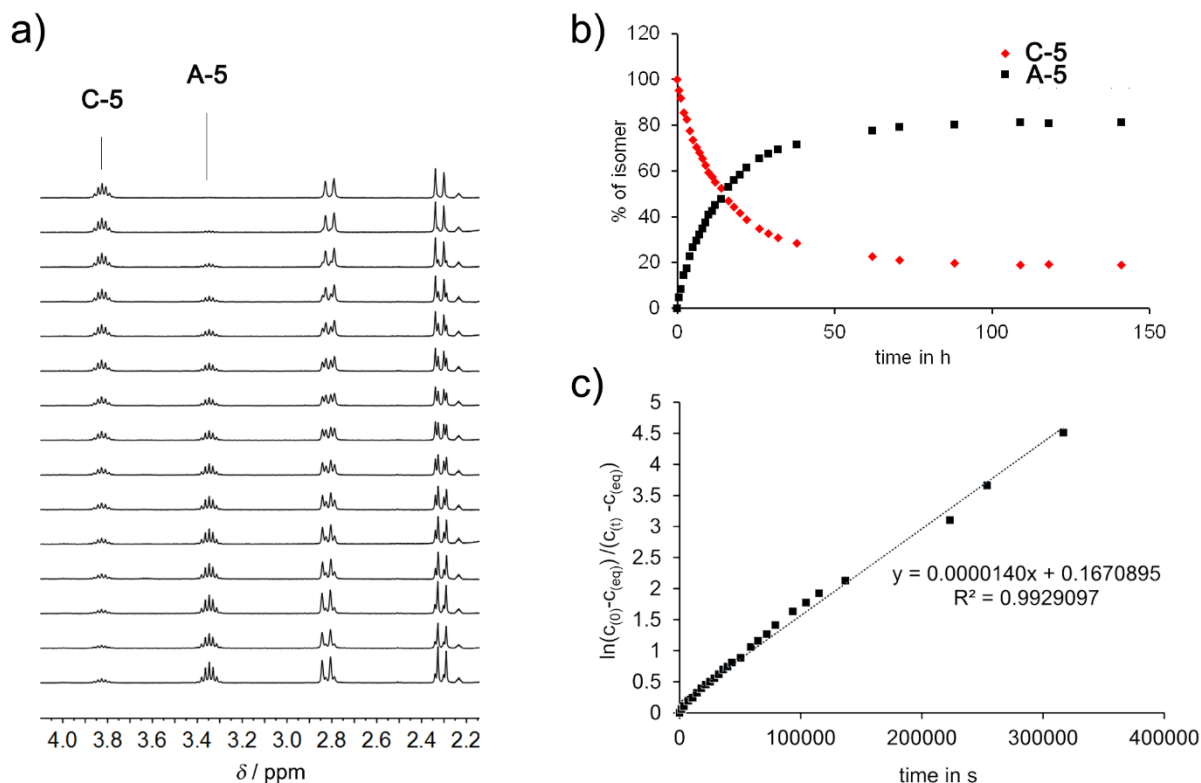
Figure 54:   Thermal isomerization of isomer **C-5** to the stable isomer **A-5** at 100 °C monitored by ^{1}H NMR spectroscopy. a) ^{1}H NMR spectra (400 MHz) of a toluene-d_8 solution (3.8 mM) of **5** acquired at ambient temperature. Illustrative spectra recorded at different time points during heating a motor **5** solution to 100 °C over the course of 141 h in the dark. Only the *iso*-propyl septets are shown exemplarily. b) Interconversion of **C** to **A** isomer with time. The **C/A** ratio was determined by integration of the septet signals. The experiment began with pure racemic isomer **C**. Equilibrium was established with a ratio of 19/81 of **C/A** within 58 h of heating to 100 °C. The obtained ratio can be translated to an energy difference of 1.1 kcal·mol^{-1}. c) First order kinetic analysis taking into account the establishment of a dynamic equilibrium allowed for the calculation of $\Delta G^\ddagger_{C\text{-}A}$ = 31.5 kcal·mol^{-1}. The slope of the linearly fitted experimental data of 0.0000140 can be used to derive the rate constant k$_{(Z\rightarrow E)}$ = 0.00000268156 s^{-1}. Adapted with permission from *Angew. Chem. Int. Ed.* **2017**, *56*, 14536-14539. Copyright 2017 Wiley and Sons.

4.11   Mechanism of Hemithioindigo-Motor Rotation

High energy barriers for the thermal double-bond isomerizations are a prerequisite for unidirectional rotary motion at ambient temperatures. Thus, it can be guaranteed that thermal canceling out of the photo induced isomerizations is prevented. For investigation of the rotation cycle low temperature conditions are indispensable, since theoretical assessment already predicted energy barriers of the thermal helix inversions should not exceed 16 kcal·mol^{-1} for any motor. The fully directional rotation cycle consists of four distinct isomerizations (**A** to **B** to **C** to **D** to **A**), each of which is capable of transferring population from one to another intermediate as long as adequate energy supply is available. The elucidation of

rotary motion requires deciphering the sequence of intermediate population occurring in the presence of light and thermal energy input and, in case of thermally driven processes, the observation of the decay kinetics and their overall completeness. Since experimental access by ^{1}H NMR spectroscopy to the metastable intermediate **B-1** was hampered by its fast decay even at –100 °C, the synthesis and investigation of sterically more hindered molecular motors was pursued. Especially motor derivatives **4** and **5** hold great promise as their calculated $\Delta G^{\ddagger}_{\textbf{B-C}}$ of 12.82 kcal·mol^{-1} and 13.55 kcal·mol^{-1} should be sufficiently high for observation of intermediate **B** at low temperature conditions of –105 °C. A general scheme of the rotation cycle is depicted in Figure 55.
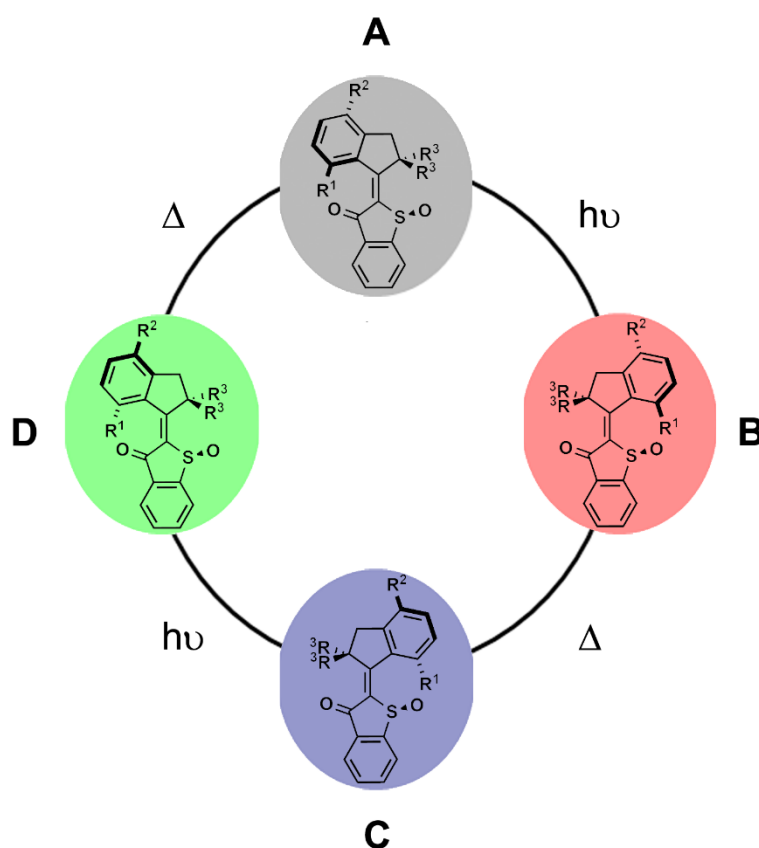
Figure 55: Rotation cycle of HTI-based molecular motors. Isomer **A** is converted by visible light input to metastable isomer **B**, which is consecutively transferred to stable isomer **C** with *Z*-configured double bond via a thermal helix inversion step. Another photoisomerization delivers isomer **D**. A second helix inverting ratcheting step recovers the starting point isomer **A**. As long as sufficient thermal energy and light input is available, a fully 360° unidirectional rotation around the central double bond occurs.

4.12   Motor behaviour under irradiation and at low temperatures

For low-temperature ¹H NMR spectroscopic analysis of the rotation cycle it is necessary to separate stable isomers **A** and **C** in order to investigate each isomer under irradiation condition on its own. Separation of the stable isomers was achieved by using HPLC. The experimental setup used for the motor investigation consists of a 400 MHz NMR spectrometer, which is capable of temperature tuning with limits up to -80 to –105 °C and an *in situ* irradiation technique. A glass fiber with one end coupled to a high power LED source, inserts directly with the other blank end into the motor solution of the NMR tube. Thus, concomitant irradiation and ¹H NMR recording at various temperatures is possible. For further details on the experimental setup, see chapter Materials and Methods.

4.13   Irradiation of isomer C-5

A NMR sample loaded with a solution of isomer **C-5** (CD_2Cl_2/CS_2 4/1) was cooled to –105°C. A series of ¹H NMR spectra was recorded during continuous high power irradiation with 470 nm. The very first spectrum was recorded in the dark. The results of the irradiation experiments are summarized in Figure 56. Only the indicative septet signals of the *iso*-propyl group of the spectrum are discussed. It can be nicely observed that soon after irradiation begins a new set of signals starts to build up. Since the isomer **A** signal of the septet is known to appear at 3.1 ppm at this low temperature, it can be derived that the new set of signals arising (new septet at 2.6 ppm) by irradiation cannot be assigned to signals from isomer **A**. After prolonged irradiation the new set of signals dominates in population with residual signals of the starting isomer **C** still being visible. In an additional annealing experiment, which is depicted in Figure 56b, thermal behaviour of the new species in the dark was investigated. A solution of **5** was irradiated with 470 nm to the pss at –70 °C (Figure 56b, spectrum 1). Afterwards the sample was allowed to warm up to 23 °C for 2 min in the dark and was recooled to –70 °C for recording of a ¹H NMR spectrum (Figure 56b, spectrum 2). The light induced new set of signals completely vanished, while signals of isomer **A** (septet at 3.1 ppm) can be observed. After the annealing, signal intensities of the originally formed photoproduct are now completely transferred to the signal intensities of isomer **A** The signals of isomer **C** remain constant during the annealing experiment. Therefore the new set of signals can be assigned to the metastable isomer **D**, which was generated by irradiation with 470 nm starting from isomer **C**. Accumulation during the irradiation was possible because temperatures of –70 °C prevented its decay. By allowing the sample to warm up to ambient temperatures a helical inversion step transferred isomer **D** to isomer **A**. As after the annealing experiment no residual signals of isomer **D** were observable, it can be stated that conversion shows at least 95% completeness. A conservative uncertainty of 5% is assumed, based on the accuracy of ¹H NMR spectroscopy.
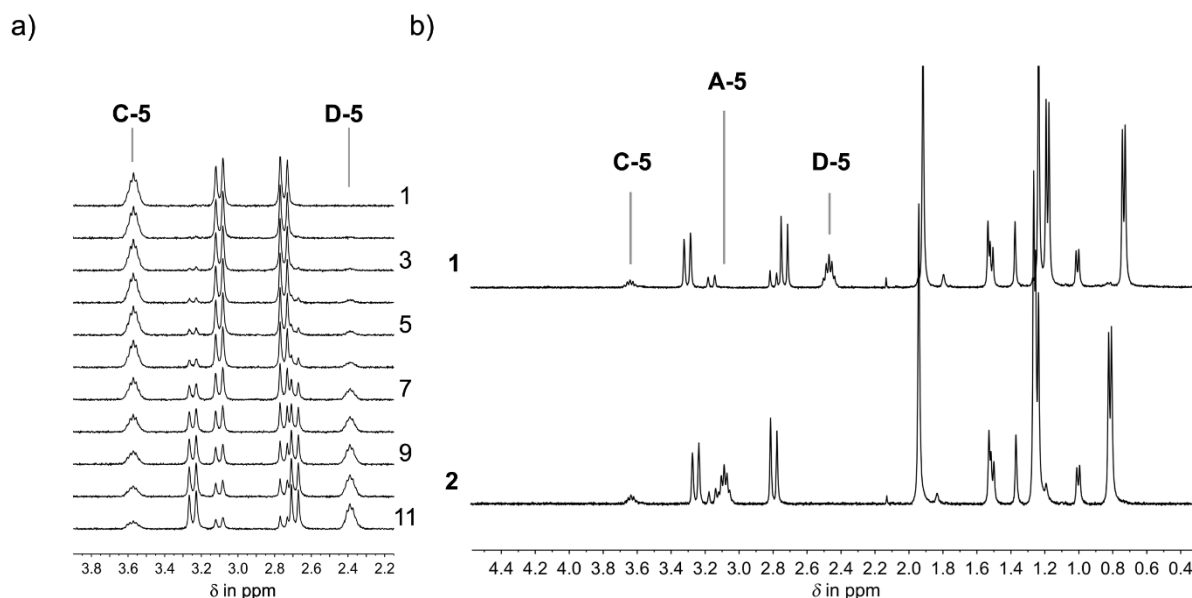
Figure 56: Irradiation experiments of **C-5** at low temperature monitored by ^{1}H NMR spectroscopy. a) A series of ^{1}H NMR spectra was acquired at –105 °C during high power irradiation (470 nm LED) of a CD_2Cl_2/CS_2 solution (4/1, 2.8 mM) of racemic **C-5**. The septet signals of the *iso*-propyl groups are shown exemplarily. Under irradiation exclusive formation of isomer **D** can be observed. b) Annealing experiment for the investigation of the completeness of **D** to **A** conversion. ^{1}H NMR spectra of a CD_2Cl_2/CS_2 (4/1) solution of **5** were acquired at –70 °C. 1. High power irradiation (470 nm LED) of a **C-5** solution (2.8 mM) resulted a mixture of **D** and **C** isomers. 2. The sample was allowed to warm up to 23 °C for 2 min and was kept in the dark. After recooling the sample to –70 °C the ^{1}H NMR spectrum was recorded. It could be observed, that isomer **D** was completely converted to isomer **A**. The signal intensities of isomer **C** remain constant. Adapted with permission from *Angew. Chem. Int. Ed.* **2017**, *56*, 14536-14539. Copyright 2017 Wiley and Sons.

The same experiments conducted for motor **1**[38] and **2**[1] revealed analogous behaviour and are fully consistent with the results of motor **5**. No irradiation experiments with pure **C-3** and **C-4** were performed.

From the experimental results, the conclusion can be drawn, that photoisomerization from **C** to **D** is most likely associated with a directional rotation around the central double bond. It has to be mentioned, however, that this conclusion is a deduced interpretation of the experimental outcomes and not the result of a directly observed rotation process. Since photoisomerization of HTI-based molecular motors occurs on fs and ps timescale, as measured by time resolved ultrafast absorption spectroscopy,[102] a direct observation of the excited state rotational processes is not possible by experimental means available at present. Nevertheless, several arguments allow the assumption that **C** to **D** photoisomerization is a directional process. The helical pretwisting should be the driving force for a directional light-induced

process, which prevents mechanically a backward rotation by sterical hindrance. This can be translated into a high energy barrier omitting backwards rotation in the excited state. Under the assumption a backward rotation would be induced by irradiation, the directly resulting isomers should be isomer **B** or **A**. The irradiation experiment of **C-5** conducted at –105 °C provided suitable thermal conditions for the possible observation of both isomers. But the outcome of all irradiation experiments with isomers **C** was the exclusive formation of isomer **D**. For the directionality of the thermal isomerizations an analogous statement can be drawn, with the difference, that theoretical calculations supply valuable insights into the helix inversion process by transition state structures and their corresponding relative energies. These energies can be confirmed by kinetic analysis of the thermal processes and allow the deduction of their inherent directionality. Hence, more information about the intrinsic mechanical rotor motion is available for the helix inversion steps than for the photoisomerization processes at present.

4.14   Thermal D to A isomerization of motors 3, 4 and 5

By applying an *in situ* irradiation technique in combination with variable temperature ^{1}H NMR spectroscopy it is possible to accumulate isomers **D** to great extent (see Figures 57-59).Their thermal decay in the dark can be monitored by a series of ^{1}H NMR spectra recorded during this process. In most cases an additional annealing experiment was performed at the end of the decay recording in order to determine full completeness (taking into account 95% accuracy of ^{1}H NMR spectroscopy) of this thermal helix inversion. Integration of indicative signals and a logarithmic plot of the integral's differential against time furnished the first order rate constant $k_{(D \to A)}$ as the slope of the resulting graph. The Gibbs free energy of activation $\Delta G^{\ddagger}_{\text{D-A}}$, associated with the thermal **D** to **A** helix inversion can be determined from the first order rate constant $k_{(D \to A)}$ by using the Eyring equation:

$$k_{(D \to A)} = \frac{k_B\, T}{h}\ e^{\frac{-\Delta G^{\ddagger}_{D-A}}{RT}} \qquad\qquad \text{(eq. 16)}$$

with k_B = Boltzmann constant ($1.381 \cdot 10^{-23}$ J·K^{-1})

T = temperature in K

h = Planck constant ($6.626 \cdot 10^{-34}$ J·s)

R = gas constant (8.314459 J·mol^{-1}·K^{-1})

$k_{(D \to A))}$ = rate constant of either the thermal **D** to **A** isomerization

Rearrangement of Equation 16 and insertion of the gas constant R, the *Boltzmann* constant k_B and the *Planck* constant h as well as the temperature delivers $\Delta G^{\ddagger}_{\text{D-A}}$:

$$\Delta G^{\ddagger}_{\textbf{D-A}} \text{ (in J} \cdot \text{mol}^{-1}) = 8.314 \cdot T \cdot \left[23.760 + \ln\left(\frac{T}{k(E/ZSM \rightarrow E/ZSP)}\right)\right] \qquad \text{(eq. 17)}$$

The first order kinetic analyses of the **D** to **A** conversion for motors **3** to **5** are depicted in Figures 57, 58, 59.
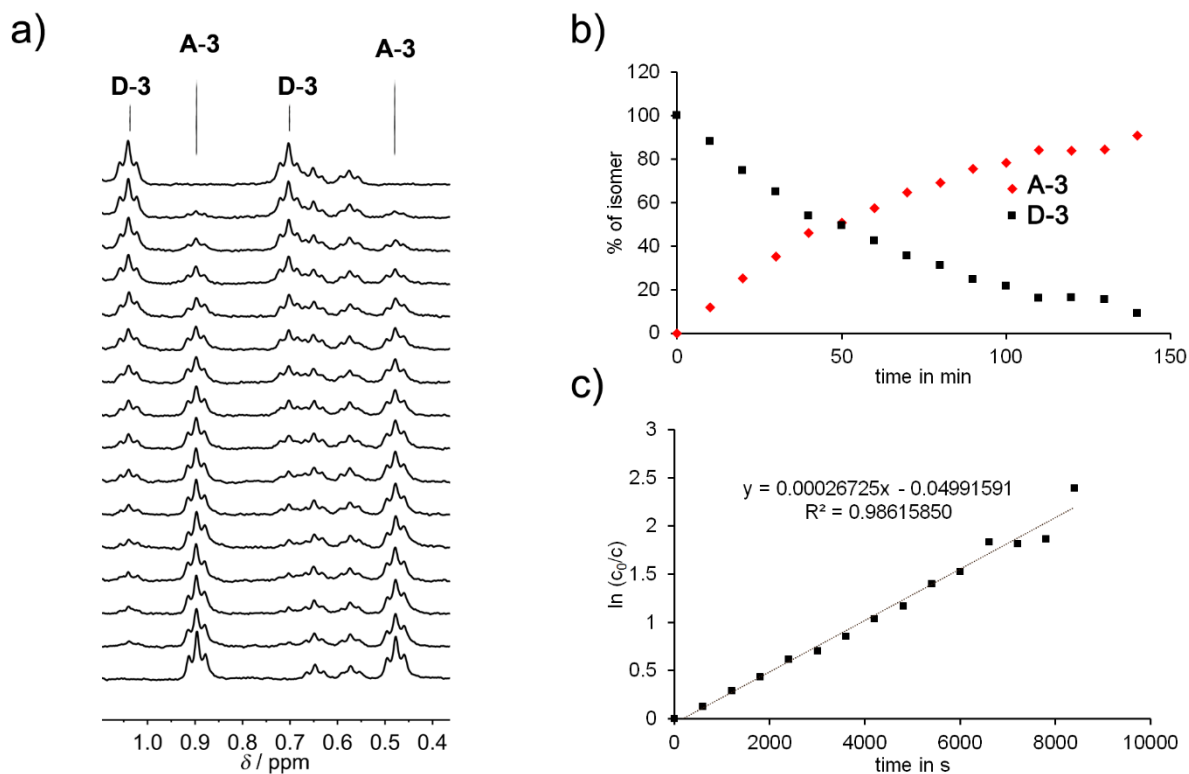
Figure 57:   Thermal decay kinetics of racemic **D-3**. a) A series of ^{1}H NMR spectra (400 MHz, –70 °C) of a **3** solution in CD$_2$Cl$_2$ at different time points records the thermal **D** to **A** conversion. A selection of triplet signals is shown exemplarily. Only signal intensities of isomer **D** and **A** are changing, while the intensities of isomer **C** remain constant throughout the experiment. At the end of decay recording an annealing experiment (warm up of the solution to 23°C for 2 minutes and recooling the sample to –70 °C) showed full conversion (>95%) as can be observed in the last spectrum. b) The spectra were taken in 10 min time intervals over the course of 2.5 h. Integration of indicative triplet signals yielded the isomeric ratio at different time points. (Total sum of **A** and **C** isomers is normalized to 100% arbitrarily) c) First order kinetic analysis sgives good agreement with the obtained data. The linear fit delivers the first order rate constant $k_{(\textbf{D}\rightarrow\textbf{A})} = 0.000267 \text{ s}^{-1}$ as the slope of the curve.
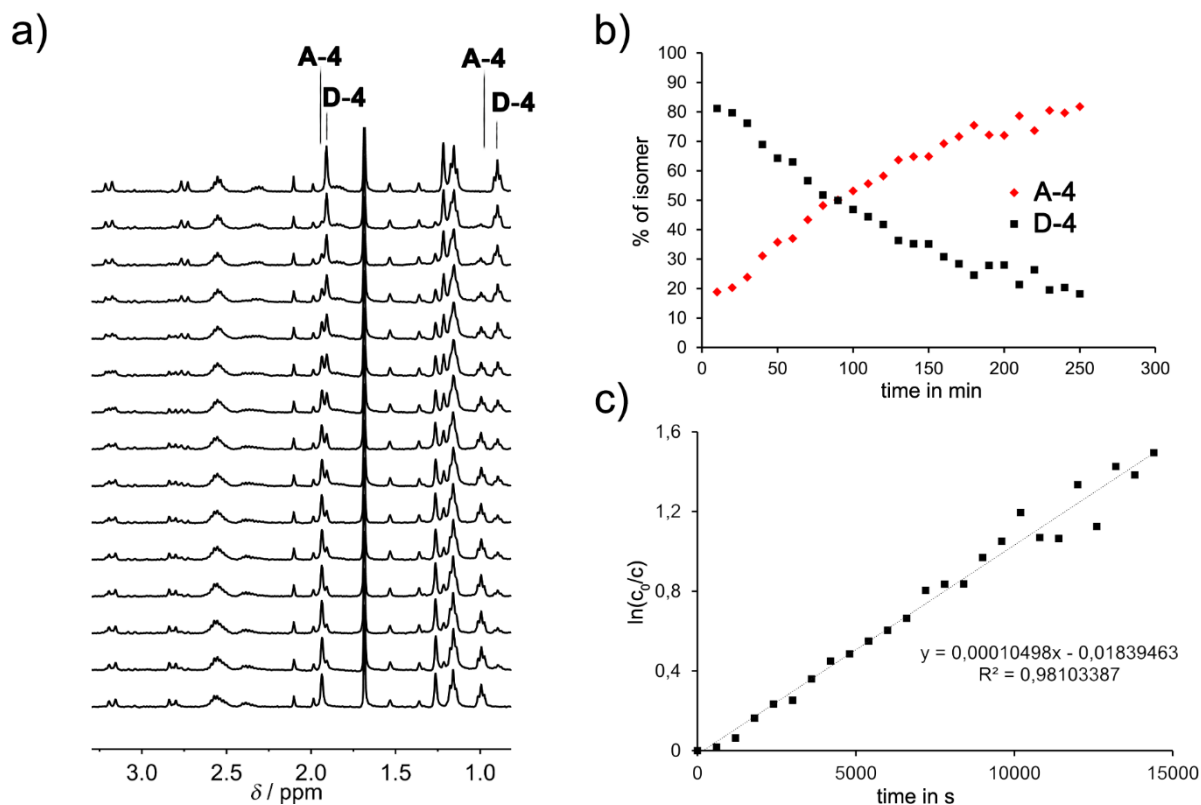
Figure 58: Thermal decay kinetics of racemic **D-4**. a) A series of ^{1}H NMR spectra (400 MHz, –70 °C) of a motor **4** solution in CD$_2$Cl$_2$ at different time points records the thermal **D** to **A** conversion. The aliphatic part of the spectrum is shown exemplarily. Only signal intensities of isomer **D** and **A** are changing, while the intensities of isomer **C** (small singulets at 1.54 and 1.36 ppm) remain constant throughout the experiment. At the end of decay recording an annealing experiment (warm up of the solution to 23°C for 3 minutes and recooling of the sample to –70 °C) showed full conversion (>95%), as it can be observed in the last spectrum. b) The spectra were taken in 5 min time intervals over the course of 3.5 h. Integration of indicative triplet signals yielded the isomeric ratio at different time points. (Total sum of **A** and **C** isomers is normalized to 100% arbitrarily) c) First order kinetic analysis gives good agreement with the obtained data. The linear fit delivers the first order rate constant $k_{(\mathbf{D} \rightarrow \mathbf{A})} = 0.00010$ s^{-1} as the slope of the curve.
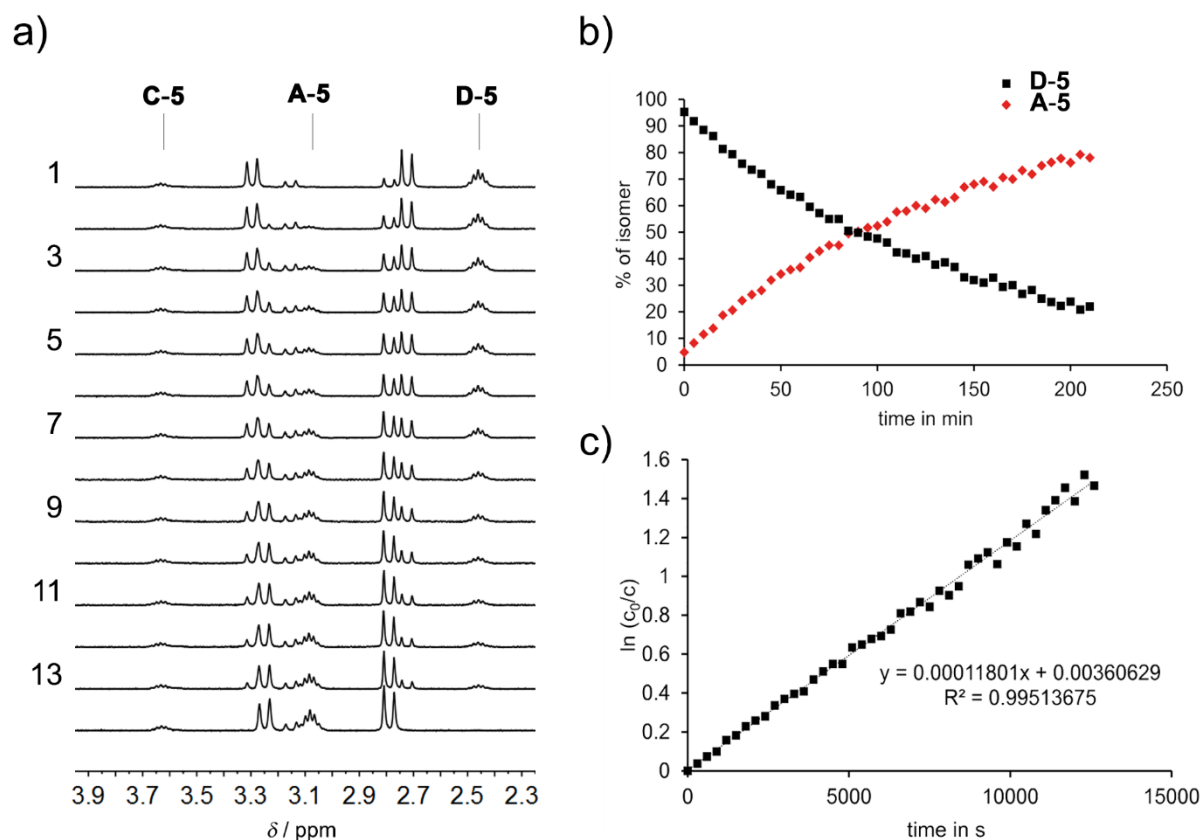
Figure 59: Thermal decay kinetics of racemic **D-5**. a) A series of ^{1}H NMR spectra (400 MHz, –70 °C) of a solution of **5** (14.3 mM) in CD_2Cl_2/CS_2 (4/1 mixture) at different time points records the thermal **D** to **A** conversion. Only signal intensities of isomer **D** and **A** are changing while the intensities of isomer **C** remain constant throughout the experiment. At the end of decay recording an annealing experiment (warm up of the solution to 23 °C for 3 min and recooling the sample to –70 °C) showed full conversion (>95%), as can be observed in the last spectrum. b) The spectra were taken in 5 min time intervals over the course of 3.5 h. Integration of the *iso*-propyl septets yielded the isomeric ratio at different time points. (Total sum of **A** and **C** isomers is normalized to 100% arbitrarily) c) First order kinetic analysis gives good agreement with the obtained data. The linear fit delivers the first order rate constant $k_{(\mathbf{D}\rightarrow\mathbf{A})}$ = 0.00012 s^{-1} as the slope of the curve. Adapted with permission from *Angew. Chem. Int. Ed.* **2017**, *56*, 14536-14539. Copyright 2017 Wiley and Sons.

The rate constants $k_{(\mathbf{D}\rightarrow\mathbf{A})}$ can be translated to the corresponding $\Delta G^{\ddagger}_{\mathbf{D}\text{-}\mathbf{A}}$. Thus, motor **3** encounters a free activation energy of the thermal **D** to **A** helix inversion of 14.30 kcal·mol^{-1}, for motor **4** 15.43 kcal·mol^{-1} were found, and **5** furnishs a thermal energy barrier of 15.39 kcal·mol^{-1}. Motors **3** and **4** were measured in pure CD_2Cl_2, while motors **2** and **5** were investigated in a 4/1 mixture of CD_2Cl_2 and CS_2. A detailed discussion of substitution effects on the thermal behavior of HTI-based molecular motors with comparison to theoretical results is given in chapter 2.19. The overall accuracy of the theoretical description, however, revealed very good agreement with the observed experimental rate constants.

Thus, experiment confirms the likely conversion of isomer **D** to **A** as a directional process via a planar transition state predicted by theoretical calculations. In summary, the sense of rotational motion is preserved in the helical inverting step, which leads to a fully directional 180° movement from **C** to **A**. The annealing experiments demonstrated the completeness of all investigated **D** to **A** conversions, which positively influences the degree of unidirectionality of the overall rotation process. For motors **3** to **5** a lower limit of 1.19 kcal·mol^{-1} energy difference between isomer **D** and **A** was found according to Equation 15 when using K= 95/5 **A/D** to take into account the accuracy of NMR spectroscopy. Identical experiments for motor **1** and **2** revealed analogous behavior and can be found in references 1 and 32.[1, 38]

4.15   Irradiation of isomer A of motors 3, 4 and 5

After the first 180° of rotation was proven as an unidirectional process triggered by light input, the second part of the rotation cycle was investigated next. Therefore isomers **A** of motors **3**, **4**, and **5** were exposed to 470 nm irradiation at low temperatures and the temporal evolution was monitored by ^{1}H NMR spectroscopy. Since observation of isomer **B** of motor **1** was precluded by its fast decay, motors **3**-**5** with increased sterical hindrance in close proximity to the rotation axle offered the potential chance for the first observation of the elusive intermediate **B**. In particular, theoretical assessment renders motors **4** and **5**, with calculated barriers of 12.82 and 13.55 kcal·mol^{-1} for **B** to **C** inversion, the preferential candidates for snapshotting isomer **B**. The observation could then finally confirm the overall directionality and the profound molecular displacements occurring during the second part of the motor operation.

In Figure 60 the intermediate populations following irradiation of pure **A** isomers of motors **3** to **4** are summarized. No intermediate **B** was observed at –80 °C in case of motors **3** and **4** (also in case of motor **2** at –105 °C[38]). Further investigations on motor **4** by irradiation experiments at –100 °C in diethyl ether-d_{10} did not deliver detectable signals of isomer **B**, either. For all experiments conducted with **3** to **4**, irradiation of pure isomer **A** solutions lead to the direct formation of isomer **C**. By prolonged irradiation increased concentration of isomer **C** leads to light-induced **C** to **D** isomerization. Hence, the signals of isomer **D** starts to grow in intensity, too. In case of motor **4** (see Figure 60b) it is also observable, that signals of isomer **C** reach maximum intensities and decline until a steady state is reached. These results match the experiments carried out with methoxy substituted motor **1**[1] as well as with motor **2**.[38]
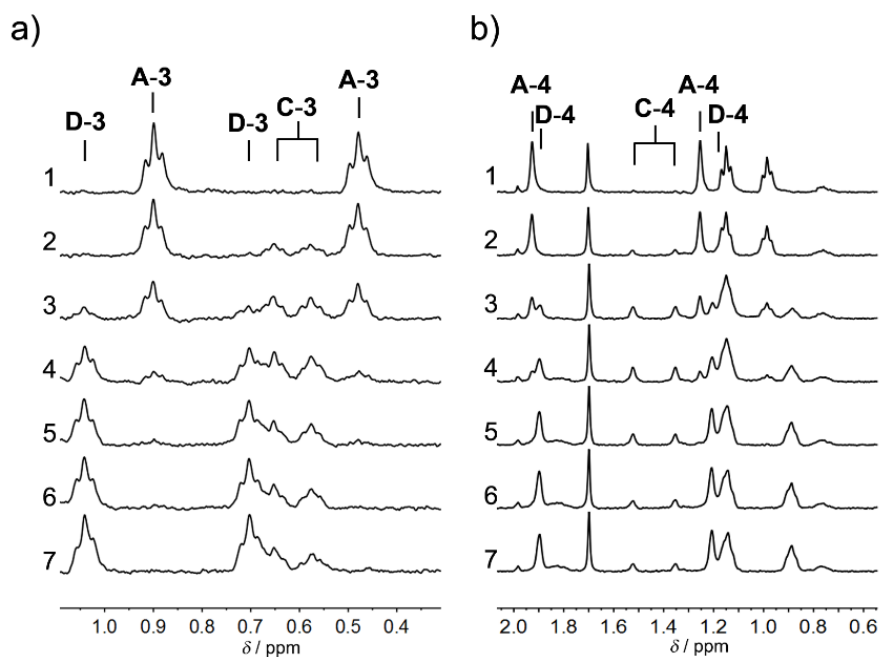
Figure 60: Irradiation experiments of isomers **A-3** and **A-4** at low temperatures. a) ^{1}H NMR spectra (–80 °C, 400 MHz) acquired during 470 nm irradiation (12 min) of a CD$_2$Cl$_2$ solution of isomer **A-3**. The aliphatic sections of the spectra are shown. 1: no light. 2: 1 min of irradiation. Isomer **C** signals are observed first. 3: 2 min. Isomer **D** signals build up. 4: 5 min. 5: 7 min. 6: 8 min. 7: 12 min (established pss). c) ^{1}H NMR spectra (–80 °C, 400 MHz) acquired during 470 nm irradiation (10 min) of a CD$_2$Cl$_2$ solution of isomer **A-4**. The aliphatic sections of the spectra are shown. 1: no light. 2: 30 sec of irradiation. Isomer **C** signals are observed first. 3: 2 min. Isomer **D** signals build up: 3.5 min 5: 6 min. 6: 8 min. 7: 9.5 min. Pss is reached.

The sequence of upcoming intermediates allows for anticipation of an overall directional process and can be derived by following arguments. Isomer **A**, if irradiated, is converted first to isomer **C**, before isomer **D** can be observed, which in turn is the photoproduct of isomer **C** excitation. Isomer **D** accumulates at the low temperature, as it encounters a too-high energy barrier for its thermal helix inversion back to isomer **A**. Apparently, it seems that **C** is the direct photoproduct of isomer **A**. On the other hand irradiation of isomer **C** (experimental data available for motors **1**, **2**, and **5**[1, 38]) does not lead to direct emergence of **A**, but results exclusively in **D**, which is transferred thermally in a second consecutive process to **A**. These observations make evident, that at least three different isomers are for sure present, which interconvert in a sequential manner. This allows the conclusion that light and thermal energy supply a unidirectional process. With respect to the apparent **A** to **C** photoreaction, a contradiction is found, as **C** seems to be part of two different photoequilibria depending on the starting isomer (with **D** when starting from **C** and **A** when starting from **A**). These arguments strongly support the theoretically predicted existence of another intermediate **B**, which explains the apparent direct

photoproduct **C** from irradiation of isomer **A**, as the results of a coupled photoreaction towards **B** and a thermally driven fast isomerization from **B** to the observable isomer **C**.

Since motors **2** to **4** failed to enable detection of intermediate **B**, the last promising candidate was *iso*-propyl substituted motor **5**. A sequence of ^{1}H NMR spectra acquired under irradiating conditions (470 nm) of an isomer **A-5** solution (CD$_2$Cl$_2$/ CS$_2$) at –105 °C is depicted in Figure 61. The spectral development can be nicely followed via the septet signals of the *iso*-propyl groups, because other signals are strongly overlapping and disentanglement is difficult. The evolution of the septet signals is representative for the development of the whole sets of signals. The first spectrum was recorded under non-irradiation conditions exhibiting solely the signals of isomer **A**. Soon after irradiation began, a new and unknown septet signal (first appearance in spectrum 3) can be observed in up to 25% intensity, followed by the rise of a second signal, which can be associated with the formation of isomer **C** (see spectrum 6). In spectrum 11 the increase of previously identified isomer **D** septet signal could be detected, too. Hence, in the last spectrum of the irradiation experiment four septet signals are clearly visible, while three can be assigned to isomers **A**, **C** and **D** unambiguously. Since the unknown intermediate is populated first, the direct photoproduct of isomer **A** and can therefore be assigned to the elusive isomer **B**. The consecutive evolution of isomer **C**, as the thermal product from **B** further supports this assignment. To get more information about the nature of this new intermediate and for validation of the assignment, this thermal conversion was scrutinized next.
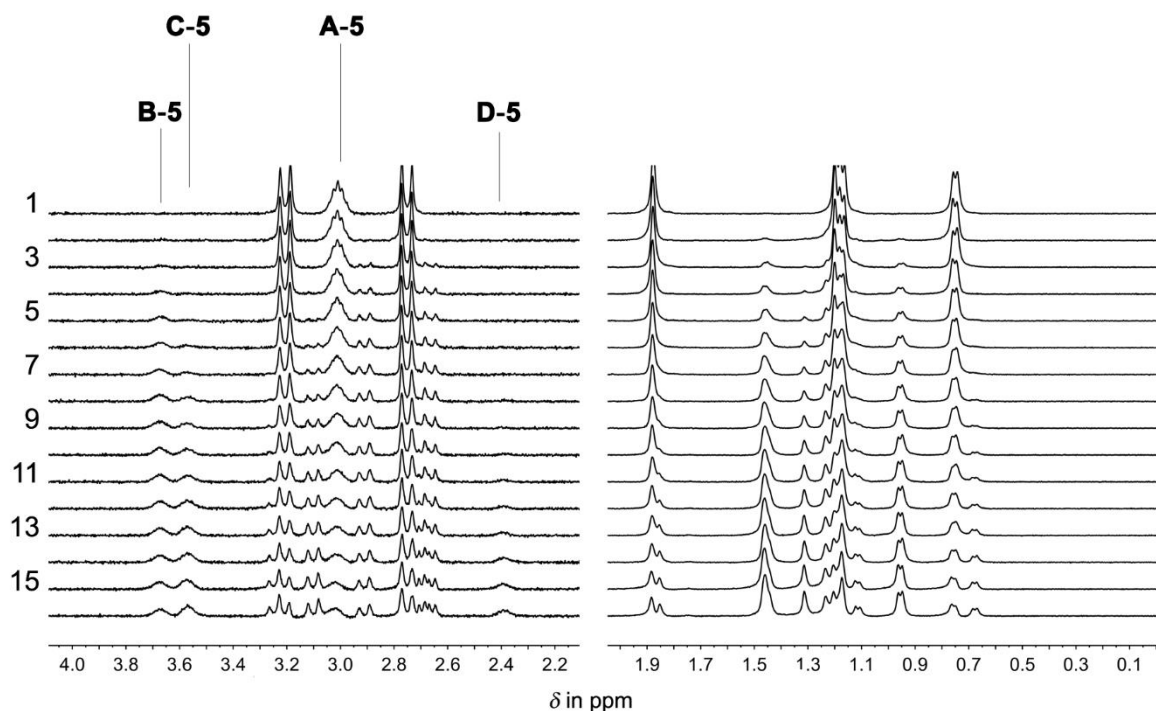
Figure 61: Irradiation experiments of isomers **A-5** at –105 °C. A series of ^{1}H NMR spectra (–105 °C, 400 MHz) was acquired in 8 s time interval during 470 nm irradiation of a CD_2Cl_2/CS_2 solution (4/1, 2.7 mM) of **A-5**. Signals of the aliphatic section of the spectra are shown exemplarily. The spectral evolution can be nicely followed by the *iso*-propyl septets. Irradiation initially leads to the formation of isomer **B** (spectra 2, 3), then the signals of isomer **C** appear with prolonged irradiation (spectrum 4). The last signals sets occurring can be assigned to isomer **D**, after isomer **C** is populated sufficiently to undergo its photoreaction (spectrum 9). Adapted with permission from *Angew. Chem. Int. Ed.* **2017**, *56*, 14536-14539. Copyright 2017 Wiley and Sons.

4.16 Thermal B to C isomerization of motor 5

After a new set of signals was observed by irradiation of a solution of **A-5** at –105 °C, the irradiation was stopped after sufficient population of the new intermediate was achieved. The thermal decay of this intermediate was recorded by a series of ^{1}H NMR spectra and is shown in Figure 62. Since the sequence of isomer appearance already indicated thermal isomer **C** formation from photogenerated isomer **B**, light exclusion would unambiguously prove this assumption. Indeed, while isomer **B** is decaying with time, isomer **C** is increasing in intensity in the dark. After 8 min (see last spectrum of Figure 62a) no residual signal of isomer **B** can be detected, allowing to evidence full completeness of this thermal conversion (at least 95%, taking into account the accuracy of ^{1}H NMR spectroscopy). A first order kinetic analysis of the thermal decay of isomer **B** revealed a thermal barrier of 11.3 kcal·mol^{-1}. Thus, good agreement with theoretically obtained $\Delta G^{\ddagger}_{B-C}$ of 13.56 kcal·mol^{-1} could be obtained, which allows the conclusion, that the thermally driven process is also a helix inverting step in this case, too. A lower limit for the

124

energy difference between isomer **B** and **C** can be calculated from the degree of completeness at –105° C to be 0.98 kcal·mol^{-1} according to Equation 15 and using $K = 95/5$ as a conservative estimate.
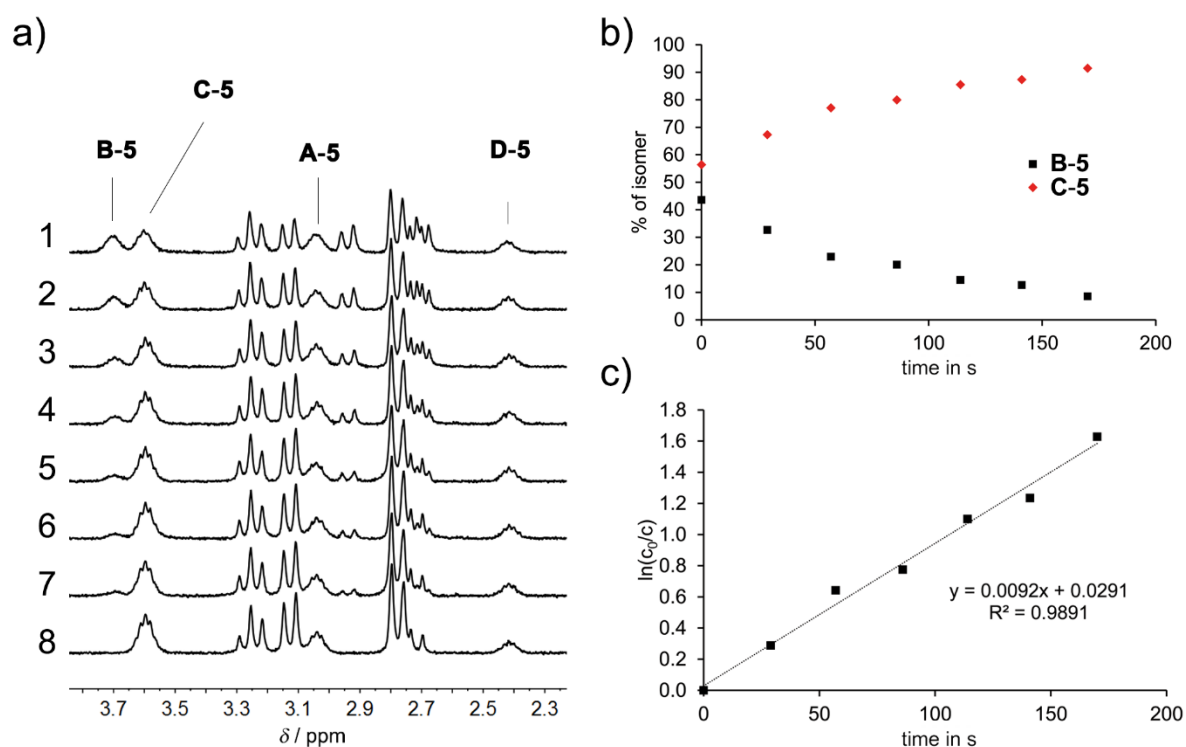
Figure 62:   Decay kinetics of intermediate **B-5**. a) A series of indicative ^{1}H NMR spectra (400 MHz, – 105 °C) of a motor **5** solution in CD$_2$Cl$_2$ at different time points illustrates the thermal **B** to **C** conversion. The *iso*-propyl septet signals are shown exemplarily. Only signal intensities of isomer **B** and **C** are changing, while the intensities of isomer **A** and **D** remain constant throughout the experiment. Spectra were taken in 8 s time intervals. The last spectrum was recorded 8 min after the irradiation was stopped. It shows full conversion (>95%). b) Integration of the septet signals yielded the isomeric ratio at different time points. (Total sum of **A** and **C** isomers is taken to 100% arbitrarily) c) First order kinetic analysis shows good agreement with the obtained data. The linear fit delivers the first order rate constant $k_{(\mathbf{B}\rightarrow\mathbf{C})} = 0.0092$ s^{-1} as the slope of the curve. Adapted with permission from *Angew. Chem. Int. Ed.* **2017**, *56*, 14536-14539. Copyright 2017 Wiley and Sons.

4.17 Spectral disentanglement of mixed spectra of motor 5

Since structural information of isomer **B-5**, as well as of isomer **D-5**, is limited by their thermal instabilities, the mixed spectra obtained from irradiation of an **A-5** solution at –105 °C were disentangled for identification of further isomer **B-5** signals. A pure ^{1}H NMR spectrum of intermediate **D-5** was obtained by spectral subtraction from a mixed spectrum containing 20% isomer **C-5** and 80% isomer **D-5**. Assignment of stable isomer **A-5** and **C-5** is easily accessible, since separation of these isomers was achieved by established chromatographic methods. The pure spectra of **A-5**, **C-5** and **D-5** allow for identification of isomer **B-5** signals.
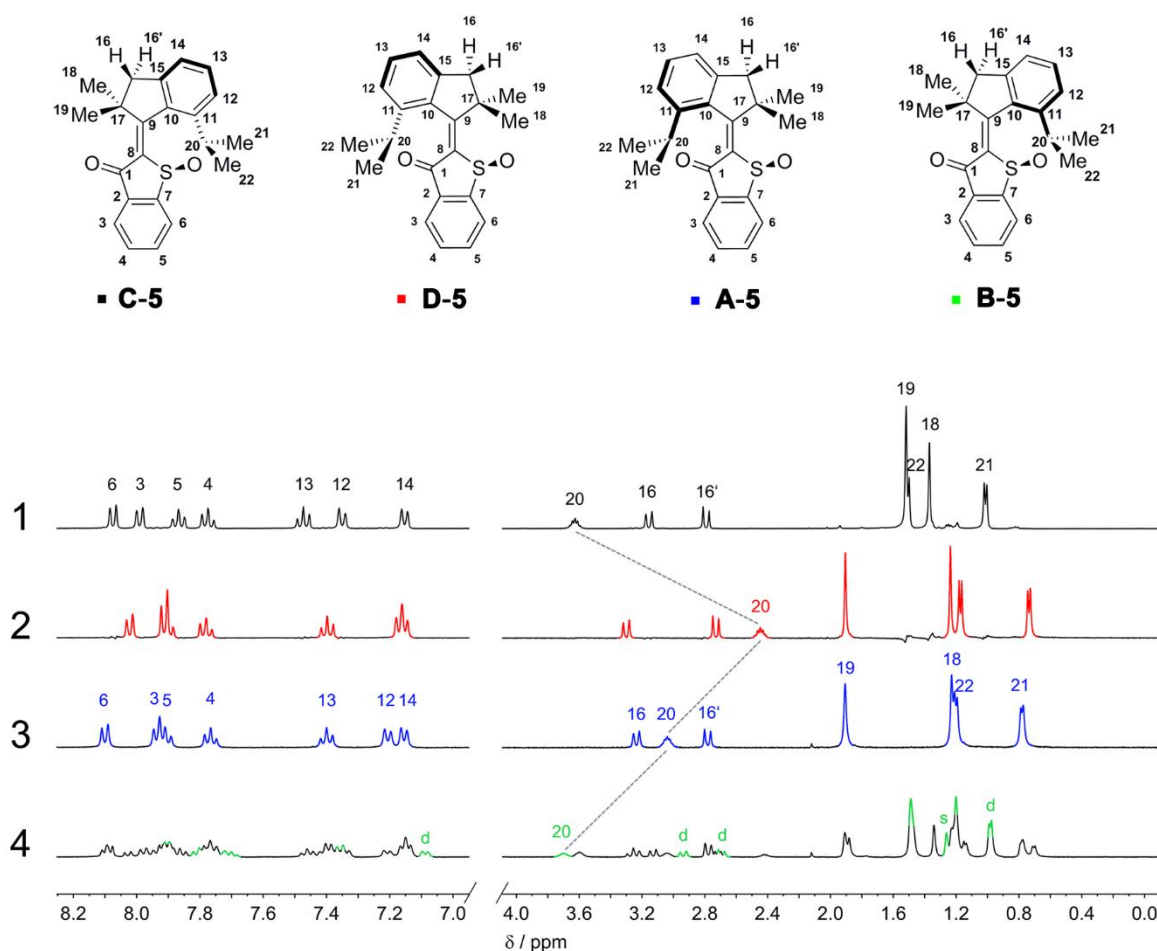
Figure 63:   Spectral disentanglement for identification of intermediate contribution to the mixed spectrum.[II] ^{1}H NMR spectra (CD$_2$Cl$_2$/CS$_2$ (4/1), 400 MHz) were acquired at –105 °C. 1: Isomer **C-5** (black). 2: Isomer **A-5** (red). 3: Isomer **D-5** (blue). Obtained by spectral subtraction from a mixed spectrum of **C** and **D** (20/80). 4: Mixed spectrum containing all four isomers obtained by irradiation (470 nm) of **A-5**. Signals of **B-5** are highlighted in green. Adapted with permission from *Angew. Chem. Int. Ed.* **2017**, *56*, 14536-14539. Copyright 2017 Wiley and Sons.

Additional information on isomer composition was obtained from the spectral evolution with time under irradiation (Figure 64). It allowed for identification of **B-5** signals in strongly overlapping regions, as it is the case with singlet signals at 1.5 ppm and doublet signals at 1.0 ppm (spectrum 2) and in the aromatic region. Also during the decay of isomer **B-5**, spectral changes at 7.9 ppm (spectrum 5) revealed isomer **B-5** signal contribution in the mixed spectrum (spectrum 4).

.
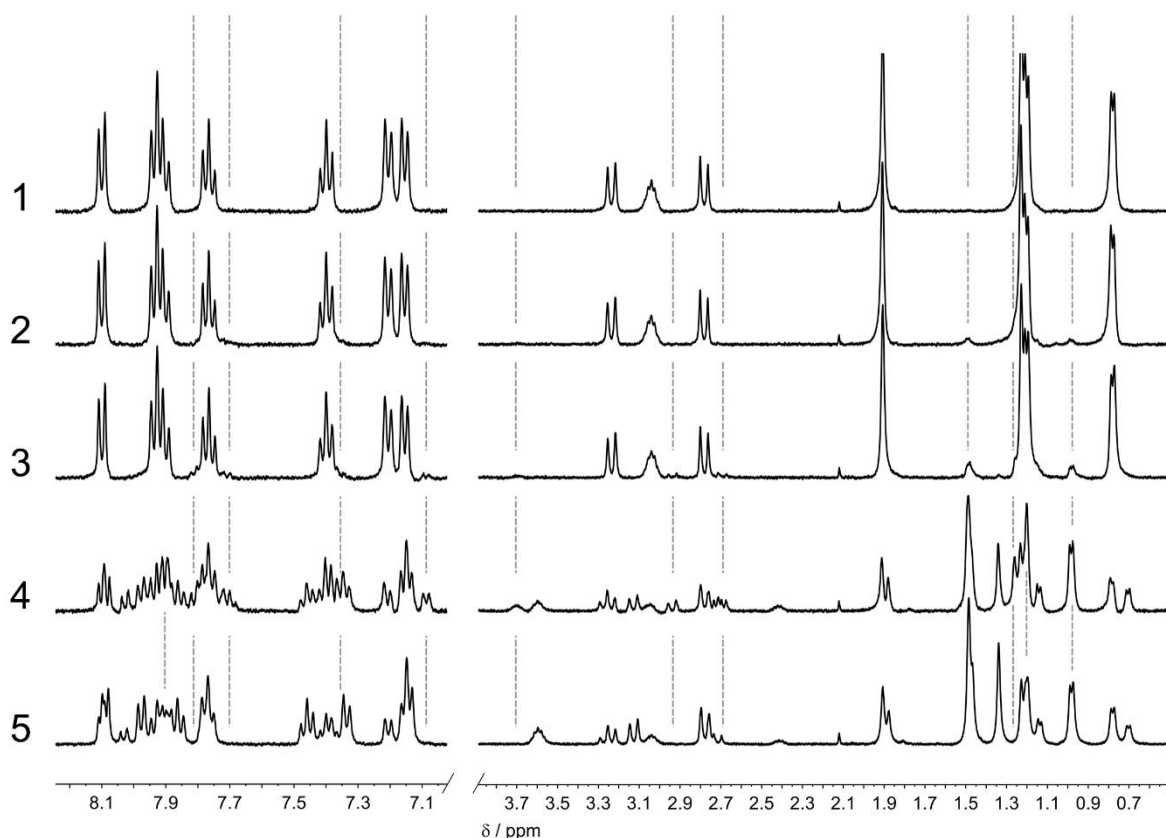
Figure 64:   Spectral evolution under irradiation conditions at –105 °C and after thermal decay of **B**-5. ^{1}H NMR spectra (CD$_2$Cl$_2$/CS$_2$ (4/1), 400 MHz) are presented.[II] 1: Spectrum of **A-5**. 2: 8 s of irradiation with 470 nm. 3: 16 s of irradiation. 4: 107 s of irradiation. 5: Spectrum obtained after the thermal decay of isomer **B-5** was finished. Reprinted with permission from *Angew. Chem. Int. Ed.* **2017**, *56*, 14536-14539. Copyright 2017 Wiley and Sons.

Comparison to calculated NMR spectra showed good agreement with the experimental results. It can be observed that the septet signals of the *iso*-propyl groups are very sensitive to structural changes and exhibit the largest spectral shifts. The very same trend can be observed for the calculated shifts, reproducing qualitatively the relative shift differences of the septet signals obtained by experimental means. **B-5** exhibits the most downfield shifted septet signal followed by isomer **C-5** and **A-5** septets. Also the distinct upfield shift of isomer **D-**5 is well reproduced in the theoretical description.
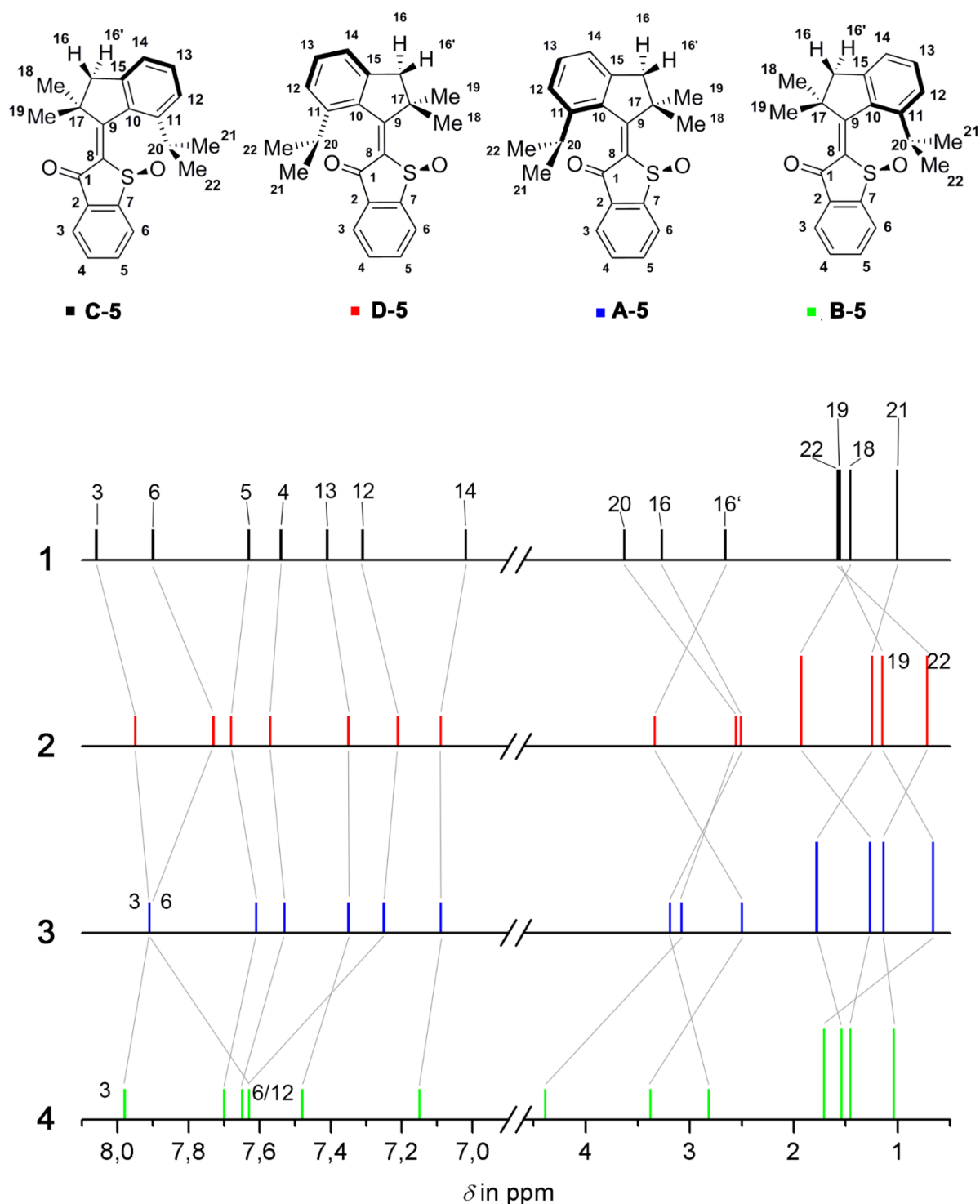
Figure 65: The ^{1}H NMR spectra of all four isomers **A** to **D** of motor **5** were calculated at the B97-2/6-311++G(d,p) level of theory based on optimized minimum structures at the MPW1K/6-311G(d,p) level of theory.[IX] Assignment of the signals to the (*S*)-configured isomers of **5**. The spectral changes of individual signals were indicated by grey lines. 1: Isomer **C-5** (black). 2: Isomer **A-5** (red). 3: Isomer **D-5** (blue). 4: Isomer **B-5** (green). Adapted with permission from *Angew. Chem. Int. Ed.* **2017**, *56*, 14536-14539. Copyright 2017 Wiley and Sons.

4.18   Energy profile of motor 5

Motor **5** revealed sufficient sterical hindrance to successfully decelerate the thermal **B** to **C** isomerization. Hence, it was possible to accumulate isomer **B-5** at –105 °C under irradiation conditions. This enabled on the one hand the observation of isomer **B-5** as the direct photoproduct of isomer **A-5** and on the other hand the recording of its decay. It could be shown, that isomer **C-5** is thermally generated from isomer **B-5** with an associated $\Delta G^{\ddagger}_{\text{B-C}}$ of 11.3 kcal·mol^{-1}. This helical inverting step was proven to proceed quantitatively at –105 °C, which can be translated into an energy difference of at least 0.98 kcal·mol^{-1} (Equation 15, K=95/5). The chemical shifts of the new intermediate were qualitatively reproduced by the calculated NMR spectrum of isomer **B-5**. Thus, theoretical and experimental results strongly supports the assignment of the new isomer as the elusive intermediate **B-5**. These previously missing key features now complete the ground state energy profile of the whole rotation cycle as it is depicted in Figure 66.
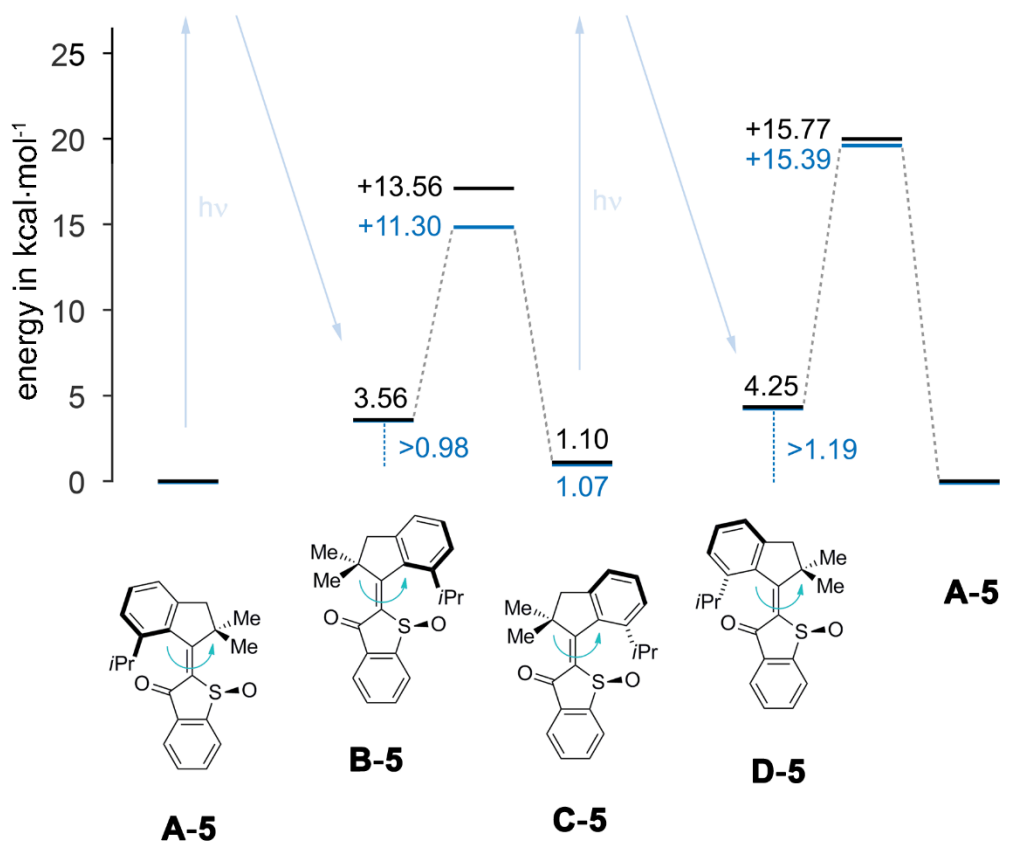
Figure 66:   Ground state energy profile of motor **5**. Only (*S*)-configured isomers are shown exemplarily. Energies are given in kcal·mol^{-1}. Experimentally determined values are highlighted in blue, calculated values (at the MPW1K/6-311G(d,p) level of theory)[IX] in black. Thermal processes are indicated as dashed black lines, while photo-induced processes are depicted as blue arrows. Adapted with permission from *Angew. Chem. Int. Ed.* **2017**, *56*, 14536-14539. Copyright 2017 Wiley and Sons.

In summary, the rotation cycle of HTI-based motors **1**-**5** consists of four distinct isomerization steps. Irradiation of isomer **C** leads to isomer **D** via photoisomerization, while **D** is converted to the next intermediate **A** through a thermal helix inversion. Full conversion of **D** to **A** finishes the first 180° of unidirectional rotation. Since the energy barrier for this process is sufficiently high, its observation was possible for all investigated motor derivatives. Unidirectionality of the second 180° of rotation can be explained analogously to the first 180° of rotation (see chapter 2.13). Helical pre-twisting is considered as the determinant for directional photo-induced rotation around the central double bond. Experimental observation of initial formation of isomer **B**, if isomer **A** is irradiated, strongly supports this assumption. Since the sulfoxide stereocenter is maintaining its stereochemical information, the second photoisomerization exhibits the same directionality as the two previous isomerization steps. The directionality of the final thermal **B** to **C** helix inversion can be derived from an experimentally validated theoretical description, which postulates a planar-type transition state between the two isomers. Only a helical inversion, which is accompanied by a further rotation of the double bond with suitable directionality, is able to generate isomer **C**. As this process restores the starting point of the rotation cycle, a fully directional 360° rotation around the central double bond is thereby completed. Repetitive motion occurs as long as sufficient thermal energy and light is available.

4.19   Substituent effects on thermal ground state features

In a comparative study, including the original methoxy-substituted motor **1**, a profound deduction of substituent effects on the thermally driven processes can be drawn. At least for derivative **5** the whole ground state process could be elucidated by low temperature ^{1}H NMR spectroscopy. It allowed for the determination of the thermal barrier of the **B** to **C** isomerization, which made a validation of the theoretical assessment for this fast thermal helix inversion possible. It was found, that theory is in good agreement with the experiment. Further experiments using transient absorption measurements for determination of the decay constants of intermediates **B-1**, **B-2** and **B-5** also confirmed that theory gives reliable results. For the following discussion, support by theoretical assessment is helpful for features of the energy profile, which are hardly accessible by experimental means. Theory derived findings of the discussion, however, have to be handled cautiously, since validation by experimental means is missing.

a)

b)

motor	A	B	$\Delta G^{*}_{B\text{-}C}$	C	D	$\Delta G^{*}_{D\text{-}A}$
1	0.81	3.35	5.53	0.00	3.51	13.45
2	0.00	4.61	10.10	1.41	4.31	15.16
3	0.00	5.29	8.12	0.99	3.69	14.20
4	0.00	3.87	11.95	1.24	4.30	15.79
5	0.00	3.56	13.55	1.10	4.25	15.76

c)

motor	A	B	$\Delta G^{*}_{B\text{-}C}$	C	D	$\Delta G^{*}_{D\text{-}A}$
1	0.81[4]	>1.73[1]	5.76[1]	0.00[4]	>1.73[1]	13.14[3] 13.32[1]
2	0.00[4]	>1.73[1]	9.50[1]	1.29[4]	>1.13[2]	14.38[2] 15.04[5]
3	0.00[4]	-	-	0.87[4]	>1.13[3]	14.30[3] 14.64[5]
4	0.00[4]	-	<11.30[2]	1.11[4]	>1.19[3]	15.43[3] 15.28[2]
5	0.00[4]	>1.73[1]	11.30[2] 11.99[1]	1.07[4]	>1.19[2]	15.39[2]
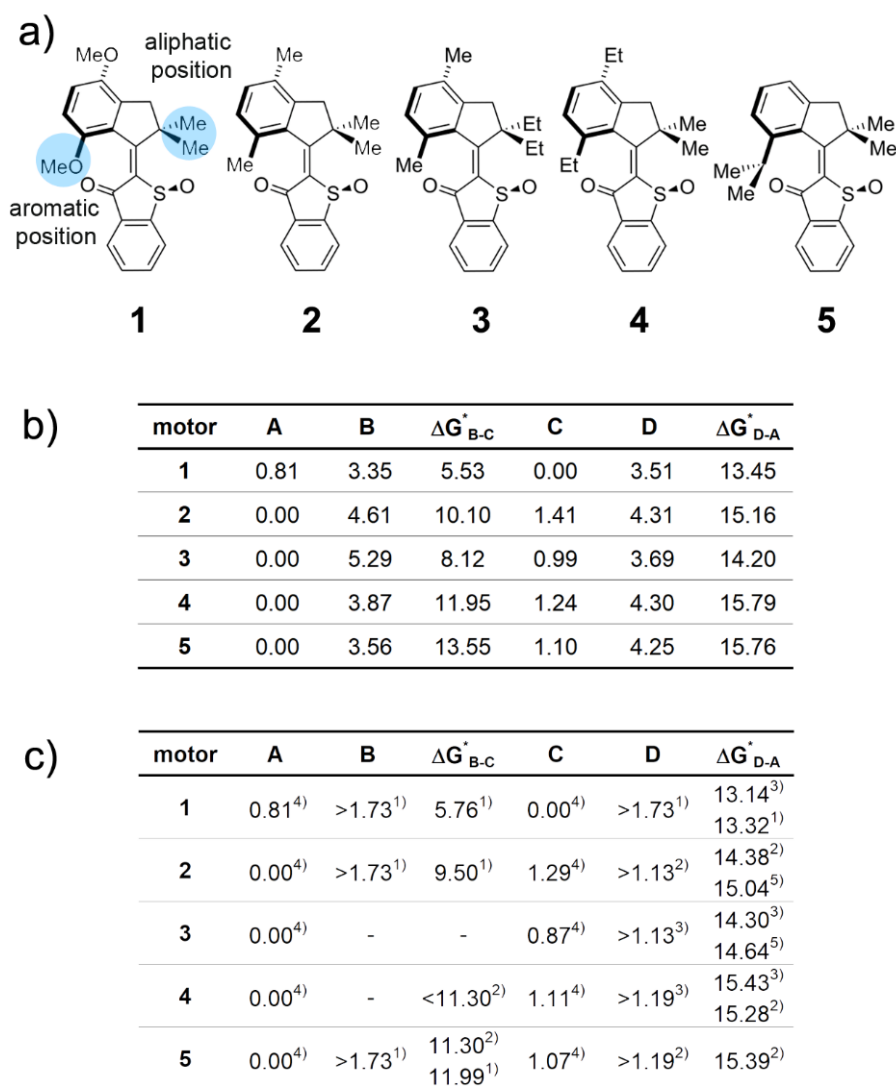
Figure 67: HTI-based molecular motors **1-5** and experimentally as well as theoretically determined energy values of their ground state profiles are presented. Theoretical descriptions of motors **1**, **2** and **5** were delivered by *Stefan Thumser*.[IX] a) Structures of isomers **A** with (*S*) configuration are depicted exemplarily. b) Theoretically obtained energies of the ground state profile. Optimization was performed on the MPW1K/6-311G(d,p) level of theory. Energies are given in kcal·mol⁻¹. c) Experimentally determined energies by low temperature ¹H NMR spectroscopy as well as ultrafast transient absorption measurements. Energies are given in kcal·mol⁻¹. [1] Values obtained by transient absorption spectroscopy in CH₂Cl₂ at 23 °C. [2] Measured in a mixture of CD₂Cl₂/CS₂ (4/1 ratio) by low temperature ¹H NMR spectroscopy (**2**: –80°C; **4, 5**: –70°C) [3] Measured in CD₂Cl₂ by low temperature ¹H NMR spectroscopy (**1**: –90°C; **3**: –80°C; **4**: –70°C). [4] Measured in toluene-*d₈* (**1, 3 ,4** and **5**) or in xylene-*d₁₀* (**2**) at 100 °C by ¹H NMR spectroscopy. [5]) Measured in CD₂Cl₂ by ¹H NMR spectroscopy of a mixed solution of motor **2** and **3** at –80 °C.

Valuable insights into substitution effects on the energy barriers for the **D** to **A** helix inversions are available by exploration of motors **1** to **5**. The thermal **D** to **A** conversions were studied for all derivatives. Only in case of derivatives **1**, **2**, and **5** the **B** to **C** conversion was followed either by low temperature ^{1}H NMR spectroscopy or by transient absorption spectroscopy. Especially derivatives **3** and **4**, as they are regioisomeric forms, offer the potential to explore the differences between sterical hindrance at the aromatic or aliphatic position. Figure 67 shows a summary of experimentally and theoretically obtained energy values of the ground state profile. Comparative data are available for most thermal helix inversions and deviations results from different experimental setups, temperature and solvents. For comparison between different motors experimental data were used with most conformity.

Significant increase of the **D** to **A** thermal barrier of 1.9 kcal·mol^{-1} is observed by substitution of a methoxy group with a methyl group at the aromatic position as it is the case for derivatives **1** and **2**. Determined decay constants show a further increase of $\Delta^{\ddagger}G^{0}_{\mathbf{D\text{-}A}}$ of 1 kcal·mol^{-1}, when comparing **2** with **4** and **5**. Interestingly derivative **3** is characterized by a decrease of its energy barrier for the thermal **D** to **A** conversion compared to motor **2** despite increase in sterical hindrance (at the aliphatic side of the rotor fragment). This intricate detail was deciphered by unambiguous direct experimental comparison. Motors **2** and **3** were mixed in eqimolar concentration and were loaded in a single NMR tube. After isomer **D** accumulation by irradiation with 450 nm light, the decays of **D-2** and **D-3** were recorded simoultaneously by ^{1}H NMR spectroscopy at –80 °C. The results as well as the first order kinetic analyses are shown in Figure 68a and 68b. This experiment could unambiguously prove, that speed increase is observed in case of sterical increase at the aliphatic position by comparing motor **2** with motor **3**. Whereas a speed decrease is observed in case of increased sterical hindrance at the aromatic position by comparing motors **2** and **4**. Thus, two opposing effects result for the regioisomers **3** and **4**.
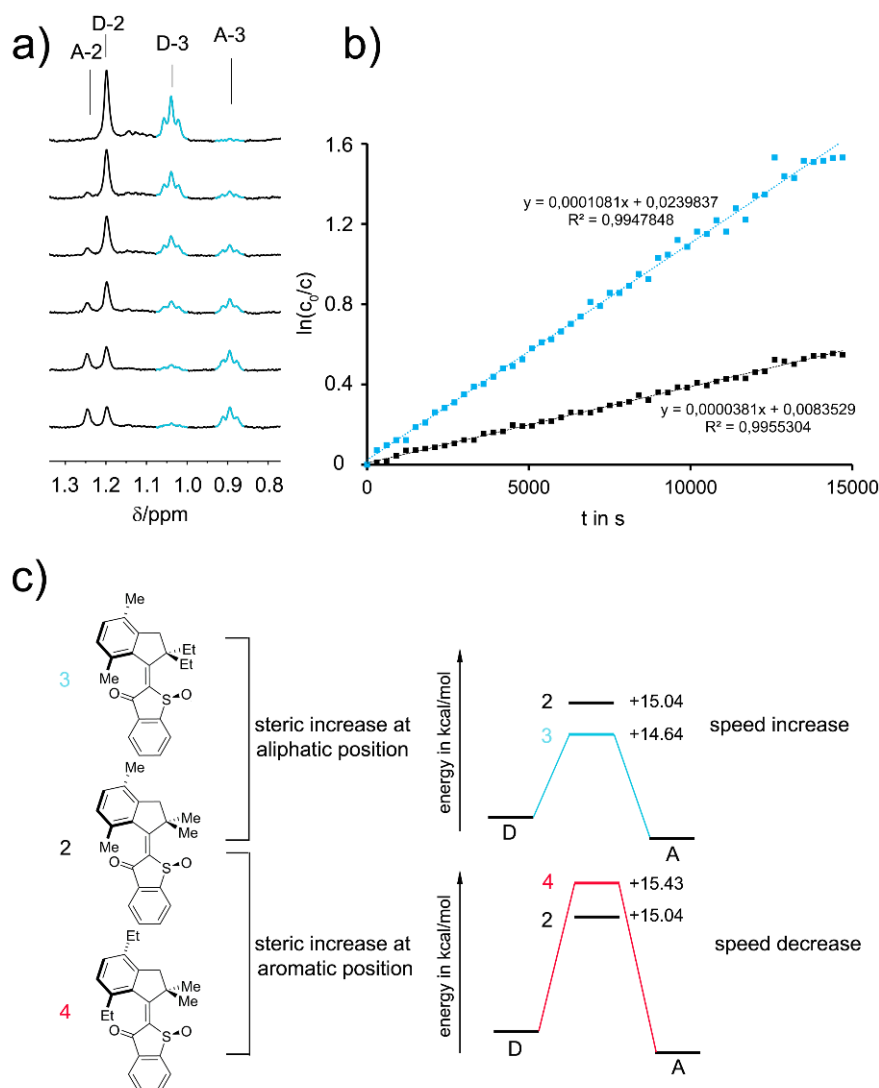
Figure 68: The energy barriers of thermal **D** to **A** isomerization of motors **2**, **3**, and **4** are compared. a) An extract of the ^{1}H NMR spectra recorded by the thermal decay of photo-generated isomers **D-2** and **D-3** is shown. Faster decay of isomer **D-3** (triplet signal) in comparision to isomer **D-2** (singlet signal) is observed. b) Decays of isomers **D** can be mathematically reproduced with a first-order kinetic anlysis and it was confirmed that **D-3** exhibit a smaller half-live as it was observed for **D-2**. c) In summary, increased sterical hindrance at the aliphatic position leads to a decreased energy barrier for the thermal **D** to **A** conversion (**2**: 15.0 kcal·mol^{-1}, **3**: 14.6 kcal·mol^{-1}) as elucidated by comparison of motor **2** and **3**. By comparision of the thermal decays of **D-2** with **D-4** (**2**: 15.0 kcal·mol^{-1}, **4**: 15.4 kcal·mol^{-1}) it was found that increased sterics at the aromatic position leads to an increased energy barrier for the **D** to **A** conversion.

Comparing motors **4** and **5**, almost the same energy barriers were found- again despite significant increase in sterical hindrance (at the aromatic side of the rotor fragment).

For the thermal **B** to **C** conversion, limited data are available for derivatives **1**, **2**, and **5**. Fundamentally increased barriers, rising from 5.77 to 9.50 kcal·mol^{-1} can be observed, if motor **1** is compared with **2**. Further increase of 1.7 kcal·mol^{-1} is achieved by introduction of an *iso*-propyl group as it is the case for motor **5**.

In summary, the range for speed manipulation by substitution is by far larger in the case of **B** to **C** conversion (5.5 kcal·mol^{-1} for $\Delta^{\ddagger}G^0_{\textbf{B-C}}$), than it is observed for the **D** to **A** inversion (2.3 kcal·mol^{-1} for $\Delta^{\ddagger}G^0_{\textbf{D-A}}$). There are three different scenarios which could affect the deceleration of the inversion process: 1. An increase of the transition state energy. 2. A stabilization of the metastable isomer. 3. A combination of both influences. From the available data it cannot be stated, if solely the transitions state energies are influenced by different substitution pattern or if ground state manipulations are participating, too. The group of *Feringa*[156] already reported on ground state energy variation of metastable states leading to unexpected speed increase of thermally driven motor processes of overcrowded alkenes. Experimental access to the relative energy differences between stable and metastable states is, in terms of calculated differences of 3-4 kcal·mol^{-1}, hardly feasible for distinguishing between the three scenarios.

Further interpretation of substitution effects can only be derived from calculated data, since experimental access to fast thermal processes and relative energies of metastable states is limited by experimental conditions. The structures of all assessed HTI-based molecular motors and a summary of their theoretically obtained energies of the ground state profile are depicted in Figure 67. Theoretical descriptions of motors **1**, **2** and **5** were delivered by *Stefan Thumser*.[IX]

An overall trend, with exception of derivative **3**, of increased thermal barriers for both thermal isomerization processes can be observed, as illustrated in Figure 67b. Theoretical description confirms that manipulation of the thermal motor behaviour by increased sterical hindrance is possible. The thermal barrier for the **B** to **C** inversion increase significantly from 5.53 to 13.55 kcal·mol^{-1}, while the increase of the thermal barrier of the **D** to **A** conversion from 13.45 to 15.82 kcal·mol^{-1} is lower in magnitude. Theoretical description of motor derivative **3** with increased sterical hindrance at the aliphatic position predicts lower barriers than derivative **2** and **4**. In comparison to tetramethylated derivative **2** the decreased thermal barriers for the **D** to **A** and **B** to **C** conversion exhibit counterintuitive speed increase by increased sterical hindrance. This was confirmed for the **D** to **A** inversion by a direct comparision experiment via ^{1}H NMR spectroscopy. Motor **4**, however, shows opposite behaviour in agreement to the observed overall trend. Furthermore, theory predicts a very similar thermal barrier for **D** to **A** isomerization in case of derivative **4** and **5**, although an ethyl group is replaced by an *iso*-propyl group, which was confirmed by experimental measurements.

The different thermal energy barriers for helix inversions, can be caused either by the direct change of the transition state energies or by a stabilization/destabilization of the metastable isomers. By comparing the minima as well as transition state energies of derivatives **2**, **4**, and **5**, which represent a series of

increased sterical hindrance at the aromatic position by introduction of alkyl substituents, a trend can be observed. While isomer **B** is stabilized from **2** to **5**, the transition state is destabilized. Both effects lead to an increased thermal barrier as can be seen in Figure 69a. The ground state profile of motors **2** and **3** are illustrated in Figure 69b. It can be seen, that the decreased thermal barrier of **3** could be a consequence of the destabilization of metastable isomer **B**. An additional manipulation of the transition state energy however is also predicted by theoretical assessment.
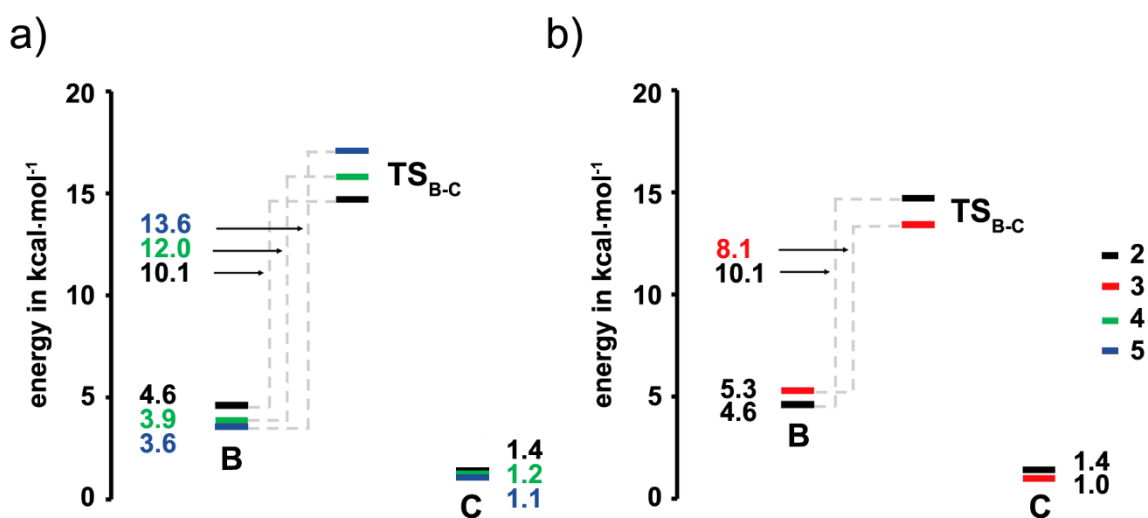
Figure 69:   Theoretically obtained energies on the MPW1K/6-311G(d,p) level of theory for isomers **B**, **C**, and transitions state **TS$_{B-C}$** of derivatives **2** to **5**. a) Energy profile of **B** and **C**, which are connected by **TS$_{B-C}$** of motor **2**, **4** and **5**. Increased sterical bulk lead to stabilization of isomer **B** and to a destabilization of **TS$_{B-C}$**. b) Energy profile of **B** and **C**, which are connected by **TS$_{B-C}$** of motor **2** and **3**. Increased sterical bulk leads to destabilization of isomer **B** and to a stabilization of **TS$_{B-C}$**.

In summary, theoretical calculation predicts an increase of thermal barriers for the helical inverting steps, if the sterical bulk at the aromatic position is enhanced. A slight decrease of the thermal barrier for **B** to **C** conversion should be available by introducing ethyl groups at the aliphatic position. Since motor **1** exhibits the fastest thermal isomerization rates, a possible improvement in terms of thermal speed increase would be the synthesis of a methoxy and ethyl group bearing motor derivative.

4.20   Ultrafast transient absorption measurements of derivatives 1, 2 and 5

Since two of four motor rotation steps are light induced conversions, efficient motor behavior is strongly correlated to exited state processes. Therefore, a mechanistic study based on ultrafast transient absorption spectroscopy[229-232] of three motor derivatives **1**, **2**, and **5** was performed in order to elucidate the full rotation cycle as well as substituent effects on photophysical key features of motor behavior.

135

Further, it became evident, that under realistic irradiation conditions the overall rotation frequency of HTI-based molecular motors is not limited by the highest thermal barrier of ground state helix inversions but rather from the quantum yields of the photoreactions.[102] The comparison of the transient data of derivatives **1**, **2**, and **5** allowed valuable insights into excited state behaviour of HTI motors and provided elaborate design principles for future development of new motor derivatives.

The great time-resolution capabilities of ultrafast transient absorption spectroscopy allowed for investigation of excited state processes as well as fast thermal ground state processes, e. g. the **B** to **C** helix inversion of all three motor derivatives at ambient temperatures. Thus, it could be shown, that the existence of isomer **B** is a common feature of HTI based motors and not exceptionally observable for motor **5**. For derivative **1**, however, the identification of isomer **B** and the spectral reconstruction of thermal **B** to **C** conversion was challenging, because the fast isomer **B** decay was overlapped with a long-living broad signal of a triplet state. In the following, the transient absorption data on µs time scale of **A-1** is shown as well as the interpretations and possible conclusions, which were drawn, before the global analysis of the data revealed isomer **B** existence. Further, the transient data of motor **2** are shown and the results of motors **1**-**3** are discussed in terms of future improvements of the HTI motor design. The transient absorption measurements of all three derivatives as well as the spectral analysis was carried out by *Roland Wilcken*.[XII] Main contributors to the investigation of motor derivative **1** were *Roland Wilcken*[XII], *Monika Schildhauer*[VIII] and *Manuel Güntner*[III]. The results on derivative **1** can be found in reference 102.[102] For related studies on overcrowded alkenes see references 149-151, 155 and 233-236. [149-151, 155, 233-236]

4.20.1 Transient absorption measurements of motor 1 on µs time scale

The transient absorption measurements on the µs time scale conducted after fs excitation of isomer **A-1** revealed a slowly decaying bathochromic absorption (decay time 100 ns), which hints at population of a triplet state ^{3}**A-1*** (Figure 70). This unprecedented result was surprising since theoretical assessment predicted a fourth ground state isomer **B**, which did not fit to the observed spectral developments. No traces of this missing intermediate **B-1** were detected at first glance. After complete decay of the triplet state ^{3}**A-1***, partial recovery of the ground state bleach as well as the product spectrum of isomer **C-1** could be observed.
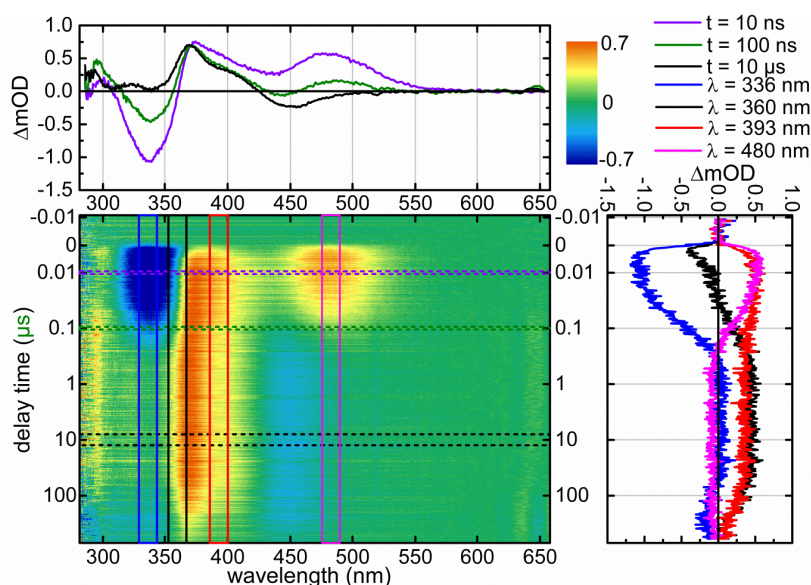
Figure 70:   Transient absorption spectra of motor **1** in CH₂Cl₂ at 22 °C recorded on ns/µs time scale.[XII] Three selected spectra at 10 ns, 100 ns and 10 µs are shown (top). The 2D plot of the transient spectra with elapsed time is shown at the left side. At the right side the kinetic traces at four different wavelengths are shown. Color codes are used for assignment of kinetic traces (right) to the corresponding wavelengths in the left 2D plot. Reprinted with permission from *J. Am. Chem. Soc.* **2018**, *140*, 5311-5318. Copyright 2018 American Chemical Society.

Three different possible scenarios can be derived from these first observations: In the first, the intermediate **B-1** spectrum is overlapped by the broad triplet spectrum ³**A-1***, with intermediate **B-1** converting to **C-1** on a similar or a shorter timescale compared to the triplet state population. In the second, no isomer **B-1** formation is induced by irradiation and excited isomer **A-1** is directly converted to isomer **C-1**. In this case the triplet state ³**A-1*** is just an additional deexcitation channel. The last scenario contemplates the possibility of triplet state contribution to the photoisomerization process, which would imply triplet state population from excited isomer **A-1** and a consecutive deexcitation to the ground state accompanied by partial double-bond isomerization. Further, the consequences for motor unidirectionality and mode of action have to be taken into account for scenarios 2 and 3. Full directionality for scenario 1 is discussed in chapter 2.18. If no isomer **B-1** exists, as it is the case in scenario two, a backwards rotation should deliver isomer **D-1**. Since direct and exclusive formation of isomer **C-1** results from excitation of isomer **A-1**, another reaction path, which differs from the mechanism of **C-1** to **A-1** conversion, would be present. From the data it cannot be stated, if the observed **A-1** to **C-1** conversion is a forward rotation around the double bond, but it can be stated that it does not cancel out the movement accompanied by the **C-1** to **A-1** conversion. Scenario 3 results in similar considerations, although a triplet state would be intermediately populated. Also in this case a different reaction path for **A-1** to **C-1** conversion as for **C-1** to **A-1** transfer would be the consequence. Scenario two and three describe a three state mechanism, with interconversion in a defined sequence. If a 360°

unidirectional rotation around the central double bond is the driving motion for sequencial three state population, cannot be derived from the data. Further considerations on alternative motion possibilities is given in the introduction chapter 2.1.

Low temperature ^{1}H NMR spectroscopy measurements showed the existence of isomer **B** for motor derivative **5**. It seems unlikely that derivative **1** should exhibit distinct deviation from the theoretical prediction. Thus, the decay of the long lasting absorption feature in the transient absorption spectra of **A-1** was investigated in greater detail for identification of a fast decaying hidden species. More sophisticated analysis of the transient data was achieved by using a sum of exponential functions for global fitting of the temporal development at all wavelengths. For further details on spectral analysis see reference 102 and 237.[102, 237] It was finally possible to disentangle the bathochromic absorption from the **B-1** spectrum. The thus obtained decay time found for the **B-1** species, is in good agreement with the theoretical description, which supports the isomer identification.

4.20.2 Transient absorption measurements of motor derivative 2

Unambiguous identification of isomer **B** can be obtained from the transient data of motor **2** and **5**. The lifetime of isomer **B** is in these cases sufficiently long to enable to extraction of the isomer **B** spectrum unambiguously from the transient absorption (TA) spectra and not only by the decay associated difference spectrum (DADS) from the global fit. Since spectral behavior of motor **2** is quite similar to motor **5**, only the data of **2** are shown exemplarily. TA measurements and and spectral analysis was performed by *Roland Wilcken*.[XII]
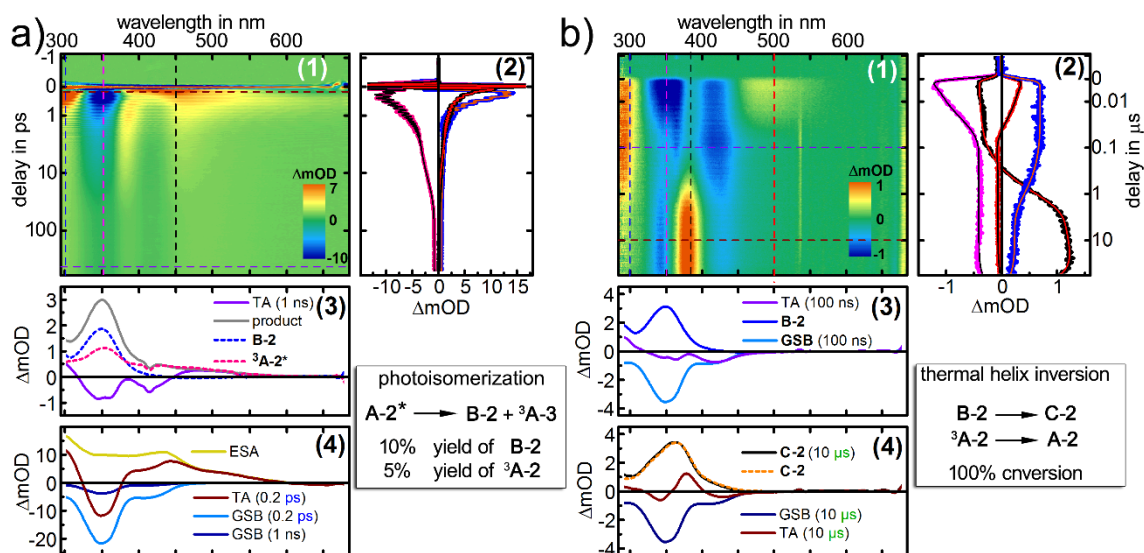
Figure 71: Transient absorption spectra of motor **A-2** after 420 nm fs-pulse excitation in CH_2Cl_2 at 22 °C are shown.[XII] a) Transient measurements on the fs/ps timescale. 1: 2D plot of the transient spectra versus elapsed time. 2: Kinetic traces at different wavelengths. 3: Spectral disentanglement of the ^{3}**A-2*** triplet spectrum as well as the **B-2** spectrum is. 4: Excited state absorption (ESA) spectrum at 200 fs. b) Transient absorptions at the μs time scale. 1: 2D plot of the transient spectra versus elapsed time. 2: Kinetic traces at different wavelengths. 3: Spectral reconstruction of **B-2** from the TA at 100 ns. 4: Reconstruction of isomer **C-2** spectrum at 10 μs.

A solution of **A-2** was excited with a 420 nm fs laser pulse (35fs) and the spectral changes were recorded on the fs and ps times scale (Figure 71a). After excitation strong excited state absorption (ESA) bands can be observed at 300 nm and 450 nm respectively. The absorption features of the ESA reveal rapid spectral changes on the 100 fs time scale. The decay of the ESA is described by a time constant of only 330 fs (Figure 71 inset 1 and 3). Consecutive thermal ground state relaxation happens with a time constant of 8 ps. The remaining spectral features are dominated by a red shifted absorption band, which was already observed for motor **1**. Theoretical calculations on the CASSCF level of theory were performed for motor **1** and the results confirm the assignment of this absorption to a triplet state.[102] Since their lifetimes and spectra reveal great similarity, the redshifted absorption band can be assigned to a triplet state ^{3}**A-2*** in this case, too. The triplet spectrum is overlapping with the spectrum of isomer **B-2**, which contributes mostly in the shorter wavelengths regions (350 nm). By subtraction of the isomer **B-2** spectrum, which can be obtained at later delay times (100 ns, Figure 71b inset 3) from the product spectrum at 1000 ps, the spectrum of the triplet state ^{3}**A-2*** is extracted (Figure 71a inset 4). Comparison of the ground state bleach (GSB) at 200 fs delay time with GSB at 1000 ps shows that 17% of the excited molecules populates either the triplet state ^{3}**A-2*** or isomer **B-2**. The ratio of triplet state and isomer **B** population was found to be 40/60, which can be translated into the corresponding quantum yields $\phi_{A/3A}$ of $7 \pm 2\%$ for ^{3}**A-2*** triplet generation as well as $\phi_{A/B}$ of $10 \pm 2\%$ for the **A-2** to **B-2** photoisomerization.

Measurements on the ns time scale (420 nm light pulse with 2.5 ns duration) allowed the total decay of the triplet state ^{3}**A-2*** to be observed (Figure 71b). The remaining TA signal is solely the sum of the GSB and the absorption spectrum of isomer **B-2**. That allows for spectral reconstruction of the isomer **B** spectrum at 100 ns, which was used for spectrum identification of the triplet state at earlier decay times (1000 ps). (Figure 71b inset 3). Unlike motor derivate **1**, derivative **2** shows a much longer lifetime of metastable isomer **B**, which exceeds the lifetime of the triplet state sufficiently. At later delay time of 10 µs the final product spectrum is extracted, which is revealed to be identical with the steady state absorption spectrum of isomer **C-2**. Global analysis confirms the existence of two decaying species, which are assigned to the triplet decay with a time constant of 25 ns and the **B** to **C** conversion with a time constant of 990 ns. As the triplet decay leads solely to GSB recovery it can be stated, that also in the case of motor **2**, triplet state formation can be regarded as a minor loss channel for photons but it does not interfere with the overall directionality of the motor rotation. Full conversion for the **B** to **C** helix inversion is confirmed, since no GSB recovery can be observed for this process. Thus, the ratcheting step from **B-2** to **C-2** reveals 100% completeness at 22 °C, which is an important prerequisite for overall directionality at ambient temperature.
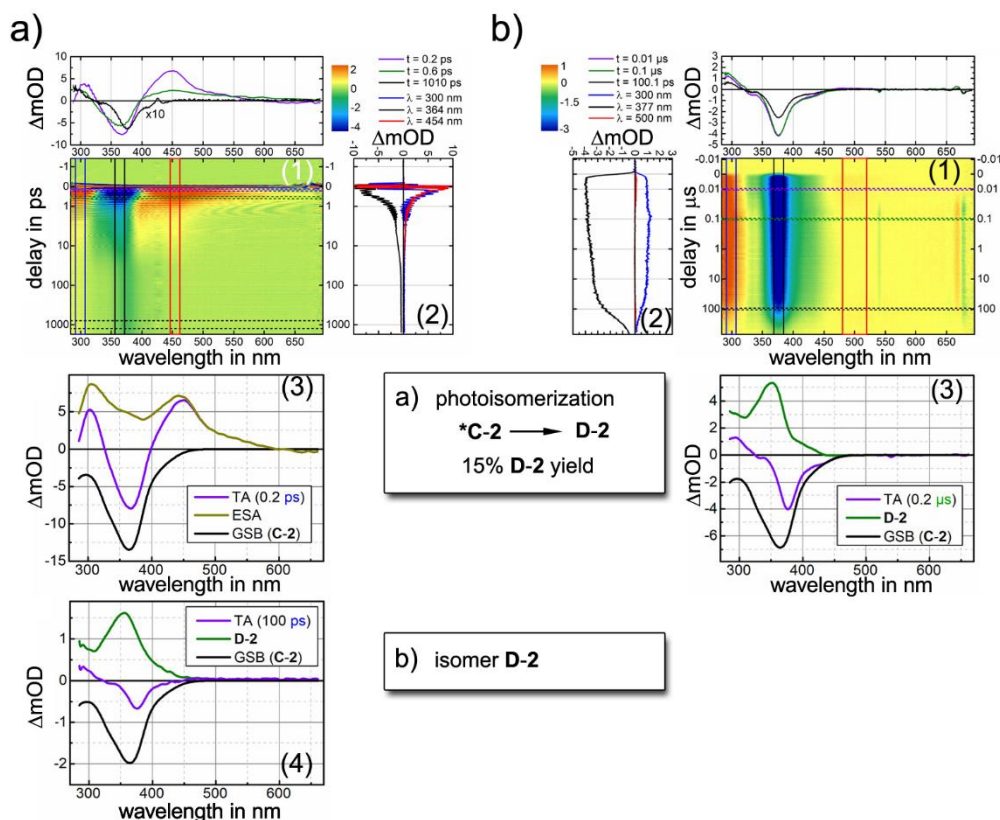
Figure 72:   Transient absorption spectra of motor **C-2** recorded after 420 nm fs-pulse excitation in CH₂Cl₂ at 22 °C.[XII] a) Transient measurements on the fs/ps timescale. 1: Selected absorption spectra at different delay times and 2D plot of the transient spectra versus elapsed time. 2: Kinetic traces at different wavelengths. 3: ESA spectrum at 200 fs. 4: Spectral disentanglement of the **D-2** spectrum. b) Transient absorptions at the µs time scale. 1: Selected absorption spectra at different delay times and 2D plot of the transient spectra versus elapsed time. 2: Kinetic traces at different wavelengths. 3: Spectral reconstruction of **D-2** from the TA at 200 ns.

The ultrafast dynamics were also investigated for isomer **C-2**. A CH₂Cl₂ solution of **C-2** was excited with a 420 nm fs light pulse and the spectral changes were recorded on the fs to µs time scale. Initially after excitation the ESA absorptions at 300 and 450 to 600 nm can be detected. Again the absorption features of the ESA are dramatically changing within a very short time (80 fs). A time constant of 370 fs is found for the deexcitation into the ground state. Consecutively, thermal cooling of the ground state can be observed with a time constant of 5.2 ps. Only in the ns timescale measurements traces of red shifted remaining absorption bands were detected, which could hint at triplet state formation after **C-2** excitation. In the fs timescale measurements this weak absorption is not observed and its contribution to the transient signals can be neglected. From the TA measurements at the µs time scale the **D-2** spectrum can be obtained at 100 ps delay time by spectral analysis (Figure 72a inset 4). For the light induced formation of **D-2** a quantum yield $\phi_{C/D}$ of $15 \pm 3\%$ is found. The thermal energy barrier for the

D to **A** conversion was determined to be 14.38 kcal·mol^{-1} by low temperature ^{1}H NMR meassurements, which leads to prolonged life time also at ambient temperature exceeding the temporal resolution capabilities of the pulsed laser setup. Thus, the signal of isomer **D-2** remains constant at the μs timescale (Figure 72b inset 1).

4.20.3   Ultrafast excited state dynamics of HTI motors

Transient measurements of the three motor derivatives reveal overall similar behavior after excitation. But there are also distinct differences between methoxy-bearing motor **1** and the alkylated analogues **2** and **5** with regard to the ultrafast excited state dynamics at early delay times. In Figure 73 the excited state absorption developments are illustrated for isomers **A-1** and **A-2**. Measurements of **A-2** show very similar behavior to **A-1**. The ESA decay of isomer **A**-1 proceeds with a time constant of 1.5 ps and a consecutive ground state thermal relaxation with 7 ps timescale. The ESA dynamics are dominated by simple fading of the absorption. Derivative **2**, however, shows rapid spectral evolution within 200 fs with a decreasing absorption band at 450 nm as well as an increasing red shifted absorption (>550 nm). Overall, the ESA of **A-2** decays much faster with a time constant of 330 fs. Thermal cooling with a time constant of 7 ps, however, is again consistent with motor **1**. The ESA dynamics after excitation of the corresponding **C** isomers are very similar to those obtained for the isomers **A**.

The obtained transient data allow for interpretation of the excited state processes. After excitation to the Franck-Condon region structural rearrangements within the molecule lead to reduced potential energy and population of an excited state minimum. Motors **2** and **5** exhibit almost barrier free access to a subsequent conical intersection, which consequently results in immediate deexciation to the ground state. Derivative **1** shows much longer ESA decay times, which can be translated into a higher barrier towards the conical intersection. This delivers a consistent picture for the fastest photoisomerization speeds measured for HTI derivatives so far (derivatives **2** and **5**). Analogous behavior is observed for the isomers **C**, with ultrafast photoisomerization of alkylated motors and a prolonged ESA lifetime of methoxy-bearing derivative **1**.
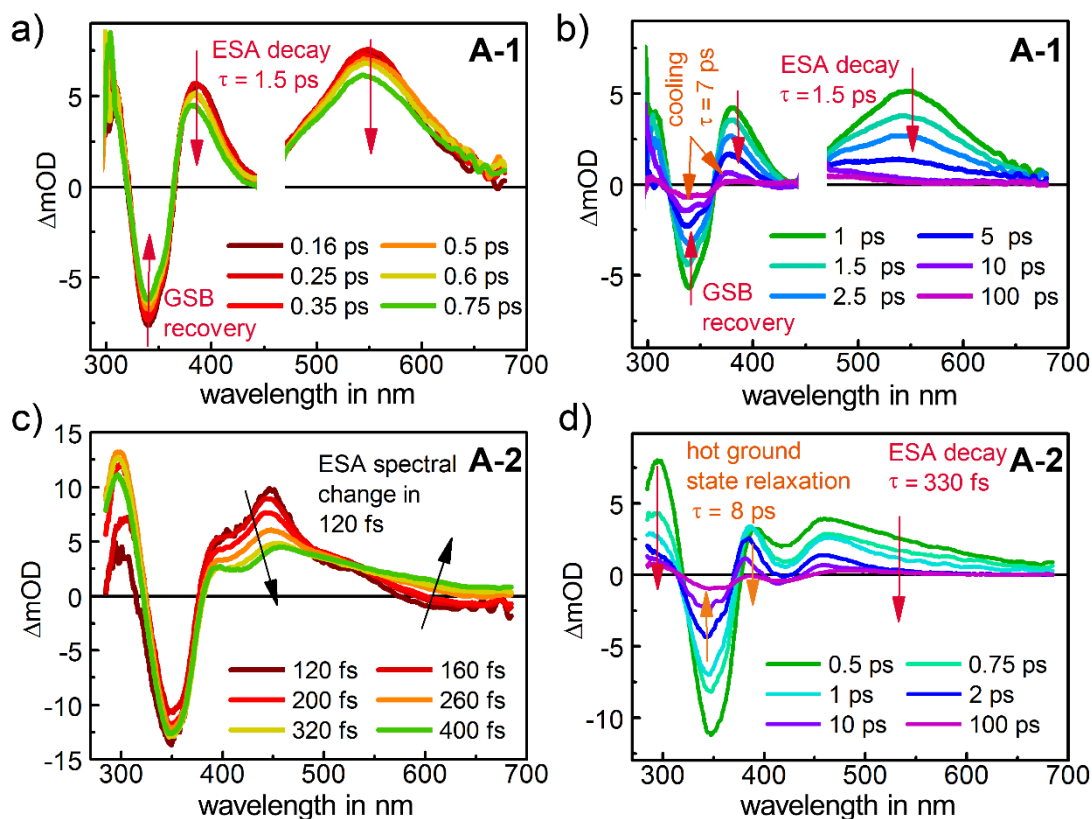
Figure 73:   ESA dynamics of motor derivatives **A-1** and **A-2** after excitation in CH_2Cl_2 at 22 °C.[XII] a) Spectral dynamics of **A-1** at early delay times show a dominant fading of the absorption. b) Decay of the ESA of motor **A-1** happens with a time constant of 1.5 ps and a consecutive ground state cooling with a time constant of 7 ps. c) The ESA of **A*-2** is evolving rapidly within few hundred fs. d) Ultrafast decay of the ESA of **A-2** happens within 330 fs. A 8 ps time constant is found for hot ground state relaxation.

4.20.4   Steady state absorption spectra of all intermediates

As already described, from the transient measurements performed by *Roland Wilcken*[XII], the steady state absorption spectra of intermediates **B** and **D** can be extracted. Since the extinction coefficients of stable isomers **A** and **C** as well as the concentrations of the investigated solutions are known, the molar absorptivity of the metastable isomers can be determined, too. In the following Figure 74 all intermediate spectra of motors **1**, **2**, and **5** are summarized.
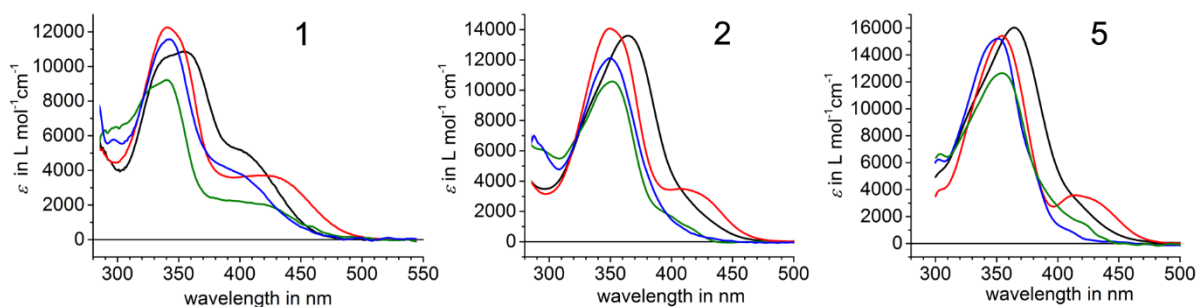
Figure 74:   Molar absorption spectra of all isomers of motors **1** (left), **2** (middle), and **5** (right) in CH_2Cl_2.at ambient temperature.[XII] **A** isomers are shown in red, **B** isomers in blue, **C** isomers in black, and **D** isomers in green. Spectra of metastable isomers are extracted from the TA measurements. Stable isomers **A** and **C** were measured by steady state absorption spectroscopy.

All derivatives reveal similar absorptions, with the characteristic bathochromic shoulder of the **A** isomers as well as a bathochromic absorption maximum of the **C** isomers. A less pronounced bathochromic shoulder of isomer **C** is present in the absorption spectrum of motor **1**, but is essentially missing for derivatives **2** and **5**. In all cases metastable isomers exhibit decreased absorptions in comparison to the stable isomers. In particular, for motor **1** spectral features for a specific double bond configuration (red shifted absorption plateau for **A** and red-shifted shoulder for **C**) are maintained in isomer **D** and isomer **B**, while a bathochromic shoulder is only rudimentary preserved in the absorption spectra of isomers **D-2** and **D-5**. Methoxy substituted motor **1** shows absorptions up to 500 nm, while absorptions of **2** and **5** are hypsochromically shifted. **2** and **5** reveal marginally increased extinction coefficients at shorter wavelengths.

4.20.5 Comparison of motors 1, 2, and 5

With the transient data and the data obtained from the low temperature ^{1}H NMR spectroscopic measurements, photophysical and thermal properties can be linked to different substitution pattern in close proximity to the central double bond. In Table 11, the key features of motors **1**, **2**, and **5** are summarized. It was already discussed in chapter 2.19 on the basis of low temperature ^{1}H NMR spectroscopy and theoretical assessments that increased sterical hindrance at the aromatic position of the rotor part leads to decreased rates for the thermal helix inversions. For the **D** to **A** inversion, this was elucidated by ^{1}H NMR spectroscopy. With the transient data, increasing thermal barriers with increased sterical hindrance, e.g. a time constant of 3 ns for **1** and 125 µs for **5**, can be confirmed for the **B** to **C** conversion at ambient temperature, too. The effect of sterical hindrance on the **B** to **C** conversion is more distinct. For example the **B**/**C** conversion of **5** is 43,000 times slower than the **B**/**C** conversion of motor **1**, while for the **D**/**A** conversion motor **5** is only 25 times slower than for motor **1**. The TA measurements also allow for the observation of the completeness of both helix inversions at ambient temperature, which is a prerequisite for full directionality.

Table 11:   Quantum yields and time constants derived from the TA measurements[XII] as well as ^{1}H NMR spectroscopy are summarized for motor derivatives **1**, **2**, and **5**. The time constants $\tau_{A/B}$ and $\tau_{C/D}$ for the photoisomerizations are derived from the excited state lifetime of A^* and C^*. $\phi_{A/B}$ and $\phi_{C/D}$ denote the corresponding quantum yields of the photoisomerizations. The decay times of the triplet states are given with $\tau_{3A/A}$, while the quantum yields of triplet formation are given as $\phi_{A/3A}$. Extrapolated half-lives of isomers **D-2** and **D-5** are denoted as $\tau_{D/A}$. [a) b)] The $\Delta G^{\ddagger}_{D-A}$ of these processes were measured at low temperature (–70 °C for derivative **5** and –80 °C for derivative **2**) with ^{1}H NMR spectroscopy. The yields $\phi_{D/A}$ are determined by the accuracy of this measurement. [c)] $\phi_{C/D}$ for **3** determined by using a home-build steady state quantum yield determination setup.

	1	**2**	**5**		**1**	**2**	**5**
$\tau_{A/B}$	1.5 ps	330 fs	470 fs	$\phi_{A/B}$	7%	10%	9%[c)]
$\tau_{B/C}$	3 ns	990 ns	125 µs	$\phi_{B/C}$	100%	100%	100%
$\tau_{3A/A}$	100 ns	25 ns	20 ns	$\phi_{A/3A}$	8%	7%	6%
$\tau_{C/D}$	7.9 ps	370 fs	270 fs	$\phi_{C/D}$	24%	15%	11%[c)]
$\tau_{D/A}$	1.2 ms	7.4 ms[a)]	41.1 ms[b)]	$\phi_{D/A}$	100%	>95%[a)]	>95%[b)]

The ultrafast ESA evolutions of derivatives **2** and **5** were already discussed in the previous chapter. For the isomers **A** the corresponding quantum yields significantly decrease from 24% for derivative **1** to 15% for **2** and 11% for **5**. For the isomers **C**, however, a slightly increased quantum yield (7% for **1**, 10% for **2**, and 9% for **5**) can be observed. Also the triplet decay becomes faster with a marginal decreasing quantum yield for this process (8% for **1**, 7% for **2**, and 6% for **5**).

A rate model[102, 238] established by *Roland Wilcken*[XII] is used for the simulation of rotation frequencies under realistic irradiation conditions with 100 mW LED input power. It was found, that in this case, the rotational speed is not dominated by the thermal barriers of the helical inverting steps but rather by the amount of available photons. It can be calculated, that thermal limits are reached, if irradiation intensity is 1000 W·cm^{-2}.[102] Such intensities would most probably lead to decomposition of the molecular motors. Since it is not possible to increase irradiation intensity over a certain limit, photonic efficiency is the only possibility for speed increase under realistic irradiation conditions. Photonic efficiency can be achieved by increased quantum yields and increased molar absorptivity. Equation 18 describes the dependency of rotational frequencies *f* of quantum yield and absorption behavior:

$$f = \frac{1}{2} \cdot \frac{Abs \cdot N_{ph}}{N_{mol}} \cdot \phi_{A/B} \cdot \phi_{C/D} \qquad \text{(eq. 18)}$$

with $\quad Abs = 1 - 10^{d \cdot [\varepsilon_A c_A + \varepsilon_B c_B + \varepsilon_C c_C + \varepsilon_D c_D]}$ (eq. 19)

d = path length of cuvette $\qquad\qquad \varepsilon_{A/B/C/D}$ = extinction coefficients

$c_{A/B/C/D}$ = concentration –

and $\quad N_{Ph} = P_0 \cdot \frac{\lambda}{h \cdot c} \cdot \Delta t$ (eq. 20)

N_{Ph} = photon flux $\qquad\qquad\qquad P_0$ = incoming light power

λ = wavelength $\qquad\qquad\qquad\quad c$ = speed of light

h = Planck constant $\qquad\qquad\quad \Delta t$ = elapsed time

and $\quad N_{mol} = c \cdot V \cdot N_A$ (eq. 21)

c = concentration of the motor solution $\qquad V$ = volume of motor solution

N_A = Avogadro constant

N_{mol} = number of molecules

For frequency determination, the overall number absorbed photons as well the number of molecules have to be taken into account. If photons were absorbed, the photonic efficiency determines if a rotation occurs or not. This efficiency is dependent on the molar absorption behavior (*Abs*) and the quantum yields. As a full rotation includes two photoisomerizations the number of photons is divided by 2. Irradiation is considered to be monochromatic, and illumination area is exchanged fast with the surroundings (vigorous stirring).

Under typical conditions (100 mW light power at 350 nm and 2 mL of a 0.1 mM solution in a 10x10 mm cuvette, 22 °C), rotation frequencies of 12 mHz for motor **1**, 11 mHz for motor **2** and 7 mHz for

motor **3** are calculated. Different absorptions are found to be negligible, while the quantum yields dominates the varying rotation frequencies.

The rotational frequencies under realistic irradiation conditions of motors **1**, **2**, and **5** vary only little, while the overall maximum rates, which are determined by the highest thermal barrier show distinct deviations. 1 KHz rotation is found for derivative **1**, 114 Hz for derivative **2** and only 20 Hz for motor **5** at 20 °C as the maximum attainable rotation speeds. Thus, the intrinsic differences of the molecular motors become evident only at reduced temperature where thermal processes are significantly slowed down and thermal limits dominate over photonic efficiency.

In summary, molecular motor **1** exhibits superior motor functionality, since light induced processes as well as thermal processes ensure rapid conversion of intermediates. Astonishingly, alkylated motors show only little reduced rotation frequencies, although their theoretical maximum rotation rates are considerably diminished. The formula for frequency determination allows for a qualitative comparison of motor performances, which takes into account the most important aspects, ie. available photons, absorption behaviour, and quantum yields. From the obtained data several important conclusions for the future development of HTI-based molecular motors can be drawn. For molecular motors with high rotational frequencies, which works under photonic limits at ambient temperature, reduced thermal barriers for rapid ratcheting steps are essential. In the case of HTI based motors methoxy substituted motor **1** shows fastest thermal conversions, although all derivatives investigated exhibit motor function under photonic limits at ambient temperature. Further increase of rotation frequency can be obtained by enhanced absorptions and improved quantum yields for both photoreactions. Herein lies a distinct difference to superior HTI based photoswitches. As it was already discussed in chapter 2.8, the efficient switching performance of unsubstituted HTI is determined by the combination of a high quantum yield for *Z* to *E* isomerization and a low quantum yield for *E* to *Z* isomerization. The latter of which is fully compensated by the favourable photochromism. For molecular motors both photoreactions have to be efficient for high rotation frequencies and photochromism is not very relevant. As methoxy substituted derivative **1** reveals increased quantum yields for the **C** to **D** isomerization, motor designs with further increased electron density should be contemplated. The quantum yield of **A** to **B** photoisomerization shows only little variations with the different substitution pattern in motors **1**, **2**, and **5**. If the slight increase in efficiency of the **A** to **B** isomerizations, observed for methyl bearing motor **2** is in fact induced by its greater sterical hindrance and not by the electronic effects of the methyl group, superior quantum yield of future motor designs could be available by a moderate sterical increase at the aromatic position of the rotor part.

5.   Mixed indigoids as potential molecular motors

Future applications of molecular motors in sensitive environments (e.g biological systems) beyond fundamental research will require functionality under non damaging conditions. A convenient region for signaling ranges from 600 - 900 nm (biooptical window), as tissue degradation is minimized and scattering as well as absorption is diminished. Hence, penetration depths of several cm are possible at these wavelengths. However, most of molecular rotary motors developed so far are operational only under UV light input, which renders bio-applications difficult. HTI-based molecular motors, e. g. the methoxy substituted derivative **1** can be operated with wavelengths of up to 500 nm. For further improvement of the absorption a more pronounced indigoid chromophore can be contemplated. In Figure 75 the molecular structure of potential molecular motors based on mixed indigoid chromophores is illustrated. The synthesis of derivatives **86** and **87** is described in detail in the experimental part. Experimental data shown in this chapter were obtained for these derivatives **86** and **87**, while theoretical investigation was performed for **88** and **89** without the *tert*-butyl substitution at the thioindigo fragment. Derivatives **88** and **89** can be regarded as suitable model compounds for **86** and **87** since the structural differences should not exhibit sterical influence on the conformation of the double bond. The transition state of **88** was assessed with assistance of *Stefan Thumser*.[IX]

R₁= *t*Bu: **86**
R₁= H: **88**

R₂= *t*Bu: **87**
R₂= H: **89**
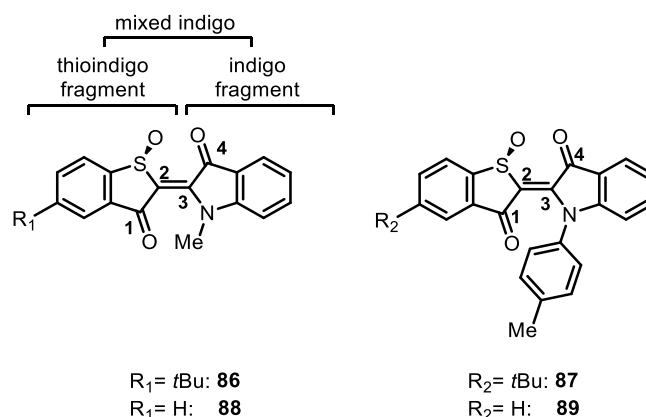
Figure 75:   Molecular designs of potential molecular motors based on a mixed indigoid chromophores. Only (*R*)-configured derivatives are shown. Arbitrary numbering is shown exemplarily and is used in Table 12 for identification of dihedral angles of the double bonds.

The molecular design exhibits fundamental features important for motor functionality, e. g. a double bond and a stereocenter in close proximity to the potential rotational axle. For unidirectional rotation, a pronounced helical twist around the central double is essential for the presence of two diasteromeric isomers for each double bond configuration. Thus, theoretical calculations were performed for mixed indigoids **88** and **89** in order to elucidate, if four ground state minima can be found. **88** is bearing a methyl group at the nitrogen, while **89** is tolyl substituted.

5.1 Theoretical investigation on mixed indigos 88 and 89

The theoretical assessment was performed on the B3LYP/6-311+G(d,p) level of theory. Indeed for both mixed indigos **88** and **89** four different ground state minima were found, which were confirmed to be stationary points by frequency analysis. The obtained structures exhibit slightly distorted double bonds, which allows for distinct geometrical classification of all four isomers. The double bond configuration is defined by *cis/trans* notation, the *R/S* descriptor determines the configuration of the sulfoxide stereocenter, and *P/M* is describing the helical twist of the double bond. Only (*R*)-configured enantiomers were assessed theoretically. Transition states for the *P/M* helical inversions with *cis* configuration for **88** and **89** were found, which connect the metastable c*is* isomers with their stable diastereomeric counterparts. One imaginary mode was obtained for each *cis*-configured transition state, showing that they are first order saddle points on the hyper-potential energy surface. In both cases, **88** and **89**, no transitions states for the helix inversions with *trans* configuration could be obtained. For convenience reasons **A** to **D** nomenclature is introduced, analogously to the HTI based motors. **A** stands for the enantiomeric pair *trans*-(*R*)-*M/ trans*-(*S*)-*P*, **B** for *cis*-(*R*)-*P/ cis*-(*S*)-*M*, **C** for *cis*-(*R*)-*M/ cis*-(*S*)-*P* and **D** for *trans*-(*R*)-*P/ trans*-(*S*)-*M*. Only (*R*)-configured minima are shown in Figure 77. Helicity for these molecules is defined by the distortion of the central double bond and can be determined easiest at the opposite side of the sulfoxide stereocenter, since double bond twisting is more pronounced (isomers **A/D**: C4-C3-C2-N, isomers **B/C**: C4-C3-C2-C1, atom numbering can be found in Figure 75).

5.1.1 Double bond twisting and obtained minimum structures

Double bond twisting is assumed to be a prerequisite for unidirectional photoisomerization.[239] In Figure 76 all possibilities for twisted double bonds in the proposed mixed indigoid chromophores are summarized. If both sides of the double bond exhibit the same helical twist (structures I and II in Figure 76), unidirectional photoswitching is possible. It is assumed, that rotation around the double bond in the excited state proceeds along the vector with minimal sterical hindrance. Thus, for structure I a clockwise rotation results because the groups marked in red in Figure 76 avoid the sterical hindrance of the groups marked in blue in Figure 76. Analogously, structure II rotates in counterclockwise direction. If both sides of the double bond exhibit different twisting as it is the case with structure III and IV, the sterical clash with the blue groups while rotating cannot be circumvented in the excited state. Two possibilities could result from that twisting configuration. In asymmetric molecules one side with increased distortion could dominate over the other side with minimal twisting and dictate the directionality of the isomerization after excitation. The second possibility is, if sterical hindrance of the four substituents is high enough for suppression of the rotation, no photoisomerization should occur. No preferential direction should result from a planar double bond as illustrated with structure V. It can be assumed, that amplitudes of populated vibrational modes at the time point of photon absorption could influence the direction of rotation in this case.
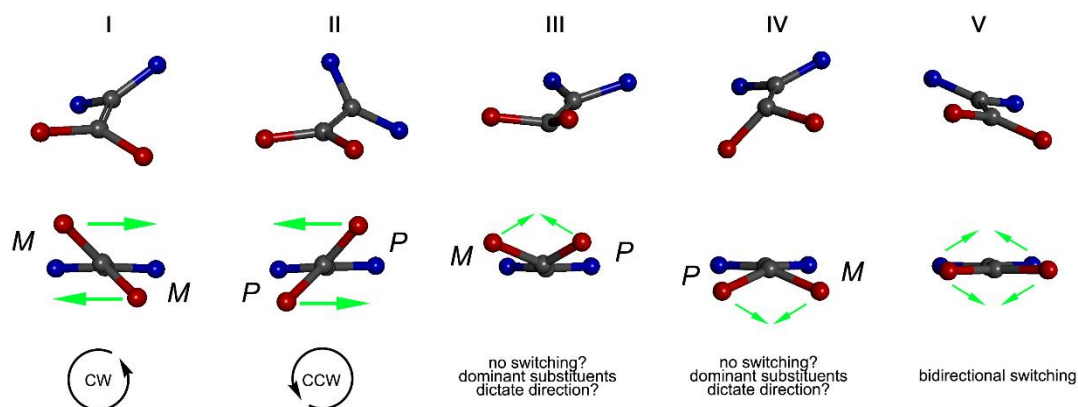
Figure 76: Five different twisting conformations of a fourfold substituted double bond are possible. The helical distortions result from the sterical hindrance of the double bond substituents, which are illustrated as red and blue groups. For simplicity reasons only symmetrical double bonds are shown. Green arrows illustrate the preferred direction of rotation of a substituent, which is determined by minimal sterical hindrance. Directionality is determined by rotating the red groups, while blue groups are kept static. The perspective is given by viewing from red to blue groups. Those with identical twisting on both sides should lead to directional isomerization around the double bond (structure I and II). Structure III and IV experience sterical clash, if isomerization occurs. Directionality cannot be predicted in these cases intuitively. A planar double bond (structure V) is able to undergo photoisomerization in both directions without preferred direction.

The helical twisting of the double bonds of mixed indigos **88** and **89** can be derived from the dihedral angles of the theoretically obtained minimum structures. The dihedral angles of the central double bonds are summarized in Table 12.

Table 12: Dihedral angles of the central double bonds of proposed motors **88** and **89** obtained from the calculated minimum structures on the B3LYP/6-311+G(d,p) level of theory. It becomes apparent, that all isomers exhibit suitable helical information, which should lead to directional photoisomerization. The sense of helicity is deduced from the algebraic sign of the dihedral angles. Anticipated directionality in turn is determined by the helical information as shown in Figure 77. For reconstruction of the directionality the thioindigo part is kept static and the indigo part rotates. The perspective is arbitrarily set by viewing from the indigo part to the thioindigo part.

	A-88	**B-88**	**C-88**	**D-88**	**A-89**	**B-89**	**C-89**	**D-89**
Angle C1-C2-C3-C4		24.14°	-22.22°			11.14°	-23.32°	
Angle S-C2-C3-N		21.29°	-19.38°			5.33°	-18.63°	
Angle S-C2-C3-4	-16.43°			7.00°	-19.62°			3.51°
Angle C1-C2-C3-N	-16.84°			10.73°	-16.79°			5.21°
Helicitiy	*M/M*	*P/P*	*M/M*	*P/P*	*M/M*	*P/P*	*M/M*	*P/P*
Directionality of isomerization	cw	ccw	cw	ccw	cw	ccw	cw	ccw

From the analysis of the dihedral angles it can be concluded, that a suitable helical twist for directional photoswitching is incorporated into the design of mixed indigoid molecular motors. For all isomers the helical distortion of both sides of the double bond were identical. Thus, only one helical descriptor is necessary for geometrical classification of all isomers in analogy to the HTI-based molecular motors. In comparison to dihedral angles found in the crystal structures of motor **2**, which range from 18-22° for **A** and **C** isomers, the calculated dihedral angles for mixed indigos **88** and **89** are, however, on average smaller.
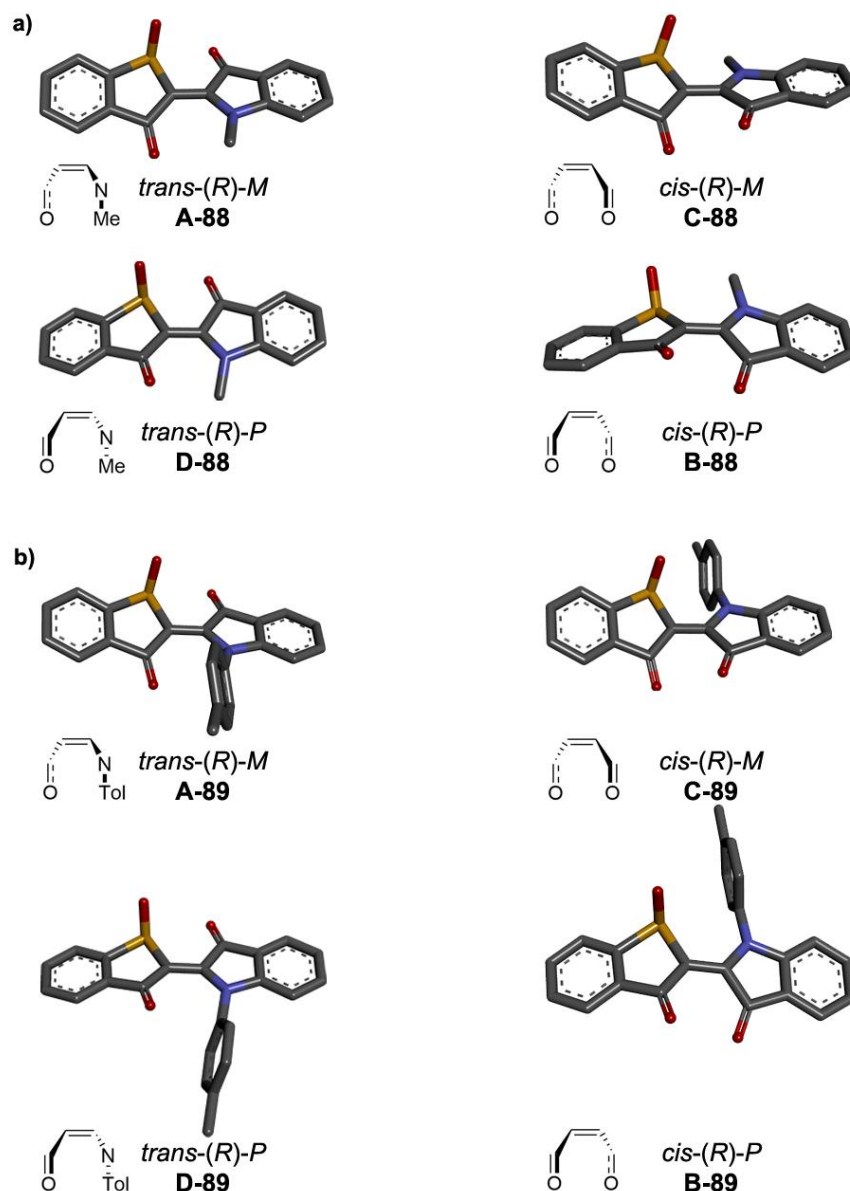
Figure 77:   Calculated minimum structures of mixed indigos **88** and **89** on the B3LYP/6-311+G(d,p) level of theory. For facile reconstruction of the helical descriptor the twisting is illustrated additionally as schematic formula. Only (*R*)-configured isomers are shown. *Trans*-configured isomers are shown left and *cis*-configured isomers are shown right. A) Isomers of **88**. b) Isomers of **89**.

5.1.2 B to C conversion of mixed indigos 88 and 89

The helical twist of mixed indigos promises directional isomerization behavior after excitation. Since metastable isomers **B** and **D** exhibit opposite isomerization directionality compared to the corresponding isomers **A** and **C** (see Table 12), the initial movements would be canceled out, if **B** and **D** undergo photoisomerization. In established rotary motor systems ratcheting steps prevent light induced back-isomerization by a fast thermal conversion of these metastable states to their diastereomeric counterparts

with opposite helicity. These thermal helix inversions ensure overall directionality. Superior motor functionality is therefore linked to certain features of these thermal ratcheting steps: In the first photo-induced isomers **B** and **D** must be sufficiently higher in energy as their corresponding diastereomers **A** and **C**. This leads to 100% completeness of both thermal conversions, which is an important condition for all light-induced and thermal rotations exhibiting same directionality. In the second, the thermal energy barriers for helix inversion should be sufficiently low (<16 kcal·mol^{-1}) for high rotation frequencies with the photon flux being the only limitation under realistic irradiation conditions. Fast thermal decay of metastable isomers results in low concentrations of these intermediates, which diminishes the possibility for their photon absorption and thus backwards reaction. This is another important condition for superior motor behavior. However, temporal resolution capabilities of conventional experimental setups require thermal barriers of > 6 kcal·mol^{-1} to be able to follow these motions with conventional spectroscopy methods. At this limit the observation of motor functionality becomes challenging. For mixed indigos **88** and **89** only transition states with *cis* configuration were found. With minimum structures **B** and **C** as well as the transition state structure **TS$_{B-C}$** for mixed indigos **88** and **89** the helix inversion processes and their inherent directionality can be predicted theoretically.
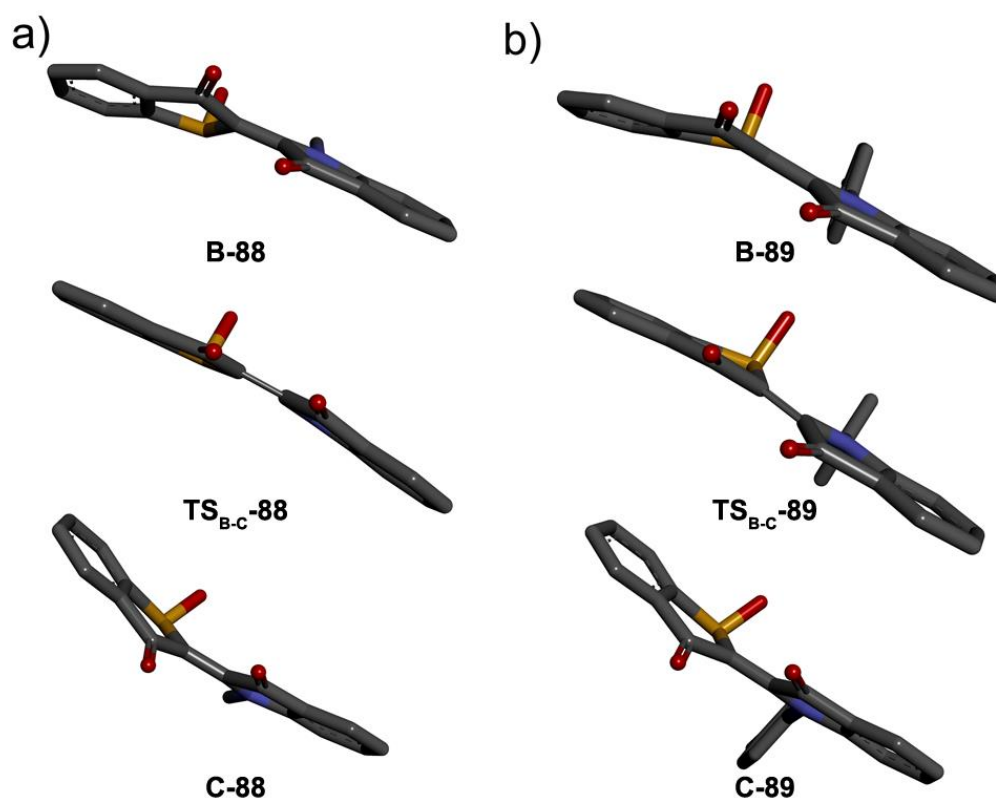
Figure 78:   Minimum structures **B** and **C** as well as transitions state structures **TS$_{B-C}$** for mixed indigos **88** and **89**. Structures were obtained on the B3LYP/6-311+G(d,p) level of theory. The helix inverting steps proceed by intermediate planarization of the central double bond, as it can be seen from the transition state structures. **B** to **C** conversion describes a clockwise rotation while **C** to **B** occurs in counter clockwise fashion.

The helix inversion from **B** to **C** isomers is predicted from the theoretical treatment to occur in clockwise direction in accordance to the directionality anticipated for the photoisomerzation steps from **A** to **B** and **C** to **D**. The order of mass transfer of this thermal process is given by the relative energy difference of isomers **B** and **C**. All determined energies are summarized in Figure 79 and are discussed below. No conclusions can be drawn for thermal **D** to **A** conversion since no transition state structures could be found in the calculations. Most probably a very low lying transition state with planar geometry exists, which enables interconversion of isomers **D** and **A**. Thus, a clockwise transfer from **D** to **A** would be an obvious explanation. The order of mass transfer is again given by the relative energy difference between the interconverting species (isomer **D** and **A**).

5.1.3   Ground state energy profiles of mixed indigos 88 and 89

In Figure 79 the calculated energies for all ground state minima as well as the transition states TS_{B-C} are illustrated. Most prominent and strongly differing from the energy profiles of HTI-based molecular motors are the decreased energy barriers found for mixed indigos, as well as declined energy differences between the diastereomeric pairs **A/D** and **C/B** with identical double bond configuration. Only 2.56 kcal·mol^{-1} was found for the free activation energy $\Delta G^{\ddagger}_{B-C}$ of the thermal **B** to **C** conversion for **88** and surprisingly an even lower barrier of 2.13 kcal·mol^{-1} was found for **89**. Originally, **89** was anticipated to exhibit higher energy barriers than methyl substituted mixed indigo **88**. However, theoretically obtained structures of **89** show almost perpendicular orientation of the tolyl-ring in relation to the indigo core. This could lead to reduced sterical hindrance with the carbonyl group/ sulfoxide moiety in comparison to methyl substituted derivative **88**. In summary, the thermal barriers found for mixed indigos are far below the resolution limits accessible by conventional experimental means available at present. As no transition state TS_{D-A} with *trans* configuration was found, it is assumed that this barrier is at least in the same range as the barrier TS_{B-C}. With no straight-forward experimental access to metastable states **B** and **D** evidencing unidirectional rotation remains challenging.

Energy differences of only 0.77 kcal·mol^{-1} and 1.48 kcal·mol^{-1} were found between isomers **B** and **C**, while in both cases isomer **B** is higher in energy. Isomer **D-88** is 2.18 kcal·mol^{-1} above the global minimum **A-88** and an energy difference of 1.74 kcal·mol^{-1} between metastable **D-89** and the global minimum **A-89** was found. From the obtained data it can be derived, that the photoproducts **B** and **D** are higher in energy, which allows for directed population transfer towards the stable isomers **A** and **C**, while overall directionality is preserved. In general, the energy differences however are decreased in comparison to HTI based motors **1-5**, which diminishes the yield of population transfer. Sufficient energy differences in case of HTI based motors between metastable and stable isomers yield 100% mass transfer. In the case of mixed indigos **88** and **89** residual population of metastable states was predicted to be 2% to 21% at 23 °C. Under operational conditions the intermediate concentration of metastable isomers increases, if the energy difference to its corresponding diastereomer is small. Thus, absorption

probabilities of these metastable states rise and lead to loss of photons as well as partial backwards rotation. If both metastable states are considerably populated under irradiation, the possibility of 360° antidirectional rotation is rising. For determination of rotational frequencies the magnitude of antidirectional rotation has to be subtracted from the frequency rate of directional motions. This scenario, however, can be neglected for both mixed indigos, since at least one thermal step proceeds with >90%. In summary, it has to be taken into account, that small energy differences between metastable and stable isomers lead to reduced rotation frequencies, but motor functionality is not disturbed as long as the light induced isomers **B** and **D** are higher in energy as their diastereomeric counterparts **C** and **A**. Considering these aspects mixed indigo **89** exhibits superior thermal behavior in comparison to **88**, since the calculated energy differences allow for almost quantitative population transfer of over 90% in both ratcheting steps.
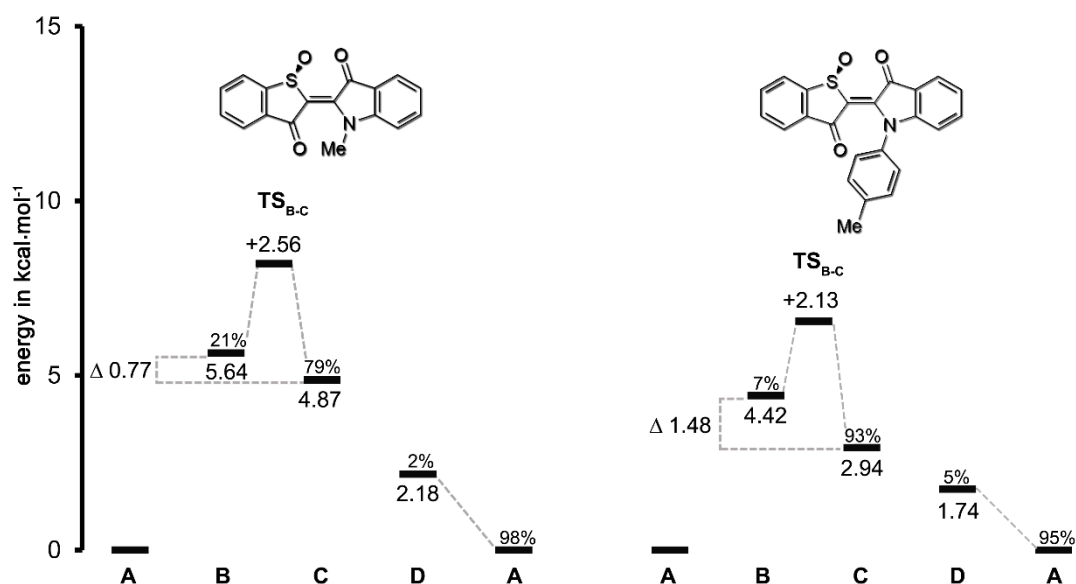
Figure 79: Ground state energy profile of mixed indigos **88** and **89**. Energies are obtained from theoretical calculations on the the B3LYP/6-311+G(d,p) level of theory and are given in kcal·mol^{-1}. Since the energy differences between metastable and stable isomers are relatively small, the population ratios at 25 °C are given, too.

5.2 Conformational analysis in solution

The theoretical assessment revealed helical twisting of the central double bond. Though no experimental evidences could be obtained for validation of the theoretically obtained helical distortion, NMR spectra could be recorded for both mixed indigos **86** and **87**. Thus, it was possible to exclude most isoindigoid structures for mixed indigos **86** and **87** (Figure 80). All possible structural isomers are given below. The corresponding double bond isomers of these structures are not depicted.

R = Me: **90**
R = Tol: **91**

R = Me: **92**
R = Tol: **93**

R = Me: **94**
R = Tol: **95**

R = Me: **96**
R = Tol: **97**

R = Me: **98**
R = Tol: **99**
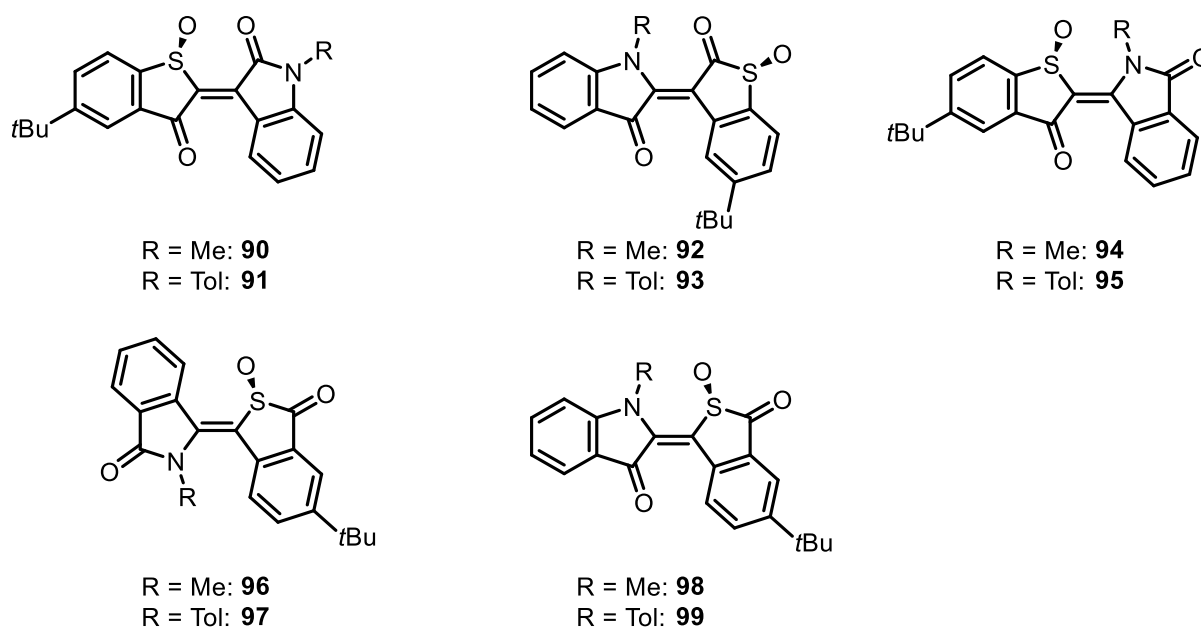
Figure 80: Structural isomers of mixed indigos **86** and **87**.

The HMBC spectra (Figure 81) show couplings between the aromatic protons in *ortho* position to both carbonyl groups. Therefore structures **90-93**, with either one carbonyl disconnected from the phenyl rings can be excluded. For mixed indigo **86** a coupling between the methyl group protons and the quaternary carbon atom at 155 ppm is oserved in the HMBC spectrum, which strongly suggests, that the nitrogen atom is directly connected to the phenyl ring and *ortho* to the position of the carbonyl function. The ^{13}C NMR spectra show chemical shifts for the carbonyl of over 185 ppm. This strong downfield shifts renders amidic carbonyls rather unlikely, which are present in structures **90/91** and **94-97**. Less information is available for exclusion of structures **98/99**. However, for HTI-based molecular motors the signals of the protons in *ortho* positions to sulfoxides exhibit the strongest downfield shifts for all motors **1** to **5**. Also in case of mixed indigos **86** and **87** these protons are strongest downfield shifted, even in comparison to the protons in *ortho* position to the carbonyl functions.

Under the premise of overall structural continuity during chemical synthesis in combination with the findings from the conformational analysis, mixed indigos **86** and **87** furnish with high probability the

proposed structures. For unambiguous identification further investigations have to be carried out, including NOESY spectra of mixed indigos **86** and **87** and of the precursor molecule **85**, as well as crystal structure analysis.
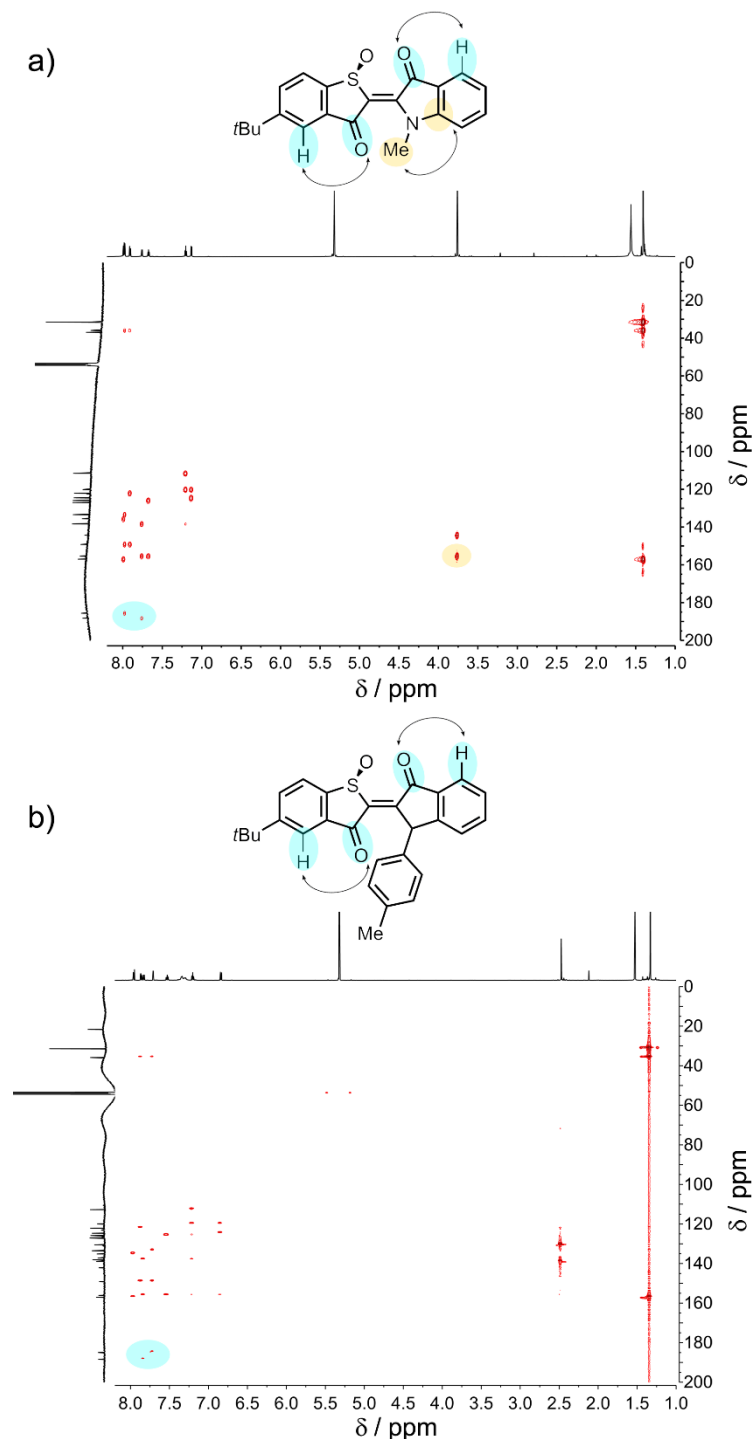
Figure 81: HMBC NMR spectra (800 MHz in case of **86** and 600 MHz in case of **87**) in CD$_2$Cl$_2$ at ambient temperature. Only hydrogens indicative for structural elucidation are shown for clairity. a) HMBC spectrum of mixed indigo **86**. Relevant couplings are highlighted in blue and orange. b) HMBC spectrum of mixed indigo **87**. Relevant couplings are highlighted in blue.

5.3 Photophysical properties of mixed indigos 86 and 87

Photoisomerization is the central feature of light-driven molecular motors. Therefore, absorption spectra of indigos **86** and **87** were measured and the photosensitivity was tested by irradiation of the sample THF solution with 595 nm and 450 nm LEDs respectively. A sample of **86** was irradiated with 595 nm light for 2 min some spectral changes could be observed. No further spectral changes could be observed under prolonged irradiation, which confirms pss establishment. Irradiation with 450 nm led to partial reconstruction of the initial absorption spectrum, but full recovery under prolonged irradiation was not possible. The same observations were made for mixed indigo **87**. The corresponding spectra are given in Figure 82.
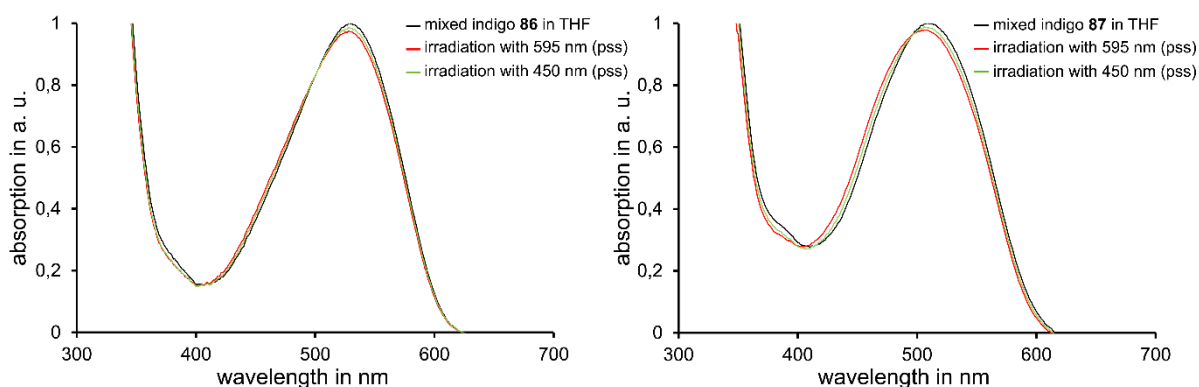
Figure 82:   Absorption spectra of mixed indigos **86** (left) and **87** (right) in dry THF at 18 °C. Black spectra were obtained in the dark. Red spectra show the pss after 2 min of irradiation with 595 nm. Green spectrua show the pss after 450 nm of irradiation. For **86** isosbestic points at 501 nm and 407 nm and for **87** at 497 nm and 407 nm were observed.

The irradiation experiments revealed reversible light sensitivity for **86** and **87**. Also for interconverting species typical isosbestic points are observable, which hints at photoisomerization between *cis* and *trans* isomers. From the calculated data of **88** and **89**, it is anticipated that the *trans* isomers in case of **86** and **87** are the overall thermodynamic minima. They also should exhibit sufficient energy difference to the less stable *cis* isomers, which would result in 100% population of *trans* isomer at equilibrating conditions. A low energy barrier of 21 kcal·mol^{-1} for the thermal recovery of the initial absorption of **86** in THF was measured, which allows for interconversion at ambient temperature. For **87** no significant thermal conversion could be observed at 18 °C over the course of 30 min. Furthermore, ^{1}H NMR spectra of **86** and **87** in CD_2Cl_2 showed only one set of signals, which proves in combination with the observed thermal behavior, the presence of only one isomer. Therefore, it can be stated for **86**, that the signals observed in the ^{1}H NMR spectrum can be attributed to the *trans* isomers. Likewise the absorption spectrum, which was recorded before irradiation and did not show any changes with time (Figure 82 left: black spectrum) can be attributed to be a pure *trans* spectrum. As no thermal conversion in case of mixed indigo **87** could be observed the linkage between ^{1}H NMR spectrum and absorption spectrum

cannot be made unequivocally as it is the case for **86**. In analogy to **86**, it is assumed that the absorption spectrum recorded before irradiation (Figure 82 right: black colored spectrum) is also most likely a pure *trans* isomer spectrum. This identification of the set of signals observed in the ^{1}H NMR spectrum to be *trans* isomer signals can be supported also in this case by theoretical calculation.

In both cases irradiation with 595 nm lead to a bathochromic shift, which can be consequently described as a *trans* to *cis* isomerization as well as spectral changes observed after 450 nm irradiation result from a *cis* to *trans* isomerization. Thus, it can be derived, that the pure spectrum of the *cis*-**86** is hypsochromically shifted. In analogy spectral changes observed for **87** can be explained likewise. For substituted indigos a similar hypsochromic shift was interpreted to be the result of a *trans* to *cis* isomerization after irradiation.[39, 85] However further investigation are needed for identification of the pure absorption spectra of the assumed *cis* isomers of **86** and **87**.

In comparison to other photoswitches (see Figure 52) the observed photochromism seems largely diminished. The pure spectra of the *cis* isomers of **86** and **87** are not available, but with regard to the low photochromism it can be assumed, that the pure isomer spectra are strongly overlapping, which leads to low isomeric yields in the pss. Also solutions in MeCN and CH_2Cl_2 of mixed indigo **87** showed reduced photochromism, similar to the spectral changes observed for THF solutions.

The absorption maximum of methyl- substituted mixed indigo **86** of 529 nm is bathochromically shifted in comparison to tolyl-substituted mixed indigo **87**, which exhibits an absorption maximum of 509 nm in THF. The theoretical calculation of mixed indigo **89** showed an almost perpendicular tolyl-ring in relation to the indigo core structure. Thus, conjugation across the C-N bond is largely suppressed. No mesomerically mediated donor contribution of the tolyl substituent to the chromophoric core structure is consequently possible. The inductive effect of a tolyl substituent is smaller than the inductive effect of a methyl group since sp^2 hybridized carbon linked substituents exhibit reduced group electronegativity than sp^3 hybridized carbon linked substituents. This could explain the bathochromic shift of the absorption maximum of **86**, since donor strength of the nitrogen atom is increased by the methyl group. The different inductive effects of methyl and twisted tolyl groups should also influence the thermal stability of metastable isomers. The obtained data describing the thermal stability is given in the following chapter.

5.4   Thermal double-bond isomerization in mixed indigoids

For mixed indigo **86** the thermal recovery of the initial absorption spectrum was monitored after irradiation with 595 nm in dry THF at 18 °C (Figure 83). As described in the chapter above, the initial spectrum can be most likely assigned to a pure *trans* isomer spectrum and the observed conversion can be ascribed to a thermal *cis* to *trans* isomerization. For mixed indigo **87** no thermal back isomerization could be observed over the course of 30 min at 18 °C. Therefore, the energy barrier should be >23 kcal·mol⁻¹. The thermal recovery of **86** was monitored over the course of 50 min, while the absorption at 530 nm was measured in 2 minutes time intervals. The initial amount of photogenerated *cis* isomer was set arbitrarily to 100%. First order kinetic analysis without assuming an isomer equilibrum gave good agreement with the obtained data and a thermal barrier of 21.15 kcal·mol⁻¹ was found. It is at least 2 kcal·mol⁻¹ lower than the energy barrier of the *cis* to *trans* isomerization of mixed indigo **87**. Also in the case of indigos, alkylated derivatives revealed decreased thermal barriers in comparison to indigos bearing aromatic substituents at the nitrogen atoms.[85] According to the observations made for the absorption spectra of mixed indigos **86** and **87**, the differences in the thermal stability of the metastable *cis* isomers can likely be explained by the varying inductive effects of methyl and tolyl-substituents. In comparison to substituted indigo derivatives the measured life times of the assumed *cis*-isomers of mixed indigos **86** and **87** are very similar (see chapter 4.7). It seems that the substitution of a nitrogen atom with a sulfoxide moiety does not significantly influence the double bond character of the central bond. HTI derived molecular motors **1-5**, however, reveal much higher energy barriers for thermal double bond isomerizations of >30 kcal·mol⁻¹.
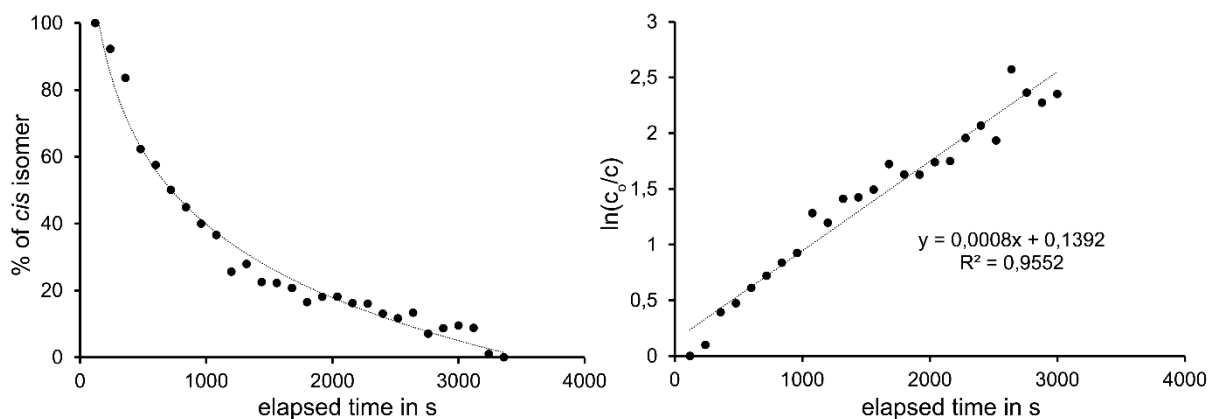
Figure 83:   The thermal decay of photogenerated *cis*-**86** was monitored by UV/vis spectroscopy at 530 nm over the course of 50 min at 18 °C in dry THF. Left: The absorption increase at 530 nm is taken as measure for decreasing amount of *cis* isomer, which is plotted against time. Right: Logarithmic plot of the quotient between initial *cis* isomer content and decreasing amount of *cis* isomer against time. Good agreement of the obtained data with the first order kinetic analysis was found. The slope of the linear fit describes the first order rate constant $k_{(cis \rightarrow trans)} = 0.008$ s⁻¹.

6. Indigo-based photoswitches

6.1 Aim

The successful application of photoswitches for biomedicinal purposes is inevitably connected to their absorption profile. This can be traced back to the high sensitivity of biological tissues to DNA damages induced by UV light as well as the low penetration potential of high frequency light in tissue, which limits the range of light inputs. Hence, it is necessary to develop photoswitches with red shifted extinction. The indigo dye, with its outstanding absorption and already incorporated double bond with isomerization potential, could therefore be a suitable candidate. The photophysical properties of indigo has been investigated for the last century,[123-127, 133, 240-242] and a very efficient deexcitation pathway[128, 131] was found, which is characterized by a proton transfer in the excited state. The outstanding photostability of indigo[130, 137] was referred to this effective deexcitation process. Thus, photoisomerization, as competitor to ESPT, is also effectively suppressed.

In the past, several efforts have been made to unravel the photoisomerization potential of indigo. Apparently, the persuaded strategy was the suppression of ESPT. By substitution of the hydrogen atoms, connected to the nitrogens, by methyl- or acetyl groups, indeed isomerization by irradiation was provoked. Unfortunately another drawback could be observed after revelation of the photoisomerization potential. The thermal stability of the photogenerated *cis* isomer is highly decreased by the distinct push pull character induced by the four substituents around the central double bond and the unfavourable co-alignement of the two carbonyl dipoles. Hence, the double bond character is diminished, leading to a low energy barrier for thermal *cis* to *trans* as well as *trans* to *cis* isomerization. In combination with a fairly destabilized *cis* isomer, this leads to fast thermal off-switching in the dark, which first of all complicates investigation as well as excludes certain applications. In 2015 austrian scientists reported about BOC protected indigos,[86] which undergo photoisomerization and show remarkable thermal stability. Unfortunately the absorption features were strongly influenced by the strong electron withdrawing character of the BOC protection group. But it was successfully shown, that the thermal stability of the *cis* isomer could be manipulated by suitable electronic effects.

In the literature a promising protocol[139-140] was found, which describes the synthesis of several indigo derivatives with aryl substitution at the nitrogen atoms. Since the photoisomerization potential was not investigated in this report, the simple one step synthesis was reproduced in order to investigate the isomerization behaviour. The synthesis delivered di-arylated indigo as well as mono-arylated indigo. Therefore, it was also possible to examine the behaviour of indigos with one hydrogen atom left accessible for ESPT, as well.

6.2   Synthetic approach

The synthesis, described in the literature[140] is based on a Cu-catalyzed *Ullmann* coupling reaction between indigo and different aryl halides at elevated temperatures. Depending on the nature of the aryl halide used for the coupling reaction, the ratio between mono- and di-arylated indigo varies. For sterically hindered as well as electron deficient halides, increased or exclusive formation of mono-substituted products was observed in the presented study. The general reaction scheme, as well as the different aryl halides used for the exploration of indigoid photoswitches is presented in Scheme 21.
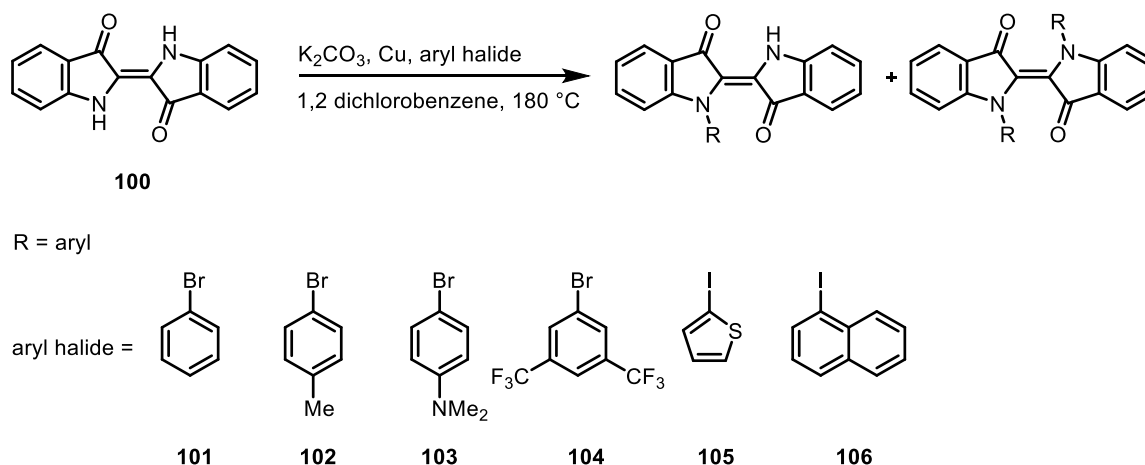
Scheme 21:   Synthesis of mono- and di-arylated indigos by a Cu-mediated *Ullmann* type coupling reaction
                   at elevated temperatures. Aryl halides **101**-**106** were used for the synthesis of mono- and di-
                   substituted indigos.

Several mono-arylated indigos and di-aryled indigos were prepared by adaptation of the reported protocol as summarized in Figure 84 and Table 13. Mono-substituted *N*-phenyl indigo **111** was isolated with 14% yield when phenyl bromide **101** was used as aryl halide (entry 1). Access to the di-substituted analogue should be possible after treatment of indigo **100** with phenyl iodide according to the literature.[140] From the data obtained, it cannot be verified if *N,N'*-diphenyl indigo could also be accessible using of phenyl bromide **101**. Maybe prolonged reaction time or varying amounts of Cu or K$_2$CO$_3$ could allow its access with phenyl bromide **101** as arylation agent. By reducing the amount of added 4-bromo-*N*-dimethylaniline **103**, mono-substituted indigo **109** was obtained in 9% yield (entry 3). In entry 6, however, three equivalents of **103** were used and only di-substituted indigo **110** was isolated in 11% yield. Indigo **107** and **108** could be obtained from the same reaction mixture in 24% and 13% respectively, as can be seen in entry 2. Coupling reactions of aryl halides **104**-**106** with indigo delivered mono-arylated indigos **112**-**114** exclusively in poor to moderate yields. No twofold arylated indigos could be isolated. In Table 13 the results of the *Ullmann*- coupling reactions are summarized.
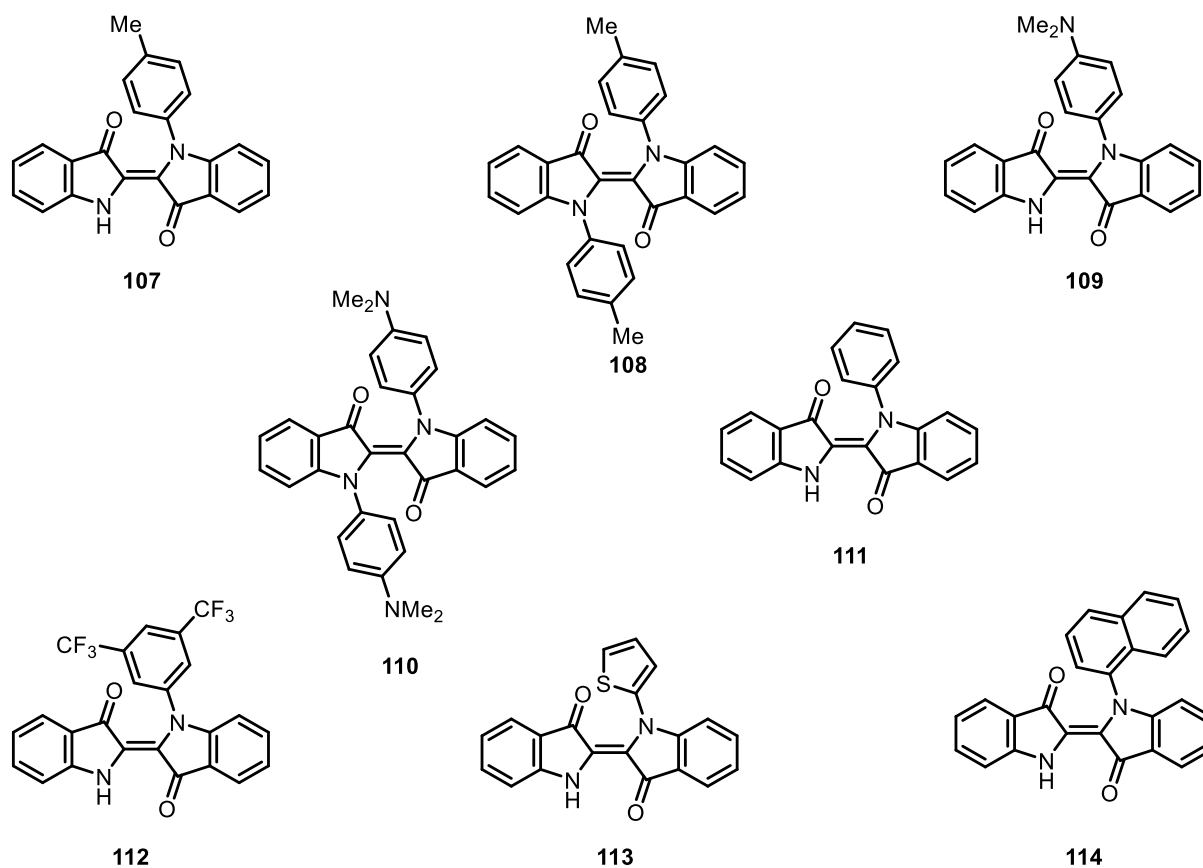
Figure 84:   Indigos **107 - 114** were synthesized by a Cu-catalyzed *Ullmann*-coupling reaction of indigo with aryl halides at elevated temperatures.

A common feature opf all reactions is the low yield of arylated indigos ranging from of 3% to 32%. It could likely be explained by the poor solubility of indigo and the required high temperature of 180 °C, which increases decomposition at prolonged reaction times. It was also not possible to obtain twofold arylated indigos with electron deficient substituents as well as sterically more hindered derivatives, e.g. naphtyl bearing indigos. Improvements of the reaction conditions were tested by solvent variation and reduced catalyst load as well as a *Chan-Lam* coupling[222] approach. Since the research group of *Hecht* reported on improved synthetic strategies,[85] including the successful synthesis of a twofold arylated indigo with electron withdrawing groups in the meantime, these efforts were halted.

Table 13:   Experimental conditions for the arylation of indigo and corresponding yields. All reactions were carried out at 180 °C in 1,2 dichlorbenzene. Indigos **108** and **110** bear two aryl substituents at the nitrogen atom, while the other derivatives are mono- substituted. All used aryl halides coupling partners are depicted in Scheme 21.

entry	1		2	3	4	5	6	7
indigo	**107**	**108**	**109**	**110**	**111**	**112**	**113**	**114**
Aryl halide	**102**	**102**	**103**	**103**	**101**	**104**	**105**	**106**
equiv. halide	1.5	1.5	1	3	3.6	3	4	4
equiv. Cu	0.1	0.1	5.2	2.5	5	1	0.1	0.1
Time [h]	11	11	5	5	12.5	5	8.5	17
yield [%]	24	13	9	11	14	32	3	17

In order to study the thermal *cis* to *trans* isomerization of twofold arylated indigos and its dependency on the electronic characteristics of the aryl substituents, a nonsymmetric indigo with both, electron deficient and electron rich substituents was envisioned. Indigo **116** is available by *Chan-Lam* coupling reaction of mono-substituted indigo **109** with 4-cyanophenylboronic acid **115** in a good yield of 77%. The reaction is depicted in Scheme 22.
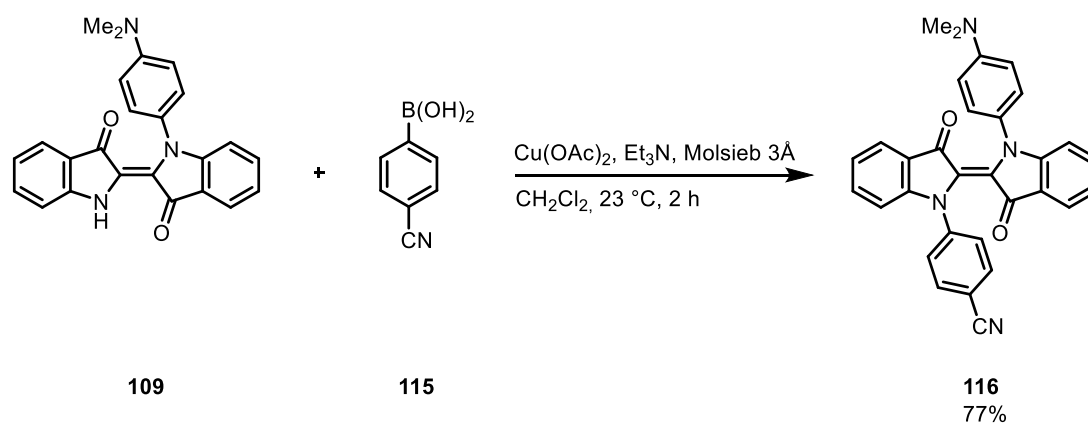
Scheme 22:   Synthesis of nonsymmetric indigo **116** by Cu catalyzed *Chan-Lam* cross coupling reaction between mono-substituted indigo **109** and 4-cyanophenyl boronic acid **115** in the presence of Et$_3$N.

6.3   Theoretical description

In the theoretical assessment of mono- and di-arylated indigos *cis*- and *trans*-configured isomers were found to be minimum structures. For the *trans* and *cis* isomers of di-arylated indigos enantiomeric pairs exist, exhibiting opposite twisting of the central double bond. Also for the *cis* isomer of mono-arylated indigos two enantiomeric forms exist, while the corresponding *trans* isomer exhibits almost planar structure and hence no helical information. No transition state calculations were performed for elucidation of the thermal barriers of helical inversions, but indigos are likely to invert readily at ambient temperatures. In most cases the *trans* isomers of **107** and **108** were lowest in energy, while the extent of *trans*-stabilization depends on the applied DFT-functional. Only for indigo **107** did B3LYP and MPW1K functionals predict the *cis* isomer to be more stable. In Table 14 a summary of the *cis* and *trans* isomer minimum energies obtained by applying different DFT functionals or with implementation of implicit solvent effects is given. For di-arylated indigo **108** an energy difference of 0.86 kcal·mol^{-1} could be obtained experimentally from the observed ratio of 81/19 *trans* to *cis* isomers at 25 °C measured by ^{1}H NMR spectroscopy. Thus, DFT functional ωB97X-D and implementation of THF solvent effects with a calculated energy difference of 0.32 kcal·mol^{-1} gives the best results, compared to experimentally determined energy difference. For mono-arylated indigo **107** only one set of signals was observed in the ^{1}H NMR spectrum, which is ascribed to the *trans* isomer of **107**. This means, that at least 95% population of the *trans* isomer is present in THF solution, which can be translated into a minimal energy difference of >1.75 kcal·mol^{-1} at 23 °C. Again ωB97X-D was found to be in best agreement to the experimentally determined energy values. Thus, for assessment of other mono- and di-arylated indigos **107-114** and **116** the DFT functional ωB97X-D with implementation of THF solvent effects was applied.

Table 14: Calculated minimum energies of the *cis* and *trans* isomers of di-arylated and mono-arylated indigos **107** and **108** with different DFT functionals or with implementation of THF solvent effects (IEFPCM). In all cases a 6-311G(d,p) basis set was used. Energies in Hartree can be translated to energies in kcal·mol^{-1} by multiplication with the factor 627.15. ΔG^0 can be consecutively obtained as the energetic difference between the metastable and most stable isomer.

indigo	functional	THF solvent effects (IEFPCM)	G^0 in Hartree	G^0 in kcal·mol^{-1}	ΔG^0
cis-**108**	ωB97X-D	yes	−1415.884358	−887971.88	0.32
trans-**108**	ωB97X-D	yes	−1415.884866	−887972.19	0.00
cis-**108**	ωB97X-D	no	−1415.866394	−887960.61	0.07
trans-**108**	ωB97X-D	no	−1415.866502	−887960.68	0.00
cis-**108**	B3LYP	no	−1416.350508	−888264.22	4.82
trans-**108**	B3LYP	no	−1416.358189	−888269.04	0.00
cis-**108**	MPW1K	no	−1415.900372	−887981.92	4.31
trans-**108**	MPW1K	no	−1415.907250	−887986.23	0.00
cis-**107**	ωB97X-D	yes	−1145.650859	−718494.94	3.16
trans-**107**	ωB97X-D	yes	−1145.655894	−718498.09	0.00
cis-**107**	ωB97X-D	no	−1145.635220	−718485.13	5.54
trans-**107**	ωB97X-D	no	−1145.644061	−718490.67	0.00
cis-**107**	B3LYP	no	−1146.408281	−718969.95	0.00
trans-**107**	B3LYP	no	−1146.408178	−718969.89	0.06
cis-**107**	MPW1K	no	−1146.037544	−718737.44	0.00
trans-**107**	MPW1K	no	−1146.036501	−718736.79	0.65

In Tables 14 and 15 the minimum energies of the *cis* and *trans* isomers of di-arylated and mono-arylated indigos **107-114** using the ωB97X-D/6-311+G(d,p) level of theory with implementation of implicit THF solvent effects (IEFPCM) are summarized. All structures were found to be minimum structures since frequency analysis confirmed them to be stationary points with no imaginary frequency. Among the di-arylated indigos **108**, **110**, and **116** only for **108** the *trans* isomer was found to be the thermodynamic minimum. Indigo **110** shows the *trans* isomer slightly higher in energy than the *cis* isomer, while indigo **116** with nonsymmetric substitution furnishes the *trans* isomer ca. 2 kcal·mol^{-1} above the corresponding *cis* isomer. Interestingly the isomeric ratio obtained by ^{1}H NMR spectroscopy revealed in case of indigo **116** the highest content of *cis* isomer in CD$_2$Cl$_2$ solution found for di-arylated indigos. At least the experimentally observed trends are qualitatively reproduced in the calculation. NMR analysis of indigo **108** revealed a similar isomeric ratio than it was observed for indigo **110**.

Table 15:   Calculated minimum energies of the *cis* and *trans* isomers of several di-arylated and mono-arylated indigos on the ωB97X-D/6-311+G(d,p) level of theory with implementation of THF solvent effects (IEFPCM). Energies in Hartree can be translated to energies in kcal·mol^{-1} by multiplication with the factor 627.15. ΔG^0 can be consecutively obtained by the energetic difference between metastable and most stable isomer.

indigo	energy in Hartree	energy in kcal·mol^{-1}	ΔG^0
cis-**108**	−1415.884358	−887971.88	0.32
trans-**108**	−1415.884866	−887972.19	0.00
cis-**110**	−1605.093068	−1006634.12	0.00
trans-**110**	−1605.092978	−1006634.06	0.06
cis-**116**	−1563.434587	−980508.00	0.00
trans-**116**	−1563.431486	−980506.06	1.94
cis-**107**	−1145.650859	−718494.94	3.16
trans-**107**	−1145.655894	−718498.09	0.00
cis-**111**	−1106.358027	−693852.44	3.69
trans-**111**	−1106.363909	−693856.13	0.00
cis-**109**	−1240.257115	−777827.25	2.17
trans-**109**	−1240.260576	−777829.42	0.00
cis-**112**	−1780.459133	−1116614.95	6.06
trans-**112**	−1780.468802	−1116621.01	0.00
cis-R_a-**113**	−1427.160074	−895043.44	3.32
cis-S_a-**113**	−1427.160071	−895043.44	3.32
trans-R_a-**113**	−1427.164676	−895046.33	0.43
trans-S_a-**113**	−1427.165365	−895046.76	0.00
cis-R_a-**114**	−1259.937943	−790170.08	3.88
cis-S_a-**114**	−1259.937751	−790169.96	4.00
trans-R_a-**114**	−1259.944125	−790173.96	0.00
trans-S_a-**114**	−1259.944064	−790173.92	0.04

For mono-arylated indigos higher relative energy differences with the *trans* isomers as the thermodynamic minima were calculated in consistency with experimental observations. For mono-arylated indigos **113** and **114** two different minima for each double bond configuration were found with opposite axial chirality of the nonsymmetric aryl substituents. Since the central double bond is slightly twisted, a small but negligible energy difference resulted. These diastereomers were termed with the additional descriptors R_a/S_a. Electronically neutral substituted derivatives like phenyl, tolyl, naphtyl and thiophenyl groups attached to indigos **111**, **107**, **114**, **113** show an energy difference of 3-4 kcal·mol^{-1} between the stable *trans* and the metastable *cis* isomers Indigo **109** with strong electron-donating *p*-aniline moieties shows a declined energy difference of only 2.17 kcal·mol^{-1}, while electron withdrawing 3,5-trifluoromethylphenyl substitution in case of **112** leads to a large energy difference of 6.06 kcal·mol^{-1}.

In Figure 85 the calculated minimum structures of indigo **107** and **108** are illustrated exemplarily. The *trans* isomers show great similarity with the obtained structures in the crystalline state (see chapter 4.4). The aryl substituents reveal helical distortion resulting from the sterical repulsion with the indigo core

chromophore. Di-arylated indigos are strongly twisted around the central double bond, while mono-arylated indigos exhibit almost planar structures analogous to the structures found in the crystalline state. As it is illustrated for indigos **107** and **108**, calculated ground state minima of other indigos reveal very similar structures.
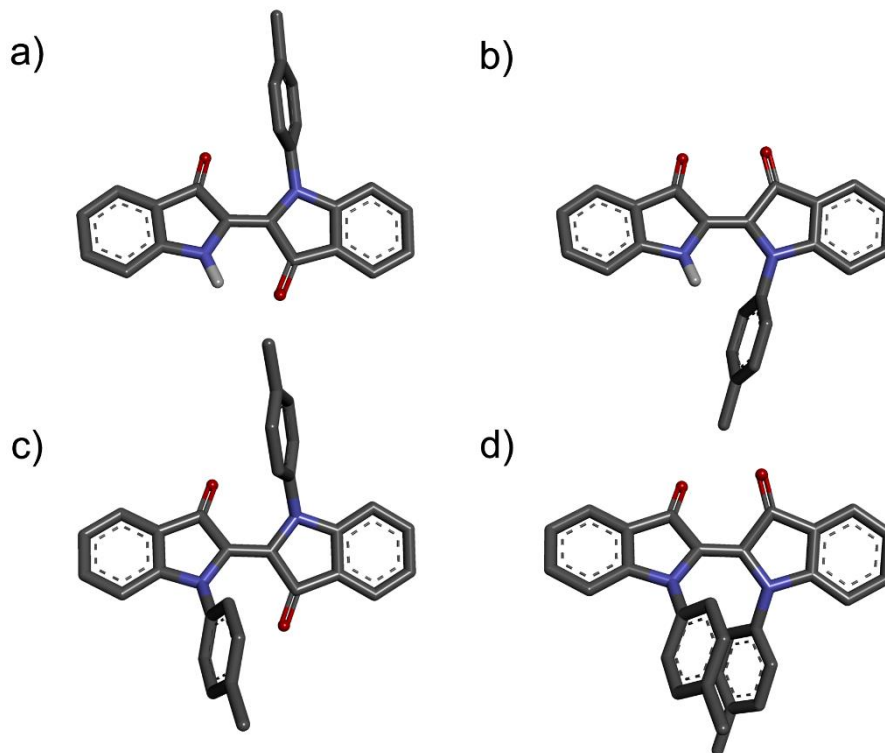
Figure 85: Calculated minimum structures of *trans* indigo **107** (a), *cis* indigo **107** (b), *trans* indigo **108** (c), and *cis* indigo **108** (d) on the ωB97X-D/6-311+G(d,p) level of theory with implementation of implicit THF solvent effects (IEFPCM). Carbon bound hydrogens were omitted in this illustration for clarity reasons.

Selected bond-lengths, distances and dihedral angles found for all theoretical assessed indigos are summarized in Table 16 for di-arylated indigos and in Table 17 for mono-arylated indigos. Data were obtained from optimized structures on the ωB97X-D/6-311+G(d,p) level of theory with implementation of implicit THF solvent effects (IEFPCM).

Table 16:   Selected bond lengths and torsional angles in the optimized geometries of di-arylated indigos **108**, **110**, and **116**. Optimized geometries of *cis* and *trans* isomers were obtained on the ωB97X-D/6-311+G(d,p) level of theory with implementation of THF solvent effects (IEFPCM).
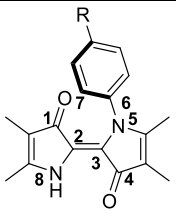
numbering	bond lengths/ angles	*trans-*108	*cis-*108	*trans-*110	*cis-*110	*trans-*116	*cis-*116
	bond lengths						
	double bond [Å]						
	C(2)-C(2')[a]	1,3596	1.3642	1.3603	1.3654	1,359	1,365
	carbonyls [Å]						
	C(1)-O(1)	1,213	1,209	1.2137	1.210	1,212	1.210
	C(1')-O(1')	1,213	1,209	1.2128	1.210	1,213	1.208
	torsional angles [°]						
	N-aryl axis						
	C(5)-C(4)-N(3)-C(2)/	47,89	37,92	44.65	40.11	46.03	41.49
	C(5')-C(4')-N(3')-C(2')	47,88	37,92	52.02	40.10	42.78	34.00
	double bond						
	trans: C(1)-C(2)-C(2')-N(3') *cis*: N(4)-C(2)-C(2')-N(4')	23,85	12,79	25.10	13.86	22.19	12.69
	trans: C(1')-C(2')-C(2)-N(3) *cis*: C(1)-C(2)-C(2')-C(1')	23,86	34,02	24.08	33.60	23.44	34.49

R₁ (structure diagram)

O 5' 4'
1 N3'
2'
N3 2'
4 5
O
R₂
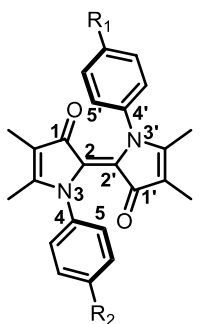
108: R₁=R₂=Me
110: R₁=R₂=N(Me)₂
116: R₁ =CN
        R₂ =N(Me)₂

From the geometry optimization it can be derived that the structures of di-arylated indigos **108**, **110**, and **116** show great similarity. Torsional angles of the N-aryl axis of ca. 30-50 ° were found, while the *cis* isomers show slightly reduced dihedral angles compared to the *trans* isomers. For the *trans* isomers a double bond twisting of over 20° was found for both double bond sides. For the *cis* isomers the torsional angles of the double bond differ substantially from each other (ca. 20°), with a larger torsional angle for the carbonyls bearing side of the double bond (C(1)-C(2)-C(2')-C(1')).

Table 17: Selected bond lengths, torsional angles and distances in the optimised structures of mono-arylated indigos **107**, **109**, and **111**-**114**. Optimized geometries of *cis* and *trans* isomers were obtained on the ωB97X-D/6-311+G(d,p) level of theory with implementation of implicit THF solvent effects (IEFPCM).

indigo/ numbering	bond lengths [Å]		torsional angles [°]		distance [Å]
	double bond	carbonyl	N-Aryl axis	double bond	H-bridge
(structure R)	C(2)-C(3)	C(1)-O(1) C(4)-O(4)	C(7)-C(6)-N(5)-C(3)	*trans*: C(1)-C(2)-C(3)-N(5) C(4)-C(3)-C(2)-N(8) *cis*: N(8)-C(2)-C(3)-N(5) C(1)-C(2)-C(3)-C(4)	H(8)- O(4)
cis-**107**	1.3600	1.209 1.211	55.25	3.65 14.32	-
trans-**107**	1.3581	1.211 1.224	48.22	6.49 8.90	2.02115
cis-**111**	1.3597	1.208 1.211	52.16	3.77 15.42	-
trans-**111**	1.3579	1.211 1.224	48.20	6.24 8.77	2.0230
cis-**109**	1.3608	1.209 1.211	68.02	3.83 11.52	-
trans-**109**	1.359	1.211 1.225	53.69	6.43 8.02	2.00475
cis-**112**	1.3588	1.207 1.210	40.07	3.60 18.65	-
trans-**112**	1.3572	1.211 1.223	43.26	5.30 8.76	2.04343
cis-S_a-**113**	1.3585	1.207 1.210	−115.48	−3.65 −13.27	-
cis-R_a-**113**	1.3584	1.207 1.210	115.46	3.62 13.22	-
trans-R_a-**113**	1.3589	1.209 1.224	61.79	4.68 5.91	1.9791
trans-S_a-**113**	1.3581	1.209 1.224	−128.64	5.48 7.45	2.0057
cis- R_a -**114**	1.3590	1.2085 1.211	59.28	4.08 15.43	-
cis- S_a -**114**	1.3596	1.209 1.210	−111.09	3.49 10.54	-
trans- R_a -**114**	1.3572	1.211 1.224	54.56	5.91 8.08	2.03
trans- S_a -**114**	1.3600	1.210 1.225	−115.15	2.91 3.19	1.97

For mono-arylated indigos again very similar structures were obtained in the theoretical description, independent of the nature of the aryl substituent. Structures of **107**, **110**, and **111** are also in good agreement with their respective structures in the crystalline state. In the theoretical assessment the carbonyl bonds of the arylated fragment of the chromophore exhibit elongation in relation to the other carbonyl function. This can be stated for *cis* and *trans* isomers. The same elongation is observed for the structures of *trans*-**107**, *trans*-**110**, and *trans*-**111** in the crystalline state (see chapter 4.4). Since both isomers exhibit elongation in the calculation a possible explanation involving a NH-carbonyl hydrogen bond cannot support the bond length increase found for the *cis* isomers. Thus, a more plausible explanation could be the influences of the aryl group, which could increase the electron density of the carbon atom of the carbonyl group and hence lead to longer bonds for *trans* and *cis* isomers. However no significant differences in the carbonyl bond length could be found for aryl substituents with varying electronic character. Torsion around the N-aryl axis was found to be slightly more pronounced, as it is the case for the di-arylated indigos, which is consistent with the analysis of the crystal structures of **107**, **110**, and **111**. With exception of indigo **112**, *cis* isomers exhibit marginally increased twisting of the N-aryl axis compared to the *trans* isomers. Torsional angles of the central double bond were found to be very similar for the *trans* isomers, with the dihedral angle of the double bond side in vicinity to the aryl substituent slightly decreased. For the *cis* isomers clearly stronger distortions were found for the double bond side bearing the carbonyl groups. Distances of the hydrogen bonds are similar to the ones observed in the crystalline state. In Figure 86 a structure superposition^c is shown, demonstrating the similarity between the calculated minimum structures of the *trans* isomers of mono- and di-arylated indigos **107** and **108** with the structures in the crystalline state.
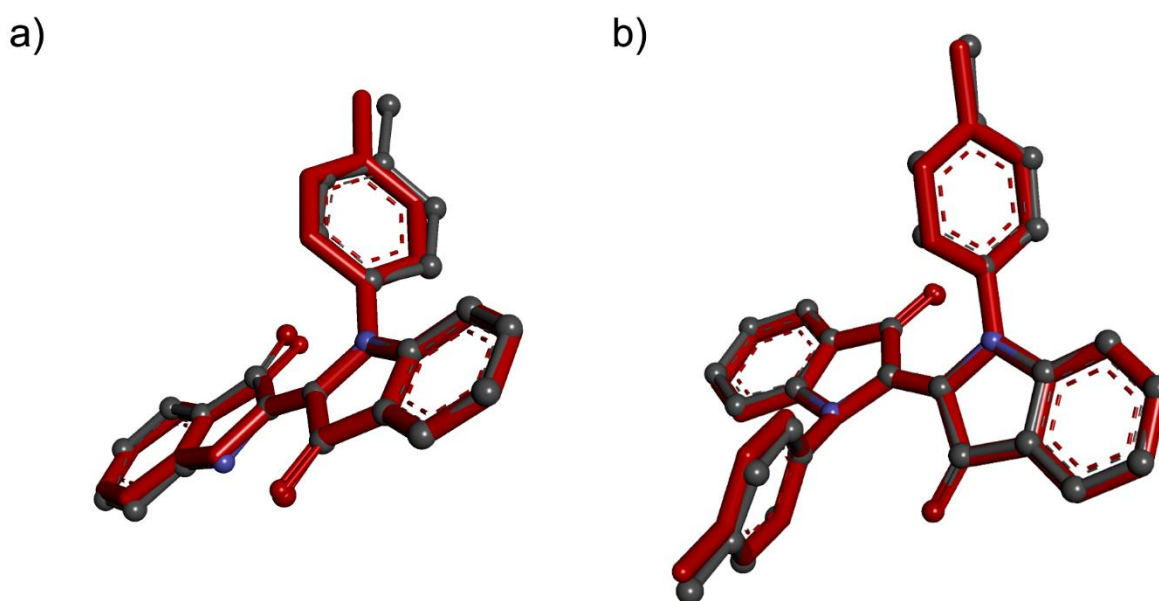
Figure 86:   Superposition of calculated structures (red) and the structures in the crystalline state (grey). a) *Trans-N-(p-*tolyl) indigo **107**. b) *Trans-N,N'-(p-*tolyl) indigo **108**.

Calculations of absorption spectra were performed on the TD-B3LYP/6-311+G(d,p) IEFPCM(THF) level of theory based on structures optimized on the ωB97X-D/6-311+G(d,p) level of theory with implementation of THF solvent effects (IEFPCM). Good agreement between calculated absorption maxima and the experimentally determined maxima was found. Since no pure spectra of the *cis*-**107** and *cis*-**108** as well as of *trans*-**108** were accessible, comparison was only possible with the spectra obtained either in thermal equilibrium conditions for *trans*-**108**, or with *cis*-enriched spectra, representing pss after irradiation. As calculations showed that the absorption spectrum of the *cis* isomer of mono-arylated indigo **107** is shifted to shorter wavelengths, the photogenerated species with bathochromically shifted absorption, was assigned to the *cis* isomer. All light sensitive mono-arylated indigos reveal bathochromically shifted absorptions after irradiation, which allowed the assumption, that in all cases *cis* isomers are generated by irradiation from the thermodynamically stable *trans* isomers. Figure 87 depicts the calculated absorption spectra of indigo **107** and **108**, as well as calculated and experimentally determined absorption maxima.
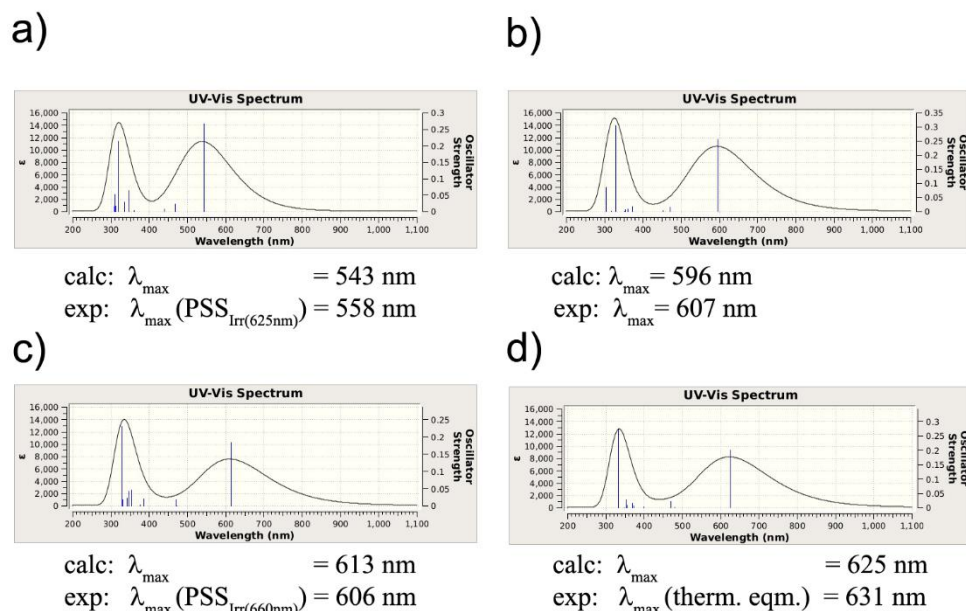
Figure 87:   Calculated absorption spectra of *trans-N*-(*p*-tolyl) indigo **107** and *trans-N,N'*-(*p*-tolyl) indigo **108** on the TD-B3LYP/6-311+G(d,p) IEFPCM(THF) level of theory. Minimum structures were obtained on the ωB97X-D/6-311+G(d,p) level of theory with implementation of THF solvent effects (IEFPCM). Very good agreement of calculated absorption maxima with experimental values was observed, the corresponding maxima values are compared under the respective absorption spectra. L. A. Huber, P. Mayer, H. Dube: Photoisomerization of Mono-Arylated Indigo and Water-Induced Acceleration of Thermal *cis* to *trans* Isomerization. *ChemPhotoChem.* **2018**, *2*, 458-464. Copyright Wiley-VCH Verlag GmbH & Co. KGaA. Adapted with permission.

In Figure 88, the HOMOs and LUMOs of mono- and di-arylated indigos **107** and **108** are illustrated exemplarily. It was found that the $S_0 - S_1$ transition is essentially a HOMO to LUMO excitation, which can be described as a π-π* transition.
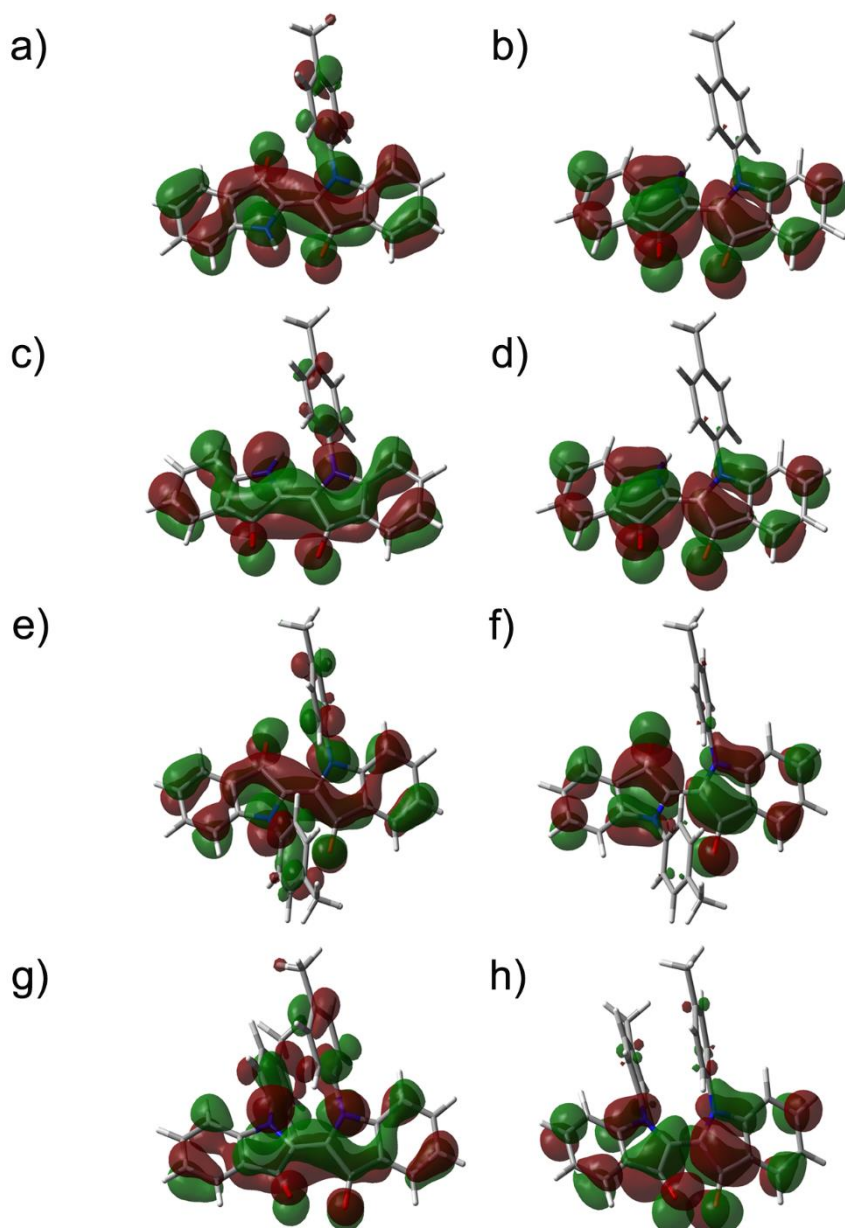
Figure 88: HOMOs and LUMOS obtained from the theoretical description of the *cis* and *trans* isomers of mono- and di-arylated indigos **107** and **108**. Orbitals were obtained on the TD-B3LYP/6-311+G(d,p) IEFPCM(THF) level of theory on the basis of optimized structures on the ωB97X-D/6-311+G(d,p) level of theory with implementation of THF solvent effects (IEFPCM). a) HOMO of *trans*-**107**. b) LUMO of *trans*-**107**. c) HOMO of *cis*-**107**. d) LUMO of *cis*-**107**. e) HOMO of *trans*-**108**. f) LUMO of *trans*-**108**. g) HOMO of *cis*-**108** h) LUMO of *cis*-**108**. L. A. Huber, P. Mayer, H. Dube: Photoisomerization of Mono-Arylated Indigo and Water-Induced Acceleration of Thermal *cis* to *trans* Isomerization. *ChemPhotoChem.* **2018**, *2*, 458-464. Copyright Wiley-VCH Verlag GmbH & Co. KGaA. Reprinted with permission.

6.4 Conformational analysis in the crystalline state

Structures in the crystalline state could be obtained for the *trans* isomers of di-arylated indigos **108** and **110** as well as for mono-arylated indigos **107**, **109**, and **111**. The structures of indigo **108** and **110** are shown in Figure 89. All structures were measured and refined by *Peter Mayer*.[VII] Theoretically obtained structures show great similarity to the corresponding crystal structures. All indigos exhibit strongly distorted aryl substituents in relation to the indigo core structure. No *cis* isomers in the crystalline state could be obtained, which strongly affirms that *trans* isomers are thermodynamic global minimum structures of di-arylated and mono-arylated indigos as predicted by theoretical calculation.

108   **110**
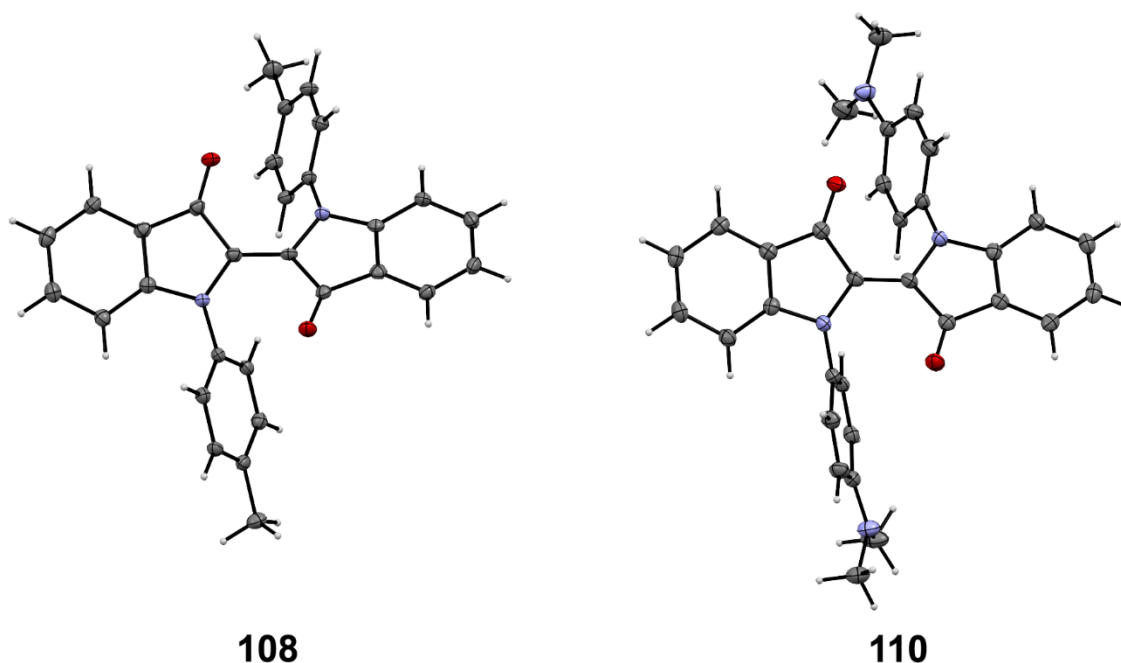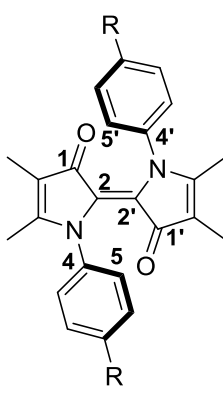
Figure 89:   Structures in the crystalline state of *trans* isomers of di-arylated indigos **108** (left) and **110** (right).[VII]

Selected bond lengths and dihedral angles of di-arylated indigos **108** and **110** as well as unsubstituted indigo **100**[243] (CCDC 1180367) are summarized in Table 18. Structures of di-arylated indigos **108** and **110** show great similarity. A slight difference can be found in the torsional angles of the N-aryl axis, which is between –40° to –46° for indigo **108**. A stronger torsion could be found for derivative **110** with almost 50°. Both di-arylated indigos are characterized by a slightly reduced double bond length in comparison to unsubstituted indigo. Bond length of the carbonyl functions are reduced in both cases in comparison to unsubstituted indigo, which could hint at the absence of a hydrogen bridge in di-arylated indigos **108** and **110**. Both di-arylated indigos show strongly twisted double bonds in comparison to indigo **100**, which is almost planar. Interestingly the double bond of unsubstituted indigo possesses a slight helical distortion, which results in opposite helicity as depicted in Figure 76 structures 3 and 4.

Table 18:   Comparison of torsional angles, bond length of di-arylated indigos **108**, **110**, and indigo **100** (CCDC 1180367). Arbitrary labelling of relevant atoms is given on the left side.

Numbering	Bond lengths/ angles	*trans*-**108**	*trans*-**110**	*trans*-**100**
	bond length in Å (central double bond)			
	C(2)-C(2')[a]	1.3668	1.371	1.375
	bond length in Å (carbonyl groups)			
	C(1)-O(1)	1.2249	1.224	1.268
	C(1')-O(1')	1.2344	1.224	1.268
	torsional angles (N-Aryl axis)			
	C(5)-C(4)-N-C(2)/	–40.73	–49.76	
	C(5')-C(4')-N-C(2')	–45.95	–49.76	
	torsional angles (central double bond)			
	C(1)-C(2)-C(2')-N	–25.22	–23.38	5.82
	C(1')-C(2')-C(2)-N	–26.68	–23.38	–5.82

Structures in the crystalline state could be obtained for mono-arylated indigos **107**, **109**, and **111** (Figure 91). They show a highly planar indigo core structure, while di-arylated indigos **108** and **110** reveal stronger distortions across the central double bonds. A comparison between structures of mono- and di-arylated indigos **107** and **108** is given in Figure 90. The torsional angles of the central double bond of mono-arylated indigos are quite similar to the dihedral angle found for unsubstituted indigo. **107**, **109**, and **111** show strong twisting of the aromatic substituents with increased torsional angles as compared to di-arylated indigos. A possible explanation could be, that in case of di-arylated indigos the pronounced double bond twisting allows for a slight planarization of the aryl substituents, since sterical hindrance to the carbonyl groups is reduced.

107   **108**
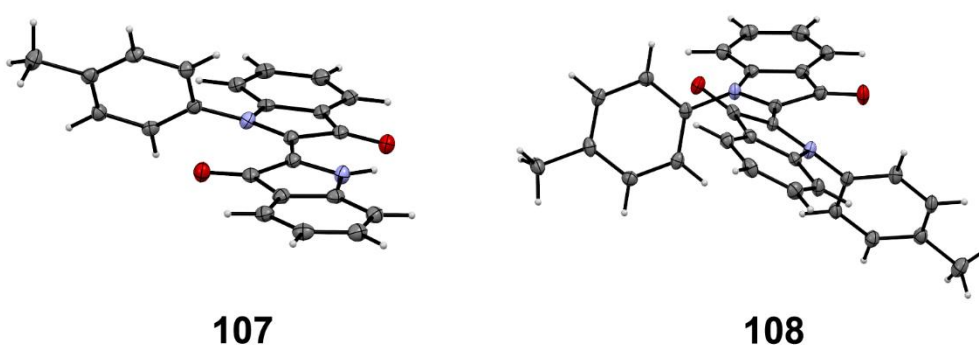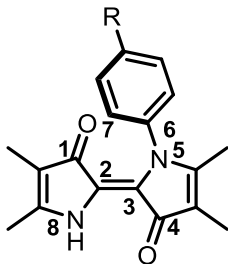
Figure 90:   Side view of *trans*-**107** and *trans*-**108** structures in the crystalline state. Mono-arylated compounds possess a highly planar indigo core structure, while di-arylated analoga reveal a twisted central double bond.

Table 19: Comparison of torsional angles, bond lengths and distances in the structures of mono-arylated indigos **107**, **109**, and **111**. Arbitrary labelling of relevant atoms is given on the left side.

numbering	bond lengths/ angles/distances	*trans*-**111**	*trans*-**107**	*trans*-**109**
	bond length in Å (central double bond)			
	C(2)-C(3)	1.3684	1.3674	1.3739
	bond length in Å (carbonyl groups)			
	C(1)-O(1)	1.2193	1.2235	1.2143
	C(4)-O(4)	1.2374	1.2432	1.2355
	distance in Å (H bridge)			
	H(8)- O(4)	2.1904	1.9164	2.056
	torsional angles (N-aryl axis)			
	C(7)-C(6)-N(5)-C(3)	–54.51	–131.53	–63.68
	torsional angles (central double bond)			
	C(1)-C(2)-C(3)-N(5)	–5.67	0.73	–2.12
	C(4)-C(3)-C(2)-N(8)	–7.88	4.38	–5.22

In Table 19 selected distances, torsional angles and bond lengths in the structures of mono-arylated indigos are summarized. As it was already observed for di-arylated indigos the double bond lengths of mono-arylated indigos are marginally reduced in comparison to unsubstituted indigo. Shorter bond lengths of the carbonyl group in close proximity to the aryl substituent were also found. The carbonyls situated next to the hydrogen bearing nitrogens are slightly elongated. Twisting of the N-aryl axis, which is slightly more pronounced as observed for di-arylated indigos, was found for all mono-arylated indigos.
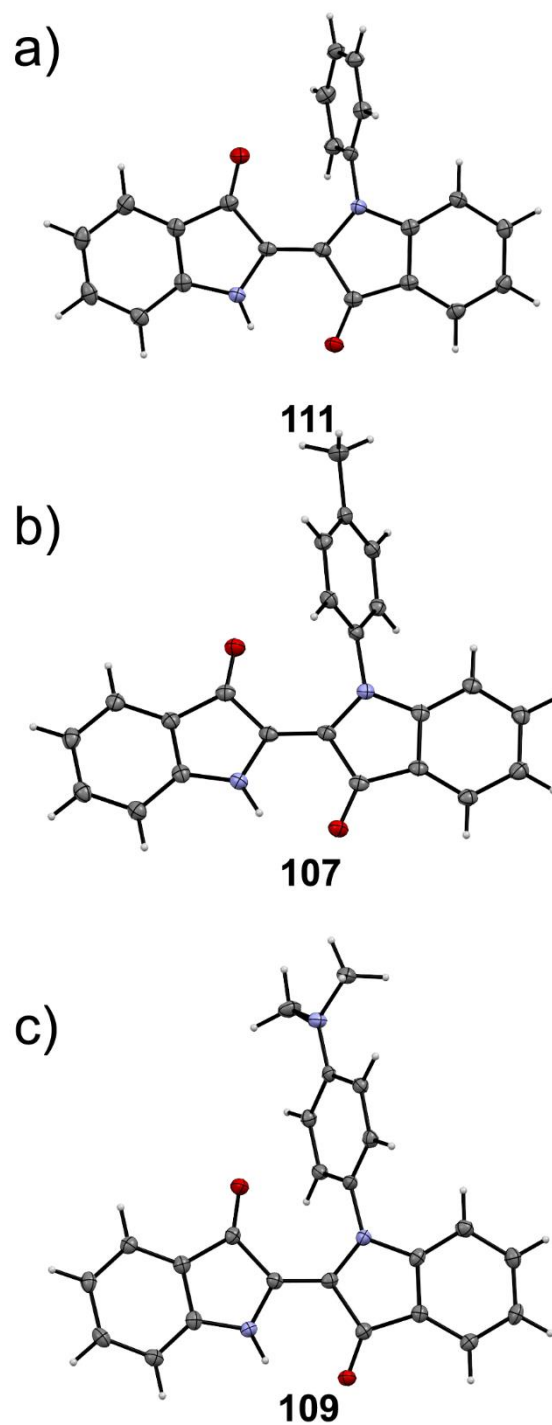
Figure 91:   Structures in the crystalline state of *trans* isomers of mono-arylated indigos **111** (a), **107** (b), and **109** (c).

6.5 Conformational analysis in solution

Only a single set of signals was observed in the ^{1}H NMR spectra of all investigated mono-arylated indigos. In combination with sufficient thermal half-lives, experimentally observed for the corresponding metastable *cis* isomers, the observed set of signals can be clearly identified as the *trans* isomers. Taking into account the uncertainty of NMR measurements at least 95% of this isomer is populated, which can be translated into an estimated energy difference of at least 1.74 kcal·mol^{-1} between the stable and metastable isomers. In combination with the theoretical assessment, which resulted in the *trans* isomers as the thermodynamic minima for all investigated mono-arylated indigos, the observed signals were assigned to the *trans* isomers. No indicative cross peak signals between the two fragments at either side of the double bond could be observed in the NOESY spectra, which would have proven the double bond configuration unambiguously (see Figure 96). In Figure 92 the ^{1}H NMR spectrum of mono-arylated indigo **107** is shown exemplarily together with the assignment of the hydrogen signals. A broad signal of the amine function is observed, which hints at fast dynamics on NMR time scale. The distinct downfield shift of this signal is induced by strong electron withdrawing effects of the carbonyl groups.
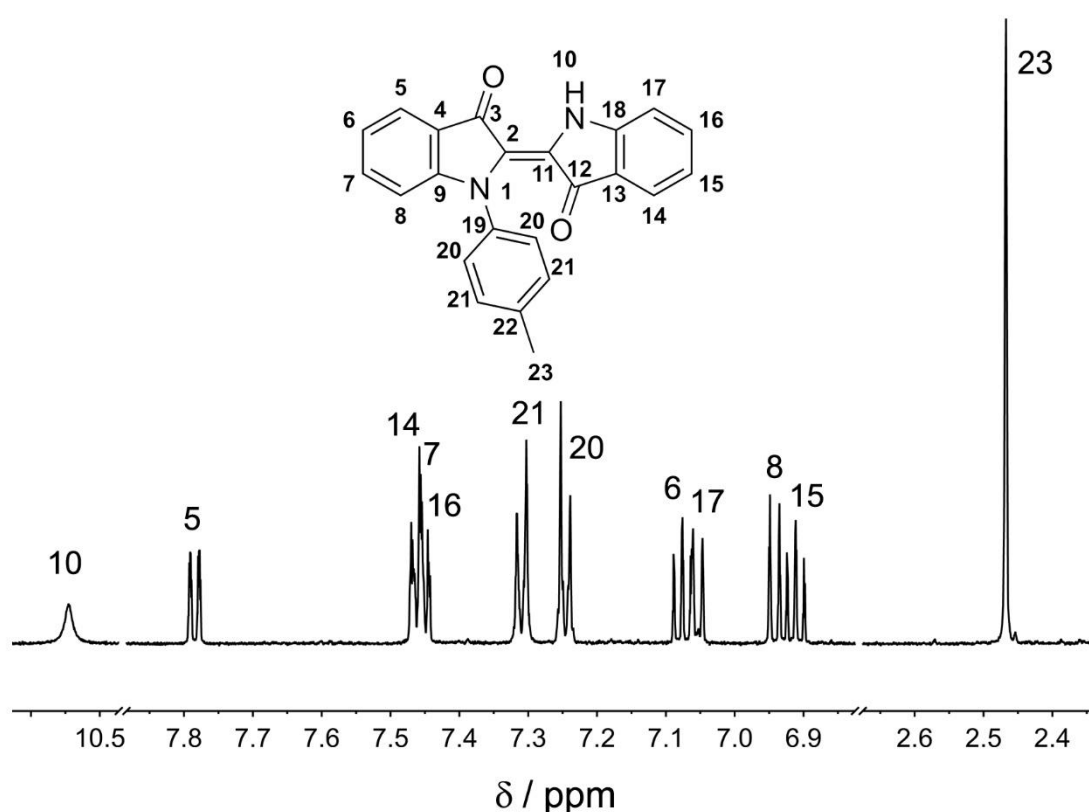
Figure 92: ^{1}H NMR spectrum (600 MHz, CD$_2$Cl$_2$, 27 °C) of mono-arylated indigo **107** and the corresponding assignment of the signals. Arbitrary numbering is identical with the numbering in the experimental part.

For di-arylated indigos two sets of signals were observed in the ^{1}H NMR spectra, which demonstrates that the relative energy difference of *cis* and *trans* isomer is decreased compared to mono-arylated indigos. This trend was also observed in the theoretical calculations. In Figure 93 the ^{1}H NMR spectrum of di-arylated **108** with assignment of the signals is depicted exemplarily. No indicative cross peak signals in the NOESY spectra could be observed, which would have proven the double bond configuration unambiguously (see Figure 97). Identification of each isomer was also aggravated by ambiguous results from the theoretical assessment, which revealed the *trans* isomer as the thermodynamic minimum for indigo **108**, while the *cis* isomer was identified as the minimum for indigos **110** and **116**. However, comparison of the theoretically obtained minimum structures with the chemical shifts of indigo **108** gave valuable information and allowed for identification of the isomers.
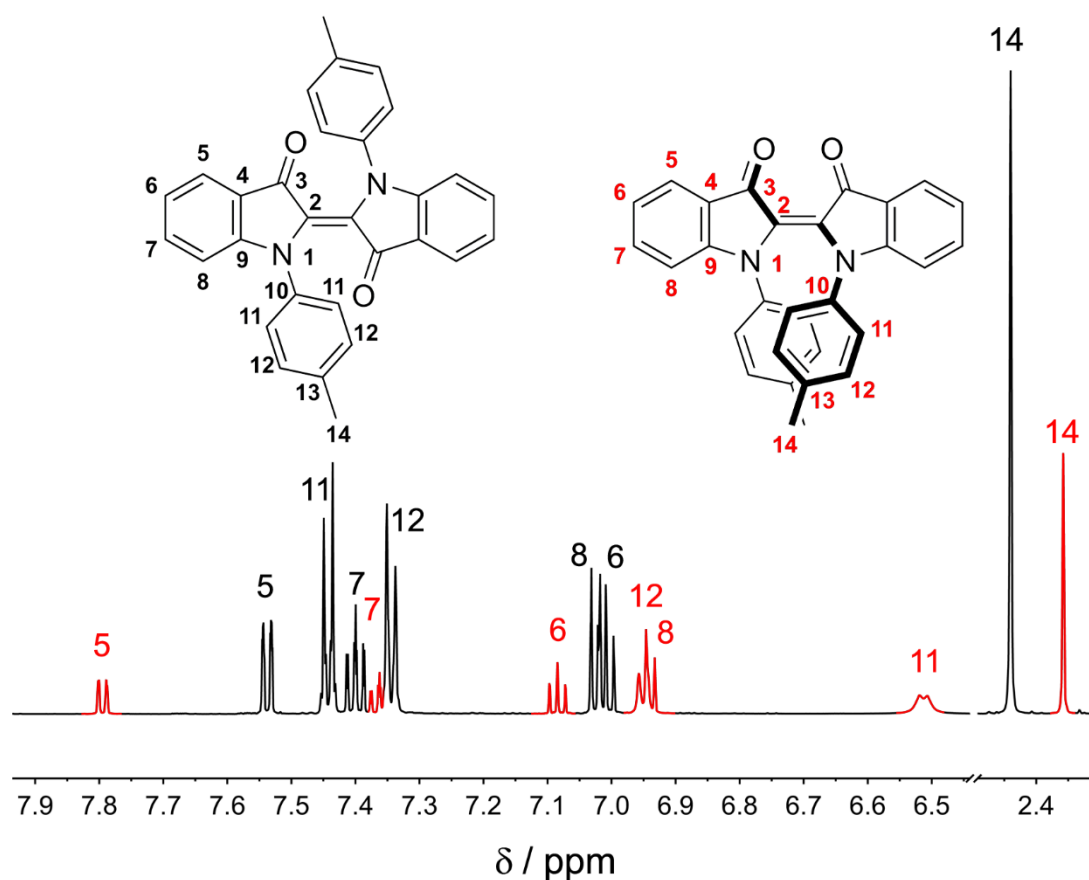
Figure 93:   ^{1}H NMR spectrum (600 MHz, CD$_2$Cl$_2$, 27 °C) of di-arylated indigo **108** and the corresponding assignment of the signals. Arbitrary numbering is identical with the numbering in the experimental part. For the *cis* isomer of **108** the signals as well as the assignments are depicted in red. An isomeric ratio of 73% / 29% *trans* / *cis* was found.
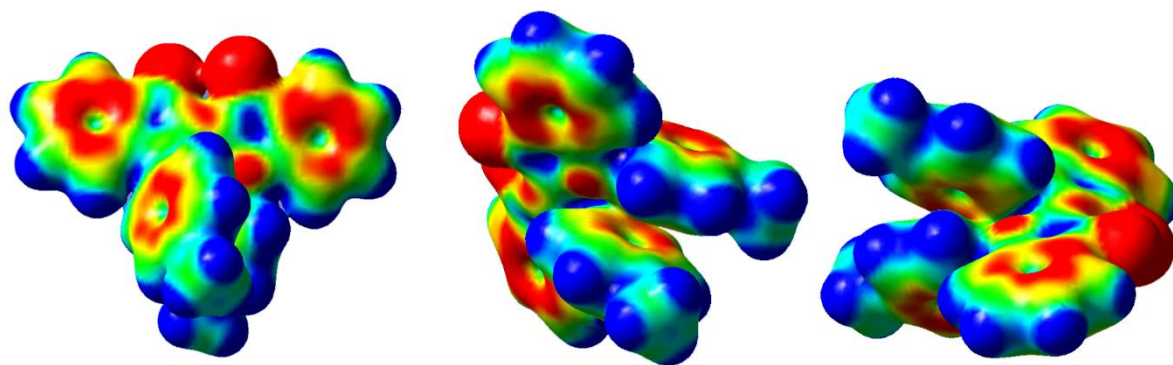
Figure 94: Electrostatic potential surfaces (ESP) of di-arylated indigo **108** from three different perspectives. ESPs were generated with the following parameters: Density = 0.01, MO = 0.02, and a lowest/highest limit of $1.000e^{-4}$ and $6.000e^{-2}$ for the electron density.

In Figure 94 the electrostatic potential (ESP) from the optimized structure of *cis*-**108** is depicted and illustrate the conformation leading to distinct NMR shifts. The *cis* isomer revealed close proximity of the aryl substituents, which leads to a helical distortion of the central double bond. The aryl substituents show a parallel alignment with distinct twisting around the N-aryl axis (for details on twisting angles see Table 16). Thus, hydrogens 11 in *ortho* position of the substituents pointing to the other aryl group are especially close to the π surface of the neighboring aryl ring and experience the ring current of its aromatic system, which consequently leads to the distinct upfield shift of these signals. Hydrogens 11 which are pointing in opposite direction are in vicinity to the lone pair situated at the nitrogen atom. It is possible, that this molecular arrangement also contributes to the upfield shift of the hydrogens 11 signal. Further it can be observed from the ¹H NMR spectrum, that the hydrogens 12 in *meta* position exhibit upfield shifted signals but with lower magnitude. Hydrogens 12 are partly overlapped from the doublet derived from hydrogen 8. Both hydrogens 12 and 11 exhibit broad signals in comparison to the sharp signals derived from the *trans* isomers, which hints at dynamic processes happening on the NMR time scale. Two different molecular displacements can be contemplated for explanation of the signal broadening: A rotation around the N-aryl axes or a helical inversion of the central double bond. At –40 °C it can be observed that the doublets from hydrogen 11 and 12 completely vanish as it can be seen in Figure 95, while the ¹H NMR spectrum at –60 °C hints at signal splitting which should lead to 4 signals. However, only two signals are clearly observable. It is likely that the two residual signals are hidden or overlapping. The low temperature ¹H NMR spectra confirm signal broadening observed at ambient temperatures as a consequence of dynamic conformational processes. Nevertheless, the characteristic upfield shift was used for the identification of the *cis* isomer and *trans* isomer signals. Thus, an isomeric ratio of 73% *trans* isomer and 27% *cis* isomer could be determined for CD₂Cl₂ solution

of **108**, which can be translated into an energy difference of 2.5 kcal·mol⁻¹ at 27 °C. Additionally, it was found that the isomer composition is dependent on the solvent used for ¹H NMR spectrum recording. More details are given in chapter 4.6.
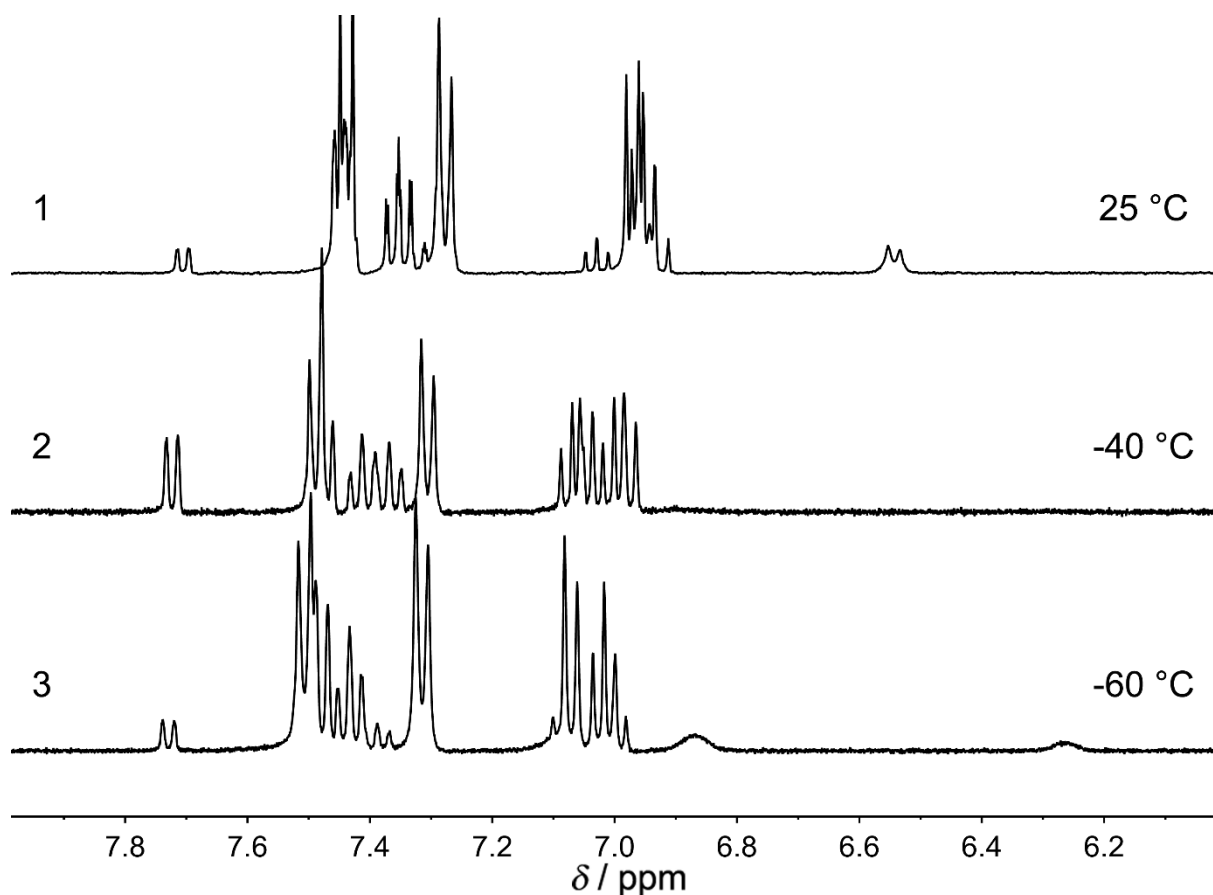
Figure 95:   ¹H NMR spectroscopy (400 MHz, THF-d_8) of indigo **108** at various temperatures. 1. At 25 °C only one doublet can be observed for hydrogens 11. The doublet from hydrogen 12 is hidden under the signals belonging to the indigo core at 7.00 ppm. 2: ¹H NMR spectrum at –40 °C (concentration of *cis* isomer is higher than observed for spectrum 1 and 3, because the solution was irradiated with 625 nm before the spectrum was recorded). The doublets of hydrogens 11 and 12 has completely vanished, which hints at further deceleration of the dynamic conformational changes. 3: ¹H NMR spectrum at –60 °C two new signals are observable. Further doublets are either overlapped or hidden under the signals derived from the indigo core signals. The reappearance of these signals hints at slower conformational processes at –60 °C than observable on the NMR timescale. Thus, diasterotopicity of hydrogens 11 and 12 is now frozen out, leading to a total of four individual signals for these protons.

In Figure 96 and 97 the NOESY as well as the HMBC spectra of indigos **107** and **108** are shown exemplarily. From the analysis of the NOESY spectra no indicative cross signals could be observed for unambiguous assignment of the configuration of the central double bond of mono- and di-arylated indigos. However, the NOESY spectra delivered valuable information for identification of the two hemispheres for mono-and di-arylated indigos. For mono-arylated indigo a cross peak signal of the N-bound hydrogen 10 and the adjacent aromatic hydrogen atom 17 was observed, as well as a cross peak signal between hydrogen 11 from the aryl substituent and the aromatic hydrogen 8 of the indigo core. In the HMBC spectrum, the hemispheres are distinguishable from the cross peak signals observed for the carbonyl groups. Interestingly, hydrogen 5 revealed significant downfield shift as it is the case for hydrogen 14, which can be attributed to the different deshielding effects by the carbonyl groups. For di-arylated indigos cross peaks signals between hydrogen 11 and 12 as well as between 12 and 14 allowed for identification of the *meta* hydrogens of the tolyl group, which are hidden under the doublet signal of hydrogen 8 as well as unambiguous entanglement of these signals to the methyl group with minor intensities, represented by the singlet at 2.35 ppm. Again the HMBC spectrum confirms the observation in the NOESY spectrum by the indicative cross peak signals of the carbonyl groups. In summary, the NMR analysis confirmed the molecular structures obtained from the crystallographic analysis in the solid state.
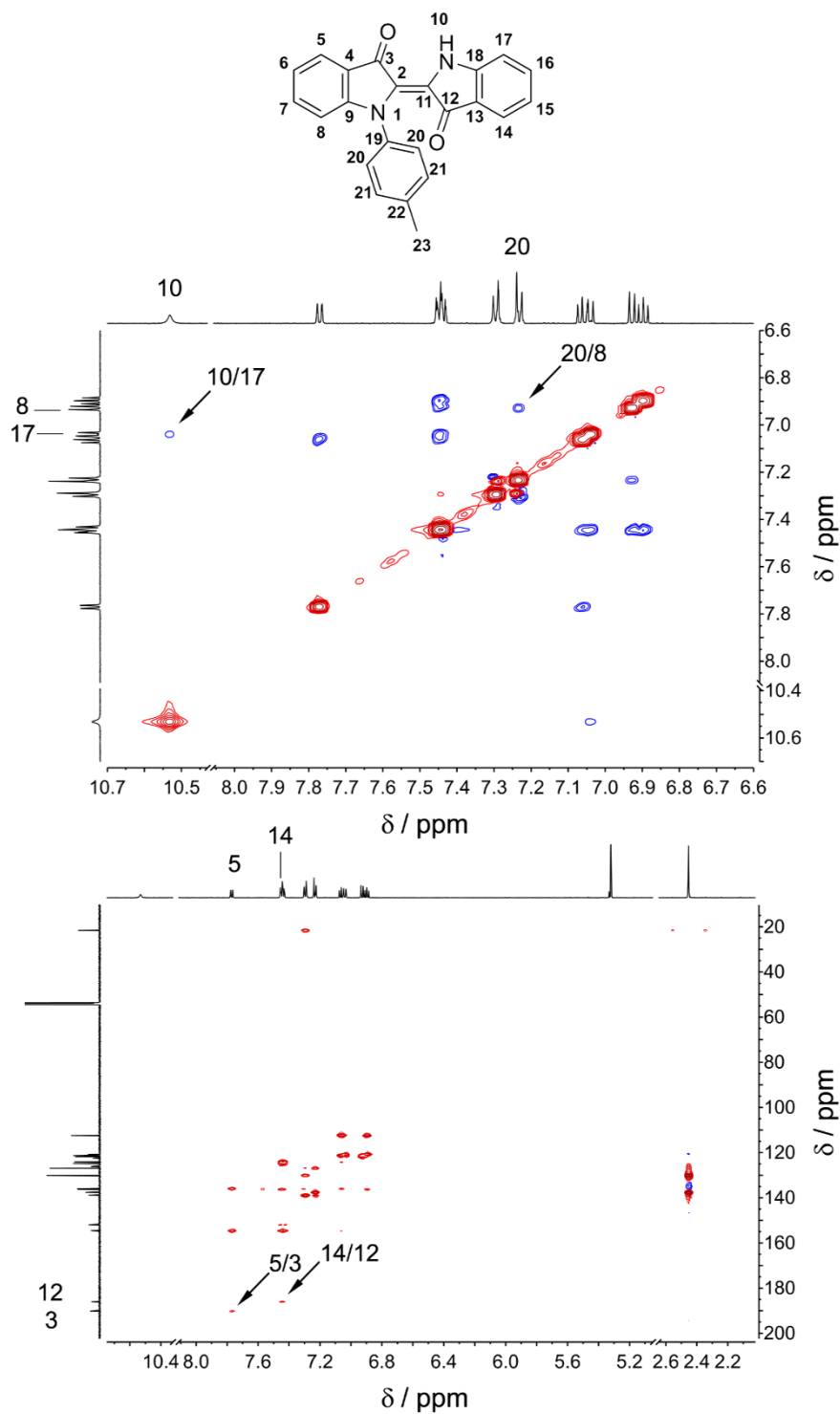
Figure 96:   NOESY spectrum (top) and HMBC spectrum (down) (600 MHz, CD$_2$Cl$_2$, 27 °C) of mono-arylated indigo **107**. Indicative signals are highlighted with black arrows.
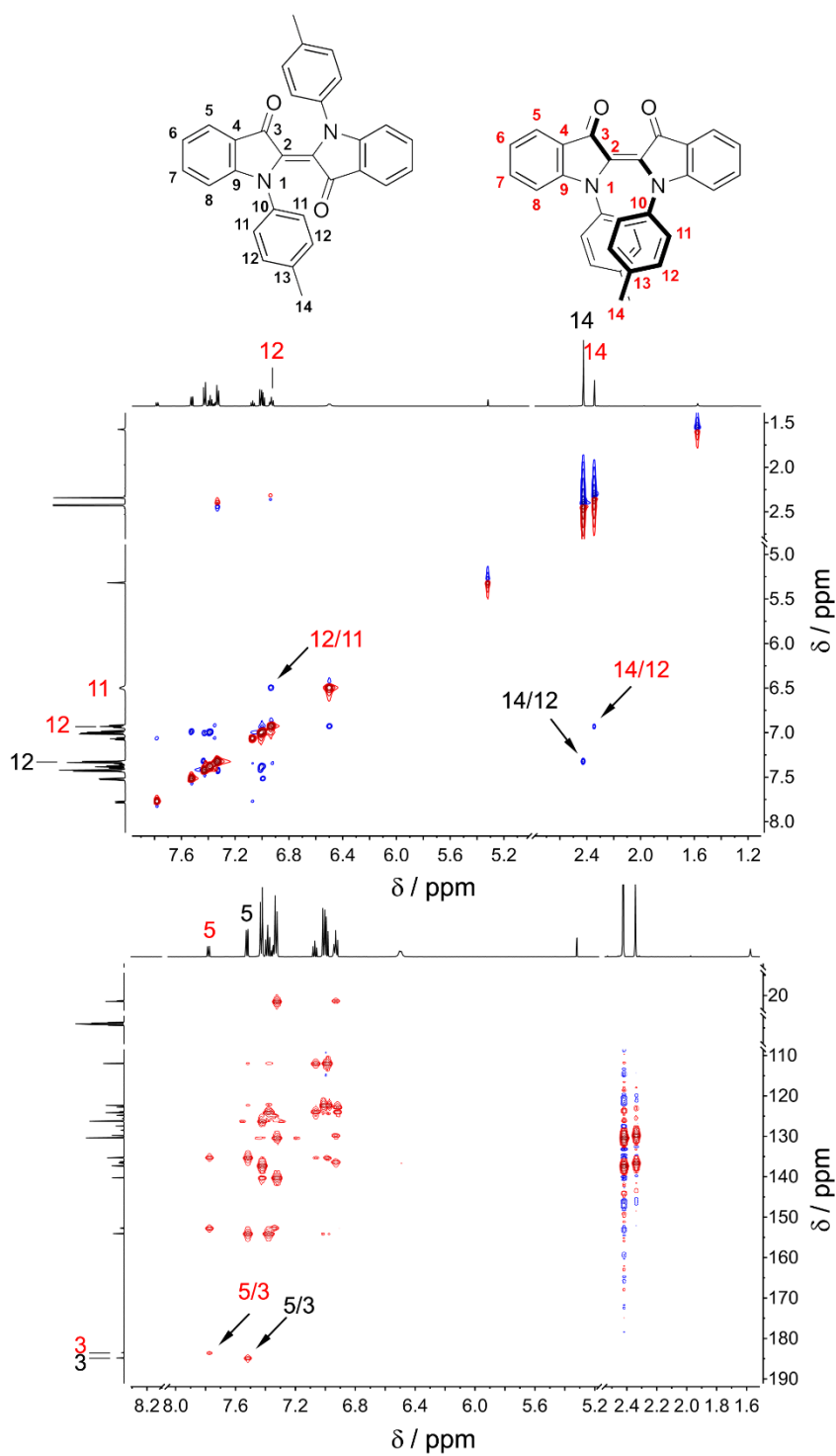
Figure 97:   NOESY spectrum (top) and HMBC spectrum (down) (600 MHz, CD$_2$Cl$_2$, 27 °C) of di-arylated indigo **108**. Indicative signals are highlighted with black arrows.

6.5.1 Fast deuterium exchange of mono-arylated indigo 107

The broad signal of the nitrogen bound hydrogen already hinted at a possible hydrogen exchange on the time scale of ^{1}H NMR experiment. Therefore, it was tested if a hydrogen deuterium exchange is happening after addition of D_2O to a solution of indigo **107** in THF. Low temperature ^{1}H NMR spectroscopy was used because of the possible chance of recording the exchange dynamics - in case of small rate constants. However, no dynamics could be observed. In the first spectrum the N-H signal is clearly observable at 11 ppm. The first spectrum was recorded at –80 °C. Afterwards D_2O was added to the NMR solution while the NMR sample was kept at –80 °C in a cooling bath. After rapid transfer of the sample into the NMR spectrometer a ^{1}H NMR spectrum was recorded. Unfortunately, spectrum quality suffered from sample transfer and the first recorded spectrum at –80 °C exhibited insufficient signal to noise ratio and resolution for unambiguous determination of signal intensity of the N-bound hydrogen. After warming up to –60 °C another ^{1}H NMR spectrum was recorded with sufficient spectral resolution. The signal at 11 ppm had vanished completely, which proves that a fast deuterium exchange took place after addition of D_2O. The sample was further warmed up to –40 °C and 22 °C and ^{1}H NMR spectra were recorded (spectrum 3 and 4 in Figure 98), which confirmed the absence of the N-H signal. The residual water signal was shifted from 2.48 to 3.25 ppm. Comparison of the residual water signal of a sample containing indigo **107**, THF-d_8, and D_2O (spectrum 4) with the water signal of a sample containing THF-d_8 and D_2O (spectrum 6) indicates again interactions of mono-arylated indigo **107** with water. The interactions could be solely represented by the exchange of the N-bound hydrogen but could also be influenced by additional interactions of water with the carbonyl groups of indigo **107**.
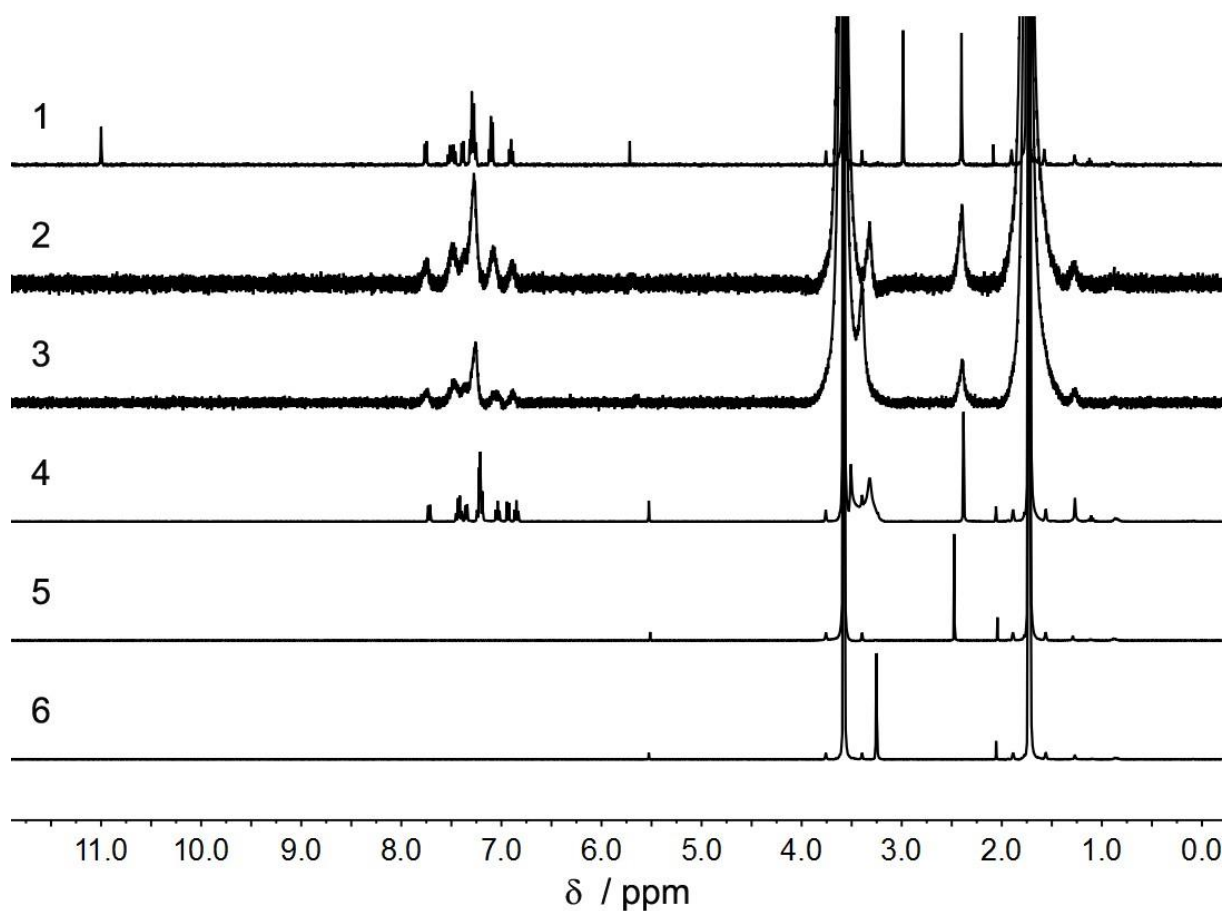
Figure 98: ¹H NMR spectra (400 MHz) recorded during deuterium exchange of the N-bound hydrogen of mono-arylated indigo **107** (1.9 mM, 0.8 mL THF-d_8) after D_2O addition to the THF-d_8 solution. 1) ¹H NMR spectrum of *trans-N*-(*p*-tolyl) indigo **107** before D_2O addition. The N-H signals can be observed at 11 ppm. 2) ¹H NMR spectrum recorded at –60 °C after D_2O addition (1700 equiv.) to the solution of indigo **107** (1.5 mM, 1 mL THF-d_8). 3) ¹H NMR spectrum recorded at –40 °C after D_2O addition. 4) ¹H NMR spectrum recorded at 22 °C after D_2O addition. No signal of the N-H group can be observed after D_2O addition (spectra 2-4), which proves very fast deuterium exchange. 5) ¹H NMR spectrum of pure THF-d_8 without D_2O. 6) ¹H NMR spectrum of THF-d_8 with D_2O. The water signal is significantly shifted downfield from 2.48 to 3.25 ppm. L. A. Huber, P. Mayer, H. Dube: Photoisomerization of Mono-Arylated Indigo and Water-Induced Acceleration of Thermal *cis* to *trans* Isomerization. *ChemPhotoChem.* **2018**, *2*, 458-464. Copyright Wiley-VCH Verlag GmbH & Co. KGaA. Reprinted with permission.

6.5.2 Isomeric ratios of di-arylated indigos in different solvents

It was found for di-arylated indigos **108**, **110**, and **116** that the isomeric ratio in thermal equilibrium varies with different solvents. Isomeric ratios were obtained by ^{1}H NMR spectroscopy with integration of indicative methyl groups. Identification of the *cis* isomer signals was derived from the distinct upfield shifts of the aromatic protons of the aryl substituent. In case of indigo **116** isomer identification was aggravated by an almost 50/50 mixture of *cis* and *trans* isomer. Nevertheless, the derived conclusion are the same if assignment is done *vice versa*. Obtained isomeric ratios in different solvents are summarized in Table 20.

Table 20: Summary of varying *cis* isomer content in equilibrium in different solvents of di-arylated indigos **108**, **110**, and **116**.

indigo	benzene-d_6	toluene-d_8	THF-d_8	CD$_2$Cl$_2$	DMSO-d_6
108	-	10%	19%	29%	26%
110	-	7%	30%	-	-
116	24%	-	27%	54% (46%)*	-

*distinct identification of the *cis*-**116** in the ^{1}H NMR spectrum was hampered by spectral overlap of indicative signals. Thus, it cannot be fully excluded that *cis* isomer content is 46%. Argumentation however does not change in this case.

For indigo **108** the *cis* isomer content in apolar toluene solution was found to be 10%, while more polar THF and CD$_2$Cl$_2$ solutions deliver increased content of *cis* isomer. Even higher polarity as it is the case with DMSO however does not yield a further increased *cis* isomer content. Obtained data for indigos **110** and **116** also supports a beneficial influence of more polar solvents on the *cis* isomer content. It can be concluded that solvent polarity influences the isomeric ratio for di-arylated indigos to a certain extent, but the isomeric ratio of **108** in DMSO hints at more specific interactions, which are not linearly represented by the solvent polarity. A general influence of solvent polarity can be explained by better solvation of the *cis* isomer having a distinctly larger dipole moment in comparison with the corresponding *trans* isomers. It was also observed that aromatic solvents as toluene and benzene deliver lowest *cis* isomer contents. This could be caused by their inherent low polarities and or or by representing a competitive partner for aromatic interactions of the aryl substituents, which diminishes intramolecular stabilization of the *cis* isomer. For indigo **116** the highest *cis* isomer content was observed in aromatic solvents as well as in CH$_2$Cl$_2$. In contrast to **108** and **110**, the *cis* isomer of **116** was found to be ca. 2 kcal·mol^{-1} lower in energy compared to the *trans* isomer in the theoretical description, which qualitatively reproduces the observed experimental trends. A possible stabilization by polar aromatic interactions was already discussed in chapter 4.5. In summary, the at present only fragmentary information allowes for several possible hypotheses, as stabilization of the large dipole moment of the *cis* isomer in more polar solvents and/or stabilization of intramolecular polar aromatic interactions. Further experimental data are necessary for a profound study of solvent effects on the isomeric ratio of di-arylated indigos.

6.6   Photophysical properties

In the following the extinction coefficients and emission spectra of mono-arylated indigos and di-arylated indigo **108** are reported. The molar absorption spectra and absorption was well as emission spectra are shown in Figures 99 and 100, respectively.
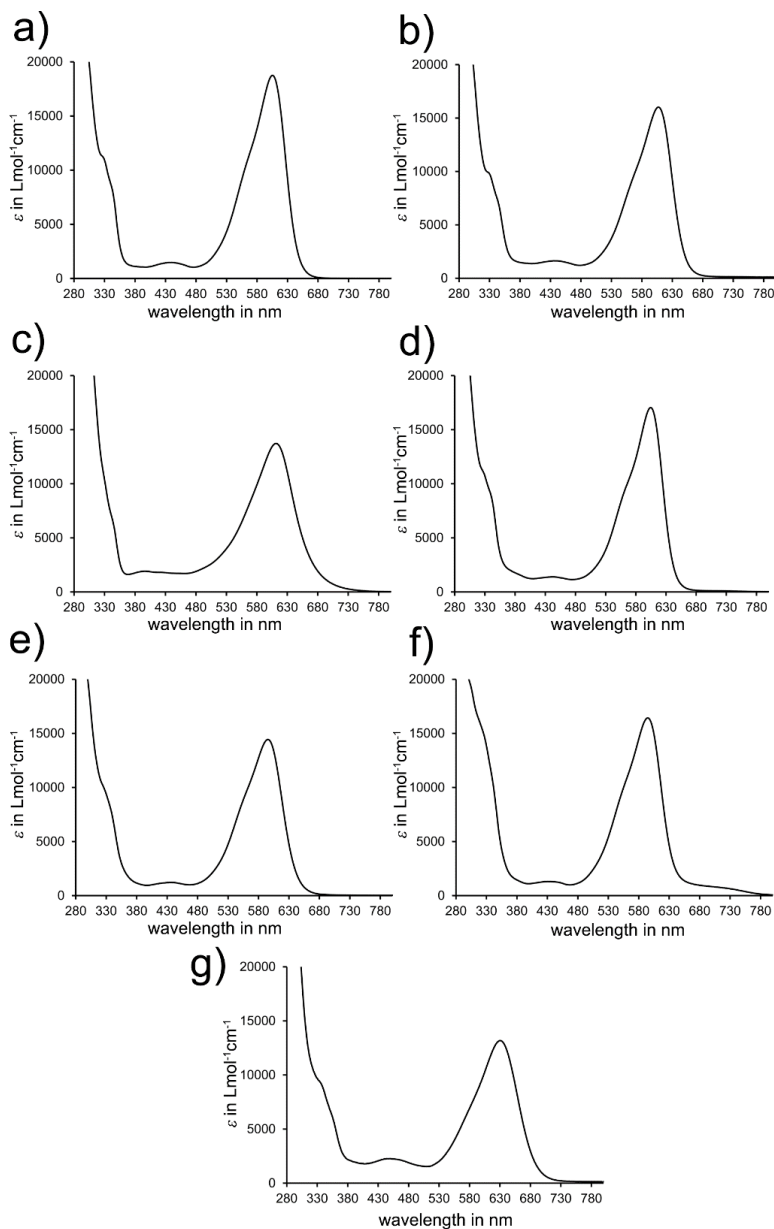
Figure 99:   Extinction coefficients of mono- and di-arylated indigos in dry THF at ambient temperatures. a) *Trans-N*-phenyl indigo **111**. b) *Trans-N*-(*p*-tolyl) indigo **107**. c) *Trans-N*-(*p*-(dimethylamino)phenyl) indigo **109**. d) *Trans-N*-(naphthalen-1-yl) indigo **114** e) *Trans-N*-(thiophen-2-yl) indigo **113**. f) *Trans-N*-(3,5-bis(trifluoromethyl)phenyl) indigo **112**. g) Extinctions of a 82/18 *trans*/*cis* mixture of *N,N'*-di(*p*-tolyl) indigo **108**. L. A. Huber, P. Mayer, H. Dube: Photoisomerization of Mono-Arylated Indigo and Water-Induced Acceleration of Thermal *cis* to *trans* Isomerization. *ChemPhotoChem.* **2018**, *2*, 458-464. Copyright Wiley-VCH Verlag GmbH & Co. KGaA. Adapted with permission.
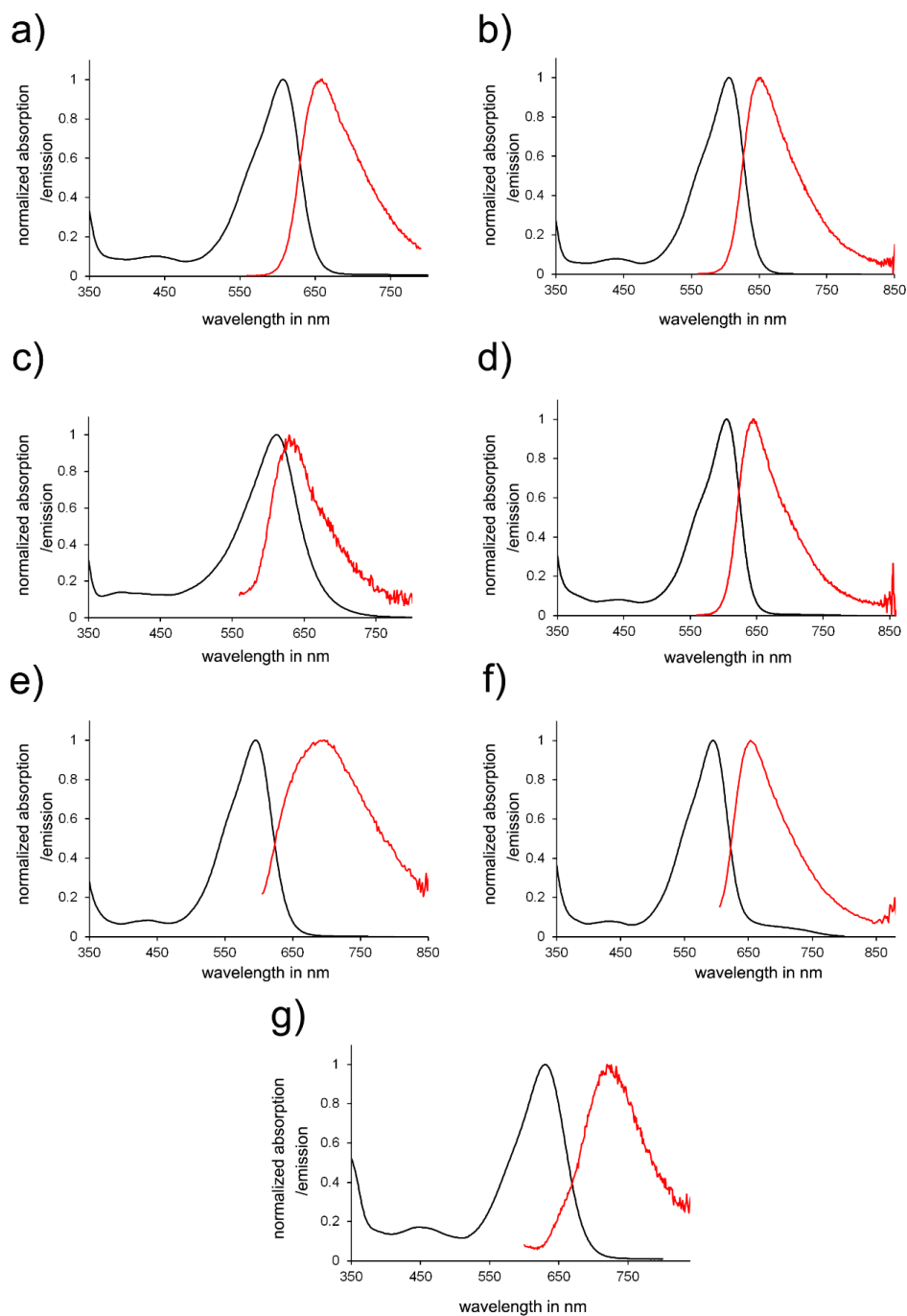
Figure 100: Emission spectra of mono- and di-arylated indigos in dry THF at ambient temperature. a) *Trans-N*-phenyl indigo **111**. b) *Trans-N*-(*p*-tolyl) indigo **107**. c) *Trans-N*-(*p*-(dimethylamino)phenyl) indigo **109**. d) *Trans-N*-(naphthalen-1-yl) indigo **114** e) *Trans-N*-(thiophen-2-yl) indigo **113**. f) *Trans-N*-(3,5bis(trifluoromethyl)phenyl) indigo **112**. g) Emission of a 82/18 *trans/cis* mixture of *N,N'*-di(*p*-tolyl) indigo **108**. L. A. Huber, P. Mayer, H. Dube: Photoisomerization of Mono-Arylated Indigo and Water-Induced Acceleration of Thermal *cis* to *trans* Isomerization. *ChemPhotoChem.* **2018**, *2*, 458-464. Copyright Wiley-VCH Verlag GmbH & Co. KGaA. Adapted with permission.

Table 21: Absorption maxima λ_{max}, emission maxima Em_{max}, Stokes shifts as well as the extinction coefficient ε of indigos **107-114** and **116** measured in THF [a], *i*Hexane[b], or CH_2Cl_2[c] at ambient temperatures.

Indigo	λ_{max} [nm]	Em_{max} [nm]	Stokes Shift [nm]	ε (λ_{max}) [Lmol⁻¹cm⁻¹]
107	607[a]	667[a]	60[a]	16000[a]
108	630[a], 619[b], 641[c]	720[a]	90[a]	13200[a]
109	611[a]	643[a]	32[a]	13700[a]
110	630[b]	-	-	-
111	605[a]	661[a]	56[a]	18700[a]
112	595[a]	653[a]	58[a]	16400[a]
113	595[a]	712[a]	117[a]	14400[a]
114	604[a]	654[a]	50[a]	17000[a]
116	619[b]	-	-	-

In Table 21 selected photophysical properties measured at ambient temperatures are summarized for indigos **107**-**114** and **116**. Mono-arylated indigos exhibit an absorption maximum of around 600 nm, while di-arylated indigos show an increased red shift with an absorption maximum of 630 nm. For mono-aryalated indigos a minor effect of the electronic character of the aryl substituent can be observed. The electron donating *p*-aniline moiety leads to a bathochromic shift of the absorption maximum (611 nm), while thiophene and electron withdrawing 3,5-trifluoromethylbenzene moieties exhibit maxima at shorter wavelengths (595 nm in both cases). Neutral substituents in indigos **107**, **111** and **114**, lead to absorption maxima of 604 to 607 nm. Most mono-arylated indigos revealed a Stokes shift of 50-60 nm, while a reduced Stokes shift of only 32 nm could be observed for *p*-aniline bearing indigo **109**. The opposite effect was observed with thiophene bearing indigo, which provides a Stokes shift of 117 nm. In this case the fluorescence spectrum deviates from the absorption mirror image, observed for the other indigos. The emission band is broadened and visible up to 850 nm. The extinction coefficients range from 13,000 to 19,000, while *N,N'*-di(*p*-tolyl) indigo **108** is less absorbing than *N*-(*p*-tolyl) indigo **107**. Similar substituents effects on the absorption of several mono- and di-arylated indigos were already reported by *Matsumoto* and *Tanaka*.[140] The influence of the electronic character of aryl substituents on di-arylated indigos is illustrated in Figure 101, where absorptions of indigo **108**, **110**, and **116** are compared. It can be observed analogous to mono-arylated indigos, that electron rich *p*-aniline moieties lead to a bathochromic shift in comparison to *N,N'*-di(*p*-tolyl) indigo **108**. Indigo **116**, with electron donating and electron withdrawing aryl substituents shows an identical absorption maximum as observed for indigo **108** but with a broader absorption band. It seems that the opposing electronic effects of the aryl substituents are canceling out each other or simply have no large effect. Absorption spectra of indigo **108** were measured in *i*-hexane, THF, and CH_2Cl_2 in order to compare the absorption behavior

in different solvents. A moderate positive solvatochromism was found, with an absorption maximum of 619 nm in *i*-hexane, 630 nm in THF, and 641 nm in CH_2Cl_2.
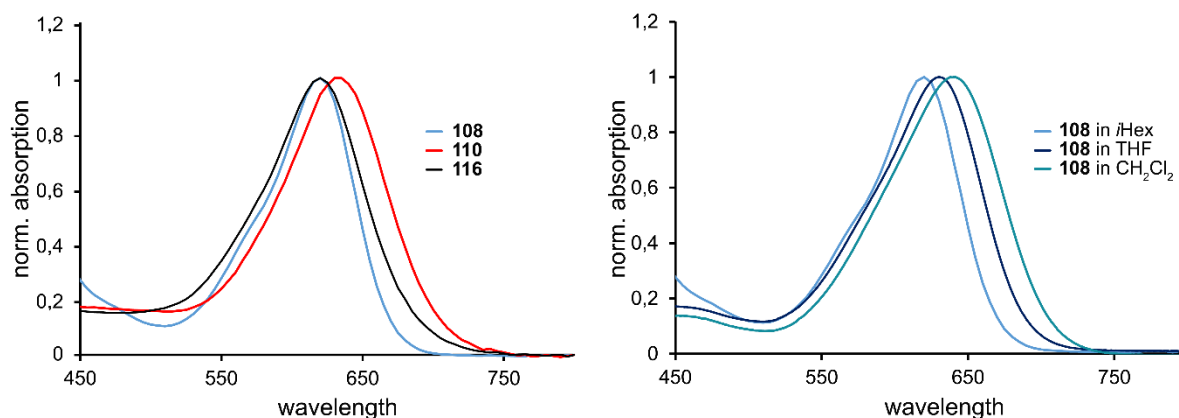
Figure 101:   Absorption spectra of di-arylated indigos **108**, **110** and **116**. Left: Comparison of the absorption spectra of di-arylated indigos in *i*-hexane. Right: Positive solvatochromism observed for indigo **108**.

6.6.1   Fluorescence quantum yield

The fluorescence quantum yield of mono-arylated indigo **107** was determined in order to investigate the varying influences of H_2O and D_2O addition to a THF solution of indigo **107** on its photophysical properties. Fluorescence quantum yields of ca. 0.77% were found and are all in the same range, which was also previously observed for other indigoid HTI photoswitches.[105] D_2O addition increased the fluorescence quantum yield to 1.01% while the same amount of H_2O furnished a decrease to 0.71%. The results are shown in Table 22.

Table 22:   Summary of determined fluorescence quantum yields for mono-arylated indigo **107** measured in dry THF, in THF with H_2O content of 0.09 M, and in THF with D_2O content of 0.09 M. Fluorescence quantum yield increase upon D_2O addition while H_2O addition showed a decrease in fluorescence quantum yield. L. A. Huber, P. Mayer, H. Dube: Photoisomerization of Mono-Arylated Indigo and Water-Induced Acceleration of Thermal *cis* to *trans* Isomerization. *ChemPhotoChem.* **2018**, *2*, 458-464. Copyright Wiley-VCH Verlag GmbH & Co. KGaA. Adapted with permission.

solvent	ϕ_{fl} in %	averaged ϕ_{fl} in %	deviation to ϕ_{fl} in dry THF in %
dry THF	0.77		
dry THF	0.77		
dry THF	0.76	0.77	-
dry THF	0.78		
THF with 0.09 M H$_2$O	0.70		
THF with 0.09 M H$_2$O	0.71	0.71	8
THF with 0.09 M D$_2$O	1.00		
THF with 0.09 M D$_2$O	1.01	1.01	31

Rhodamine 101 inner salt **117** (Figure 102) with a fluorescence quantum yield ϕ_{fl} of 0.915[244] in EtOH was used as reference for determination of ϕ_{fl} of mono-arylated indigo **107**. Therefore an UV/vis absorption spectrum of a solution of **117** in EtOH was recorded. After dilution (1:200) a fluorescence spectrum was recorded. For determination of the fluorescence quantum yield of mono-arylated indigo **107** an absorption spectrum and a fluorescence spectrum, with identical settings (same excitation and emission slits and identical excitation wavelength) as used for the measurement of the Rhodamine 101 emission spectrum, were recorded.
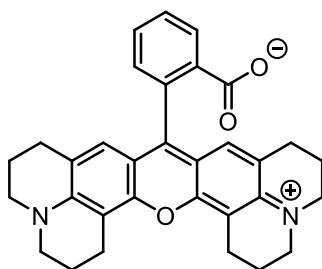
Figure 102:   Rhodamine 101 inner salt **117** was used as a standard reference for fluorescence quantum yield ϕ_{fl} determination.

An UV/vis absorption spectrum of indigo **107** in THF was recorded at a concentration resulting in an OD <1. Consecutively, a fluorescence spectrum was measured with 520 nm excitation wavelength and suitable excitation and emission slit widths.

Equation 22 was used for calculation of the fluorescence quantum yield $\phi_{\text{fl,I}}$ of indigo **107**.

$$\phi_{fl,I} = \frac{F_I f_R n_I^2}{F_R f_I n_R^2} \phi_{fl,R} \quad ^{[245]}$$

(eq. 22)

The subscripts *R* and *I* stand for Rhodamine 101 reference and for indigo **107**, respectively. *F* represents the fluorescence photon flux $q_{\text{P}}(\lambda_{\text{em}})$ at the detector, which is calculated by Equation 23. $f(\lambda_{ex})$ denotes the absorbance at the excitation wavelength, which is given by Equation 24. The refraction index of the solvent is represented by *n*.

$$F = \int_{\lambda_{em1}}^{\lambda_{em2}} q_{p,\lambda}^f (\lambda_{em}) \, d\lambda_{em} = (hc)^{-1} \int_{\lambda_{em1}}^{\lambda_{em2}} \frac{I_u(\lambda_{em})}{s(\lambda_{em})} \lambda_{em} \, d\lambda_{em}$$

(eq. 23)

The photon flux *F* is the integral of the emission $I_{\text{u}}(\lambda_{\text{em}})$ and is multiplied with λ_{em} to account for the energy of emitted photons.[246] After multiplying the obtained corrected emission spectrum $I_{\text{u}}(\lambda_{\text{em}})$ with the photon energy λ_{em}/hc, it is divided by $s(\lambda_{\text{em}})$, the spectral responsivity of the emission correction. In the calculation of the quantum yield the term *hc* and $s(\lambda_{\text{em}})$ cancel each other out.

The fraction of the excitation light, which is absorbed by the chromophore is represented by the absorption factor $f(\lambda_{\text{ex}})$ in Equation 22. $f(\lambda_{\text{ex}})$ is dependent on the absorption $A(\lambda_{\text{ex}})$, which can be calculated by usage of the *Lambert-Beer*-law with the extinction coefficient ε, the concentration *c*, and the optical path length *d*.

$$f(\lambda_{ex}) = 1 - 10^{-A(\lambda_{ex})} = 1 - 10^{-\varepsilon(\lambda_{ex})cd}$$

(eq. 24)

6.6.2 Photoisomerization behaviour

For mono- and di-arylated indigos **107** and **108** a considerable photochromism with reduction of the maximum absorption intensity could be observed after irradiation of their THF solutions. The unique absorption features of substituted indigos allowed for addressability above 600 nm. Similar photochromism is provided by indigos with equally neutral substituents as it is the case for mono-arylated indigos **111** and **114**. In Figure 103 the cuvettes of THF solutions of indigos **107** and **108** before and after irradiation as well as the corresponding absorption spectra are shown. The considerable spectral changes can be followed by the naked eye. Distinctly different absorption spectra with bathochromic shifts for *cis* isomers were also predicted by theoretical calculations and allowed for identification of spectral features derived from individual *cis* or *trans* isomer absorptions. Since the thermal back isomerization happens within minutes for mono- and di-arylated indigos the identification of pure isomer spectra as well as the establishement of the isomeric yields in the pss was not possible. Therefore, quantum yields of the photoisomerization reactions could also not be determined.
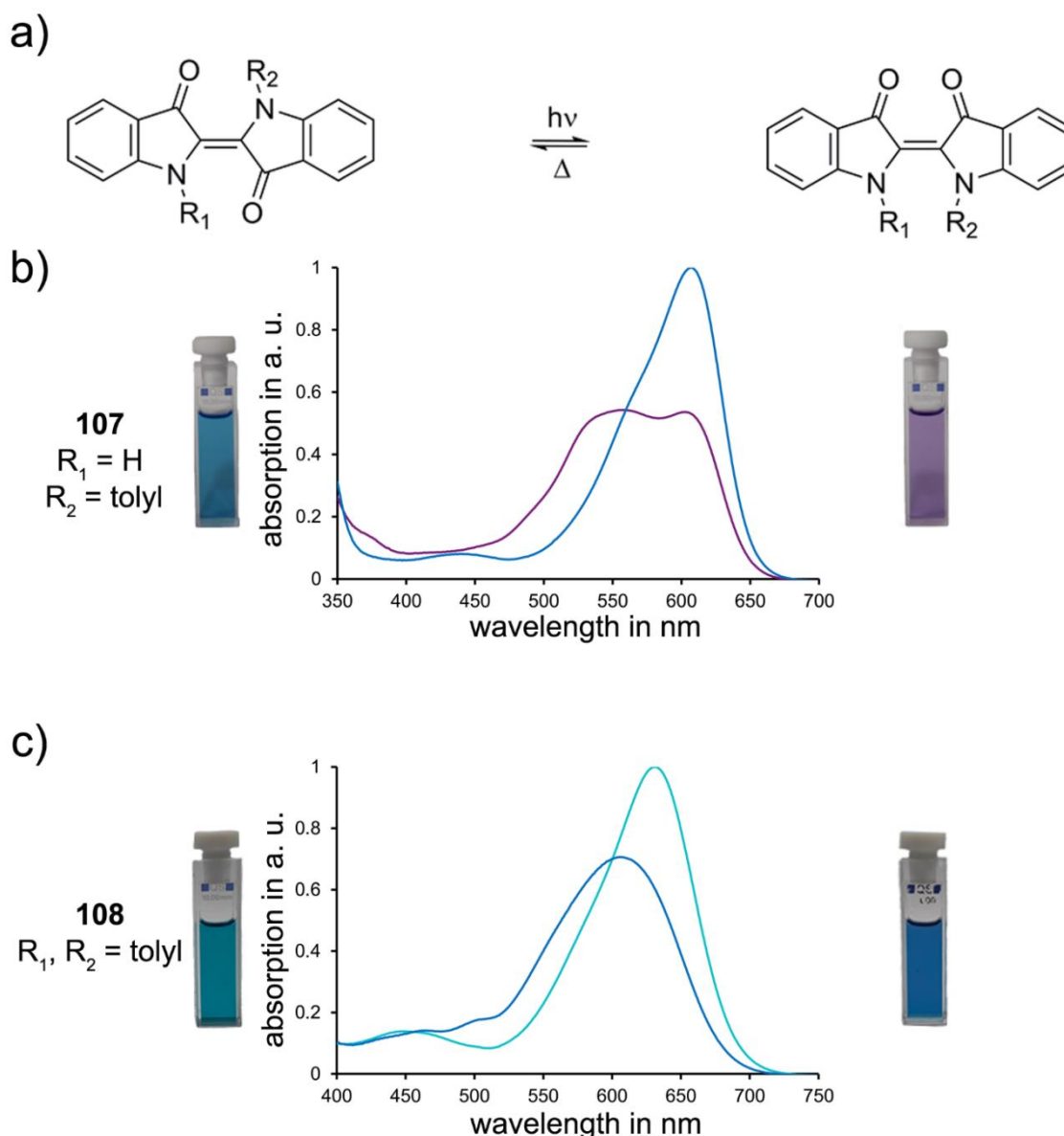
Figure 103: Spectral changes occuring after irradiation of mono- and di-arylated indigo **107** and **108**, respectively a) Illustration of light induced *trans* to *cis* isomerization of substituted indigos with thermal *cis* to *trans* isomerization. b) A solution of mono-arylated indigo **107** in dry THF was irradiated with 625 nm until the pss was reached. The left cuvette contains *trans*-**107** solution, while the right cuvette contains *cis* enriched THF solution obtained after irradiation to the pss. The corresponding absorption spectra are shown in the middle c) A solution of di-arylated indigo **108** in dry THF was irradiated with 660 nm until the pss was reached. The left cuvette contains *trans*-/*cis*-**108** (71/29 ratio) solution in its thermal equilibrium, while the right cuvette contains a *cis* enriched THF solution obtained after irradiation to the pss. The corresponding absorption spectra are shown in the middle. L. A. Huber, P. Mayer, H. Dube: Photoisomerization of Mono-Arylated Indigo and Water-Induced Acceleration of Thermal *cis* to *trans* Isomerization. *ChemPhotoChem.* **2018**, *2*, 458-464. Copyright Wiley-VCH Verlag GmbH & Co. KGaA. Adapted with permission.

For mono-arylated indigo **109** with strong electron donating aryl substitution as well as for indigo **112** with strong electron withdrawing aryl substitution no spectral changes were observed under irradiation conditions. In Table 23 several different solvents were tested for these two derivatives in order to further investigate if the photoisomerization potential is dependent on solvent effects. However, in all cases, no spectral changes could be observed. Since it was already observed for indigos with electronically neutral substituents that water is highly influencing the photoisomerization, water free solvents were tested as well. From the obtained data it cannot be fully excluded at present if the observation of a possible photoisomerization is hampered by a fast thermal *cis* to t*rans* isomerization. Therefore, low temperature ^{1}H NMR spectroscopy with *in situ* irradiation was applied to scrutinize if photoisomerization occurs at decreased temperatures (–40 °C to –60 °C) in THF. No *cis* isomer signals could be observed under these conditions. However, low temperature was only tested in case of THF as solvent. Since deuterated THF generally contains certain amounts of water and much higher concentrations of indigo are used for the irradiation experiments by ^{1}H NMR spectroscopy, it cannot be generally concluded that indigo **109** and **112** are not capable of photoisomerization. Further experiments are needed for investigation of a possible photoisomerization behaviour of **109** and **112** under different conditions.

Table 23: Summary of tested solvents for investigation of the photoisomerization potential of indigos **109** and **112**. L. A. Huber, P. Mayer, H. Dube: Photoisomerization of Mono-Arylated Indigo and Water-Induced Acceleration of Thermal *cis* to *trans* Isomerization. *ChemPhotoChem.* **2018**, *2*, 458-464. Copyright Wiley-VCH Verlag GmbH & Co. KGaA. Adapted with permission.

solvent	indigo		irradiation wavelength [nm]
	109	**112**	
n-hexane [a]	no isomerization	no isomerization	625 (**109, 112**)
toluene [b]	no isomerization	no isomerization	625 (**109**), 660 (**112**)
THF [b]	no isomerization	no isomerization	625 (**109**), 660 (**112**)
1,4-dioxane [c]	no isomerization	no isomerization	625 (**109**), 660 (**112**)
acetonitrile [b]	no isomerization	no isomerization	625 (**109, 112**)
CH$_2$Cl$_2$ [b,d]	no isomerization	no isomerization	625 (**109**), 660 (**112**)
DMF [b]	no isomerization	no isomerization	625 (**109**), 660 (**112**)
MeOH [b]	no isomerization	no isomerization	625 (**109**), 660 (**112**)

[a] spectroscopic grade

[b] stored over molecular sieve 4Å

[c] freshly opened, anhydrous grade

[d] filtered over Al$_2$O$_3$ (neutral) straight before measurement

In *i*-hexane solutions, photoisomerization was observed for all investigated di-arylated indigos **108**, **110**, and **116**. For indigo **110**, no photoisomerization in CH_2Cl_2 and dry THF was found. Figure 104 depicts the maximum spectral changes achieved by irradiation. In case of indigo **116** 680 nm were used for irradiation while indigo **108** and **116** were irradiated with 660 nm.
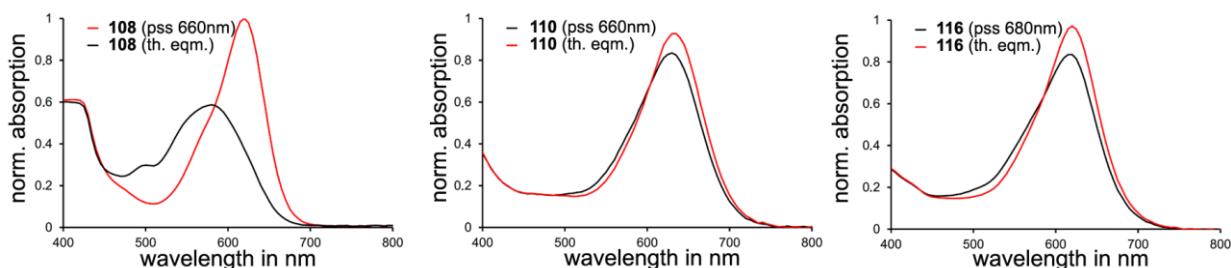
Figure 104: Absorption spectra of *i*-hexane solutions of di-arylated indigos **108**, **110**, and **116** in thermal equilibrium at ambient temperature (red) and after irradiation (black) with 660 nm (**108** and **110**) or 680 nm (**116**).

For di-arylated indigo **108** pronounced spectral changes were recorded after irradiation in comparison to indigos **110** and **116**. It can thus be assumed that the yield of the *cis* isomer obtained in the photoreaction is also larger in case of indigo **108**. Since the thermal *cis* to *trans* isomerization is fast and happens within minutes, determination of the pure isomer spectra was not feasible. Therefore, no isomeric yields in the pss could be obtained for di-arylated indigos by absorption spectroscopy. The thermal recoveries and the kinetic analysis for indigos **108**, **110**, and **116** in *i*-hexane can be found in chapter 4.7.2.

For mono-arylated indigos **107**, **111**, **113**, and **114** photoisomerization was induced by irradiating dry THF solutions with 625 nm light. In Figure 105 the observed spectral changes after irradiation are shown. In all cases hypsochromic shifts of the absorptions are accompanied by substantial loss in intensities. Again the occurring absorption features can be interpreted as increased concentration of *cis* isomer in solution. The hypsochromism upon irradiation confirmed the predictions of the theoretical calculations, which determined a blue-shifted absorption of the *cis* isomer for indigo **107** and the *trans* isomers to be the thermodynamic minima for all mono-arylated indigos. Absorption spectra were calculated for **107** exemplarily and it can be assumed that other mono-arylated indigos exhibit consistent photochromic behavior. Pronounced absorption changes were found for indigos **107** and **111**. Indigo **113** with substituted thiophene moiety showed minor spectral changes upon irradiation. Also in case of indigo **114** less pronounced absorption changes can be observed upon irradiation. From the absorption spectra no isomeric yield in the pss could be obtained as well as no pure isomer spectra since thermal

cis to *trans* isomerization happens on minutes time scale at ambient temperature. For investigation of isomeric yields low temperature ^{1}H NMR spectroscopy with *in situ* irradiation was performed.
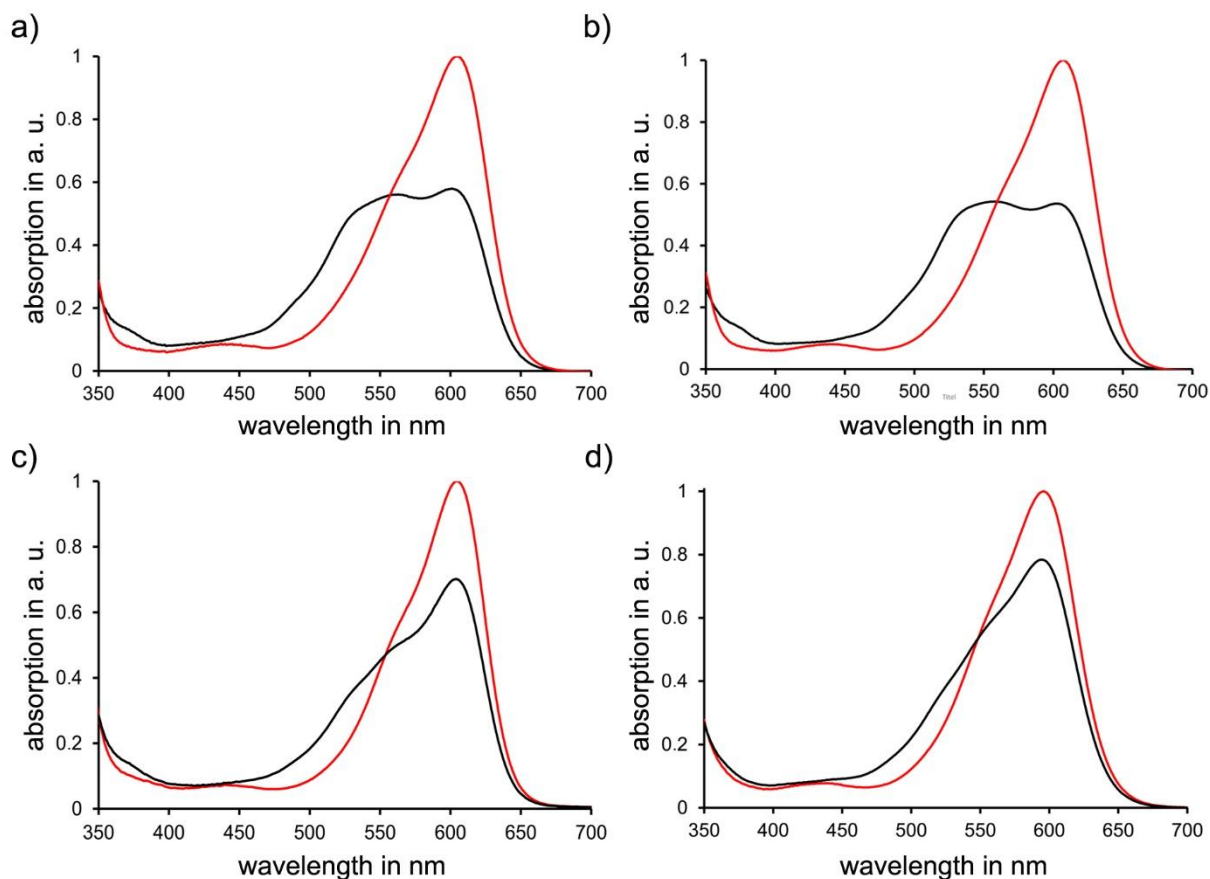
Figure 105:   Absorption spectra of mono-arylated indigos in dry THF solutions before (red) and after (black) irradiation with 625 nm. The red spectra corresponding to 100% *trans* isomer, which was determined by ^{1}H NMR spectroscopy. Black spectra were obtained after reaching the pss a) Indigo **111**. b) Indigo **107**. c) Indigo **114**. d) Indigo **113**.

6.6.3   Isomeric yields in the pss of indigos 107, 108, and 111

Fast thermal *cis* to *trans* isomerization at ambient temperatures impeded physical separation of *cis* and *trans* isomers as well as recording of the corresponding absorption spectra of pure *cis* isomers as well as pure *trans* isomer in case of di-arylated indigo **108**. Furthermore, irradiation experiments performed to determine the isomer composition changes by ^{1}H NMR spectroscopy at ambient temperature was also hampered by thermal instability of *cis*-configured indigos. Therefore, also the disentanglement of the absorption spectra via determination of the underlying isomeric compositions after irradiation were not possible at ambient temperatures. For circumvention of thermal limitations for determination of isomeric ratios in the pss low temperature ^{1}H NMR spectroscopy was performed with an *in situ* irradiation technique. Thus, sample irradiation as well as spectrum recording can be performed at constantly low temperatures without the necessity for sample transfer and warming up of the solution. Additionally, for di-arylated indigo **108** a sample solution was irradiated while keeping the sample containing NMR tube in a cooling bath at –60 °C. Freezing the sample solution after irradiation with rapid transfer to the precooled NMR device allowed for determination of the isomeric ratio in the pss for indigo **108**. This more complicated method was performed since no glass fiber coupled high power LED with 660nm was available for *in situ* irradiation. In Figures 106-109 formation of *cis* isomers of mono-arylated indigos **107** and **111** as well as di-arylated indigo **108** under irradiation conditions followed by ^{1}H NMR spectroscopy are shown. Irradiation was stopped when the pss was reached. Rising signals of the *cis* isomers are highlighted in red. A moderate isomeric yield of 36% and 38% in the pss could be obtained at –60 °C for mono-arylated indigos **111** and **107**. For di-arylated indigo **108** a good isomeric yield of 72% *cis* isomer content under 660 nm irradiation (–40 °C) was reached and only 43% *cis* isomer content was found under 625 nm (–60 °C) irradiation. The different ratios of isomer content can most likely be attributed to the more suitable 660nm wavelength of irradiation, because spectral overlap with the *cis* isomer is diminished at longer wavelengths. A temperature effect however cannot be fully excluded.
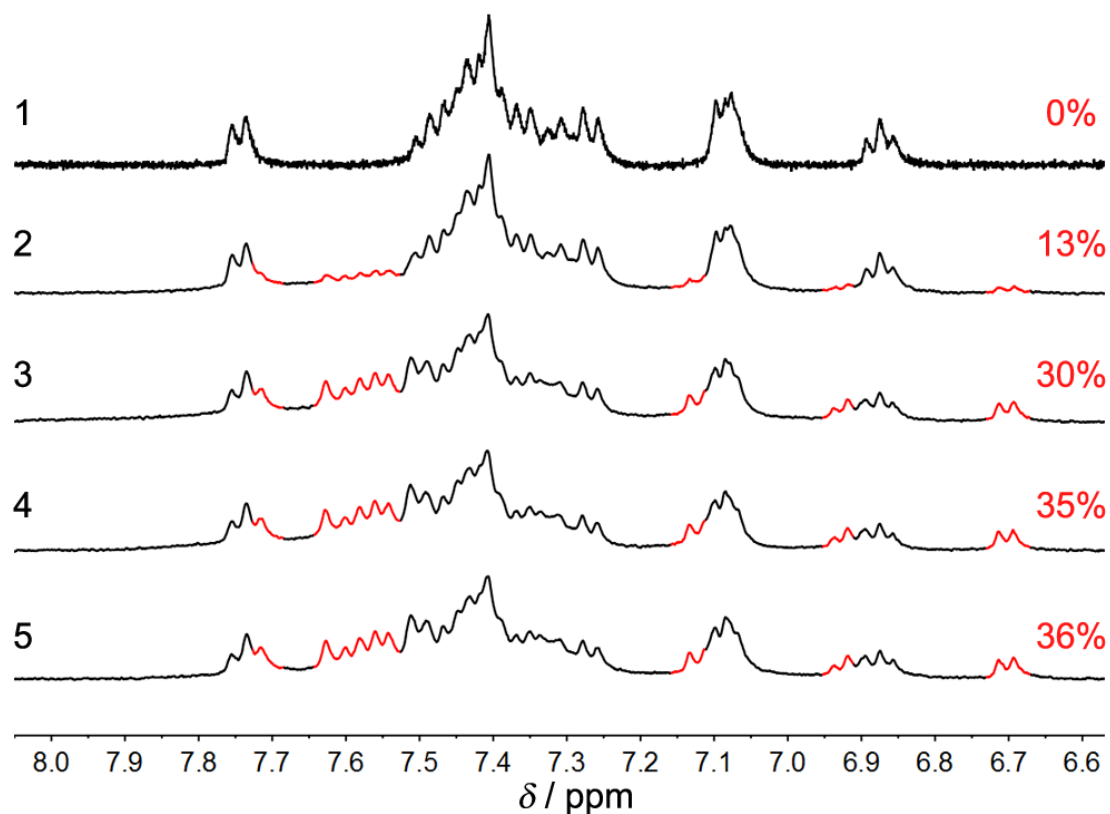
Figure 106: A 3.2 mM solution of *trans-N*-phenyl indigo **111** was irradiated with 625 nm and changes in isomeric composition were followed by ^{1}H NMR spectroscopy (400 MHz, THF-d_8, –60 °C). The aromatic part of the spectrum is shown exemplarily and signals of *cis*-**111** are highlighted in red. 1: Only the signals of *trans*-**111** can be observed. 2: Spectrum obtained after 10 min of irradiation. 13% *cis*-**111** was generated. 3: 30% *cis* isomer content was reached after 60 min of irradiation. 4: 35% of *cis*-**111** can be observed after 90 min of irradiation. 5: 35% *cis* isomer yield in the pss after irradiating the sample for 110 min was obtained. Signals of increasing *cis* isomer and decreasing *trans* isomer are partly overlapping. At 7.5-6.6 ppm as well as at 6.7 ppm the *cis*-**111** derived signals can be clearly observed. No *cis*-**111** N-H signal could be identified. L. A. Huber, P. Mayer, H. Dube: Photoisomerization of Mono-Arylated Indigo and Water-Induced Acceleration of Thermal *cis* to *trans* Isomerization. *ChemPhotoChem.* **2018**, *2*, 458-464. Copyright Wiley-VCH Verlag GmbH & Co. KGaA. Adapted with permission.
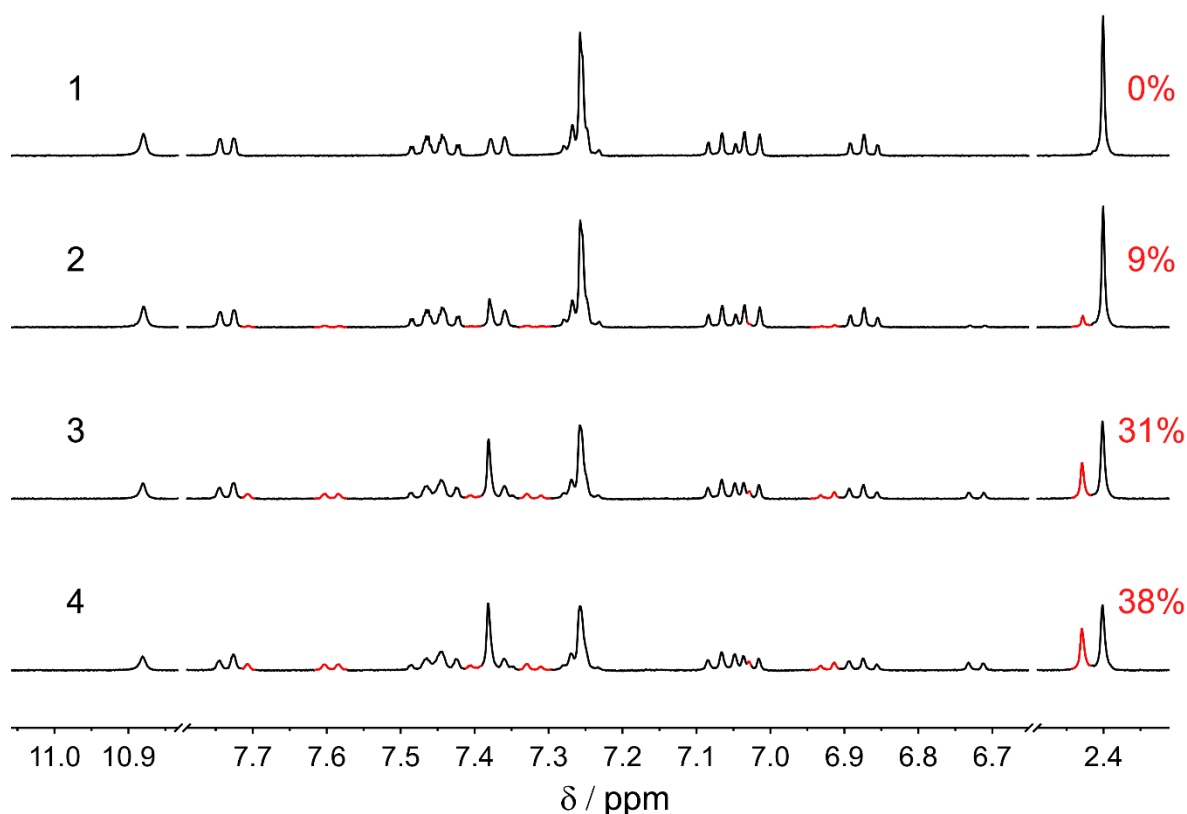
Figure 107: A 3.2 mM solution of *trans-N*-tolyl indigo **107** was irradiated with 625 nm and changes in the isomeric composition were followed by ^{1}H NMR spectroscopy (400 MHz, THF-d_8, –60 °C). Signals of *cis*-**107** are highlighted in red.1: Only the signals of *trans*-**107** can be observed. 2: Spectrum obtained after 9 min of irradiation. 9% *cis*-**107** was generated. 3: 31% *cis* isomer content was reached after 30 min of irradiation. 4: 38% of *cis*-**107** can be observed after 110 min of irradiation and the pss was reached at this time. Signals of increasing cis isomer and decreasing *trans* isomer are partly overlapping. At 7.6 ppm as well as at 2.4 ppm the *cis*-**107** derived signals can be clearly observed. No *cis*-**107** N-H signal could be identified. L. A. Huber, P. Mayer, H. Dube: Photoisomerization of Mono-Arylated Indigo and Water-Induced Acceleration of Thermal *cis* to *trans* Isomerization. *ChemPhotoChem.* **2018**, *2*, 458-464. Copyright Wiley-VCH Verlag GmbH & Co. KGaA. Adapted with permission.
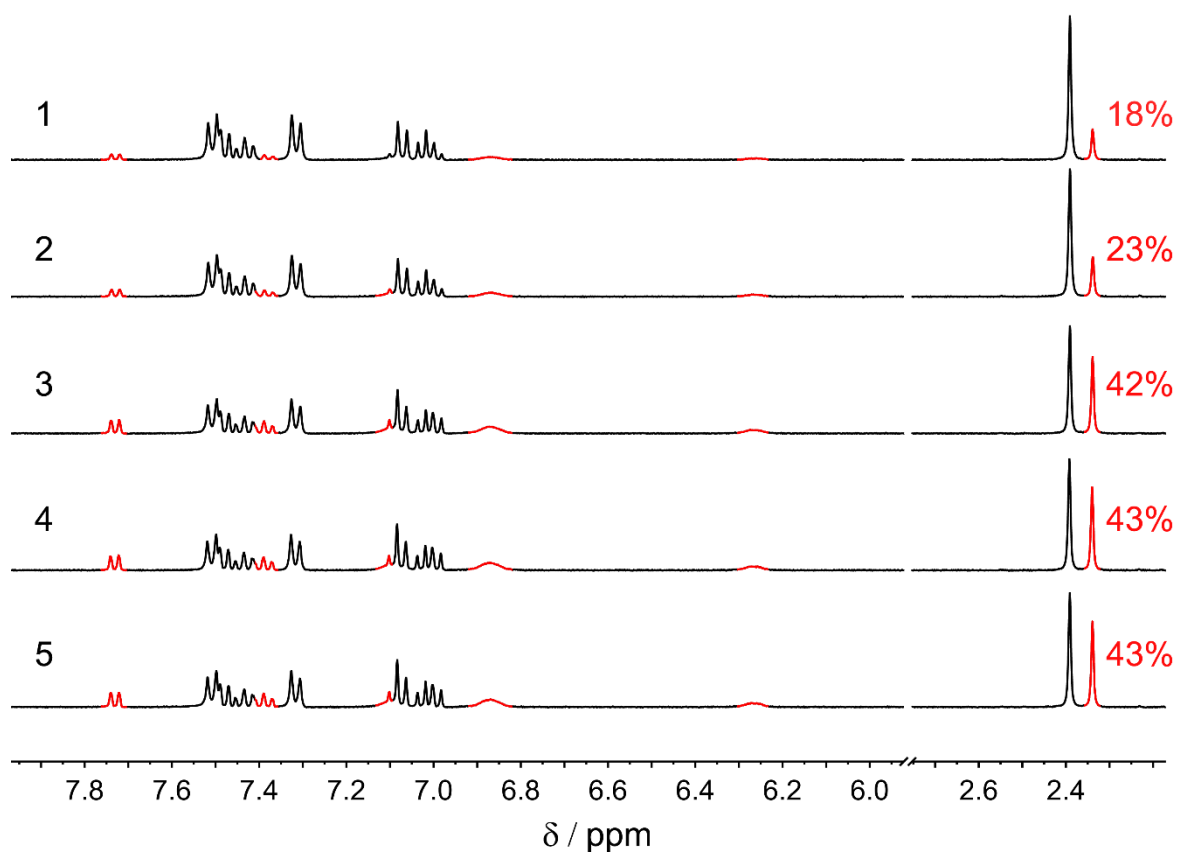
Figure 108:   A 2.5 mм solution of *N,N'*-di(*p*-tolyl) indigo **108** was irradiated in situ with 625 nm and the progress of photoisomerization was recorded by ¹H NMR spectroscopy at –60 °C. 1: 18% *cis* isomer content in the thermal equilibrium. 2: After 5 min of irradiation 23% *cis* isomer content was obtained. 3: After 50 min of irradiation 42% *cis* isomer content was obtained. 4: After 80 min of irradiation 43% *cis* isomer content was obtained. 1: After 95 min of irradiation 43% *cis* isomer content was confirmed to be the isomeric yield in the pss.
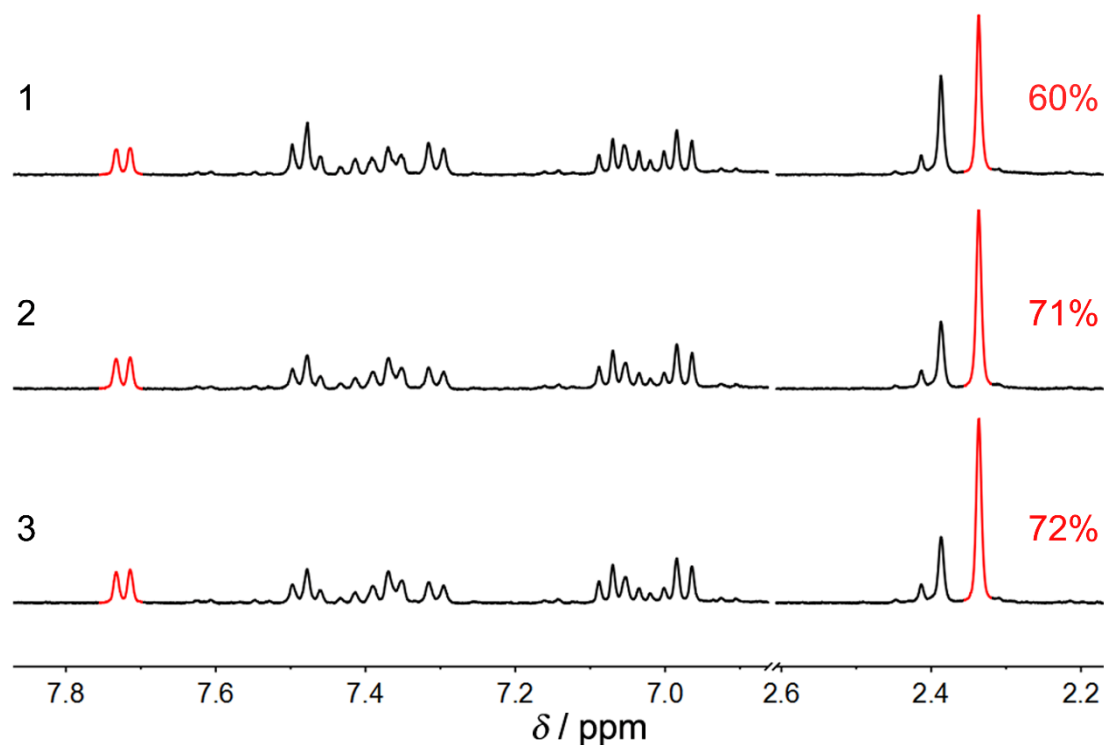
Figure 109:   A solution of *N,N'*-di(*p*-tolyl) indigo **108** was irradiated with 660 nm light while the sample containing NMR tube was kept in a cooling bath at –40 °C. Afterwards the isomeric composition was recorded by ^{1}H NMR spectroscopy (400 MHz, THF-d_8, –40 °C). Rapid transfer of the NMR tube to the precooled NMR device ensured the suppression of thermal back isomerization. The aromatic part of the spectrum is shown exemplarily and signals of *cis*-**108** are highlighted in red.1: After 30 min of irradiation 60% *cis* isomer content was obtained. 2: Spectrum obtained after 60 min of irradiation. 71% *cis*-**108** was generated. 3: 72% *cis* isomer content was reached in the pss after 90 min of irradiation. *Cis/trans* isomeric ratio can be nicely observed at the methyl group signals at 2.3-2.4 ppm. L. A. Huber, P. Mayer, H. Dube: Photoisomerization of Mono-Arylated Indigo and Water-Induced Acceleration of Thermal *cis* to *trans* Isomerization. *ChemPhotoChem.* **2018**, *2*, 458-464. Copyright Wiley-VCH Verlag GmbH & Co. KGaA. Adapted with permission.

6.7 Thermal stability of *cis* isomers

A reduced thermal stability of metastable *cis* isomers of mono- and di-arylated indigos was observed in comparison to the HTI-based molecular motors, which is displayed in thermal back isomerization at ambient temperature after irradiation. Therefore, it was possible to record the thermal decay of the photogenerated *cis* isomers unambiguously by UV/vis spectroscopy. In Figure 110 the thermal recoveries of indigos **111**, **107**, **113** and **108** in dry THF at ambient temperatures are summarized exemplarily.
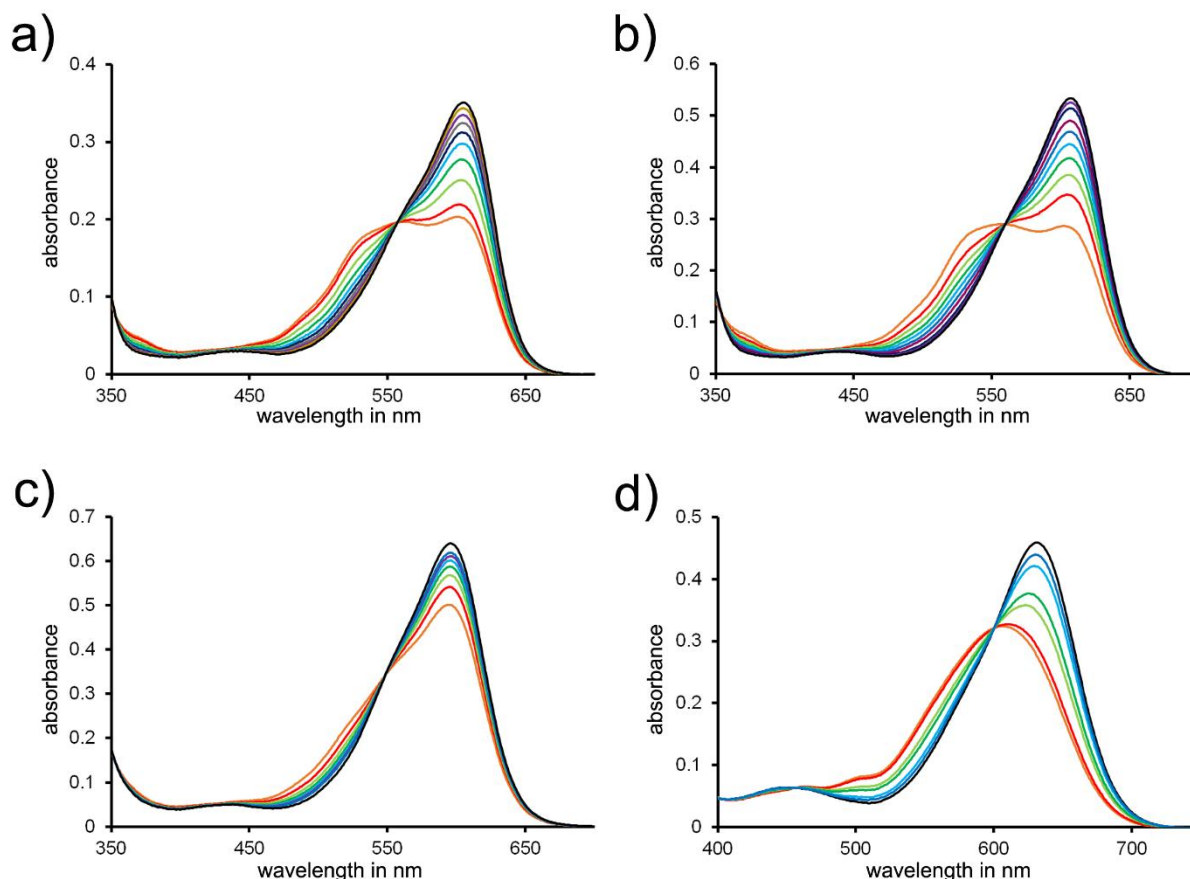
Figure 110:   Thermal recoveries of stable *trans* isomers observed via absorption spectroscopy after irradiation (625 nm for mono-arylated indigos **107**, **111**, and **113** and 660 nm for di-arylated indigo **108**) of indigo solutions in dry THF at ambient temperatures. a) *Cis* isomer of *N*-phenyl indigo **111** decays within 7 min. Spectra were recorded in 50 s time intervals. b) *Cis* isomer of *N*-(*p*-tolyl) indigo **107** decays within 20 min at 25 °C. Spectra were recorded in 1 min time intervals. c) *Cis* isomer of *N*-(thiophen-2-yl) indigo **113** decays within 12 min. Spectra were recorded in 2 min time intervals. d) *Cis* isomer of *N,N'*-(*p*-tolyl) indigo **108** decays within 10 min at 24 °C. Black spectrum was recorded before irradiation. L. A. Huber, P. Mayer, H. Dube: Photoisomerization of Mono-Arylated Indigo and Water-Induced Acceleration of Thermal *cis* to *trans* Isomerization. *ChemPhotoChem.* **2018**, *2*, 458-464. Copyright Wiley-VCH Verlag GmbH & Co. KGaA. Reprinted with permission.

6.7.1 Water induced acceleration of *cis* to *trans* isomerization

For mono-arylated indigo **107** it was found that the speed of thermal *cis* to *trans* isomerization was greatly influenced by water addition to the solvent. Therefore, a series of kinetic measurements was performed with increasing water content of an indigo **107** solution in THF. For comparison, a THF solution of di-arylated indigo **108** with increased water content was investigated, too. In Figures 111 to 114 the kinetic analyses of the thermal *cis* to *trans* isomerizations of mono- and di-arylated indigo and their water content dependencies are illustrated. The absorption changes over time were recorded at 605 nm for mono-arylated indigo **107** and at 630 nm for di-arylated indigo **108** using UV/vis spectroscopy. The initial amounts of *cis* isomers was arbitrarily set to 100% for convenience. *Cis* isomer was accumulated by irradiation with 625 nm for **107** and with 660 nm for **108** until the pss was reached prior to kinetic measurements. Spectral changes directly represent the increase of *trans* isomer as well as decrease of *cis* isomer concentration over time. The relative absorption changes were calculated according to the following equation:

$$relative\ absorption\ change = \frac{absorption\ at\ t_x - absorption\ at\ t_{start}}{absorption\ at\ t_{end} - absorption\ at\ t_{start}} \qquad \text{(eq. 25)}$$

With t_x as the time point of measurement, t_{start} as the time point of the first measurement and t_{end} as the time point of the last measurement. For the relative absorption change the initial amount of *cis* isomer content was set to 100% arbitrarily. Thus, the *cis* isomer content can be calculated by applying Equation 26:

$$\%\ of\ cis\ isomer = (1 - relative\ absorption\ change) * 100 \qquad \text{(eq. 26)}$$

A first order kinetic analysis was performed according to the following equation:

$$\ln(\%cis_0 / \%cis_t) = kt \qquad \text{(eq. 27)}$$

The first order rate constant is represented by k and t as the elapsed time. In Table 24 the original measurement data of a kinetic analysis is shown exemplarily.

Table 24:   Kinetic data describing the thermal *cis* to *trans* isomerization of indigo **107** in the dark in THF with a water content of 0.37 M water. L. A. Huber, P. Mayer, H. Dube: Photoisomerization of Mono-Arylated Indigo and Water-Induced Acceleration of Thermal *cis* to *trans* Isomerization. *ChemPhotoChem.* **2018**, *2*, 458-464. Copyright Wiley-VCH Verlag GmbH & Co. KGaA. Reprinted with permission.

Absorption monitored at 605 nm	relative changes	percentage of *cis* isomer (*%cis*)	ln (*%cis $_0$* / *%cis $_t$*)	t in s
0.298646539	0	100	0	0
0.336151511	0.308278831	69.17211689	0.36857234	12
0.358696461	0.493591089	50.64089106	0.680410812	24
0.375326991	0.630288714	36.97112857	0.995032887	36
0.386541486	0.722468263	27.75317368	1.281819986	48
0.394570679	0.788465651	21.15343485	1.553367889	60
0.400711805	0.838943738	16.1056262	1.826001522	72
0.405684382	0.879816727	12.01832734	2.118737423	84
0.409712106	0.912923328	8.707667176	2.440966264	96
0.412887752	0.93902612	6.097387954	2.797309711	108
0.415084004	0.95707861	4.292139018	3.148384972	120
0.416775823	0.970984813	2.90151873	3.539935886	132
0.418063343	0.981567814	1.843218593	3.993656907	144
0.418847561	0.988013837	1.198616308	4.424002371	156
0.419568777	0.993942003	0.605799728	5.106376016	168
0.419706792	0.995076438	0.492356236	5.313722953	180
0.42021957	0.999291315	0.070868512	7.252099243	192
0.420285374	0.999832199	0.016780146	8.692729045	204
0.420305789	1	0	#DIV/0!	216

a)

b)

c)
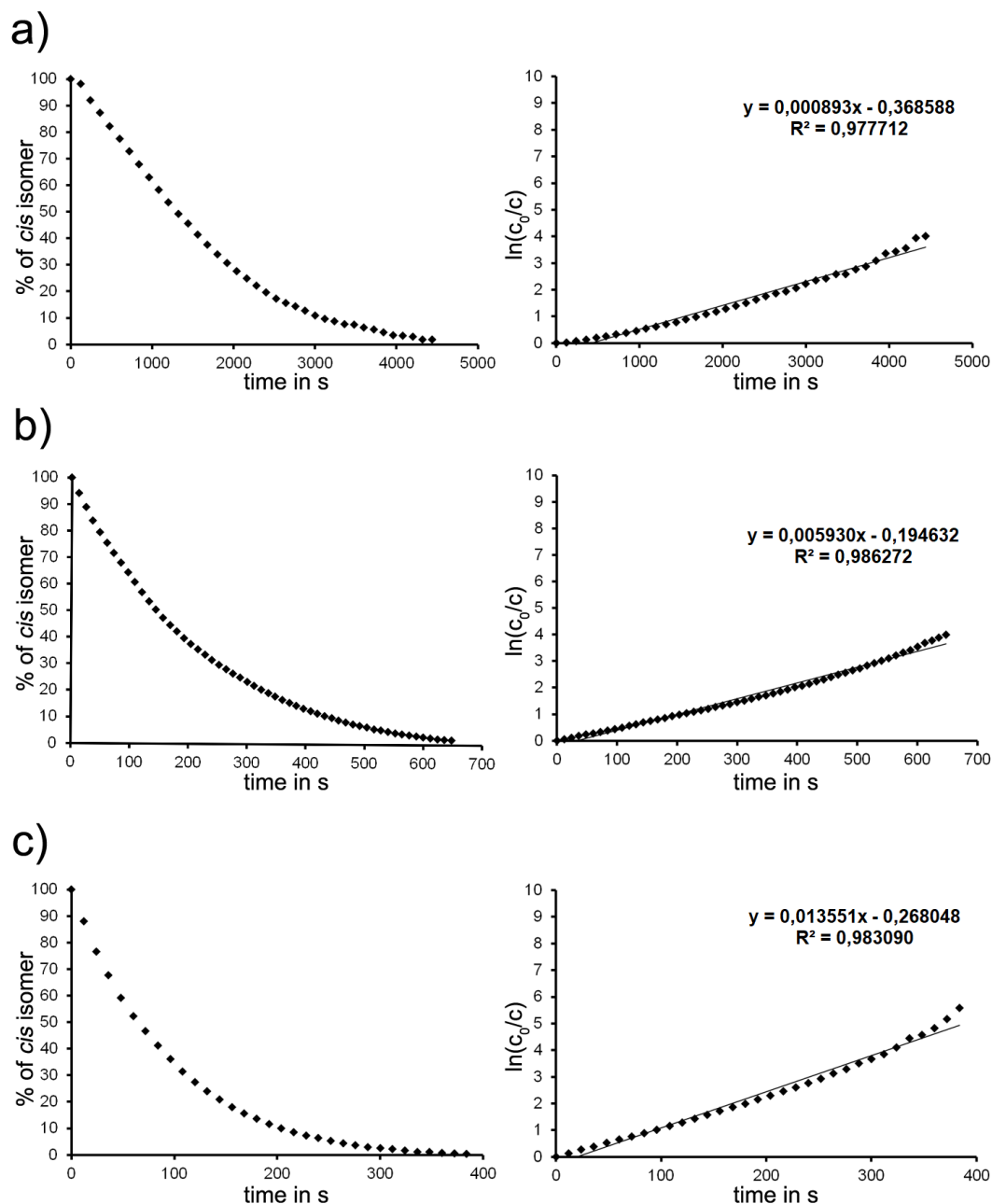
Figure 111:   The thermal decays (left graphs) of the metastable *cis* isomers of mono-arylated indigo **107** at 23.5 °C in THF with increasing water content. Good agreement of the first order kinetic analysis (right graphs) with experimentally assessed absorption decay was found. a) Decay of *cis* isomer in dry THF. The residual water content was set to 0 м. b) Decay of *cis*-**107** in THF with 0.09 м water. c) Decay of *cis*-**107** in THF with 0.18 м water. L. A. Huber, P. Mayer, H. Dube: Photoisomerization of Mono-Arylated Indigo and Water-Induced Acceleration of Thermal *cis* to *trans* Isomerization. *ChemPhotoChem.* **2018**, *2*, 458-464. Copyright Wiley-VCH Verlag GmbH & Co. KGaA. Adapted with permission.

Figure 112: The thermal decays (left graphs) of the metastable *cis* isomers of mono-arylated indigo **107** at 23.5 °C in THF with increasing water content. Good agreement of the first order kinetic analysis (right graphs) with experimentally assessed absorption decay was found. a) Decay of *cis*-**107** in THF with 0.37 M water. b) Decay of *cis*-**107** in THF with 0.73 M water. c) Decay of *cis*-**107** in THF with 1.44 M water. L. A. Huber, P. Mayer, H. Dube: Photoisomerization of Mono-Arylated Indigo and Water-Induced Acceleration of Thermal *cis* to *trans* Isomerization. *ChemPhotoChem.* **2018**, *2*, 458-464. Copyright Wiley-VCH Verlag GmbH & Co. KGaA. Adapted with permission.
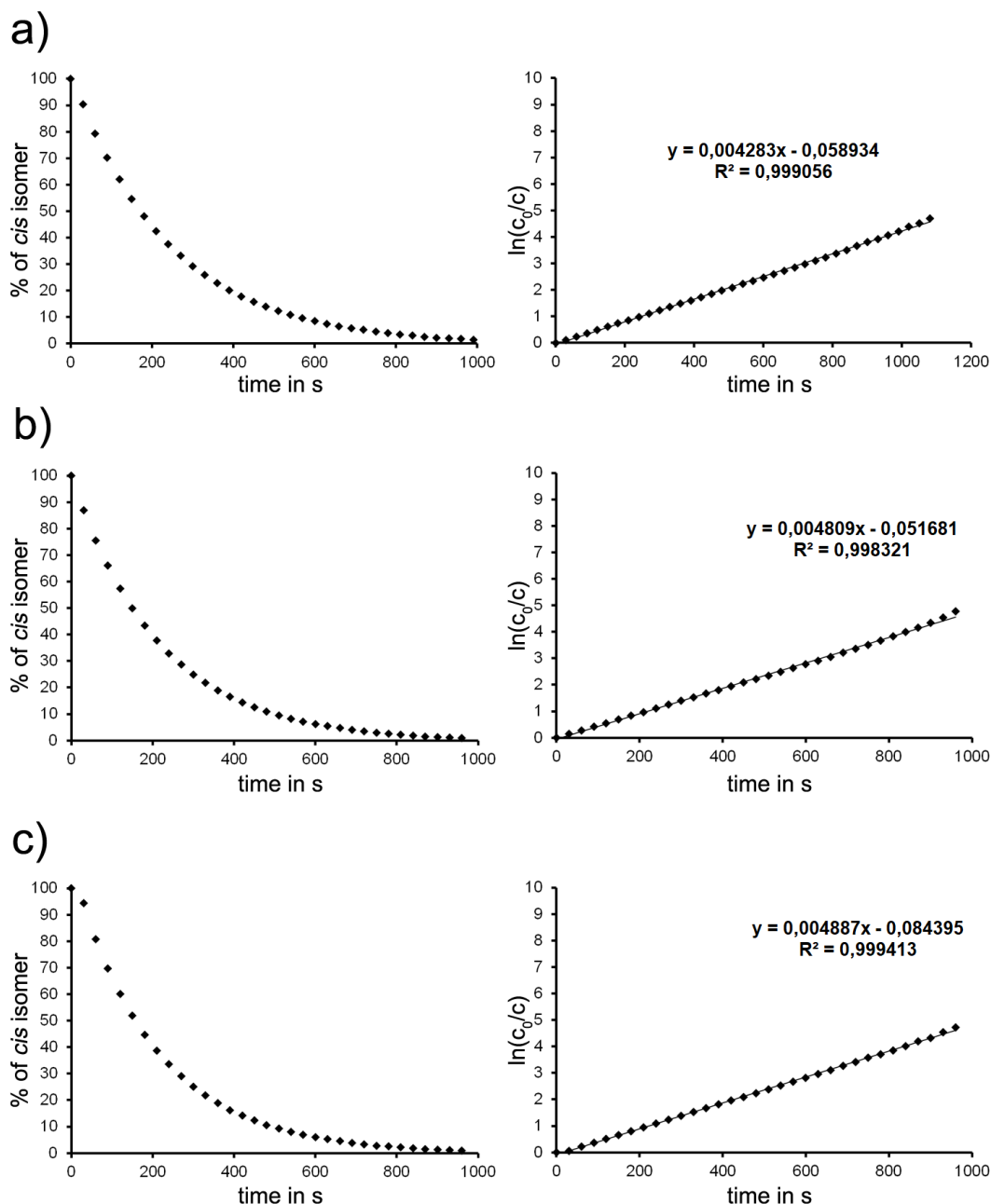
Figure 113: The thermal decays (left graphs) of the metastable *cis* isomers of di-arylated indigo **108** at 23.5 °C in THF with increasing water content. Good agreement of the first order kinetic analysis (right graphs) with experimentally assessed absorption decay was found. a) Decay of *cis* isomer in dry THF. The residual water content was set to 0 ʍ. b) Decay of *cis*-**108** in THF with 0.09 ʍ water. c) Decay of *cis*-**108** in THF with 0.18 ʍ water. L. A. Huber, P. Mayer, H. Dube: Photoisomerization of Mono-Arylated Indigo and Water-Induced Acceleration of Thermal *cis* to *trans* Isomerization. *ChemPhotoChem.* **2018**, *2*, 458-464. Copyright Wiley-VCH Verlag GmbH & Co. KGaA. Adapted with permission.

Figure 114: The thermal decays (left graphs) of the metastable *cis* isomers of di-arylated indigo **108** at 23.5 °C in THF with increasing water content. Good agreement of the first order kinetic analysis (right graphs) with experimentally assessed absorption decay was found. a) Decay of *cis*-**108** in THF with 0.37 M water. b) Decay of *cis*-**108** in THF with 0.73 M water. c) Decay of *cis*-**108** in THF with 1.44 M water. L. A. Huber, P. Mayer, H. Dube: Photoisomerization of Mono-Arylated Indigo and Water-Induced Acceleration of Thermal *cis* to *trans* Isomerization. *ChemPhotoChem.* **2018**, *2*, 458-464. Copyright Wiley-VCH Verlag GmbH & Co. KGaA. Adapted with permission.
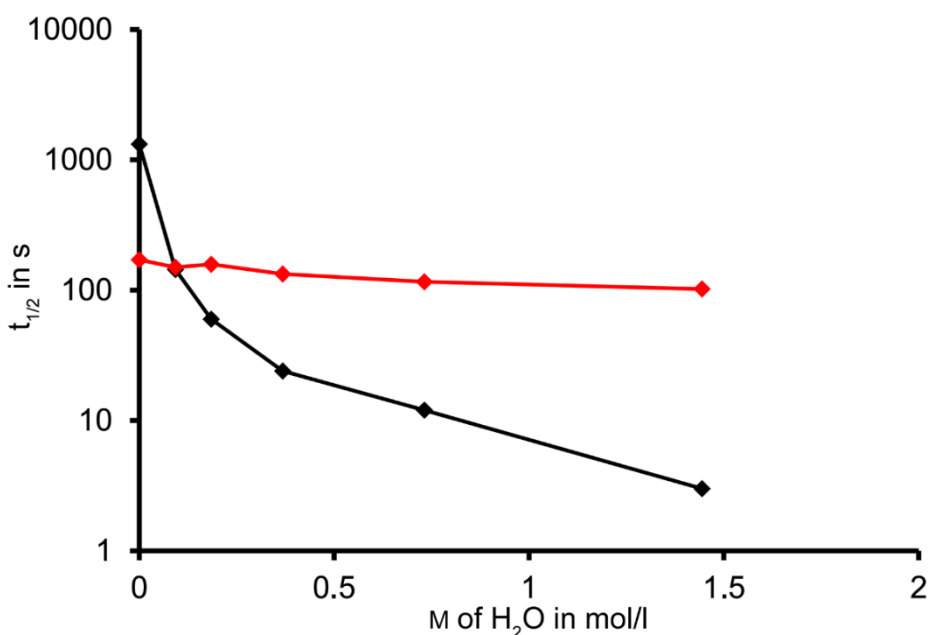
Figure 115: The half-lives of metastable *cis* isomers of mono-arylated indigo **107** (black) and di-arylated indigo **108** (red) at 23.5 °C in THF solutions containing increasing amounts of water (x-axis). A strong acceleration of the thermal decay of the *cis* isomer of mono-arylated indigo **107** with increased concentration of water in THF can be observed, while di-arylated indigo **108** shows only little speed increase. Note that the y-axis is logarithmic L. A. Huber, P. Mayer, H. Dube: Photoisomerization of Mono-Arylated Indigo and Water-Induced Acceleration of Thermal *cis* to *trans* Isomerization. *ChemPhotoChem.* **2018**, *2*, 458-464. Copyright Wiley-VCH Verlag GmbH & Co. KGaA. Adapted with permission.

From the kinetic measurements performed in THF solutions containing increasing amounts of water (summarized in Figure 115) it can be clearly observed that the speed of the thermal *cis* to *trans* isomerization is highly dependent on the water content for mono-arylated indigo **107**. Thus, addition of 5 µl of water to 3 mL of an indigo **107** solution in THF (0.09 M water content) caused an almost 10-fold speed increase of the thermal recovery of the *trans* isomer. Further water addition delivered a minimal half-life of 3 s at a water concentration of 1.44 M. For di-arylated indigo **108**, however, only minor acceleration could be observed. This could likely be explained by the general increase of overall solvent polarity or more specific (hydrogen bonding) interactions with the carbonyl groups resulting from the water addition. On the basis of these results a direct influence of the N-H group of indigo **107**, which is replaced by an N-Aryl group in case of indigo **108** is most likely be responsible for the strong water sensitivity of the kinetic stability of *cis*-**107**. Further confirmation of a specific interaction with the N-H group can be derived from deuteration experiments. As already discussed in chapter 4.5.1 fast and quantitative exchange of the N-bound hydrogen was observed by ^{1}H NMR spectroscopy if D_2O was added to the indigo **107** solution. Next it was scrutinized if D_2O addition also influences the thermal decay of the *cis* isomer. Indeed it was found that addition of the same amount of D_2O in comparison to

water (as it was used in a control experiment) leads to a five-fold decelerated decay compared to the control experiment with water. In Figure 116 the decay kinetics of the deuteration experiments are illustrated.
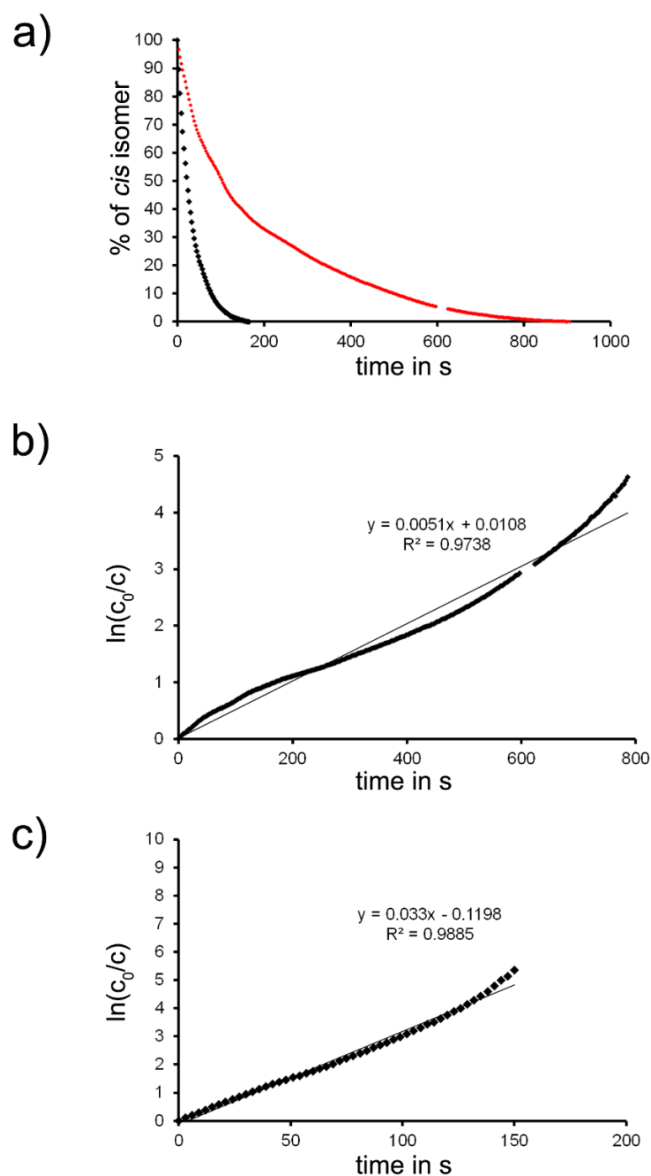
Figure 116:   Comparison of the thermal decays of *cis*-**107** after D_2O (red) and H_2O (black) addition at 24 °C. D_2O/H_2O containing THF solutions of indigo **107** were irradiated with 625 nm to the pss and the thermal recovery was monitored at 605 nm by UV/vis spectroscopy. a) Thermal decay of *cis*-**107** in THF with a H_2O content of 0.18 M (black) and thermal decay of *cis*-**107** with D_2O content of 0.18 M (red) versus elapsed time. b) First order kinetic analysis of thermal *cis* to *trans* isomerization of **107** in THF with a D_2O content of 0.18 M. Good agreement with experimental data was observed. c) First order kinetic analysis of thermal *cis* to *trans* isomerization of **107** in THF with a H_2O content of 0.18 M. Good agreement with experimental data was observed. L. A. Huber, P. Mayer, H. Dube: Photoisomerization of Mono-Arylated Indigo and Water-Induced Acceleration of Thermal *cis* to *trans* Isomerization. *ChemPhotoChem.* **2018**, *2*, 458-464. Copyright Wiley-VCH Verlag GmbH & Co. KGaA. Reprinted with permission.

The observed isotope effect can be explained by decreased donating power of the nitrogen atom if bound to a deuterium instead of hydrogen, which consequently leads to less reduction of the central double bond character. This can be traced back either to an increased bond strength between nitrogen and deuterium and decreased acidity or to reduced intra- and intermolecular hydrogen bonding in case of deuteration of the nitrogen. In summary, the minor effects of water on the kinetic stability of di-arylated *cis*-**108** in combination with the observations made in the deuteration experiments strongly suggest that the N-H group of mono-arylated indigos is responsible for the high sensitivity of the kinetic stability of *cis*-**107** towards the water content in the solution.

6.7.2   Thermal stabilities of the *cis* isomers of di-arylated indigos 108, 110 and 116

Direct comparison of the thermal stability of *cis* isomers of di-arylated indigos **108**, **110**, and **116** was undertaken in *i*-hexane. In Figure 117 the thermal conversion of metastable *cis* isomers versus elapsed time as well as the logarithmic plots of the first order kinetic analysis of this process for di-arylated indigos **108**, **110**, and **116** are illustrated. Thermal energy barriers were determined to be 21.0 kcal·mol^{-1} for **108**, 20.1 kcal·mol^{-1} for **110**, and 21.8 kcal·mol^{-1} for **116**. Generally a good agreement of the experimental data with the first order kinetic treatment was found. The increase of the thermal isomerization speed of indigo **110**, bearing strong electron donating aryl substituents in comparison to indigo **108** with neutral substituents, can most likely be traced back to the reduced double bond character of the central bond caused by the increased donating power of the aryl substituted nitrogen atoms. Indigo **116** with electron withdrawing and electron donating aryl substituents exhibits the highest energy barrier for thermal *cis* to *trans* isomerization of all three investigated indigos. A mechanistic explanation could be the increased electron deficiency of one nitrogen atom caused by the benzonitrile moiety. Consequently the donating power of this nitrogen atom is reduced, which increases the double bond character of the central bond and hence the energy barrier for thermal isomerization. It seems that this effect could not be fully compensated by the opposing effects of the electron donating *p*-aniline moiety, leading to a higher energy barrier as it is the case for indigo **108** with neutral substituents. Thus, dominance of electron withdrawing effects over electron donating effects could be considered. An alternative explanation could be a positive polar aromatic interaction of the two aryl substituents in the *cis* conformation. This would results in a stabilization of the *cis* isomer, while consecutively increasing the energy barrier of thermal *cis* to *trans* isomerization. ^{1}H NMR spectroscopic analysis delivered an equilibrium content of 54% / 46% *cis* isomer of **116** at ambient temperature, while **108** and **110** show only 30% *cis* isomer content in CD$_2$Cl$_2$ (for comparison *N,N'*-di-(*p*-(cyano)phenyl indigo exhibit only 13% *cis* isomer in CD$_2$Cl$_2$ solution according to the literature.[85] These data are consistent with a possible stabilization of the *cis* isomers through a positive aryl interaction. The theoretical description showed highly twisted structures for the *cis* isomers of di-arylated indigos with tilted aryl substituents in a parallel arrangement. Thus, hydrogen atoms in *ortho* position to the N-aryl axis are situated over

the π surface of the neighbouring aryl substituent. NMR spectral analysis showed a significant upfield shift for these hydrogen atoms, proving the spatial vicinity to the neighbouring aryl substituents as predicted by the theoretical calculation. Thus, in principle, structural preorganization for an attractive parallel displaced polar aromatic interaction is provided. For profound validation of this assumption, however, the thermal decay kinetics in *i*-hexane of a symmetrical disubstituted indigo bearing two benzonitrile moieties are inevitable.
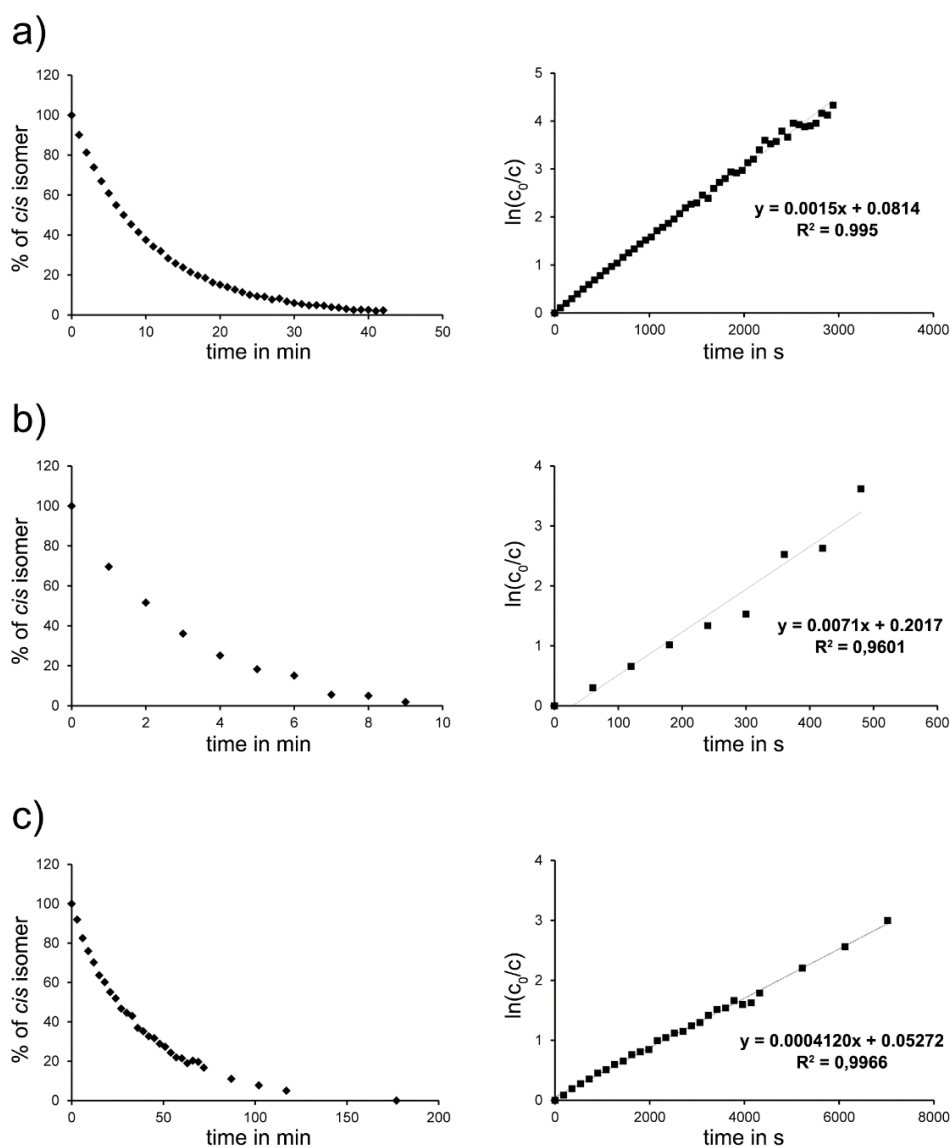
Figure 117:   The thermal decays of the metastable *cis* isomers of di-arylated indigos in *i*-hexane were monitored by UV/vis spectroscopy at 21 °C. On the left side the decrease of photogenerated *cis* isomer concentration is plotted against time. The graphs on the right side show the logarithmic plots of the first order kinetic analysis. Good agreement of the kinetic model with experimental data was found. a) *N,N'*-di(*p*-tolyl) indigo **108**. Accumulation of *cis* isomer with 660 nm. b) *N,N'*-di(*p*-dimethylaminophenyl) indigo **110**. Accumulation of *cis* isomer with 660 nm. c) *N*-(*p*-(dimethylamino)phenyl)-*N'*-(*p*-(cyano)phenyl) indigo **116.** Accumulation of *cis* isomer with 680 nm.

Huang et al. already reported on the thermal behaviour of di-arylated indigos.[85] A considerable series of substituted indigos, with aryl substituents of varying electronic character was investigated, which showed that reduced electron densities lead to increased energy barriers for the thermal *cis* to *trans* isomerization. Further effects of possible aryl interactions are not discussed. One example where the decay times of a push-/pull-substituted indigo is compared to its electron deficient analogue shows dominating electronic effects of the aryl substituents. In this case, however, rather moderate donors and acceptors were used, thus it cannot be fully concluded whether aryl-interactions contributes to the energy barrier height if strong electron donors and acceptors are used.

6.8   Influence of H_2O and D_2O on the photoisomerization of mono-(*p*-tolyl) indigo 107

From the investigation on the thermal stability of the *cis*-**107** and *cis*-**108,** it was found that increased water content of the indigo solution in THF resulted in an acceleration of the thermal *cis* to *trans* isomerization in the dark. The effect observed for mono-arylated indigo **107** is much stronger than for di-arylated indigo **108**, which hints at specific interactions of the unique N-H functionality of mono-arylated indigo. The half-life dependency on the water concentration is shown in Figure 118a. Moreover it was found that the effect of D_2O on the thermal stability is roughly 5 times smaller in comparison to H_2O. Because of these severe effects of water addition and deuteration on the ground state properties of mono-arylated indigos, it was investigated next, if the photoisomerization efficiency suffers from H_2O addition, too. It was found, that increased concentration of water reduces the spectral changes, which can be achieved by irradiation. At a concentration of 3.1 M of water, no light induced absorption changes can be observed. In Figure 118b the spectral changes achieved by 2 min of irradiation of indigo solutions in THF with varying water content is summarized. Diminished spectral changes can be most likely traced back to a reduced content of *cis* isomer after irradiation. One reason for this observation is the decreased thermal stability which resulted in increased speed rates for thermal *cis* to *trans* conversion occurring readily during irradiation and spectrum recording. At a critical limit of water concentration the thermal *cis* to *trans* isomerization outcompetes light induced *cis* isomer generation. An additional reason could be a decreased quantum yield of photoisomerization. From the obtained data no further disentanglement as well as quantification of this two processes determining the isomeric yield after irradiation can be made, especially since fast decay of *cis* isomer impeded quantum yield measurements at ambient temperature. Next it was investigated how D_2O addition is influencing the isomerization efficiency. For small amounts of D_2O (0.09 M) in the THF solution it was found, that the photoisomerization is much more efficient in comparison to the photoisomerization observed for an indigo solution with the same amount of water. More interestingly, it was additionally found, that photoisomerization efficiency after D_2O addition is even superior to the efficiency observed for a dry THF solution of indigo **107**. The spectra of these irradiation experiments are shown in Figure 118c. In order to decipher if the thermal stability of the *cis* isomer of the D_2O containing indigo solution is

responsible for the increased photoisomerization efficiency, kinetic measurements were performed where solutions of indigo **107** in dry THF and in THF containing 0.09 M D_2O were compared (Figure 118d). It was verified that the *cis* isomer possessed a longer half- life in dry THF and a faster decay in D_2O containing THF solution. From these results it can be excluded that increased photoisomerization efficiency in D_2O containing THF solutions is a consequence of higher thermal stability of the *cis* isomer. As expected, the contrary is the case. Thus, only increased quantum yield of photoisomerization remained for explanation of increased photoisomerization efficiency in the presence of D_2O. Additionally, emission spectra were recorded for further investigation of the excited state behaviour, (Figure 118e). A solution of indigo *trans*-**107** containing 0.09 M D_2O shows an increased fluorescence quantum yield of 1.01% in comparison to a solution in dry THF with the same indigo concentration. A solution of indigo **107** in THF containing 0.09 M H_2O yielded in a decrease of the fluorescence quantum yield to 0,7%, which confirms that an isotope effect of deuterium is the reason for the increase of the fluorescence quantum yield in the presence of D_2O.
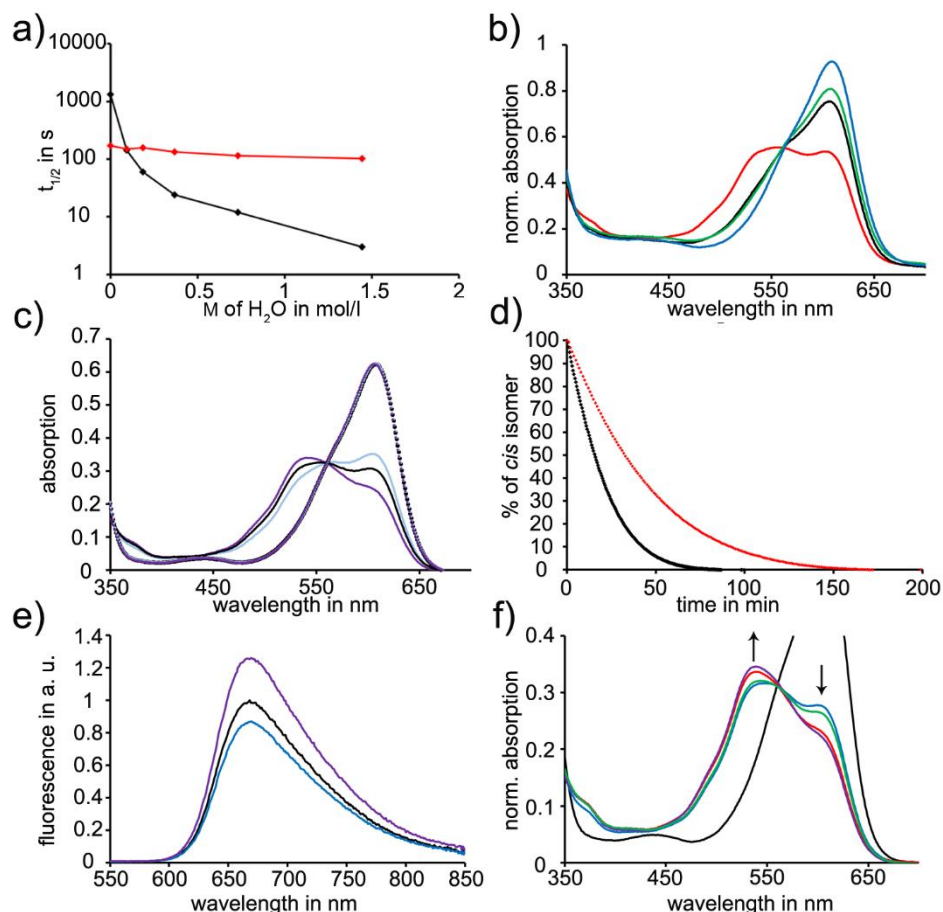
Figure 118: Results of experiments concerning H_2O and D_2O effects on the thermal stability of *cis*-**107** as well as on the photochemical behavior of **107**. a) The dependency of the half-life of mono-arylated *cis*-**107** (black) and of di-arylated indigo *cis*-**108** (red) on the water content in THF solutions at 23.5 °C. b) Absorption spectra (23 °C) of indigo **107** (27 μM) in dry THF after 2 min of irradiation with 625 nm (red), of **107** in THF containing 0.78 M of D_2O after 2 min of irradiation with 625 nm (black), of **107** in THF containing 1.55 M of D_2O after 2 min of irradiation with 625 nm (green) and of **107** in dry THF solution before irradiation (blue). c) After irradiation with 625 nm absorption spectra of the isomer composition in the pss were recorded for **107** in dry THF (black), for **107** in THF containing 0.09 M D_2O (violet) and for **107** in THF containing 0.09 M H_2O (blue). d) The thermal *cis* to *trans* conversion of *cis*-**107**, enriched by 625 nm irradiation of a **107** solution in dry THF (red) and of a **107** solution in THF containing 0.09 M D_2O (black) was followed by UV/vis absorption spectroscopy. e) Fluorescence spectra of indigo **107** solutions (50 μM) in dry THF (black), in THF containing 0.09 M D_2O (violet), in THF containing 0.09 M H_2O (blue). f) Absorption spectra of an indigo **107** solution (36 μM) after irradiation with 625 nm in dry THF (blue), in THF containing 24 equiv. D_2O (green), in THF containing 240 equiv. D_2O (red), in THF containing 2400 equiv. D_2O (violet). The absorption spectrum of *trans*-**107** solution in dry THF without irradiation is shown in black. L. A. Huber, P. Mayer, H. Dube: Photoisomerization of Mono-Arylated Indigo and Water-Induced Acceleration of Thermal *cis* to *trans* Isomerization. *ChemPhotoChem.* **2018**, *2*, 458-464. Copyright Wiley-VCH Verlag GmbH & Co. KGaA. Adapted with permission.

These findings allow the discussion of two possible explanations (Figure 119). Either the exchange of hydrogen by deuterium directly enhances the transfer rate of exited molecules into the excited state minimum (S_{PI}), from which the molecules can relax to the ground state by photoisomerization. This would b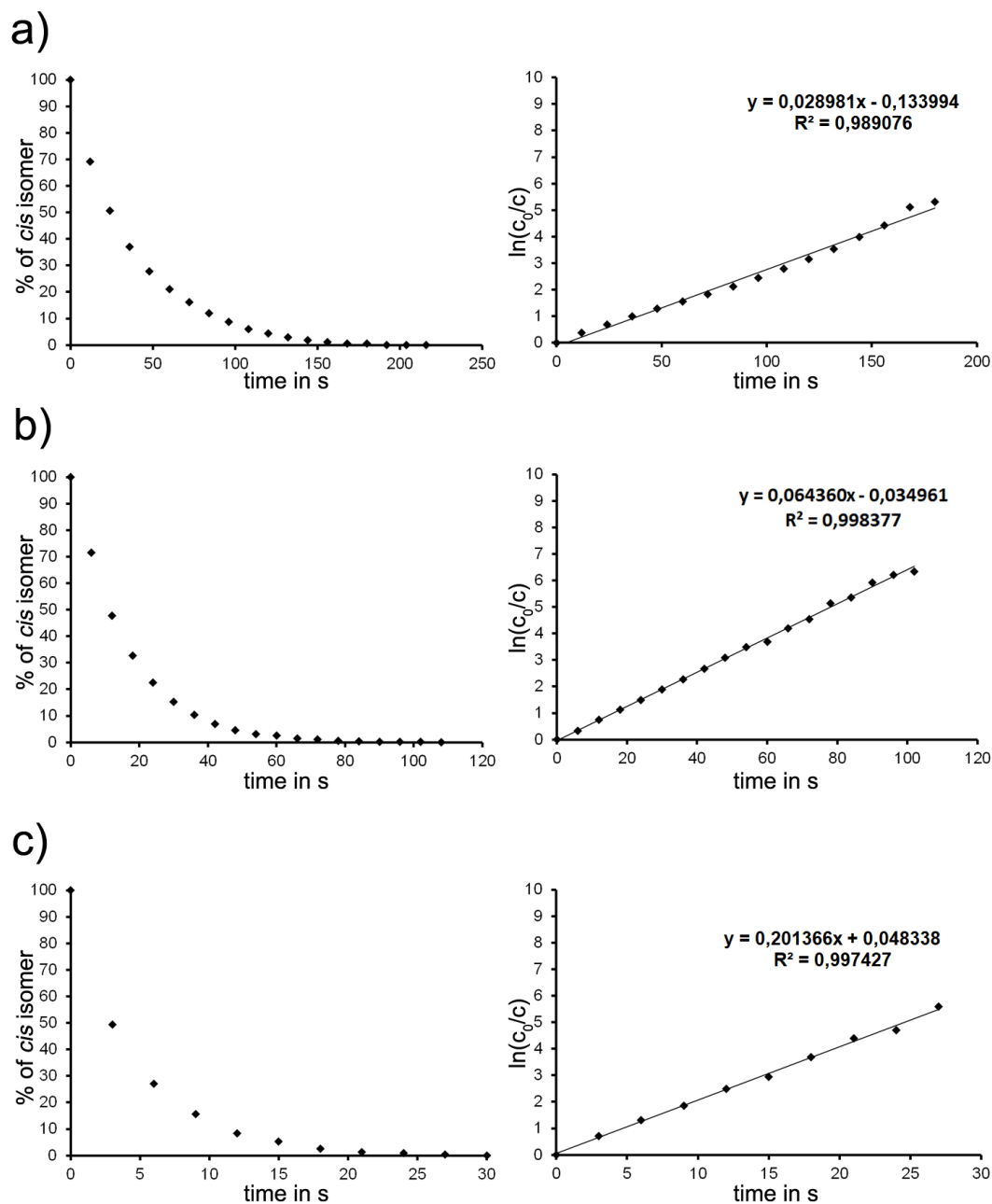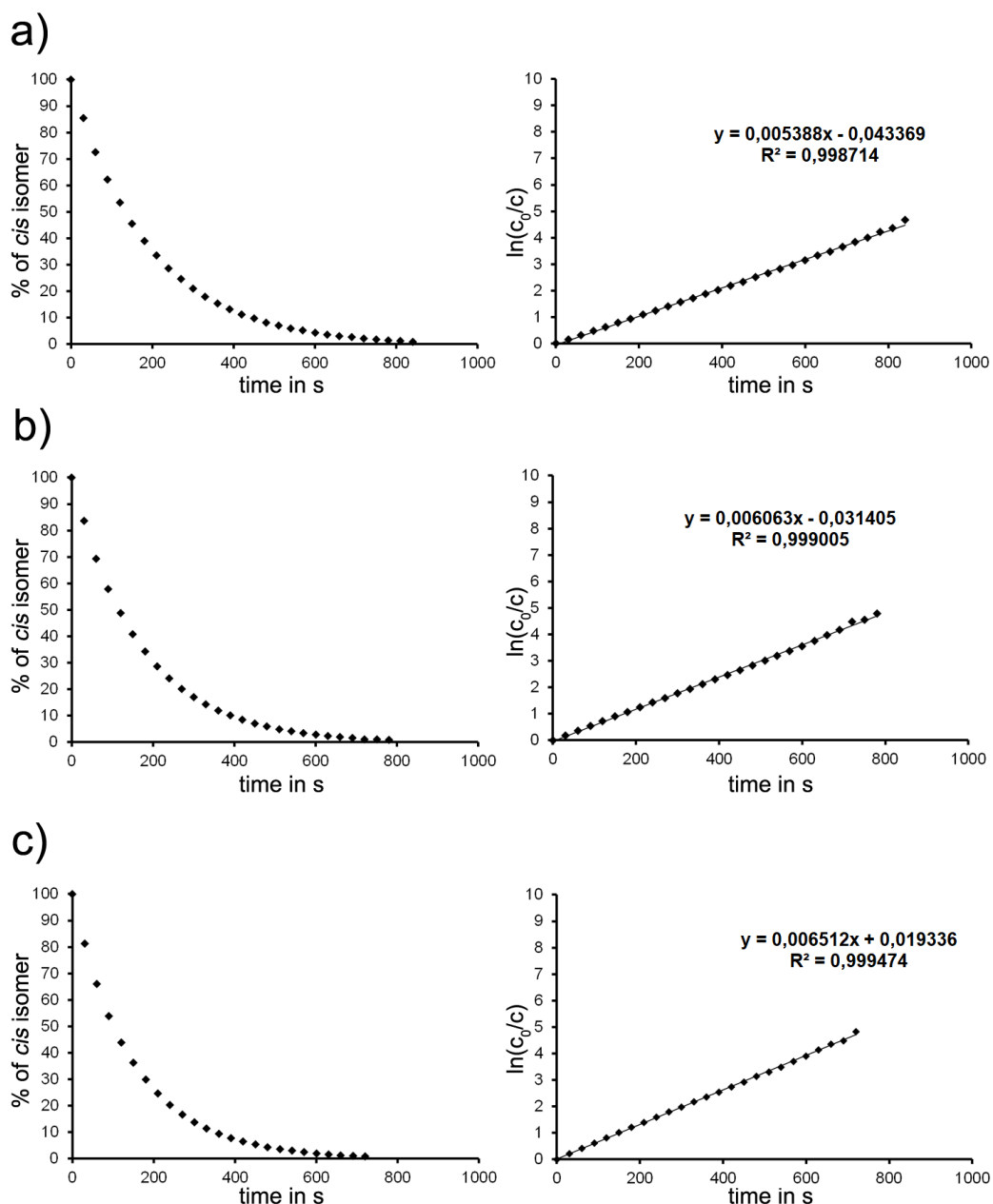e possible by lowering the energy of the S_{PI} excited state minimum region, which leads to a reduced barrier with respect to the S_1 minimum populated primarily after excitation and which is not affected by deuteration. This hypothesis, however, cannot satisfyingly explain the increased fluorescence because under the assumption that the S_1 excited state minimum is the only emitting state, an accelerated transfer to the S_{PI} minimum region would reduce the fluorescence quantum yield compulsorily. Hence, it has to be assumed that emission is an additional deexcitation pathway of the S_{PI}, which is uncommon because effective deexcitation by photoisomerization should by far outcompete emission from this minimum region.

The second explanation is based on several studies with indigo,[123-124, 133, 136-137] where an exited state proton transfer was shown to be an effective deexitation channel. Given that indigo **107** possesses the same molecular scaffold it seems likely that it is capable to undergo proton transfer after excitation, too (Figure 119a). A hydrogen deuterium exchange could increase the barrier of an excited state proton transfer and reduce the transfer rate to its excited state minimum region (S_{PT}). In Figure 119b the N-H deuteration scenario is depicted. The consequence is that depopulation of the S_1 minimum has to take place augmented by photoisomerization or emission. Hence, the quantum yields of photoisomerization and fluorescence should increase, as it was indeed observed by UV/vis and fluorescence spectroscopy. Further experiments were conducted to get deeper insight into the nature of the excited state proton transfer. If its transfer rate is manipulated by addition of D_2O it is not necessarily an intramolecular proton transfer but it could also be a proton transfer to D_2O. If the latter is the case the yield of this process should, because of its bimolecular nature, be enhanced by an increased content of D_2O. Pronounced proton transfer should consequence lower photoisomerization efficiency, which can be monitored by UV/vis spectroscopy. In order to answer this question, irradiation experiments with indigo **107** solutions in THF with increasing concentration of D_2O were conducted (Figure 118f). After addition of 23 equivalents of D_2O with respect to the concentration of indigo **107**, enhanced photoisomerization efficiency could be observed by UV/vis spectroscopy. Further D_2O addition, up to 2200 equivalents, resulted again in increased photoisomerization. Therefore, it can be concluded that within the concentration range observed in this experiment, the proton transfer is dominantly an intramolecular transfer. Minor contribution of intermolecular proton transfer with water is also possible but is outcompeted by the intramolecular fashion within the investigated concentration range.
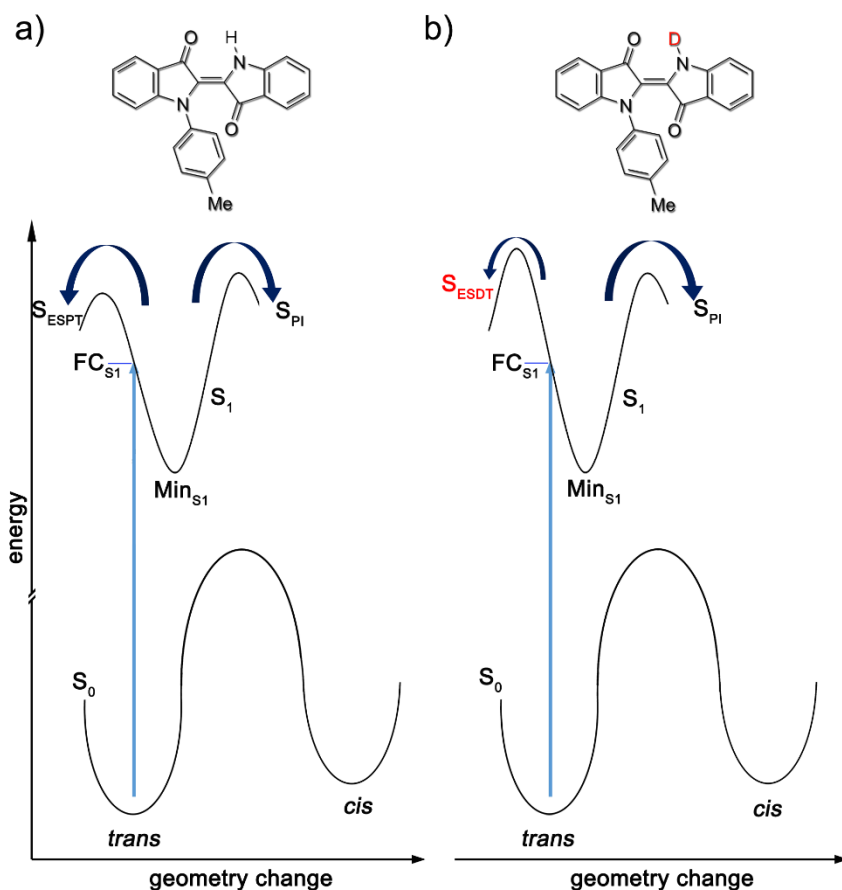
Figure 119:   Possible explanation for the excited state behavior of mono-arylated indigo **107** with regard to H_2O and D2O sensitivities. S_0: ground state. S_1: first excited state. FC_{S1}: Vertical excitation into Frank Condon region. Min_{S1}: Minimum of S_1 populated after initial relaxation. S_{ESPT}: Excited state populated by ESPT. S_{PI}: Excited state populated by rotation around the central double bond (PI=Photoisomerization). $CoIn_{SPI}$: conical intersection between S_0 and S_{PI}. S_{ESDT}: excited state populated by deuterium transfer. It is assumed that two effective deexcitation pathways are present for indigo **107**. For indigo, the often discussed ESPT leads to an enol form in the excited state, which readily converts back to the ground state. Hot ground state relaxation restores the initial ground state S_0. A second pathway, which can be directly followed by absorption spectroscopy after irradiation, is photoisomerization. After population of the corresponding S_{PI}, a fast deexcitation pathway via transition of a conical intersection to the ground state takes place. A 90° distorted double bond leads either back to the *trans* isomer or to the *cis* isomer by further hot ground state relaxation. The ratio between these two competing deexcitation processes is defined by the relative barrier heights (green bars) in the excited state. After D2O addition it is assumed that replacement of hydrogen by deuterium leads to aggravated excited state enol formation (population of S_{ESDT}) since an excited state deuterium transfer (ESDT) has to take place in this case. The isotope effect of deuterium most likely reduces the acidity of the amine function and increase the bond strength of the N-D motif in comparison to the N-H motif. In consequence the excited state barrier is increased. Thus, deexcitation via photoisomerization takes place augmentedly, which is not or only little affected by the isotope effect of deuterium.

7. Outlook

Based on the results, it can be stated that HTI-based molecular motors are capable of directional rotary motion by a four step mechanism, similar to the Feringa type molecular motors. The herein presented molecules were able to significantly increase thermal barriers of the helix inverting steps in comparison to motor **1**, which allowed for detection of the missing intermediate **B** of the rotation cycle. Nevertheless, compared to Feringa's first generation motors thermal barriers are still relatively low, which aggravates accumulation and maintenance of metastable isomer concentration with opposite helicity, as it is the case for the stable isomers. Thus, applications at ambient temperature, which exploit the possibility to switch between opposite helical information with light is not possible so far. For realization of this aim, it is necessary to raise at least one thermal barrier (15.75 kcal·mol^{-1} in case of motor **5**) by at least 10 kcal·mol^{-1}. The increase of sterical hindrance was shown to be a promising strategy for reduction of the speed of the helical inversions. Therefore, several molecular designs can be contemplated for further thermal speed decrease. Molecular setups are depicted in Figure 120.
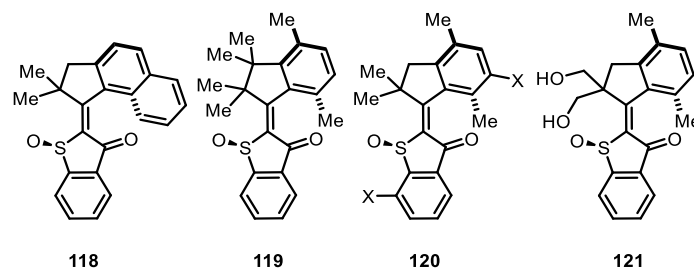
Figure 120: Molecular setups for further thermal speed decrease. The approach to increase the sterical hindrance is further extended to other positions at proximal or remote position to the rotation axle.

Since aromatic and aliphatic positions on the rotor fragment in close proximity to the double bond were already investigated for thermal speed decrease, other positions can be regarded for installation of sterical hindrance. Structure **118** could provide higher thermal barriers by replacing floppy alkyl or alkoxy groups by a rigid naphthyl ring, which is used by the group of *Feringa*. A different approach is depicted with structure **119**, with further methyl groups at the second aliphatic position. Transition state structures of motor **2** (see Figure 45) reveal an eclipsed conformation of the hydrogens and the methyl groups. That means these substituents have to be pushed against each other during the helical inversion. By increasing the sterics at this position, this mechanical movement should be aggravated. Indeed, first theoretical calculations for **119** showed a higher calculated barrier of 16.36 kcal·mol^{-1} for the **D** to **A** conversion, as it is the case for motor **5** (calc. 15.76 kcal·mol^{-1}). *Fabian Huck* already reported in his master thesis[247] on higher experimentally determined barriers, e.g. 16.23 kcal·mol^{-1} for **D** to **A** conversion, as it was found for motor **5**, measured for a motor derivative with twofold bromine substitution (substitution pattern analogue to structure **120**). It is not yet clear, which substituent

dominates the thermal barrier, or if this is a cumulative effect. Nevertheless, it is a promising example for remote influences on the thermal barriers. Structure **121** provides two hydroxy groups, which could stabilize metastable structures in order to rise thermal barriers for helix inversions. Thus, it represents a different strategy, as it is shown with the other molecular designs. Structure **121** could furnish other promising advantages such as an increased photochromism. The group of *Newhouse* already reported on these features if one isomer exhibits intramolecular hydrogen bonding.[82] Finally, the diol motif could be regarded as a connecting positon with other molecular subcomponents by acetal formation, which would also allow for facile functionalization.

As HTI based motors already work under photonic limitations, reducing thermal barriers for additional overall speed increase under realistic irradiation conditions is not possible. This could instead be achieved by increased quantum yields and increased absorption behavior. The investigation by ultrafast transient absorption spectroscopy already indicated, that this aim could be achieved by substitution of the rotor fragment with electron-donating groups. Further improvements for faster motor performance would be the possibility to drive fully directional 360° rotation with only one photon. This would require one double-bond isomerization to occur thermally, which is technically possible. Nevertheless, it is a very intricate aim, since the energy profile of the motor must allow for three sequential thermal steps delivering the starting point of the cycle.

Shifting the addressability of molecular motors is a worthwhile aim, since application in sensitive environments require mild conditions. A possibility is to use a hemiindigo scaffolds for the motor design, as it was already shown by *Petermayer et al*, that this substance class comprises superior switching features with outstanding redshifted absorption.[73] A possible synthetic approach, which is founded on the positive results for HTI-based molecular motors, is shown in Scheme 23. The synthesis starts with the preparation of a propargylic alcohol from a Boc-protected acetylene derivative. After Meyer-Schuster rearrangement with eventually deprotected amine function, the ring closing reaction could be tested next. At this stage, similar to the sulfur containing analogues, an Umpolung approach should be considered. Eventually Boc-protection could provide sufficient electron withdrawing effect for nucleophilic attack of the β-carbon atom of the enone function. If not, further electron withdrawing substituents such as hydroxy or chloride substituents can be considered. Of course the molecular design includes, also in this case, a stereocenter, which is placed at the rotor fragment.
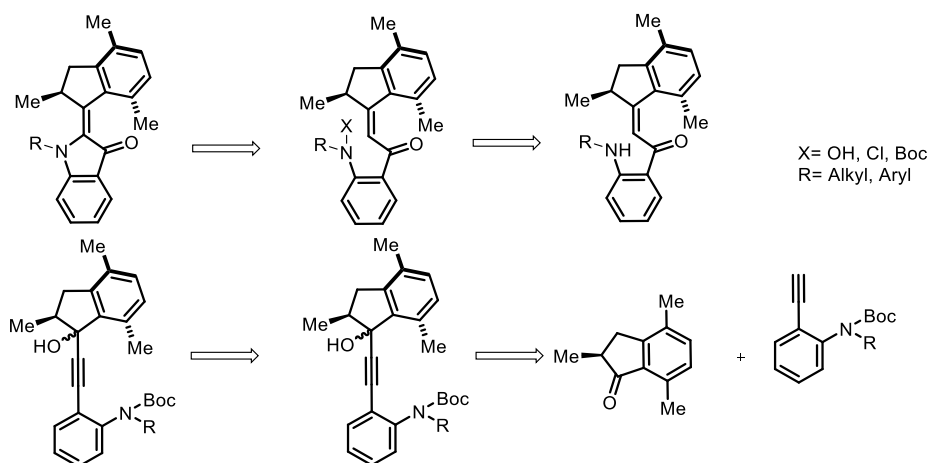
Scheme 23:   Retrosynthesis of a potential hemiindigo-based molecular motor.

The pK_a value of mono-arylated *cis* indigos is most likely smaller as it is the case for the corresponding *trans* isomers, since the absence of a possible hydrogen bridge leads to a more loosely bound hydrogen at the nitrogen atom of the *cis* isomer. A possible application could therefore be the manipulation of the reaction rate of an acid catalyzed reaction by *cis* isomer accumulation via light input. An acceleration of the reaction speed could therefore reversely prove the pK_a differences of the *cis* and *trans* isomers. It was also shown in this thesis, that addition of water to the mono-aryl indigo solution influences the thermal barrier of *cis* to *trans* isomerization. The presented results in this thesis strongly hints at the N-H group, governing this behavior. A mechanistic explanation could be an interaction of the N-H group with water, which could reduce the double bond character of the central double bond and would therefore accelerate thermal *cis* to *trans* isomerization. If an amine or a hydroxy group is coupled over an alkyl chain to the N-aryl substituent, this function could intramolecularly trigger the thermal back isomerization (Figure 121). The consequence would be a sequential motion of a light induced double rotation followed by a kinking of the triggering group for induction of the thermal *cis* to *trans* isomerization. This could be verified, if varying chain lengths of the triggering group are influencing the speed of the thermal *cis* to *trans* isomerization in dry solvents. A very long chain as well as a very short chain should lead to a higher thermal energy barrier, as energy-costly bending of the chain is neede. Nature evenly use cascade reactions for the transduction of a stimulus, and this would be an interesting synthetic example for an artificial analogue.
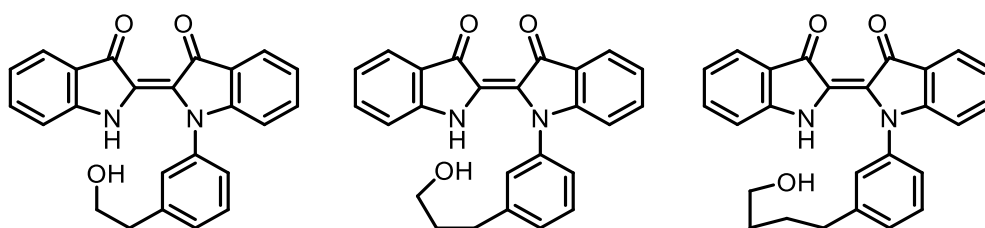
Figure 121:   Proposal for sequential motion of the mono-arylated indigos with triggering units for thermal *cis* to *trans* isomerization. In the *cis* isomeric structures the hydroxy function can interact with the N-H group, which could trigger the thermal *cis* to *trans* isomerization.

8. Materials and General Methods

Reagents and solvents were obtained from *ABCR*, *Acros*, *Chempur Fluka*, *Merck*, *Sigma-Aldrich* or *TCI* in the qualities *puriss.*, *p.a.*, or *purum* and used as received. Technical solvents were distilled before using for column chromatography on a rotary evaporator (*Vacuubrand* CVC 3000). Reaction control was performed on *Merck* Silica 60 F254 TLC plates and detection was done by irradiation with UV light (254 nm or 366 nm).

The THF used for spectrometric investigation of arylated indigos was continuously refluxed and freshly distilled from sodium benzophenone ketyl under N2 atmosphere and stored over activated molecular sieve 4Å for at least one week before usage.

Column chromatography was performed with silica gel 60 (*Merck*, particle size 0.063- 0.200 mm) or with neutral aluminium oxide (*Sigma Aldrich*, activated, neutral, Brockmann I). For eluation distilled technical solvents were used.

High Performance Liquid Chromatography (HPLC) was performed on a Shimadzu HPLC system consisting of a LC-20AP solvent delivery module, a CTO-20A column oven, a SPD-M20A photodiode array UV/vis detector and a CBM-20A system controller using a semipreparative CHIRALPAK® IC column (particle size 5 µm) from Diacel was performed or on a Merck-Hitachi LaChrom Series HPLC system consisting of a D-7000 interface, a L-7150 solvent delivery module, a L-7350 column oven, a L-7420 UV-vis detector and a L-7455 diode array detector using a preparative Machery-Nagel VP 250/21 NUCLEODUR Sphinx RP 5 µm column and HPLC grade solvents (2-PrOH, *n*-heptane and MeCN) from *Sigma-Aldrich*, VWR and *ROTH*.

^{1}H NMR and ^{13}C NMR spectra were measured on a JEOL ECX 400 (400 MHz), Varian VNMRS 400 (400 MHz), Varian VNMRS 600 (600 MHz), or Bruker AVANCE III HD 800 (800 MHz) NMR spectrometer. Deuterated solvents were obtained from *Cambridge Isotope Laboratories* and used without further purification. Chemical shifts (δ) are given relative to tetramethylsilane as external standard. Residual solvent signals in the ^{1}H and ^{13}C NMR spectra were used as internal reference. CDCl$_3$: δ_H = 7.260 ppm, δ_C = 77.16 ppm; CD$_2$Cl$_2$: δ_H = 5.320 ppm, δ_C = 53.84 ppm; toluene-d_8: δ_H = 2.080 ppm, δ_C = 20.43 ppm; *o*-xylene-d_{10}: δ_H = 2.083 ppm, Et$_2$O-d_{10}: δ_H = 1.110 ppm. For low temperature measurements (–105 °C) of molecular motors a 4/1 mixture of CD$_2$Cl$_2$/CS$_2$ was used and the residual solvent signals of CD$_2$Cl$_2$ was used as internal reference. For pss determination of arylated indigos THF-d_8 was used and the residual solvent signals of THF served as internal reference. The resonance multiplicity is marked as s (singlet), d (doublet), t (triplet), q (quartet), sep (septet) and m (multiplet) and br (broad signal). The chemical shifts are given in parts per million (ppm) on the delta scale (δ) and the coupling constant values (J) are in hertz (Hz). Arbitrary numbering of the molecules and signal assignment is given in the experimental part.

Electron Impact (EI) mass spectra were measured on a *Finnigan MAT95Q* or on a *Finnigan MAT90* mass spectrometer. **Electrospray ionisation (ESI) mass spectra** were measured on a *Thermo Finnigan LTQ-FT*. The most important signals are reported in *m/z* units and the molecular ion is signed as *M*.

Elemental analyses were performed on an *Elementar Vario EL* apparatus in the micro analytical laboratory of the LMU department of chemistry

Infrared spectra were recorded on a *Perkin Elmer Spectrum BX-FT-IR* instrument equipped with a Smith *DuraSamplIR II* ATR-device. Transmittance values are qualitatively described by wavenumber (cm^{-1}) as very strong (vs), strong (s), medium (m), and weak (w).

UV/vis spectra were measured on a *Varian Cary 5000* spectrophotometer. The spectra were recorded in a quartz cuvette (1 cm). Spectral grade solvents were obtained from *VWR* and *Merck*. Absorption wavelengths (λ) are reported in nm and the extinction coefficients (ε) L·mol^{-1}·cm^{-1} in brackets. Shoulders are declared as sh.

Electronic circular dichroism (ECD) spectra were measured on a *Jasco J-810 Spectropolarimeter*.

Melting points (m.p.) were measured on a *Büchi B-540 melting point* apparatus in open capillaries.

Photoisomerization experiments: Irradiations of solutions were conducted either in NMR tubes in different deuterated solvents (CD$_2$Cl$_2$, toluene-*d$_8$*) or in UV/vis cuvettes. Photoproducts were then either detected by NMR or absorption spectroscopy. Irradiations in cuvettes were conducted using LEDs from Roithner Lasertechnik GmbH (305 nm, 365 nm, 385 nm, 405 nm, 420 nm, 435 nm, 450 nm, 470 nm, 490 nm, 505 nm, 625 nm) as well as a LED from Thorlabs (M660D2, 660 nm). For *in situ* irradiation in NMR spectrometer either a Mightex FCS-0470-200 LED (470 nm) or a Prizmatix ultra high power LED 625 nm (UHP-T-625-DI) was used as light source and the light was transmitted by a fiber-optic cable from Thorlabs (FT1500UMT, 0.39 NA, 1500 μm, one SMA, one blank end), which pointed directly into the NMR tube during NMR measurements.

(*E*/*Z*)-2-(2,2,4,7-Tetramethyl-2,3-dihydro-1*H*-inden-1-ylidene)benzo[*b*]thiophen-3(2*H*)-one 1-oxide (*E*/*Z*-2)[IV] [38]
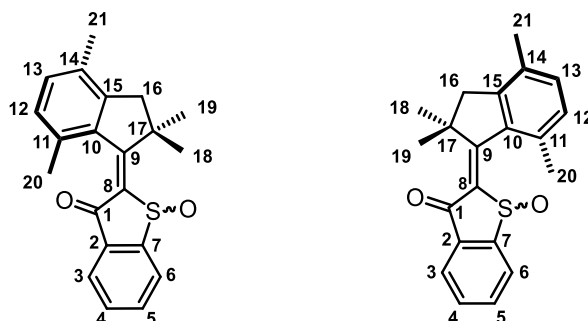
Compound **19** (9.40 mg, 0.029 mmol, mixture of *E* and *Z* isomers) was dissolved in c. AcOH (1.0 mL) at 23 °C and sodium perborate tetrahydrate was added (17.2 mg, 0.112 mmol). After the reaction mixture was stirred for 3 h at 23 °C a saturated aqueous NaHCO$_3$ solution (20 mL) was added. The aqueous phase was extracted with EtOAc (3 x 20 mL) and the combined organic phases were dried over Na$_2$SO$_4$. The solvent was removed *in vacuo* and the crude product was purified by column chromatography (SiO$_2$, *i*Hex:EtOAc, 8:2 v/v) to obtain compound **2** (9.00 mg, 0.027 mmol, 93%) as yellow solid. Separation of the *Z* and *E* isomers as well as the enantiomers was conducted using chiral HPLC (CHIRALPAK IC, *i*Pr:*n*Hept, 5:95 v/v).

E isomer: R_f = 0.41 (*i*Hex:EtOAc 1:1); m.p. 171 °C (mixed crystal of *Z* and *E* isomers); ^{1}H NMR (800 MHz, CD$_2$Cl$_2$) δ = 8.08 (d, ^3J(H,H) = 7.7 Hz, 1H, H-C(6)), 8.01 (d, ^3J(H,H) = 7.6 Hz, 1H, H-C(3)), 7.87 (td, ^3J(H,H) = 7.7 Hz, ^4J(H,H) = 1.1 Hz, 1H, H-C(5)), 7.75 (td, ^3J(H,H) = 7.5 Hz, ^4J(H,H) = 0.9 Hz, 1H, H-C(4)), 7.21 (d, ^3J(H,H) = 7.7 Hz, 1H, H-C(13)), 7.07 (d, ^3J(H,H) = 7.7 Hz, 1H, H-C(12)), 3.19 (d, ^3J(H,H) = 15.1 Hz, 1H, H$_2$-C(16)), 2.82 (d, ^3J(H,H) = 15.1 Hz, 1H, H$_2$-C(16')), 2.28 (s, 3H, H$_3$-C(21)), 2.18 (s, 3H, H$_3$-C(20)), 2.01 (s, 3H, H$_3$-C(19)), 1.34 (s, 3H, H$_3$-C(18)) ppm; ^{13}C NMR (201 MHz, CD$_2$Cl$_2$): δ = 183.8 (C(1)), 175.7 (C(9)), 149.9 (C(7)), 147.6 (C(15)), 141.0 (C(8)), 138.9 (C(11)), 138.6 (C(10)), 135.7 (C(5)), 135.6 (C(2)), 133.3 (C(13)), 132.9 (C(4)), 131.8 (C(14)), 129.8 (C(12)), 127.4 (C(6)), 125.9 (C(3)), 53.0 (C(17)), 49.2 (C(16)), 28.5 (C(18)), 27.1 (C(19)), 21.9 (C(20)), 18.4 (C(21)) ppm; IR: $\tilde{\nu}$ = 2959w, 2923w, 2864w, 1675vs, 1589s, 1539vs, 1492m, 1451m, 1380w, 1364w, 1324w, 1278s, 1214vs, 1189w, 1174w, 1119m, 1085m, 1073m, 1040vs, 1012m, 996m, 953w, 940w, 864m, 813m, 800w, 787w, 760s, 745s, 710m, 691m, 669s, 653s cm^{-1}; HR-EI-MS calc. [C$_{21}$H$_{20}$O$_2$S]: 336.1184, found: 336.1180; elemental analysis calc. (%) for C$_{21}$H$_{20}$O$_2$S: C 74.97, H 5.99, S 9.53; found: C 74.91, H 6.06, S 9.59.

Z isomer: R_f = 0.33 (*i*Hex:EtOAc 1:1); ^{1}H NMR (800 MHz, CD$_2$Cl$_2$) δ = 8.03 (d, ^3J(H,H) = 7.7 Hz, 1H, H-C(6)), 8.02 (d, ^3J(H,H) = 7.6 Hz, 1H, H-C(3)), 7.85 (td, ^3J(H,H) = 7.6 Hz, ^4J(H,H) = 1.1 Hz, 1H,

H-C(5)), 7.75 (td, ^3J(H,H) = 7.5 Hz, ^4J(H,H) = 0.9 Hz, 1H, H-C(4)), 7.26 (d, ^3J(H,H) = 7.7 Hz, 1H, H-C(13)), 7.17 (d, ^3J(H,H) = 7.7 Hz, 1H, H-C(12)), 3.10 (d, ^3J(H,H) = 15.6 Hz, 1H, H_2-C(16)), 2.81 (d, ^3J(H,H) = 15.6 Hz, 1H, H_2-C(16')), 2.61 (s, 3H, H_3-C(20)), 2.26 (s, 3H, H_3-C(21)), 1.61 (s, 3H, H_3-C(19)), 1.44 (s, 3H, H_3-C(18)) ppm; ^{13}C NMR (201 MHz, CD_2Cl_2): δ = 184.5 (C(1)), 177.5 (C(9)), 150.6 (C(7)), 148.8 (C(15)), 143.2 (C(8)), 138.0 (C(10)), 136.4 (C(2)), 135.9 (C(11)), 135.5 (C(5)), 133.9 (C(13)), 133.0 C((4)), 132.3 (C(14)), 131.1 (C(12)), 127.5 (C(6)), 125.5 (C(3)), 53.3 (C(17)), 20.1 (C(16)), 27.7 (C(18)), 26.4(C(19)), 22.7 (C(20)), 18.4 (C(21)) ppm; IR: $\tilde{v}$ = 3009w, 2956w 2917w, 2859w, 1667s, 1585m, 1531vs, 1490w, 1472w, 1455m, 1447m, 1379m, 1360w, 1328w, 1314w, 1275s, 1208vs, 1173w, 1157w, 1117m, 1086s, 1073m, 1061s, 1045vs, 1019w, 975w, 941w, 923w, 896w, 882w, 817s, 791m, 761vs, 747m, 708s, 691w, 661m, 653s cm^{-1}.

Concise protocol for the synthesis of HTI motor **2** without isolation of synthetic intermediates[38]

Compound **17** (160 mg, 0.48 mmol) was dissolved in THF (2 mL) at 23 °C and c. H_2SO_4 (3 drops) was added. After the reaction mixture was stirred for 15 h saturated aqueous $NaHCO_3$ solution (40 mL) was added. The aqueous phase was extracted with EtOAc (3 x 100 mL) and the combined organic phases were dried over $MgSO_4$. The solvent was removed *in vacuo*. The residue was dissolved in c. AcOH (3 mL) and sodium perborate tetrahydrate was added (306 mg, 1.99 mmol). After the reaction mixture was stirred for 45min at 23 °C a saturated aqueous $NaHCO_3$ solution (100 mL) was added. The aqueous phase was extracted with EtOAc (3 x 150 mL) and the combined organic phases were dried over $MgSO_4$. The solvent was removed *in vacuo*. The residue was dissolved in dry CH_2Cl_2 (3 mL) and the solution was cooled to –50 °C. Oxalyl chloride was added (55 µL, 0.65 mmol) and the reaction mixture was stirred for 1 h at –50 °C. Saturated aqueous $NaHCO_3$ solution (50 mL) was added and the aqueous phase was extracted with CH_2Cl_2 (3 x 100 mL). The combined organic phases were dried over $MgSO_4$ and the solvent was removed *in vacuo*. The residue was dissolved in c. AcOH (3 mL) and sodium perborate tetrahydrate was added (268 mg, 1.70 mmol). After the reaction mixture was stirred for 4 h at 23 °C a saturated aqueous $NaHCO_3$ solution (100 mL) was added. The aqueous phase was extracted with EtOAc (3 x 150 mL) and the combined organic phases were dried over $MgSO_4$. The solvent was removed *in vacuo* and the crude product was purified by column chromatography (Al_2O_3, *i*Hex:EtOAc 9:1) to obtain compound **1** (66 mg, 0.20 mmol, 41%) as a yellow solid.

(*E*/*Z*)-2-(2,2-diethyl-4,7-dimethyl-2,3-dihydro-1*H*-inden-1-ylidene)-1-(λ¹-oxidanyl)-1,2-dihydro-3*H*-1λ³-benzo[*b*]thiophen-3-one (3)
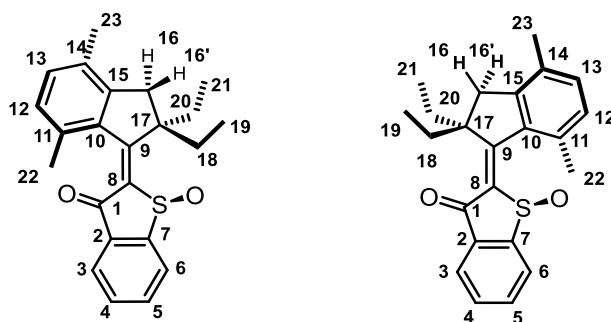
Compound **38** (0.15 g, 0.42 mmol) was dissolved in dry THF (2.8 mL) at 23 °C and c. H$_2$SO$_4$ (14 µL) was added. After the reaction mixture was stirred for 20 minutes saturated aqueous NaHCO$_3$ solution (20 mL) was added. The aqueous phase was extracted three times with CH$_2$Cl$_2$ (3 x 50 mL) and the combined organic phases were dried over MgSO$_4$. The volatiles were removed *in vacuo*. The residue was dissolved in c. AcOH (4.5 mL) and sodium perborate tetrahydrate (0.26 g, 1.7 mmol) was added. After the reaction mixture was stirred for 45 min at 23 °C a saturated aqueous NaHCO$_3$ solution (50 mL) was added. The aqueous phase was extracted with CH$_2$Cl$_2$ (3 x 50 mL) and the combined organic phases were dried over MgSO$_4$. The volatiles were removed *in vacuo*. The residue was dissolved in dry CH$_2$Cl$_2$ (4.0 mL) and the solution was cooled to –50 °C. Oxalyl chloride (40 µL, 0.46 mmol) was added and the stirred reaction mixture was allowed to warm up to –25 °C over the course of 2 h. Oxalyl chloride (4 µL, 0.048 mmol) was added again and the reaction mixture was stirred at –25 °C for 30 min. Saturated NaHCO$_3$ solution (50 mL) was added and the aqueous phase was extracted three times with CH$_2$Cl$_2$ (3 x 50 mL). The combined organic phases were dried over MgSO$_4$ and the volatiles were removed *in vacuo*. The residue was dissolved in c. AcOH (5 mL) and sodium perborate tetrahydrate was added (0.26 mg, 1.7 mmol). After the reaction mixture was stirred for 1.5 h at 23 °C a saturated aqueous NaHCO$_3$ solution (50 mL) was added. The aqueous phase was extracted three times with CH$_2$Cl$_2$ (3 x 50 mL) and the combined organic phases were dried over MgSO$_4$. The solvent was removed *in vacuo* and the crude product was purified by column chromatography (SiO$_2$, *i*Hex to *i*Hex:EtOAc 4:1 v/v) to obtain compound **3** (121 mg, 0.33 mmol, 79%) as a yellow solid.

E/Z mixture: m.p. 146 °C (isomer composition 2/1); IR (isomer composition 2/1): $\tilde{v}$ = 2971m, 2919w, 1664s, 1589m, 1528vs, 1493m, 1449m, 1432m, 1373w, 1329w, 1275s, 1214s, 1194m, 1156w, 1117m, 1076s, 1046vs, 976w, 925m, 885w, 860w, 811s, 798m, 786m, 770w, 747s, 738m, 709s, 688m, 670m cm^{-1}; EI-MS (70 eV): *m/z* (%): 364 (2) [*M*], 347 (100), 333 (33); HR-EI-MS calc. [C$_{23}$H$_{24}$O$_2$S]: 364.1497, found: 364.1486.

E-isomer: R_f = 0.56 (*i*Hex:EtOAc 1:1); ^{1}H NMR (800 MHz, CD_2Cl_2) δ = 8.07 (d, ^3J(H,H) = 7.5 Hz, 1H, H-C(6)), 8.00 (d, ^3J(H,H) = 7.8 Hz, 1H, H-C(3)), 7.87 (t, ^3J(H,H) = 7.5 Hz, 1H, H-C(5)), 7.75 (t, ^3J(H,H) = 7.5 Hz, 1H, H-C(4)), 7.23 (d, ^3J(H,H) = 7.6 Hz, 1H, H-C(13)), 7.08 (d, ^3J(H,H) = 7.7 Hz, 1H, H-C(12)), 3.23 (d, ^3J(H,H) = 16 Hz, 1H, H_2-C(16)), 2.79 (d, ^3J(H,H) = 15.9 Hz, 1H, H_2-C(16')), 2.51 (dq, ^3J(H,H) = 7.3 Hz, 1H, H_2-C(20) or H_2-C(20')), 2.31 (s, 3H, H_3-C(23)), 2.26 (dq, ^3J(H,H) = 7.3 Hz, 1H, H_2-C(20') or H_2-C(20)), 2.23 (s, 3H, H_3-C(22)), 1.99 (dq, ^3J(H,H) = 7.2 Hz, 1H, H_2-C(18) or H_2-C(18)), 1.82 (qd, 1H, H_2-C(18') or H_2-C(18)), 1.01 (t, ^3J(H,H) = 7.2 Hz, 3H, C(21)), 0.57 (t, ^3J(H,H) = 7.5 Hz, 3H, C(19)) ppm; ^{13}C NMR (100 MHz, CD_2Cl_2): δ = 183.3 (C(1)), 174.9 (C(9)), 149.6 (C(7)), 149.3 (C(15)), 141.5 (C(8)), 140.1 (C(10)), 138.9 (C(11)), 135.6 (C(5)), 135.4 (C(2)), 133.6 (C(13)), 133.0 (C(4)), 131.3 (C(14)), 129.9 (C(12)), 127.4 (C(6)), 126.0 (C(3)), 60.2 (C(17)), 42.0 (C(16)), 33.8 (C(18)), 30.6 (C(20)), 22.0 (C(22)), 18.5 (C(23)), 10.4 (C(19) or C(21)), 10.4 (C(21) or C(19)) ppm.

Z-isomer: R_f = 0.47 (*i*Hex:EtOAc 1:1).

(*E,Z*)-2-(4,7-diethyl-2,2-dimethyl-2,3-dihydro-1*H*-inden-1-ylidene)-1-(λ^1-oxidanyl)-1,2-dihydro-3*H*-1λ^3-benzo[*b*]thiophen-3-one (4)
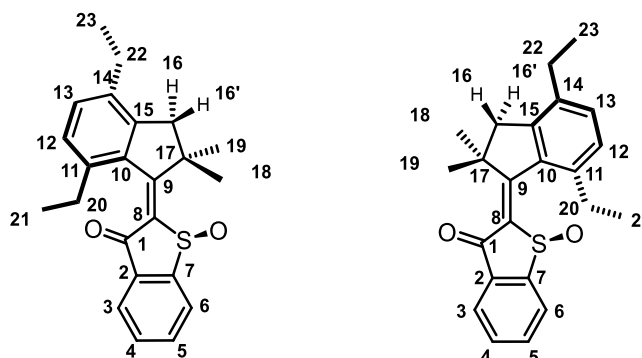
Compound **42** (0.17 g, 0.47 mmol) was dissolved in dry THF (3.2 mL) at 23 °C and c. H_2SO_4 (16 µL) was added. After the reaction mixture was stirred for 20 minutes saturated aqueous $NaHCO_3$ solution (20 mL) was added. The aqueous phase was extracted three times with CH_2Cl_2 (3 x 50 mL) and the combined organic phases were dried over $MgSO_4$. The volatiles were removed *in vacuo.* The residue was dissolved in c. AcOH (5 mL) and sodium perborate tetrahydrate (0.29 g, 1.90 mmol) was added. After the reaction mixture was stirred for 45 min at 23 °C a saturated aqueous $NaHCO_3$ solution (50 mL) was added. The aqueous phase was extracted three times with CH_2Cl_2 (3 x 50 mL) and the combined organic phases were dried over $MgSO_4$. The volatiles were removed *in vacuo*. The residue was dissolved in dry CH_2Cl_2 (4.5 mL) and the solution was cooled to –50 °C. Oxalyl chloride (44 µL, 0.52 mmol) was added and the stirred reaction mixture was allowed to warm up to –25 °C over the course of 2 h. Oxalyl chloride (8 µL, 0.095 mmol) was added again and the reaction mixture was stirred at –25 °C for 1 h. Saturated $NaHCO_3$ solution (50 mL) was added and the aqueous phase was extracted three times with CH_2Cl_2 (3 x 50 mL). The combined organic phases were dried over $MgSO_4$ and the volatiles were removed *in vacuo*. The residue was dissolved in c. AcOH (5 mL) and sodium perborate tetrahydrate (0.29 mg, 1.9 mmol) was added. After the reaction mixture was stirred for 1 h at 23 °C a saturated aqueous $NaHCO_3$ solution (50 mL) was added. The aqueous phase was extracted three times with CH_2Cl_2 (3 x 50 mL) and the combined organic phases were dried over $MgSO_4$. The solvent was removed *in vacuo* and the crude product was purified by column chromatography (SiO_2, *i*Hex to *i*Hex:EtOAc 4:1 v/v) to obtain compound **4** (118 mg, 0.32 mmol, 69%) as a yellow solid.

E/Z mixture: m.p. (*E/Z* isomer composition 3/2) 82 °C; IR (*E/Z* isomer composition 3/2): $\tilde{\nu}$ = 2961m, 1673s, 1650m, 1588s, 1572m, 1537vs, 1492m, 1450s, 1381m, 1279m, 1213vs, 1119m, 1073s, 1041vs, 865m, 830m, 786m, 754s, 707m, 674s, 654s cm^{-1}; EI-MS (70 eV): *m/z* (%): 364 (3) [*M*], 347 (100), 335 (49); HR-EI-MS calc. [$C_{23}H_{24}O_2S$]: 364.1497, found: 364.1497.

E-isomer: R_f = 0.55 (*i*Hex:EtOAc 1:1); ^{1}H NMR (800 MHz, CD$_2$Cl$_2$) δ = 8.09 (d, ^3J(H,H) = 7.8 Hz, 1H, H-C(6)), 8.00 (d, ^3J(H,H) = 7.6 Hz, 1H, H-C(3)), 7.88 (t, ^3J(H,H) = 7.5 Hz, 1H, H-C(5)), 7.75 (t, ^3J(H,H) = 7.5 Hz, 1H, H-C(4)), 7.30(d, ^3J(H,H) = 7.8 Hz, 1H, H-C(13)), 7.22 (d, ^3J(H,H) = 7.8 Hz, 1H, H-C(12)), 3.21 (d, ^3J(H,H) = 14.9 Hz, 1H, H$_2$-C(16)), 2.87 (d, ^3J(H,H) = 14.9 Hz, 1H, H$_2$-C(16')), 2.63 (m, 3H, H$_2$-C(20) or H$_2$-C(20') and H$_2$-C(22) and H$_2$-C(22')), 2.53 (dq, ^3J(H,H) = 7.3 Hz, 1H, H$_2$-C(20') or H$_2$-Cv(20)), 2.02 (s, 3H, H$_3$-C(18)), 1.35 (s, 3H, H$_3$-C(19)), 1.25 (t, ^3J(H,H) = 7.6 Hz, 3H, H$_3$-C(23)), 1.07 (t, 3H, H$_3$-C(21)) ppm; ^{13}C NMR (100 MHz, CD$_2$Cl$_2$): δ = 183.7 (C(1)), 175.6 (C(9)), 149.7 (C(7)), 146.4 (C(15)), 145.0 (C(11)), 140.3 (C(8)), 138.1 (C(10)), 137.9 (C(14)), 135.8 (C(5)), 135.4 (C(2)), 132.9 (C(4)), 132.0 (C(13)), 127.4 (C(6)), 127.4 (C(12)), 126.0 (C(3)), 53.0 (C(17)), 48.8 (C(16)), 28.5 (C(19)), 27.1 (C(20) and C(18)), 25.9 (C(22)), 15.3 (C(21)), 14.8 (C(23)) ppm.

Z-isomer: R_f = 0.51 (*i*Hex:EtOAc 1:1).

2-(7-isopropyl-2,2-dimethyl-2,3-dihydro-1*H*-inden-1-ylidene)-1-(λ^1-oxidanyl)-1,2-dihydro-3*H*-1λ^3-benzo[*b*]thiophen-3-one (5)[38]
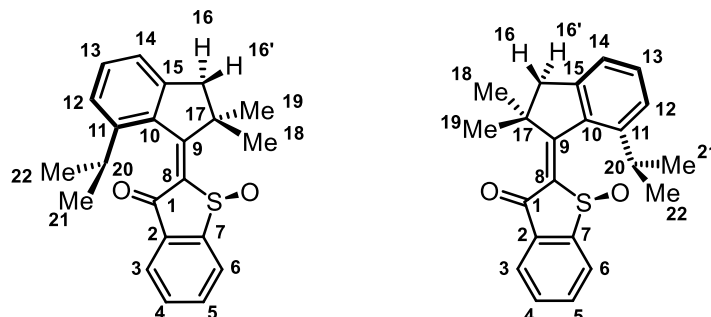
Compound ***E*-63** (81 mg, 0.22 mmol) was dissolved in dry CH_2Cl_2 (1.5 mL) and the solution was cooled to –50 °C. Oxalyl chloride was added (25 μL, 0.29 mmol) and the stirred reaction mixture was allowed to warm up to –30 °C within 2 h. The solution changed its color successively from yellow to an intensive red. Saturated aqueous $NaHCO_3$ solution (20 mL) was added and the aqueous phase was extracted three times with EtOAc (3 x 50 mL). The combined organic phases were dried over $MgSO_4$ and the solvent was removed *in vacuo*. Quantitative purification with conventional column chromatography (SiO_2, *i*Hex to *i*Hex:EtOAc 50:1) of compound HTI **64** was not successful and the prepurified material was used in the next synthetic step. Prepurified compound **64** (49 mg, 0.15 mmol) was dissolved in c. AcOH (2 mL) at 23 °C and sodium perborate tetrahydrate was added (69 mg, 0.45 mmol). After the reaction mixture was stirred for 2.5 h at 23 °C a saturated aqueous $NaHCO_3$ solution (50 mL) was added. The aqueous phase was extracted three times with EtOAc (3 x 100 mL) and the combined organic phases were dried over $MgSO_4$. The solvent was removed *in vacuo* and the crude product was purified by column chromatography (SiO_2, *i*Hex to *i*Hex:EtOAc 50:1 to 10:1 to 5:1) to obtain compound **5** (27 mg, 0.08 mmol, 36% over two steps) as a yellow solid.

E isomer: R_f = 0.26 (*i*Hex:EtOAc 7:3); m.p. 178 °C; ^{1}H NMR (800 MHz, CD_2Cl_2) δ = 8.09 (d, ^3J(H,H) = 7.7 Hz, 1H, H-C(6)), 7.97 (d, ^3J(H,H) = 7.6 Hz, 1H, H-C(3)), 7.89 (t, ^3J(H,H) = 7.5 Hz, 1H, H-C(5)), 7.75 (t, ^3J(H,H) = 7.4 Hz, 1H, H-C(4)), 7.42 (t, ^3J(H,H) = 7.6 Hz, 1H, H-C(13)), 7.26 (d, ^3J(H,H) = 7.8 Hz, 1H, H-C(12)), 7.17 (d, ^3J(H,H) = 7.3 Hz, 1H, H-C(14)), 3.27 (d, ^3J(H,H) = 14.8 Hz, 1H, H-C(16)), 3.20 (sep, ^3J(H,H) = 6.8 Hz, 1H, H_2-C(20)), 2.80 (d, ^3J(H,H) = 14.8 Hz, 1H, H_2-C(16')), 1.99 (s, 1H, H_3-C(19)), 1.32(s, 3H, H_3-C(18)), 1.31 (d, ^3J(H,H) = 6.7 Hz, 3H, H_3-C(22)), 0.87 ppm (d, ^3J(H,H) = 6.8 Hz, 3H, H_3-C(21)); ^{13}C NMR (200 MHz, CD_2Cl_2): δ = 183.4 (C(1)), 175.0 (C(9)), 151.9 (C(11)), 149.7 (C(7)), 148.2 (C(15)), 139.5 (C(8)), 137.5 (C(10)), 136.0 (C(5)), 135.3 (C(2)), 133.0 (C(4) and C(13)), 127.5 (C(6)), 126.0 (C(3)), 124.3 (C(12)), 122.9 (C(14)), 53.8 (C(17)), 50.5 (C(16)), 31.0 (C(20)), 27.9 (C(21) and C(18)), 26.9 (C(19)), 19.2 (C(22)) ppm; IR: $\tilde{\nu}$ = 3059w, 2955w, 2934w,

2870w, 1674s, 1589m, 1548vs, 1464m, 1452m, 1384w, 1362w, 1322w, 1278m, 1222s, 1200m, 1176w, 1164m, 1122m, 1076m, 1037vs, 1005m, 972w, 949w, 911w, 893w, 865m, 837w, 802m, 794vs, 783m, 770m, 753vs, 715s, 693s, 676s cm^{-1}; EI-MS (70 eV): *m/z* (%): 350 (4) [*M*], 333 (12), 307 (100), 291 (32), 183 (21); HR-EI-MS calc. [$C_{22}H_{22}OS$]: 350.1341, found: 350.1332; elemental analysis calc. (%) for $C_{22}H_{22}O_2S$: C 75.40, H 6.33, O 9.13, S 9.15; found: C 75.41, H 6.49, S 9.21.

Z isomer: R_f = 0.19 (*i*Hex:EtOAc 7:3); ^{1}H NMR (800 MHz, CD$_2$Cl$_2$) δ = 8.04 (d, ^3J(H,H) = 7.7 Hz, 1H, H-C(6)), 8.02 (d, ^3J(H,H) = 7.8 Hz, 1H, H-C(3)), 7.85 (t, ^3J(H,H) = 7.5 Hz, 1H, H-C(5)), 7.76 (t, ^3J(H,H) = 7.5 Hz, 1H, H-C(4)), 7.48 (t, ^3J(H,H) = 7.6 Hz, 1H, H-C(13)), 7.38 (d, ^3J(H,H) = 7.9 Hz, 1H, H-C(12)), 7.17 (d, ^3J(H,H) = 7.3 Hz, 1H, H-C(14)), 3.72 (sep, ^3J(H,H) = 6.6 Hz, 1H, H-C(20)), 3.19 (d, ^3J(H,H) = 15.3 Hz, 1H, H$_2$-C(16)), 2.81 (d, ^3J(H,H) = 15.3 Hz, 1H, H$_2$-C(16')), 1.59 (s, 3H, H$_3$-C(19)), 1.55 (d, ^3J(H,H) = 6.7 Hz, 3H, H$_3$-C(22)), 1.41(s, 3H, H$_3$-C(18)), 1.03 (d, ^3J(H,H) = 6.7 Hz, 3H, H$_3$-C(21)) ppm; ^{13}C NMR (200 MHz, CD$_2$Cl$_2$): δ = 184.4 (C(1)), 177.3 (C(9)), 150.9 (C(7)), 150.4 (C(11)), 149.6 (C(15)), 144.6 (C(8)), 137.0 (C(10)), 136.5 (C(2)), 135.5 (C(5)), 133.6 (C(13)), 133.1 (C(4)), 127.6 (C(6)), 125.6 (C(3) and C(12)), 123.1 (C(14)), 54.4 (C(17)), 51.4 (C(16)), 31.2 (C(20)), 27.7 (C(21)), 27.1 (C(18)), 26.4 (C(19)), 21.3 (C(22)) ppm; IR: $\tilde{v}$ = 2962m, 2867w, 1672vs, 1587m, 1543vs, 1475m, 1462m, 1388w, 1362w, 1309w, 1275s, 1215s, 1193w, 1164m, 1118m, 1076vs, 1046vs, 980m, 971m, 935w, 881w, 822w, 796m, 788m, 779s, 769s, 753vs, 705s, 667w cm^{-1}.

Analytical data of intermediate compound 64 after purification by HPLC:[38]
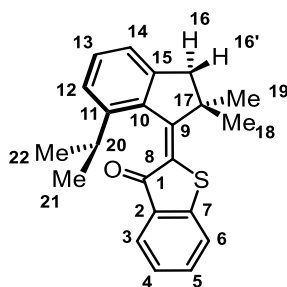
E isomer: R_f = 0.16 (*i*Hex:EtOAc 50:1); m.p. 59 °C; ^{1}H NMR (800 MHz, CD$_2$Cl$_2$) δ = 7.79 (d, ^3J(H,H) = 7.7 Hz, 1H, H-C(3)), 7.55 (t, ^3J(H,H) = 7.6 Hz, 1H, H-C(5)), 7.49 (d, ^3J(H,H) = 7.9 Hz, 1H, H-C(6)), 7.31 (t, ^3J(H,H) = 7.6 Hz, 1H, H-C(13)), 7.26 (t, ^3J(H,H) = 7.5 Hz, 1H, H-C(4)), 7.20 (d, ^3J(H,H) = 7.8 Hz, 1H, H-C(12)), 7.10 (d, ^3J(H,H) = 7.3 Hz, 1H, H-C(14)), 3.27 (sep, ^3J(H,H) = 6.9 Hz, 1H, H-C(20)), 3.15 (d, ^3J(H,H) = 14.8 Hz, 1H, H$_2$-C(16) or H$_2$-C(16')), 2.69 (d, ^3J(H,H) = 14.8 Hz, 1H, H$_2$-C(16') or H$_2$-C(16)), 1.69 (s, 3H, H$_3$-C(18) or H$_3$-C(19)), 1.34 (d, ^3J(H,H) = 6.7 Hz, 3H, H$_3$-C(21) or H$_3$-C(22)), 1.15 (s, 3H, H$_3$-C(19) or H$_3$-C(18)), 0.85 (d, ^3J(H,H) = 6.9 Hz, 3H, H$_3$-C(22) or H$_3$-C(21)) ppm; ^{13}C NMR (100 MHz, CD$_2$Cl$_2$): δ = 186.8 (C(1)), 161.5 (C(9)), 151.2 (C(11)), 147.1 (C(15)), 145.2 (C(7)), 138.4 (C(10)), 134.9 (C(5)), 132.4 (C(8)), 131.2 (C(13)), 127.0 (C(3)), 125.3 (C(4)), 123.8 (C(6)), 123.6 (C(12)), 122.5 (C(14)), 52.4 (C(17)), 50.2 (C(16)), 31.3 (C(20)), 28.0 (C(21) or C(22)), 27.3 (C(18) or C(19)), 26.5 (C(19) or C(18)), 19.3 (C(22) or C(21)) ppm; IR: $\tilde{v}$ = 2954w, 1667m, 1587m, 1531m, 1450s, 1380w, 1359w, 1312w, 1281s, 1217w, 1162w, 1110w, 1074m, 1049s, 1031m, 1012m, 866w, 840m, 788m, 777m, 764m, 741vs, 724m, 692m, 668m; EI-MS (70 eV): *m/z* (%): 334 (2) [*M*], 307 (26), 291 (100), 261 (12); HR-EI-MS calc. [C$_{22}$H$_{22}$OS]: 334.1391, found: 334.1378.

Z isomer: R_f = 0.22 (*i*Hex:EtOAc 50:1).

Concise protocol for the synthesis of HTI motor 5[38]

A solution of compound **16** (143 mg, 0.96 mmol) in dry THF (1.4 mL) was cooled to –78°C and *n*BuLi (0.36 mL, 0.81 mmol, 2.25 M in hexane) was added slowly under an Argon atmosphere. The reaction mixture was allowed to warm up to 0 °C within 10 min. Then a solution of compound **55** (150 mg, 0.74 mmol) in dry THF (1.6 mL) was added to the reaction mixture. After 20 min of stirring at 0 °C under Argon atmosphere a solution of saturated aqueous NH$_4$Cl solution (50 mL) was added to the reaction mixture. The aqueous phase was extracted three times with EtOAc (3 x 100mL) and the

combined organic phases were dried over $MgSO_4$. The solvent was removed in *vacuo* and the crude product was purified by column chromatography (SiO_2, *i*Hex to *i*Hex:EtOAc, 50:1 to 25:1 v/v). Purified compound **61** (206 mg, 0.59 mmol) was dissolved in THF (4 mL) at 23 °C and c. H_2SO_4 (20 µL) was added. The reaction mixture turned green and then changed its color to a dark yellow within minutes. After the reaction mixture was stirred for 40 minutes saturated aqueous $NaHCO_3$ solution (40 mL) was added. The aqueous phase was extracted three times with EtOAc (3 x 100 mL) and the combined organic phases were dried over $MgSO_4$. The solvent was removed *in vacuo*. The residue was dissolved in c. AcOH (7 mL) and sodium perborate tetrahydrate was added (268 mg, 1.74 mmol). After the reaction mixture was stirred for 1.5 h at 23 °C a saturated aqueous $NaHCO_3$ solution (100 mL) was added. The aqueous phase was extracted three times with CH_2Cl_2 (3 x 150 mL) and the combined organic phases were dried over $MgSO_4$. The solvent was removed *in vacuo*. The residue was dissolved in dry CH_2Cl_2 (3.8 mL) and the solution was cooled to –50 °C. Oxalyl chloride was added (60 µL, 0.72 mmol) and the reaction mixture was stirred for 2 h at –50 °C. The solution changed its color successively from yellow to an intensive red. Saturated aqueous $NaHCO_3$ solution (50 mL) was added and the aqueous phase was extracted three times with EtOAc (3 x 100 mL). The combined organic phases were dried over $MgSO_4$ and the solvent was removed *in vacuo*. The residue was dissolved in c. AcOH (7 mL) and sodium perborate tetrahydrate was added (272 mg, 1.77 mmol). After the reaction mixture was stirred for 3 h at 23 °C a saturated aqueous $NaHCO_3$ solution (100 mL) was added. The aqueous phase was extracted three times with EtOAc (3 x 150 mL) and the combined organic phases were dried over $MgSO_4$. The solvent was removed *in vacuo* and the crude product was purified by column chromatography (SiO_2, *i*Hex to *i*Hex:EtOAc 50:1 to 25:1 to 10:1 to 5:1) to obtain compound **5** (133 mg, 0.38 mmol, 52%) as a yellow solid.

2,2,4,7-Tetramethyl-2,3-dihydro-1*H*-inden-1-one (10)[I] [202]
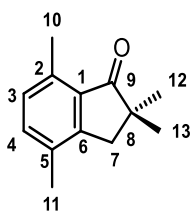
To a solution of 4,7-dimethyl-2,3-dihydro-1H-inden-1-one **24** (1.0 g, 6.2 mmol) in dimethoxyethane (15 mL) NaH (60% w/w in mineral oil, 0.75 mg, 19 mmol) was added at 23 °C and stirred for 40 min. Then methyl iodide (1.4 mL, 22 mmol) was added successively to the reaction mixture and after 40 min of stirring at 23 °C a saturated aqueous NH$_4$Cl solution (50 mL) was added. The aqueous phase was extracted three times with EtOAc (3 x 50 mL) and the combined organic phases were dried over Na$_2$SO$_4$. The solvent was removed *in vacuo* and the crude product was purified by column chromatography (SiO$_2$, *i*Hex:EtOAc, 98:2 v/v) to obtain compound **12** (1.1 g, 5.8 mmol, 92%) as a pale yellow solid.

R_f = 0.47 (*i*Hex:EtOAc 95:5); m.p. 41 °C; ^{1}H NMR (400 MHz, CDCl$_3$) δ = 7.25 (d, ^3J(H,H) = 7.5 Hz, 1H, H-C(4)), 7.03 (d, ^3J(H,H) = 7.5 Hz, 1H, H-C(3)), 2.83 (s, 2H, H$_2$-C(7)), 2.60 (s, 3H, H$_3$-C(10)), 2.28 (s, 3H, H$_3$-C(11)), 1.22 (s, 6H, H$_3$-C(12) and H$_3$-C(13)) ppm; ^{13}C NMR (100 MHz, CDCl$_3$): δ = 212.8 (C(9)), 151.8 (C(6)), 136.7 (C(2)), 134.6 (C(4)), 132.8 (C(5)), 132.5 (C(1)), 129.5 (C(3)), 45.3 (C(8)), 41.5 (C(7)), 25.7 (C(12) and C(13)), 18.1 (C(10)), 17.6 (C(11)) ppm; IR: $\tilde{\nu}$ = 2963w, 1694vs, 1584m, 1491m, 1462m, 1436m, 1373m, 1328w, 1287w, 1244m, 1156m, 1076w, 984m, 928m, 816vs, 788m, 667w cm^{-1}; HR-EI-MS calc. [C$_{13}$H$_{16}$O]: 188.1201, found: 188.1197.

2-ethynyl thioanisole (16)[198]
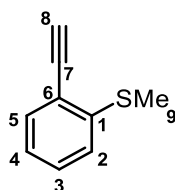
To a solution of 2-iodo thioanisole (1.5 g, 6.0 mmol) in a mixture of THF (18 mL) and N(Et)$_3$ (9.0 mL) CuI (91 mg, 0.48 mmol) and Pd(P(Ph)$_3$)$_2$Cl$_2$ (0.13 mg, 0.18 mmol) were added. The reaction mixture was degassed with N$_2$ for 10 min and TMS-acetylene (0.80 g, 7.8 mmol) was added. After the reaction mixture was stirred for 30 min at 23 °C, saturated aqueous NH$_4$Cl solution (150 mL) was added. The reaction mixture was extracted three times with EtOAc (3 x 150 mL). The combined organic phases were washed again with saturated aqueous NH$_4$Cl solution (100 mL) and water (100 mL) and dried over MgSO$_4$. The volatiles were removed *in vacuo*. The product was purified by column chromatography (SiO$_2$, *i*Hex:EtOAc, 200:1 v/v). After removing the volatiles *in vacuo* the residue was dissolved in MeOH (18 mL) and KF (0.52 g, 9.0 mmol) was added. After the reaction mixture was stirred for 16 h, saturated aqueous NH$_4$Cl solution was added. The aqueous phase was extracted three times with EtOAc (3 x 150 mL) and the combined organic phases were separated and dried over MgSO$_4$. The volatiles were removed *in vacuo* and the crude product was purified by column chromatography (SiO$_2$, *i*Hex:EtOAc, 50:1 v/v) to obtain compound **16** (0.82 g, 92%) as a colourless liquid.

R_f = 0.38 (*i*Hex); ^{1}H NMR (600 MHz, CDCl$_3$) δ = 7.46 (d, ^3J(H,H) = 7.7 Hz, 1H, H-C(2) or H-C(5)), 7.32 (d, ^3J(H,H) = 7.6 Hz, 1H, H-C(3) or H-C(4)), 7.18 (d, ^3J(H,H) = 7.7 Hz, 1H, H-C(5) or H-C(2)), 7.10 (t, ^3J(H,H) = 7.7 Hz, 1H, H-C(4) or H-C(3)), 3.47 (s, 1H, H-C(8)), 2.50 (s, 3H, H$_3$-C(9)) ppm; ^{13}C NMR (150 MHz, CDCl$_3$): δ = 142.0 (C(1)), 133.3 ((C(3) or (C(5)), 129.4 (C(5) or (C(3)), 124.5 (C(2) or (C(4))), 124.5 (C(4) or (C(2))), 120.4 (C(6)), 88.6 (C(8)), 81.2 (C(7)), 15.3 (C(9)) ppm; IR: $\tilde{v}$ = 3279m, 3058w, 2983w, 2919w, 2100w, 1913w, 1580w, 1560w, 1462s, 1431s, 1320w, 1277w, 1262m, 1195w, 1163w, 1128m, 1069m, 1038m, 968w, 954w, 960w, 781w, 747vs, 721m, 673s cm^{-1}; EI-MS (70 eV): *m/z* (%): 147 (100) [*M*], 89 (22); HR-EI-MS calc. [C$_9$H$_8$S]: 148.0347, found: 148.0336.

2,2,4,7-Tetramethyl-1-((2-(methylthio)phenyl)ethynyl)-2,3-dihydro-1*H*-inden-1-ol (17)[I] [38]
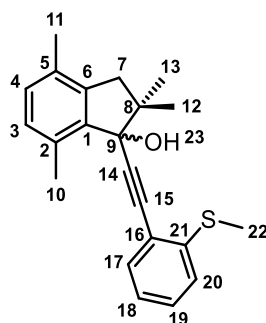
A solution of compound **16** (173 mg, 1.17 mmol) in dry THF (1.5 mL) was cooled to –78°C and *n*BuLi (2.5 M in hexane, 0.47 mL, 1.17 mmol) was added slowly under an argon atmosphere. The reaction mixture was allowed to warm up to 0 °C within 15 min. Then a solution of 2,2,4,7-Tetramethyl-2,3-dihydro-1H-inden-1-one **12** (220 mg, 1.17 mmol) in dry THF (1.5 mL) was added slowly to the reaction mixture. After 50 min of stirring at 0 °C under an argon atmosphere a saturated aqueous NH₄Cl solution (20 mL) was added to the reaction mixture. The aqueous phase was extracted with EtOAc (3 x 20 mL) and the combined organic phases were dried over Na₂SO₄. The solvent was removed *in vacuo* and the crude product was purified by column chromatography (SiO₂, *i*Hex:EtOAc, 98:2 v/v) to obtain compound **17** (380 mg, 1.13 mmol, 97%) as a colorless oil.

R_f = 0.18 (*i*Hex:EtOAc 95:5); ¹H NMR (800 MHz, CD₂Cl₂) δ = 7.40 (d, ^3J(H,H) = 7.6 Hz, 1H, H-C(17)), 7.31 (t, ^3J(H,H) = 7.7 Hz, 1H, H-C(19)), 7.16 (d, ^3J(H,H) = 7.9 Hz, 1H, H-C(20)), 7.09 (t, ^3J(H,H) = 7.5 Hz, 1H, H-C(18)), 6.99 (d, ^3J(H,H) = 7.6 Hz, 1H, H-C(4)), 6.93 (d, ^3J(H,H) = 7.6 Hz, 1H, H-C(3)), 2.80 (d, ^3J(H,H) = 15.2 Hz, 1H, H₂-C(7)), 2.69 (d, ^3J(H,H) = 15.2 Hz, 1H, H₂-C(7)), 2.61 (s, 3H, H₃-C(10)), 2.46 (s, 3H, H₃-C(22)), 2.30 (m, 1H, H-O(23)), 2.21 (s, 3H, H₃-C(11)), 1.31 (s, 3H, H₃-C(12) or H₃-C(13)), 1.26 (s, 3H, H₃-C(13) or H₃-C(12)) ppm; ¹³C NMR (201 MHz, CD₂Cl₂): δ = 142.3 (C(21)), 142.2 (C(1)), 141.8 (C(6)), 133.3 (C(2)), 132.9 (C(17)), 132.3 (C(5)), 129.8 (C(4)), 129.7 (C(3)), 129.4 (C(19)), 124.6 (C(18)), 124.5 (C(20)), 121.3 (C(16)), 96.6 (C(14)), 85.5 (C(15)), 82.9 (C(9)), 48.7 (C(8)), 43.6 (C(7)), 26.8 (C(12) or C(13)), 22.4 (C(13) or C(12)), 18.8 (C(11)), 18.7 (C(10)), 15.4 (C(22)) ppm; IR: $\tilde{v}$ = 3409w, 1959m, 2923m, 2867w, 1582w, 1496m, 1463s, 1434s, 1380m, 1364m, 1336w, 1278m, 1258w, 1236w, 1174m, 1118w, 1050s, 1033s, 985m, 965m, 926m, 906m, 867m, 807s, 785m, 748vs, 720m, 680m cm⁻¹; HR-EI-MS calc. [C₂₂H₂₄OS]: 336.1548, found: 336.1544; elemental analysis calc. (%) for C₂₂H₂₄OS: C 78.53, H 7.19, S 9.53, O 4.75; found: C 78.59, H 7.26, S 9.78.

(*E/Z*)-1-(2-(Methylthio)phenyl)-2-(2,2,4,7-tetramethyl-2,3-dihydro-1*H*-inden-1-ylidene)ethan-1-one (*E/Z*-18)[IV] [38]
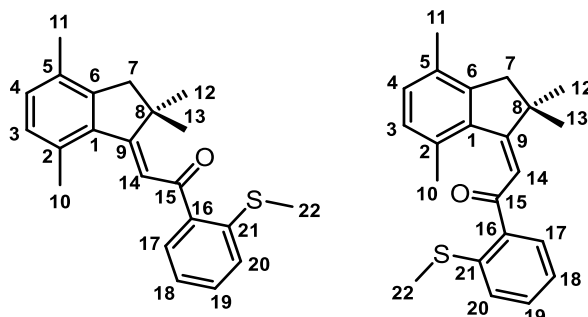
Compound **17** (56.5 mg, 0.168 mmol) was dissolved in THF at 23 °C (1.0 mL) and c. H_2SO_4 (20 μL) was added. After the reaction mixture was stirred for 15 h at 23 °C a saturated aqueous $NaHCO_3$ solution (20 mL) was added. The mixture was extracted three times with EtOAc (3 x 20 mL) and the combined organic phases were dried over Na_2SO_4. The solvent was removed *in vacuo* and the crude product was purified by column chromatography (SiO_2, *i*Hex:EtOAc, 98:2 v/v) to obtain compound **18** (51.7 mg, 0.154 mmol, 92%) as a mixture of *E* (91%) and *Z* (9%) isomers, both as yellow crystals.

E isomer: R_f = 0.37 (*i*Hex:EtOAc 95:5); m.p. 111-112 °C; ^1H NMR (800 MHz, CD_2Cl_2) δ = 7.83 (dd, $^3J(H,H)$ = 7.7 Hz, $^4J(H,H)$ = 1.4 Hz, 1H, H-C(17)), 7.47 (ddd, $^3J(H,H)$ = 8.1, 7.3 Hz, $^4J(H,H)$ = 1.5 Hz 1H, H-C(19)), 7.36 (d, $^3J(H,H)$ = 8.1 Hz, 1H, H-C(20)), 7.18 (ddd, $^3J(H,H)$ = 7.7, 7.3 Hz, $^4J(H,H)$ = 1.1 Hz 1H, H-C(18)), 7.05 (d, $^3J(H,H)$ = 7.9 Hz, 1H, H-C(4)), 7.04 (s, 1H, H-C(14)), 6.98 (d, $^3J(H,H)$ = 7.7 Hz, 1H, H-C(3)), 2.84 (s, 2H, H_2-C(7)), 2.50 (s, 3H, H_3-C(10)) 2.46 (s, 3H, H_3-C(22)), 2.23 (s, 3H, H_3-C(11)), 1.42 (s, 6H, H_3-C(12) and H_3-C(13)); ^{13}C NMR (201 MHz, CD_2Cl_2): δ = 194.5 (C(15)), 167.5 (C(9)), 146.3 (C(6)), 142.4 (C(21)), 138.4 (C(1)), 137.4 (C(16)), 133.6 (C(2)), 132.6 (C(5)), 132.3 (C(19)), 131.6 (C(17)), 130.8 (C(4)), 130.7 (C(3)), 125.5 (C(20)), 124.0 (C(18)), 122.3 (C(14)), 49.0 (C(7)), 45.2 (C(8)), 27.8 (C(12) and C(13)), 22.4 (C(10)), 18.7 (C(11)), 16.3 (C(22)) ppm; IR: $\tilde{v}$ = 2920w, 1642s, 1606m, 1586m, 1554m, 1493w, 1458m, 1446m, 1435m, 1376w, 1357w, 1332w, 1311m, 1280w, 1262w, 1248m, 1208s, 1132m, 1084w, 1027m, 977w, 886m, 841m, 810s, 774m, 746vs, 676s cm^{-1}; HR-EI-MS calc. [$C_{22}H_{24}OS$]: 336.1548, found: 336.1542; elemental analysis calc. (%) for $C_{22}H_{24}OS$: C 78.53, H 7.19, S 9.53; found: C 78.60, H 7.37, S 9.68.

Z isomer: R_f = 0.26 (*i*Hex:EtOAc 95:5); m.p. 146-147 °C; ^1H NMR (800 MHz, CD_2Cl_2) δ = 7.89 (dd, $^3J(H,H)$ = 7.7 Hz, $^4J(H,H)$ = 1.5 Hz, 1H, H-C(17)), 7.48 (ddd, $^3J(H,H)$ = 8.1, 7.3 Hz, $^4J(H,H)$ = 1.5 Hz 1H, H-C(19)), 7.36 (d, $^3J(H,H)$ = 8.0 Hz, 1H, H-C(20)), 7.19 (dd, $^3J(H,H)$ = 8.4, 7.5 Hz, 1H, H-C(18)), 7.04 (d, $^3J(H,H)$ = 7.6 Hz, 1H, H-C(4)), 6.90 (d, $^3J(H,H)$ = 7.6 Hz, 1H, H-C(3)), 6.53 (s, 1H, H-C(14)), 2.80 (s, 2H, H_2-C(7)), 2.44 (s, 3H, H_3-C(22)), 2.24 (s, 3H, H_3-C(11)), 1.97 (s, 3H, H_3-C(19)), 1.28 (s,

239

6H, H$_3$-C(12) and H$_3$-C(13)); ^{13}C NMR (201 MHz, CD$_2$Cl$_2$): δ = 194.0 (C(15)), 165.6 (C(9)), 144.8 (C(6)), 143.2 (C(21)), 137.8 (C(1)), 136.2 (C(16)), 135.0 (C(2)), 132.5 (C(19)), 132.0 (C(17)), 131.6 (C(5)), 130.9 (C(4)), 129.3 (C(3)), 125.3 (C(20)), 123.8 (C(14)), 119.8 (C(14)), 48.0 (C(8)), 46.1 (C(7)), 28.1 (C(12) and C(13)), 22.1 (C(10)), 18.5 (C(11)), 16.2 (C(22)) ppm; IR: $\tilde{v}$ = 2962w, 2916w, 1646s, 1601s, 1585m, 1432s, 1310w, 1262m, 1224s, 1206s, 1135s, 1082w, 1046w, 1025m, 1012m, 946w, 846w, 820m, 190w, 768vs, 744s, 699w, 672m cm^{-1}.

(*E*/*Z*)-2-(2,2,4,7-Tetramethyl-2,3-dihydro-1*H*-inden-1-ylidene)benzo[*b*]thiophen-3(2*H*)-one (*E*/*Z*-19)[38]
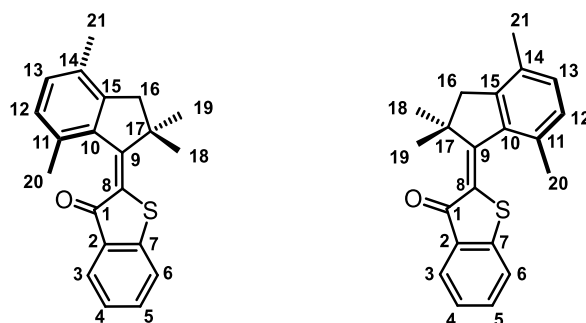
Compound **25** (mixture of *E* (78%) and *Z* (22%) isomers, 113 mg, 0.320 mmol) was dissolved in dry CH$_2$Cl$_2$ (3.0 mL) and the solution was cooled to –50 °C. Oxalyl chloride was added (30 µL, 0.350 mmol) and the stirred reaction mixture was allowed to warm up to –30°C within 2 h. The solution changes its color successively from yellow to an intense orange. A saturated aqueous NaHCO$_3$ solution (40 mL) was added and the mixture was extracted with CH$_2$Cl$_2$ (3 x 40 mL). The combined organic phases were dried over Na$_2$SO$_4$ and the solvent was removed *in vacuo*. The crude product was purified two times by column chromatography (SiO$_2$, *i*Hex:EtOAc, 98:2 v/v) to obtain compound **19** (90 mg, 0.280 mmol, 88%) as a mixture of *E* (87%) and *Z* (13%) isomers, both as an orange solid.

E isomer: R_f = 0.60 (*i*Hex:EtOAc 95:5); ^{1}H NMR (800 MHz, CD$_2$Cl$_2$) δ = 7.83 (d, ^3J(H,H) = 7.7 Hz, 1H, H-C(3)), 7.56 (td, ^3J(H,H) = 7.5 Hz, ^4J(H,H) = 1.3 Hz, 1H, H-C(5)), 7.51 (d, ^3J(H,H) = 7.94 Hz, 1H, H-C(6)), 7.27 (td, ^3J(H,H) = 7.4 Hz, ^4J(H,H) = 0.9 Hz, 1H, H-C(4)), 7.11 (d, ^3J(H,H) = 7.8 Hz, 1H, H-C(12)), 7.02 (d, ^3J(H,H) = 7.7 Hz, 1H, H-C(13)), 3.08 (d, ^3J(H,H) = 15.2 Hz, 1H, H$_2$-C(16)), 2.75 (d, ^3J(H,H) = 15.2 Hz, 1H, H$_2$-C(16)), 2.26 (s, 3H, H$_3$-C(20)), 2.15 (s, 3H, H$_3$-C(21)), 1.74 (s, 3H, H$_3$-C(18) or H$_3$-C(19)), 1.17 (s, 3H, H$_3$-C(19) or H$_3$-C(18)) ppm; ^{13}C NMR (201 MHz, CD$_2$Cl$_2$): δ = 186.6 (C(1)), 162.0 (C(9)), 145.8 (C(10)), 144.2 (C(7)), 138.7 (C(15)), 137.2 (C(14)), 134.1 (C(5)), 132.0 (C(2)), 131.0 (C(12)), 130.6 (C(11)), 128.7 (C(13)), 126.2 (C(3)), 125.9 (C(8)), 124.6 (C(4)), 123.2 (C(6)), 50.7 (C(17)), 48.2 (C(16)), 26.8 (C(18) or C(19)), 26.1 (C(19) or C(18)), 21.6 (C(21)), 17.9 (C(20)) ppm.

Z isomer: R_f = 0.68 (*i*Hex:EtOAc 95:5); ^{1}H NMR (800 MHz, CD$_2$Cl$_2$) δ = 7.80 (d, ^3J(H,H) = 7.7 Hz, 1H, H-C(3)), 7.51 (td, ^3J(H,H) = 7.5 Hz, ^4J(H,H) = 1.3 Hz, 1H, H-C(5)), 7.41 (d, ^3J(H,H) = 7.94 Hz, 1H, H-C(6)), 7.25 (td, ^3J(H,H) = 7.4 Hz, ^4J(H,H) = 0.9 Hz, 1H, H-C(4)), 7.15 (d, ^3J(H,H) = 7.8 Hz, 1H, H-C(13)), 7.07 (d, ^3J(H,H) = 7.7 Hz, 1H, H-C(12)), 2.91 (s, 2H, H$_2$-C(16)), 2.44 (s, 3H, H$_3$-C(20)), 2.24 (s, 3H, H$_3$-C(21)), 1.51 (s, 6H, H$_3$-C(18) and H$_3$-C(19)) ppm.

Mix of 8:2 *E*:*Z* isomers: m.p. 138 °C; IR: $\tilde{v}$ = 2956w, 2915w, 2857w, 1656s, 1586m, 1520s, 1489w, 1448s, 1377w, 1362w, 1311w, 1278s, 1209m, 1172m, 1114w, 1073s, 1038m, 1012m, 931w, 890w, 864w, 814w, 794w, 755s, 742vs, 728m, 713w, 690m, 663m cm^{-1}; HR-EI-MS calc. [C$_{21}$H$_{20}$OS]: 320.1235, found: 320.1229; elemental analysis calc. (%) for C$_{21}$H$_{20}$OS: C 78.71, H 6.29, S 10.00, O 4.99; found: C 78.88, H 6.56, S 10.22.

9-((2-(methylthio)phenyl)ethynyl)-9*H*-fluoren-9-ol (21)
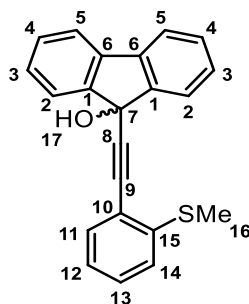
To a solution of 2-ethinyl thioanisole **16** (37 mg, 0.25 mmol) in dry DME (2 mL) *n*BuLi (0.10 mL, 0.25 mmol, 2.5 M in hexane) was added successively at –78 °C under Argon atmosphere. After the solution was stirred for 30 min at –78 °C a solution of fluorenone (45 mg, 0.25 mmol) in DME (1.0 mL) was added. The reaction mixture was allowed to warm up to 23 °C and was stirred for 20 h. A saturated aqueous NH$_4$Cl (30 mL) solution was added to the reaction mixture. The aqueous phase was extracted three times with EtOAc (3 x 50 mL) and the combined organic phases were dried over MgSO$_4$. The volatiles were removed *in vacuo* and the crude product was purified by column chromatography (SiO$_2$, *i*Hex:EtOAc, 50:1 v/v) to obtain compound **21** (46 mg, 0.14 mmol, 56%) as a colourless liquid.

^{1}H NMR (400 MHz, CDCl$_3$) δ = 7.82 (d, ^3J(H,H) = 7.4 Hz, 2H, H-C(2) or H-C(5)), 7.64 (d, ^3J(H,H) = 7.2 Hz, 2H, H-C(5) or H-C(2)), 7.41 (t, ^3J(H,H) = 7.4 Hz, 2H, H-C(3) or H-C(4)), 7.38 (t, ^3J(H,H) = 7.4 Hz, 2H, H-C(4) or H-C(3)), 7.36 (d, ^3J(H,H) = 7.7 Hz, 1H, H-C(11) or H-C(14)), 7.26 (t, ^3J(H,H) = 7.7 Hz, 1H, H-C(12) or H-C(13)), 7.12 (d, ^3J(H,H) = 7.9 Hz, 1H, H-C(14) or H-C(11)), 7.03 (t, ^3J(H,H) = 7.5 Hz, 1H, H-C(13) or H-C(12)), 2.73 (s, 1H, H-O(17)), 2.44 (s, 3H) ppm; ^{13}C NMR (100 MHz, CDCl$_3$): δ = 147.1, 142.5, 139.3, 132.8, 129.8, 129.2, 128.7, 124.7, 124.2, 124.2, 120.5, 120.4,

15.2, (C(16)) ppm; EI-MS (70 eV): *m*/*z* (%): 281 (100) [*M*], 328 (14), 311 (5); HR-EI-MS calc. [$C_{22}H_{16}OS$]: 328.0922, found: 328.0912.

2-(9*H*-fluoren-9-ylidene)-1-(2-(methylthio)phenyl)ethan-1-one (22)
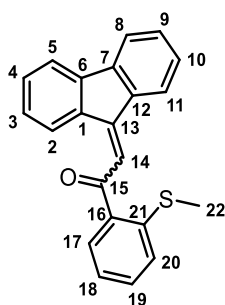
Compound **21** (34 mg, 0.10 mmol) was dissolved in ethanol (1.0 mL) and one drop of c. H_2SO_4 was added. After the reaction mixture was stirred for 2 h aqueous saturated NH_4Cl solution (2.0 mL) was added and the aqueous phase was extracted three times with EtOAc (3 x 15 mL). The combined organic phases were dried over $MgSO_4$ and the volatiles were removed *in vacuo*. After purification by column chromatography (SiO$_2$, *i*Hex:EtOAc, 50:1 v/v) compound **22** could be obtained as yellow solid.

^{1}H NMR (400 MHz, CD$_2$Cl$_2$) δ = 8.24 (d, ^{3}J(H,H) = 7.9 Hz, 1H), 7.93 (d, ^{3}J(H,H) = 7.6 Hz, 1H, H-C(17)), 7.77 (d, ^{3}J(H,H) = 7.6 Hz, 1H), 7.68 (d, ^{3}J(H,H) = 7.5 Hz, 2H), 7.54 (t, ^{3}J(H,H) = 8.2 Hz, 1H, H-C(19)), 7.51 (s, 1H, H-C(14)), 7.44 (d, ^{3}J(H,H) = 7.8 Hz, 1H, H-C(20)), 7.44 (t, ^{3}J(H,H) = 7.5 Hz, 1H), 7.39 (t, 1H, ^{3}J(H,H) = 7.4 Hz), 7.32 (t, 1H, ^{3}J(H,H) = 7.5 Hz), 7.23 (t, 1H, ^{3}J(H,H) = 7.8 Hz, 1H), 7.22 (t, 1H, ^{3}J(H,H) = 7.7 Hz, H-C(18)), 2.51 (s, 3H, H$_3$-C(22)) ppm; ^{13}C NMR (100 MHz, CD$_2$Cl$_2$): δ = 193.9 (C(15)), 145.5, 143.1 (C(21)), 142.7, 141.2, 139.3, 136.5, 135.9, 133.1 (C(19)), 131.9 (C(17)), 131.2, 130.9, 128.4, 128.0, 127.9, 126.0 (C(20)), 124.3 (C(18)), 122.1, 121.8, 120.4, 120.3, 16.5 (C(22)) ppm.

2-(9*H*-fluoren-9-ylidene)benzo[*b*]thiophen-3(2*H*)-one (23)
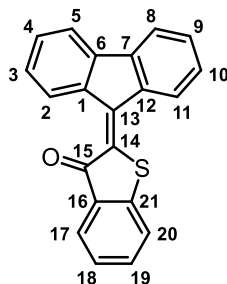
Compound **21** (46 mg, 0.14 mmol) was dissolved in c. AcOH (0.20 mL) and one drop of c. H_2SO_4 was added. After the reaction mixture was stirred for 30 min saturated aqueous NH_4Cl (2 mL) was added and the aqueous phase was extracted three times with EtOAc (3 x 5 mL). The combined organic phases were dried over $MgSO_4$ and the volatiles were removed *in vacuo.* The crude product was purified by column chromatography (SiO_2, *i*Hex:EtOAc, 50:1 v/v).

^{1}H NMR (400 MHz, CD_2Cl_2) $\delta = 9.39$ (d, $^3J(H,H) = 8.0$ Hz, 1H, H-C(2)), 8.23 (d, $^3J(H,H) = 7.7$ Hz, 1H, H-C(11)), 7.94 (d, $^3J(H,H) = 7.7$ Hz, 1H, H-C(17)), 7.71 (d, $^3J(H,H) = 7.4$ Hz, 1H, H-C(8)), 7.68 (d, $^3J(H,H) = 7.5$ Hz, 1H, H-C(5)), 7.66 (t, $^3J(H,H) = 8.1$ Hz, 1H, H-C(19)), 7.57 (d, $^3J(H,H) = 7.8$ Hz, 1H, H-C(20)), 7.45 (t, $^3J(H,H) = 7.6$ Hz, 1H, H-C(9)), 7.43 (t, $^3J(H,H) = 7.4$ Hz, 1H, H-C(4)), 7.39 (t, $^3J(H,H) = 8.0$ Hz, 1H, H-C(10)), 7.36 (t, $^3J(H,H) = 7.8$ Hz, 1H, H-C(18)), 7.34 (t, $^3J(H,H) = 7.6$ Hz, 1H, H-C(3)) ppm; ^{13}C NMR (201 MHz, CD_2Cl_2): $\delta = 189.6$ (C(15)), 143.8 (C(21)), 143.6 (C(13) or C(14)), 143.3 (C(7)), 141.6 (C(6)), 139.5 (C(12)), 137.1 (C(1)), 135.8 (C(19)), 133.2 (C(14) or C(13)), 131.5 (C(4)), 131.4 (C(16)), 131.0 (C(9)), 129.3 (C(2)), 129.0 (C(3)), 128.5 (C(11)), 128.2 (C(10)), 127.3 (C(17)), 126.4 (C(18)), 123.9(C(20)), 120.6 (C(8)), 119.9 (C(5)) ppm; EI-MS (70 eV): *m/z* (%): 312 (53) [*M*], 311 (100), 164 (9); HR-EI-MS calc. [$C_{21}H_{11}OS^{.}$]: 311.0531, found: 311.0524.

4,7-dimethyl-2,3-dihydro-1*H*-inden-1-one (24)[I] [203]
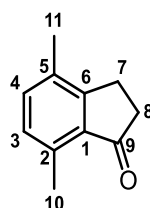
Aluminium chloride (8.0 g, 60 mmol) was suspended in CH_2Cl_2 (20 mL) and 3-chloropropanoyl chloride (6.4 g, 50 mmol) was added at 0 °C. The reaction mixture was stirred for 30 min and a solution of *p*-xylene (5.3 mg, 50 mmol) in CH_2Cl_2 (15 mL) was added at 0 °C. The reaction mixture was allowed to warm up to 23 °C and was stirred for 1 h. Water (50 mL) and saturated aqueous sodium oxalate solution was added (50 mL). The aqueous phase was extracted six times with Et_2O (6 x 100 mL). The combined organic phases were washed with saturated aqueous NaCl solution and dried over Na_2SO_4. The volatiles were removed *in vacuo*. The crude product was dissolved in c. H_2SO_4 (40 mL) and the reaction mixture was stirred for 1 h at 95 °C. Saturated aqueous Na_2CO_3 solution (250 mL) was added and the aqueous phase was extracted four times with Et_2O (4 x 100 mL). The combined organic phases were dried over Na_2SO_4 and the volatiles were removed *in vacuo*. After column chromatography (SiO₂, *i*Hex:EtOAc, 50:1 v/v) compound **24** was obtained as a colourless solid (6.7 g, 42 mmol, 84%).

M.p. 77-78 °C; ^1H NMR (800 MHz, CD_2Cl_2) δ = 7.25 (d, ^3J(H,H) = 7.4 Hz, 1H, H-C(4)), 7.02 (d, ^3J(H,H) = 7.4 Hz, 1H, H-C(3)), 2.96 (t, ^3J(H,H) = 5.9 Hz, 2H, H_2-C(8)), 2.63 (t, ^3J(H,H) = 5.9 Hz, 2H, H_2-C(7)), 2.56 (s, 3H, H_3-C(10)), 2.30 (s, 3H, H_3-C(11)) ppm; ^{13}C NMR (201 MHz, CD_2Cl_2): δ = 208.6 (C(9)), 155.4 (C(6)), 136.1 (C(2)), 134.7 (C(4)), 134.7 (C(1)), 133.6 (C(5)), 129.6 (C(3)), 37.2 (C(7)), 24.8 (C(8)), 18.2 (C(10)), 17.7 (C(11)) ppm; IR: $\tilde{v}$ = 2920w, 1698vs, 1583m, 1495m, 1441m, 1377m, 1328m, 1281w, 1245s, 1224m, 1083m, 1008m, 988m, 898m, 828vs cm⁻¹; EI-MS (70 eV): *m/z* (%): 160 (100) [*M*], 145 (8); HR-EI-MS calc. [$C_{11}H_{12}O$]: 160.0888, found: 160.0883.

(*E*/*Z*)-1-(2-(Methylsulfinyl)phenyl)-2-(2,2,4,7-tetramethyl-2,3-dihydro-1*H*-inden-1-ylidene)ethan-1-one (*E*/*Z*-25)[38]
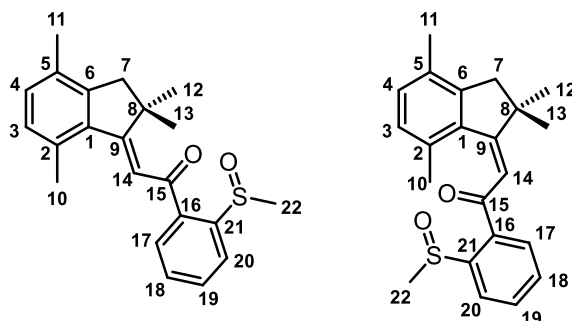
Compound **18** (mixture of *E* (91%) and *Z* (9%) isomers, 117 mg, 0.350 mmol) was dissolved at 23 °C in c. AcOH (4 mL) and sodium perborate tetrahydrate was added (215 mg, 1.40 mmol). After the reaction mixture was stirred for 45 min at 23 °C a saturated aqueous NaHCO$_3$ solution (100 mL) was added. The aqueous phase was extracted three times with EtOAc (3 x 70 mL) and the combined organic phases were dried over MgSO$_4$. The solvent was removed *in vacuo* and the crude product was purified by column chromatography (SiO$_2$, *i*Hex:EtOAc, 9:1 to 2:1 to 1:1 v/v) to obtain compound **25** as a mixture of *E* (78%) and *Z* (22%) isomers (113 mg, 0.320 mmol, 92%) as a yellow solid.

E isomer: R_f = 0.16 (*i*Hex:EtOAc 1:1); m.p. 160-161 °C; ^{1}H NMR (800 MHz, CD$_2$Cl$_2$) δ = 8.35 (dd, ^3J(H,H) = 7.9 Hz, ^4J(H,H) = 1.1 Hz, 1H, H-C(20)), 7.99 (dd, ^3J(H,H) = 7.7 Hz, ^4J(H,H) = 1.2 Hz, 1H, H-C(17)), 7.82 (ddd, ^3J(H,H) = 7.9, 7.4 Hz, ^4J(H,H) = 1.3 Hz, 1H, H-C(19)), 7.60 (td, ^3J(H,H) = 7.6 Hz, ^4J(H,H) = 1.2 Hz, 1H, H-C(18)), 7.19 (s, 1H, H-C(14)), 7.09 (d, ^3J(H,H) = 7.6 Hz, 1H, H-C(4)), 7.01 (d, ^3J(H,H) = 7.6 Hz, 1H, H-C(3)), 2.90 (d, ^3J(H,H) = 16.5 Hz, 1H, H$_2$-C(7)), 2.89 (s, 3H, H$_3$-C(22)), 2.84 (d, ^3J(H,H) = 16.5 Hz, 1H, H$_2$-C(7)), 2.54 (s, 3H, H$_3$-C(10)), 2.23 (s, 3H, H$_3$-C(11)), 1.45 (s, 3H, H$_3$-C(12) or H$_3$-C(13)), 1.40 (s, 3H, H$_3$-C(13) or H$_3$-C(12)) ppm; ^{13}C NMR (201 MHz, CD$_2$Cl$_2$): δ = 193.1 (C(15)), 170.7 (C(9)), 151.2 (C(21)), 146.9 (C(6)), 138.1 (C(1)), 136.7 (C(16)), 133.9 (C(2)), 133.9 (C(19)), 132.7 (C(5)), 131.4 (C(4)), 130.9 (C(3)), 130.8 (C(17)), 130.5 (C(18)), 124.7 (C(20)), 119.8 (C(14)), 49.0 (C(7)), 45.5 (C(8)), 45.3 (C(22)), 28.7 (C(12) or C(13)), 26.7 (C(13) or C(12)), 22.5 (C(10)), 18.6 (C(11)) ppm; IR: $\tilde{\nu}$ = 2922w, 1646s, 1610s, 1494w, 1463w, 1434w, 1380w, 1359w, 1340w, 1314w, 1284w, 1254m, 1214m, 1173w, 1133w, 1070s, 1042m, 1022vs, 954w, 889w, 846m, 810s, 780m, 750s, 730s, 702m, 667m cm^{-1}; HR-EI-MS calc. [C$_{22}$H$_{24}$O$_2$S]: 352.1497, found: 352.1498; elemental analysis calc. (%) for C$_{22}$H$_{24}$O$_2$S: C 74.96, H 6.86, S 9.10, O 9.08; found: C 74.70, H 6.85, S 9.31.

2,2-Diethyl-4,7-dimethyl-2,3-dihydro-1*H*-inden-1-one (26)[X] [208]
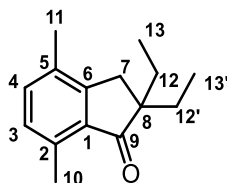
To a solution of compound **12** (0.24 mg, 1.5 mmol) in THF (10 mL) sodium hydride (60% in mineral oil, 0.11 g, 4.5 mmol) was added at 0 °C. The reaction mixture was stirred for 30 min at 23 °C before ethyl iodide (0.94 g, 6.0 mmol) was added at 0 °C. After stirring the reaction mixture for 24 h at 23 °C an aqueous HCl solution (50 mL, 0.1 M) was added. The aqueous phase was extracted three times with EtOAc (3x100 mL). The combined organic layers were washed with saturated aqueous NaHCO$_3$ solution, water and brine and dried over MgSO$_4$. The volatiles were removed *in vacuo*. The crude product was purified by column chromatography (SiO$_2$, *i*Hex:EtOAc, 99:1 v/v) to afford compound **26** (0.27 g, 1.26 mmol, 84%) as a yellow oil.

R_f = 0.20 (*i*Hex:EtOAc 50:1); ^{1}H NMR (600 MHz, CDCl$_3$): δ = 7.22 (d, ^3J(H,H) = 7.5 Hz, 1H, H-C(4)), 6.99 (d, ^3J(H,H) = 7.5 Hz, 1H, H-C(3)), 2.79 (s, 2H, H$_2$-C (7)), 2.59 (s, 1H, H-C(10)), 2.30 (s, 3H, H$_3$-C(11)), 1.63 (m, 4H, H$_2$-C(12) and C(12')), 0.76 (t, ^3J(H,H) = 7.6 Hz, 6H, H$_3$-C(13) and H$_3$-C(13')) ppm; ^{13}C NMR (150 MHz, CDCl$_3$): δ = 212.8 (C(9)), 152.9 (C(6)), 135.9 (C(2)), 134.6 (C(1)), 134.4 (C(4)), 132.4 (C(5)), 129.3 (C(3)), 53.1 (C(8)), 35.4 (C(7)), 30.0 (C(12) and C(12')), 18.1 (C(10)), 17.6 (C(11)), 8.8 (C(13) and C(13')) ppm; IR: $\tilde{\nu}$ = 2963m, 2919m, 2878m, 1649vs, 1585m, 1495, 1460m, 1379, 1322w, 1246s, 1232m, 1158w, 1078m, 1038m, 985m, 965m, 920m, 817s, 789m, 725w, 692w, 663w cm^{-1}; HR-ESI-MS calc. [C$_{15}$H$_{20}$O]: 216.1514; found: 216.1506.

4,7-diethyl-2,3-dihydro-1*H*-inden-1-one (27)[248]
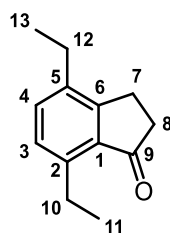
Aluminium chloride (2.4 g, 18 mmol) was suspended in CH_2Cl_2 (5.0 mL) and 3-chloropropanoyl chloride was added at 0 °C. The reaction mixture was stirred for 15 min and a solution of 1,4-diethylbenzene (2.0 g, 15 mmol) was added in CH_2Cl_2 (5.0 mL) at 0 °C. The reaction mixture was allowed to warm up to 23 °C and was stirred for 1 h. Saturated aqueous sodium oxalate solution was added (50 mL). The aqueous phase was extracted three times with EtOAc (3x100 mL). The combined organic phases were dried over Na_2SO_4. The volatiles were removed *in vacuo*. The crude product was dissolved in c. H_2SO_4 (12 mL) and the reaction mixture was stirred for 1 h at 95 °C. Saturated aqueous Na_2CO_3 solution (250 mL) was added and the aqueous phase was extracted three times with EtOAc (3 x 100 mL). The combined organic phases were dried over Na_2SO_4 and the volatiles were removed *in vacuo*. After column chromatography (SiO_2, *i*Hex:EtOAc, 100:1 to 50:1 v/v) compound **27** was obtained as a colourless solid (2.6 g, 14 mmol, 93%).

R_f = 0.42 (*i*Hex:EtOAc 25:1); ^1H NMR (400 MHz, CD_2Cl_2) δ = 7.32 (d, ^3J(H,H) = 7.6 Hz, 1H, H-C(4)), 7.11 (d, ^3J(H,H) = 7.6 Hz, 1H, H-C(3)), 3.03 (q, ^3J(H,H) = 7.5 Hz, 2H, H_2-C(10)), 3.0 (t, ^3J(H,H) =5.8 Hz, 2H, H_2-C(7)), 2.67 (q, ^3J(H,H) = 7.5 Hz, 2H, H_2-C(12)), 2.62 (t, ^3J(H,H) =5.7 Hz, 2H, H_2-C(8)), 1.25 (t, ^3J(H,H) =7.6 Hz, 3H, H_3-C(13), 1.18 (t, ^3J(H,H) =7.5 Hz, 3H, H_3-C(11)) ppm; ^{13}C NMR (100 MHz, $CDCl_3$): δ = 208.3 (C(9)), 155.0 (C(6)), 142.8 (C(2)), 139.6 (C(5)), 134.1 (C(1)), 133.3 (C(4)), 128.2 (C(3)), 37.2 (C(8)), 25.0 (C(10)), 25.0 (C(12)), 24.4 (C(7)), 15.5 (C(11)), 14.5 (C(13)) ppm; EI-MS (70 eV): *m/z* (%): 188 (85) [*M*], 173 (100), 159 (38); HR-EI-MS calc. [$C_{13}H_{16}O$]: 188.1201, found: 188.1195.

4',7'-diethylspiro[cyclopropane-1,2'-inden]-1'(3'*H*)-one (28)
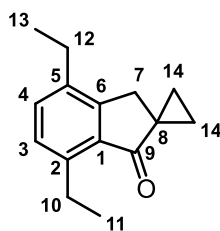
To a solution of triethylamine (0.14 mL, 1.0 mmol) in THF (5.0 mL) *n*BuLi (0.40 mL, 1.0 mmol, 2.5 M in hexane) was added at –78 °C. The stirred solution was allowed to warm up to 0 °C over the course of 30 min. The reaction mixture was cooled to –78 °C and a solution of compound **27** (94 mg, 0.50 mmol) in THF (5.0 mL) was added successively. The reaction mixture was allowed to warm up to 0 °C and 1,2-dibromoethane (43 µl, 0.50 mmol) was added. After the reaction mixture was stirred for 4 days at 23 °C saturated aqueous NH_4Cl solution (20 mL) was added and the aqueous phase was extracted three times with EtOAc (3 x 30 mL). The combined organic phases were dried over $MgSO_4$ and the volatiles were removed *in vacuo*. The crude product was purified by column chromatography (SiO_2, *i*Hex:EtOAc, 100:1 v/v) to obtain compound **28** as a pale yellow liquid (14 mg, 70 µmol, 14%).

R_f = 0.47 (*i*Hex:EtOAc 25:1); ^{1}H NMR (400 MHz, $CDCl_3$) δ = 7.33 (d, ^3J(H,H) = 7.6 Hz, 1H, H-C(4)), 7.14 (d, ^3J(H,H) = 7.7 Hz, 1H, C(3)), 3.11 (s, 2H, H_2-C(7)), 3.06 (q, ^3J(H,H) = 7.4 Hz, 2H, H_2-C(10)), 2.66 (q, ^3J(H,H) = 7.6 Hz, 2H, H_2-C(12)), 1.32 (tdd, ^3J(H,H) = 3.9 Hz, 2H, H_2-C(14)), 1.25 (t, ^3J(H,H) = 7.6 Hz, 3H, H_3-C(13)), 1.19 (t, ^3J(H,H) = 7.5 Hz, 3H, H_3-C(11)), 1.10 (tdd, ^3J(H,H) = 3.5 Hz, 2H, H_2-C(14)) ppm; ^{13}C NMR (100 MHz, $CDCl_3$): δ = 207.2 (C(9)), 152.8 (C(6)), 142.2 (C(2)), 139.0 (C(5)), 134.5 (C(1)), 132.6 (C(4)), 128.2 (C(3)), 34.9 (C(7)), 29.8 (C(8)), 25.2 (C(12)), 25.0 (C(10)), 18.0 (C(14)), 15.6 (C(11)), 14.5 (C(13)) ppm; EI-MS (70 eV): *m/z* (%): 214 (74) [*M*], 199 (100), 185 (69); HR-EI-MS calc. [$C_{15}H_{18}O$]: 214.1358, found: 214.1345.

2,2-diisopropyl-4,7-dimethyl-2,3-dihydro-1*H*-inden-1-one (29)
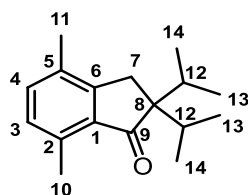
To a solution of compound **24** (0.30 g, 1.9 mmol) in dimethoxyethane (8.0 mL) NaH (60% w/w in mineral oil, 0.19 g, 4.8 mmol) was added at 23 °C and stirred for 30 min. Then *iso*-propyl iodide (0.65 g, 3.8 mmol) was added successively to the reaction mixture. After the reaction mixture was stirred for 24 h at 23 °C saturated aqueous NH_4Cl solution (50 mL) was added. The aqueous phase was extracted three times with EtOAc (3 x 100 mL) and the combined organic phases were dried over Na_2SO_4. The solvent was removed *in vacuo* and the crude product was purified by column chromatography (SiO₂, *i*Hex) to obtain compound **29** (0.20 g, 0.82 mmol, 43%) as a pale yellow liquid.

R_f = 0.36 (*i*Hex); ¹H NMR (400 MHz, CD₂Cl₂) δ = 7.22 (d, ^3J(H,H) = 7.5 Hz, 1H, H-C(4)), 6.98 (d, ^3J(H,H) = 7.5 Hz, 1H, H-C(3)), 2.73 (s, 2H, H₂-C(7)), 2.55 (s, 3H, H₃-C(10)), 2.31 (s, 3H, H₃-C(11)), 2.19 (sep, 2H, H-C(12)), 0.87 (d, ^3J(H,H) = 6.7 Hz, 6H, H₃-C(13) or H₃-C(14)), 0.78 (d, ^3J(H,H) = 7.9 Hz, 6H, H₃-C(14) or H₃-C(13)) ppm; ¹³C NMR (100 MHz, CDCl₃): δ = 212.9 (C(9)), 154.1 (C(6)), 136.5 (C(1)), 135.5 (C(2)), 134.5 (C(4)), 132.7 (C(5)), 129.6 (C(3)), 58.5 (C(8)), 33.7 (C(7)), 32.8 (C(12)), 18.3 (C(10)), 18.2 (C(13) or C(14)), 17.8 (C(11)), 17.4 (C(14) or C(13)) ppm; EI-MS (70 eV): *m/z* (%): 244 (8) [*M*], 201 (39), 187 (100); HR-EI-MS calc. [C₁₇H₂₄O]: 244.1827, found: 244.1816.

7-bromo-2,2-dimethyl-2,3-dihydro-1*H*-inden-1-one (31)
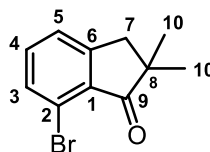
7-bromo-2,3-dihydro-1H-inden-1-one (0.11 g, 0.50 mmol) was dissolved in THF (6.0 mL) and KO*t*Bu (0.11 g, 1.0 mmol) was added at 0 °C and the reaction mixture was stirred for 10 min. Methyl iodide (0.14 g, 1.0 mmol) was added and the reaction mixture was stirred for 20 min. Saturated aqueous NH$_4$Cl solution (20mL) was added and the aqueous phase was extracted three times with EtOAc (3 x 20 mL). The combined organic phases were dried over MgSO$_4$ and the volatiles were removed *in vacuo*. The crude product was purified by column chromatography (SiO$_2$, *i*Hex:EtOAc, 100:1 to 50/1 v/v) to obtain compound **31** as a pale yellow liquid (46 mg, 0.19 mmol, 38%).

R_f = 0.54 (*i*Hex:EtOAc 25:1); m.p. 60 °C; ^{1}H NMR (400 MHz, CD$_2$Cl$_2$) δ = 7.52 (d, ^3J(H,H) = 7.3 Hz, 1H, H-C(5)), 7.41 (m, 2H, H-C(4) and H-C(3)), 2.96 (s, 2H, H$_2$-C(7)), 1.21 (s, 6H, H$_3$-C(10)) ppm; ^{13}C NMR (100 MHz, CD$_2$Cl$_2$): δ = 208.6 (C(9)), 155.7 (C(6)), 135.7 (C(4)), 133.2 (C(2)), 132,9 (C(5)), 126.4 (C(3)), 120.3 (C(1)), 46.6 (C(8)), 42.5(C(7)), 25.6 (C(10)) ppm; IR: $\tilde{\nu}$ = 2966m, 2867w, 1705vs, 1588s, 1563s, 1452s, 1435m, 1417m, 1380m, 1360w, 1324m, 1301w, 1284w, 1246m, 1215m, 1198m, 1165s, 1122s, 1056m, 1014w, 988s, 943m, 916w, 888w, 866vs, 847m, 787vs, 775vs, 733s, 678s cm^{-1}; EI-MS (70 eV): *m/z* (%): 238 (38) [*M*], 222 (90); HR-EI-MS calc. [C$_{11}$H$_{11}$BrO]: 237.9993, found:237.9986.

4,7-diethyl-2,2-dimethyl-2,3-dihydro-1*H*-inden-1-one (34)
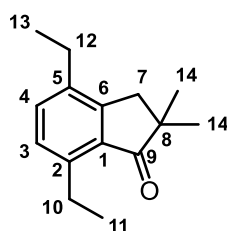
To a solution of compound **27** (0.10 g, 0.53 mmol) in dimethoxyethane (2 mL) NaH (60% w/w in mineral oil, 43 mg, 1.1 mmol) was added at 23 °C and the reaction mixture stirred for 30 min. Then methyl iodide (0.15 g, 1.1 mmol) was added successively. After the reaction mixture was stirred for 5 h at 23 °C a saturated aqueous NH$_4$Cl solution (20 mL) was added. The aqueous phase was extracted three times with EtOAc (3 x 50 mL) and the combined organic phases were dried over MgSO$_4$. The volatiles were removed *in vacuo* and the crude product was purified by column chromatography (SiO$_2$, *i*Hex:EtOAc, 100:1 v/v) to obtain compound **34** (63 mg, 0.29 mmol, 55%) as a pale yellow liquid.

R_f = 0.62 (*i*Hex:EtOAc 25:1); ^{1}H NMR (400 MHz, CD$_2$Cl$_2$) δ = 7.33 (d, ^3J(H,H) = 7.6 Hz, 1H, H-C(4)), 7.12 (d, 1H, ^3J(H,H) = 7.6 Hz, H-C(3)), 3.02 (q, ^3J(H,H) = 7.5 Hz, 2H, H$_2$-C(10)), 2.88 (s, 2H, H$_2$-C(7)), 2.64 (q, ^3J(H,H) = 7.6 Hz, 2H, H$_2$-C(12)), 1.23 (t, ^3J(H,H) = 7.6 Hz, 3H, H$_3$-C(13)), 1.18 (s, 6H, H$_3$-C(14)), 1.18 (t, ^3J(H,H) = 7.6 Hz, 6H, H$_3$-C(11)) ppm; ^{13}C NMR (100 MHz, CDCl$_3$): δ = 212.5 (C(9)), 151.8 (C(6)), 143.4 (C(2)), 139.5 (C(5)), 133.4 (C(4)), 132.3 (C(1)), 128.3 (C(3)), 41.4 (C(7)), 25.9 (C(14)), 25.1 (C(12)), 24.9 (C(10)), 15.5 (C(11)), 14.5 (C(13)) ppm; IR: $\tilde{v}$ = 2962m, 2927m, 2866w, 1698m, 1578m, 1494m, 1458m, 1407w, 1377m, 1358w, 1323w, 1295w, 1279w, 1231m, 1169w, 1089w, 1060w, 1016m, 978m, 946w, 911m, 835s, 808m, 714w, 666w cm^{-1}; EI-MS (70 eV): *m/z* (%): 216 (39) [*M*], 201 (100); HR-EI-MS calc. [C$_{15}$H$_{20}$O]: 216.1514, found:216.1508.

2,2-bis(hydroxymethyl)-4,7-dimethyl-2,3-dihydro-1*H*-inden-1-one (36)
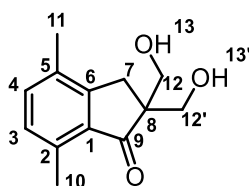
Compound **24** (0.30 g, 1.9 mmol) was dissolved in a mixture of MeOH (12 mL) and H_2O (12 mL). K_2CO_3 (0.56 g, 3.8 mmol) and formaline (37%, 0.57 mL, 7.6 mmol) were added and the reaction mixture was stirred for 3 h at 50 °C. Saturated aqueous NH_4Cl solution (50 mL) was added and the aqueous phase was extracted three times with CH_2Cl_2 (3 x 50 mL). The combined organic phases were dried over $MgSO_4$ and the volatiles were removed *in vacuo*. The crude product was purified by column chromatography (SiO_2, *i*Hex:EtOAc, 9:1 to 1:1 v/v) to obtain compound **36** (0.29 g, 1.3 mmol, 68%)

R_f = 0.21 (*i*Hex:EtOAc 1:1); m.p. 147 °C; ^{1}H NMR (400 MHz, MeOD) δ = 7.34 (d, ^3J(H,H) = 7.5 Hz, 1H, H-C(4)), 7.08 (d, ^3J(H,H) = 7.4 Hz, 1H, H-C(3)), 3.81 (d, ^3J(H,H) = 10.7 Hz, 2H, H_2-C(12)), 3.70 (d, ^3J(H,H) = 10.7 Hz, 2H, H_2-C(12)), 3.16 (s, 2H, H_2-C(7)), 2.60 (s, 3H, H_3-C(10)), 2.39 (s, 3H, H_3-C(11)) ppm; ^{13}C NMR (100 MHz, MeOD): δ = 211.6 (C(9)), 155.3 (C(6)), 134.0 (C(5)), 135.9 (C(4)), 136.8 (C(2)), 135.4 (C(1)), 130.2 (C(3)), 65.4 (C(12)), 58.8(C(8)), 32.6 (C(7)), 18.2 (C(10)), 17.5 (C(11)) ppm; IR: $\tilde{v}$ = 3370m, 2921w, 2872w, 2493m, 1679vs, 1583s, 1499s, 1473m, 1452m, 1369m, 1337m, 1256s, 1163m, 1093s, 1070s, 1043s, 1012s, 962m, 929s, 874m, 839vs, 788m, 670s cm^{-1}; EI-MS (70 eV): *m/z* (%): 220 (46) [*M*], 172 (100), 159 (28); HR-EI-MS calc. [$C_{13}H_{16}O_3$]:220.1099, found: 220.1094.

2,2-diethyl-4,7-dimethyl-1-((2-(methylthio)phenyl)ethynyl)-2,3-dihydro-1*H*-inden-1-ol (38)
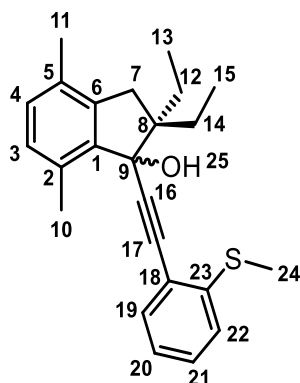
A solution of compound **16** (89 mg, 0.60 mmol) in dry THF (1.5 mL) was cooled to –78°C and *n*BuLi (0.18 g, 0.60 mmol, 2 M in hexane,) was added slowly under an argon atmosphere. The solution was allowed to warm up to 0 °C within 15 min. Then a solution of compound **26** (0.13 g, 0.60 mmol) in dry THF (1.0 mL) was added slowly to the solution of lithiated **16**. After 80 min of stirring at 0 °C reaction control by TLC showed incomplete conversion of indanone **26**. The reaction mixture was added to a freshly prepared lithium acetylide solution (89 mg of **16** and 0.2 mL of 2 M *n*BuLi in hexane, prepared as described above) in THF (1 mL) at 0 °C. After the reaction mixture was stirred for 40 min at 0° C, the reaction mixture was allowed to warm up to 23 °C and was stirred for additional 90 min. A saturated aqueous NH$_4$Cl solution (10 mL) was added and the aqueous phase was extracted three times with CH$_2$Cl$_2$ (3 x 20 mL). The combined organic phases were dried over MgSO$_4$. The solvent was removed *in vacuo* and the crude product was purified by column chromatography (SiO$_2$, *i*Hex to *i*Hex:EtOAc, 50:1 to 25:1 v/v) to obtain compound **38** (0.16 g, 0.45 mmol, 75%) as a colourless oil.

R_f = 0.51 (*i*Hex:EtOAc 9:1); ^{1}H NMR (600 MHz, CD$_2$Cl$_2$) δ = 7.37 (d, ^3J(H,H) = 7.7 Hz, 1H, H-C(19)), 7.29 (t, ^3J(H,H) = 8.1 Hz, 1H, H-C(21)), 7.15 (d, ^3J(H,H) = 8.0 Hz, 1H, H-C(22)), 7.08 (t, ^3J(H,H) = 7.5 Hz, 1H, H-C(20)), 6.97 (d, ^3J(H,H) = 7.6 Hz, 1H, H-C(4)), 6.91 (d, ^3J(H,H) = 7.6 Hz, 1H, H-C(3)), 2.68 (d, ^3J(H,H) = 15.8 Hz, 1H, H$_2$-C(7)), 2.59 (s, 3H, H$_3$-C(10)), 2.45 (s, 3H, H$_3$-C(24)), 2.24 (s, 1H, H-O(25)), 2.20 (s, 3H, H$_3$-C(11)), 2.09 (dq, ^3J(H,H) = 7.4 Hz, 1H, H$_2$-C(12) or H$_2$-C(14)), 1.88 (dq, ^3J(H,H) = 7.3 Hz, 1H, H$_2$-C(14) or H$_2$-C(12)), 1.63 (dq, ^3J(H,H) = 7.5 Hz, 1H, H$_2$-C(12) or H$_2$-C(14)), 1.54 (dq, ^3J(H,H) = 7.6 Hz, 1H, H$_2$-C(14) or H$_2$-C(12)), 1.01 (t, ^3J(H,H) = 7.5 Hz, 3H, H$_3$-C(15) or C(13)), 0.90 (t, ^3J(H,H) = 7.5 Hz, 3H, H$_3$-C(13) or H$_3$-C(15)) ppm; ^{13}C NMR (150 MHz, CD$_2$Cl$_2$): δ = 143.1 (C(1)), 142.3 (C(23)), 141.3 (C(6)), 132.9 (C(19)), 132.8 (C(2)), 131.8 (C(5)), 129.8 (C(3)), 129.7 (C(4)), 129.3 (C(21)), 124.6 (C(20)), 124.5 (C(22)), 121.4 (C(18)), 97.3 (C(16)), 86.0 (C(17)), 82.8 (C(9)), 39.6 (C(7)), 28.3 (C(12) or C(14)), 25.2 (C(14) or C(12)), 18.9 (C(10)), 18.7 (C(11)), 15.4 (C(24)), 10.1 (C(13) or C(15)), 9.9 (C(15) or C(13)) ppm; IR: $\tilde{v}$ = 3443w, 2960m, 2920m, 2876w, 1581w, 1494m, 1462s, 1434s, 1378m, 1321w, 1265m, 1199w, 1162m, 1122w, 1070m, 1037m, 990m,

965s, 905m, 856w, 807s, 747vs, 720s, 681m cm^{-1}; EI-MS (70 eV): m/z (%): 364 (2) [M], 349 (6), 317 (100); HR-EI-MS calc. [$C_{24}H_{28}OS$]: 364.1861, found: 364.1859.

4,7-diethyl-2,2-dimethyl-1-((2-(methylthio)phenyl)ethynyl)-2,3-dihydro-1*H*-inden-1-ol (42)
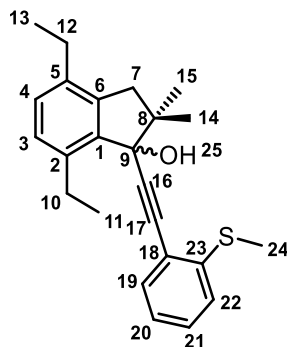
A solution of compound **16** (89 mg, 0.60 mmol) in dry THF (1.5 mL) was cooled to –78°C and *n*BuLi (0.18 g, 0.60 mmol, 2 M in hexane,) was added slowly under an argon atmosphere. The solution was allowed to warm up to 0 °C within 15 min. Then a solution of compound **34** (0.13 g, 0.60 mmol) in dry THF (1.0 mL) was added slowly to the solution of lithiated **16**. After 80 min of stirring at 0 °C reaction control by TLC showed incomplete conversion of indanone **34**. The reaction mixture was added to a freshly prepared lithium acetylide solution (89 mg of **16** and 0.2 mL of 2 M *n*BuLi in hexane, prepared as described above) in THF (1 mL) at 0 °C. After the reaction mixture was stirred for 30 min a saturated aqueous NH_4Cl solution (5 mL) was added and the aqueous phase was extracted three times with EtOAc (3 x 20 mL). The combined organic phases were dried over $MgSO_4$. The solvent was removed *in vacuo* and the crude product was purified by column chromatography (SiO_2, *i*Hex to *i*Hex:EtOAc, 50:1 to 25:1 v/v) to obtain compound **42** (0.19 g, 0.53 mmol, 89%) as a colourless oil.

R_f = 0.51 (*i*Hex:EtOAc 9:1); ^{1}H NMR (600 MHz, CD_2Cl_2) δ = 7.39 (d, ^3J(H,H) = 7.6 Hz, 1H, H-C(19)), 7.31 (t, ^3J(H,H) = 8.0 Hz, 1H, H-C(21)), 7.16 (d, ^3J(H,H) = 8.2 Hz, 1H, H-C(22)), 7.09 (t, ^3J(H,H) = 7.6 Hz, 1H, H-C(20)), 7.07 (d, ^3J(H,H) = 8.1 Hz, 1H, H-C(4)), 7.03 (d, ^3J(H,H) = 7.8 Hz, 1H, H-C(3)), 3.10 (m, ^3J(H,H) = 7.1 Hz, 2H, H_2-C(10)), 2.83 (d, ^3J(H,H) =15.1 Hz, 1H, H_2-C(7)), 2.71 (d, ^3J(H,H) =14.9 Hz, 1H, H_2-C(7)), 2.56 (q, ^3J(H,H) = 7.6 Hz, 2H, H_2-C(12)), 2.46 (s, 3H, H_3-C(24)), 2.25 (s, 1H, H-O(25)), 1.29 (s, 3H, H_3-C(14) or C(15)), 1.29 (t, ^3J(H,H) =7.6 Hz, 3H, H_3-C(11)), 1.27 (s, 3H, H_3-C(15) or C(14)), 1.17 (t, ^3J(H,H) =7.6 Hz, 3H, H_3-C(13)) ppm; ^{13}C NMR (150 MHz, CD_2Cl_2): δ = 142.4 (C(23)), 141.9 (C(1)), 141.3 (C(6)), 139.9 (C(2)), 138.5 (C(5)), 132.8 (C(19)), 129.4 (C(21)), 128.4 (C(4)), 128.2 (C(3)), 124.6 (C(20)), 124.4 (C(22)), 121.3 (C(18)), 96.9 (C(16)), 85.1 (C(17)), 82.8 (C(9)), 48.8 (C(8)), 43.0 (C(7)), 26.7 (C(14) or C(15)), 26.4 (C(12)), 25.1 (C(10)), 22.2 (C(15) or C(14)), 16.3 (C(11)), 15.4 (C(24)), 15.0 (C(13)) ppm; IR: $\tilde{v}$ = 3434w, 2961m, 2926m, 2867m, 1582w, 1493m,

1463s, 1434m, 1364m, 1321w, 1264w, 1239w, 1169m, 1119w, 1076m, 1026s, 990m, 963m, 898m, 860w, 826s, 783m, 748vs, 720m, 681m cm^{-1}; EI-MS (70 eV): m/z (%): 364 (8) [M], 335 (10), 317 (100); HR-EI-MS calc. [$C_{24}H_{28}OS$]: 364.1861, found: 364.1856.

7-isopropyl-2,2-dimethyl-2,3-dihydro-1H-inden-1-one (55)[38]
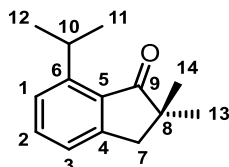
To a solution of compound **60** (500 mg, 2.87 mmol) in dimethoxyethane (15 mL) NaH was added (344 mg, 8.61 mmol) at 23 °C and the reaction mixture was stirred for 10 min. MeI (0.54 mL, 8.61 mmol) was added to the reaction mixture and after 90 min of stirring at 23 °C a saturated aqueous NH$_4$Cl solution (200 ml) was added. The aqueous phase was extracted with EtOAc (3 x 150 mL) and the combined organic phases were dried over MgSO$_4$. The solvent was removed *in vacuo* and the crude product was purified by column chromatography (aluminium oxide neutral, *i*Hex to *i*Hex:EtOAc, 100:1 v/v, no dryload). Compound **55** (336 mg, 1.66 mmol, 58%) was obtained as a faint yellow liquid.

R_f = 0.39 (*i*Hex:EtOAc 100:1); ^{1}H NMR (400 MHz, CD$_2$Cl$_2$) δ = 7.50 (t, ^3J(H,H) = 7.6 Hz, 1H, H-C(2)), 7.29 (d, ^3J(H,H) = 7.6 Hz, 1H, H-C(1)), 7.24 (d, ^3J(H,H) = 7.6 Hz, 1H, H-C(3)), 4.14 (sep, ^3J(H,H) = 6.9 Hz, 1H, H-C(10)), 2.94 (s, 1H, H-C(7)), 1.22 (d, ^3J(H,H) = 6.9 Hz, 6H, H$_3$-C(11, 12)), 1.18 (s, 1H, H$_3$-C(13), H$_3$-C(14)) ppm; ^{13}C NMR (100 MHz, CD$_2$Cl$_2$): δ = 212.2 (C(9)), 153.7 (C(4)), 151.2 (C(6)), 134.9 (C(2)), 131.9 (C(5)), 124.5 (C(3)), 45.8 (C(8)), 42.8 (C(7)), 27.8 (C(10)), 25.8 (C(13), C(14)) ppm; IR: $\tilde{v}$ = 3062w, 3032w, 2961m, 2926w, 2867w, 1702vs, 1591s, 1478m, 1460m, 1431w, 1380m, 1360w, 1319m, 1295w, 1264w, 1192m, 1168m, 1108w, 1087w, 1043w, 1000m, 960w, 929s, 894w, 862w, 848w, 782s, 752w, 706s, 666w cm^{-1}; EI-MS (70 eV): m/z (%): 202 (57) [M], 187 (100), 174 (17), 159 (23); HR-EI-MS calc. [$C_{14}H_{18}O$]: 202.1358, found: 202.1348.

2-Isopropyl-*N*-methoxy-*N*-methylbenzamide (58)[38, 214]
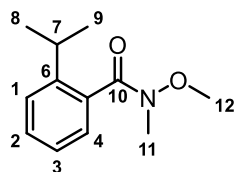
To a solution of 2-*iso*-propylbenzoic acid **57** (1.00 g, 6.10 mmol) in CH_2Cl_2 (10.0 mL) oxalyl chloride (0.65 mL, 7.58 mmol) and three drops of DMF were added. After the reaction mixture was stirred at 23 °C for 90 min the volatiles were removed *in vacuo*. The residue was dissolved again in CH_2Cl_2 (10 mL) before *N,O*-dimethylhydroxylamine hydrochloride (0.85 g, 8.70 mmol) and triethylamine (2.60 mL) were added. After the reaction mixture was stirred at 23 °C for 90 min a saturated aqueous $NaHCO_3$ solution (250 mL) was added. The aqueous phase was extracted three times with CH_2Cl_2 (3 x 150 mL) and the combined organic phases were separated and dried over $MgSO_4$. The solvent was removed *in vacuo* and the crude product was purified by column chromatography (SiO_2, CH_2Cl_2) to obtain 2-*iso*-propyl-*N*-methoxy-*N*-methylbenzamide **58** (1.12 g, 5.40 mmol, 89%) as a colorless liquid.

R_f = 0.12 (CH_2Cl_2); ^1H NMR (800 MHz, CD_2Cl_2): δ = 7.36 (m, 2H, H-C(1), H-C(2)), 7.20 (m, 2H, H-C(3), H-C(4)), 3.30 (m, 6H, H_3-C-N(11) and H_3-C-O(12)), 2.93 (br s, 1H, H-C(7)), 1.22 (d, ^3J(H,H) = 6.9 Hz, 6H, H_3-C(8) and H_3-C(9)) ppm; ^{13}C NMR (201 MHz, CD_2Cl_2): δ = 172.0 (C(10)), 146.2 (C(6)), 135.5 (C(5)), 129.7 (C(2)), 126.4 (C(3) or C(4)), 126.0 (C(1)), 125.8 (C(4) or C(3)), 61.5 (C(12)), 32.6 (C(11)), 31.5 (C(7)), 24.3 (C(8) and C(9)) ppm; IR: $\tilde{v}$ = 2963m, 2934w, 2871w, 1649vs, 1600m, 1576w, 1490m, 1460m, 1446m, 1410m, 1376s, 1362s, 1304w, 1278w, 1222w, 1198m, 1167w, 1116w, 1092w, 1058m, 1032m, 986s, 948w, 924w, 896w, 884w, 872w, 779m, 760vs, 736m, 692m cm^{-1}; ESI-MS (70 eV): *m/z* (%): 208 (100) [*M*], 156 (50), 149(15); HR-ESI-MS calc. [$C_{12}H_{18}NO_2^+$]: 208.1332, found: 208.1332; elemental analysis calc. (%) for $C_{12}H_{17}NO_2$: C 69.54, H 8.27, N 6.76, O 15.44; found: C 69.36, H 8.32, N 6.76.

1-(2-Isopropylphenyl)prop-2-en-1-one (59)[38, 214]
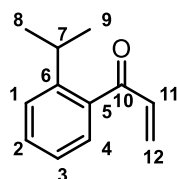
To a stirred solution of 2-*iso*-propyl-*N*-methoxy-*N*-methylbenzamide **58** (1.88 g, 9.10 mmol) in dry THF (15 mL) a solution of vinylmagnesium bromide (9.10 mL, 9.10 mmol, 1 M in THF) was added slowly at 0 °C. After stirring the reaction mixture for 1 h at 0 °C a solution of vinylmagnesium bromide (9.10 mL, 1 M in THF) was added again. After stirring the reaction mixture for additional 2.5 h at 0 °C reaction control by GC-MS showed full conversion and the reaction mixture was slowly added to a stirred aqueous HCl solution (200 mL, 2 M). The aqueous phase was extracted with CH_2Cl_2 (3 x 100 mL) and the combined organic phases were washed twice with an aqueous HCl solution (2 x 100 mL, 2 M) and twice with pure H_2O (2 x 100 mL). After drying the organic phases with $MgSO_4$, the solvent was removed *in vacuo*. The crude product was purified by column chromatography (SiO_2, *i*Hex:EtOAc, 7:3 v/v, no dryload) to obtain compound **59** (1.20 g, 6.70 mmol, 74%) as colorless oil.

R_f = 0.12 (*i*Hex); ^{1}H NMR (400 MHz, CD_2Cl_2): δ = 7.42 (m, 2H, H-C(3), H-C(4)), 7.25 (m, 2H, H-C(1) and H-C(2)), 6.69 (dd, ^3J(H,H) = 17.5 Hz, ^3J(H,H) = 10.6 Hz, 1H, H-C(11)), 6.03 (m, 2H, 2 x H-C(12)), 3.13 (sep, 1H, H-C(7)), 1.21 (m, 6H, H₃-C(8) and H₃-C(9)) ppm; ^{13}C NMR (100 MHz, CD_2Cl_2): δ = 198.6 (C(10)), 147.8 (C(6)), 138.6 (C(5)), 138.3 (C(11)), 132.3 (C(12)), 130.9 (C(4)), 128.0 (C(2)), 126.7 (C(3)), 125.7(C(1)), 30.5 (C(7)), 24.4 (C(8) and C(9)) ppm; IR: $\tilde{\nu}$ = 3066w, 3024w, 2964m, 2930w, 2870w, 1676m, 1659vs, 1604m, 1573w, 1485w, 1463w, 1444m, 1400s, 1385w, 1364w, 1292s, 1263m, 1225m, 1201m, 1074w, 1033w, 990s, 961s, 947m, 811m, 758vs, 743m, 719w cm⁻¹; EI-MS (70 eV): *m/z* (%): 174 (>1) [*M*], 159 (100), 131 (40); HR-EI-MS calc. [$C_{12}H_{14}O$]: 174.1045, found: 174.1037.

7-Isopropyl-2,3-dihydro-1*H*-inden-1-one (60)[38, 214]
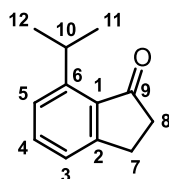
Compound **59** (650 mg, 3.7 mmol) was dissolved in 1,2-dichloroethane and the solution was heated to 80 °C. Then c. H_2SO_4 (1.20 mL) was added. After stirring the obtained mixture for 15 min at 80 °C a saturated aqueous $NaHCO_3$ solution (200 mL) was added and the aqueous phase was extracted three times with CH_2Cl_2 (3 x 150 mL). The organic phases were washed with water (1 x 150 mL) and dried over $MgSO_4$. The solvent was removed *in vacuo* and the crude product was purified by filtering through a short pad of neutral aluminium oxide (*i*Hex:EtOAc, 9:1 v/v, 400 mL) to obtain compound **60** (516 mg, 2.96 mmol, 80%) as colorless crystals.

R_f = 0.17 (*i*Hex:EtOAc 50:1); m.p. 30 °C; ^1H NMR (400 MHz, CD_2Cl_2) δ = 7.50 (t, $^3J(H,H)$ = 7.6 Hz, 1H, H-C(4)), 7.29 (d, $^3J(H,H)$ = 7.5 Hz, 2H, H-C(5), H-C(3)); 4.16 (sep, $^3J(H,H)$ = 6.9 Hz, 1H, H-C(10)), 3.07 (m, 2H, H-C(8)), 2.62 (m, 2H, H-C(7)), 1.23 (d, $^3J(H,H)$ = 6.9 Hz, 6H, H_3-C(11, 12)) ppm; ^{13}C NMR (100 MHz, CD_2Cl_2): δ = 208.0 (C(9)), 156.9 (C(2)), 150.6 (C(6)),134.8 (C(4)), 133.6(C(1)), 124.6 (C(5)), 124.2 (C(3)), 37.5 (C(7)), 27.6 (C(10)), 25.8 (C(8)), 23.4 (C(11), C(12)) ppm; IR: $\tilde{v}$ = 2963w, 2926w, 2869w, 1697vs, 1590s, 1477m, 1461m, 1406w, 1361w, 1316m, 1290w, 1263w, 1240m, 1220m, 1189s, 1167m, 1108w, 1087w, 1049m, 1031w, 991w, 943m, 858w, 833m, 777s, 732m, 673w cm^{-1}; EI-MS (70 eV): *m/z* (%) 174 (80) [*M*], 159 (100), 146 (36); HR-EI-MS calc. [$C_{12}H_{14}O$]: 174.1045, found: 174.1045.

7-isopropyl-2,2-dimethyl-1-((2-(methylthio)phenyl)ethynyl)-2,3-dihydro-1*H*-inden-1-ol (61)[38]
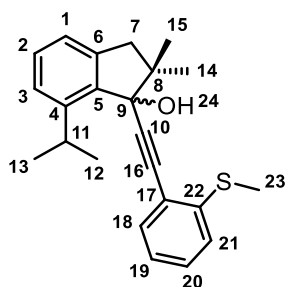
A solution of compound **16** (143 mg, 0.96 mmol) in dry THF (1.4 mL) was cooled to –78°C and *n*BuLi (0.36 mL, 0.81 mmol, 2.25 M in hexane) was added slowly under an Argon atmosphere. The reaction mixture was allowed to warm up to 0 °C within 10 min. Then a solution of compound **55** (150 mg, 0.74 mmol) in dry THF (1.6 mL) was added to the reaction mixture. After 20 min of stirring at 0 °C under Argon atmosphere a solution of saturated aqueous NH_4CO_3 solution (50 mL) was added to the reaction mixture. The aqueous phase was extracted with EtOAc (3 x 100 mL) and the combined organic phases were dried over $MgSO_4$. The solvent was removed in *vacuo* and the crude product was purified by column chromatography (SiO_2, *i*Hex to *i*Hex:EtOAc, 50:1 to 25:1 v/v) to obtain compound **61** (214 mg, 0.61 mmol, 82%) as colorless oil.

R_f = 0.48 (*i*Hex:EtOAc 9:1); ^{1}H NMR (400 MHz, CD_2Cl_2) δ = 7.39 (d, ^3J(H,H) = 7.6 Hz, 1H, H-C(18)), 7.31 (t, ^3J(H,H) = 7.6 Hz, 1H, H-C(20)), 7.25 (t, ^3J(H,H) = 7.8 Hz, 1H, H-C(2)), 7.20 (d, ^3J(H,H) = 7.9 Hz, 1H, H-C(3)), 7.17 (d, ^3J(H,H) = 7.9 Hz, 1H, H-C(21)), 7.09 (t, ^3J(H,H) = 7.5 Hz, 1H, H-C(19)), 7.04 (d, ^3J(H,H) = 7.0 Hz, 1H, H-C(1)) 4.14 (sep, ^3J(H,H) = 6.9 Hz, 1H, H-C(11)), 2.90 (d, ^3J(H,H) = 15.1 Hz, 1H, H-C(7)), 2.73 (d, ^3J(H,H) = 15.1 Hz, 1H, H-C(7)), 2.47 (s, 3H, H-C(23)), 2.27 (s, 1H, H-O(24)), 1.31 (d, ^3J(H,H) = 6.7 Hz, 3H, H-C(12, 13)), 1.31 (s, 3H, H-C(14, 15)), 1.30 (d, ^3J(H,H) = 6.9 Hz, 3H, H-C(12, 13)), 1.27 (s, 3H, H-C(14, 15)) ppm; ^{13}C NMR (100 MHz, CD_2Cl_2): δ = 147.8 (C(4)), 143.2 (C(6)), 142.4 (C(22)), 141.4 (C(5)), 132.9 (C(18)), 129.4 (C(20)), 124.8 (C(3)), 124.6 (C(19)), 124.5 (C(21)), 121.3(C(17)), 96.9 (C(10)), 85.3 (C(16)), 82.7 (C(9)), 49.2 (C(8)), 45.0 (C(7)), 28.7 (C(11)), 26.6 (C(14 or 15)), 24.7 (C(12 or 13)), 24.6 (C(13 or 14)), 22.2 (C(15 or 14)), 15.4 (C(23)) ppm; IR: $\tilde{v}$ = 3434w, 3059w, 2962m, 2926w, 2867w, 1592w, 1583w, 1476m, 1464s, 1434m, 1382m, 1364m, 1341w, 1265m, 1234w, 1213w, 1152m, 1131w, 1078m, 1048m, 1036m, 1018m, 989m, 968m, 918w, 903m, 859w, 837w, 802w, 783m, 748vs, 720s, 703m, 680m cm^{-1}; EI-MS (70 eV): *m/z* (%): 350 (19) [*M*], 335 (34), 307 (72), 303 (100); HR-EI-MS calc. [$C_{23}H_{26}OS$]: 350.1704 found: 350.1699.

(*E*/*Z*)-2-(7-isopropyl-2,2-dimethyl-2,3-dihydro-1*H*-inden-1-ylidene)-1-(2-(methylthio)phenyl)ethan-1-one (*E*/*Z*-62)[38]
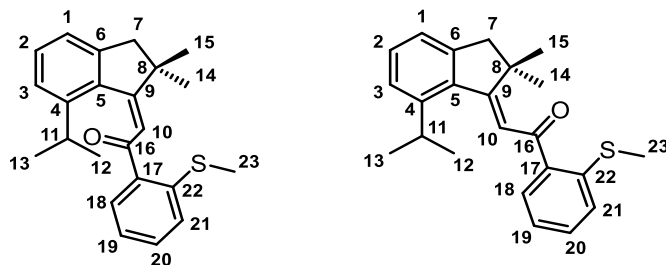
Compound **61** (206 mg, 0.59 mmol) was dissolved in THF at 23 °C (4 mL) and c. H_2SO_4 (20 µL) was added. The reaction mixture turned green and then changed its color to a dark yellow within minutes. After the reaction mixture was stirred for 40 min at 23 °C a saturated aqueous $NaHCO_3$ solution (40 mL) was added. The aqueous phase was extracted with EtOAc (3 x 100 mL) and the combined organic phases were dried over $MgSO_4$. The solvent was removed *in vacuo* and compound **62** (204 mg, 0.58 mmol, 99%) was obtained without the need for further purification as a mixture of *E* (86%) and *Z* (14%) isomers, both as yellow crystals.

E isomer: R_f = 0.2 (*i*Hex:EtOAc 50:1); m.p. 117 °C; ^{1}H NMR (400 MHz, CD_2Cl_2) δ = 7.87 (d, ^3J(H,H) = 7.8 Hz, 1H, H-C(18)), 7.48 (t, ^3J(H,H) = 7.7 Hz, 1H, H-C(20)), 7.36 (d, ^3J(H,H) = 8.0 Hz, 1H, H-C(21)), 7.29 (t, ^3J(H,H) = 7.8 Hz, 1H, H-C(2)), 7.25 (d, ^3J(H,H) = 7.8 Hz, 1H, H-C(3)), 7.18 (t, ^3J(H,H) = 7.8 Hz, 1H, H-C(19)), 7.11 (d, ^3J(H,H) = 7.0 Hz, 1H, H-C(19)), 6.99 (s, 1H, H-C(10)), 3.55 (sep, ^3J(H,H) = 6.7 Hz, 1H, H-C(11)), 2.90 (s, 2H, H_2-C(7)), 2.46 (s, 3H, H_3-C(23)), 1.36 (s, 6H, H_3-C(14) and H_3-C(15)), 1.28 (d, 6H, ^3J(H,H) = 6.8 Hz, H_3-C(12) and H_3-C(13)) ppm; ^{13}C NMR (100 MHz, CD_2Cl_2): δ = 194.5 (C(16)), 165.1 (C(9)), 148.0 (C(4)), 147.1 (C(6)), 143.0 (C(22)), 137.8 (C(5)), 136.5 (C(17)), 132.6 (C(20)), 132.0 (C(18)), 130.4 (C(2)), 125.3 (C(21)), 124.7 (C(3)), 123.9 (C(19)), 123.1 (C(10)), 123.1 (C(1)), 50.1 (C(7)), 46.4 (C(8)), 29.5 (C(11)), 27.6 (C(14) and C(15)), 24.0 (C(12) and C(13)), 16.2 (C(23)) ppm; IR: $\tilde{v}$ = 2960m, 2857m, 1648vs, 1586vs, 1459m, 1433s, 1382m, 1362w, 1305m, 1263m, 1232m, 1212vs, 1189m, 1168m, 1136m, 1081w, 1028s, 986m, 855w, 810w, 774m, 754s, 743m, 677m cm^{-1}; EI-MS (70 eV): *m*/*z* (%): 350 (0.7) [*M*], 335 (1), 307 (100), 291 (4), 151 (17); HR-EI-MS calc. [$C_{23}H_{26}OS$]: 350.1704, found: 350.1706.

Z isomer: R_f = 0.1 (*i*Hex:EtOAc 50:1); ^{1}H NMR (400 MHz, CD_2Cl_2) δ = 7.80 (d, ^3J(H,H) = 7.7 Hz, 1H, H-C(18)), 7.45 (t, ^3J(H,H) = 7.7 Hz, 1H, H-C(20)), 7.34 (d, ^3J(H,H) = 8.1 Hz, 1H, H-C(21)), 7.24 (t, ^3J(H,H) = 7.6 Hz, 1H, H-C(2)), 7.12 (t, ^3J(H,H) = 7.7 Hz, 1H, H-C(19)), 7.09 (d, ^3J(H,H) = 7.5 Hz, 1H, H-C(1)), 7.06 (d, ^3J(H,H) = 7.8 Hz, 1H, H-C(3)), 6.38 (s, 1H, H-C(10)), 2.93 (sep, ^3J(H,H) = 6.8 Hz, 1H, H-C(11)), 2.83 (s, 2H, H_2-C(7)), 2.43 (s, 3H, H_3-C(23)), 1.26 (s, 6H, H_3-C(14) and H_3-C(15)), 0.94

(d, 6H, ^3J(H,H) = 6.8 Hz, H$_3$-C(12) and H$_3$-C(13)) ppm; ^{13}C NMR (100 MHz, CD$_2$Cl$_2$): δ = 193.6 (C(16)), 164.8 (C(9)), 148.5 (C(4)), 145.6 (C(6)), 143.3 (C(22)), 137.4 (C(5)), 135.9 (C(17)), 131.8 (C(18)), 132.4 (C(20)), 130.4 (C(2)), 125.5 (C(21)), 123.0 (C(1)), 123.7 (C(19) and C(3)), 123.0. (C(1)), 118.8 (C(10)), 49.2 (C(8)), 47.7 (C(7)), 31.1 (C(11)), 27.3 (C(14) and C(15)), 23.5 (C(12) and C(13)), 16.4 (C(23)) ppm.

(*E*)-2-(7-isopropyl-2,2-dimethyl-2,3-dihydro-1*H*-inden-1-ylidene)-1-(2-(methylsulfinyl)phenyl)ethan-1-one (*E*-63)[38]
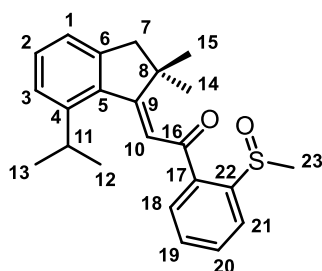
Compound **62** (107 mg, 0.31 mmol, mixture of *E* and *Z* isomers) was dissolved in c. AcOH (3.4 mL) at 23 °C and sodium perborate tetrahydrate was added (143 mg, 0.93 mmol). After the reaction mixture was stirred for 2 h at 23 °C a saturated aqueous NaHCO$_3$ solution (50 mL) was added. The aqueous phase was extracted three times with CH$_2$Cl$_2$ (3 x 100 mL) and the combined organic phases were dried over MgSO$_4$. The solvent was removed *in vacuo* and the crude product was purified by column chromatography (SiO$_2$, *i*Hex to *i*Hex:EtOAc 9:1 to 7:3) to obtain compound **63** (81 mg, 0.22 mmol, 71%) exclusively in the *E* isomeric form as a yellow solid.

E isomer: R_f = 0.12 (*i*Hex:EtOAc 7:3); m.p. 126 °C; ^{1}H NMR (400 MHz, CD$_2$Cl$_2$) δ = 8.37 (d, ^3J(H,H) = 7.9 Hz, 1H, H-C(21)), 7.99 (d, ^3J(H,H) = 7.7 Hz, 1H, H-C(18)), 7.82 (t, ^3J(H,H) = 7.7 Hz, 1H, H-C(20)), 7.60 (t, ^3J(H,H) = 7.5 Hz, 1H, H-C(19)), 7.32 (t, ^3J(H,H) = 7.2 Hz, 1H, H-C(2)), 7.27 (t, ^3J(H,H) = 7.8 Hz, 1H, H-C(3)), 7.13 (d, ^3J(H,H) = 7.3 Hz, 1H, H-C(1)), 7.12 (s, 1H, H-C(10)), 3.56 (sep, ^3J(H,H) = 7.1 Hz, 1H, H-C(11)), 2.98 (d, ^3J(H,H) = 16.1 Hz, 1H, H$_2$-C(7)), 2.89 (s, 3H, H$_3$-C(23)), 2.88 (d, ^3J(H,H) = 16.2 Hz, 1H, H$_2$-C(7)), 1.39 (s, 3H, H$_3$-C(14) or C(15)), 1.34 (s, 3H, H$_3$-C(15) or C(14)), 1.32 (d, ^3J(H,H) = 7.0 Hz, 3H, H$_3$-C(12) or C(13)), 1.30 ppm, (d, ^3J(H,H) = 7.0 Hz, 3H, H$_3$-C(13) or C(12)) ppm; ^{13}C NMR (100 MHz, CD$_2$Cl$_2$): δ = 193.4 (C(16)), 168.4 (C(9)), 151.4 (C(22)), 148.2 (C(6)), 147.6 (C(4)), 137.5 (C(5)), 136.1 (C(17)), 134.1 (C(20)), 130.9 (C(2) and C(18)), 130.6 (C(19)), 124.8 (C(3)), 124.8 (C(21)), 123.2 (C(1)), 120.7 (C(10)), 50.1 (C(7)), 46.7 (C(8)), 45.2 (C(23)), 29.6 (C(11)), 28.5 (C(14) or C(15)), 26.8 (C(15) or C(14)), 24.2 (C(12) or C(13)), 23.7 (C(13) or C(12)) ppm; IR: $\tilde{\nu}$

= 2952w, 2918w, 2867w, 1646s, 1605m, 1592m, 1567m, 1477w, 1434w, 1412w, 1379w, 1360w, 1334w, 1300m, 1253m, 1232m, 1214m, 1189w, 1168m, 1133w, 1115w, 1068s, 1023vs, 983m, 951m, 932w, 922m, 892w, 848w, 809m, 784m, 775s, 753vs, 743s, 712w, 678m, 668m cm^{-1}; EI-MS (70 eV): m/z (%): 366 (0.5) [M], 350 (3), 323 (88), 307 (100)); HR-EI-MS calc. [$C_{23}H_{26}O_2S$]: 366.1654, found: 366.1638.

3,3',5,5'-tetramethyl-1,1'-biphenyl (68)[217]
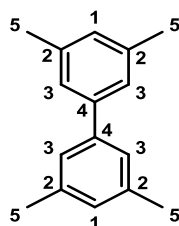
(3,5-dimethylphenyl)boronic acid (0.30 g, 2.0 mmol) was dissolved in MeOH (40 mL) and Pd(OAc)$_2$ (23 mg, 0.10 mmol) was added. After the reaction mixture was stirred at 23 °C for 3 h, saturated aqueous NH$_4$Cl solution (100 mL) was added. The aqueous phase was extracted three times with EtOAc (3 x 100 mL) and the combined organic phases were dried over MgSO$_4$. The volatiles were removed *in vacuo* and the crude product was purified by column chromatography (SiO$_2$, *i*Hex) to obtain compound **68** as a white solid (0.17 g, 0.81mmol, 81%).

R_f = 0.60 (*i*Hex); ^{1}H NMR (400 MHz, CD$_2$Cl$_2$) δ = 7.19 (s, 4H, H-C(3)), 6.98 (s, 2H, H-C(1)), 2.36 (s, 12H, H$_3$-C(5)) ppm; ^{13}C NMR (100 MHz, CD$_2$Cl$_2$): δ = 141.8 (C(4)), 138.7 (C(2)), 129.3 (C(1)), 125.5 (C(3)), 21.7 (C(5)) ppm; IR: $\tilde{v}$ = 3013w, 2911m, 2858w, 1732w, 1596s, 1446m, 1370w, 1100w, 1037w, 946w, 897w, 883w, 875w, 849m, 836m, 731m, 707w, 695s, 690vs; EI-MS (70 eV): m/z (%): 210 (100) [M], 195 (45); 180 (21); HR-EI-MS calc. [$C_{16}H_{18}$]: 210.1409, found: 210.1396.

1,3,6,8-tetramethyl-9*H*-fluorene (69)
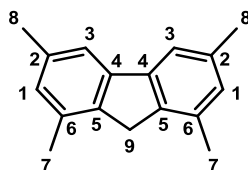
Compound **68** (0.96 g, 4.6 mmol) was dissolved in CH_2Cl_2 (150 mL) and $AlCl_3$ (0.61 g, 4.6 mmol) was added. After the reaction mixture was stirred for 4 d at 23 °C, saturated aqueous $NaHCO_3$ solution (300 mL) was added. The aqueous phase was extracted three times with CH_2Cl_2 (3 x 200 mL) and the combined organic phases were dried over $MgSO_4$. The volatiles were removed *in vacuo* and the crude product was purified by column chromatography (SiO_2, *i*Hex) to obtain compound **69** as white solid (0.57 g, 2.6 mmol, 53%).

R_f = 0.52 (*i*Hex); ^{1}H NMR (400 MHz, CD_2Cl_2) δ = 7.43 (s, 2H, H-C(3)), 6.96 (s, 2H, H-C(1)), 3.58 (s, 2H, H_2-C(9)), 2.44 (s, 3H, H_3-C(8)), 2.40 (s, 3H, H_3-C(7)) ppm; ^{13}C NMR (100 MHz, CD_2Cl_2): δ = 142.3 (C(4)), 140.1 (C(5)), 137.1 (C(2)), 134.5 (C(6)), 129.1 (C(1)), 118.5 (C(3)), 34.5 (C(9)), 21.8 (C(8)), 19.1 (C(7)) ppm; IR: $\tilde{v}$ = 3004w, 2912w, 2360w, 1717w, 1613w, 1589w, 1455m, 1398w, 1371w, 1303w, 1254w, 1174w, 1036w, 957w, 925w, 872w, 842vs, 800m, 761w, 727w, 689s, 667w. EI-MS (70 eV): *m/z* (%): 222 (82) [*M*], 207 (100); HR-EI-MS calc. [$C_{17}H_{18}$]: 222.1409, found: 222.1407.

1,3,6,8-tetramethyl-9*H***-fluoren-9-one (70)**
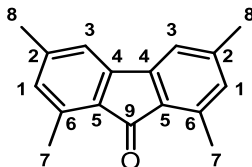
Compound **69** (0.13 g, 0.59 mmol) was dissolved in pyridine (2.5 mL). $FeCl_3$ (20 mg, 0.12 mmol) and a *tert*-butyl hydroperoxide solution in nonane (0.2 mL, 6 M, 1.2 mmol) were added. After the reaction mixture was stirred for 17 h, saturated aqueous $NaHCO_3$ solution (30 mL) was added. The aqueous phase was extracted three times with EtOAc (3 x 30 mL) and the combined organic phases were dried over $MgSO_4$. The volatiles were removed *in vacuo* and the crude product was purified by column chromatography (SiO_2, *i*Hex) to obtain compound **70** (0.11 g, 0.45 mmol, 79%) as yellow solid.

R_f = 0.6 (*i*Hex:EtOAc 50:1); ^{1}H NMR (600 MHz, CD_2Cl_2) δ = 7.17 (s, 2H, H-C(3)), 6.85 (s, 2H, H-C(1)), 2.54 (s, 6H, H_3-C(7)), 2.36 (s, 6H, H_3-C(8)) ppm; ^{13}C NMR (150 MHz, CD_2Cl_2): δ = 196.1 (C(9)), 145.0 (C(4) and C(2)), 139.1 (C(6)), 132.7 (C(1)), 129.8 (C(5)), 119.0 (C(3)), 22.2 (C(8)), 17.8 (C(7)) ppm; IR: $\tilde{v}$ = 2914w, 1687s, 1589s, 1449m, 1372m, 1293m, 1239m, 1172s, 1137w, 1117m, 1030m, 973w, 874s, 849vs, 804m, 666vs; EI-MS (70 eV): *m/z* (%): 236 (100) [*M*], 221 (42), 193 (33); HR-EI-MS calc. [$C_{17}H_{16}O$]: 236.1201, found: 236.1190.

2-bromo-1,3,6,8-tetramethyl-9H-fluoren-9-one (71)
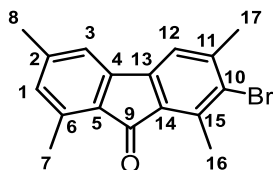
To a solution of **70** (20 mg, 0.085 mmol) in CH_2Cl_2 (2 mL) a Br_2 solution in dry CH_2Cl_2 (40 μL, 2 M) was added. After the reaction mixture was stirred for 3 days at 23 °C saturated aqueous $Na_2S_2O_4$ (10 mL) was added and the aqueous phase was extracted three times with CH_2Cl_2 ((3 x 20 mL)). The combined organic phases were dried over $MgSO_4$ and the volatiles were removed *in vacuo* and the crude product was purified by column chromatography. Compound 71 was obtained as a yellow solid. Yield was not determined.

^{1}H NMR (400 MHz, CDCl$_3$) δ = 7.22 (s, 1H, H-C(12)), 7.13 (s, 1H, H-C(3)), 6.85 (s, 1H, H-C(1)), 2.72 (s, 3H, H$_3$-C(16)), 2.56 (s, 3H, H$_3$-C(7)), 2.46 (s, 3H, H$_3$-C(17)), 2.36 (s, 3H, H$_3$-C(8)) ppm; ^{13}C NMR (100 MHz, CDCl$_3$): δ = 195.1 (C(9)), 144.8 (C(2)), 144.0 (C(11)), 143.8 (C(13)), 143.0 (C(4)), 139.5 (C(15)), 139.3 (C(6)), 132.6 (C(1)), 130.7 (C(14)), 129.7 (C(10)), 129.0 (C(5)), 119.9 (C(12)), 118.6 (C(3)), 25.2 (C(17)), 22.1 (C(8)), 17.8 (C(7)), 17.2 (C(16)) ppm; EI-MS (70 eV): *m/z* (%): 314 (55) [*M*], 3235 (29), 207 (100);); HR-EI-MS calc. [C$_{17}$H$_{15}$BrO]: 314.0306, found: 314.0297.

1,3,6,8-tetramethyl-9-((2-(methylthio)phenyl)ethynyl)-9*H*-fluoren-9-ol (72)
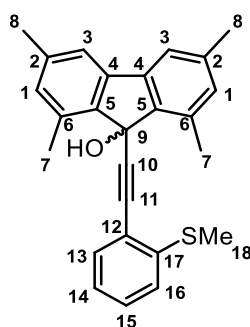
To a solution of 2-ethinyl thioanisole **16** (36 mg, 0.21 mmol) in dry THF (0.50 mL) under Argon atmosphere, *n*BuLi (0.10 mL, 0.25 mmol, 2.5 M in hexane) was added successively at –78 °C. After the solution was stirred for 30 min at –78 °C, a solution of fluorenone **70** (45 mg, 0.25 mmol) in THF (1 mL) was added. The reaction mixture was allowed to warm up to 23 °C and was stirred for 20 h. To the reaction mixture, a saturated aqueous NH$_4$Cl solution (20 mL) was added. The aqueous phase was extracted three times with EtOAc (3 x 20 mL) and the combined organic phases were dried over MgSO$_4$. The volatiles were removed *in vacuo* and the crude product was purified by column chromatography (SiO$_2$, *i*Hex:EtOAc, 50:1 v/v) to obtain compound **72** (50 mg, 0.13 mmol, 62%) as a colourless liquid.

^{1}H NMR (400 MHz, CDCl$_3$) δ = 7.32 (t, ^3J(H,H) = 7.5 Hz, 1H, H-C(14) or H-C(15)), 7.27 (d, ^3J(H,H) = 7.4 Hz, 1H, H-C(13) or H-C(16)), 7.28 (s, 2H, H-C(1) or H-C(3)), 7.13 (d, ^3J(H,H) = 8.0 Hz, 1H, H-C(16) or H-C(13)), 7.04 (t, ^3J(H,H) = 7.5 Hz, 1H, H-C(15) or H-C(14)), 6.95 (s, 2H, H-C(3) or H-C(1)), 2.70 (s, 6H, H$_3$-C(7) or H$_3$-C(8)), 2.43 (s, 3H, H$_3$-C(18)), 2.38 (s, 6H, H$_3$-C(8) or H$_3$-C(7)) ppm; EI-MS (70 eV): *m/z* (%): 383 (57) [*M*-1], 369 (41), 353 (14).

1-(2-(methylsulfinyl)phenyl)-2-(1,3,6,8-tetramethyl-9*H*-fluoren-9-ylidene)ethan-1-one (74)
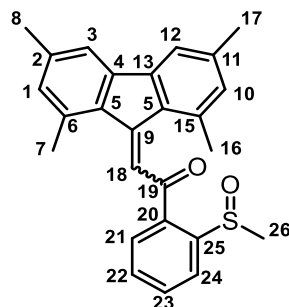
Compound **72** (50 mg, 0.13 mmol) was dissolved in THF (1 mL) and two drops of H_2SO_4 were added. After the solution was stirred for 10 min at 23 °C, saturated aqueous $NaHCO_3$ solution (5 mL) was added and the aqueous phase was extracted three times with EtOAc (3 x 10 mL). The combined organic phases were dried over $MgSO_4$ and the volatiles were removed *in vacuo*. The crude product was dissolved in c. AcOH (2 mL) and sodium perborate tetrahydrate (20 mg, 0.13 mmol) was added. After the reaction mixture was stirred for 7 h at 23 °C, saturated aqueous $NaHCO_3$ solution (20 mL) was added and the aqueous phase was extracted three times with EtOAc (3 x 20 mL). The combined organic phases were dried over $MgSO_4$ and the volatiles were removed *in vacuo*. The crude product was purified by column chromatography to obtain compound **74** (15 mg, 0.037 mmol, 29%) as a yellow solid.

^{1}H NMR (400 MHz, CDCl$_3$) δ = 8.40 (d, 1H, ^3J(H,H) = 7.9 Hz, H-C(21) or H-C(24)), 8.18 (d, 1H, ^3J(H,H) = 7.7 Hz, H-C(24) or H-C(21)), 7.89 (t, 1H, ^3J(H,H) = 7.7 Hz, H-C(22) or H-C(23)), 7.68 (t, ^3J(H,H) = 7.5 Hz, 1H, H-C(23) or H-C(22)), 7.53 (s, 1H, H-C(10)), 7.36 (s, 1H, H-C(1) or H-C(3) or H-C(10) or H-C(12)), 7.33 (s, 1H, H-C(3) or H-C(10) or H-C(12) or H-C(1)), 6.91 (s, 1H, H-C(10) or H-C(12) or H-C(1) or H-C(3)), 6.85 (s, 1H, H-C(12) or H-C(1) or H-C(3) or H-C(10)), 2.88 (s, 3H, H$_3$-C(26), 2.66 (s, 3H, H$_3$-C(7) or H$_3$-C(8) or H$_3$-C(16) or H$_3$-C(17)), 2.39 (s, 3H, H$_3$-C(8) or H$_3$-C(16) or H$_3$-C(17) or H$_3$-C(7)), 2.38 (s, 3H, H$_3$-C(16) or H$_3$-C(17) or H$_3$-C(7) or H$_3$-C(8)), 1.98 (s, 3H, H$_3$-C(17) or H$_3$-C(7) or H$_3$-C(8) or H$_3$-C(16)) ppm; EI-MS (70 eV): *m/z* (%): 400 (3) [*M*], 383 (62), 369 (27); HR-EI-MS calc. [$C_{26}H_{24}O_2S$]: 400.1497, found: 400.1510.

1-ethynyl-2-(methylsulfinyl)benzene (77)
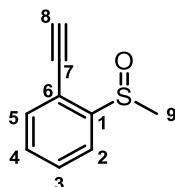
To a solution of compound **16** (0.61 g, 4.1 mmol) in c. acetic acid (10 mL) sodium perborate tetrahydrate (0.56 g, 4.1 mmol) was added. After the reaction mixture was stirred at 23 °C for 4.5 h additional sodium perborate tetrahydrate (0.12 g, 0.88 mmol) was added. The reaction mixture was stirred for 3 h at 23 °C and saturated aqueous $NaHCO_3$ solution (30 mL) was added. The aqueous phase was extracted three times with EtOAc (3 x 50 mL). The combined organic phases were dried over $MgSO_4$ and the volatiles were removed *in vacuo*. The crude product was purified by column chromatography (SiO_2, *i*Hex:EtOAc, 1:1 v/v) to obtain compound **77** (0.59g, 3.6 mmol, 87%) as a colorless solid

R_f = 0.25 (*i*Hex:EtOAc 1:1); ^{1}H NMR (400 MHz, CD_2Cl_2) δ = 7.93 (d, ^3J(H,H) = 7.9 Hz, 1H, H-C(2)), 7.63 (t, ^3J(H,H) = 7.6 Hz, 1H, H-C(3) or H-C(4)), 7.56 (d, ^3J(H,H) = 7.7 Hz, 1H, H-C(5)), 7.47 (t, ^3J(H,H) = 7.5 Hz, 1H, H-C(4) or H-C(3)), 3.60 (s, 1H, H-C(8)), 2.79 (s, 3H, H_3-C(9)) ppm; ^{13}C NMR (100 MHz, CD_2Cl_2): δ = 149.0 (C(1)), 133.8 ((C(5)), 130.8 (C(3) or H-C(4)), 130.7 (C(4) or H-C(3)), 123.7 (C(2)), 118.5 (C(6)), 86.4 (C(8)), 79.0 (C(7)), 42.7 (C(9)) ppm; IR: $\tilde{v}$ = 3469w, 3282w, 3198w, 3055w, 2917w, 2360w, 2099w, 1651w, 1461m, 1433w, 1414m, 1291w, 1257w, 1187w, 1158w, 1126m, 1066vs, 1027vs, 951s, 879w, 759vs, 660s cm^{-1}; EI-MS (70 eV): m/z (%): 164 (5) [*M*], 149 (31), 121 (100); HR-EI-MS calc. [C_9H_8OS]: 164.0296, found: 164.0288.

2-((4-(*tert*-butyl)phenyl)thio)acetic acid (81)[249]
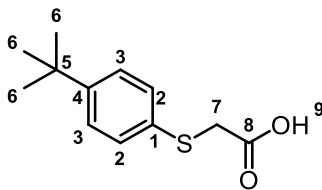
Bromoacetic acid (1.8 g, 13 mmol) was dissolved in acetone (25 mL) and K_2CO_3 (10 g, 72 mmol) was added. After the reaction mixture was stirred for 15 min 4-*tert*-butylbenzenethiol (2.0 g, 12 mmol) was added at 0 °C. After the reaction mixture was stirred for 75 min, the volatiles were removed *in vacuo* and water (30 mL) was added. The aqueous phase was extracted three times with EtOAC (3 x 50 mL) to remove unreacted 4-*tert*-butylbenzenethiol. The organic phases were removed. 2M aqueous HCl solution was added to the aqueous phase until pH is 1. The aqueous phase was extracted again three times with EtOAc (3 x 100 mL). These combined organic phases were dried over $MgSO_4$ and the volatiles were removed *in vacuo*. Compound **81** was obtained as colorless solid (2.6 g, 12 mmol, 100%).

R_f = 0.20 (EtOAc); m.p. 61 °C; ^{1}H NMR (400 MHz, CD_2Cl_2): δ = 7.35 (s, 4H, H-C(2) and H-C(3)), 3.66 (s, 2H, H_2-C(7)), 1.30 (s, 9H, H_3-C(6)) ppm; ^{13}C NMR (100 MHz, CD_2Cl_2): δ = 175 (C(8)), 151.3 (C(4)), 131.4 (C(1)), 130.6 (C(2) or C(3)), 126.8 (C(3) or C(2)), 37.3 (C(7)), 35.0 (C(5)), 31.5 (C(6)) ppm; IR: $\tilde{v}$ = 2960m, 2866m, 1723vs, 1497m, 1463m, 1400m, 1380m, 1364s, 1296s, 1268m, 1196vs, 1178s, 1122s, 1013s, 905s, 886vs, 828s, 810vs, 788s, 740m, 724m, 660s cm^{-1}; EI-MS (70 eV): *m/z* (%): 224 (27) [*M*], 209 (100); HR-EI-MS calc. [$C_{12}H_{16}O_2S$]: 224.0871, found: 244.0867.

5-(*tert*-butyl)benzo[*b*]thiophen-3(2*H*)-one (82)[249]
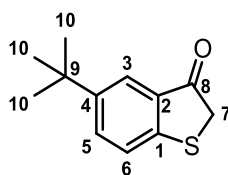
2-((4-(tert-butyl)phenyl)thio)acetic acid **81** (1.0 g, 4.5 mmol) was dissolved in CH_2Cl_2 (6.0 mL). Oxalyl chloride (0.68 g, 5.4 mmol) and two drops of DMF were added. After the solution was stirred for 70 min at 23 °C the volatiles were removed *in vacuo*. The residue was dissolved in DCE (6 mL) and $AlCl_3$ (0.9 g, 6.7 mmol) was added at 0 °C. The reaction mixture was stirred for 1 h at 0 °C. After the reaction mixture was stirred for additional 40 min at 23 °C, 1M aqueous HCl solution solution (30 mL) was added successively. The aqueous phase was extracted three times with CH_2Cl_2 (3 x 100 mL). The combined organic phases were dried over $MgSO_4$ and the volatiles were removed *in vacuo*. The crude product **82** was obtained as a yellow solid and used without further purification in the next synthetic step.

^{1}H NMR (600 MHz, CD_2Cl_2): δ = 7.76 (d, [4]*J*(H,H) = 2.1 Hz, 1H, H-C(3)), 7.65 (d, [3]*J*(H,H) = 7.6 Hz, [4]*J*(H,H) = 2.1 Hz, 1H, H-C(5)), 7.39 (d, [3]*J*(H,H) = 8.3 Hz, 1H, H-C(6)), 3.79 (s, 2H, H_2-C(7)), 1.33 (s, 9H, H-C(10)) ppm; ^{13}C NMR (151 MHz, CD_2Cl_2): δ = 200.5 (C(8)), 151.8 (C(1)), 149.0 (C(4)), 134.2 (C(5)), 131.4 (C(2)), 124.7 (C(6)), 123.2 (C(3)), 40.3 (C(7)), 35.1 (C(9)), 31.5 (C(10)) ppm; EI-MS (70 eV): *m/z* (%): 191 (100), 206 (28) [*M*]; HR-EI-MS calc. [$C_{12}H_{14}OS$]: 206.0765 found: 206.0758.

5-(*tert*-butyl)-1-(λ^1-oxidanyl)-1,2-dihydro-3*H*-1λ^3-benzo[*b*]thiophen-3-one (83)
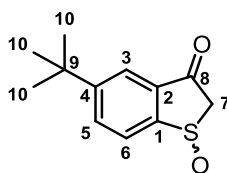
Compound **82** (0.83g, 4.0 mmol) was dissolved in c. AcOH (6.0 mL) and sodium perborate tetrahydrate (0.62 g, 4.0 mmol) was added. After the reaction mixture was stirred for 5 h at 23 °C, aqueous saturated NaHCO$_3$ solution (200 mL) was added. The aqueous phase was extracted three times with EtOAc (3 x 200 mL). The combined organic phases were dried over MgSO$_4$ and the volatiles were removed *in vacuo*. The crude product was purified by column chomatography (SiO$_2$, *i*Hex:EtOAc, 1:1 v/v) to afford compound **83** (0.51 g, 2.3 mmol, 57% over two steps) as a colorless solid.

R_f = 0.21 (*i*Hex:EtOAc 1:1); ^{1}H NMR (400 MHz, CD$_2$Cl$_2$): δ = 7.97 (m, 2H, H-C(5) and H-C(6)), 7.95 (d, ^4J(H,H) = 1.6 Hz, 1H, H-C(3)), 4.30 (d, ^3J(H,H) = 17.6 Hz, 1H, H$_2$-C(7)), 3.58 (d, ^3J(H,H) = 17.6 Hz, 1H, H-C(7)), 1.38 (s, 9H, H$_3$-C(10)) ppm; ^{13}C NMR (100 MHz, CD$_2$Cl$_2$): δ = 194.9 (C(8)), 157.8 (C(4)), 151.9 (C(1)), 134.9 (C(5)), 133.9 (C(2)), 127.9 (C(6)), 122.7 (C(3)), 62.3 (C(7)), 35.9 (C(9)), 31.4 (C(10)) ppm; IR: $\tilde{v}$ = 3048w, 2994w, 2951m, 2903w, 1710vs, 1595m, 1571w, 1479m, 1463m, 1417w, 1361m, 1289w, 1254w, 1224s, 1181m, 1159m, 1113w, 1078w, 1041w, 1020vs, 925w, 907w, 869m, 854s, 793w, 746w, 731w, 705m cm^{-1}; EI-MS (70 eV): *m/z* (%): 222 (15) [*M*], 207 (37); HR-EI-MS calc. [C$_{12}$H$_{14}$O$_2$S]: 222.0715, found: 222.0707.

(E)-2-(5-(*tert*-butyl)-1-(λ^1-oxidanyl)-3-oxo-1,3-dihydro-2*H*-1λ^3-benzo[*b*]thiophen-2-ylidene)indolin-3-one (85)
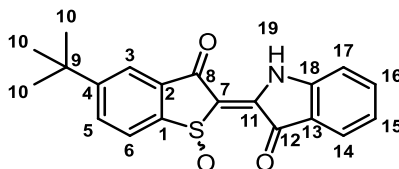
Compound **83** (0.20 g, 1.3 mmol) and indoxyl acetate **84** (0.23 g, 1.3 mmol) were dissolved in c. AcOH (15 mL) and Mn(OAc)$_3$ (1.0 g, 3.9 mmol) was added. After the reaction mixture was stirred for 4.5 h at 23 °C, saturated aqueous NH$_4$Cl solution (50 mL) was added. The aqueous phase was extracted three times with CH$_2$Cl$_2$ (3 x 100 mL). The combined organic phases were dried over NaSO$_4$ and the volatiles were removed *in vacuo*. The crude product was purified by column chromatography (SiO$_2$, *i*Hex:EtOAc, 7:3 v/v) to afford compound **85** as a red solid (30 mg, 0.085 mmol, 7%).

^{1}H NMR (400 MHz, CD$_2$Cl$_2$): δ = 10.32 (s, 1H, H-N(19)), 8.00 (d, ^4J(H,H) = 2.2 Hz, 1H, H-C(3)) 8.00 (d, ^3J(H,H) = 7.6 Hz, 1H, H$_2$-C(6)), 7.93 (d, ^3J(H,H) = 8.1 Hz, ^4J(H,H) = 1.9 Hz, 1H, H-C(5)), 7.78 (d, ^3J(H,H) = 7.5 Hz, 1H, H-C(14)), 7.62 (t, ^3J(H,H) = 7.9 Hz, 1H, H-C(16), 7.17 (t, ^3J(H,H) = 7.3 Hz, 1H, H-C(15)), 7.12 (d, ^3J(H,H) = 7.9 Hz, 1H, H-C(17)), 1.41 (s, 9H, H$_3$-C(10)) ppm; EI-MS (70 eV): *m*/*z* (%): 351 (5) [*M*], 335 (100), 320 (99); HR-EI-MS calc. [C$_{20}$H$_{17}$NO$_3$S]: 351.0929, found: 351.0910.

(*E*)-2-(5-(*tert*-butyl)-1-(λ^1-oxidanyl)-3-oxo-1,3-dihydro-2*H*-1λ^3-benzo[*b*]thiophen-2-ylidene)-1-methylindolin-3-one (86)
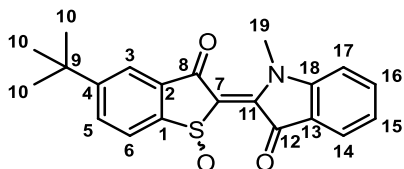
Compound **85** (8.0 mg, 23 µmol) was dissolved in DMF (1.5 mL) and K_2CO_3 (10 mg) was added. The reaction mixture was stirred for 15 min and methyl iodide (8 µl, 0.12 mmol) was added. After the reaction mixture was stirred for 45 min at 23 °C, saturated aqueous NH_4Cl solution (5 mL) was added. The aqueous phase was extracted three times with CH_2Cl_2 (3 x 10 mL). The combined organic phases were dried over $MgSO_4$ and the volatiles were removed *in vacuo*. The crude product was purified by column chromatography (SiO_2, deactivated with NEt_3, *i*Hex:EtOAc, 8:2 to 7:3 to 1:1 v/v) to obtain compound **86** as a red solid (1.9 mg, 5.4 µmol, 23%).

R_f = 0.4 (EtOAc); ^{1}H NMR (800 MHz, CD_2Cl_2): δ = 7.99 (d, ^3J(H,H) = 8.1 Hz, 1H, H-C(6)), 7.97 (d, ^4J(H,H) = 1.9 Hz, 1H, H-C(3)), 7.91 (d, ^3J(H,H) = 8.1 Hz, ^4J(H,H) = 2.0 Hz, 1H, H-C(5)) 7.76 (d, ^3J(H,H) = 7.4 Hz, 1H, H-C(14)), 7.67 (t, ^3J(H,H) = 8.0 Hz, 1H, H-C(16), 7.20 (t, ^3J(H,H) = 7.4 Hz, 1H, H-C(15)), 7.13 (d, ^3J(H,H) = 8.1 Hz, 1H, H-C(17), 3.76 (s, 3H, H$_3$-C(19)), 1.40 (s, 9H, H$_3$-C(10)) ppm; ^{13}C NMR (100 MHz, CD_2Cl_2): δ = 188.2 (C(12)), 185.6 (C(8)), 157.0 (C(4)), 155.4 (C(18)), 149.2 (C(1)), 144.3 (C(11)), 138.3 (C(16)), 135.6 (C(2)), 133.4 (C(5)), 127.0 (C(6)), 125.9 (C(14)), 124.6 (C(15)), 122.5 (C(7)), 122.1 (C(3)), 120.1 (C(13)), 111.6 (C(17)), 36.9 (C(19)), 35.9 (C(9)), 31.5 (C(10)) ppm; EI-MS (70 eV): *m/z* (%): 365 (1) [*M*], 349 (100), 334 (74); HR-EI-MS calc. [$C_{21}H_{19}NO_3S$]: 365.1086, found: 365.1076.

(*E*)-2-(5-(*tert*-butyl)-1-(λ^1-oxidaneyl)-3-oxo-1,3-dihydro-2*H*-1λ^3-benzo[*b*]thiophen-2-ylidene)-1-(*p*-tolyl)indolin-3-one (87)
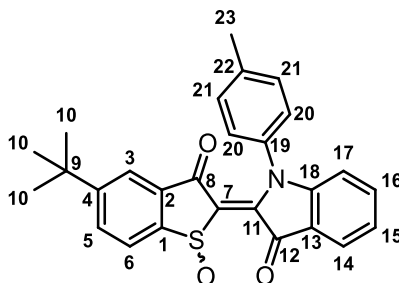
Compound **85** (6 mg, 17 µmol) was dissolved in CH_2Cl_2 (1 mL) and Et_3N (4.6 µL, 34 µmol), $Cu(OAc)_2$ (3.4 mg, 17 µmol) and *p*-tolyl boronic acid (2.3 mg, 17 µmol) were added. After the reaction mixture was stirred for 3.5 h at 23 °C, saturated aqueous NH_4Cl (3 mL) solution was added. The aqueous phase was extracted three times with CH_2Cl_2 (3 x 5 mL). The combined organic phases were dried over $MgSO_4$ and the volatiles were removed *in vacuo*. The crude product was purified by column chromatography (SiO_2, deactivated with Et_3N, *i*Hex:EtOAc, 8:2 to 7:3 to 1:1 v/v) to obtain compound **87** as a red solid (2.1 mg, 4.8 µmol, 28%).

R_f = 0.63 (EtOAc); ^{1}H NMR (600 MHz, CD_2Cl_2): δ = 7.96 (d, ^3J(H,H) = 8.2 Hz, 1H, H-C(6)), 7.86 (d, ^4J(H,H) = 1.9 Hz, ^3J(H,H) = 8.2 Hz, 1H, H-C(5)), 7.83 (d, ^3J(H,H) = 7.5 Hz, 1H, H-C(14)), 7.71 (d, ^4J(H,H) = 1.8 Hz, 1H, H-C(3)), 7.53 (t, ^3J(H,H) = 8.3 Hz, 1H, H-C(16), 7.32 (m, 4H, H-C(20) and H-C(21)), 7.20 (t, ^3J(H,H) = 7.4 Hz, 1H, H-C(15), 6.84 (d, ^3J(H,H) = 8.2 Hz, 1H, H-C(17)), 2.47 (s, 3H, H_3-C(23)), 1.33 (s, 9H, H_3-C(10)) ppm; ^{13}C NMR (150 MHz, CD_2Cl_2): δ = 188.4 (C(12)), 185.0 (C(8)), 157.0 (C(4)), 156.1 (C(18)), 149.2 (C(1)), 142.1 (C(7) or C(11) or C(19)), 138.9 (C(22)), 138.1 (C(16)), 137.3 (C(11) or C(19) or C(7)), 135.2 (C(2)), 133.5 (C(5)), 130.5 (C(20) and C(21)), 127.1 (C(6)), 125.9 (C(14)), 124.7 (C(15)), 123.1 (C(19) or C(7) or C(11)), 122.1 (C(3)), 112.8 (C(17)), 35.9 (C(9)), 31.4 (C(10)), 21.6 (C(23)) ppm; EI-MS (70 eV): *m/z* (%): 441 (0.5) [*M*], 425 (100), 410 (35); HR-EI-MS calc. [$C_{27}H_{23}NO_3S$]: 441.1399, found: 441.1391.

trans-N-(p-tolyl) indigo (107) and N,N'-di(p-tolyl) indigo (108)[39]
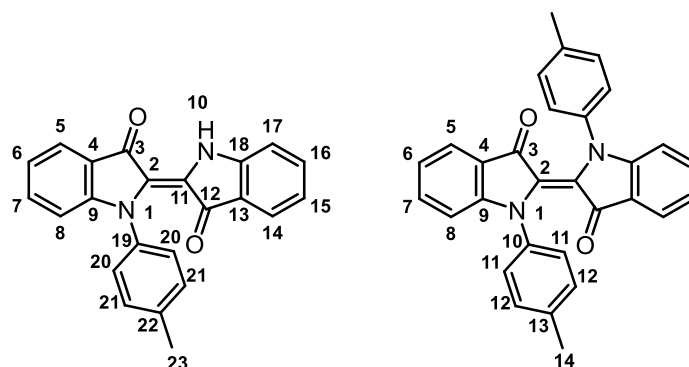
Indigo (200 mg, 0.76 mmol), K_2CO_3 (210 mg, 1.5 mmol), and copper (5.3 mg, 0.083 mmol) were dispersed in 1,2-dichlorobenzene (4 ml) and 4-bromotoluene (0.14 ml, 1.14 mmol) was added. The stirred mixture was heated to 180 °C under reflux for 11 h. Subsequently, water was added (50 mL) and the aqueous phase was extracted three times with CH_2Cl_2 (3 x 150 mL). The combined organic phases were separated and dried over $MgSO_4$. The volatiles were removed *in vacuo* and the crude product was purified by column chromatography (SiO_2, iHex to iHex:EtOAc, 20:1 to 9:1 v/v) to obtain *trans-N-(p-tolyl)* indigo **107** (65 mg, 0.18 mmol, 24%) as a blue solid and a mixture of *cis* and *trans* isomer of *N,N'-di(p-tolyl)* indigo **108** (42 mg, 0.095 mmol, 13%) as a blue-green solid.

trans-N-(p-tolyl) indigo (**107**):

R_f = 0.54 (iHex:EtOAc 4:1); m.p. 254 °C; ^1H NMR (600 MHz, CD_2Cl_2): δ = 10.53 (s, 1H, H-N(10)), 7.77 (d, 1H, $^3J(H,H)$ = 7.7 Hz, H-C(5)), 7.44 (d, 1H, H-C(14)), 7.44 (t, 1H, H-C(7)), 7.44 (t, 1H, H-C(16)), 7.30 (d, $^3J(H,H)$ = 8.6 Hz, 2H, H-C(21)), 7.23 (d, $^3J(H,H)$ = 8.3 Hz, 2H, H-C(20)), 7.06 (t, $^3J(H,H)$ = 7.9 Hz, 1H, H-C(6)), 7.04 (d, $^3J(H,H)$ = 8.4 Hz, 1H, H-C(17)), 6.93 (d, $^3J(H,H)$ = 8.3 Hz, 1H, H-C(8)) 6.90 (t, $^3J(H,H)$ = 7.4 Hz, 1H, H-C(15)), 2.45 (s, 3H, H_3-C(23)) ppm; ^{13}C NMR (151 MHz, CD_2Cl_2): δ = 190.2 (C(3)), 186.0 (C(12)), 154.5 (C(9)), 152.0 (C(18)), 138.9 (C(19)), 137.6 (C(22)), 136.3 (C(16)), 136.0 (C(7)), 130.1 (C(21)), 126.9 (C(20)), 126.2 (C(2) or C(11)), 124.8 (C(14)), 124.0 (C(5)), 122.5 (C(11) or C(2)), 121.8 (C(6)), 121.3 (C(4)), 121.3 (C(15)), 120.7 (C(13)), 112.4 (C(17)), 112.3 (C8)), 21.6 (C(23)) ppm; IR: $\tilde{v}$ = 1695m, 1637m, 1601s, 1516m, 1476s, 1461s, 1392s, 1320m, 1303m, 1288m, 1216w, 1178s, 1150m, 1102m, 1063vs, 911s, 879m, 850m, 814m, 786m, 752m, 742vs, 718m, 694s cm^{-1}; EI-MS (70 eV): *m/z* (%): 352 (100) [*M*], 337 (33), 309 (21); HR-EI-MS calc. [$C_{23}H_{16}N_2O_2$]: 352.1212, found: 352.1199.

N,N'-di(*p*-tolyl) indigo (**108**) (mixture of *cis* und *trans* isomer):

R_f = 0.15 (*i*Hex:EtOAc 9:1); m.p. 261 °C; IR: $\tilde{v}$ = 1646s, 1600s, 1532w, 1510s, 1459s, 1334m, 1305s, 1290s, 1255s, 1188s, 1100m, 1044vs, 924vs, 811m, 755vs, 746vs, 716m, 708m, 690s cm^{-1}; EI-MS (70 eV): *m/z* (%): 442 (100) [*M*], 425 (36), 413 (28); HR-EI-MS calc. [$C_{30}H_{22}N_2O_2$]: 442.1681, found: 442.1677.

cis-N,N'-di(*p*-tolyl) indigo (*cis*-**108**):

^{1}H NMR (600 MHz, CD_2Cl_2): δ = 7.78 (d, ^3J(H,H) = 7.6 Hz, 1H, H-C(5)), 7.34 (t, ^3J(H,H) = 7.2 Hz, 1H, H-C(7)), 7.07 (t, ^3J(H,H) = 7.4 Hz, 1H, H-C(6)), 6.93 (d, 2H, H-C(12)), 6.93 (d, ^3J(H,H) = 8.1 Hz, 1H, H-C(8)), 6.50 (d, 2H, H-C(11)), 2.34 (s, 3H, H_3-C(14)) ppm; ^{13}C NMR (151 MHz, CD_2Cl_2): δ = 183.5 (C(3)), 152.7 (C(9)), 136.6 (C(13)), 136.3 (C(10)), 135.2 (C(7)), 129.8(C(12)), 128.5 (C(2)), 125.6 (C(11)), 124.8 (C(5)), 123.9 (C(4)), 122.8 (C(6)), 112.0 (C(8)), 21.3 (C(14)) ppm.

trans-N,N'-di(*p*-tolyl) indigo (*trans*-**108**):

^{1}H NMR (600 MHz, CD_2Cl_2): δ = 7.52 (d, ^3J(H,H) = 7.6 Hz, 1H, H-C(5)), 7.43 (d, ^3J(H,H) = 8.4 Hz, 2H, H-C(11)), 7.39 (t, ^3J(H,H) = 7.8 Hz, 1H, H-C(7)), 7.33 (d, ^3J(H,H) = 8.0 Hz, 2H, H-C(12)), 7.01 (d, ^3J(H,H) = 8.3 Hz, 1H, H-C(8)), 6.99 (t, ^3J(H,H) = 7.2 Hz, 1H, H-C(6)), 2.43 (s, 3H, H_3-C(14)) ppm; ^{13}C NMR (151 MHz, CD_2Cl_2): δ = 184.8 (C(3)), 154.0 (C(9)), 140.3 (C(10)), 137.3 (C(13)), 135.3 (C(7)), 130.4 (C(12)), 127.4 (C(2)), 126.3 (C(11)), 124.1 (C(5)), 122.3 (C(6)), 122.3 (C(4)), 112.0 (C(8)), 21.5 (C(14)) ppm.

trans-*N*-(*p*-(dimethylamino)phenyl) indigo (109)[39]
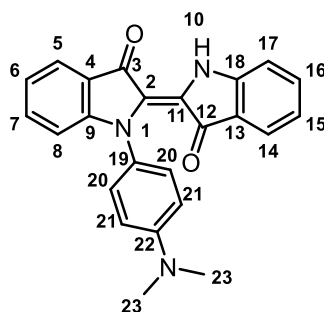
Indigo (300 mg, 1.1 mmol), K_2CO_3 (473 mg, 2.2 mmol), and copper (362 mg, 5.7 mmol) were dispersed in 1,2-dichlorobenzene (24 ml) and 4-bromo-*N*,*N*-dimethylaniline (228 mg, 1.1 mmol) was added. The stirred mixture was heated to 180 °C under reflux for 5 h. Subsequently, water (50 mL) was added and the aqueous phase was extracted three times with EtOAc (3 x 150 mL). The combined organic phases were separated and dried over $MgSO_4$. The volatiles were removed *in vacuo* and the crude product was purified by column chromatography (SiO$_2$, *i*Hex:EtOAc, 9:1 to 4:1 v/v) to obtain *trans-N*-(*p*-(dimethylamino)phenyl) indigo **109** (38 mg, 0.24 mmol, 9%) as a blue solid. No bis-arylated indigo could be isolated.

R_f = 0.33 (*i*Hex:EtOAc 4:1); m.p. 284 °C; ^{1}H NMR (600 MHz, CD$_2$Cl$_2$): δ = 10.56 (s, 1H, H-N(10)), 7.74 (d, ^3J(H,H) = 7.6 Hz, 1H, H-C(5)), 7.45 (d, ^3J(H,H) = 7.9 Hz, 1H, H-C(14)), 7.43 (t, ^3J(H,H) = 7.3 Hz, 1H, H-C(6)), 7.42 (t, ^3J(H,H) = 7.0 Hz, 1H, H-C(15)), 7.19 (d, ^3J(H,H) = 9.0 Hz, 1H, H-C(20)), 7.03 (t, ^3J(H,H) = 7.3 Hz, 1H, H-C(7)), 7.03 (d, ^3J(H,H) = 8.0 Hz, 1H, H-C(17)), 6.89 (t, ^3J(H,H) = 7.3 Hz, 1H, H-C(16)), 6.86 (d, ^3J(H,H) = 8.3 Hz, 1H, H-C(8)), 6.77 (d, ^3J(H,H) = 9.2 Hz, 1H, H-C(21)), 3.03 (s, 6H, H$_3$-C(23)) ppm; ^{13}C NMR (151 MHz, CD$_2$Cl$_2$): δ = 190.5 (C(3)), 186.0 (C(12)), 155.1 (C(9)), 151.9 (C(18)), 150.1 (C(22)), 136.1 (C(6)), 135.9(C(15)), 130.3 (C(19)), 128.0 (C(20)), 125.9 (C(2) or C(11)), 124.7 (C(14)), 123.8 (C(5)), 123.2 (C(11) or C(2)), 121.5 (C(7)), 121.1 (C(16)), 121.1 (C(4)), 120.8 (C(13)), 112.4 (C(8)), 112.4 (C(21)), 112.4 (C(17)), 40.9 (C(23)) ppm; IR: $\tilde{v}$ = 3325w, 2804w, 1696w, 1640m, 1600vs, 1522s, 1475s, 1461s, 1382m, 1318s, 1292s, 1219m, 1191m, 1174s, 1149m, 1132s, 1098m, 1045vs, 954m, 927m, 909vs, 880m, 858m, 809m, 744vs, 710s, 696vs cm^{-1}; EI-MS (70 eV): *m/z* (%): 381 (100) [*M*], 366 (4), 337 (16); HR-EI-MS calc. [C$_{24}$H$_{19}$N$_3$O$_2$]: 381.1477, found: 381.1475.

N,N'-di(*p*-(dimethylamino)phenyl) indigo (110)
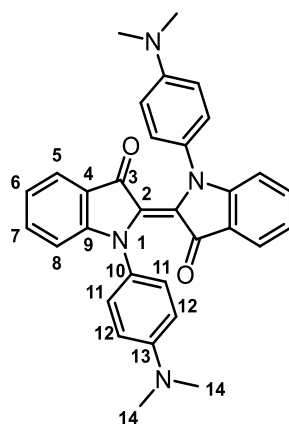
Indigo (0.20 g, 0.76 mmol), K_2CO_3 (0.32 mg, 2.3 mmol), and copper (0.12 g, 1.9 mmol) were dispersed in 1,2-dichlorobenzene (16 ml) and 4-bromo-dimethylaniline (0.46 g, 2.3 mmol) was added. The stirred mixture was heated to 180 °C under reflux for 5 h. Subsequently, water (50 mL) was added and the aqueous phase was extracted three times with CH_2Cl_2 (3 x 150 mL). The combined organic phases were separated and dried over $MgSO_4$. The volatiles were removed *in vacuo* and the crude product was purified by column chromatography to obtain N,N'-di(*p*-(dimethylamino)phenyl) indigo **110** (42 mg, 0.084 mmol, 11%) as a green solid in *cis* and *trans* configuration with dynamic exchange.

EI-MS (70 eV): *m/z* (%): 500 (100) [*M*], 486 (17); HR-EI-MS calc. [$C_{32}H_{28}N_4O_2$]: 500.2212, found: 500.2205.

cis-N,N'-di(*p*-(dimethylamino)phenyl) indigo (*cis*-**110**):

^{1}H NMR (600 MHz, CD_2Cl_2): δ = 7.76 (d, ^3J(H,H) = 7.5 Hz, 2H, H-C(5) or H-C(8)), 7.34 (t, ^3J(H,H) = 8.4 Hz, 2H, H-C(6) or H-C(7)), 7.05 (t, ^3J(H,H) = 7.4 Hz, 2H, H-C(7) or C(6)), 6.91 (d, ^3J(H,H) = 8.4 Hz, 2H, H-C(8) or H-C(5)), 6.52 (d, ^3J(H,H) = 7.9 Hz, 4H, H-C(11) or H-C(12)), 6.48 (d, ^3J(H,H) = 8.6 Hz, 4H, H-C(12) or C(11)), 2.95 (s, 12H, H-C(14) ppm.

trans-N,N'-di(*p*-(dimethylamino)phenyl) indigo (*trans*-**110**):

^{1}H NMR (600 MHz, CD_2Cl_2): δ = 7.53 (d, ^3J(H,H) = 7.6 Hz, 2H, H-C(5) or H-C(8)), 7.39 (d, ^3J(H,H) = 9 Hz, 4H, H-C(11) or H-C(12)), 7.38 (t, ^3J(H,H) = 8.3 Hz, 2H, H-C(6) or C(7)), 6.98 (t, ^3J(H,H) = 7.4 Hz, 2H, H-C(7) or H-C(6)), 6.97 (d, ^3J(H,H) = 8.2 Hz, 2H, H-C(8) or H-C(5)), 6.82 (d, ^3J(H,H) = 9 Hz, 4H, H-C(12) or C(11)), 3.02 (s, 12H, H-C(14)) ppm.

trans-N-phenyl indigo (111)[39, 140]
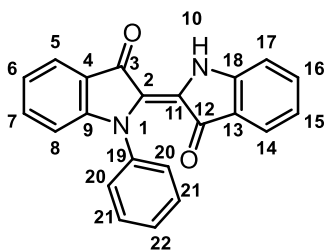
Indigo (0.20 g, 0.76 mmol), K_2CO_3 (0.32 g, 2.3 mmol), and copper (0.42 g, 3.8 mmol) were dispersed in 1,2-dichlorobenzene (4.0 ml) and phenyl bromide (0.26 g, 1.7 mmol) was added. The reaction mixture was stirred at 180 °C for 7 h. Again phenyl bromide (0.15g, 1 mmol) was added and the reaction mixture was stirred at 180 °C for additional 5.5 h. Subsequently, water (50 mL) was added and the aqueous phase was extracted three times with EtOAc (3 x 150 mL). The combined organic phases were separated and dried over $MgSO_4$. The volatiles were removed *in vacuo* and the crude product was purified by column chromatography (SiO$_2$, *i*Hex to *i*Hex:EtOAc, 10:1 v/v) to obtain *trans-N*-(phenyl) indigo **111** (38 mg, 0.11 mmol, 14%) as a blue solid. No bis-arylated indigo could be isolated.

R_f = 0.49 (*i*Hex:EtOAc 4:1); m.p. 263 °C; ^{1}H NMR (600 MHz, CD$_2$Cl$_2$): δ = 10.53 (s, 1H, H-N(10)), 7.78 (d, ^3J(H,H) = 7.7 Hz, 1H, H-C(5)), 7.49 (t, ^3J(H,H) = 7.2 Hz, 2H, H-C(21)), 7.45 (t, ^3J(H,H) = 7.1 Hz, 1H, H-C(7)), 7.45 (t, ^3J(H,H) = 7.3 Hz, 1H, H-C(16)), 7.44 (d, ^3J(H,H) = 7.2 Hz, 1H, H-C(14)), 7.42 (t, ^3J(H,H) = 7.3 Hz, 1H, H-C(22)), 7.36 (d, ^3J(H,H) = 8.2 Hz, 2H, H-C(20)), 7.08 (t, ^3J(H,H) = 6.9 Hz, 1H, H-C(6)), 7.04 (d, ^3J(H,H) = 8.4 Hz, 1H, H-C(17)), 6.96 (d, ^3J(H,H) = 8.3 Hz, 1H, H-C(8)), 6.90 (t, ^3J(H,H) = 8.0 Hz, 1H, H-C(15)) ppm; ^{13}C NMR (151 MHz, CD$_2$Cl$_2$): δ = 190.1 (C(3)), 186.0 (C(12)), 154.3 (C(9)), 152.0 (C(18)), 141.5 (C(19)), 136.3 (C(16)), 136.0 (C(7)), 129.6 (C(21)), 127.7 (C(22)), 127.1 (C(20)), 126.3 (C(2) or C(11)), 124.8 (C(14)), 124.1 (C(5)), 122.3 (C(11) or C(2)), 121.9 (C(6)), 121.4 (C(4)), 121.4 (C(15)), 120.7 (C(13)), 112.4 (C(17)), 112.2 (C(8)) ppm; IR: $\tilde{v}$ = 3319m, 1699w, 1639s, 1602vs, 1495m, 1474s, 1461vs, 1376s, 1317s, 1291s, 1214m, 1181s, 1152m, 1128s, 1098m, 1046vs, 1018vs, 922s, 900vs, 858m, 844m, 791m, 770s, 756s, 747vs, 717s, 696vs, 660s cm^{-1}; EI-MS (70 eV): m/z (%): 338 (100) [*M*], 309 (29); HR-EI-MS calc. [C$_{22}$H$_{14}$N$_2$O$_2$]: 338.1055, found: 338.1048.

***trans*-*N*-(3,5-bis(trifluoromethyl)phenyl) indigo (112)**[39]
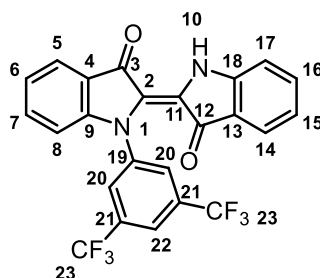
Indigo (200 mg, 0.76 mmol), K_2CO_3 (316 mg, 2.3 mmol), and copper (50 mg, 0.78 mmol) were dispersed in 1,2-dichlorobenzene (16 ml) and 1-iodo-3,5-bis(trifluoromethyl)benzene (0.4 ml, 2.3 mmol) was added. The stirred mixture was heated to 180 °C under reflux for 5 h. Subsequently, water (50 mL) was added and the aqueous phase was extracted three times with CH_2Cl_2 (3 x 150 mL). The combined organic phases were separated and dried over $MgSO_4$. The volatiles were removed *in vacuo* and the crude product was purified by column chromatography (SiO_2, *i*Hex:EtOAc, 4:1 v/v) to obtain *trans*-*N*-(3,5-bis(trifluoromethyl)phenyl) indigo **112** (114 mg, 0.24 mmol, 32%) as a blue solid. No bis-arylated indigo could be isolated.

R_f = 0.5 (*i*Hex:EtOAc 4:1); m.p. 275 °C; ^1H NMR (600 MHz, CD_2Cl_2): δ = 10.49 (s, 1H, H-N(10)), 7.94 (s, 1H, H-C(22)), 7.85 (s, 2H, H-C(20)), 7.85 (d, 1H, H-C(5)), 7.52 (t, ^3J(H,H) = 8.2 Hz, 1H, H-C(7)), 7.48 (t, ^3J(H,H) = 8.2 Hz, 1H, H-C(16)), 7.46 (d, ^3J(H,H) = 7.5 Hz, 1H, H-C(14)), 7.17 (t, ^3J(H,H) = 7.5 Hz, 1H, H-C(6)), 7.06 (d, ^3J(H,H) = 7.9 Hz, 1H, H-C(17)), 6.94 (d, ^3J(H,H) = 8.7 Hz, 1H, H-C(8)), 6.93 (t, ^3J(H,H) = 7.6 Hz, 1H, H-C(15)) ppm; ^{13}C NMR (151 MHz, CD_2Cl_2): δ = 189.3 (C(3)), 186.4 (C(12)), 153.2 (C(9)), 152.3 (C(18)), 143.0 (C(19)), 136.9 (C(16)), 136.3(C(7)), 132.9 (q, C(23)), 127.6 (C(20)), 126.9 (C(2) or C(11)), 125.1 (C(14)), 124.6 (C(4)), 124.5 (C(5)), 123.0 (C(6)), 122.8 (C(21)), 121.9 (C(15)), 121.4 (sep, C(22)), 121.2 (C(2) or C(11)), 120.4 (C(13)), 112.6 (C(17)), 111.6 (C(8)) ppm; IR: $\tilde{\nu}$ = 3350w, 1698w, 1640m, 1620m, 1604m, 1573w, 1515w, 1479m, 1459m, 1380s, 1348m, 1320w, 1280s, 1211m, 1157s, 1124vs, 1107s, 1068s, 1014m, 976s, 927m, 895m, 880m, 862m, 844m, 760m, 746vs, 716m, 708m, 700s, 693s, 680vs cm^{-1}; EI-MS (70 eV): *m/z* (%): 474 (100) [*M*], 446 (8); HR-EI-MS calc. [$C_{24}H_{12}F_6N_2O_2$]: 474.0803, found: 474.0794.

trans-N-(thiophen-2-yl) indigo (113)[39]
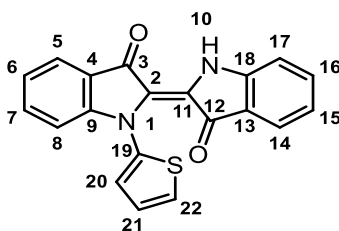
Indigo (200 mg, 0.76 mmol), K_2CO_3 (210 mg, 1.5 mmol), and copper (5.3 mg, 0.083 mmol) were dispersed in 1,2-dichlorobenzene (4 ml) and 2-iodothiophene (0.17 ml, 1.5 mmol) was added. The stirred mixture was heated to 180 °C under reflux for 7 h. 2-iodothiophene (0.17 ml, 1.5 mmol) was added again and the mixture was stirred for additional 1.5 h. Reaction monitoring by TLC revealed progressed decomposition. Subsequently, water (50 mL) was added and the aqueous phase was extracted three times with CH_2Cl_2 (3 x 150 mL). The combined organic phases were separated and dried over $MgSO_4$. The volatiles were removed *in vacuo* and the residue was prepurified by a short patch of silica (*i*Hex to CH_2Cl_2). After removing the volatiles purification by column chromatography (SiO_2, deactivated with NEt_3, *i*Hex:EtOAc, 9:1 v/v) afford *trans-N*-(thiophen-2-yl) indigo **113** (7.3 mg, 0.03 mmol, 3%) as a blue solid. No bis-arylated indigo could be isolated.

R_f = 0.47 (*i*Hex:EtOAc 4:1); m.p. 279 °C; ^{1}H NMR (600 MHz, CD_2Cl_2): δ = 10.57 (s, 1H, H-N(10)), 7.78 (d, $^3J(H,H)$ = 7.6 Hz, 1H, H-C(5)), 7.53 (t, $^3J(H,H)$ = 8.4 Hz, 1H, H-C(7)), 7.49 (d, $^3J(H,H)$ = 7.6 Hz, 1H, H-C(14)), 7.46 (t, $^3J(H,H)$ = 8.1 Hz, 1H, H-C(16)), 7.28 (dd, $^3J(H,H)$ = 5.6 Hz, $^4J(H,H)$ = 1.4 Hz, 1H, H-C(22)), 7.13 (dd, $^3J(H,H)$ = 3.7 Hz, $^4J(H,H)$ = 1.5 Hz, 1H, H-C(21)), 7.12 (t, $^3J(H,H)$ = 7.6 Hz, 1H, H-C(6)), 7.10 (dd, $^3J(H,H)$ = 5.6 Hz, $^4J(H,H)$ = 3.7 Hz, 1H, H-C(20)), 7.06 (d, $^3J(H,H)$ = 8.2 Hz, 1H, H-C(8)), 7.04. (d, $^3J(H,H)$ = 8.1 Hz, 1H, H-C(17)), 6.92 (t, $^3J(H,H)$ = 7.4 Hz, 1H, H-C(15)) ppm; ^{13}C NMR (151 MHz, CD_2Cl_2): δ = 189.4 (C(3)), 186.5 (C(12)), 154.2 (C(9)), 152.1 (C(18)), 142.9 (C(19)), 136.6 (C(16)), 136.2(C(7)), 127.2 (C(2) or C(11)), 126.0 (C(20)), 125.7 (C(21)), 125.0 (C(14)), 123.8 (C(22)), 123.2 (C(11) or C(2)), 122.6 (C(6)), 121.6 (C(15)), 121.6 (C(4)), 120.6 (C(13)), 112.7 (C(8)), 112.5 (C(17)) ppm; IR: $\tilde{v}$ = 3294m, 2918m, 1699w, 1601s, 1542m, 1474s, 1460s, 1433m, 1379s, 1316s, 1305s, 1264m, 1221m, 1172s, 1147m, 1117m, 1095m, 1045vs, 1015vs, 926m, 904m, 894m, 876s, 852m, 791m, 744s, 722s, 694vs cm^{-1}; EI-MS (70 eV): *m/z* (%): 344 (100) [*M*], 314 (20); HR-EI-MS calc. [$C_{20}H_{12}N_2O_2S$]: 344.0619, found: 344.0613.

trans-N-naphtyl indigo (114)[140]

Indigo (200 mg, 0.76 mmol), K_2CO_3 (210 mg, 1.5 mmol), and copper (4.9 mg, 0.077 mmol) were dispersed in 1,2-dichlorobenzene (4 ml) and 1-iodonaphthalene (0.38 g, 1.5 mmol) was added. The stirred mixture was heated to 180 °C. After the reaction mixture was stirred for 4 h, additional 1-iodonaphthalene (0.38 g, 1.5 mmol) was added and the reaction mixture was stirred at 180 °C for 13 h. Subsequently, water (50 mL) was added and the aqueous phase was extracted three times with CH_2Cl_2 (3 x 150 mL). The combined organic phases were separated and dried over $MgSO_4$. The volatiles were removed *in vacuo* and the crude product was purified by column chromatography (SiO_2, *i*Hex:EtOAc, 9:1 to 4:1 v/v) to obtain *trans-N-(p-*(naphtyl) indigo **114** (51 mg, 0.17 mmol, 17%) as a blue solid. No bis-arylated indigo could be isolated.

R_f = 0.44 (*i*Hex:EtOAc 4:1); m.p. 271 °C; ^{1}H NMR (600 MHz, CD_2Cl_2): δ = 10.64 (s, 1H, H-N(10)), 8.04 (d, [3]J(H,H) = 8.3 Hz, 1H, H-C(24)), 8.01 (d, [3]J(H,H) = 8.3 Hz, 2H, H-C(22)), 7.85 (d, [3]J(H,H) = 7.8 Hz, 1H, H-C(5)), 7.76 (d, [3]J(H,H) = 8.4 Hz, 1H, H-C(27)), 7.57 (t, [3]J(H,H) = 6.8 Hz, 1H, H-C(25)), 7.54 (t, [3]J(H,H) = 7.3 Hz, 1H, H-C(21)), 7.47 (t, [3]J(H,H) = 8.2 Hz, 2H, H-C(26)), 7.41 (d, [3]J(H,H) = 7.3 Hz, 1H, H-C(20)), 7.41 (t, [3]J(H,H) = 7.2 Hz, 1H, H-C(16)), 7.35 (t, [3]J(H,H) = 7.1 Hz, 1H, H-C(7)), 7.28 (d, [3]J(H,H) = 7.6 Hz, 1H, H-C(14)), 7.07 (t, [3]J(H,H) = 7.0 Hz, 1H, H-C(6)), 7.02 (d, [3]J(H,H) = 8.1 Hz, 1H, H-C(17)), 6.82 (t, [3]J(H,H) = 7.6 Hz, 1H, H-C(15)), 6.47 (d, [3]J(H,H) = 8.1 Hz, 1H, H-C(8)) ppm; ^{13}C NMR (151 MHz, CD_2Cl_2): δ = 189.9 (C(3)), 186.0 (C(12)), 154.5 (C(9)), 152.0 (C(18)), 138.0 (C(19)), 136.3 (C(16)), 136.0 (C(7)), 134.8 (C(23)), 132.1 (C(28)), 129.1 (C(24)), 129.0 (C(22)), 127.3 (C(26)), 126.9 (C(25)), 126.2 (C(2) or C(11)), 126.0 (C(21)), 125.1 (C(20)), 124.8 (C(14)), 124.0 (C(5)), 123.7 (C(27)), 123.1 (C(11) or C(2)), 121.7 (C(6)), 121.3 (C(15)), 121.0 (C(4)), 120.5 (C(13)), 112.6 (C(8)), 112.3 (C(17)) ppm; IR: $\tilde{v}$ = 1988w, 1697w, 1641m, 1605s, 1458s, 1388m, 1318m, 1294s, 1176s, 1140s, 1101m, 1059vs, 1041s, 907m, 854m, 800m, 788m, 762m, 748vs, 696s, 661m cm^{-1}; EI-MS (70 eV): *m/z* (%): 388 (100) [*M*], 359 (29); HR-EI-MS calc. [$C_{26}H_{16}N_2O_2$]: 388.1212, found: 388.1210.

N-(*p*-(dimethylamino)phenyl)-*N'*-(*p*-(cyano)phenyl) indigo (116)

A round bottom flask was charged with *trans-N*-(*p*-(dimethylamino)phenyl) indigo **109** (18 mg, 0.047 mmol), 4-cyanophenyl boronic acid (21 mg, 0.14 mmol), $Cu(OAc)_2$ (0.12 g, 1.9 mmol) and molecular sieves 3Å. Et_3N (13 µL) and CH_2Cl_2 (3 mL) were additionally added. After the reaction mixture was stirred for 2 h at 23 °C, saturated aqueous NH_4Cl solution (10 mL) was added and the aqueous phase was extracted three times with CH_2Cl_2 (3 x 20 mL). The combined organic phases were dried over $MgSO_4$ and the volatiles were removed *in vacuo*. The crude product was purified by column chromatography (SiO_2, iHex:EtOAc, 7:3 v/v) to obtain *N*-(*p*-(dimethylamino)phenyl)-*N'*-(*p*-(cyano)phenyl) indigo **116** (18 mg, 0.036 mmol, 77%) as a blue solid.

Mixture of *cis*-**116** and *trans*-**116**:

^{1}H NMR (600 MHz, CD_2Cl_2): δ = 7.81 (d, $^3J(H,H)$ = 8.7 Hz, 2H), 7.78 (d, $^3J(H,H)$ = 7.5 Hz, 1H), 7.66 (d, $^3J(H,H)$ = 8.8 Hz, 2H), 7.59 (d, $^3J(H,H)$ =7.5 Hz, 1H), 7.52-7.34 (m, 9H), 7.18-7.03 (m, 5H), 7.03-6.95 (m, 3H), 6.90 (d, $^3J(H,H)$ = 8.3 Hz, 1H), 6.84-6.75 (m, 4H), 6.43 (bs, 4H), 3.02 (s, 6H, H_3-C(23), *cis* or *trans*), 2.96 (s, 6H, H_3-C(23), *trans* or *cis*) ppm; EI-MS (70 eV): *m/z* (%): 482 (62) [*M*], 468 (9); HR-EI-MS calc. [$C_{31}H_{22}N_4O_2$]: 482.1743, found: 482.1739.

9. Crystal structural data
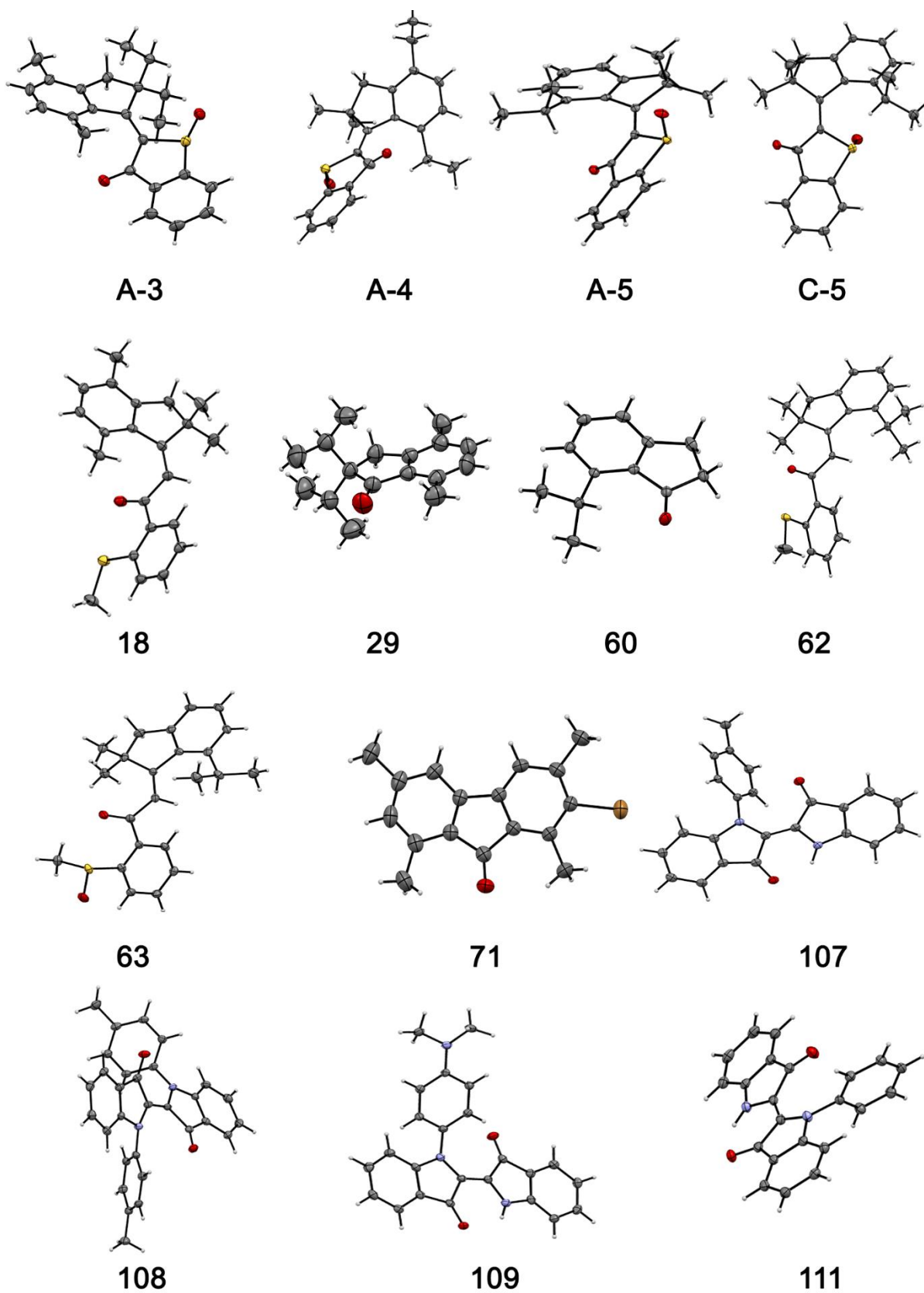
Figure 122:   Structures in the crystalline state of several compounds.

Table 25: Crystal structural data of **3**, **4**, **A-5**.

	A-3	A-4	A-5
net formula	$C_{23}H_{24}O_2S$	$C_{23}H_{24}O_2S$	$C_{22}H_{22}O_2S$
M_r/g mol^{-1}	364.48	364.48	350.45
crystal size/mm	$0.504 \times 0.292 \times 0.118$	$0.100 \times 0.070 \times 0.050$	$0.090 \times 0.060 \times 0.030$
T/K	143(2)	100.(2)	100.(2)
radiation	MoKα	MoKα	MoKα
diffractometer	'Oxford XCalibur'	'Bruker D8 Venture TXS'	'Bruker D8 Venture TXS'
crystal system	orthorhombic	monoclinic	orthorhombic
space group	'P b c a'	'P 1 21/n 1'	'P b c a'
a/Å	8.6063(3)	16.122(3)	15.3941(4)
b/Å	15.0198(6)	10.590(2)	9.7375(3)
c/Å	28.9494(10)	22.889(5)	24.1083(6)
α/°	90	90.00(3)	90
β/°	90	99.95(3)	90
γ/°	90	90.00(3)	90
V/Å^3	3742.1(2)	3849.1(14)	3613.84(17)
Z	8	8	8
calc. density/g cm^{-3}	1.294	1.258	1.288
μ/mm^{-1}	0.187	0.182	0.191
absorption correction	multi-scan	Multi-Scan	Multi-Scan
transmission factor range	0.95631–1.00000	0.8147–0.9705	0.9239–0.9705
refls. measured	20510	11339	26154
R_{int}	0.0464	0.0000	0.0412
mean $\sigma(I)/I$	0.0386	0.0640	0.0282
θ range	4.224–26.371	3.193–28.277	3.140–27.482
observed refls.	2780	9087	3397
x, y (weighting scheme)	0.0437, 2.4437	0.1030, 15.6691	0.0362, 2.5607
hydrogen refinement	constr	constr	constr
Flack parameter			
refls in refinement	3776	11339	4139
parameters	239	498	230
restraints	0	18	0
$R(F_{obs})$	0.0414	0.0964	0.0383
$R_w(F^2)$	0.1110	0.2516	0.0935
S	1.036	1.023	1.044
shift/error$_{max}$	0.001	0.001	0.001
max electron density/e Å^{-3}	0.265	4.574	0.316
min electron density/e Å^{-3}	−0.360	−1.067	−0.432

Table 26: Crystal structural data of **C-5**, **18**, **29**.

	C-5	18	29
net formula	$C_{22}H_{22}O_2S$	$C_{22}H_{24}OS$	$C_{17}H_{24}O$
M_r/g mol^{-1}	350.45	336.47	244.36
crystal size/mm	$0.100 \times 0.080 \times 0.050$	$0.410 \times 0.330 \times 0.240$	$0.100 \times 0.080 \times 0.050$
T/K	100.(2)	123(2)	298.(2)
radiation	MoKα	MoKα	MoKα
diffractometer	'Bruker D8 Venture TXS'	'Oxford XCalibur'	'Bruker D8 Venture TXS'
crystal system	monoclinic	monoclinic	orthorhombic
space group	'P 1 21/c 1'	'C c'	'P 21 21 21'
a/Å	9.7600(3)	9.7733(4)	6.6141(11)
b/Å	12.8063(4)	12.8417(7)	12.469(2)
c/Å	29.0798(9)	14.5554(7)	18.338(3)
α/°	90	90	90
β/°	91.5140(10)	96.016(4)	90
γ/°	90	90	90
V/Å^3	3633.40(19)	1816.72(15)	1512.4(4)
Z	8	4	4
calc. density/g cm^{-3}	1.281	1.230	1.073
μ/mm^{-1}	0.190	0.183	0.064
absorption correction	Multi-Scan	'multi-scan'	Multi-Scan
transmission factor range	0.9287–0.9705	0.96808–1.00000	0.92–1.00
refls. measured	37824	5995	15561
R_{int}	0.0584	0.0261	0.0450
mean $\sigma(I)/I$	0.0466	0.0421	0.0360
θ range	3.181–26.372	4.243–27.478	3.274–26.336
observed refls.	6153	3434	2148
x, y (weighting scheme)	0.0517, 4.6660	0.0331, 0.6775	0.0517, 0.1914
hydrogen refinement	constr	constr	constr
Flack parameter		0.07(4)	0.5
refls in refinement	7405	3675	3068
parameters	459	222	169
restraints	0	2	0
$R(F_{obs})$	0.0504	0.0353	0.0477
$R_w(F^2)$	0.1302	0.0825	0.1210
S	1.028	1.040	1.036
shift/error$_{max}$	0.001	0.001	0.001
max electron density/e Å^{-3}	1.714	0.231	0.120
min electron density/e Å^{-3}	−0.522	−0.162	−0.147

Table 27:　　　Crystal structural data of **60**, **62**, **63**.

	60	62	63
net formula	$C_{12}H_{14}O$	$C_{23}H_{26}OS$	$C_{23}H_{26}O_2S$
M_r/g mol^{-1}	174.23	350.50	366.50
crystal size/mm	$0.100 \times 0.090 \times 0.080$	$0.090 \times 0.070 \times 0.040$	$0.100 \times 0.060 \times 0.040$
T/K	100.(2)	100.(2)	100.(2)
radiation	MoKα	MoKα	MoKα
diffractometer	'Bruker D8 Venture TXS'	'Bruker D8 Venture TXS'	'Bruker D8 Venture TXS'
crystal system	monoclinic	orthorhombic	triclinic
space group	'P 1 21/n 1'	'P 21 21 21'	'P -1'
a/Å	9.5696(9)	8.7429(2)	7.7096(4)
b/Å	9.6593(8)	9.8261(3)	14.8613(8)
c/Å	11.2211(10)	22.6473(6)	17.8548(8)
α/°	90	90	71.328(2)
β/°	111.861(3)	90	89.714(2)
γ/°	90	90	80.319(2)
V/Å^3	962.64(15)	1945.60(9)	1907.82(17)
Z	4	4	4
calc. density/g cm^{-3}	1.202	1.197	1.276
μ/mm^{-1}	0.074	0.174	0.184
absorption correction	Multi-Scan	Multi-Scan	Multi-Scan
transmission factor range	0.9285–0.9705	0.9331–0.9705	0.7980–0.9705
refls. measured	10783	16197	6779
R_{int}	0.0359	0.0331	0.0000
mean $\sigma(I)/I$	0.0322	0.0332	0.0819
θ range	3.193–28.268	3.246–27.484	3.141–25.350
observed refls.	2095	4211	5118
x, y (weighting scheme)	0.0369, 0.4345	0.0333, 0.4700	0.0235, 3.4259
hydrogen refinement	constr	constr	constr
Flack parameter		−0.03(2)	
refls in refinement	2387	4437	6779
parameters	120	231	480
restraints	0	0	8
$R(F_{obs})$	0.0407	0.0299	0.0684
$R_w(F^2)$	0.1062	0.0740	0.1452
S	1.085	1.049	1.117
shift/error$_{max}$	0.001	0.001	0.001
max electron density/e Å^{-3}	0.368	0.213	0.413
min electron density/e Å^{-3}	−0.208	−0.217	−0.480

Table 28: Crystal structural data of **71**, **107**, **108**.

	71	107	108
net formula	$C_{17}H_{15}BrO$	$C_{23}H_{16}N_2O_2$	$C_{30}H_{22}N_2O_2$
M_r/g mol^{-1}	315.20	352.38	442.49
crystal size/mm	$0.050 \times 0.040 \times 0.030$	$0.100 \times 0.070 \times 0.030$	$0.100 \times 0.080 \times 0.070$
T/K	296.(2)	100.(2)	100.(2)
radiation	MoKα	MoKα	MoKα
diffractometer	'Bruker D8 Venture TXS'	'Bruker D8 Venture TXS'	'Bruker D8 Venture TXS'
crystal system	orthorhombic	monoclinic	triclinic
space group	'P b c m'	'P 1 21/n 1'	'P -1'
a/Å	8.666(3)	8.7751(6)	9.4986(5)
b/Å	22.841(6)	8.7228(5)	10.3849(6)
c/Å	7.053(2)	21.3314(16)	11.8292(7)
α/°	90	90	96.508(2)
β/°	90	98.818(2)	93.309(2)
γ/°	90	90	108.300(2)
V/Å^3	1396.1(7)	1613.48(19)	1095.31(11)
Z	4	4	2
calc. density/g cm^{-3}	1.500	1.451	1.342
μ/mm^{-1}	2.933	0.094	0.085
absorption correction	Multi-Scan	Multi-Scan	Multi-Scan
transmission factor range	0.81–0.92	0.8639–0.9705	0.8517–0.9705
refls. measured	10310	19370	4340
R_{int}	0.0430	0.0570	0.0609
mean σ(I)/I	0.0313	0.0371	0.0516
θ range	3.395–26.372	3.313–26.351	3.484–26.372
observed refls.	1147	2625	3757
x, y (weighting scheme)	0.0377, 0.6796	0.0316, 1.3401	0.0445, 0.8182
hydrogen refinement	constr	H(C) constr, H(N) refall	constr
Flack parameter			
refls in refinement	1543	3282	4340
parameters	119	249	310
restraints	0	0	0
$R(F_{obs})$	0.0323	0.0419	0.0552
$R_w(F^2)$	0.0853	0.1065	0.1332
S	1.041	1.057	1.108
shift/error$_{max}$	0.001	0.001	0.001
max electron density/e Å^{-3}	0.285	0.203	0.275
min electron density/e Å^{-3}	−0.312	−0.238	−0.293

Table 29: Crystal structural data of **109** and **111**.

	109	111
net formula	$C_{24}H_{19}N_3O_2$	$C_{22}H_{14}N_2O_2$
M_r/g mol^{-1}	381.42	338.35
crystal size/mm	$0.100 \times 0.080 \times 0.030$	$0.100 \times 0.020 \times 0.020$
T/K	100.(2)	103.(2)
radiation	MoKα	MoKα
diffractometer	'Bruker D8 Venture TXS'	'Bruker D8 Venture TXS'
crystal system	triclinic	monoclinic
space group	'P -1'	'P 1 21/c 1'
a/Å	9.8377(4)	9.9721(4)
b/Å	9.8422(5)	6.2669(2)
c/Å	10.9824(5)	25.1386(10)
α/°	111.910(2)	90
β/°	105.0000(10)	92.2510(10)
γ/°	103.3610(10)	90
V/Å^3	886.96(7)	1569.80(10)
Z	2	4
calc. density/g cm^{-3}	1.428	1.432
μ/mm^{-1}	0.093	0.093
absorption correction	Multi-Scan	Multi-Scan
transmission factor range	0.94–1.00	0.95–1.00
refls. measured	10834	14511
R_{int}	0.0269	0.0423
mean $\sigma(I)/I$	0.0306	0.0299
θ range	3.344–26.371	3.244–25.338
observed refls.	3151	2284
x, y (weighting scheme)	0.0470, 0.5391	0.0422, 0.5889
hydrogen refinement	H(C) constr, H(N) refall	H(C) constr, H(N) refall
Flack parameter		
refls in refinement	3598	2848
parameters	268	239
restraints	0	0
$R(F_{obs})$	0.0412	0.0364
$R_w(F^2)$	0.1060	0.0930
S	1.030	1.037
shift/error$_{max}$	0.001	0.001
max electron density/e Å^{-3}	0.332	0.187
min electron density/e Å^{-3}	−0.296	−0.212

10. Theoretically obtained geometries

Table 30: Cartesian coordinates of theoretically obtained geometries of **A-3**-I, **A-3**-II, **B-3**-I on the MPW1K/6-311G(d,p) level of theory in the gaseous phase.

	A-3-I		**A-3**-II		**B-3**-I
C	-3.22771 -0.27687 0.06511	C	-3.21944 0.32157 -0.05154	C	2.87413 0.82954 -0.46147
O	-0.89589 2.03977 -1.18405	O	-0.98603 -2.14651 1.08461	O	1.74473 -1.78262 1.5989
C	-4.53666 -0.57088 0.38821	C	-4.51432 0.68293 -0.36309	C	3.90277 1.40622 -1.17328
C	-3.81113 1.93569 -0.6474	C	-3.89445 -1.89684 0.55443	C	4.23639 -1.05038 0.13902
C	-5.12526 1.65831 -0.33001	C	-5.19506 -1.55197 0.24792	C	5.2715 -0.49496 -0.58956
C	-5.48205 0.41931 0.193	C	-5.4996 -0.27625 -0.21657	C	5.10428 0.71984 -1.24157
C	-2.8585 0.95517 -0.42737	C	-2.90219 -0.94628 0.38341	C	3.03178 -0.37515 0.18907
C	-1.4043 1.10048 -0.62986	C	-1.45579 -1.16017 0.58063	C	1.80123 -0.83137 0.86644
C	-0.7109 -0.10551 -0.13766	C	-0.71348 0.04026 0.15039	C	0.67987 0.06171 0.49876
C	0.62453 -0.30538 -0.04082	C	0.62728 0.18402 0.04366	C	-0.60813 -0.30749 0.30924
C	1.33497 -1.65642 -0.05107	C	1.40595 1.49674 0.07745	C	-1.11068 -1.75104 0.18713
C	3.97233 2.21677 -0.00707	C	3.8669 -2.46411 -0.18149	C	-4.08632 1.75498 -0.82355
C	4.0437 0.89734 -0.42536	C	3.99538 -1.17643 0.31707	C	-3.89628 0.41244 -1.11012
C	2.8713 0.16591 -0.36315	C	2.85244 -0.39844 0.31725	C	-2.72539 -0.159 -0.64413
C	2.71884 -1.289 -0.62434	C	2.7517 1.04068 0.67961	C	-2.35835 -1.59557 -0.70889
C	1.61627 2.03258 0.55032	C	1.51394 -2.15464 -0.6941	C	-2.01105 1.89244 0.43188
C	2.80098 2.75052 0.49869	C	2.67015 -2.92068 -0.70171	C	-3.18631 2.45654 -0.04298
C	1.47728 -2.21121 1.38396	C	1.60617 1.93191 -1.39445	C	-0.17136 -2.77434 -0.46802
C	1.65423 0.72875 0.03245	C	1.61121 -0.88804 -0.10056	C	-1.74626 0.57433 0.03005
C	0.69623 -2.75879 -0.90553	C	0.80913 2.64062 0.89976	C	-1.49981 -2.29728 1.57442
H	4.86241 2.82881 -0.03204	H	4.73268 -3.11004 -0.20682	H	-4.98389 2.24871 -1.16713
H	2.81062 3.7573 0.88909	H	2.63531 -3.90171 -1.15168	H	-3.42075 3.47122 0.24288
H	2.75917 -1.50003 -1.69274	H	2.75095 1.16978 1.76172	H	-3.17285 -2.23523 -0.36807
H	3.5102 -1.87554 -0.15833	H	3.5861 1.62234 0.2937	H	-2.13547 -1.89915 -1.73133
H	0.48159 -2.46548 1.7401	H	2.13674 1.12989 -1.90778	H	0.5837 -3.0939 0.24135
H	2.03441 -3.14576 1.29249	H	0.62324 2.00849 -1.8547	H	-0.79193 -3.65307 -0.65433
H	-0.16411 -3.17777 -0.38731	H	-0.02112 3.09089 0.35817	H	-1.91127 -3.29528 1.41114
H	1.42612 -3.57004 -0.92967	H	1.57165 3.41882 0.93332	H	-0.57956 -2.42355 2.13967
H	-3.50751 2.89144 -1.04434	H	-3.63097 -2.88185 0.90594	H	4.34394 -1.98858 0.66027
H	-5.88526 2.4086 -0.48129	H	-5.98525 -2.27724 0.36199	H	6.21937 -1.00574 -0.65294
H	-6.51318 0.22605 0.44479	H	-6.52112 -0.02972 -0.46084	H	5.92465 1.13985 -1.8024
H	-4.80802 -1.53543 0.78686	H	-4.74521 1.67529 -0.71636	H	3.78139 2.36271 -1.65657
S	-1.88537 -1.44448 0.1289	S	-1.83153 1.43667 -0.05836	S	1.32381 1.6512 -0.0746
O	-1.76187 -1.99563 1.50983	O	-1.67769 2.04184 -1.41358	O	1.69468 2.57007 1.04096
C	0.44426 2.649 1.23709	C	0.30703 -2.68272 -1.39365	C	-1.21697 2.66194 1.438
H	-0.23155 1.89804 1.63744	H	-0.33739 -1.88222 -1.74689	H	-0.5654 2.0281 2.02822
C	5.32616 0.28049 -0.8837	C	5.30661 -0.64283 0.79863	H	-1.90416 3.16708 2.11257
H	5.22855 -0.14619 -1.88059	H	5.23795 -0.28469 1.82445	C	-4.91481 -0.3915 -1.85241
H	6.12472 1.01584 -0.91184	H	6.07576 -1.40859 0.76332	H	-4.48402 -0.86528 -2.73304
H	0.78894 3.27036 2.05943	H	0.61225 -3.27749 -2.25042	H	-5.32343 -1.18592 -1.22859
H	-0.12555 3.27049 0.5514	H	-0.28209 -3.31108 -0.73077	H	-5.74196 0.23166 -2.17895
H	5.63919 -0.52423 -0.21905	H	5.6431 0.19387 0.18734	H	-0.5811 3.41946 0.98996
C	2.15659 -1.32239 2.40697	C	2.35176 3.23876 -1.59465	C	-2.48369 -1.47373 2.38236
H	1.57753 -0.42481 2.60799	H	2.52852 3.39656 -2.65602	H	-2.07202 -0.50422 2.65233
H	2.25518 -1.86223 3.34602	H	1.78092 4.09089 -1.23548	H	-3.41614 -1.2975 1.84935
H	3.15332 -1.01094 2.10025	H	3.3225 3.25123 -1.10145	H	-2.72708 -1.99363 3.30612
C	0.3148 -2.39851 -2.32863	C	0.39357 2.31955 2.32416	C	0.48977 -2.36149 -1.77035
H	-0.0814 -3.2733 -2.83875	H	1.23468 1.99749 2.93409	H	1.03757 -3.20091 -2.19226
H	-0.44765 -1.62575 -2.36378	H	-0.0252 3.20588 2.79478	H	-0.23137 -2.03722 -2.51864
H	1.16443 -2.04299 -2.90758	H	-0.35902 1.53805 2.37026	H	1.19772 -1.5486 -1.63526

Table 31:   Cartesian coordinates of theoretically obtained geometries of **B-3**-II, **B-3**-III, **C-3**-I on the MPW1K/6-311G(d,p) level of theory in the gaseous phase.

	B-3-II			**B-3**-III			**C-3**-I	
C	-2.90132 -0.83616 -0.43381		C	-2.97943 -0.76226 -0.51281		C	3.00261 -0.8945 -0.17049	
O	-1.67643 1.83709 1.49046		O	-1.70565 1.76655 1.56696		O	1.71966 2.079 1.20623	
C	-3.95278 -1.41574 -1.1093		C	-4.03724 -1.27847 -1.22836		C	4.10742 -1.60783 -0.59004	
C	-4.20397 1.10935 0.08552		C	-4.22359 1.20813 0.05526		C	4.35665 0.97085 0.48824	
C	-5.26102 0.55033 -0.60768		C	-5.2856 0.71328 -0.67827		C	5.47139 0.26882 0.07783	
C	-5.13458 -0.69887 -1.20145		C	-5.19149 -0.51716 -1.31531		C	5.34619 -1.00662 -0.46399	
C	-3.01883 0.40232 0.15926		C	-3.06509 0.45785 0.12356		C	3.11372 0.37777 0.34394	
C	-1.77053 0.85273 0.80703		C	-1.81778 0.83396 0.8181		C	1.81906 1.00259 0.6703	
C	-0.68171 -0.0957 0.48803		C	-0.75462 -0.13253 0.46633		C	0.72013 0.08683 0.32989	
C	0.62221 0.21431 0.30658		C	0.56114 0.13045 0.31482		C	-0.60233 0.37093 0.22372	
C	1.20204 1.62164 0.12215		C	1.20066 1.51488 0.13646		C	-1.18095 1.75148 -0.08665	
C	4.03929 -2.04882 -0.5886		C	3.89454 -2.24142 -0.58163		C	-4.0685 -1.96371 -0.09169	
C	3.89529 -0.73233 -1.00076		C	3.776 -0.93235 -1.02884		C	-3.99054 -0.68469 -0.61807	
C	2.73732 -0.08673 -0.60771		C	2.63776 -0.2522 -0.63985		C	-2.79871 -0.0081 -0.42555	
C	2.40287 1.34622 -0.81134		C	2.30317 1.17451 -0.89499		C	-2.5136 1.40336 -0.78567	
C	1.94517 -2.00965 0.64183		C	1.80872 -2.13057 0.65805		C	-1.82802 -1.84275 0.83376	
C	3.10864 -2.65017 0.23755		C	2.95578 -2.80607 0.26067		C	-3.02892 -2.50641 0.64237	
C	0.3154 2.69753 -0.51302		C	0.26943 2.61197 -0.39855		C	-1.44671 2.54962 1.20368	
C	1.73047 -0.72699 0.11816		C	1.62974 -0.85238 0.11624		C	-1.6993 -0.59098 0.20949	
C	1.69025 2.07756 1.51447		C	1.80741 1.87706 1.50933		C	-0.31995 2.61448 -1.01892	
H	4.92571 -2.59803 -0.87162		H	4.76708 -2.81609 -0.85724		H	-4.97899 -2.53221 -0.21423	
H	3.30774 -3.64146 0.61696		H	3.1335 -3.7954 0.65543		H	-3.16595 -3.47087 1.10837	
H	3.24677 1.99517 -0.58518		H	3.16585 1.83175 -0.81462		H	-2.41649 1.51463 -1.86467	
H	2.13127 1.54199 -1.84838		H	1.90902 1.29177 -1.90513		H	-3.31595 2.07169 -0.47353	
H	-0.38298 3.08523 0.22098		H	-0.49581 2.14405 -1.01951		H	-0.48233 2.81665 1.62625	
H	0.98542 3.52335 -0.75464		H	-0.25796 3.06503 0.43405		H	-1.92956 3.47952 0.89773	
H	0.82925 2.05957 2.17944		H	0.98688 1.87687 2.22518		H	-0.91717 3.50044 -1.24443	
H	2.39444 1.33338 1.8876		H	2.47947 1.07152 1.80514		H	0.54409 2.97462 -0.47142	
H	-4.27969 2.07413 0.56194		H	-4.27591 2.15594 0.56754		H	4.42491 1.9643 0.90245	
H	-6.19428 1.08496 -0.68857		H	-6.1978 1.28354 -0.75623		H	6.45068 0.71117 0.17157	
H	-5.9717 -1.12137 -1.735		H	-6.03242 -0.89005 -1.87901		H	6.22912 -1.53599 -0.78666	
H	-3.86334 -2.39747 -1.54676		H	-3.97382 -2.24622 -1.70026		H	4.00592 -2.59716 -1.00717	
S	-1.37108 -1.6869 -0.02703		S	-1.48242 -1.68022 -0.12122		S	1.33435 -1.524 -0.20803	
O	-1.76194 -2.56722 1.11211		O	-1.90762 -2.59867 0.97396		O	0.93218 -1.74426 -1.62611	
C	1.10878 -2.65874 1.69725		C	0.94477 -2.74146 1.71388		C	-0.83443 -2.44603 1.77577	
H	0.4659 -1.95187 2.20884		H	0.32881 -2.00447 2.21697		H	-0.18407 -1.69618 2.21548	
H	1.76706 -3.11678 2.43168		H	1.57932 -3.2231 2.45395		H	-0.20253 -3.18277 1.28653	
C	4.94802 -0.03391 -1.80036		C	4.83447 -0.28339 -1.86234		C	-5.14001 -0.05082 -1.33273	
H	4.54425 0.36409 -2.72986		H	4.42901 0.09019 -2.80114		H	-4.85937 0.25676 -2.33868	
H	5.37241 0.80472 -1.24932		H	5.2823 0.56433 -1.34509		H	-5.97672 -0.73808 -1.41416	
H	5.76008 -0.70976 -2.05132		H	5.62957 -0.98446 -2.09793		H	-1.3651 -2.94961 2.57968	
H	0.45728 -3.43392 1.30612		H	0.26173 -3.48779 1.32031		H	-5.48916 0.83917 -0.81025	
C	2.33219 3.45188 1.57229		C	2.54425 3.19929 1.61072		C	0.12208 1.9695 -2.32219	
H	1.62269 4.24156 1.34028		H	1.87723 4.04712 1.48024		H	0.64284 1.02839 -2.16708	
H	2.70575 3.63832 2.57651		H	2.98971 3.29009 2.59887		H	-0.71518 1.76171 -2.98595	
H	3.17677 3.54934 0.89246		H	3.35116 3.28644 0.85546		H	0.79225 2.63835 -2.8573	
C	-0.4309 2.31097 -1.77744		C	0.92704 3.70672 -1.22751		C	-2.29381 1.86492 2.25862	
H	-0.93824 3.18068 -2.18846		H	0.18803 4.4679 -1.46792		H	-1.80293 0.97927 2.65579	
H	0.2334 1.92981 -2.55095		H	1.74094 4.20021 -0.70567		H	-2.46723 2.54298 3.09118	
H	-1.18553 1.54967 -1.60281		H	1.31862 3.33439 -2.17088		H	-3.26613 1.55698 1.87845	

Table 32: Cartesian coordinates of theoretically obtained geometries of **C-3**-II, **C-3**-III, **D-3**-I on the MPW1K/6-311G(d,p) level of theory in the gaseous phase.

	C-3-II				**C-3**-III				**D-3**-I		
C	-3.02783	-0.88675	0.16535	C	3.10943	-0.82789	-0.26063	C	-3.19206	0.27951	0.06867
O	-1.64981	2.05765	-1.18304	O	1.65777	1.98068	1.28452	O	-0.90604	-2.07726	-1.17521
C	-4.15389	-1.56833	0.58115	C	4.24307	-1.44208	-0.75386	C	-4.49555	0.59912	0.38283
C	-4.32223	1.03241	-0.45878	C	4.34689	1.12744	0.36983	C	-3.79967	-1.96499	-0.51525
C	-5.45775	0.36234	-0.0519	C	5.48906	0.52559	-0.117	C	-5.10779	-1.66525	-0.18611
C	-5.37248	-0.92424	0.47092	C	5.43494	-0.74491	-0.68192	C	-5.45145	-0.39507	0.25989
C	-3.09914	0.39608	-0.33012	C	3.1481	0.44038	0.27663	C	-2.84334	-0.97647	-0.3763
C	-1.78571	0.98113	-0.65548	C	1.82587	0.95077	0.68075	C	-1.39866	-1.11983	-0.6464
C	-0.71744	0.02424	-0.33199	C	0.78558	-0.02719	0.32516	C	-0.68764	0.10097	-0.1914
C	0.61449	0.26026	-0.24586	C	-0.5499	0.16943	0.25197	C	0.63958	0.21567	0.02589
C	1.25912	1.61618	0.04069	C	-1.24626	1.51118	0.00291	C	1.47099	1.49608	0.13135
C	4.01357	-2.18115	-0.05178	C	-3.87768	-2.35407	-0.02883	C	3.82702	-2.50928	-0.04414
C	3.98067	-0.91537	0.51174	C	-3.85823	-1.08976	-0.59928	C	3.95669	-1.19974	-0.48359
C	2.80473	-0.20251	0.36111	C	-2.70146	-0.35354	-0.42375	C	2.83224	-0.40201	-0.38018
C	2.55421	1.20164	0.77543	C	-2.44347	1.04458	-0.85873	C	2.73064	1.05907	-0.65135
C	1.76073	-1.97419	-0.93075	C	-1.64619	-2.10209	0.89107	C	1.50895	-2.18421	0.59894
C	2.9463	-2.67591	-0.77925	C	-2.81475	-2.82855	0.71734	C	2.64836	-2.97125	0.51087
C	1.60313	2.25528	-1.32212	C	-1.721	2.01076	1.38497	C	0.85993	2.75219	-0.48595
C	1.68056	-0.73671	-0.27295	C	-1.5857	-0.86112	0.24332	C	1.60705	-0.89117	0.0763
C	0.44745	2.57631	0.91551	C	-0.39175	2.54848	-0.74023	C	1.87134	1.71589	1.60398
H	4.91027	-2.77707	0.03787	H	-4.76067	-2.96758	-0.1346	H	4.67923	-3.17128	-0.09706
H	3.0476	-3.63141	-1.27203	H	-2.90451	-3.78816	1.20431	H	2.614	-3.97564	0.90639
H	2.41474	1.2649	1.85401	H	-2.16293	1.05494	-1.91217	H	3.61642	1.60661	-0.33605
H	3.38859	1.85504	0.52844	H	-3.31129	1.69104	-0.75258	H	2.58676	1.25373	-1.7158
H	2.26491	1.57179	-1.85576	H	-2.34985	1.23651	1.82532	H	0.41458	2.49927	-1.44524
H	0.68197	2.32179	-1.89565	H	-0.83608	2.09355	2.01309	H	0.03963	3.11279	0.12927
H	1.11631	3.40096	1.16419	H	0.20547	3.09313	-0.01687	H	2.45116	0.85505	1.93442
H	-0.35479	3.00855	0.32705	H	0.31551	2.01417	-1.3752	H	2.5489	2.56807	1.63594
H	-4.35943	2.03344	-0.85848	H	4.35999	2.11488	0.80344	H	-3.5096	-2.94029	-0.87324
H	-6.4221	0.83861	-0.13353	H	6.43389	1.04343	-0.06609	H	-5.87224	-2.4207	-0.27742
H	-6.27093	-1.42835	0.79125	H	6.33755	-1.19477	-1.06519	H	-6.479	-0.1779	0.50666
H	-4.08351	-2.56641	0.9836	H	4.19712	-2.42863	-1.18711	H	-4.76525	1.5924	0.70533
S	-1.38099	-1.57314	0.18579	S	1.5022	-1.60146	-0.19387	S	-1.85378	1.46896	-0.00436
O	-0.98069	-1.82807	1.598	O	1.05094	-1.92807	-1.57382	O	-2.05138	2.19956	-1.29089
C	0.72886	-2.52618	-1.86265	C	-0.60633	-2.6363	1.82341	C	0.31681	-2.73089	1.31266
H	0.09705	-1.74602	-2.27581	H	-0.02228	-1.84055	2.27613	H	-0.33354	-1.94291	1.68187
H	0.08131	-3.24872	-1.37265	H	0.08716	-3.30459	1.31892	C	5.25155	-0.66798	-1.00987
C	5.15985	-0.33617	1.22479	C	-5.03165	-0.54283	-1.34716	H	5.13525	-0.26032	-2.01251
H	4.90527	-0.05176	2.24432	H	-4.75912	-0.26823	-2.36471	H	5.63833	0.13197	-0.37951
H	5.97746	-1.04925	1.27079	H	-5.83393	-1.27256	-1.4018	H	0.63896	-3.32894	2.16134
H	1.22502	-3.03373	-2.68581	H	-1.08794	-3.20031	2.6177	C	0.72414	1.9437	2.56893
H	5.52601	0.55866	0.72281	H	-5.42705	0.35114	-0.86658	H	0.04647	1.09288	2.59149
C	-0.10677	2.00175	2.20901	C	-1.14677	3.5383	-1.61599	H	1.10504	2.08561	3.57771
H	-0.70437	2.75254	2.72079	H	-0.44774	4.26899	-2.01701	H	0.14061	2.82443	2.31347
H	-0.7325	1.12889	2.04754	H	-1.62587	3.05788	-2.46549	C	1.83837	3.89977	-0.6734
H	0.6814	1.69866	2.89584	H	-1.91089	4.08639	-1.0732	H	1.32065	4.75075	-1.10845
C	2.24299	3.63016	-1.25665	C	-2.46536	3.33231	1.41548	H	2.27443	4.23274	0.26622
H	2.52717	3.94994	-2.25665	H	-2.81432	3.52834	2.42701	H	2.65242	3.63873	-1.3457
H	1.55818	4.37555	-0.86158	H	-1.82622	4.16312	1.12922	H	-0.27301	-3.36287	0.65372
H	3.14369	3.64532	-0.64539	H	-3.3395	3.33698	0.76698	H	6.00481	-1.44902	-1.05254

Table 33:　　　　Cartesian coordinates of theoretically obtained geometries of **D-3**-II, **D-3**-III, **TS**$_{\text{D-A}}$-**3**-I on the MPW1K/6-311G(d,p) level of theory in the gaseous phase.

	D-3-II		**D-3**-III		**TS**$_{\text{D-A}}$-**3**-I
C	-3.1633　0.21023　0.32019	C	-3.22186　0.39684　0.20954	C	3.09953　-0.31003　0.26973
O	-0.92882　-1.78999　-1.50797	O	-1.14336　-1.99972　-1.29832	O	1.36964　2.28026　-1.23801
C	-4.44103　0.4188　0.79174	C	-4.48319　0.76493　0.62519	C	4.26327　-0.74855　0.86297
C	-3.76254　-1.92023　-0.59958	C	-3.98685　-1.7782　-0.44766	C	3.73739　1.98605　0.50526
C	-5.04394　-1.73513　-0.11522	C	-5.25319　-1.4307　-0.01681	C	4.89627　1.5645　1.13127
C	-5.37882　-0.5772　0.57486	C	-5.49781　-0.17128　0.51585	C	5.15667　0.21159　1.30872
C	-2.8225　-0.93454　-0.36637	C	-2.971　-0.8495　-0.32147	C	2.8352　1.02664　0.08915
C	-1.40145　-0.96922　-0.76998	C	-1.5547　-1.05118　-0.68924	C	1.55908　1.27293　-0.62541
C	-0.69049　0.17634　-0.16554	C	-0.75582　0.10366　-0.21832	C	0.69698　0.05365　-0.48947
C	0.64569　0.32039　-0.00074	C	0.58129　0.1348　-0.0302	C	-0.62357　-0.18108　-0.28541
C	1.3689　1.65239　0.20025	C	1.46215　1.38143　0.10062	C	-1.09027　-1.61654　0.08921
C	3.95941　-2.25657　-0.14268	C	3.63353　-2.74374　0.01045	C	-4.31252　1.81257　0.47883
C	4.0757　-0.88868　-0.32468	C	3.85327　-1.43115　-0.38003	C	-4.13536　0.4557　0.63425
C	2.90989　-0.14953　-0.22399	C	2.76314　-0.58254　-0.3272	C	-2.89566　-0.05662　0.28008
C	2.80923　1.33114　-0.24077	C	2.75372　0.88344　-0.58145	C	-2.59871　-1.50025　0.27967
C	1.57213　-2.1079　0.27978	C	1.29722　-2.31988　0.51868	C	-2.07315　2.07961　-0.45744
C	2.74805　-2.83564　0.18866	C	2.40096　-3.15975　0.47707	C	-3.31118　2.57976　-0.08237
C	0.84553　2.83016　-0.635	C	0.91265　2.64042　-0.58217	C	-0.8206　-2.68261　-0.98882
C	1.65714　-0.73724　-0.02045	C	1.48676　-1.01928　0.03479	C	-1.81747　0.71241　-0.18637
C	1.33189　2.06262　1.68439	C	1.67458　1.5804　1.61796	C	-0.49946　-2.07011　1.44055
H	4.84079　-2.8779　-0.20905	H	4.4546　-3.44576　-0.00757	H	-5.2519　2.27242　0.74896
H	2.71714　-3.89207　0.41034	H	2.29383　-4.16992　0.84362	H	-3.5052　3.62512　-0.26762
H	3.54396　1.79322　0.41886	H	3.64416　1.38359　-0.20818	H	-2.9262　-2.00232　1.18842
H	2.9964　1.72789　-1.23803	H	2.70131　1.08217　-1.65245	H	-3.13949　-1.97452　-0.54122
H	-0.06839　3.23385　-0.2076	H	0.30515　2.35069　-1.43533	H	0.20026　-3.0503　-0.93547
H	1.59396　3.61762　-0.52398	H	0.23112　3.148　0.0993	H	-1.44579　-3.53758　-0.72419
H	1.89669　2.99263　1.76624	H	0.68748　1.69407　2.06749	H	0.55813　-2.28146　1.3256
H	0.30206　2.30962　1.93772	H	2.09136　0.66014　2.02637	H	-0.9696　-3.02683　1.67493
H	-3.48158　-2.80571　-1.14774	H	-3.7741　-2.74586　-0.87415	H	3.52854　3.03079　0.33772
H	-5.79416　-2.4934　-0.27537	H	-6.06193　-2.14003　-0.0958	H	5.61212　2.29193　1.48047
H	-6.3857　-0.44762　0.9399	H	-6.49409　0.08434　0.84142	H	6.07102　-0.0949　1.79226
H	-4.7063　1.33013　1.30393	H	-4.67774　1.75185　1.01439	H	4.47435　-1.80058　0.97358
S	-1.86883　1.45001　0.33941	S	-1.8301　1.52206　0.09969	S	1.86671　-1.34118　-0.51103
O	-2.22101　2.38945　-0.76722	O	-2.08455　2.32601　-1.13153	O	2.29686　-1.53582　-1.92624
C	0.35954　-2.80996　0.79457	C	0.04735　-2.82789　1.15769	C	-1.20336　3.05419　-1.18116
H	-0.32932　-2.1266　1.28403	H	-0.56397　-2.02135　1.55321	H	-0.67905　2.59995　-2.0095
C	5.3944　-0.23269　-0.5804	C	5.2035　-0.94999　-0.8064	H	-0.45115　3.49734　-0.53798
H	5.37605　0.35155　-1.49892	H	5.173　-0.51163　-1.80238	C	-5.22726　-0.43432　1.1346
H	5.66244　0.44783　0.22727	H	5.58549　-0.18636　-0.12978	H	-4.93246　-0.96066　2.04163
H	0.65877　-3.5636　1.5181	H	0.30154　-3.49308　1.97875	H	-6.12146　0.13936　1.35892
C	1.8649　1.05525　2.6844	C	2.53794　2.75096　2.04883	H	-1.82706　3.85689　-1.56324
H	2.89256　0.7677　2.47243	H	2.07933　3.70585　1.80758	H	-5.49304　-1.19095　0.3974
H	1.84271　1.47893　3.68585	H	2.67665　2.7221　3.12736	C	-1.12027　-2.24574　-2.40964
H	1.26836　0.14611　2.69893	H	3.52709　2.72618　1.59634	H	-1.05189　-3.09309　-3.08689
C	0.60612　2.55945　-2.10763	C	1.94406　3.6493　-1.06724	H	-2.12025　-1.82481　-2.50601
H	0.40218　3.49403　-2.62376	H	1.42877　4.5213　-1.46251	H	-0.40385　-1.50209　-2.74754
H	1.462　2.0938　-2.59388	H	2.61344　3.99106　-0.284	C	-0.69801　-1.11035　2.59802
H	-0.26132　1.92413　-2.25121	H	2.55466　3.24898　-1.87268	H	-1.74812　-0.89174　2.7802
H	-0.18256　-3.30145　-0.00875	H	-0.5587　-3.38066　0.44462	H	-0.28954　-1.53553　3.51181
H	6.18654　-0.97011　-0.669	H	5.9202　-1.76565　-0.82276	H	-0.19293　-0.16355　2.42081

Table 34:   Cartesian coordinates of theoretically obtained geometries of **TS_{D-A}-3**-II, **TS_{B-C}-3**-I, **TS_{B-C}-3**-II on the MPW1K/6-311G(d,p) level of theory in the gaseous phase.

	TS_{D-A}-3-II				TS_{B-C}-3-I				TS_{B-C}-3-II		
C	-3.09517	-0.30296	-0.20647	C	3.11408	0.83552	-0.13677	C	3.13437	-0.85737	0.07476
O	-1.44282	2.34389	1.25953	O	1.71894	-2.2867	0.55529	O	1.61252	2.23437	-0.49364
C	-4.25225	-0.79397	-0.77064	C	4.26363	1.56817	-0.34726	C	4.31167	-1.55585	0.24364
C	-3.80239	1.96519	-0.50474	C	4.32468	-1.22878	-0.12435	C	4.27733	1.24548	0.08335
C	-4.95497	1.49016	-1.10423	C	5.48383	-0.51472	-0.35439	C	5.46408	0.56506	0.271
C	-5.1778	0.12556	-1.23633	C	5.45347	0.87154	-0.46183	C	5.48083	-0.82338	0.34766
C	-2.86708	1.04623	-0.07195	C	3.13542	-0.52988	-0.01831	C	3.10908	0.51072	-0.01282
C	-1.59194	1.34268	0.62698	C	1.81273	-1.12777	0.25041	C	1.76096	1.07006	-0.23086
C	-0.68876	0.1528	0.47737	C	0.73677	-0.10052	0.08989	C	0.72557	0.00145	-0.09053
C	0.62796	-0.0528	0.23067	C	-0.6103	-0.29078	-0.02025	C	-0.62496	0.1593	0.02992
C	1.1672	-1.49825	0.01239	C	-1.21603	-1.71118	0.06998	C	-1.24612	1.57491	0.02007
C	4.31233	2.00304	-0.44509	C	-4.31325	1.83351	-0.29822	C	-4.28948	-2.02393	-0.00531
C	4.13868	0.65541	-0.66419	C	-4.21502	0.46236	-0.27828	C	-4.21721	-0.65257	0.07137
C	2.88747	0.12989	-0.37357	C	-2.93565	-0.07178	-0.2202	C	-2.94768	-0.09667	0.13404
C	2.57574	-1.29972	-0.54211	C	-2.69763	-1.52282	-0.23188	C	-2.73047	1.35073	0.29114
C	2.02546	2.24475	0.3764	C	-1.88149	2.09382	-0.24833	C	-1.8577	-2.2454	0.10814
C	3.27945	2.75582	0.07648	C	-3.16986	2.60612	-0.29293	C	-3.13469	-2.78022	0.03289
C	1.24688	-2.14851	1.41049	C	-0.67354	-2.74085	-0.93831	C	-0.72071	2.53938	1.09945
C	1.79875	0.87277	0.10243	C	-1.74629	0.67636	-0.17505	C	-1.74715	-0.82579	0.10256
C	0.43581	-2.40724	-0.99793	C	-1.08834	-2.24805	1.51169	C	-1.1358	2.11694	-1.42676
H	5.26261	2.47079	-0.6572	H	-5.28134	2.31119	-0.33487	H	-5.24881	-2.51649	-0.06626
H	3.45544	3.80087	0.27912	H	-3.27995	3.67813	-0.33439	H	-3.2276	-3.85469	0.01726
H	2.63025	-1.57547	-1.59582	H	-3.32013	-2.05045	0.48929	H	-3.35268	1.94124	-0.37842
H	3.30177	-1.92859	-0.02907	H	-2.95939	-1.92669	-1.2109	H	-3.0079	1.64677	1.30403
H	1.91286	-1.537	2.02125	H	-1.3935	-3.56111	-0.93008	H	-1.45259	3.34606	1.15721
H	0.27368	-2.09513	1.89537	H	0.26154	-3.16056	-0.59719	H	0.20961	2.99889	0.79918
H	-0.39466	-2.92883	-0.5413	H	-1.63416	-3.19334	1.53394	H	-0.1368	1.96062	-1.81046
H	1.15352	-3.18208	-1.26759	H	-0.05145	-2.4859	1.709	H	-1.80449	1.51021	-2.03991
H	-3.62481	3.02057	-0.37143	H	4.32246	-2.30223	-0.02109	H	4.23796	2.32039	0.00578
H	-5.69559	2.1852	-1.46747	H	6.42518	-1.03303	-0.44728	H	6.39006	1.11184	0.35478
H	-6.08807	-0.22219	-1.69915	H	6.37148	1.41155	-0.63358	H	6.41942	-1.33681	0.4866
H	-4.43404	-1.85465	-0.84435	H	4.23778	2.64412	-0.41579	H	4.32215	-2.63333	0.28793
S	-1.82222	-1.26817	0.59795	S	1.49989	1.52803	0.11577	S	1.54027	-1.60282	-0.1619
O	-2.2225	-1.39666	2.0301	O	1.46428	2.0589	1.51495	O	1.50661	-2.12123	-1.56494
C	1.08966	3.22326	1.00203	C	-0.82301	3.15026	-0.31377	C	-0.77555	-3.27072	0.23367
H	0.59617	2.8195	1.87478	H	-0.20112	3.17032	0.57837	H	-0.12966	-3.29518	-0.64176
H	0.30941	3.54014	0.31857	H	-0.18356	3.03049	-1.18063	H	-0.16284	-3.10569	1.11229
C	5.23982	-0.21196	-1.18305	C	-5.42039	-0.42009	-0.31948	C	-5.43631	0.21115	0.09551
H	4.95262	-0.71534	-2.10526	H	-5.39087	-1.09644	-1.1726	H	-5.49953	0.78307	1.02084
H	6.13071	0.37438	-1.38683	H	-6.32894	0.16996	-0.39246	H	-6.33722	-0.38843	0.01027
H	1.64803	4.10633	1.29665	H	-1.30229	4.12026	-0.39438	H	-1.22707	-4.25246	0.33112
H	5.50847	-0.98705	-0.46607	H	-5.49413	-1.03702	0.57529	H	-5.4332	0.9291	-0.72392
C	1.72071	-3.59075	1.43107	C	-1.61507	-1.32603	2.59634	C	-1.48701	3.58477	-1.58305
H	1.80517	-3.93336	2.45941	H	-2.6597	-1.05653	2.45007	H	-0.77711	4.21786	-1.05839
H	1.02179	-4.25281	0.92644	H	-1.53748	-1.81248	3.56587	H	-1.4532	3.86094	-2.63434
H	2.69646	-3.71916	0.96623	H	-1.03978	-0.40407	2.64789	H	-2.4848	3.82079	-1.21496
C	-0.02987	-1.71321	-2.26286	C	-0.51905	-2.22447	-2.35672	C	-0.56177	1.92719	2.47858
H	0.7743	-1.1547	-2.73972	H	-0.258	-3.03704	-3.03066	H	-0.28968	2.6957	3.19844
H	-0.39812	-2.43976	-2.98334	H	-1.43303	-1.7678	-2.73504	H	-1.47796	1.4578	2.8353
H	-0.83406	-1.00774	-2.06642	H	0.2681	-1.477	-2.42509	H	0.21879	1.17056	2.49583

Table 35:   Cartesian coordinates of theoretically obtained geometries of **A-4**-I, **A-4**-II, **B-4**-I on the MPW1K/6-311G(d,p) level of theory in the gaseous phase.

	A-4-I		**A-4**-II		**B-4**-I
C	-3.38973 -0.47051 -0.19137	C	-3.42291 -0.50748 -0.05641	C	2.98724 0.42683 -0.8965
O	-0.85946 1.60672 -1.482	O	-1.03955 1.65208 -1.48408	O	2.18758 -1.40733 1.99303
C	-4.73199 -0.67371 0.05663	C	-4.73716 -0.74228 0.29303	C	3.93286 0.80369 -1.82535
C	-3.81446 1.66169 -1.20194	C	-3.96211 1.6451 -0.96386	C	4.52519 -1.07073 0.17403
C	-5.16037 1.4734 -0.96244	C	-5.28092 1.42541 -0.62214	C	5.47677 -0.71864 -0.76401
C	-5.6128 0.32012 -0.32904	C	-5.66202 0.24614 0.01035	C	5.18203 0.20981 -1.75432
C	-2.92772 0.67957 -0.79366	C	-3.02967 0.66785 -0.65873	C	3.27324 -0.49017 0.09182
C	-1.45693 0.74935 -0.88746	C	-1.57269 0.7671 -0.86917	C	2.12915 -0.75537 0.98489
C	-0.86426 -0.41979 -0.20578	C	-0.90796 -0.41033 -0.27365	C	0.9288 -0.07108 0.46372
C	0.43444 -0.63098 0.09223	C	0.41395 -0.60725 -0.08858	C	-0.35447 -0.46171 0.61424
C	1.09955 -1.97411 0.37125	C	1.1195 -1.94688 0.09351	C	-0.86241 -1.85254 0.98938
C	3.86769 1.76106 0.07583	C	3.79335 1.84777 -0.34055	C	-3.917 1.20773 -0.79839
C	3.9135 0.40142 -0.19979	C	3.8382 0.49329 -0.64211	C	-3.70291 -0.16657 -0.78248
C	2.71056 -0.27786 -0.13999	C	2.65842 -0.2088 -0.49043	C	-2.4996 -0.59404 -0.25458
C	2.47918 -1.74391 -0.28058	C	2.43936 -1.67401 -0.65801	C	-2.03014 -1.99007 -0.02058
C	1.47937 1.72116 0.50629	C	1.45401 1.75242 0.30078	C	-1.80667 1.67193 0.30748
C	2.69443 2.38995 0.44679	C	2.64725 2.44607 0.14682	C	-3.01285 2.09147 -0.24351
C	1.25101 -2.14563 1.88523	C	1.39427 -2.16164 1.58447	C	0.08324 -3.027 0.81189
C	1.50139 0.37203 0.13123	C	1.46519 0.41249 -0.10559	C	-1.53161 0.3058 0.20116
C	0.44931 -3.21268 -0.22188	C	0.44193 -3.17789 -0.48461	C	-1.40025 -1.82665 2.41961
H	4.78279 2.33528 0.04306	H	4.68819 2.44327 -0.45566	H	-4.84042 1.58981 -1.21022
H	2.73317 3.43284 0.71808	H	2.68858 3.48654 0.42714	H	-3.26381 3.14107 -0.20229
H	2.43876 -2.03724 -1.33085	H	2.31965 -1.93165 -1.71204	H	-2.81143 -2.64385 0.36364
H	3.25075 -2.34592 0.19601	H	3.25369 -2.27877 -0.26424	H	-1.65544 -2.43962 -0.94133
H	1.78699 -3.07001 2.09464	H	1.95907 -3.08249 1.72124	H	-0.50642 -3.94273 0.8042
H	1.80824 -1.32017 2.32177	H	1.97189 -1.34 2.00143	H	0.61583 -2.9701 -0.13615
H	0.27064 -2.19594 2.35107	H	0.45517 -2.24319 2.12492	H	0.80859 -3.0983 1.61167
H	-0.41765 -3.53576 0.34619	H	-0.37135 -3.53323 0.14067	H	-0.58904 -1.63929 3.1179
H	0.16497 -3.06501 -1.26141	H	0.07247 -3.00353 -1.49274	H	-2.15705 -1.05644 2.54847
H	1.17109 -4.02748 -0.18662	H	1.1763 -3.98065 -0.53335	H	-1.84625 -2.78959 2.66215
H	-3.43704 2.55165 -1.68024	H	-3.639 2.55529 -1.44387	H	4.73269 -1.77934 0.96036
H	-5.87101 2.22776 -1.26129	H	-6.02537 2.17505 -0.83944	H	6.45882 -1.16321 -0.72762
H	-6.66791 0.19678 -0.14061	H	-6.69622 0.09815 0.27962	H	5.93944 0.47829 -2.4742
H	-5.07814 -1.57228 0.54213	H	-5.0284 -1.66079 0.77724	H	3.71145 1.54236 -2.57942
S	-2.11274 -1.6741 0.11691	S	-2.10626 -1.6961 0.11006	S	1.37384 1.2062 -0.7412
O	-2.10604 -2.05169 1.56026	O	-1.97608 -2.11635 1.53569	O	1.65967 2.54118 -0.14275
C	0.26634 2.42093 1.0439	C	0.28126 2.41922 0.95631	C	-1.00451 2.64671 1.12067
H	-0.18012 3.01175 0.24533	H	-0.23762 3.02531 0.21497	H	-0.76156 3.51701 0.51534
C	0.53503 3.30072 2.25446	C	0.64044 3.26855 2.16525	C	-1.75981 3.07451 2.37307
H	1.16865 4.15144 2.0172	H	1.24583 4.13183 1.90116	H	-1.162 3.77669 2.94956
H	-0.40171 3.69635 2.63994	H	-0.26488 3.64364 2.63678	H	-2.70481 3.5572 2.13398
H	1.01541 2.7388 3.05241	H	1.18901 2.69001 2.90526	H	-1.97777 2.21846 3.00857
C	5.20296 -0.27656 -0.55436	C	5.11912 -0.16796 -1.05659	H	-0.04946 2.22688 1.40684
H	6.03106 0.30309 -0.14989	H	4.90397 -1.00417 -1.71985	C	-4.72354 -1.11739 -1.33203
H	5.25022 -1.2529 -0.0732	H	5.70953 0.53836 -1.63862	H	-4.76912 -2.00846 -0.70697
C	5.38786 -0.44282 -2.05686	C	5.94119 -0.65411 0.12994	H	-5.70728 -0.65427 -1.27611
H	5.38238 0.52347 -2.55594	H	5.38527 -1.37545 0.72509	C	-4.43616 -1.5229 -2.77168
H	6.33148 -0.9351 -2.2823	H	6.86267 -1.12899 -0.20015	H	-5.1934 -2.21032 -3.14248
H	4.58702 -1.03875 -2.48862	H	6.20367 0.17442 0.78392	H	-4.42205 -0.65207 -3.42313
H	-0.47832 1.67578 1.31445	H	-0.42883 1.65607 1.26657	H	-3.4684 -2.01197 -2.85703

Table 36:   Cartesian coordinates of theoretically obtained geometries of **B-4**-II, **B-4**-III, **C-4**-I on the MPW1K/6-311G(d,p) level of theory in the gaseous phase.

	B-4-II		**B-4**-III		**C-4**-I
C	3.11283 0.47717 -0.76273	C	3.01101 0.53496 -0.81103	C	-3.09645 0.61434 -0.67069
O	2.10193 -1.67875 1.82233	O	2.25313 -1.82977 1.67536	O	-2.13077 -1.87116 1.62817
C	4.12086 0.94169 -1.57942	C	3.94221 1.09035 -1.66126	C	-4.10875 1.21608 -1.39101
C	4.55452 -1.17934 0.20248	C	4.56625 -1.13545 -0.07389	C	-4.62147 -0.95782 0.30707
C	5.56866 -0.73845 -0.62613	C	5.50395 -0.60236 -0.93783	C	-5.64407 -0.36409 -0.40398
C	5.35247 0.31208 -1.50886	C	5.19356 0.49981 -1.72408	C	-5.38746 0.70876 -1.25191
C	3.32057 -0.5617 0.11882	C	3.31223 -0.55609 -0.02474	C	-3.33667 -0.46507 0.15176
C	2.11818 -0.90673 0.90117	C	2.17938 -0.9968 0.81212	C	-2.12197 -1.00908 0.78526
C	0.96453 -0.13504 0.39666	C	0.97011 -0.23279 0.44431	C	-0.94247 -0.27019 0.31101
C	-0.3313 -0.51304 0.41509	C	-0.31045 -0.65094 0.53093	C	0.35879 -0.60171 0.45857
C	-0.88011 -1.92931 0.58061	C	-0.79624 -2.09603 0.63226	C	0.91433 -2.01124 0.63573
C	-3.76251 1.39522 -1.01965	C	-3.93377 1.18714 -0.46981	C	3.93464 1.45846 -0.21196
C	-3.57442 0.02264 -1.14533	C	-3.68973 -0.15321 -0.7325	C	3.82172 0.09217 -0.42998
C	-2.42026 -0.49184 -0.58934	C	-2.46551 -0.6418 -0.31061	C	2.59165 -0.47439 -0.15105
C	-1.98645 -1.91618 -0.50467	C	-1.97933 -2.04828 -0.36621	C	2.20474 -1.91149 -0.21237
C	-1.72917 1.67523 0.27708	C	-1.80638 1.48426 0.67334	C	1.65744 1.64506 0.60384
C	-2.88587 2.18567 -0.30348	C	-3.03468 1.96433 0.23984	C	2.89557 2.20193 0.31508
C	0.05918 -3.09168 0.31211	C	0.1572 -3.20055 0.21175	C	1.26453 -2.23851 2.10611
C	-1.46903 0.32458 0.02924	C	-1.50402 0.16859 0.29447	C	1.50528 0.28907 0.28513
C	-1.50306 -2.07123 1.96889	C	-1.30907 -2.3599 2.04751	C	0.05847 -3.15181 0.11252
H	-4.6407 1.84776 -1.45847	H	-4.86733 1.63209 -0.77707	H	4.87598 1.94749 -0.41883
H	-3.11701 3.23139 -0.16443	H	-3.32017 2.9719 0.49706	H	3.06673 3.24455 0.5309
H	-2.79661 -2.59757 -0.25194	H	-2.74825 -2.77445 -0.10678	H	1.9823 -2.20664 -1.23837
H	-1.56321 -2.25176 -1.4531	H	-1.62032 -2.30172 -1.3655	H	2.97927 -2.58033 0.15888
H	-0.54095 -3.98656 0.15292	H	-0.42564 -4.10189 0.02683	H	1.73894 -3.21132 2.22315
H	0.64986 -2.92684 -0.58765	H	0.67637 -2.9491 -0.7118	H	1.94922 -1.47753 2.47431
H	0.73267 -3.27863 1.13813	H	0.89344 -3.42436 0.97233	H	0.36128 -2.22175 2.70917
H	-0.7329 -1.99048 2.73118	H	-0.48709 -2.30394 2.75596	H	-0.76412 -3.38436 0.77608
H	-2.25502 -1.30669 2.14993	H	-2.06999 -1.63941 2.33813	H	-0.33954 -2.92109 -0.87385
H	-1.97654 -3.04709 2.0615	H	-1.74186 -3.35727 2.10178	H	0.68299 -4.03944 0.02078
H	4.70014 -1.9846 0.90522	H	4.78613 -1.98325 0.5557	H	-4.79195 -1.79599 0.96406
H	6.53851 -1.20882 -0.58711	H	6.48728 -1.04089 -1.00205	H	-6.65238 -0.73508 -0.30827
H	6.15773 0.64791 -2.14348	H	5.94021 0.90693 -2.38796	H	-6.19907 1.15424 -1.80582
H	3.95991 1.77308 -2.24738	H	3.70867 1.96058 -2.25407	H	-3.90607 2.0492 -2.04522
S	1.50747 1.27278 -0.60537	S	1.39971 1.25989 -0.47825	S	-1.39889 1.17 -0.68022
O	1.78115 2.51208 0.17652	O	1.69191 2.43913 0.38734	O	-0.84612 1.02318 -2.05438
C	-0.96629 2.53057 1.24721	C	-1.00964 2.28422 1.66887	C	0.62162 2.46386 1.32442
H	-0.64926 3.44908 0.75875	H	-0.018 1.87022 1.79611	H	-0.14156 1.79936 1.72017
C	-1.80488 2.85432 2.47754	C	-0.87734 3.76631 1.36665	C	1.18048 3.29709 2.4677
H	-1.23292 3.46813 3.16951	H	-0.28131 4.24347 2.13992	H	1.71926 2.67499 3.17879
H	-2.71225 3.39665 2.22127	H	-0.36239 3.92021 0.42442	H	1.85871 4.07275 2.12256
H	-2.09935 1.94574 2.99904	H	-1.84023 4.27189 1.33565	H	0.36975 3.7908 2.99838
H	-0.05015 2.04652 1.55878	H	-1.51948 2.15958 2.62757	H	0.11103 3.11548 0.61615
C	-4.60261 -0.84407 -1.8094	C	-4.67758 -1.05937 -1.41234	C	4.9725 -0.70715 -0.96277
H	-5.07147 -0.28296 -2.61656	H	-4.18758 -1.52521 -2.26886	H	5.90345 -0.20435 -0.70592
H	-4.1171 -1.70028 -2.27493	H	-4.91559 -1.88125 -0.7342	H	5.00371 -1.67891 -0.47142
C	-5.67549 -1.32811 -0.84254	C	-5.96526 -0.40608 -1.87047	C	4.90153 -0.90335 -2.47151
H	-6.40638 -1.95386 -1.35018	H	-6.60514 -1.13597 -2.35932	H	4.9083 0.05446 -2.98645
H	-5.24111 -1.90848 -0.03134	H	-6.52293 0.01183 -1.03496	H	5.74747 -1.48651 -2.82894
H	-6.20218 -0.48752 -0.39646	H	-5.77592 0.39493 -2.58214	H	3.98987 -1.42173 -2.7589

Table 37:　　　Cartesian coordinates of theoretically obtained geometries of **C-4**-II, **D-4**-I, **D-4**-II on the MPW1K/6-311G(d,p) level of theory in the gaseous phase.

	C-4-II		**D-4**-I		**D-4**-II
C	-3.20361 0.60403 -0.51894	C	3.38499 -0.41364 0.03427	C	3.41427 -0.43029 0.15685
O	-2.01926 -2.01239 1.51738	O	0.84357 1.47262 -1.48993	O	1.00526 1.53092 -1.48318
C	-4.27897 1.22965 -1.11721	C	4.72846 -0.5796 0.29419	C	4.7326 -0.61375 0.51512
C	-4.61943 -1.07081 0.45254	C	3.77847 1.67138 -1.08238	C	3.89852 1.69793 -0.83571
C	-5.7042 -0.45407 -0.13629	C	5.126 1.5282 -0.81258	C	5.22015 1.53683 -0.46625
C	-5.53337 0.68208 -0.92104	C	5.59568 0.41311 -0.12964	C	5.63233 0.39162 0.20382
C	-3.35993 -0.53638 0.23884	C	2.91155 0.68726 -0.64519	C	2.99806 0.70056 -0.51074
C	-2.0906 -1.09294 0.7406	C	1.44432 0.68482 -0.81379	C	1.54882 0.71263 -0.79498
C	-0.96488 -0.29272 0.23637	C	0.86402 -0.44499 -0.0458	C	0.90738 -0.44515 -0.12328
C	0.35038 -0.60019 0.26669	C	-0.4305 -0.60253 0.29702	C	-0.41043 -0.6104 0.11023
C	0.94586 -2.00452 0.30257	C	-1.12074 -1.88149 0.76405	C	-1.13682 -1.90514 0.46702
C	3.8141 1.59802 -0.5411	C	-3.85625 1.75665 -0.2027	C	-3.77666 1.78485 -0.58428
C	3.71878 0.24275 -0.8269	C	-3.89012 0.37203 -0.29439	C	-3.80767 0.40328 -0.71855
C	2.53079 -0.37457 -0.48646	C	-2.69405 -0.28764 -0.07684	C	-2.63802 -0.26942 -0.42178
C	2.17159 -1.81383 -0.62237	C	-2.45878 -1.75833 0.00512	C	-2.4132 -1.74368 -0.38532
C	1.6078 1.66695 0.4665	C	-1.49714 1.7827 0.36525	C	-1.47493 1.77662 0.18552
C	2.80365 2.27717 0.11292	C	-2.704 2.43373 0.14835	C	-2.65669 2.44237 -0.11312
C	1.403 -2.32605 1.72527	C	-0.46255 -3.21052 0.44152	C	-0.45794 -3.22238 0.13887
C	1.46237 0.32947 0.07538	C	-1.50028 0.39835 0.16727	C	-1.46499 0.40019 -0.06001
C	0.078 -3.12627 -0.24132	C	-1.36781 -1.7848 2.27136	C	-1.49798 -1.87204 1.95391
H	4.71733 2.12973 -0.80531	H	-4.76584 2.31717 -0.36556	H	-4.66274 2.35771 -0.81911
H	2.96154 3.31258 0.37026	H	-2.75255 3.50397 0.27421	H	-2.70851 3.50969 0.03509
H	1.88461 -2.03851 -1.65068	H	-3.25881 -2.29123 0.51622	H	-3.24905 -2.29615 0.03945
H	2.98207 -2.48846 -0.35378	H	-2.35114 -2.20118 -0.98594	H	-2.23086 -2.13999 -1.38555
H	1.90435 -3.29232 1.73907	H	-1.19609 -4.00085 0.59558	H	-1.2029 -4.01466 0.20016
H	2.09585 -1.57553 2.09981	H	-0.10651 -3.26145 -0.58221	H	-0.0229 -3.23056 -0.85509
H	0.54414 -2.37499 2.38841	H	0.37673 -3.42795 1.09595	H	0.32689 -3.47275 0.84688
H	-0.69082 -3.42562 0.45893	H	-0.42358 -1.76458 2.81125	H	-0.59749 -1.88097 2.56423
H	-0.39305 -2.83626 -1.17862	H	-1.93128 -0.89249 2.53175	H	-2.07685 -0.98814 2.20938
H	0.71206 -3.98932 -0.43991	H	-1.92762 -2.65592 2.60656	H	-2.08408 -2.75343 2.2075
H	-4.72339 -1.95724 1.05808	H	3.39012 2.5226 -1.61914	H	3.55535 2.57293 -1.36497
H	-6.69495 -0.85595 0.00652	H	5.82294 2.28537 -1.13571	H	5.94175 2.3035 -0.70069
H	-6.39302 1.1452 -1.37984	H	6.65201 0.31549 0.06674	H	6.66957 0.28054 0.47897
H	-4.14259 2.11163 -1.72272	H	5.09485 -1.45695 0.80348	H	5.05599 -1.5136 1.01416
S	-1.52265 1.20058 -0.61481	S	2.13809 -1.66225 0.34694	S	2.1443 -1.68454 0.31663
O	-1.07288 1.16158 -2.03307	O	2.29614 -2.65872 -0.75236	O	2.38721 -2.63457 -0.80799
C	0.61542 2.41136 1.31704	C	-0.31992 2.55596 0.88408	C	-0.34356 2.52625 0.82628
H	-0.11002 1.70687 1.71409	H	0.12221 3.12002 0.06419	H	0.16087 3.12308 0.06784
C	1.24705 3.16386 2.47851	C	-0.65543 3.48783 2.03863	C	-0.77286 3.40979 1.98784
H	1.8361 2.49602 3.10298	H	0.24965 3.96336 2.4098	H	0.09771 3.8731 2.44668
H	1.897 3.96883 2.14636	H	-1.33881 4.28038 1.74548	H	-1.43717 4.21079 1.6745
H	0.47243 3.60924 3.09844	H	-1.11239 2.94453 2.86295	H	-1.2884 2.83194 2.75193
H	0.04903 3.10641 0.69812	C	-5.15898 -0.35435 -0.62654	C	-5.06624 -0.31042 -1.1141
C	4.86795 -0.50661 -1.43234	H	-5.237 -1.25598 -0.0198	H	-5.62212 0.31405 -1.81208
H	4.49093 -1.31559 -2.0557	H	-6.00746 0.27112 -0.35411	H	-4.81787 -1.22294 -1.65345
H	5.41486 0.16088 -2.09659	C	-5.25046 -0.72611 -2.10025	C	-5.95306 -0.64541 0.07806
C	5.8205 -1.06806 -0.38474	H	-6.18634 -1.24953 -2.31044	H	-6.857 -1.16118 -0.23885
H	5.30765 -1.75303 0.28712	H	-5.21866 0.16262 -2.72594	H	-5.43299 -1.28452 0.78858
H	6.64184 -1.60716 -0.85183	H	-4.43306 -1.37126 -2.3988	H	-6.24764 0.25815 0.60715
H	6.24222 -0.27008 0.22232	H	0.44629 1.85954 1.21484	H	0.39553 1.81621 1.18819

Table 38: Cartesian coordinates of theoretically obtained geometries of **D-4**-III, **TS**$_{D-A}$-**4**-I, **TS**$_{D-A}$-**4**-II on the MPW1K/6-311G(d,p) level of theory in the gaseous phase.

	D-4-III				TS$_{D-A}$-4-I				TS$_{D-A}$-4-II		
C	3.41602	-0.40265	0.07629	C	3.14341	-0.56683	0.62172	C	-3.23465	-0.6012	-0.54206
O	0.85657	1.58942	-1.27141	O	1.70994	1.70736	-1.545	O	-1.69109	1.64239	1.58162
C	4.75647	-0.5662	0.35244	C	4.20463	-0.91703	1.42781	C	-4.345	-0.94996	-1.27981
C	3.77642	1.82205	-0.7432	C	3.84982	1.72124	0.53768	C	-3.97627	1.668	-0.33697
C	5.11997	1.6797	-0.4536	C	4.90402	1.39195	1.36989	C	-5.08196	1.34105	-1.10035
C	5.60446	0.49652	0.0901	C	5.07971	0.08634	1.81005	C	-5.26453	0.04542	-1.56654
C	2.92794	0.76636	-0.46587	C	2.96239	0.72374	0.1832	C	-3.0467	0.67942	-0.0783
C	1.46655	0.74467	-0.67759	C	1.79285	0.85183	-0.71151	C	-1.8183	0.80674	0.73368
C	0.90218	-0.48939	-0.07748	C	0.8935	-0.32327	-0.52556	C	-0.91308	-0.34415	0.45075
C	-0.39324	-0.71393	0.21657	C	-0.44732	-0.50079	-0.56112	C	0.43032	-0.49391	0.39096
C	-1.06357	-2.05877	0.48182	C	-1.12576	-1.87898	-0.70187	C	1.1427	-1.86201	0.43404
C	-3.88215	1.60445	-0.01621	C	-4.01229	1.63976	0.36368	C	3.87436	1.75433	-0.71786
C	-3.86654	0.25272	-0.321	C	-3.87066	0.27394	0.52956	C	3.75118	0.38965	-0.90652
C	-2.65117	-0.39453	-0.16697	C	-2.66981	-0.28415	0.12611	C	2.59681	-0.2061	-0.43248
C	-2.38366	-1.85558	-0.29235	C	-2.36873	-1.73629	0.16134	C	2.32089	-1.66181	-0.50526
C	-1.53099	1.61623	0.60326	C	-1.78356	1.83725	-0.60413	C	1.72306	1.87054	0.42491
C	-2.75573	2.24981	0.46579	C	-3.00084	2.37919	-0.20522	C	2.89431	2.45229	-0.05021
C	-0.36379	-3.31483	-0.0037	C	-1.5121	-1.94601	-2.18904	C	1.63097	-1.9751	1.88804
C	-1.485	0.27576	0.2038	C	-1.59204	0.4588	-0.39441	C	1.54253	0.4957	0.18381
C	-1.35466	-2.18091	1.97931	C	-0.43396	-3.1875	-0.35395	C	0.454	-3.17183	0.08439
H	-4.79822	2.16628	-0.11	H	-4.9348	2.12378	0.6505	H	4.75584	2.27049	-1.07063
H	-2.84505	3.2821	0.76801	H	-3.15798	3.43425	-0.37503	H	3.03835	3.50686	0.13385
H	-3.18436	-2.47197	0.11324	H	-2.15755	-2.07245	1.17783	H	2.04468	-1.95674	-1.5197
H	-2.24193	-2.14785	-1.33425	H	-3.19004	-2.34471	-0.21378	H	3.17523	-2.26995	-0.21424
H	-1.08073	-4.13458	0.01661	H	-2.07549	-2.85917	-2.37278	H	2.22351	-2.88164	1.99844
H	0.02004	-3.21412	-1.01363	H	-2.12202	-1.09911	-2.49108	H	2.24283	-1.1263	2.18077
H	0.46312	-3.60381	0.63875	H	-0.61875	-1.96529	-2.80814	H	0.78241	-2.03735	2.56464
H	-0.4264	-2.22037	2.54516	H	0.41156	-3.41475	-0.99769	H	-0.33981	-3.44186	0.77566
H	-1.94441	-1.34461	2.34573	H	-0.11886	-3.23242	0.68301	H	0.06852	-3.18544	-0.9294
H	-1.9041	-3.10066	2.17105	H	-1.16886	-3.97752	-0.50814	H	1.2135	-3.95024	0.15703
H	3.37799	2.72696	-1.17426	H	3.70956	2.72455	0.16782	H	-3.82829	2.66273	0.05252
H	5.80217	2.49118	-0.65238	H	5.60328	2.15362	1.67701	H	-5.81609	2.09643	-1.3325
H	6.65762	0.40144	0.30395	H	5.91432	-0.15093	2.45107	H	-6.13904	-0.19057	-2.15247
H	5.13545	-1.49362	0.75198	H	4.35416	-1.93717	1.74475	H	-4.49777	-1.96324	-1.61655
S	2.19996	-1.71591	0.18151	S	1.97917	-1.72022	-0.09825	S	-1.99857	-1.75004	0.05426
O	2.41505	-2.54817	-1.03792	O	2.62151	-2.27598	-1.32503	O	-2.53899	-2.35959	1.30453
C	-0.41907	2.33981	1.31209	C	-0.85588	2.81321	-1.25972	C	0.83199	2.80514	1.18403
H	0.46757	1.71709	1.35747	H	-1.46444	3.45972	-1.89106	H	1.4767	3.43302	1.79826
C	-0.0707	3.70337	0.73517	C	-0.11256	3.68057	-0.25245	C	0.00919	3.7038	0.27046
H	0.74787	4.15097	1.29496	H	-0.80461	4.29051	0.32551	H	0.65115	4.34709	-0.32874
H	0.22742	3.61676	-0.30406	H	0.45406	3.0763	0.45133	H	-0.60028	3.12183	-0.41591
H	-0.9139	4.38764	0.79206	H	0.585	4.34208	-0.76038	H	-0.65692	4.33384	0.85485
C	-5.08205	-0.51056	-0.76763	H	-0.15397	2.31222	-1.90769	H	0.18343	2.26713	1.85731
H	-4.84515	-1.01986	-1.70296	C	-4.96993	-0.54459	1.13928	C	4.84926	-0.40268	-1.5528
H	-5.27597	-1.30701	-0.04634	H	-5.91894	-0.03852	0.97001	H	4.43026	-1.25502	-2.08467
C	-6.34319	0.30795	-0.95271	H	-5.04408	-1.50678	0.63491	H	5.33262	0.21779	-2.30614
H	-7.15781	-0.32633	-1.29228	C	-4.77974	-0.76831	2.63397	C	5.89418	-0.88422	-0.55442
H	-6.65828	0.77688	-0.02281	H	-4.7478	0.18027	3.16506	H	5.44889	-1.51855	0.20901
H	-6.20477	1.09193	-1.69438	H	-5.59434	-1.35949	3.04677	H	6.67656	-1.45416	-1.05093
H	-0.73738	2.4679	2.34884	H	-3.84871	-1.291	2.84056	H	6.35994	-0.04257	-0.04688

Table 39:   Cartesian coordinates of theoretically obtained geometries of **TS_B-C-4**-I, **TS_B-C-4**-II, **TS_B-C-4**-III
on the MPW1K/6-311G(d,p) level of theory in the gaseous phase.

	TS_B-C-4-I		TS_B-C-4-II		TS_B-C-4-III
C	-3.30262 0.54655 -0.06859	C	-3.30155 0.57905 0.08422	C	3.34101 0.57925 -0.02559
O	-1.79255 -2.59087 -0.30832	O	-1.86658 -2.55774 -0.44798	O	1.88712 -2.56496 0.3901
C	-4.47719 1.26611 -0.00124	C	-4.45552 1.30902 0.27745	C	4.50404 1.31461 -0.12051
C	-4.46483 -1.53837 0.10431	C	-4.48544 -1.49665 0.21726	C	4.54174 -1.4905 -0.04622
C	-5.65002 -0.83501 0.19156	C	-5.64889 -0.78382 0.43016	C	5.71589 -0.77275 -0.15962
C	-5.65578 0.55447 0.1371	C	-5.63384 0.60636 0.45784	C	5.69684 0.61738 -0.19384
C	-3.28753 -0.82362 -0.02418	C	-3.30767 -0.7915 0.04715	C	3.35026 -0.79048 0.01824
C	-1.93827 -1.40877 -0.14529	C	-1.9807 -1.38615 -0.20413	C	2.01012 -1.39175 0.15739
C	-0.89714 -0.33835 -0.055	C	-0.91763 -0.33707 -0.1258	C	0.94814 -0.35105 -0.00958
C	0.44493 -0.48765 0.14302	C	0.43192 -0.51707 -0.03308	C	-0.39149 -0.5477 -0.19382
C	1.05658 -1.89772 0.31387	C	1.02881 -1.94225 0.01989	C	-0.95869 -1.98493 -0.28626
C	4.13442 1.64032 -0.09015	C	4.11877 1.55716 -0.5199	C	-4.14668 1.45427 -0.00608
C	4.04656 0.28984 0.1679	C	4.0343 0.20004 -0.29286	C	-4.01824 0.09906 -0.20976
C	2.77178 -0.24076 0.28808	C	2.76768 -0.31365 -0.05892	C	-2.72671 -0.3901 -0.33098
C	2.51621 -1.64341 0.66735	C	2.51112 -1.72315 0.29215	C	-2.42298 -1.79539 -0.65905
C	1.70622 1.90121 -0.01382	C	1.71906 1.85594 -0.17738	C	-1.73558 1.80272 -0.15378
C	2.99125 2.40852 -0.15034	C	2.99311 2.34721 -0.42762	C	-3.03233 2.26885 -0.00868
C	0.45967 -2.73942 1.43972	C	0.49251 -2.84041 1.1322	C	-0.33319 -2.87177 -1.36073
C	1.57765 0.49193 0.14103	C	1.57902 0.44378 -0.0743	C	-1.55952 0.39049 -0.23394
C	0.10153 3.1395 1.4731	C	0.27249 3.01332 1.52198	C	-1.12462 4.28165 -0.47562
C	1.04908 -2.61004 -1.04395	C	0.92413 -2.57692 -1.372	C	-0.94355 -2.61747 1.11081
H	5.10085 2.10972 -0.20523	H	5.07513 2.01214 -0.73398	H	-5.12671 1.89455 0.11037
H	3.09611 3.47307 -0.29001	H	3.10461 3.41415 -0.54149	H	-3.18834 3.32906 0.08248
H	-0.70981 3.86391 1.48075	H	-0.51667 3.75116 1.64806	H	-0.25367 4.91015 -0.64373
H	-0.28213 2.20837 1.87927	H	-0.10027 2.06349 1.89351	H	-1.78313 4.38978 -1.33534
H	0.88257 3.49544 2.14225	H	1.11486 3.30534 2.14616	H	-1.63553 4.67595 0.39971
H	3.17059 -2.35622 0.17255	H	3.12363 -2.43075 -0.26135	H	-3.05579 -2.51362 -0.14469
H	2.68398 -1.75226 1.74047	H	2.73574 -1.87031 1.34944	H	-2.57729 -1.9459 -1.72921
H	1.12052 -3.58842 1.61061	H	1.15708 -3.69919 1.21959	H	-0.97372 -3.74343 -1.49016
H	0.42549 -2.16289 2.36282	H	0.51392 -2.3142 2.08528	H	-0.30524 -2.34484 -2.31321
H	-0.52312 -3.12802 1.22567	H	-0.50318 -3.2142 0.95409	H	0.6563 -3.22616 -1.12047
H	0.05035 -2.75155 -1.43016	H	-0.0996 -2.68166 -1.70047	H	0.0534 -2.6997 1.51763
H	1.63224 -2.03976 -1.76534	H	1.47151 -1.97606 -2.0964	H	-1.55787 -2.02858 1.79016
H	1.51291 -3.58905 -0.93233	H	1.37597 -3.56741 -1.34384	H	-1.36968 -3.61788 1.05031
H	-4.4339 -2.61606 0.12888	H	-4.47201 -2.5742 0.17622	H	4.5294 -2.56795 -0.00249
H	-6.58322 -1.36516 0.29866	H	-6.58146 -1.30678 0.57241	H	6.65976 -1.29152 -0.2179
H	-6.59305 1.08498 0.19984	H	-6.55479 1.14479 0.61842	H	6.62582 1.15985 -0.27493
H	-4.47846 2.34294 -0.05952	H	-4.44188 2.38734 0.28249	H	4.48595 2.39284 -0.13134
S	-1.69431 1.25195 -0.3312	S	-1.70366 1.27743 -0.25218	S	1.71772 1.27169 0.16184
O	-1.61082 1.61321 -1.781	O	-1.71714 1.72291 -1.68064	O	1.60436 1.73152 1.58155
C	0.6504 2.96545 0.06364	C	0.69804 2.92981 0.06259	C	-0.66477 2.84835 -0.28085
H	1.12049 3.90095 -0.23018	H	1.16345 3.8755 -0.20487	H	-0.03412 2.81982 0.60753
H	-0.12719 2.81644 -0.67634	H	-0.1422 2.84639 -0.61695	H	-0.03493 2.58471 -1.12428
C	5.27822 -0.5584 0.28841	C	5.26865 -0.6523 -0.26875	C	-5.22083 -0.79571 -0.27428
H	5.13073 -1.32404 1.04812	H	6.03218 -0.17065 -0.87738	H	-5.06134 -1.582 -1.0102
H	6.09875 0.06435 0.64111	H	5.06912 -1.6143 -0.738	H	-6.07006 -0.21513 -0.63097
C	5.67468 -1.21086 -1.02973	C	5.81452 -0.87339 1.13583	C	-5.56752 -1.41492 1.07354
H	6.5693 -1.81832 -0.91145	H	6.71508 -1.48309 1.11121	H	-6.44215 -2.05705 0.99541
H	4.88126 -1.85048 -1.40992	H	6.06164 0.07499 1.60752	H	-4.7444 -2.01269 1.45876
H	5.87584 -0.45704 -1.7874	H	5.08903 -1.37678 1.7703	H	-5.78015 -0.6423 1.80883

Table 40: Cartesian coordinates of theoretically obtained geometries of **A-88**, **B-88**, **C-88** on the B3LYP/6-311+G(d,p) level of theory in the gaseous phase.

	A-88		B-88		C-88
C	-4.24941 -1.36942 -0.42782	C	4.24559 -1.58408 -0.32225	C	4.16268 1.55299 -0.55448
C	-5.4435 -0.70149 -0.16487	C	5.44087 -0.86745 -0.37627	C	5.36033 0.83998 -0.58539
C	-5.41847 0.63295 0.25145	C	5.42599 0.52507 -0.26111	C	5.36822 -0.52389 -0.28018
C	-4.22232 1.33895 0.41317	C	4.23689 1.24174 -0.08859	C	4.20123 -1.21332 0.06395
C	-3.03856 0.66602 0.13295	C	3.0556 0.51242 -0.0308	C	3.01546 -0.48794 0.0943
C	-3.05823 -0.67202 -0.27395	C	3.06309 -0.87894 -0.14947	C	3.00077 0.87491 -0.2142
H	-4.23177 -2.40697 -0.73997	H	4.2225 -2.66387 -0.41149	H	4.1213 2.61032 -0.78873
H	-6.39152 -1.21282 -0.27703	H	6.38179 -1.38599 -0.51325	H	6.28476 1.33741 -0.85169
H	-6.35361 1.14026 0.46043	H	6.36098 1.07165 -0.311	H	6.30434 -1.06975 -0.31491
H	-4.23685 2.36739 0.74775	H	4.25222 2.32108 -0.01366	H	4.23491 -2.27257 0.28183
C	-1.66749 -1.09755 -0.44475	C	1.66901 -1.34738 -0.07537	C	1.61057 1.35002 -0.11399
O	-1.23402 -2.16302 -0.81507	O	1.2472 -2.45695 -0.26919	O	1.17184 2.43303 -0.40137
N	-1.71256 1.1467 0.2072	N	1.7391 0.98465 0.15185	N	1.71869 -0.93008 0.41979
C	-0.82242 0.14628 -0.10073	C	0.8377 -0.05055 0.15815	C	0.80646 0.0939 0.32188
C	0.54223 0.13886 -0.16897	C	-0.52782 0.00912 0.2066	C	-0.55127 0.03129 0.42985
C	2.88437 0.76326 -0.25302	C	-2.81964 -0.80479 0.12856	C	-2.85205 0.767 0.20507
C	4.02817 1.55862 -0.34618	C	-3.91034 -1.66838 0.20085	C	-3.95571 1.61325 0.1023
C	2.99016 -0.58524 0.05895	C	-2.98585 0.49018 -0.33926	C	-2.98134 -0.58276 -0.0922
C	5.26459 0.9778 -0.09151	C	-5.15651 -1.20648 -0.21236	C	-5.16429 1.0827 -0.33605
H	3.92795 2.60737 -0.5998	H	-3.76623 -2.67424 0.57763	H	-3.84511 2.66235 0.35011
C	4.21833 -1.17772 0.32342	C	-4.22399 0.97532 -0.73566	C	-4.18037 -1.13149 -0.5272
C	5.35755 -0.37833 0.24932	C	-5.31291 0.10523 -0.67364	C	-5.27387 -0.27641 -0.65615
H	6.16603 1.57676 -0.14979	H	-6.01663 -1.86483 -0.17274	H	-6.03104 1.72576 -0.43606
H	4.28618 -2.2268 0.58653	H	-4.34585 1.99743 -1.07475	H	-4.26053 -2.185 -0.76837
H	6.32931 -0.81278 0.45519	H	-6.29239 0.45265 -0.98184	H	-6.22162 -0.67054 -1.00479
S	1.41573 -1.49891 0.02451	S	-1.4758 1.50716 -0.28613	S	-1.4764 -1.55093 0.22343
C	1.49306 1.23829 -0.43223	C	-1.42836 -1.12803 0.5543	C	-1.48095 1.18002 0.61421
O	1.21456 2.37042 -0.80825	O	-1.12458 -2.13744 1.15074	O	-1.21334 2.25888 1.09797
C	-1.42417 2.42934 0.84171	C	1.48585 2.38266 0.49132	C	1.47617 -2.26636 0.94695
H	-2.17982 3.15229 0.53416	H	2.29112 2.73538 1.13859	H	1.30367 -2.98307 0.14265
H	-1.44761 2.32771 1.9321	H	1.45153 3.00932 -0.40424	H	2.33342 -2.57183 1.54864
H	-0.45269 2.78666 0.51555	H	0.54092 2.47851 1.02263	H	0.60119 -2.24649 1.59614
O	1.19126 -2.06535 1.40154	O	-1.64911 2.5046 0.8446	O	-1.03424 -2.24623 -1.04413

Table 41: Cartesian coordinates of theoretically obtained geometries of **D-88**, **TS_{B-C}-88**, **A-89** on the B3LYP/6-311+G(d,p) level of theory in the gaseous phase.

	D-88			TS_{B-C}-88			A-89	
C	4.38314 1.2232 0.09731		C	-4.34022 1.502 -0.05676		C	-3.57702 -3.09321 -0.04593	
C	5.51873 0.42407 0.22769		C	-5.4979 0.74896 -0.24446		C	-4.87504 -2.59031 -0.05811	
C	5.38508 -0.95505 0.40863		C	-5.41132 -0.641 -0.3604		C	-5.08799 -1.20931 -0.13501	
C	4.13329 -1.57745 0.46321		C	-4.18934 -1.31735 -0.28979		C	-4.0317 -0.29769 -0.20964	
C	3.0123 -0.76803 0.32563		C	-3.04334 -0.55217 -0.09709		C	-2.7423 -0.81487 -0.21451	
C	3.13879 0.61137 0.14881		C	-3.12509 0.83467 0.00544		C	-2.52008 -2.19318 -0.1265	
H	4.45235 2.29584 -0.04094		H	-4.36719 2.58137 0.03648		H	-3.37646 -4.15545 0.03017	
H	6.50546 0.86935 0.19515		H	-6.46334 1.23596 -0.30483		H	-5.72185 -3.26324 -0.00318	
H	6.27509 -1.56496 0.51513		H	-6.31635 -1.21843 -0.51203		H	-6.10356 -0.82943 -0.1339	
H	4.05753 -2.646 0.61581		H	-4.15895 -2.39353 -0.39334		H	-4.21578 0.76713 -0.25558	
C	1.78448 1.18312 0.06306		C	-1.76684 1.36072 0.20564		C	-1.07087 -2.41135 -0.08983	
O	1.46808 2.34338 0.04491		O	-1.45857 2.50273 0.4132		O	-0.44968 -3.4475 -0.03043	
N	1.65237 -1.14237 0.32677		N	-1.70338 -0.97591 0.02166		N	-1.50961 -0.11558 -0.27966	
C	0.8377 -0.05055 0.15815		C	-0.83985 0.09862 0.11849		C	-0.45891 -1.00906 -0.20631	
C	-0.52782 0.00912 0.2066		C	0.5326 0.09155 0.09609		C	0.87833 -0.78063 -0.29213	
C	-2.81964 -0.80479 0.12856		C	2.86206 0.81959 -0.07315		C	3.02958 0.30119 -0.55765	
C	-3.91034 -1.66838 0.20085		C	3.96979 1.66493 -0.12332		C	3.98578 1.27604 -0.8465	
C	-2.98585 0.49018 -0.33926		C	3.02757 -0.54823 -0.19504		C	3.40464 -0.89407 0.04271	
C	-5.15651 -1.20648 -0.21236		C	5.23153 1.10243 -0.28329		C	5.30879 1.03657 -0.49405	
H	-3.76623 -2.67424 0.57763		H	3.82294 2.73442 -0.02884		H	3.67715 2.19843 -1.32451	
C	-4.22399 0.97532 -0.73566		C	4.27927 -1.13182 -0.34292		C	4.72163 -1.14429 0.40605	
C	-5.31291 0.10523 -0.67364		C	5.3859 -0.28556 -0.38738		C	5.67223 -0.16164 0.13457	
H	-6.01663 -1.86483 -0.17274		H	6.10637 1.74107 -0.32333		H	6.06748 1.78246 -0.70113	
H	-4.34585 1.99743 -1.07475		H	4.39413 -2.20706 -0.41344		H	4.99983 -2.07256 0.89138	
H	-6.29239 0.45265 -0.98184		H	6.37749 -0.70819 -0.50219		H	6.70727 -0.32868 0.41068	
S	-1.4758 1.50716 -0.28613		S	1.48687 -1.48528 -0.09025		S	2.05053 -2.09982 0.26769	
C	-1.42836 -1.12803 0.5543		C	1.45373 1.2739 0.12257		C	1.57366 0.41587 -0.81821	
O	-1.12458 -2.13744 1.15074		O	1.16965 2.44384 0.25001		O	1.05141 1.32613 -1.43787	
C	1.26368 -2.55029 0.30451		C	-1.38523 -2.40205 0.01569		O	1.8923 -2.33697 1.74742	
H	1.98499 -3.10128 -0.3021		H	-2.25786 -2.94784 0.37122		C	-1.4451 1.29637 -0.0237	
H	1.25094 -2.9752 1.31208		H	-1.13379 -2.7531 -0.9892		C	-1.90092 2.20235 -0.97711	
H	0.27513 -2.66366 -0.13626		H	-0.56337 -2.61232 0.69808		C	-0.97774 1.75242 1.20623	
O	-1.64911 2.5046 0.8446		O	1.51813 -2.26804 1.21077		C	-1.89149 3.56288 -0.69382	
						H	-2.2358 1.84095 -1.94156	
						C	-0.95906 3.11809 1.47124	
						H	-0.6276 1.04295 1.94711	
						C	-1.41618 4.04567 0.53038	
						H	-0.59122 3.46566 2.43087	
						C	-1.36731 5.52744 0.81228	
						H	-0.43947 5.96612 0.42944	
						H	-2.19757 6.05261 0.33439	
						H	-1.40814 5.73131 1.88439	
						H	-2.2453 4.26281 -1.44351	

Table 42: Cartesian coordinates of theoretically obtained geometries of **B-89**, **C-89** and **D**-89 on the B3LYP/6-311+G(d,p) level of theory in the gaseous phase.

	B-89		C-89		D-89
C	3.37825 -3.3776 -0.17239	C	-3.28063 -3.41011 -0.18345	C	3.16468 -3.45102 0.22392
C	4.7004 -2.9413 -0.22122	C	-4.59903 -3.00803 -0.38677	C	4.51475 -3.11796 0.16394
C	4.98542 -1.57152 -0.19989	C	-4.90739 -1.64727 -0.49029	C	4.8973 -1.78065 0.00678
C	3.97813 -0.60546 -0.13108	C	-3.92598 -0.65637 -0.40058	C	3.96286 -0.74774 -0.10085
C	2.66563 -1.05938 -0.07878	C	-2.61632 -1.07613 -0.20665	C	2.61831 -1.0972 -0.05451
C	2.37179 -2.42274 -0.09529	C	-2.29903 -2.43083 -0.09286	C	2.22852 -2.42871 0.11146
H	3.12253 -4.43059 -0.19038	H	-3.00945 -4.4555 -0.09303	H	2.8333 -4.47432 0.3558
H	5.51004 -3.65856 -0.27675	H	-5.3881 -3.74578 -0.46564	H	5.27154 -3.88878 0.24159
H	6.01864 -1.24483 -0.2384	H	-5.93783 -1.34781 -0.64583	H	5.95231 -1.53317 -0.03145
H	4.21398 0.45036 -0.11718	H	-4.17945 0.39253 -0.48025	H	4.27736 0.28095 -0.21327
C	0.90952 -2.57552 -0.0567	C	-0.84692 -2.54851 0.12291	C	0.76682 -2.4572 0.17071
O	0.26817 -3.583 -0.20189	O	-0.17779 -3.54801 0.17093	O	0.02764 -3.39854 0.34366
N	1.47774 -0.29983 0.00119	N	-1.44951 -0.28712 -0.08045	N	1.48542 -0.24991 -0.13934
C	0.36532 -1.12208 0.09359	C	-0.34434 -1.08132 0.15612	C	0.32277 -0.99584 -0.03311
C	-0.94351 -0.76848 0.20919	C	0.95428 -0.68433 0.24531	C	-0.98754 -0.63362 -0.09752
C	-3.35573 -0.99833 0.02434	C	3.37159 -0.84524 0.35827	C	-3.03494 0.675 -0.1328
C	-4.60913 -1.59414 -0.09314	C	4.64536 -1.36998 0.57682	C	-3.88636 1.7769 -0.21088
C	-3.19395 0.35219 -0.24987	C	3.21958 0.35365 -0.32432	C	-3.52904 -0.57455 0.21512
C	-5.68479 -0.80987 -0.50042	C	5.74458 -0.68623 0.06934	C	-5.23672 1.59651 0.06846
H	-4.72061 -2.64828 0.13277	H	4.74889 -2.30094 1.12176	H	-3.48244 2.74306 -0.49027
C	-4.25964 1.15318 -0.63501	C	4.30594 1.04952 -0.83874	C	-4.87809 -0.77263 0.47664
C	-5.51191 0.55232 -0.76948	C	5.57567 0.51027 -0.63917	C	-5.72877 0.33055 0.40842
H	-6.66717 -1.25502 -0.60839	H	6.74263 -1.08232 0.2172	H	-5.91697 2.43893 0.01905
H	-4.12716 2.21254 -0.82296	H	4.17047 1.97586 -1.38465	H	-5.26123 -1.75599 0.72413
H	-6.36149 1.14982 -1.08009	H	6.44335 1.02573 -1.03504	H	-6.78538 0.20475 0.61633
S	-1.52053 0.98255 0.12197	S	1.49956 0.93921 -0.43618	S	-2.30034 -1.93021 0.16277
C	-2.10281 -1.68903 0.44701	C	2.09246 -1.46867 0.79694	C	-1.57703 0.69378 -0.41236
O	-2.07813 -2.79318 0.93897	O	2.02172 -2.41252 1.55564	O	-0.98286 1.66054 -0.85143
O	-1.59003 1.56849 1.5163	O	1.11539 1.02877 -1.896	O	-2.57257 -2.67075 -1.12142
C	1.52662 1.13618 -0.01285	C	-1.52914 1.1352 0.1104	C	1.65224 1.17504 -0.04295
C	1.47718 1.85631 1.17846	C	-1.5187 1.65627 1.40475	C	2.09988 1.89728 -1.14557
C	1.68902 1.80289 -1.22758	C	-1.6655 1.98437 -0.98509	C	1.4449 1.81624 1.17383
C	1.57357 3.24338 1.14577	C	-1.63518 3.02804 1.59623	C	2.3222 3.26346 -1.02897
H	1.32957 1.33712 2.11638	H	-1.41339 0.98821 2.25169	H	2.2478 1.39133 -2.09189
C	1.78872 3.18892 -1.24554	C	-1.79224 3.35459 -0.77796	C	1.66036 3.18743 1.27574
H	1.72587 1.23403 -2.14937	H	-1.62558 1.5742 -1.98507	H	1.11296 1.24644 2.03408
C	1.73254 3.93206 -0.06006	C	-1.77956 3.89923 0.50988	C	2.09978 3.93398 0.1794
H	1.50736 3.79761 2.07535	H	-1.61708 3.42743 2.60477	H	2.66208 3.82152 -1.89514
H	1.90471 3.70213 -2.19427	H	-1.884 4.01176 -1.63595	H	1.4884 3.68239 2.22572
C	1.85859 5.43564 -0.07997	C	-1.93818 5.38433 0.72553	C	2.30099 5.426 0.28329
H	1.23063 5.89603 0.68594	H	-2.99278 5.6486 0.86006	H	3.15702 5.75605 -0.31024
H	2.89154 5.74393 0.11494	H	-1.40191 5.71744 1.61679	H	1.4211 5.96328 -0.08653
H	1.57036 5.84741 -1.0493	H	-1.56474 5.9525 -0.1289	H	2.46487 5.73605 1.31743

Table 43: Cartesian coordinates of theoretically obtained geometries of **TS$_{B-C}$-89** on the B3LYP/6-311+G(d,p) level of theory in the gaseous phase and geometries of *cis*-**107** and *trans*-**107** on the ωB97X-D/6-311+G(d,p) level of theory with implementation of implicit THF solvent effects (IEFPCM).

TS$_{B-C}$-89				*cis*-**107**				*trans*-**107**			
C	3.58069	-3.20408	-0.10995	C	-4.53443	-1.80502	0.18517	C	-4.38135	1.11644	-0.55536
C	4.87257	-2.68537	-0.05695	C	-3.22697	-1.35512	0.05858	C	-3.27505	0.31062	-0.31891
C	5.0676	-1.30215	0.02589	C	-2.94933	-0.05738	-0.36913	C	-3.41942	-0.99129	0.17142
C	3.99811	-0.40356	0.06046	C	-3.97005	0.82909	-0.69283	C	-4.67619	-1.52191	0.43764
C	2.71696	-0.94049	0.01775	C	-5.27484	0.36688	-0.56673	C	-5.77516	-0.70484	0.19884
C	2.51266	-2.31643	-0.06553	C	-5.56521	-0.93201	-0.13281	C	-5.64154	0.60021	-0.28996
H	3.39423	-4.26913	-0.18344	H	-4.73079	-2.81628	0.5226	H	-4.2501	2.12203	-0.9383
H	5.72837	-3.34876	-0.08204	H	-3.75965	1.83765	-1.02713	H	-4.79456	-2.52992	0.8154
H	6.07821	-0.91098	0.06311	H	-6.09189	1.03632	-0.81162	H	-6.76742	-1.09381	0.39833
H	4.16415	0.66392	0.11966	H	-6.59659	-1.2508	-0.04693	H	-6.52529	1.20194	-0.46177
C	1.06403	-2.56177	-0.14225	C	-1.9486	-2.03774	0.32054	C	-1.84179	0.56183	-0.51829
O	0.50902	-3.60719	-0.35407	O	-1.79253	-3.15368	0.75759	O	-1.30371	1.53169	-1.00334
N	1.48019	-0.2595	0.04369	C	-0.89182	-1.00391	-0.03737	C	-1.17061	-0.71362	-0.0464
C	0.41599	-1.15015	0.02171	N	-1.58127	0.14203	-0.39613	N	-2.17711	-1.57769	0.32442
C	-0.91479	-0.86354	0.09834	C	0.46307	-1.11288	0.00658	C	0.14077	-1.06544	-0.01464
C	-3.33364	-1.09204	-0.06993	C	1.29785	-2.36339	0.13814	C	0.57059	-2.46968	0.23698
C	-4.58362	-1.68186	-0.2466	N	1.34804	-0.0498	-0.23711	N	1.2781	-0.30241	-0.29933
C	-3.20522	0.28805	-0.0751	C	2.68272	-1.8963	-0.02872	C	2.01642	-2.45878	0.04389
C	-5.68991	-0.85802	-0.4307	C	3.87863	-2.60111	0.01404	C	2.95863	-3.47772	0.14767
H	-4.66729	-2.76234	-0.23374	C	2.66329	-0.51785	-0.22308	C	2.39524	-1.14201	-0.23484
C	-4.30053	1.12545	-0.23795	C	5.0642	-1.89696	-0.1349	C	4.29441	-3.15915	-0.02625
C	-5.55013	0.53467	-0.42528	H	3.86983	-3.67409	0.16787	H	2.63983	-4.49018	0.36694
H	-6.67077	-1.29559	-0.57679	C	3.8438	0.20537	-0.35708	C	3.73868	-0.80833	-0.38805
H	-4.19107	2.2037	-0.21766	C	5.03514	-0.50899	-0.31261	C	4.66856	-1.8334	-0.28403
H	-6.42332	1.16202	-0.56395	H	6.01475	-2.41525	-0.10876	H	5.05413	-3.9277	0.04317
S	-1.51946	0.87339	0.28534	H	3.83971	1.27995	-0.48905	H	4.05021	0.21035	-0.57877
C	-2.05704	-1.83298	0.15072	H	5.97018	0.02966	-0.41811	H	5.71965	-1.59649	-0.40526
O	-2.01464	-3.02392	0.35847	O	0.93119	-3.50568	0.30025	O	-0.16296	-3.40846	0.51869
O	-1.4898	1.25253	1.75193	C	1.05409	1.33026	-0.03099	C	1.41324	1.10052	-0.06882
C	1.44751	1.17582	-0.03759	C	0.61606	1.7784	1.21207	C	1.0523	1.64863	1.1554
C	1.44679	1.94892	1.1204	C	1.20447	2.22973	-1.08025	C	1.9489	1.90923	-1.06114
C	1.48872	1.78936	-1.29047	C	0.31582	3.11978	1.39214	C	1.21479	3.00888	1.37423
C	1.46744	3.33675	1.01751	H	0.49576	1.07046	2.02416	H	0.63393	1.01355	1.92833
H	1.38919	1.46805	2.08776	C	0.91601	3.5748	-0.88246	C	2.12593	3.26515	-0.82424
C	1.50811	3.17543	-1.37885	H	1.53482	1.86943	-2.04768	H	2.20662	1.47666	-2.02075
H	1.49446	1.17827	-2.1856	C	0.46489	4.04035	0.35208	C	1.75912	3.83843	0.39326
C	1.49812	3.97223	-0.22665	H	-0.03868	3.45965	2.35942	H	0.9184	3.43243	2.32832
H	1.44248	3.93245	1.92323	H	1.03373	4.26985	-1.70687	H	2.54107	3.89163	-1.6069
H	1.52815	3.6467	-2.35586	H	-1.14877	0.97792	-0.75021	H	-1.98285	-2.53238	0.59288
C	1.5432	5.4772	-0.32781	C	0.16771	5.49979	0.57059	C	1.96701	5.30765	0.65112
H	1.062	5.94776	0.53191	H	1.02292	5.99845	1.03675	H	2.95005	5.48597	1.09822
H	2.57794	5.83531	-0.36234	H	-0.04019	6.00846	-0.37233	H	1.91645	5.8831	-0.27537
H	1.04494	5.83098	-1.23311	H	-0.69077	5.63311	1.23207	H	1.21565	5.69896	1.33995

Table 44:   Cartesian coordinates of theoretically obtained geometries of *cis*-**108**, *trans*-**108** and *cis*-**109** at the ωB97X-D/6-311+G(d,p) level of theory with implementation of implicit THF solvent effects (IEFPCM).

	cis-**108**			*trans*-**108**			*cis*-**109**
C	4.12883 -2.84709 -0.50835	C	1.40174 -4.08623 -1.298	C	2.96359 4.12868 0.17176
C	2.92052 -2.19251 -0.31213	C	1.18951 -2.73483 -1.06556	C	2.00977 3.12617 0.05567
C	2.86521 -0.83783 -0.00005	C	2.24231 -1.87972 -0.74581	C	2.36875 1.82745 -0.30393
C	4.03422 -0.10229 0.16552	C	3.53959 -2.36301 -0.61739	C	3.69365 1.49177 -0.5636
C	5.24111 -0.76517 -0.0283	C	3.74161 -3.71762 -0.84983	C	4.63892 2.50354 -0.44719
C	5.30109 -2.11971 -0.36976	C	2.69385 -4.57786 -1.19372	C	4.2896 3.81021 -0.08426
H	4.13808 -3.90313 -0.75255	H	0.56335 -4.72686 -1.54647	H	2.66509 5.13162 0.45494
H	4.01891 0.94308 0.44155	H	4.35911 -1.71178 -0.34159	H	3.97793 0.48452 -0.8433
H	6.16376 -0.20864 0.092	H	4.74515 -4.11857 -0.75859	H	5.67975 2.27106 -0.64331
H	6.2624 -2.59622 -0.51675	H	2.8957 -5.62701 -1.37179	H	5.05869 4.56843 -0.00405
C	1.55009 -2.71694 -0.34957	C	-0.05406 -1.95362 -1.05091	C	0.55265 3.16078 0.26632
O	1.2049 -3.82271 -0.69722	O	-1.16977 -2.31223 -1.35103	O	-0.10633 4.10571 0.63461
C	0.6823 -1.52784 0.00628	C	0.38951 -0.55646 -0.70089	C	0.09574 1.74418 -0.04153
N	1.52867 -0.42319 0.13793	N	1.77876 -0.56903 -0.56864	N	1.24456 1.02793 -0.34313
C	-0.68187 -1.528 -0.00633	C	-0.38963 0.55629 -0.70082	C	-1.15984 1.22046 -0.01012
C	-1.54937 -2.71731 0.34947	C	0.05393 1.95343 -1.05096	C	-2.47816 1.95209 0.10957
N	-1.52849 -0.42353 -0.13792	N	-1.77885 0.56896 -0.56824	N	-1.46343 -0.13437 -0.20327
C	-2.91992 -2.19319 0.31209	C	-1.18959 2.73471 -1.06536	C	-3.4946 0.89504 0.00067
C	-4.12808 -2.84805 0.50831	C	-1.40179 4.08612 -1.29776	C	-4.88027 0.96689 0.05893
C	-2.86493 -0.83848 0.00009	C	-2.24237 1.87966 -0.74536	C	-2.84178 -0.32374 -0.16512
C	-5.30051 -2.12093 0.36981	C	-2.69386 4.57783 -1.1932	C	-5.60619 -0.21055 -0.04628
H	-4.13709 -3.90411 0.75246	H	-0.56342 4.7267 -1.54641	H	-5.36831 1.92602 0.18937
C	-4.03411 -0.10319 -0.16539	C	-3.53959 2.36303 -0.61666	C	-3.55376 -1.51505 -0.26007
C	-5.24085 -0.76635 0.02842	C	-3.74159 3.71765 -0.84908	C	-4.93961 -1.43214 -0.20023
H	-6.26171 -2.59766 0.5168	H	-2.89568 5.62698 -1.37123	H	-6.68827 -0.1908 -0.00581
H	-4.01903 0.9422 -0.44136	H	-4.35909 1.71185 -0.34067	H	-3.04958 -2.46648 -0.375
H	-6.16362 -0.21002 -0.09181	H	-4.74509 4.11865 -0.75762	H	-5.52083 -2.34457 -0.27425
O	-1.20393 -3.82302 0.69705	O	1.16962 2.31199 -1.35121	O	-2.67668 3.14043 0.22908
C	-1.20701 0.76531 -0.85571	C	-2.52915 -0.3561 0.21896	C	-0.55506 -1.22753 -0.08889
C	-0.49041 0.70529 -2.04473	C	-2.17809 -0.59803 1.53898	C	-0.02574 -1.58288 1.14816
C	-1.63069 1.99558 -0.36367	C	-3.64315 -0.97976 -0.32721	C	-0.18967 -1.9576 -1.21503
C	-0.18041 1.87811 -2.72012	C	-2.93833 -1.47106 2.30664	C	0.8748 -2.6263 1.25911
H	-0.1676 -0.25299 -2.43445	H	-1.31165 -0.103 1.96333	H	-0.31203 -1.02182 2.03084
C	-1.3358 3.15554 -1.06021	C	-4.40718 -1.8308 0.45298	C	0.70338 -3.01151 -1.11742
H	-2.1548 2.04271 0.58307	H	-3.88089 -0.8127 -1.37036	H	-0.60517 -1.68865 -2.17979
C	-0.59399 3.12009 -2.24157	C	-4.06639 -2.09495 1.78061	C	1.2731 -3.36829 0.12456
H	0.38976 1.82228 -3.64161	H	-2.65495 -1.65858 3.33717	H	1.26827 -2.86625 2.23696
H	-1.66333 4.11034 -0.66203	H	-5.27392 -2.31747 0.01729	H	0.95853 -3.55712 -2.01514
C	1.20686 0.76546 0.85572	C	2.52915 0.35609 0.2184	H	1.25372 0.05771 -0.60717
C	0.49021 0.70532 2.0447	C	2.17836 0.59798 1.5385	N	2.17921 -4.38974 0.22518
C	1.63019 1.99595 0.36371	C	3.64294 0.97991 -0.32803	C	2.64194 -4.81894 1.53034
C	0.17984 1.87805 2.72009	C	2.93867 1.47109 2.30599	H	3.35292 -5.63309 1.40518
H	0.16764 -0.25305 2.4344	H	1.31208 0.10284 1.96304	H	3.15462 -4.00783 2.05751
C	1.33494 3.15582 1.06024	C	4.40704 1.83104 0.452	C	1.82014 -5.17641 2.1636
H	2.15432 2.04324 -0.58302	H	3.88045 0.81288 -1.37123	C	2.48132 -5.20397 -0.93554
C	0.59309 3.12015 2.24158	C	4.06652 2.09513 1.7797	H	3.23571 -5.94057 -0.66635
H	-0.39036 1.82204 3.64155	H	2.6555 1.65857 3.33659	H	1.59805 -5.73731 -1.3095
H	1.6622 4.11072 0.66208	H	5.27361 2.31782 0.01611	H	2.88717 -4.59703 -1.75105
C	0.21881 4.39349 2.95231	C	4.90613 3.02711 2.61344		
H	-0.04214 4.20543 3.9954	H	5.90394 2.61022 2.77892		
H	1.03735 5.11627 2.92749	H	5.03163 3.99286 2.1167		
H	-0.64657 4.86099 2.47169	H	4.45123 3.20609 3.58937		
C	-0.22011 4.39354 -2.95232	C	-4.90592 -3.02683 2.61453		
H	0.04078 4.20557 -3.99544	H	-5.90368 -2.60988 2.78012		
H	-1.03883 5.11612 -2.92739	H	-5.03153 -3.9926 2.11787		
H	0.6452 4.86125 -2.47178	H	-4.45089 -3.20577 3.59041		

Table 45: Cartesian coordinates of theoretically obtained geometries of *trans*-**109**, *cis*-**110** and *trans*-**110** at the ωB97X-D/6-311+G(d,p) level of theory with implementation of implicit THF solvent effects (IEFPCM).

	trans-**109**				*cis*-**110**				*trans*-**110**		
C	3.51835	-2.96428	-0.56046	C	3.36185	4.00868	-1.16722	C	0.25343	4.43453	-1.17439
C	3.0086	-1.6933	-0.32815	C	2.71422	2.84557	-0.76638	C	-0.03635	3.08203	-1.01847
C	3.81841	-0.66883	0.17229	C	1.36253	2.84707	-0.41381	C	-1.35794	2.63288	-0.90186
C	5.16179	-0.89032	0.45451	C	0.63108	4.03368	-0.41745	C	-2.42247	3.53192	-0.91253
C	5.65899	-2.16705	0.22078	C	1.28845	5.19699	-0.81895	C	-2.1206	4.88352	-1.07175
C	4.85644	-3.1997	-0.2792	C	2.63623	5.19532	-1.19937	C	-0.80156	5.34015	-1.20691
H	2.8759	-3.74464	-0.95234	H	4.41191	3.9706	-1.43377	H	1.28501	4.75633	-1.261
H	5.79469	-0.10109	0.84092	H	-0.40581	4.0638	-0.1125	H	-3.44488	3.19508	-0.80169
H	6.70337	-2.36706	0.43305	H	0.73446	6.12937	-0.83323	H	-2.9335	5.6013	-1.09108
H	5.28559	-4.1797	-0.44677	H	3.1097	6.11898	-1.51015	H	-0.60976	6.3989	-1.33388
C	1.66381	-1.14252	-0.54482	C	3.24367	1.47982	-0.59969	C	0.85479	1.91868	-0.90565
O	0.7018	-1.6815	-1.04431	O	4.34551	1.08151	-0.90965	O	2.06589	1.88202	-1.03406
C	1.76793	0.29357	-0.06825	C	2.057	0.67978	-0.09432	C	-0.08145	0.7468	-0.73647
N	3.07855	0.48813	0.31542	N	0.94842	1.5419	-0.05727	N	-1.39125	1.2338	-0.76284
C	0.84753	1.29287	-0.03123	C	2.05703	-0.67974	0.09429	C	0.26949	-0.57859	-0.78836
C	1.23584	2.70457	0.2588	C	3.24373	-1.47974	0.59964	C	-0.51929	-1.67697	-1.45453
N	-0.52001	1.26761	-0.31465	N	0.94848	-1.54189	0.05725	N	1.52935	-1.08917	-0.45901
C	0.0081	3.47318	0.09203	C	2.71432	-2.8455	0.76637	C	0.39417	-2.82892	-1.45796
C	-0.24737	4.83395	0.23531	C	3.36197	-4.00859	1.16724	C	0.21354	-4.12633	-1.92869
C	-1.01443	2.56873	-0.2108	C	1.36261	-2.84704	0.41381	C	1.58734	-2.44455	-0.83277
C	-1.54813	5.27954	0.07515	C	2.63637	-5.19524	1.19943	C	1.24435	-5.0442	-1.75836
H	0.56111	5.51561	0.47329	H	4.41203	-3.97049	1.43378	H	-0.71947	-4.39768	-2.40935
C	-2.3298	3.00498	-0.35213	C	0.6312	-4.03367	0.4175	C	2.61877	-3.36066	-0.6359
C	-2.57113	4.36395	-0.20927	C	1.28859	-5.19695	0.81903	C	2.42703	-4.65662	-1.11235
H	-1.78243	6.3321	0.17514	H	3.10987	-6.11889	1.51023	H	1.13727	-6.06009	-2.11946
H	-3.13334	2.31131	-0.56356	H	-0.4057	-4.06381	0.11256	H	3.53332	-3.07839	-0.13117
H	-3.58681	4.72709	-0.32018	H	0.73462	-6.12934	0.83335	H	3.21924	-5.38495	-0.9769
O	2.35764	3.09872	0.55178	O	4.34551	-1.0814	0.90957	O	-1.61883	-1.5859	-1.97147
C	-1.38634	0.14239	-0.16055	C	-0.19673	-1.35015	-0.78209	C	2.37481	-0.58401	0.59044
C	-1.46221	-0.52936	1.05162	C	-0.06066	-0.90472	-2.0972	C	1.88356	-0.50408	1.89344
C	-2.1995	-0.26101	-1.20879	C	-1.4715	-1.66805	-0.31643	C	3.68129	-0.2298	0.28708
C	-2.31754	-1.60577	1.21091	C	-1.16777	-0.7721	-2.92329	C	2.73982	-0.04593	2.88934
H	-0.83887	-0.21303	1.88119	H	0.92269	-0.66405	-2.48309	H	0.86616	-0.80041	2.11469
C	-3.07537	-1.32229	-1.05736	C	-2.58196	-1.56358	-1.14217	C	4.56088	0.22007	1.2936
H	-2.14028	0.25799	-2.15877	H	-1.59964	-1.98394	0.71161	H	3.97934	-0.25402	-0.74915
C	-3.14521	-2.03929	0.15465	C	-2.46525	-1.09707	-2.46957	C	4.05264	0.31251	2.60751
H	-2.34361	-2.10502	2.16958	H	-1.01189	-0.42648	-3.93537	H	2.38229	0.03094	3.91041
H	-3.69681	-1.60076	-1.89705	H	-3.54786	-1.82897	-0.73683	H	4.67679	0.67414	3.4122
H	3.41645	1.39707	0.59997	C	-0.19676	1.35012	0.78209	C	-2.52978	0.58213	-0.17768
N	-3.98261	-3.12254	0.29917	C	-0.06068	0.90468	2.09719	C	-2.55507	0.30793	1.18852
C	-4.17477	-3.70429	1.61201	C	-1.47155	1.66801	0.31644	C	-3.64955	0.2739	-0.94481
H	-4.85741	-4.54842	1.53058	C	-1.1678	0.77205	2.92328	C	-3.66881	-0.27306	1.77926
H	-3.2321	-4.08296	2.01835	H	0.92265	0.66397	2.48309	H	-1.69697	0.56118	1.80115
H	-4.59588	-2.98896	2.33208	C	-2.582	1.56355	1.14218	C	-4.77651	-0.28794	-0.36307
C	-4.95513	-3.41365	-0.73441	H	-1.59965	1.9839	-0.7116	H	-3.62605	0.45741	-2.01105
H	-5.51901	-4.30115	-0.45243	C	-2.46527	1.09704	2.46958	C	-4.81217	-0.59637	1.01519
H	-5.66516	-2.58919	-0.88866	H	-1.01191	0.42637	3.93534	H	-3.64785	-0.46369	2.84287
H	-4.46554	-3.62585	-1.6896	H	-3.5479	1.82897	0.73686	H	-5.62473	-0.5087	-0.99511
				N	-3.57725	-0.94871	-3.28739	N	-5.9176	-1.20078	1.59183
				N	-3.57725	0.94874	3.28743	N	5.87225	0.56216	0.99316
				C	-3.38888	0.70319	4.7083	C	-6.00179	-1.31388	3.03762
				H	-4.36368	0.58104	5.179	H	-6.91655	-1.8439	3.29997
				H	-2.82737	-0.22003	4.87637	H	-5.16259	-1.891	3.43777
				H	-2.85934	1.5216	5.21826	H	-6.01379	-0.3367	3.54286
				C	-4.84994	1.50871	2.86512	C	-7.14031	-1.34582	0.82065
				H	-5.17635	1.07106	1.9173	H	-7.87644	-1.8813	1.41902
				H	-5.60733	1.27077	3.61109	H	-7.57542	-0.38018	0.52308
				H	-4.8188	2.60178	2.74217	H	-6.96569	-1.93217	-0.08617
				C	-4.84984	-1.50908	-2.86523	C	6.67443	1.24188	1.99608
				H	-5.17653	-1.07154	-1.91746	H	6.76127	0.63746	2.90328
				H	-5.60719	-1.27136	-3.6113	H	7.68107	1.38729	1.6055
				H	-4.81835	-2.60213	-2.74229	H	6.26783	2.22487	2.27852
				C	-3.38888	-0.70306	-4.70823	C	6.25655	0.73261	-0.40102
				H	-4.36366	-0.58044	-5.17885	H	5.67456	1.51376	-0.90949
				H	-2.82701	0.21996	-4.87618	H	7.31147	1.00088	-0.44608
				H	-2.85971	-1.5216	-5.21838	H	6.13282	-0.20018	-0.95857

Table 46: Cartesian coordinates of theoretically obtained geometries of *cis*-**111**, *trans*-**111** and *cis*-**112** at the ωB97X-D/6-311+G(d,p) level of theory with implementation of implicit THF solvent effects (IEFPCM).

cis-**111**				*trans*-**111**				*cis*-**112**			
C	-4.52671	-1.56592	0.14879	C	-4.40608	0.93667	-0.51274	C	3.99112	-0.41447	-0.53391
C	-3.22087	-1.10643	0.04159	C	-3.22423	0.24108	-0.2927	C	2.89984	-1.15008	-0.98924
C	-2.94736	0.20161	-0.35592	C	-3.23624	-1.08962	0.1379	C	3.05564	-2.42406	-1.51779
C	-3.97002	1.08899	-0.66947	C	-4.43342	-1.76054	0.35797	C	4.34801	-2.9353	-1.56584
C	-5.27329	0.61706	-0.56394	C	-5.60936	-1.05293	0.13612	C	5.45119	-2.2095	-1.10317
C	-5.55973	-0.69197	-0.15931	C	-5.60811	0.27979	-0.29235	H	6.115	-0.35174	-0.21743
H	-4.72024	-2.58513	0.46312	H	-4.37647	1.96662	-0.8494	H	2.20863	-2.99852	-1.87173
H	-3.76263	2.10549	-0.98075	H	-4.45051	-2.79173	0.68816	H	4.50218	-3.92861	-1.97184
H	-6.09206	1.28691	-0.80175	H	-6.5575	-1.55256	0.3007	H	6.44047	-2.64674	-1.15548
H	-6.58994	-1.0181	-0.08841	H	-6.54814	0.79269	-0.45312	C	3.50068	0.88487	-0.04421
C	-1.94055	-1.7875	0.29802	C	-1.82349	0.65017	-0.45687	O	4.1412	1.75905	0.48654
O	-1.77986	-2.909	0.71811	O	-1.38431	1.69353	-0.88559	N	1.99921	0.83962	-0.30403
C	-0.88697	-0.7418	-0.03527	C	-1.027	-0.56952	-0.03507	N	1.73115	-0.42059	-0.80686
N	-1.57935	0.41008	-0.36598	N	-1.94033	-1.54866	0.2861	C	1.05855	1.78356	-0.03876
C	0.46793	-0.84758	0.0082	C	0.31355	-0.78436	-0.00923	C	1.2611	3.25218	0.2225
C	1.30518	-2.09952	0.09015	C	0.88693	-2.14562	0.18224	N	-0.32919	1.57079	-0.17571
N	1.34848	0.22682	-0.20525	N	1.36533	0.10486	-0.25753	C	-0.09894	3.81392	0.22676
C	2.68784	-1.62414	-0.07167	C	2.32382	-1.97627	-0.00491	C	-0.51871	5.12043	0.43796
C	3.88426	-2.32929	-0.06125	C	3.36672	-2.89559	0.05804	C	-1.01139	2.78508	0.0155
C	2.66594	-0.2398	-0.21745	C	2.5641	-0.61679	-0.22621	C	-1.88034	5.38206	0.44278
C	5.06854	-1.61973	-0.19247	C	4.66201	-2.43312	-0.09818	H	0.2128	5.90325	0.6017
H	3.87651	-3.40698	0.05502	H	3.15511	-3.94411	0.23296	C	-2.38012	3.02741	0.03993
C	3.84555	0.48818	-0.33178	C	3.86526	-0.13934	-0.36139	C	-2.79126	4.33866	0.25232
C	5.03756	-0.22648	-0.31994	C	4.89652	-1.0661	-0.2983	H	-2.24315	6.38999	0.60096
H	6.01946	-2.13797	-0.19065	H	5.49741	-3.12107	-0.05937	H	-3.10943	2.23912	-0.09332
H	3.84196	1.56677	-0.42403	H	4.06944	0.91328	-0.50795	H	-3.85365	4.55308	0.27096
H	5.97151	0.31658	-0.41127	H	5.91721	-0.71668	-0.40629	O	2.29795	3.86153	0.3518
O	0.94158	-3.2476	0.21327	O	0.25467	-3.16678	0.41903	C	-0.97388	0.32813	0.03115
C	1.05521	1.59421	0.07165	C	1.35511	1.50134	0.04168	C	-0.5903	-0.50538	1.07966
C	0.58082	1.96904	1.3261	C	0.94436	1.94278	1.2941	C	-1.99163	-0.06331	-0.82942
C	1.24986	2.54818	-0.92293	C	1.80303	2.40464	-0.91331	C	-1.22104	-1.72725	1.24665
C	0.28751	3.30228	1.57738	C	0.96734	3.30046	1.5835	H	0.20362	-0.19784	1.74848
H	0.43255	1.21362	2.0891	H	0.60125	1.22568	2.03131	C	-2.64053	-1.2748	-0.62199
C	0.97045	3.88407	-0.65821	C	1.84023	3.75978	-0.61218	H	-2.26229	0.57286	-1.66315
H	1.60952	2.2357	-1.89639	H	2.10159	2.04237	-1.88984	C	-2.2575	-2.11906	0.40762
C	0.48476	4.26105	0.58859	C	1.41832	4.21064	0.63357	H	0.87338	-0.6599	-1.27433
H	-0.09081	3.59372	2.54997	H	0.63939	3.64707	2.55663	H	-2.75429	-3.06833	0.55386
H	1.12333	4.62757	-1.43138	H	2.18748	4.46573	-1.35756	C	-0.73344	-2.66607	2.3166
H	0.25821	5.30137	0.78995	H	1.43886	5.26956	0.86331	C	-3.77935	-1.642	-1.53372
H	-1.15045	1.24775	-0.72023	H	-1.64927	-2.48961	0.51283	F	-4.85136	-0.86209	-1.31018
								F	-3.44848	-1.48245	-2.82546
								F	-4.17197	-2.91129	-1.37459
								F	-1.70692	-3.47209	2.76201
								F	-0.23817	-2.00955	3.37448
								F	0.24977	-3.45749	1.8512

Table 47:   Cartesian coordinates of theoretically obtained geometries of *trans*-**112**, *cis*-*R*$_a$-**113** and *cis*-*S*$_a$-**113** at the ωB97X-D/6-311+G(d,p) level of theory with implementation of implicit THF solvent effects (IEFPCM).

	trans-**112**		*cis*-*R*$_a$-**113**		*cis*-*S*$_a$-**113**
C	3.82758 -2.58807 -1.30037	C	-4.55812 -1.51207 -0.21075	C	-4.558 -1.51213 0.21034
C	3.35113 -1.35583 -0.87104	C	-3.25188 -1.06729 -0.05714	C	-3.25178 -1.06719 0.05708
C	4.21403 -0.38797 -0.3468	C	-2.97763 0.23347 0.36259	C	-2.97752 0.23348 -0.36287
C	5.57821 -0.62605 -0.2401	C	-4.00028 1.12944 0.64947	C	-4.00017 1.1292 -0.65046
C	6.04293 -1.86322 -0.67235	C	-5.30439 0.67286 0.49579	C	-5.30429 0.67245 -0.49726
C	5.18776 -2.8398 -1.19605	C	-5.59137 -0.62945 0.07079	C	-5.59126 -0.62975 -0.07193
H	3.14366 -3.32528 -1.70474	H	-4.75183 -2.5261 -0.54123	H	-4.75166 -2.52609 0.54106
H	6.25187 0.11945 0.16335	H	-3.79257 2.14082 0.97664	H	-3.7925 2.14053 -0.97782
H	7.1036 -2.0759 -0.59993	H	-6.12336 1.34987 0.71154	H	-6.12326 1.34927 -0.7136
H	5.59333 -3.78993 -1.52033	H	-6.62207 -0.9435 -0.03727	H	-6.62197 -0.9439 0.0358
C	1.99458 -0.79931 -0.86759	C	-1.97184 -1.75989 -0.27902	C	-1.97174 -1.75956 0.27971
O	0.97027 -1.28226 -1.29631	O	-1.80844 -2.88198 -0.69358	O	-1.80823 -2.88144 0.69474
C	2.15763 0.57908 -0.25178	C	-0.91622 -0.72263 0.08976	C	-0.9161 -0.72231 -0.08923
N	3.49629 0.74053 0.01204	N	-1.6084 0.42488 0.42628	N	-1.60826 0.42528 -0.42556
C	1.2401 1.55302 -0.02486	C	0.43726 -0.83643 0.06727	C	0.43736 -0.8362 -0.06723
C	1.63228 2.93752 0.34818	C	1.27646 -2.08092 -0.06419	C	1.27654 -2.08054 0.06475
N	-0.15061 1.52345 -0.20697	N	1.3243 0.23406 0.31631	N	1.32426 0.23424 -0.31748
C	0.38514 3.69732 0.33785	C	2.6624 -1.61025 0.0945	C	2.66243 -1.60998 -0.09458
C	0.1356 5.03808 0.61255	C	3.86087 -2.3113 0.05098	C	3.86093 -2.31104 -0.05095
C	-0.65339 2.81157 0.03865	C	2.64383 -0.23468 0.29323	C	2.64383 -0.23456 -0.29411
C	-1.17574 5.48144 0.59012	C	5.04341 -1.60236 0.20178	C	5.04341 -1.60218 -0.20242
H	0.95749 5.7054 0.84414	H	3.85656 -3.38399 -0.10426	H	3.85662 -3.38363 0.10495
C	-1.9765 3.2422 0.03599	C	3.81756 0.49447 0.43378	C	3.81752 0.49452 -0.43537
C	-2.21261 4.58277 0.31077	C	5.01166 -0.21522 0.38606	C	5.01162 -0.21512 -0.38749
H	-1.40589 6.51947 0.79506	H	5.99557 -2.11758 0.17334	H	5.99559 -2.11735 -0.17388
H	-2.79813 2.5679 -0.16727	H	3.80291 1.56821 0.57388	H	3.8028 1.56817 -0.57614
H	-3.23575 4.9409 0.30911	H	5.9453 0.32488 0.4953	H	5.94525 0.32489 -0.49729
O	2.76958 3.32379 0.57898	O	0.91343 -3.22473 -0.22186	O	0.91348 -3.22426 0.22313
C	-0.96935 0.37956 -0.02483	H	-1.17513 1.26856 0.7626	H	-1.1751 1.26786 -0.76478
C	-0.77976 -0.45392 1.07	C	1.04086 1.59395 0.11995	C	1.04092 1.59396 -0.1199
C	-1.98083 0.11609 -0.93572	C	0.9706 2.56176 1.07786	C	0.97074 2.56246 -1.07711
C	-1.59443 -1.56318 1.23272	S	0.8108 2.25614 -1.47612	S	0.81034 2.25486 1.47663
H	0.00908 -0.24049 1.7808	C	0.70827 3.85006 0.5335	C	0.70823 3.85033 -0.53185
C	-2.80823 -0.98165 -0.74149	H	1.09928 2.34744 2.13051	H	1.09971 2.34877 -2.12985
H	-2.10191 0.75537 -1.80112	C	0.59137 3.83118 -0.82313	C	0.59088 3.83038 0.82472
C	-2.61859 -1.83463 0.33507	H	0.60521 4.74748 1.12731	H	0.60536 4.74828 -1.12491
H	3.86952 1.61701 0.34948	H	0.37928 4.65858 -1.48348	H	0.37857 4.65725 1.48565
H	-3.25627 -2.69699 0.47262				
C	-1.32534 -2.50667 2.37209				
C	-3.9391 -1.21299 -1.70467				
F	-0.90275 -1.85961 3.46956				
F	-2.41362 -3.20959 2.7167				
F	-0.3683 -3.39637 2.05418				
F	-4.96657 -0.37846 -1.45784				
F	-3.56518 -0.99679 -2.97529				
F	-4.42221 -2.46019 -1.63577				

Table 48:   Cartesian coordinates of theoretically obtained geometries of *trans-R$_a$*-**113**, *trans-S$_a$*-**113** and *cis-R$_a$*-**114** at the ωB97X-D/6-311+G(d,p) level of theory with implementation of implicit THF solvent effects (IEFPCM).

trans-R$_a$-**113**				*trans-S$_a$*-**113**				*cis-R$_a$*-**114**			
C	-4.44905	0.98985	-0.24193	C	-4.4421	0.90523	-0.50029	C	-4.56642	-1.54255	0.11657
C	-3.26256	0.27492	-0.14253	C	-3.24561	0.22835	-0.30333	C	-3.25633	-1.08528	0.03902
C	-3.2645	-1.10674	0.06776	C	-3.22803	-1.09958	0.13303	C	-2.97544	0.22955	-0.34861
C	-4.45628	-1.81226	0.18535	C	-4.40862	-1.78784	0.38371	C	-3.99361	1.1196	-0.67869
C	-5.63737	-1.08544	0.08721	C	-5.60013	-1.09892	0.18532	C	-5.30459	0.64794	-0.60302
C	-5.64612	0.29859	-0.12266	C	-5.62876	0.23112	-0.24962	C	-5.59746	-0.66454	-0.20988
H	-4.42672	2.06065	-0.40887	H	-4.43569	1.9339	-0.84193	H	-4.762	-2.56392	0.42243
H	-4.46581	-2.88312	0.34639	H	-4.40237	-2.81742	0.71918	H	-3.78274	2.13899	-0.98112
H	-6.58173	-1.61077	0.17594	H	-6.53658	-1.61177	0.37411	H	-6.11793	1.31955	-0.85491
H	-6.58988	0.82475	-0.19341	H	-6.57982	0.72903	-0.39133	H	-6.62877	-0.99244	-0.1619
C	-1.8658	0.71645	-0.24437	C	-1.85559	0.65868	-0.49965	C	-1.97805	-1.77489	0.32243
O	-1.44528	1.82322	-0.49064	O	-1.44427	1.7084	-0.93666	O	-1.83044	-2.89646	0.74913
C	-1.05523	-0.5526	-0.02806	C	-1.02884	-0.55033	-0.09023	C	-0.91047	-0.727	0.00533
N	-1.96564	-1.57472	0.12924	N	-1.92158	-1.53913	0.25193	N	-1.59991	0.43274	-0.32852
C	0.28466	-0.77821	-0.00936	C	0.31429	-0.75067	-0.07741	C	0.45069	-0.84323	0.05388
C	0.84379	-2.1593	0.05239	C	0.90436	-2.09842	0.14992	C	1.26948	-2.11668	0.11499
N	1.36441	0.11325	-0.10042	N	1.36371	0.14385	-0.34641	N	1.35526	0.22378	-0.15823
C	2.2903	-1.99148	-0.02605	C	2.34189	-1.91959	-0.02985	C	2.66231	-1.66381	-0.07313
C	3.32223	-2.92519	-0.00678	C	3.39485	-2.82532	0.05961	C	3.84266	-2.3984	-0.09138
C	2.55457	-0.62185	-0.08229	C	2.57176	-0.56713	-0.28663	C	2.67289	-0.27317	-0.20616
C	4.62681	-2.46331	-0.04052	C	4.68489	-2.35091	-0.10624	C	5.04715	-1.71768	-0.24011
H	3.09532	-3.98392	0.03961	H	3.19561	-3.87139	0.26107	H	3.80242	-3.4762	0.01667
C	3.86151	-0.14494	-0.09768	C	3.86367	-0.07528	-0.43597	C	3.87232	0.42467	-0.3344
C	4.88184	-1.08576	-0.0795	C	4.90582	-0.98779	-0.34495	C	5.05088	-0.32158	-0.35336
H	5.45441	-3.16161	-0.02999	H	5.52787	-3.02805	-0.04647	H	5.98379	-2.26153	-0.26254
H	4.0764	0.91558	-0.11936	H	4.04831	0.97616	-0.615	H	3.89945	1.50378	-0.41011
H	5.90927	-0.74001	-0.09459	H	5.92288	-0.63113	-0.46218	H	5.99623	0.19976	-0.45643
O	0.19677	-3.19508	0.13918	O	0.28416	-3.12103	0.40993	O	0.88779	-3.25908	0.24259
H	-1.66682	-2.53528	0.23136	H	-1.61127	-2.47041	0.49371	H	-1.15737	1.27074	-0.66555
C	1.34748	1.48338	0.20932	C	1.34539	1.53039	-0.12589	C	1.08224	1.64547	0.09706
C	1.08461	2.05451	1.41528	C	1.66465	2.50238	-1.0193	C	1.36047	2.5882	-0.93057
S	1.70306	2.66988	-1.00393	S	1.02226	2.18853	1.4541	C	0.56889	2.05883	1.30145
C	1.15938	3.47405	1.36791	C	1.62935	3.80344	-0.4437	C	1.89225	2.18844	-2.18736
H	0.8356	1.47756	2.29595	H	1.89168	2.28971	-2.05487	C	1.10112	3.96349	-0.69711
C	1.49419	3.94197	0.13397	C	1.2863	3.78783	0.87263	C	0.30973	3.43141	1.535
H	0.982	4.11708	2.21902	H	1.83397	4.7121	-0.99306	H	0.3525	1.3323	2.09845
H	1.63907	4.96643	-0.17385	H	1.15792	4.62697	1.53944	C	2.15194	3.11947	-3.1622
								H	2.09026	1.11989	-2.35978
								C	1.37933	4.90615	-1.72437
								C	0.5692	4.36241	0.55997
								H	-0.10145	3.73817	2.50801
								C	1.89309	4.49192	-2.92875
								H	2.56337	2.81276	-4.13516
								H	1.17488	5.97017	-1.53328
								H	0.37103	5.43088	0.73276
								H	2.10951	5.21854	-3.72568

Table 49: Cartesian coordinates of theoretically obtained geometries of *cis-S$_a$-**114***, *trans-R$_a$-**114*** and *trans-S$_a$-**114*** at the ωB97X-D/6-311+G(d,p) level of theory with implementation of implicit THF solvent effects (IEFPCM).

	*cis-S$_a$-**114***			*trans-R$_a$-**114***			*trans-S$_a$-**114***	
C	-4.56642 -1.54255 0.11657	C	-4.43926 0.97856 -0.39589	C	-4.43926 0.97856 -0.39589
C	-3.25633 -1.08528 0.03902	C	-3.25125 0.27712 -0.21782	C	-3.25125 0.27712 -0.21782
C	-2.97544 0.22955 -0.34861	C	-3.25983 -1.08989 0.10688	C	-3.25983 -1.08989 0.10688
C	-3.99361 1.1196 -0.67869	C	-4.45773 -1.78413 0.25884	C	-4.45773 -1.78413 0.25884
C	-5.30459 0.64794 -0.60302	C	-5.64093 -1.06837 0.07835	C	-5.64093 -1.06837 0.07835
C	-5.59746 -0.66454 -0.20988	C	-5.64306 0.29637 -0.24353	C	-5.64306 0.29637 -0.24353
H	-4.762 -2.56392 0.42243	H	-4.4106 2.0321 -0.64966	H	-4.4106 2.0321 -0.64966
H	-3.78274 2.13899 -0.98112	H	-4.47302 -2.83862 0.50762	H	-4.47302 -2.83862 0.50762
H	-6.11793 1.31955 -0.85491	H	-6.5872 -1.58608 0.19086	H	-6.5872 -1.58608 0.19086
H	-6.62877 -0.99244 -0.1619	H	-6.58489 0.81486 -0.3755	H	-6.58489 0.81486 -0.3755
C	-1.97805 -1.77489 0.32243	C	-1.84855 0.71253 -0.32686	C	-1.84855 0.71253 -0.32686
O	-1.83044 -2.89646 0.74913	O	-1.41564 1.80229 -0.64553	O	-1.41564 1.80229 -0.64553
C	-0.91047 -0.727 0.00533	C	-1.04488 -0.5359 -0.0016	C	-1.04488 -0.5359 -0.0016
N	-1.59991 0.43274 -0.32852	N	-1.95782 -1.54607 0.23497	N	-1.95782 -1.54607 0.23497
C	0.45069 -0.84323 0.05388	C	0.30329 -0.77539 0.02308	C	0.30329 -0.77539 0.02308
C	1.26948 -2.11668 0.11499	C	0.84528 -2.16513 0.1441	C	0.84528 -2.16513 0.1441
N	1.35526 0.22378 -0.15823	N	1.38638 0.09601 -0.15307	N	1.38638 0.09601 -0.15307
C	2.66231 -1.66381 -0.07313	C	2.28932 -2.02421 -0.00671	C	2.28932 -2.02421 -0.00671
C	3.84266 -2.3984 -0.09138	C	3.31043 -2.97339 0.01787	C	3.31043 -2.97339 0.01787
C	2.67289 -0.27317 -0.20616	C	2.57152 -0.65534 -0.15316	C	2.57152 -0.65534 -0.15316
C	5.04715 -1.71768 -0.24011	C	4.62353 -2.53829 -0.10185	C	4.62353 -2.53829 -0.10185
H	3.80242 -3.4762 0.01667	H	3.06553 -4.02279 0.13428	H	3.06553 -4.02279 0.13428
C	3.87232 0.42467 -0.3344	C	3.88918 -0.20803 -0.25395	C	3.88918 -0.20803 -0.25395
C	5.05088 -0.32158 -0.35336	C	4.89825 -1.16754 -0.23017	C	4.89825 -1.16754 -0.23017
H	5.98379 -2.26153 -0.26254	H	5.43937 -3.25077 -0.09109	H	5.43937 -3.25077 -0.09109
H	3.89945 1.50378 -0.41011	H	4.12176 0.84464 -0.34505	H	4.12176 0.84464 -0.34505
H	5.99623 0.19976 -0.45643	H	5.92921 -0.84098 -0.31158	H	5.92921 -0.84098 -0.31158
O	0.88779 -3.25908 0.24259	O	0.1804 -3.18702 0.31355	O	0.1804 -3.18702 0.31355
H	-1.15737 1.27074 -0.66555	H	-1.64085 -2.4992 0.38208	H	-1.64085 -2.4992 0.38208
C	1.08224 1.64547 0.09706	C	1.40319 1.55156 0.05185	C	1.40319 1.55156 0.05185
C	0.85283 2.06574 1.43606	C	1.87793 2.38254 -0.99994	C	1.05653 2.06366 1.33239
C	1.04881 2.55228 -0.93325	C	0.97003 2.10157 1.23288	C	1.74623 2.40266 -0.96938
C	0.88144 1.14859 2.5224	C	2.33249 1.84031 -2.23343	C	0.69726 1.20573 2.40803
C	0.58855 3.4353 1.69613	C	1.89901 3.78916 -0.81511	C	1.06917 3.46667 1.54352
C	0.78516 3.91943 -0.67424	C	0.99075 3.5055 1.4179	C	1.75911 3.80314 -0.75919
H	1.22584 2.2306 -1.97011	H	0.60218 1.46174 2.04847	H	2.01492 2.00992 -1.96107
C	0.65625 1.58101 3.80571	C	2.7861 2.6654 -3.23245	C	0.36661 1.72656 3.63439
H	1.08719 0.08843 2.31155	H	2.31258 0.74843 -2.36814	H	0.69019 0.11904 2.23541
C	0.35907 3.85562 3.03477	C	2.37372 4.62007 -1.86654	C	0.72251 3.97881 2.82369
C	0.56024 4.35185 0.60918	C	1.44414 4.33059 0.41869	C	1.42869 4.32392 0.46733
H	0.76339 4.62688 -1.51623	H	0.63879 3.92251 2.37296	H	2.03718 4.4647 -1.59282
C	0.3924 2.94789 4.06482	C	2.80709 4.06914 -3.04753	C	0.37922 3.12684 3.84465
H	0.67776 0.87351 4.64771	H	3.13832 2.24839 -4.18746	H	0.08827 1.06502 4.46799
H	0.15483 4.91969 3.22579	H	2.38618 5.70946 -1.71315	H	0.73521 5.0682 2.97703
H	0.35454 5.41211 0.81964	H	1.46387 5.42244 0.55377	H	1.43591 5.41068 0.63959
H	0.21529 3.26965 5.10164	H	3.175 4.70905 -3.86304	H	0.11046 3.51967 4.83629

Table 50: Cartesian coordinates of theoretically obtained geometries of *cis*-**116** and *trans*-**116** at the ωB97X-D/6-311+G(d,p) level of theory with implementation of implicit THF solvent effects (IEFPCM).

	cis-**116**				*trans*-**116**		
C	-2.94808	-4.28085	-0.70363	C	-0.57952	4.3907	-0.99975
C	-2.38846	-3.04165	-0.42403	C	-0.73172	3.01679	-0.86218
C	-1.06981	-2.91393	0.00024	C	-1.99072	2.43527	-0.72506
C	-0.28069	-4.04222	0.19996	C	-3.13721	3.22076	-0.68941
C	-0.84874	-5.2804	-0.07905	C	-2.97493	4.59459	-0.82599
C	-2.16333	-5.41112	-0.53539	C	-1.71643	5.18344	-0.98685
H	-3.97845	-4.34509	-1.03374	H	0.41115	4.81746	-1.10541
H	0.73433	-3.98049	0.5665	H	-4.12176	2.79208	-0.55761
H	-0.2473	-6.17063	0.06593	H	-3.85577	5.2262	-0.80642
H	-2.56541	-6.39426	-0.74621	H	-1.63561	6.25784	-1.09531
C	-3.00488	-1.70848	-0.4638	C	0.27753	1.9552	-0.79177
O	-4.10937	-1.43651	-0.87746	O	1.47581	2.0489	-0.94957
C	-1.91036	-0.7766	-0.00801	C	-0.51744	0.69294	-0.61392
N	-0.76047	-1.55561	0.20912	N	-1.87432	1.03792	-0.61053
C	-1.97582	0.58584	-0.04858	C	-0.03582	-0.57733	-0.65992
C	-3.24365	1.39483	0.17648	C	-0.78221	-1.78223	-1.17582
N	-0.924	1.49153	-0.12887	N	1.28117	-0.9598	-0.42403
C	-2.80427	2.79274	0.09841	C	0.21655	-2.85196	-1.18773
C	-3.53959	3.96736	0.17369	C	0.09909	-4.18999	-1.54396
C	-1.42758	2.80519	-0.0986	C	1.41614	-2.32898	-0.70624
C	-2.86814	5.17278	0.03096	C	1.20922	-5.00756	-1.40232
H	-4.61133	3.92699	0.32997	H	-0.84539	-4.5717	-1.91415
C	-0.74475	4.00417	-0.26399	C	2.53095	-3.14324	-0.54104
C	-1.48817	5.17782	-0.19193	C	2.40392	-4.48015	-0.89957
H	-3.40835	6.10977	0.08469	H	1.15584	-6.05449	-1.67383
H	0.32045	4.03427	-0.44891	H	3.46123	-2.75663	-0.14645
H	-0.97579	6.12533	-0.31454	H	3.26159	-5.13315	-0.78355
O	-4.3427	0.98832	0.46836	O	-1.92863	-1.81238	-1.57587
C	0.36573	1.21303	-0.67024	C	2.16439	-0.32249	0.50464
C	0.51092	0.4646	-1.83166	C	1.7182	-0.01314	1.78277
C	1.502	1.70608	-0.03855	C	3.4664	-0.07078	0.108
C	1.76893	0.17205	-2.32926	C	2.61507	0.58596	2.65698
H	-0.3672	0.09044	-2.34578	H	0.70189	-0.23371	2.08303
C	2.7619	1.44318	-0.54011	C	4.39047	0.50303	1.00002
H	1.40094	2.27968	0.87544	H	3.73576	-0.29017	-0.91502
C	2.93404	0.63588	-1.68403	C	3.92479	0.84536	2.28585
H	1.83967	-0.42434	-3.2283	H	2.29057	0.8515	3.65695
H	3.61777	1.8407	-0.01284	H	4.58445	1.31703	3.00085
C	0.31266	-1.17354	1.04998	C	-2.89331	0.28116	0.02862
C	0.07745	-0.43185	2.20744	C	-2.68194	-0.24782	1.29863
C	1.60985	-1.55521	0.71204	C	-4.11644	0.10891	-0.61069
C	1.13801	-0.05581	3.01116	C	-3.68778	-0.96152	1.92575
H	-0.93272	-0.14513	2.47077	H	-1.73171	-0.09881	1.79544
C	2.67022	-1.19406	1.52067	C	-5.13342	-0.58633	0.01818
H	1.79056	-2.08364	-0.21445	H	-4.25494	0.49811	-1.61101
C	2.43846	-0.43519	2.66962	C	-4.91866	-1.1288	1.28728
H	0.9608	0.52706	3.90624	H	-3.52784	-1.37584	2.91313
H	3.68056	-1.469	1.24546	H	-6.08561	-0.72673	-0.47734
N	4.18554	0.30261	-2.14027	N	5.69675	0.72605	0.62365
C	5.35532	0.89929	-1.52779	C	6.54394	1.5482	1.465
H	5.40788	0.66073	-0.46076	H	6.66973	1.10078	2.45508
H	6.2492	0.49453	-1.99877	H	7.53129	1.61976	1.0119
H	5.37455	1.99193	-1.63633	H	6.14869	2.56522	1.5944
C	4.32791	-0.37766	-3.41169	C	6.06847	0.56553	-0.76818
H	5.38434	-0.55447	-3.60465	H	5.52778	1.25415	-1.43212
H	3.82675	-1.35095	-3.40014	H	7.13575	0.75261	-0.87452
H	3.9201	0.20782	-4.24623	H	5.88011	-0.45677	-1.10837
C	3.54167	-0.02551	3.4845	C	-5.96511	-1.86008	1.93692
N	4.43359	0.30858	4.13296	N	-6.80702	-2.44697	2.4601

Table 51:   Cartesian coordinates of theoretically obtained geometries of *cis*-**107** and *trans*-**107** at the ωB97X-D/6-311+G(d,p) level of theory in the gaseous phase.

	cis-**107**		*trans*-**107**
C	-4.54941 -1.77626 0.16801	C	-4.3807 1.11839 -0.4875
C	-3.24225 -1.331 0.05373	C	-3.27317 0.31127 -0.275
C	-2.95682 -0.03979 -0.38438	C	-3.41237 -1.01337 0.14972
C	-3.97102 0.84391 -0.73068	C	-4.66893 -1.5642 0.37137
C	-5.27915 0.38588 -0.61807	C	-5.77111 -0.74505 0.15669
C	-5.57599 -0.90564 -0.1743	C	-5.64117 0.58164 -0.26591
H	-4.7456 -2.78424 0.51512	H	-4.24608 2.14108 -0.82074
H	-3.75527 1.84948 -1.07242	H	-4.78638 -2.59035 0.69798
H	-6.09173 1.05383 -0.88198	H	-6.76303 -1.15088 0.32259
H	-6.60875 -1.22304 -0.09912	H	-6.52712 1.18464 -0.42182
C	-1.96539 -2.01683 0.34676	C	-1.83712 0.58709 -0.44326
O	-1.81797 -3.11651 0.81047	O	-1.30572 1.58799 -0.85994
C	-0.901 -0.98989 -0.02048	C	-1.16219 -0.70865 -0.03229
N	-1.58625 0.15774 -0.3937	N	-2.16745 -1.59609 0.29163
C	0.4498 -1.10877 0.02407	C	0.14766 -1.06398 -0.00745
C	1.27243 -2.36954 0.16153	C	0.57148 -2.47837 0.20805
N	1.34607 -0.05456 -0.24388	N	1.29112 -0.30084 -0.26213
C	2.66414 -1.914 -0.02854	C	2.0212 -2.4644 0.03378
C	3.84891 -2.63271 0.01066	C	2.96067 -3.48531 0.12162
C	2.65985 -0.53894 -0.23718	C	2.40442 -1.14188 -0.20772
C	5.04334 -1.94627 -0.15632	C	4.29851 -3.16402 -0.03088
H	3.82004 -3.70347 0.17683	H	2.63424 -4.50104 0.31257
C	3.84803 0.16704 -0.38604	C	3.7491 -0.80527 -0.33982
C	5.03125 -0.5618 -0.3453	C	4.67634 -1.83356 -0.25205
H	5.98701 -2.47745 -0.13386	H	5.05694 -3.93495 0.02758
H	3.85772 1.24123 -0.52163	H	4.05905 0.21945 -0.4996
H	5.97221 -0.03545 -0.46196	H	5.72922 -1.5953 -0.35612
O	0.89821 -3.50041 0.33962	O	-0.16641 -3.4207 0.45478
C	1.07008 1.32309 -0.02656	C	1.42315 1.10482 -0.05593
C	0.56838 1.7633 1.19572	C	1.10933 1.66405 1.1742
C	1.29409 2.24002 -1.04846	C	1.89995 1.90687 -1.08315
C	0.28313 3.10679 1.38124	C	1.25548 3.03023 1.36557
H	0.38634 1.04384 1.98577	H	0.73573 1.03159 1.97179
C	1.022 3.58711 -0.84392	C	2.06038 3.26749 -0.87496
H	1.66971 1.88756 -2.0024	H	2.11616 1.46142 -2.04694
C	0.50985 4.04208 0.36985	C	1.73659 3.85254 0.34911
H	-0.12017 3.43695 2.33291	H	0.99277 3.46395 2.32489
H	1.2003 4.29345 -1.64806	H	2.42393 3.89112 -1.68534
H	-1.14666 0.98209 -0.76252	H	-1.95806 -2.56201 0.50696
C	0.23011 5.50393 0.59741	C	1.92012 5.33172 0.56544
H	1.06321 5.97732 1.12597	H	2.96931 5.56817 0.76899
H	0.09187 6.03464 -0.34648	H	1.61975 5.8995 -0.31829
H	-0.66713 5.64608 1.20371	H	1.32927 5.68544 1.41253

Table 52: Cartesian coordinates of theoretically obtained geometries of *cis*-**107** and *trans*-**107** on the B3LYP/6-311+G(d,p) in the gaseous phase.

	cis-**107**			*trans*-**107**	
C	-4.57572 -1.82643 0.16029		C	-4.40174 1.08462 -0.5269	
C	-3.26515 -1.37492 0.06418		C	-3.28678 0.2899 -0.29032	
C	-2.99119 -0.04376 -0.24577		C	-3.42957 -1.01631 0.17959	
C	-3.99021 0.88402 -0.47268		C	-4.66502 -1.58023 0.43316	
C	-5.30973 0.42198 -0.37659		C	-5.78545 -0.7713 0.19633	
C	-5.60278 -0.90828 -0.06602		C	-5.66164 0.53773 -0.27458	
H	-4.78234 -2.86161 0.40355		H	-4.28595 2.09637 -0.89616	
H	-3.7751 1.9181 -0.71289		H	-4.77466 -2.59478 0.79635	
H	-6.12174 1.11847 -0.54781		H	-6.77222 -1.17731 0.38374	
H	-6.63546 -1.22642 0.00016		H	-6.55133 1.12987 -0.44711	
C	-1.98723 -2.08233 0.25203		C	-1.85219 0.55984 -0.47314	
O	-1.78845 -3.21907 0.58189		O	-1.30202 1.51785 -0.94459	
C	-0.90468 -0.9863 -0.02904		C	-1.15402 -0.75077 0.00849	
N	-1.58838 0.14223 -0.2805		N	-2.14627 -1.59486 0.33174	
C	0.48174 -1.09938 0.00558		C	0.19521 -1.09852 0.03917	
C	1.28676 -2.28697 0.04411		C	0.6764 -2.4382 0.15605	
N	1.37813 -0.00813 -0.11586		N	1.31958 -0.27109 -0.14726	
C	2.64394 -1.90663 -0.04266		C	2.06763 -2.43902 0.00596	
C	3.84846 -2.64493 -0.04767		C	3.05365 -3.45617 0.02062	
C	2.66732 -0.49068 -0.123		C	2.4387 -1.07019 -0.15059	
C	5.03578 -1.95428 -0.1197		C	4.36896 -3.08515 -0.10137	
H	3.84762 -3.72814 0.00987		H	2.78486 -4.50103 0.13088	
C	3.87797 0.2085 -0.18419		C	3.78847 -0.70327 -0.25077	
C	5.04242 -0.53922 -0.18403		C	4.72654 -1.71615 -0.22929	
H	5.97673 -2.48907 -0.12408		H	5.14883 -3.83577 -0.09439	
H	3.90235 1.28901 -0.23217		H	4.07902 0.33409 -0.34456	
H	5.99503 -0.02517 -0.23509		H	5.77612 -1.45976 -0.31197	
C	1.06513 1.39143 -0.00138		C	1.40113 1.1624 0.00644	
C	0.83855 1.96004 1.25365		C	1.17024 1.7394 1.25115	
C	1.01641 2.18526 -1.14883		C	1.77246 1.9491 -1.07986	
C	0.54854 3.31673 1.35122		C	1.29059 3.11813 1.39806	
H	0.88856 1.34239 2.14293		H	0.90876 1.11882 2.10098	
C	0.72988 3.54407 -1.03454		C	1.90426 3.32216 -0.91438	
H	1.20344 1.74008 -2.11946		H	1.93795 1.49132 -2.04772	
C	0.49243 4.13332 0.21332		C	1.65847 3.93241 0.32202	
H	0.37082 3.75064 2.32898		H	1.10902 3.5651 2.36914	
H	0.69626 4.15501 -1.9297		H	2.19244 3.93219 -1.76337	
H	-1.14985 1.0317 -0.48304		H	-1.9862 -2.54844 0.63085	
O	0.79893 -3.51206 0.10162		C	1.76771 5.42796 0.47888	
H	1.50899 -4.16656 0.06656		H	2.60892 5.82768 -0.09149	
C	0.2174 5.61008 0.3359		H	0.86175 5.9216 0.11224	
H	1.14088 6.15318 0.56166		H	1.89844 5.71237 1.52422	
H	-0.18658 6.02126 -0.59053		O	-0.16248 -3.47102 0.33762	
H	-0.48792 5.81964 1.14246		H	0.30303 -4.31549 0.28447	

Table 53: Cartesian coordinates of theoretically obtained geometries of *cis*-**107** and *trans*-**107** on the MPW1K/6-311G(d,p) level of theory in the gaseous phase.

	cis-**107**			*trans*-**107**	
C	-4.50326 -1.87205 0.14596		C	-4.36057 1.03909 -0.54976	
C	-3.20916 -1.4046 0.05699		C	-3.2517 0.25738 -0.30453	
C	-2.95036 -0.0813 -0.24669		C	-3.3836 -1.0305 0.18376	
C	-3.95143 0.8284 -0.47577		C	-4.60571 -1.59248 0.45002	
C	-5.25477 0.35111 -0.38794		C	-5.72087 -0.79695 0.20559	
C	-5.53247 -0.97308 -0.08339		C	-5.6074 0.49493 -0.28434	
H	-4.69591 -2.90531 0.38619		H	-4.24994 2.03977 -0.93547	
H	-3.74923 1.86056 -0.71162		H	-4.70945 -2.5964 0.82844	
H	-6.07122 1.03388 -0.56175		H	-6.70077 -1.20154 0.40303	
H	-6.55692 -1.30145 -0.02415		H	-6.49693 1.07635 -0.46177	
C	-1.92991 -2.08653 0.25308		C	-1.82758 0.52243 -0.49999	
O	-1.71384 -3.20392 0.58777		O	-1.28274 1.45249 -0.99686	
C	-0.8745 -0.98702 -0.0228		C	-1.1332 -0.76248 0.00345	
N	-1.56198 0.12105 -0.27358		N	-2.10782 -1.59688 0.33955	
C	0.50229 -1.08415 0.01295		C	0.20975 -1.08966 0.03985	
C	1.31324 -2.25061 0.05128		C	0.69611 -2.41043 0.16714	
N	1.37199 0.00878 -0.11576		N	1.31106 -0.25972 -0.16181	
C	2.65494 -1.84996 -0.04224		C	2.07806 -2.39518 0.00841	
C	3.86397 -2.56421 -0.04929		C	3.07053 -3.39402 0.02828	
C	2.65199 -0.44761 -0.12528		C	2.42502 -1.03623 -0.1601	
C	5.02796 -1.85828 -0.12537		C	4.36862 -3.0086 -0.09913	
H	3.88286 -3.64202 0.00991		H	2.81794 -4.43664 0.14676	
C	3.84235 0.27133 -0.18928		C	3.76218 -0.6508 -0.26311	
C	5.0078 -0.45104 -0.19085		C	4.70381 -1.64272 -0.23598	
H	5.97451 -2.37233 -0.13153		H	5.15599 -3.74376 -0.0888	
H	3.84455 1.34733 -0.2373		H	4.03457 0.38615 -0.36201	
H	5.94724 0.07645 -0.24383		H	5.74509 -1.37441 -0.32069	
C	1.03673 1.38608 0.00074		C	1.37289 1.15707 0.00246	
C	0.77507 1.93622 1.24552		C	1.1091 1.71674 1.23683	
C	0.98856 2.17805 -1.13506		C	1.75168 1.95046 -1.06287	
C	0.44875 3.27419 1.34423		C	1.20447 3.08616 1.39485	
H	0.82486 1.31597 2.12705		H	0.84092 1.08761 2.07201	
C	0.66707 3.51858 -1.01985		C	1.86033 3.31398 -0.8859	
H	1.20136 1.74291 -2.09949		H	1.94183 1.50271 -2.02542	
C	0.39237 4.08863 0.21755		C	1.58105 3.90647 0.34027	
H	0.24204 3.69666 2.31564		H	0.99702 3.5224 2.35992	
H	0.6332 4.13159 -1.90743		H	2.15602 3.93234 -1.71961	
H	-1.13468 1.0097 -0.46973		H	-1.94315 -2.53487 0.65921	
O	0.85515 -3.46811 0.11303		C	1.66462 5.38965 0.50826	
H	1.56554 -4.10557 0.07722		H	2.50923 5.80161 -0.03689	
C	0.07823 5.54435 0.34174		H	0.7643 5.86803 0.12551	
H	0.97972 6.10514 0.58399		H	1.76672 5.66589 1.55311	
H	-0.31917 5.94646 -0.58491		O	-0.11783 -3.43691 0.36038	
H	-0.64209 5.72846 1.13343		H	0.34693 -4.26966 0.3097	

Table 54:   Cartesian coordinates of theoretically obtained geometries of *cis*-**108** and *trans*-**108** at the ωB97X-D/6-311+G(d,p) level of theory in the gaseous phase.

	cis-**108**				*trans*-**108**		
C	4.12578	-2.84451	-0.50806	C	1.40174	-4.08623	-1.298
C	2.92016	-2.18857	-0.31564	C	1.18951	-2.73483	-1.06556
C	2.86665	-0.83231	-0.01477	C	2.24231	-1.87972	-0.74581
C	4.03611	-0.0969	0.14275	C	3.53959	-2.36301	-0.61739
C	5.24241	-0.76183	-0.04733	C	3.74161	-3.71762	-0.84983
C	5.29988	-2.11755	-0.37761	C	2.69385	-4.57786	-1.19372
H	4.12708	-3.90304	-0.74152	H	0.56335	-4.72686	-1.54647
H	4.0209	0.94968	0.41484	H	4.35911	-1.71178	-0.34159
H	6.16658	-0.20647	0.06907	H	4.74515	-4.11857	-0.75859
H	6.26039	-2.59701	-0.52138	H	2.8957	-5.62701	-1.37179
C	1.54587	-2.7176	-0.34918	C	-0.05406	-1.95362	-1.05091
O	1.19914	-3.81807	-0.69219	O	-1.16977	-2.31223	-1.35103
C	0.68013	-1.52263	0.00374	C	0.38951	-0.55646	-0.70089
N	1.52877	-0.41433	0.12249	N	1.77876	-0.56903	-0.56864
C	-0.68085	-1.52235	-0.0033	C	-0.38963	0.55629	-0.70082
C	-1.54711	-2.71688	0.34986	C	0.05393	1.95343	-1.05096
N	-1.52904	-0.41373	-0.12229	N	-1.77885	0.56896	-0.56824
C	-2.92121	-2.18739	0.31576	C	-1.18959	2.73471	-1.06536
C	-4.12713	-2.84287	0.50787	C	-1.40179	4.08612	-1.29776
C	-2.86711	-0.83119	0.01474	C	-2.24237	1.87966	-0.74536
C	-5.30092	-2.11549	0.377	C	-2.69386	4.57783	-1.1932
H	-4.12888	-3.90137	0.74147	H	-0.56342	4.7267	-1.54641
C	-4.03625	-0.09536	-0.1432	C	-3.53959	2.36303	-0.61666
C	-5.24286	-0.75982	0.04661	C	-3.74159	3.71765	-0.84908
H	-6.26165	-2.59458	0.52054	H	-2.89568	5.62698	-1.37123
H	-4.02056	0.95118	-0.41542	H	-4.35909	1.71185	-0.34067
H	-6.16678	-0.20413	-0.07013	H	-4.74509	4.11865	-0.75762
O	-1.20088	-3.81755	0.69273	O	1.16962	2.31199	-1.35121
C	-1.21017	0.76682	-0.85037	C	-2.52915	-0.3561	0.21896
C	-0.48897	0.69986	-2.03738	C	-2.17809	-0.59803	1.53898
C	-1.62962	2.00202	-0.36865	C	-3.64315	-0.97976	-0.32721
C	-0.17846	1.86604	-2.7208	C	-2.93833	-1.47106	2.30664
H	-0.15908	-0.26133	-2.41361	H	-1.31165	-0.103	1.96333
C	-1.33294	3.1571	-1.07365	C	-4.40718	-1.8308	0.45298
H	-2.14548	2.05592	0.58215	H	-3.88089	-0.8127	-1.37036
C	-0.59575	3.11227	-2.25558	C	-4.06639	-2.09495	1.78061
H	0.39613	1.80311	-3.63945	H	-2.65495	-1.65858	3.33717
H	-1.65307	4.11533	-0.67735	H	-5.27392	-2.31747	0.01729
C	1.21049	0.76644	0.85049	C	2.52915	0.35609	0.2184
C	0.48966	0.69988	2.03775	C	2.17836	0.59798	1.5385
C	1.63017	2.00142	0.36846	C	3.64294	0.97991	-0.32803
C	0.17976	1.86626	2.7211	C	2.93867	1.47109	2.30599
H	0.15959	-0.26114	2.41424	H	1.31208	0.10284	1.96304
C	1.3341	3.15671	1.07338	C	4.40704	1.83104	0.452
H	2.14574	2.05503	-0.58252	H	3.88045	0.81288	-1.37123
C	0.5973	3.1123	2.25556	C	4.06652	2.09513	1.7797
H	-0.39454	1.80365	3.63996	H	2.6555	1.65857	3.33659
H	1.65441	4.11478	0.67684	H	5.27361	2.31782	0.01611
C	0.27526	4.37055	3.01783	C	4.90613	3.02711	2.61344
H	-0.6867	4.28939	3.52868	H	5.90394	2.61022	2.77892
H	1.0367	4.57064	3.77818	H	5.03163	3.99286	2.1167
H	0.23649	5.23703	2.35394	H	4.45123	3.20609	3.58937
C	-0.27305	4.37031	-3.01791	C	-4.90592	-3.02683	2.61453
H	0.68909	4.28879	-3.52838	H	-5.90368	-2.60988	2.78012
H	-1.03413	4.57051	-3.77859	H	-5.03153	-3.9926	2.11787
H	-0.23426	5.23689	-2.35414	H	-4.45089	-3.20577	3.59041

314

Table 55: Cartesian coordinates of theoretically obtained geometries of *cis*-**108** and *trans*-**108** on the B3LYP/6-311+G(d,p) in the gaseous phase.

	cis-**108**		*trans*-**108**
C	-4.11568 -2.79992 0.69106	C	-1.52234 4.01346 -1.4757
C	-2.9157 -2.14782 0.43016	C	-1.26924 2.68393 -1.15048
C	-2.87881 -0.79394 0.08954	C	-2.30715 1.81543 -0.78943
C	-4.05925 -0.06422 -0.03793	C	-3.62355 2.26603 -0.71809
C	-5.25975 -0.72624 0.22236	C	-3.86557 3.59898 -1.04795
C	-5.29944 -2.07615 0.59151	C	-2.83514 4.46981 -1.42918
H	-4.10571 -3.85155 0.95356	H	-0.7006 4.66431 -1.75168
H	-4.05961 0.9743 -0.33798	H	-4.43008 1.60992 -0.41845
H	-6.1883 -0.17317 0.13257	H	-4.88393 3.96965 -1.00706
H	-6.25171 -2.55266 0.79096	H	-3.06628 5.49713 -1.68384
C	-1.54097 -2.67859 0.41667	C	-0.0015 1.94537 -1.0702
O	-1.18117 -3.78171 0.76327	O	1.11497 2.32648 -1.37257
C	-0.68589 -1.4896 0.01164	C	-0.40612 0.55243 -0.65557
N	-1.53876 -0.37974 -0.11693	N	-1.79805 0.53051 -0.51859
C	0.68551 -1.48976 -0.0116	C	0.40611 -0.55229 -0.65562
C	1.54035 -2.67897 -0.41642	C	0.00147 -1.94529 -1.06994
N	1.53858 -0.37998 0.11668	N	1.79811 -0.53021 -0.51909
C	2.91517 -2.1484 -0.43019	C	1.26924 -2.68379 -1.15048
C	4.11501 -2.80074 -0.69115	C	1.52234 -4.01333 -1.47565
C	2.87854 -0.79446 -0.08985	C	2.30719 -1.81517 -0.78986
C	5.29889 -2.07712 -0.59192	C	2.83518 -4.46957 -1.42949
H	4.10485 -3.85242 -0.95344	H	0.70055 -4.66427 -1.75131
C	4.0591 -0.06487 0.0373	C	3.62365 -2.26565 -0.71889
C	5.25946 -0.72712 -0.22305	C	3.86566 -3.59862 -1.04868
H	6.25106 -2.5538 -0.79143	H	3.06631 -5.4969 -1.68411
H	4.05964 0.97371 0.33714	H	4.43023 -1.60944 -0.4196
H	6.1881 -0.17417 -0.13351	H	4.88407 -3.96921 -1.00808
O	1.18039 -3.78215 -0.7627	O	-1.11506 -2.3265 -1.37203
C	1.25416 0.77052 0.91967	C	2.53782 0.39586 0.29093
C	0.61829 0.64235 2.15592	C	2.2366 0.53366 1.64452
C	1.65507 2.03476 0.486	C	3.59311 1.12089 -0.25746
C	0.39115 1.76768 2.94096	C	2.9846 1.39789 2.43901
H	0.30668 -0.33547 2.50191	H	1.42276 -0.03903 2.07403
C	1.4413 3.14902 1.28999	C	4.34678 1.96514 0.5494
H	2.10664 2.14478 -0.49183	H	3.79267 1.044 -1.3183
C	0.80562 3.0392 2.53056	C	4.05629 2.12194 1.90914
H	-0.10687 1.65046 3.89807	H	2.73686 1.50086 3.49048
H	1.75731 4.12468 0.93558	H	5.16133 2.53056 0.10862
C	-1.25403 0.77081 -0.91971	C	-2.5378 -0.39578 0.29109
C	-0.61795 0.64268 -2.15585	C	-2.2363 -0.53437 1.64451
C	-1.65478 2.03507 -0.48595	C	-3.59343 -1.12025 -0.25743
C	-0.39048 1.76807 -2.94072	C	-2.98435 -1.39885 2.43873
H	-0.30644 -0.33514 -2.50191	H	-1.42222 0.0379 2.07415
C	-1.44066 3.14939 -1.28976	C	-4.34712 -1.96472 0.54913
H	-2.10651 2.14506 0.49181	H	-3.79325 -1.04273 -1.31819
C	-0.80481 3.03961 -2.53025	C	-4.05633 -2.12233 1.90874
H	0.1077 1.65088 -3.89775	H	-2.73638 -1.50244 3.49009
H	-1.75655 4.12507 -0.93527	H	-5.16193 -2.52967 0.10826
C	-0.59451 4.24811 -3.40982	C	-4.88926 -3.03272 2.77828
H	0.32481 4.16213 -3.99382	H	-5.79924 -2.52682 3.11926
H	-1.4211 4.36601 -4.11909	H	-5.19942 -3.92791 2.2338
H	-0.53728 5.16587 -2.8202	H	-4.33815 -3.35061 3.66583
C	0.59567 4.24761 3.41033	C	4.88922 3.03193 2.7791
H	-0.32385 4.16197 3.99406	H	5.79722 2.52453 3.12311
H	1.42212 4.36498 4.11985	H	5.20266 3.9255 2.23387
H	0.53904 5.16552 2.82088	H	4.33674 3.35252 3.66483

Table 56:   Cartesian coordinates of theoretically obtained geometries of *cis*-**108** and *trans*-**108** on on the
              MPW1K/6-311G(d,p) level of theory in the gaseous phase.

	cis-**108**				*trans*-**108**		
C	-4.09623	-2.79741	0.59699	C	-1.4881	4.00877	-1.39013
C	-2.8986	-2.14862	0.37321	C	-1.24547	2.67756	-1.10852
C	-2.84716	-0.79978	0.06474	C	-2.27668	1.80819	-0.78003
C	-4.01283	-0.06603	-0.06987	C	-3.58245	2.25843	-0.69413
C	-5.21074	-0.72383	0.15211	C	-3.81439	3.59215	-0.97805
C	-5.26549	-2.07102	0.49104	C	-2.78868	4.46566	-1.32935
H	-4.0948	-3.84927	0.83628	H	-0.66631	4.66031	-1.64281
H	-4.00153	0.97347	-0.34844	H	-4.38691	1.59878	-0.41479
H	-6.13062	-0.16761	0.05514	H	-4.8259	3.96488	-0.92388
H	-6.21957	-2.54335	0.66045	H	-3.01533	5.49664	-1.54794
C	-1.5344	-2.67937	0.37513	C	0.00935	1.93443	-1.04818
O	-1.18673	-3.77554	0.70439	O	1.1154	2.3092	-1.33429
C	-0.67836	-1.49456	0.00794	C	-0.40285	0.5444	-0.67528
N	-1.51842	-0.38981	-0.10368	N	-1.78468	0.52501	-0.55306
C	0.67791	-1.49473	-0.00751	C	0.4029	-0.54437	-0.67528
C	1.53362	-2.67977	-0.37474	C	-0.00931	-1.93437	-1.04839
N	1.51828	-0.39025	0.10414	N	1.78466	-0.52515	-0.5526
C	2.89795	-2.14935	-0.37308	C	1.24546	-2.67759	-1.10846
C	4.09539	-2.79842	-0.59711	C	1.48808	-4.00879	-1.39009
C	2.84689	-0.80052	-0.06451	C	2.27664	-1.80832	-0.7796
C	5.26484	-2.07232	-0.49127	C	2.78862	-4.46578	-1.32898
H	4.09366	-3.85025	-0.83647	H	0.66632	-4.66026	-1.64306
C	4.01276	-0.06707	0.07	C	3.58237	-2.25866	-0.69335
C	5.21048	-0.72515	-0.15222	C	3.81429	-3.59238	-0.97732
H	6.21877	-2.54488	-0.66087	H	3.01526	-5.49676	-1.5476
H	4.00176	0.97241	0.34865	H	4.38678	-1.59908	-0.41372
H	6.13051	-0.16916	-0.05533	H	4.82575	-3.96519	-0.92288
O	1.18559	-3.77571	-0.70436	O	-1.11533	-2.30903	-1.33471
C	1.21858	0.76176	0.87018	C	2.51676	0.38937	0.25058
C	0.55047	0.65695	2.07872	C	2.20439	0.54038	1.58912
C	1.62698	2.00805	0.42403	C	3.5829	1.08605	-0.28672
C	0.29648	1.79057	2.82599	C	2.95025	1.39363	2.38007
H	0.2308	-0.31094	2.43079	H	1.3835	-0.01864	2.01104
C	1.38718	3.12979	1.19122	C	4.33469	1.91895	0.51644
H	2.10233	2.09669	-0.53949	H	3.79797	0.98863	-1.33808
C	0.71692	3.04421	2.40399	C	4.02817	2.0946	1.85954
H	-0.22954	1.69392	3.76434	H	2.69803	1.50387	3.42437
H	1.70873	4.09473	0.82814	H	5.165	2.45893	0.08614
C	-1.21837	0.76193	-0.87	C	-2.51676	-0.3894	0.25028
C	-0.55001	0.65668	-2.07836	C	-2.20458	-0.54001	1.58892
C	-1.62665	2.00841	-0.42427	C	-3.58269	-1.08641	-0.28699
C	-0.29565	1.79007	-2.82588	C	-2.95043	-1.39316	2.37998
H	-0.23042	-0.31135	-2.43011	H	-1.38385	0.01926	2.01083
C	-1.38649	3.12991	-1.19171	C	-4.33448	-1.91922	0.51628
H	-2.1022	2.09739	0.53911	H	-3.79759	-0.98932	-1.33842
C	-0.71596	3.04389	-2.4043	C	-4.02816	-2.09445	1.85946
H	0.23058	1.69307	-3.76407	H	-2.69836	-1.50307	3.42436
H	-1.70795	4.095	-0.82896	H	-5.16463	-2.45945	0.08599
C	-0.47673	4.26084	-3.24203	C	-4.8197	-3.03728	2.7105
H	0.41658	4.15341	-3.85122	H	-5.87251	-3.02519	2.4406
H	-1.31357	4.43697	-3.91717	H	-4.46285	-4.05938	2.58854
H	-0.36213	5.14923	-2.6265	H	-4.73742	-2.78413	3.76384
C	0.4781	4.26143	3.24145	C	4.81977	3.03751	2.71042
H	-0.41508	4.15431	3.85089	H	5.87287	3.02405	2.44166
H	1.31513	4.43759	3.91634	H	4.46412	4.05985	2.58698
H	0.36351	5.14966	2.62572	H	4.73611	2.78556	3.76394

11. References

[1]   M. Guentner, M. Schildhauer, S. Thumser, P. Mayer, D. Stephenson, P. J. Mayer, H. Dube, *Nat. Commun.* **2015**, *6*, 8406.
[2]   C. J. Davisson, L. H. Germer, *Proceedings of the National Academy of Sciences of the United States of America* **1928**, *14*, 317-322.
[3]   C. Davisson, L. H. Germer, *Phys. Rev.* **1927**, *30*, 705-740.
[4]   L. de Broglie, *Annales de Physique* **1925**, *10*, 22-128.
[5]   A. Einstein, *Ann. Phys. (Berl.)* **1905**, *322*, 132-148.
[6]   V. Balzani, P. Ceroni, A. Juris, *Photochemistry and Photophysics, Vol. 1*, Wiley-VCH, **2014**.
[7]   R. Steudel, I. Krossing, Y. Steudel, *Chemie der Nichtmetalle, Vol. 3*, Walter de Gruyter, **2008**.
[8]   M. Born, R. Oppenheimer, *Ann. Phys. (Berl.)* **1927**, *389*, 457-484.
[9]   E. Condon, *Phys. Rev.* **1926**, *28*, 1182-1201.
[10]   J. Franck, E. G. Dymond, *J. Chem. Soc. Faraday Trans.* **1926**, *21*, 536-542.
[11]   P. Klan, J. Wirz, *Photochemistry of organic compounds*, Wiley, **2009**.
[12]   G. Eber, F. Grüneis, S. Schneider, F. Dörr, *Chem. Phys. Lett.* **1974**, *29*, 397-404.
[13]   N. J. Turro, R. V., S. J.C., *Principles of molecular photochemistry*, University Science Books, Sausalito, California, **2009**.
[14]   C. R. J. Stephenson, T. P. Yoon, D. W. C. Macmillan, *Visible Light Photocatalysis in Organic Chemistry*, Wiley-VCH, **2018**.
[15]   A. Wohl, *Ber. Dtsch. Chem. Ges.* **1919**, *52*, 51-63.
[16]   A. Wohl, K. Jaschinowski, *Ber. Dtsch. Chem. Ges.* **1921**, *54*, 476-484.
[17]   K. Ziegler, A. Späth, E. Schaaf, W. Schumann, E. Winkelmann, *Liebigs Ann.* **1942**, *551*, 80-119.
[18]   K. Matyjaszewski, J. Xia, *Chem. Rev.* **2001**, *101*, 2921-2990.
[19]   G. Odian, *Principles of Polymerization*, Wiley, **2004**.
[20]   C. K. Prier, D. A. Rankic, D. W. C. MacMillan, *Chem. Rev.* **2013**, *113*, 5322-5363.
[21]   M. H. Shaw, J. Twilton, D. W. C. MacMillan, *J. Org. Chem.* **2016**, *81*, 6898-6926.
[22]   N. A. Romero, D. A. Nicewicz, *Chem. Rev.* **2016**, *116*, 10075-10166.
[23]   D. A. Nicewicz, D. W. C. MacMillan, *Science* **2008**, *322*, 77-80.
[24]   M. A. Ischay, M. E. Anzovino, J. Du, T. P. Yoon, *J. Am. Chem. Soc.* **2008**, *130*, 12886-12887.
[25]   J. M. R. Narayanam, J. W. Tucker, C. R. J. Stephenson, *J. Am. Chem. Soc.* **2009**, *131*, 8756-8757.
[26]   N. J. Turro, *Modern molecular photochemistry*, Benjamin/Cummings Publishing Company, Inc., **1978**.
[27]   B. L. Feringa, W. R. Browne, *Molecular Switches, Vol. 1*, Wiley-VCH, **2001**.
[28]   H. Dürr, H. Bouas-Laurent, *Photochromism: Molecules and Systems, Vol. 1*, Elsevier Science, **2003**.
[29]   R. A. Bissell, E. Córdova, A. E. Kaifer, J. F. Stoddart, *Nature* **1994**, *369*, 133-137.
[30]   M.-V. Martínez-Díaz, N. Spencer, J. F. Stoddart, *Angew. Chem. Int. Ed. Engl.* **1997**, *36*, 1904-1907.
[31]   J. D. Harris, M. J. Moran, I. Aprahamian, *Proc. Natl. Acad. Sci. U.S.A.* **2018**, *115*, 9414-9422.
[32]   L. Zelikovich, J. Libman, A. Shanzer, *Nature* **1995**, *374*, 790.
[33]   P. L. Anelli, N. Spencer, J. F. Stoddart, *J. Am. Chem. Soc.* **1991**, *113*, 5131-5133.
[34]   A. Dreos, Z. Wang, J. Udmark, A. Ström, P. Erhart, K. Börjesson, M. B. Nielsen, K. Moth-Poulsen, *Adv. Energy Mater.* **2018**, *8*, 1703401.
[35]   M. Mansø, A. U. Petersen, Z. Wang, P. Erhart, M. B. Nielsen, K. Moth-Poulsen, *Nat. Commun.* **2018**, *9*, 1945.
[36]   C. Philippopoulos, D. Economou, C. Economou, J. Marangozis, *Ind. Eng. Chem. Prod. Res. Dev.* **1983**, *22*, 627-633.
[37]   T. J. Kucharski, Y. Tian, S. Akbulatov, R. Boulatov, *Energy Environ. Sci.* **2011**, *4*, 4449-4472.
[38]   L. A. Huber, K. Hoffmann, S. Thumser, N. Böcher, P. Mayer, H. Dube, *Angew. Chem. Int. Ed.* **2017**, *56*, 14536-14539.
[39]   L. A. Huber, P. Mayer, H. Dube, *ChemPhotoChem* **2018**, *2*, 458-464.
[40]   K. Hüll, J. Morstein, D. Trauner, *Chem. Rev.* **2018**, *118*, 10710-10747.

[41]   M. Irie, *Chem. Rev.* **2000**, *100*, 1685-1716.
[42]   M. Irie, T. Fukaminato, K. Matsuda, S. Kobatake, *Chem. Rev.* **2014**, *114*, 12174-12277.
[43]   Y. Yokoyama, *Chem. Rev.* **2000**, *100*, 1717-1740.
[44]   H. Stobbe, *Ber. Dtsch. Chem. Ges.* **1905**, *38*, 3673-3682.
[45]   R. B. Woodward, R. Hoffmann, *J. Am. Chem. Soc.* **1965**, *87*, 395-397.
[46]   S. Kawata, Y. Kawata, *Chem. Rev.* **2000**, *100*, 1777-1788.
[47]   M. Fumio, T. Hitoshi, Y. Yasushi, S. Kazuhiro, K. Yukio, *Chem. Lett.* **1994**, *23*, 1869-1872.
[48]   M. Irie, M. Mohri, *J. Org. Chem.* **1988**, *53*, 803-808.
[49]   Y. Nakayama, K. Hayashi, M. Irie, *J. Org. Chem.* **1990**, *55*, 2592-2596.
[50]   P. J. Darcy, H. G. Heller, P. J. Strydom, J. Whittall, *J. Chem. Soc., Perkin Trans. 1* **1981**, *0*, 202-205.
[51]   K. Akira, T. Akihiko, I. Mitsuo, S. Hisao, M. Ryoka, *Bull. Chem. Soc. Jpn.* **1988**, *61*, 3569-3573.
[52]   T. Koshido, T. Kawai, K. Yoshino, *J. Phys. Chem.* **1995**, *99*, 6110-6114.
[53]   G. Berkovic, V. Krongauz, V. Weiss, *Chem. Rev.* **2000**, *100*, 1741-1754.
[54]   R. Klajn, *Chem. Soc. Rev.* **2014**, *43*, 148-184.
[55]   E. H. Baker, F. C. Tompkins, H. A. Fahim, A. M. Fleifel, F. Bergmann, A. Kalmus, E. Fischer, Y. Hirshberg, H. R. V. Arnstein, E. R. Ward, L. A. Day, R. S. Bradley, W. Tadros, M. Kamel, A. S. Bailey, D. H. Bates, H. R. Ing, M. A. Warne, E. Neale, L. T. D. Williams, H. B. Henbest, A. G. Sharpe, A. H. Lamberton, E. P. Hart, C. A. Bunton, E. A. Halevi, J. P. Thurston, J. Walker, R. A. Robinson, F. G. Mann, B. B. Smith, D. L. Hammick, A. M. Roe, S. Peat, W. J. Whelan, G. J. Thomas, *J. Chem. Soc. (Resumed)* **1952**, *0*, 4518-4548.
[56]   V. A. Krongauz, S. N. Fishman, E. S. Goldburt, *J. Phys. Chem.* **1978**, *82*, 2469-2474.
[57]   I. Cabrera, V. Krongauz, H. Ringsdorf, *Angew. Chem. Int. Ed. Engl.* **1987**, *26*, 1178-1180.
[58]   A. Dulic, C. Flytzanis, *Opt. Commun.* **1978**, *25*, 402-406.
[59]   A. Lennartson, A. Roffey, K. Moth-Poulsen, *Tetrahedron Lett.* **2015**, *56*, 1457-1465.
[60]   H. Goerner, C. Fischer, S. Gierisch, J. Daub, *J. Phys. Chem.* **1993**, *97*, 4110-4117.
[61]   A. U. Petersen, M. Jevric, J. Elm, S. T. Olsen, C. G. Tortzen, A. Kadziola, K. V. Mikkelsen, M. B. Nielsen, *Org. Biomol. Chem.* **2016**, *14*, 2403-2412.
[62]   S. L. Broman, M. Å. Petersen, C. G. Tortzen, A. Kadziola, K. Kilså, M. B. Nielsen, *J. Am. Chem. Soc.* **2010**, *132*, 9165-9174.
[63]   M. Å. Petersen, S. L. Broman, A. Kadziola, K. Kilså, M. B. Nielsen, *Eur. J. Org. Chem.* **2009**, *2009*, 2733-2736.
[64]   M. Cacciarini, A. B. Skov, M. Jevric, A. S. Hansen, J. Elm, H. G. Kjaergaard, K. V. Mikkelsen, M. Brøndsted Nielsen, *Chem. Eur. J.* **2015**, *21*, 7454-7461.
[65]   D. H. Waldeck, *Chem. Rev.* **1991**, *91*, 415-436.
[66]   H. M. D. Bandara, S. C. Burdette, *Chem. Soc. Rev.* **2012**, *41*, 1809-1825.
[67]   T. Nägele, R. Hoche, W. Zinth, J. Wachtveitl, *Chem. Phys. Lett.* **1997**, *272*, 489-495.
[68]   G. Zimmerman, L.-Y. Chow, U.-J. Paik, *J. Am. Chem. Soc.* **1958**, *80*, 3528-3531.
[69]   L. Greb, J.-M. Lehn, *J. Am. Chem. Soc.* **2014**, *136*, 13114-13117.
[70]   D. J. van Dijken, P. Kovaříček, S. P. Ihrig, S. Hecht, *J. Am. Chem. Soc.* **2015**, *137*, 14982-14991.
[71]   Q. Li, H. Qian, B. Shao, R. P. Hughes, I. Aprahamian, *J. Am. Chem. Soc.* **2018**, *140*, 11829-11835.
[72]   B. Shao, M. Baroncini, H. Qian, L. Bussotti, M. Di Donato, A. Credi, I. Aprahamian, *J. Am. Chem. Soc.* **2018**, *140*, 12323-12327.
[73]   C. Petermayer, H. Dube, *Acc. Chem. Res.* **2018**, *51*, 1153-1163.
[74]   Q.-Z. Yang, Z. Huang, T. J. Kucharski, D. Khvostichenko, J. Chen, R. Boulatov, *Nat. Nanotechnol.* **2009**, *4*, 302-306.
[75]   V. Caia, G. Cum, R. Gallo, V. Mancini, E. Pitoni, *Tetrahedron Lett.* **1983**, *24*, 3903-3904.
[76]   Z. Yu, S. Hecht, *Chem. Commun.* **2016**, *52*, 6639-6653.
[77]   A. A. Beharry, G. A. Woolley, *Chem. Soc. Rev.* **2011**, *40*, 4422-4437.
[78]   W. Feng, W. Luo, Y. Feng, *Nanoscale* **2012**, *4*, 6118-6134.
[79]   T. Muraoka, K. Kinbara, T. Aida, *Nature* **2006**, *440*, 512-515.
[80]   H. Murakami, A. Kawabuchi, K. Kotoo, M. Kunitake, N. Nakashima, *J. Am. Chem. Soc.* **1997**, *119*, 7605-7606.

[81] S. Wiedbrauk, H. Dube, *Tetrahedron Lett.* **2015**, *56*, 4266-4274.

[82] J. E. Zweig, T. R. Newhouse, *J. Am. Chem. Soc.* **2017**, *139*, 10956-10959.

[83] C. Petermayer, S. Thumser, F. Kink, P. Mayer, H. Dube, *J. Am. Chem. Soc.* **2017**, *139*, 15060-15067.

[84] A. R. Katritzky, Q.-L. Li, W.-Q. Fan, *J. Heterocycl. Chem.* **1988**, *25*, 1287-1292.

[85] C.-Y. Huang, A. Bonasera, L. Hristov, Y. Garmshausen, B. M. Schmidt, D. Jacquemin, S. Hecht, *J. Am. Chem. Soc.* **2017**, *139*, 15205-15211.

[86] D. Farka, M. Scharber, E. D. Głowacki, N. S. Sariciftci, *J. Phys. Chem. A* **2015**, *119*, 3563-3568.

[87] J. Weinstein, G. M. Wyman, *J. Am. Chem. Soc.* **1956**, *78*, 4007-4010.

[88] C. Giuliano, L. Hess, J. Margerum, *J. Am. Chem. Soc.* **1968**, *90*, 587-594.

[89] G. M. Wyman, A. F. Zenhäusern, *J. Org. Chem.* **1965**, *30*, 2348-2352.

[90] H. Görner, J. Pouliquen, J. Kossanyi, *Can. J. Chem.* **1987**, *65*, 708-717.

[91] B. Koeppe, F. Römpp, *Chem. Eur. J.* **2018**, *24*, 14382-14386.

[92] P. Friedländer, *Ber. Dtsch. Chem. Ges.* **1906**, *39*, 1060-1066.

[93] V. Izmail'ski, M. A. Mostoslavskii, *Ukr. Khim. Zh.* **1961**, *27*, 234-237.

[94] I. Kunihiro, S. Takahiro, T. Takashi, Y. Takeo, *Chem. Lett.* **1990**, *19*, 1645-1646.

[95] S. Takahiro, T. Takashi, Y. Takeo, I. Kunihiro, *Bull. Chem. Soc. Jpn.* **1992**, *65*, 657-663.

[96] Y. Takeo, S. Takahiro, T. Takashi, I. Kunihiro, *Bull. Chem. Soc. Jpn.* **1992**, *65*, 649-656.

[97] M. Benjamin, W. Sandra, O. Sven, S. Elena, N. Artur, M. Peter, d. V.-R. Regina, Z. Wolfgang, D. Henry, *Chem. Eur. J.* **2014**, *20*, 13984-13992.

[98] T. Cordes, T. Schadendorf, K. Rück-Braun, W. Zinth, *Chem. Phys. Lett.* **2008**, *455*, 197-201.

[99] T. Cordes, D. Weinrich, S. Kempa, K. Riesselmann, S. Herre, C. Hoppmann, K. Rück-Braun, W. Zinth, *Chem. Phys. Lett.* **2006**, *428*, 167-173.

[100] T. Cordes, T. Schadendorf, B. Priewisch, K. Rück-Braun, W. Zinth, *J. Phys. Chem. A* **2008**, *112*, 581-588.

[101] A. Nenov, T. Cordes, T. T. Herzog, W. Zinth, R. de Vivie-Riedle, *J. Phys. Chem. A* **2010**, *114*, 13016-13030.

[102] R. Wilcken, M. Schildhauer, F. Rott, L. A. Huber, M. Guentner, S. Thumser, K. Hoffmann, S. Oesterling, R. de Vivie-Riedle, E. Riedle, H. Dube, *J. Am. Chem. Soc.* **2018**, *140*, 5311-5318.

[103] F. F. Graupner, T. T. Herzog, F. Rott, S. Oesterling, R. de Vivie-Riedle, T. Cordes, W. Zinth, *Chem. Phys.* **2018**, *515*, 614-621.

[104] S. Wiedbrauk, B. Maerz, E. Samoylova, A. Reiner, F. Trommer, P. Mayer, W. Zinth, H. Dube, *J. Am. Chem. Soc.* **2016**, *138*, 12219-12227.

[105] S. Wiedbrauk, B. Maerz, E. Samoylova, P. Mayer, W. Zinth, H. Dube, *J. Phys. Chem. Lett.* **2017**, *8*, 1585-1592.

[106] Z. R. Grabowski, K. Rotkiewicz, W. Rettig, *Chem. Rev.* **2003**, *103*, 3899-4032.

[107] J.-S. Yang, K.-L. Liau, C.-M. Wang, C.-Y. Hwang, *J. Am. Chem. Soc.* **2004**, *126*, 12325-12335.

[108] J. F. Letard, R. Lapouyade, W. Rettig, *J. Am. Chem. Soc.* **1993**, *115*, 2441-2447.

[109] P. Mukherjee, S. Rafiq, P. Sen, *J. Photochem. Photobiol. A* **2016**, *328*, 136-147.

[110] D. W. Werst, W. F. Londo, J. L. Smith, P. F. Barbara, *Chem. Phys. Lett.* **1985**, *118*, 367-374.

[111] W. Fuß, C. Kosmidis, W. E. Schmid, S. A. Trushin, *Angew. Chem. Int. Ed.* **2004**, *43*, 4178-4182.

[112] A. Warshel, *Nature* **1976**, *260*, 679-683.

[113] I. Schapiro, O. Weingart, V. Buss, *J. Am. Chem. Soc.* **2009**, *131*, 16-17.

[114] R. S. Liu, A. E. Asato, *Proc. Natl. Acad. Sci. U.S.A.* **1985**, *82*, 259-263.

[115] J. Saltiel, T. S. R. Krishna, A. M. Turek, R. J. Clark, *Chem. Commun.* **2006**, *0*, 1506-1508.

[116] A. Gerwien, M. Schildhauer, S. Thumser, P. Mayer, H. Dube, *Nat. Commun.* **2018**, *9*, 2510.

[117] S. Wiedbrauk, T. Bartelmann, S. Thumser, P. Mayer, H. Dube, *Nat. Commun.* **2018**, *9*, 1456.

[118] M. Guentner, E. Uhl, P. Mayer, H. Dube, *Chem. Eur. J.* **2016**, *22*, 16433-16436.

[119] N. Regner, T. T. Herzog, K. Haiser, C. Hoppmann, M. Beyermann, J. Sauermann, M. Engelhard, T. Cordes, K. Rück-Braun, W. Zinth, *J. Phys. Chem. B* **2012**, *116*, 4181-4191.

[120] S. Herre, T. Schadendorf, I. Ivanov, C. Herrberger, W. Steinle, K. Rück-Braun, R. Preissner, H. Kuhn, *ChemBioChem* **2006**, *7*, 1089-1095.

[121] K. Tanaka, K. Kohayakawa, S. Iwata, T. Irie, *J. Org. Chem.* **2008**, *73*, 3768-3774.

[122] H. Dube, J. Rebek, *Angew. Chem. Int. Ed.* **2012**, *51*, 3207-3210.

[123] J. S. S. de Melo, R. Rondão, H. D. Burrows, M. J. Melo, S. Navaratnam, R. Edge, G. Voss, *ChemPhysChem* **2006**, *7*, 2303-2311.

[124] J. Pina, D. Sarmento, M. Accoto, P. L. Gentili, L. Vaccaro, A. Galvão, J. S. Seixas de Melo, *J. Phys. Chem. B* **2017**, *121*, 2308-2318.

[125] E. Wille, W. Lüttke, *Liebigs Ann. Chem.* **1980**, *1980*, 2039-2054.

[126] M. Klessinger, W. Lüttke, *Tetrahedron* **1963**, *19*, 315-335.

[127] W. Lüttke, M. Klessinger, *Chem. Ber.* **1964**, *97*, 2342-2357.

[128] W. R. Brode, E. G. Pearson, G. M. Wyman, *J. Am. Chem. Soc.* **1954**, *76*, 1034-1036.

[129] G. M. Wyman, W. R. Brode, *J. Am. Chem. Soc.* **1951**, *73*, 1487-1493.

[130] A. Baeyer, *Ber. Dtsch. Chem. Ges.* **1883**, *16*, 2188-2204.

[131] I. Iwakura, A. Yabushita, T. Kobayashi, *Chem. Phys. Lett.* **2010**, *484*, 354-357.

[132] T. Kobayashi, P. M. Rentzepis, *J. Chem. Phys.* **1979**, *70*, 886-892.

[133] M. Dittmann, F. F. Graupner, B. Maerz, S. Oesterling, R. de Vivie-Riedle, W. Zinth, M. Engelhard, W. Lüttke, *Angew. Chem. Int. Ed.* **2014**, *53*, 591-594.

[134] G. Cui, W. Thiel, *PCCP* **2012**, *14*, 12378-12384.

[135] M. Moreno, J. M. Ortiz-Sánchez, R. Gelabert, J. M. Lluch, *PCCP* **2013**, *15*, 20236-20246.

[136] S. Yamazaki, A. L. Sobolewski, W. Domcke, *PCCP* **2011**, *13*, 1618-1628.

[137] G. M. Wyman, *ChemComm* **1971**, *0*, 1332-1334.

[138] T. Elsaesser, W. Kaiser, W. Luettke, *J. Phys. Chem.* **1986**, *90*, 2901-2905.

[139] P. Friedländer, K. Kunz, *Ber. Dtsch. Chem. Ges.* **1922**, *55*, 1597-1607.

[140] Y. Matsumoto, H. Tanaka, *Heterocycles* **2003**, *60*, 1805-1810.

[141] S. Erbas-Cakmak, D. A. Leigh, C. T. McTernan, A. L. Nussbaumer, *Chem. Rev.* **2015**, *115*, 10081-10206.

[142] S. Kassem, T. van Leeuwen, A. S. Lubbe, M. R. Wilson, B. L. Feringa, D. A. Leigh, *Chem. Soc. Rev.* **2017**, *46*, 2592-2621.

[143] E. R. Kay, D. A. Leigh, F. Zerbetto, *Angew. Chem. Int. Ed.* **2007**, *46*, 72-191.

[144] R. P. Feynman, *Engl. Sci.* **1960**, *23*, 22-36.

[145] R. P. Feynman, R. B. Leighton, M. Sands, *The Feynman Lectures on Physics, Vol. 1*, Addison-Wesley, Reading, MA, **1963**.

[146] M. Smoluchowski, *Phys. Z.* **1912**, *13*, 1069-1080.

[147] T. R. Kelly, J. P. Sestelo, I. Tellitu, *J. Org. Chem.* **1998**, *63*, 3655-3665.

[148] N. Koumura, R. W. J. Zijlstra, R. A. van Delden, N. Harada, B. L. Feringa, *Nature* **1999**, *401*, 152.

[149] J. Conyard, K. Addison, I. A. Heisler, A. Cnossen, W. R. Browne, B. L. Feringa, S. R. Meech, *Nat. Chem.* **2012**, *4*, 547-551.

[150] J. Conyard, A. Cnossen, W. R. Browne, B. L. Feringa, S. R. Meech, *J. Am. Chem. Soc.* **2014**, *136*, 9692-9700.

[151] R. Augulis, M. Klok, B. L. Feringa, P. H. M. v. Loosdrecht, *Phys. Status Solidi C* **2009**, *6*, 181-184.

[152] N. Koumura, E. M. Geertsema, A. Meetsma, B. L. Feringa, *J. Am. Chem. Soc.* **2000**, *122*, 12005-12006.

[153] N. Koumura, E. M. Geertsema, M. B. van Gelder, A. Meetsma, B. L. Feringa, *J. Am. Chem. Soc.* **2002**, *124*, 5037-5051.

[154] M. K. J. ter Wiel, R. A. van Delden, A. Meetsma, B. L. Feringa, *J. Am. Chem. Soc.* **2003**, *125*, 15076-15086.

[155] M. Klok, N. Boyle, M. T. Pryce, A. Meetsma, W. R. Browne, B. L. Feringa, *J. Am. Chem. Soc.* **2008**, *130*, 10484-10485.

[156] E. M. Geertsema, N. Koumura, M. K. J. ter Wiel, A. Meetsma, B. L. Feringa, *Chem. Commun.* **2002**, 2962-2963.

[157] M. K. J. ter Wiel, R. A. van Delden, A. Meetsma, B. L. Feringa, *J. Am. Chem. Soc.* **2005**, *127*, 14208-14222.

[158] T. van Leeuwen, J. Pol, D. Roke, S. J. Wezenberg, B. L. Feringa, *Org. Lett.* **2017**, *19*, 1402-1405.

[159] R. A. van Delden, N. Koumura, A. Schoevaars, A. Meetsma, B. L. Feringa, *Org. Biomol. Chem.* **2003**, *1*, 33-35.

[160] A. Cnossen, L. Hou, M. M. Pollard, P. V. Wesenhagen, W. R. Browne, B. L. Feringa, *J. Am. Chem. Soc.* **2012**, *134*, 17613-17619.

[161] S. J. Wezenberg, K.-Y. Chen, B. L. Feringa, *Angew. Chem.* **2015**, *127*, 11619-11623.

[162] A. Faulkner, T. van Leeuwen, B. L. Feringa, S. J. Wezenberg, *J. Am. Chem. Soc.* **2016**, *138*, 13597-13603.

[163] D.-H. Qu, B. L. Feringa, *Angew. Chem.* **2010**, *122*, 1125-1128.

[164] N. Ruangsupapichat, M. M. Pollard, S. R. Harutyunyan, B. L. Feringa, *Nat. Chem.* **2010**, *3*, 53-60.

[165] S. J. Wezenberg, B. L. Feringa, *Nat. Commun.* **2018**, *9*, 1984.

[166] P. Štacko, J. C. M. Kistemaker, T. van Leeuwen, M.-C. Chang, E. Otten, B. L. Feringa, *Science* **2017**, *356*, 964-968.

[167] R. Eelkema, M. M. Pollard, N. Katsonis, J. Vicario, D. J. Broer, B. L. Feringa, *J. Am. Chem. Soc.* **2006**, *128*, 14397-14407.

[168] R. Eelkema, M. M. Pollard, J. Vicario, N. Katsonis, B. S. Ramon, C. W. M. Bastiaansen, D. J. Broer, B. L. Feringa, *Nature* **2006**, *440*, 163.

[169] J. T. Foy, Q. Li, A. Goujon, J.-R. Colard-Itté, G. Fuks, E. Moulin, O. Schiffmann, D. Dattler, D. P. Funeriu, N. Giuseppone, *Nat. Nanotechnol.* **2017**, *12*, 540-545.

[170] Q. Li, G. Fuks, E. Moulin, M. Maaloum, M. Rawiso, I. Kulic, J. T. Foy, N. Giuseppone, *Nat. Nanotechnol.* **2015**, *10*, 161-165.

[171] L. Greb, A. Eichhöfer, J.-M. Lehn, *Angew. Chem.* **2015**, *127*, 14553-14556.

[172] T. R. Kelly, X. Cai, F. Damkaci, S. B. Panicker, B. Tu, S. M. Bushell, I. Cornella, M. J. Piggott, R. Salives, M. Cavero, Y. Zhao, S. Jasmin, *J. Am. Chem. Soc.* **2007**, *129*, 376-386.

[173] T. R. Kelly, H. De Silva, R. A. Silva, *Nature* **1999**, *401*, 150.

[174] B. J. Dahl, B. P. Branchaud, *Tetrahedron Lett.* **2004**, *45*, 9599-9602.

[175] Y. Lin, B. J. Dahl, B. P. Branchaud, *Tetrahedron Lett.* **2005**, *46*, 8359-8362.

[176] G. Bringmann, A. J. Price Mortimer, P. A. Keller, M. J. Gresser, J. Garner, M. Breuning, *Angew. Chem. Int. Ed.* **2005**, *44*, 5384-5427.

[177] S. P. Fletcher, F. Dumur, M. M. Pollard, B. L. Feringa, *Science* **2005**, *310*, 80-82.

[178] C. O. Dietrich-Buchecker, J. P. Sauvage, J. P. Kintzinger, *Tetrahedron Lett.* **1983**, *24*, 5095-5098.

[179] A. Livoreil, C. O. Dietrich-Buchecker, J.-P. Sauvage, *J. Am. Chem. Soc.* **1994**, *116*, 9399-9400.

[180] D. J. Cárdenas, A. Livoreil, J.-P. Sauvage, *J. Am. Chem. Soc.* **1996**, *118*, 11980-11981.

[181] A. Livoreil, J.-P. Sauvage, N. Armaroli, V. Balzani, L. Flamigni, B. Ventura, *J. Am. Chem. Soc.* **1997**, *119*, 12114-12124.

[182] P. Reimann, *Phys. Rep.* **2002**, *361*, 57-265.

[183] M. N. Chatterjee, E. R. Kay, D. A. Leigh, *J. Am. Chem. Soc.* **2006**, *128*, 4058-4073.

[184] C. Cheng, P. R. McGonigal, W.-G. Liu, H. Li, N. A. Vermeulen, C. Ke, M. Frasconi, C. L. Stern, W. A. Goddard Iii, J. F. Stoddart, *J. Am. Chem. Soc.* **2014**, *136*, 14702-14705.

[185] H. Li, C. Cheng, P. R. McGonigal, A. C. Fahrenbach, M. Frasconi, W.-G. Liu, Z. Zhu, Y. Zhao, C. Ke, J. Lei, R. M. Young, S. M. Dyar, D. T. Co, Y.-W. Yang, Y. Y. Botros, W. A. Goddard, M. R. Wasielewski, R. D. Astumian, J. F. Stoddart, *J. Am. Chem. Soc.* **2013**, *135*, 18609-18620.

[186] M. Baroncini, S. Silvi, M. Venturi, A. Credi, *Angew. Chem.* **2012**, *124*, 4299-4302.

[187] G. Ragazzon, M. Baroncini, S. Silvi, M. Venturi, A. Credi, *Nat. Nanotechnol.* **2015**, *10*, 70-75.

[188] C. Cheng, P. R. McGonigal, S. T. Schneebeli, H. Li, N. A. Vermeulen, C. Ke, J. F. Stoddart, *Nat. Nanotechnol.* **2015**, *10*, 547-553.

[189] M. Alvarez-Pérez, S. M. Goldup, D. A. Leigh, A. M. Z. Slawin, *J. Am. Chem. Soc.* **2008**, *130*, 1836-1838.

[190] A. Carlone, S. M. Goldup, N. Lebrasseur, D. A. Leigh, A. Wilson, *J. Am. Chem. Soc.* **2012**, *134*, 8321-8323.

[191] V. Serreli, C.-F. Lee, E. R. Kay, D. A. Leigh, *Nature* **2007**, *445*, 523-527.

[192] J. V. Hernández, E. R. Kay, D. A. Leigh, *Science* **2004**, *306*, 1532-1537.

[193] M. R. Wilson, J. Solà, A. Carlone, S. M. Goldup, N. Lebrasseur, D. A. Leigh, *Nature* **2016**, *534*, 235.

[194] E. Ador, J. Crafts, *Ber. Dtsch. Chem. Ges.* **1877**, *10*, 2173-2176.

[195] M. T. Konieczny, W. Konieczny, *Heterocycles* **2004**, *65*, 451-464.

[196] G. Zheng, X. Ma, B. Liu, Y. Dong, M. Wang, *Adv. Synth. Catal.* **2014**, *356*, 743-748.

[197] K. H. Meyer, K. Schuster, *Ber. Dtsch. Chem. Ges.* **1922**, *55*, 819-823.

[198] L. Aurelio, R. Volpe, R. Halim, P. J. Scammells, B. L. Flynn, *Adv. Synth. Catal.* **2014**, *356*, 1974-1978.

[199] K. Sonogashira, Y. Tohda, N. Hagihara, *Tetrahedron Lett.* **1975**, *16*, 4467-4470.

[200] C. M. Sousa, J. Berthet, S. Delbaere, A. Polónia, P. J. Coelho, *J. Org. Chem.* **2017**, *82*, 12028-12037.

[201] H. Li, J. L. Petersen, K. K. Wang, *J. Org. Chem.* **2001**, *66*, 7804-7810.

[202] P. Lemmen, D. Lenoir, *Chem. Ber.* **1984**, *117*, 2300-2313.

[203] R. T. Hart, R. F. Tebbe, *J. Am. Chem. Soc.* **1950**, *72*, 3286-3287.

[204] D. Lenoir, P. Lemmen, *Chem. Ber.* **1980**, *113*, 3112-3119.

[205] K. Omura, D. Swern, *Tetrahedron* **1978**, *34*, 1651-1660.

[206] H. Meerwein, K. F. Zenner, R. Gipp, *Liebigs Ann.* **1965**, *688*, 67-77.

[207] R. Neidlein, B. Stackebrandt, *Liebigs Ann.* **1977**, *1977*, 914-923.

[208] D. Voßiek, master thesis, Ludwig-Maximilians Universität **2016**.

[209] T. Mahapatra, T. Das, S. Nanda, *Tetrahedron: Asymmetry* **2008**, *19*, 2497-2507.

[210] S. Thumser, master thesis, Ludwig-Maximilians Universität **2016**.

[211] E. J. Corey, P. L. Fuchs, *Tetrahedron Lett.* **1972**, *13*, 3769-3772.

[212] A. O. King, N. Okukado, E.-i. Negishi, *J. Chem. Soc., Chem. Commun.* **1977**, 683-684.

[213] M. Pompeo, R. D. J. Froese, N. Hadei, M. G. Organ, *Angew. Chem. Int. Ed.* **2012**, *51*, 11354-11357.

[214] S. Y. Liu, S. Katsumura, *Chin. Chem. Lett.* **2009**, *20*, 1204-1206.

[215] S. E. Denmark, K. L. Habermas, G. A. Hite, *Helv. Chim. Acta* **1988**, *71*, 168-194.

[216] I. N. Nazarov, I. B. Torgov, L. N. Terekhova, *Bull. Acad. Sci.* **1942**, 200.

[217] Y. Yamamoto, R. Suzuki, K. Hattori, H. Nishiyama, *Synlett* **2006**, *2006*, 1027-1030.

[218] P. Adam, *Compt. rend.* **1886**, *103*, 207.

[219] G. Rieveschl, F. E. Ray, *Chem. Rev.* **1938**, *23*, 287-389.

[220] M. Nakanishi, C. Bolm, *Adv. Synth. Catal.* **2007**, *349*, 861-864.

[221] I. Kim, C. Lee, *Angew. Chem. Int. Ed.* **2013**, *52*, 10023-10026.

[222] P. Y. S. Lam, C. G. Clark, S. Saubern, J. Adams, M. P. Winters, D. M. T. Chan, A. Combs, *Tetrahedron Lett.* **1998**, *39*, 2941-2944.

[223] M. J. Frisch, G. W. Trucks, H. B. Schlegel, G. E. Scuseria, M. A. Robb, J. R. Cheeseman, G. Scalmani, V. Barone, B. Mennucci, G. A. Petersson, H. Nakatsuji, M. Caricato, X. Li, H. P. Hratchian, A. F. Izmaylov, J. Bloino, G. Zheng, J. L. Sonnenberg, M. Hada, M. Ehara, K. Toyota, R. Fukuda, J. Hasegawa, M. Ishida, T. Nakajima, Y. Honda, O. Kitao, H. Nakai, T. Vreven, J. Montgomery, J. A., J. E. Peralta, F. Ogliaro, M. Bearpark, J. J. Heyd, E. Brothers, K. N. Kudin, V. N. Staroverov, R. Kobayashi, J. Normand, K. Raghavachari, A. Rendell, J. C. Burant, S. S. Iyengar, J. Tomasi, M. Cossi, N. Rega, J. M. Millam, M. Klene, J. E. Knox, J. B. Cross, V. Bakken, C. Adamo, J. Jaramillo, R. Gomperts, R. E. Stratmann, O. Yazyev, A. J. Austin, R. Cammi, C. Pomelli, J. W. Ochterski, R. L. Martin, K. Morokuma, V. G. Zakrzewski, G. A. Voth, P. Salvador, J. J. Dannenberg, S. Dapprich, A. D. Daniels, Ö. Farkas, J. B. Foresman, J. V. Ortiz, J. Cioslowski, D. J. Fox, Gaussian, Inc., Wallingford CT, **2009**.

[224] M. J. Frisch, G. W. Trucks, H. B. Schlegel, G. E. Scuseria, M. A. Robb, J. R. Cheeseman, G. Scalmani, V. Barone, G. A. Petersson, H. Nakatsuji, X. Li, M. Caricato, A. V. Marenich, J. Bloino, B. G. Janesko, R. Gomperts, B. Mennucci, H. P. Hratchian, J. V. Ortiz, A. F. Izmaylov, J. L. Sonnenberg, Williams, F. Ding, F. Lipparini, F. Egidi, J. Goings, B. Peng, A. Petrone, T. Henderson, D. Ranasinghe, V. G. Zakrzewski, J. Gao, N. Rega, G. Zheng, W. Liang, M. Hada, M. Ehara, K. Toyota, R. Fukuda, J. Hasegawa, M. Ishida, T. Nakajima, Y. Honda, O. Kitao, H. Nakai, T. Vreven, K. Throssell, J. A. Montgomery Jr., J. E. Peralta, F. Ogliaro, M. J. Bearpark, J. J. Heyd, E. N. Brothers, K. N. Kudin, V. N. Staroverov, T. A. Keith, R. Kobayashi, J. Normand, K. Raghavachari, A. P. Rendell, J. C. Burant, S. S. Iyengar, J. Tomasi, M. Cossi, J. M. Millam, M. Klene, C. Adamo, R. Cammi, J. W. Ochterski, R. L. Martin, K. Morokuma, O. Farkas, J. B. Foresman, D. J. Fox, Wallingford, CT, **2016**.

[225] M. Karplus, *J. Chem. Phys.* **1959**, *30*, 11-15.

[226] M. Karplus, *J. Am. Chem. Soc.* **1963**, *85*, 2870-2871.

[227] M. J. Minch, *Concepts Magn. Reson.* **1994**, *6*, 41-56.

[228] U. Megerle, R. Lechner, B. Konig, E. Riedle, *Photochem. Photobiol. Sci.* **2010**, *9*, 1400-1406.

[229] U. Megerle, I. Pugliesi, C. Schriever, C. F. Sailer, E. Riedle, *Appl. Phys. B: Lasers Opt.* **2009**, *96*, 215-231.

[230] E. Riedle, M. Beutter, S. Lochbrunner, J. Piel, S. Schenkl, S. Spörlein, W. Zinth, *Appl. Phys. B* **2000**, *71*, 457-465.

[231] E. Riedle, C. F. Sailer, *Pure Appl. Chem.* **2013**, *85*, 1487-1498.

[232] E. Riedle, M. Wenninger, in *Chemical Photocatalysis*, De Gruyter: Berlin/Bostom, **2013**, 319-375.

[233] J. Conyard, P. Stacko, J. Chen, S. McDonagh, C. R. Hall, S. P. Laptenok, W. R. Browne, B. L. Feringa, S. R. Meech, *J. Phys. Chem. A* **2017**, *121*, 2138-2150.

[234] S. Amirjalayer, A. Cnossen, W. R. Browne, B. L. Feringa, W. J. Buma, S. Woutersen, *J. Phys. Chem. A* **2016**, *120*, 8606-8612.

[235] X. Pang, X. Cui, D. Hu, C. Jiang, D. Zhao, Z. Lan, F. Li, *J. Phys. Chem. A* **2017**, *121*, 1240-1249.

[236] A. A. Kulago, E. M. Mes, M. Klok, A. Meetsma, A. M. Brouwer, B. L. Feringa, *J. Org. Chem.* **2010**, *75*, 666-679.

[237] P. Fita, E. Luzina, T. Dziembowska, C. Radzewicz, A. Grobowska, *J. Chem. Phys.* **2006**, *125*, 184508.

[238] M. Klok, W. R. Browne, B. L. Feringa, *PCCP* **2009**, *11*, 9124-9131.

[239] G. Marchand, J. Eng, I. Schapiro, A. Valentini, L. M. Frutos, E. Pieri, M. Olivucci, J. Léonard, E. Gindensperger, *J. Phys. Chem. Lett.* **2015**, *6*, 599-604.

[240] J. Seixas de Melo, R. Rondão, H. D. Burrows, M. J. Melo, S. Navaratnam, R. Edge, G. Voss, *J. Phys. Chem. A* **2006**, *110*, 13653-13661.

[241] W. Lüttke, H. Hermann, M. Klessinger, *Angew. Chem.* **1966**, *78*, 638-639.

[242] W. Lüttke, H. Hermann, M. Klessinger, *Angew. Chem. Int. Ed. Engl.* **1966**, *5*, 598-599.

[243] H. von Eller, *Bull. Soc. Chim. Fr.* **1955**, 1433.

[244] C. Würth, M. Grabolle, J. Pauli, M. Spieles, U. Resch-Genger, *Nat. Protoc.* **2013**, *8*, 1535.

[245] U. Resch-Genger, K. Rurack, *Pure Appl. Chem.* **2013**, *85*, 2005-2026.

[246] M. Grabolle, M. Spieles, V. Lesnyak, N. Gaponik, A. Eychmüller, U. Resch-Genger, *Anal. Chem.* **2009**, *81*, 6285-6294.

[247] F. Huck, master thesis, Ludwig-Maximilians-Universität **2017**.

[248] F. Baur, D. Beattie, D. Beer, D. Bentley, M. Bradley, I. Bruce, S. J. Charlton, B. Cuenoud, R. Ernst, R. A. Fairhurst, B. Faller, D. Farr, T. Keller, J. R. Fozard, J. Fullerton, S. Garman, J. Hatto, C. Hayden, H. He, C. Howes, D. Janus, Z. Jiang, C. Lewis, F. Loeuillet-Ritzler, H. Moser, J. Reilly, A. Steward, D. Sykes, L. Tedaldi, A. Trifilieff, M. Tweed, S. Watson, E. Wissler, D. Wyss, *J. Med. Chem.* **2010**, *53*, 3675-3684.

[249] G. Moncelsi, L. Escobar, H. Dube, P. Ballester, *Chem. Asian J.* **2018**, *13*, 1632-1639.